# Spin-crossover in metallomesogens of iron(II)

Dissertation

zur Erlangung des Grades

"Doktor der Naturwissenschaften"

am Fachbereich Chemie, Pharmazie und Geowissenschaften

der Johannes Gutenberg-Universität

in Mainz

## Maksym Seredyuk

geboren in Smela, Ukraine

Mainz 2008

Ich erkläre hiermit an Eides statt, dass ich diese Arbeit selbständig und ohne unerlaubte Hilfsmittel angefertigt habe.

Mainz, April 2008

1. Berichterstatter:

2. Berichterstatter:

3. Berichterstatter:

Tag der mündlichen Prüfung: 26. Mai 2008

*I am at a loss to give a distinct idea of the nature of this liquid, and cannot do so without many words.*

Edgar Allan Poe
"The Narrative of Arthur Gordon Pym of Nantucket"
(1837)

*Я вагаюся дати чітке визначення природи цієї рідини, тому мені не уникнути багатьох слів.*

Едґар Алан По
«Оповідь Артура Гордона Піма з Нантакета»
(1837)

# Table of Contents

## List of Abbreviations

| | |
|---|---|
| 1D | one-dimensional |
| 2D-WAXS | two-dimensional wide angle X-ray scattering |
| 4-R-trz | 4-substituted-1,2,4-triazole |
| 6-*Mepy* | 6-methyl-pyridin-2-yl |
| 10*Dq* | octahedral ligand-field splitting |
| *A* | percentage of population |
| A$^-$ | anion |
| C$_{18}$TOS$^-$ | 4-(octadecyloxy)benzenesulfonate anion |
| C$_n$ | alkyl substituent C$_n$H$_{2n+1}$ |
| C$_n$-6-*Mepy* | 6-methyl-5-(alkoxy)pyridin-2-yl |
| C$_n$-*py* | 5-(alkoxy)pyridin-2-yl |
| C$_n$-*tba* | 3,5-bis(alkoxy)-*N*-(4*H*-1,2,4-triazol-4-yl)benzamide |
| Col$_h$ | columnar hexagonal |
| Col$_L$ | columnar lamellar |
| Cr | crystalline phase |
| d | decomposition |
| *d* | interlayer distance |
| *d*$^{bl}$ | thickness of the ionic bilayer in the mononuclear metallomesogens |
| *d*$^{cc}$ | thickness of the coordination core in the one-dimensional metallomesogens |
| *d*$^{C-H}$ | radius of the methyl group |
| *d*$^{n=0}$ | interlayer distance extrapolated to $n = 0$ |
| DSC | Differential Scanning Calorimetry |
| ESI | Electrospray Ionization |
| EXAFS | Extended X-ray Absorption Fine Structure |
| FD | Field Desorption ionization |
| g | glass |
| h | hour(s) |
| HS | high-spin |
| Htrz | 1,2,4-4*H*-triazole |
| i | isotropization |
| *imd* | imidazole-3-yl |
| IR | infrared |
| LIESST | Light Induced Excited Spin State Trapping |
| LS | low-spin |
| *m/z* | mass-to-charge ratio |
| MALDI | Matrix Assisted Laser Desorption Ionization |
| Me | methyl group |
| MLCT | metal-to-ligand charge transfer |
| MS | Mass Spectroscopy |
| n | normal alkyl chain |
| *n* | number of carbon atoms in the alkyl chain C$_n$H$_{2n+1}$ |
| NH$_2$trz | 4-amino-1,2,4-triazole |
| N$^{im}$ | nitrogen atom of the N=C-group |
| N$^{imd}$ | nitrogen atom of the imidazole unit |
| NMR | Nuclear Magnetic Resonance |
| N$^{py}$ | nitrogen atom of the pyridine unit |
| POM | Polarizing Optical Microscopy |
| *p*-tol$^-$ | tosylate anion |
| *py* | pyridin-2-yl |

| | |
|---|---|
| R | substituent |
| s | number of water molecules per a complex molecule or a monomeric unit |
| $S_A$ | smectic A |
| $S_X$ | unknown (X) smectic phase |
| SCO | spin-crossover |
| SQUID | Superconducting Quantum Interference Device |
| $T$ | temperature (K) |
| $T_{1/2}$ | spin-transition temperature, at which $\gamma_{HS} = \gamma_{LS} = 0.5$ |
| $T_{1/2}^{LIESST}$ | critical temperature of relaxation of the high-spin metastable state |
| *tach* | *cis,cis*-1,3,5-cyclohexanetriamine |
| *tach*($C_{18}$-*py*)$_3$ | 1,3,5-*cis,cis*-tris[1-aza-2-((5-octadecyloxy)(2-pyridyl))vinyl]cyclohexane |
| *tach*(*imd*)$_3$ | 1,3,5-*cis,cis*-tris[1-aza-2-(imidazol-4-yl)vinyl]cyclohexane |
| *tach*(*py*)$_3$ | 1,3,5-*cis,cis*-tris[1-aza-2-(2-pyridyl)vinyl]cyclohexane |
| *tame* | 2,2,2-tris(aminomethyl)ethane |
| *tame*(6-*Mepy*)$_3$ | 2,2,2-tris{2-aza-3-[(6-methyl)(2-pyridyl)]prop-2-enyl}ethane |
| *tame*($C_{18}$-*py*)$_3$ | 2,2,2-tris(2-aza-3-((5-octadecyloxy)(2-pyridyl))prop-2-enyl)ethane |
| *tame*($C_n$-6-Me *py*)$_3$ | 2,2,2-tris(2-aza-3-((5-akloxy)(6-methyl)(2-pyridyl))prop-2-enyl)ethane |
| *tame*(*imd*)$_3$ | 2,2,2-tris[2-aza-3-(imidazol-4-yl)prop-2-enyl]ethane |
| *tame*(*py*)$_3$ | 2,2,2-tris[2-aza-3-(2-pyridyl)prop-2-enyl]ethane |
| *tba* | *N*-4*H*-1,2,4-triazol-4-ylbenzamide |
| TGA | thermogravimetric analysis |
| *tren* | tris(2-aminoethyl)amine |
| *tren*(6-*Mepy*)$_3$ | tris[3-aza-4-(6-methyl-2-pyridyl)but-3-enyl]amine |
| *tren*($C_n$-6-Me*py*)$_3$ | tris[3-aza-4-((5-alkoxy)(6-methyl)(2-pyridyl))but-3-enyl]amine |
| *tren*($C_n$-*py*)$_3$ | tris[3-aza-4-((5-alkoxy)(2-pyridyl))but-3-enyl]amine |
| *tren*(*py*)$_3$ | tris[3-aza-4-(2-pyridyl)but-3-enyl]amine |
| trz | 1,2,4-triazolato |
| UV/VIS | ultraviolet/visible |
| *vs* | versus |
| XANES | X-ray Absorption Near Edge Structure |
| XRD | X-Ray Diffraction |
| $\alpha$ | bite angle |
| $\Gamma$ | parameter of the cooperativity in the Slichter-Drickamer model |
| $\Gamma_{1/2}$ | half-width of the line |
| $\gamma_{HS}$ ($\gamma_{LS}$) | high-spin (low-spin) molar fraction ($0 \le \gamma \le 1$) |
| $\delta$ | isomeric shift (relative to $\alpha$-iron) |
| $\Delta E_Q$ | quadrupole splitting |
| $\Delta H^{n=0}$ | enthalpy change extrapolated to $n = 0$ |
| $\Delta H^{SCO}$ | enthalpy change due to the spin-transition |
| $\Delta S^{n=0}$ | entropy change extrapolated to $n = 0$ |
| $\Delta S^{SCO}$ | entropy change due to the spin-transition |
| $\Delta T_{80}$ | the smallest temperature range which covers 80 % of the spin-transition |
| $\Delta T_{hys}$ | width of the hysteresis loop |
| $\theta$ | twist angle between two opposite trigonal faces of the octahedron |
| $\Sigma$ | octahedron distortion expressed as a sum of *cis*-N–Fe–N angles |
| $\tau$ | tilt angle of the chains respectively to the normal of the ionic bilayer |
| $\chi_M$ | molar susceptibility |

# 1 Introduction

## 1.1 Introduction

Research on coordination compounds has shown a remarkable development in the past decades, particularly in view of functional materials, which provide new platforms for designing electron- or spin-related functions; such platforms have hardly been provided by conventional organic polymers or solid-state inorganic chemistry. In particular, the supramolecular approach afforded an amazing array of non-covalently assembled architectures through elegant control of intra- and intermolecular interactions [1, 2]. The hybrid metal-containing inorganic-organic compounds attracted great attention due to the wide variations in their structure and molecular interactions and their extraordinary ability to combine synergistically the ligand-centered and metal-centered properties. In the last decades, coordination chemists were focused among other on the phenomenon of molecular magnetism [3], reversible selective sorption [4-6], molecular recognition [1], electrical conductivity [7-10] to name a few aspects of particular interest.

Molecular bistability is defined as the property of a molecular system able to evolve from one stable state to another stable state in a reversible and detectable fashion when applying an appropriate and controllable perturbation [11]. The bistability of organic bistable molecules such as diarylethenes, stilbene, and diazonium is brought about by a structural isomerization. Presently, this effect was applied by scientists to investigate the possibility of designing and constructing motors and machines at the molecular level [12-15]. On the other hand, bistability in coordination compounds is based on two different stable electronic states, and hence, the different properties associated with them. Inorganic bistable molecules have advantages over their organic counterparts due to versatility in electronic structures and the possibility of addressing them with different physical perturbations including temperature, pressure, external fields or irradiation.

Among the coordination compounds, spin-crossover compounds are the most spectacular and representative examples of molecular bistability. Since the discovery in tris(dithiocarbamato) iron(III) complexes [16-18], spin-crossover, the transition of a complex between two states with different spin multiplicity, has evolved to fascinating field of research. It is now intensively pursued by chemists and physicists and is equally relevant for bioinorganic chemists and earth and materials scientists.

Theoretically, bistable molecules can demonstrate switchable functions through different external perturbations, where a single molecule plays the role of a switching device [19]. However, at the present time the attention of researchers is focused mostly on bulk solid state compounds. It is known that many properties of solid materials are intimately related to their structures, and changes in properties are often accompanied by structural transformations. As far as spin-crossover compounds are concerned, the possibility of target-oriented and property-directed synthesis of new materials is defined by creation of new types of ligands and exploration of new synthetic strategies. Advances in supramolecular chemistry played an important role in this endeavor. At the present time, systematic synthesis and detailed measurements of properties and structures appear to be the most common approach towards optimization of the spin-crossover properties in new materials [20-23]. However, recent efforts in spin-crossover research are guided to the construction of addressed molecular systems incorporating several switchable functions. As desired characteristics of molecular systems result frequently from the degree and nature of interaction of the constituting functional groups, the control of the spin-crossover properties by related functions should open a way to the rational design of a new generation of materials. The required function may involve such physical properties as sensitivity to external stimuli or merely a desired pattern of properties specifically adjusted to meet certain practical demands.
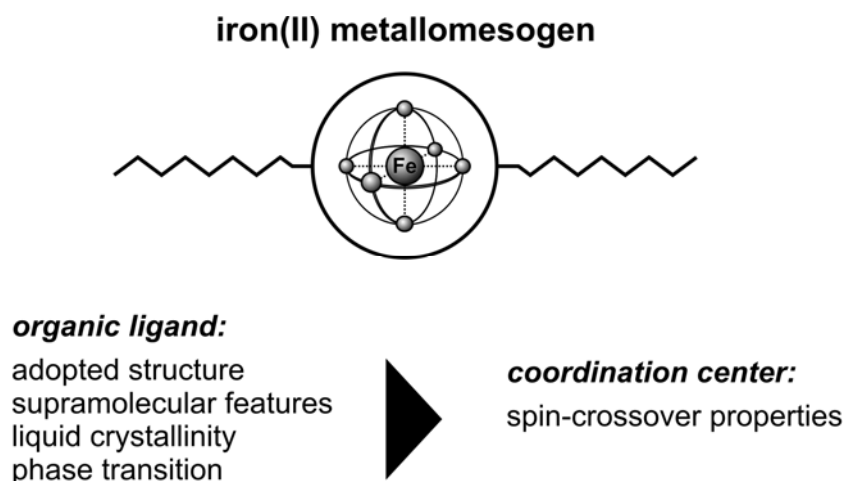


**Figure 1**. Relationship which postulates modification of the spin-crossover properties in iron(II) metallomesogens by the structural properties of the organic ligand.

The current stage of investigations includes among other interplay and synergic effects between spin-crossover and magnetic exchange [24-29], host-guest interactions [30-34], electrical conductivity [35-38]. Liquid crystalline materials in which a spin-crossover

center is incorporated into the mesogenic organic skeleton establish a separate class of compounds where the interplay is expected with structural transitions and liquid crystallinity (Figure 1). This may lead to a number of advantages in practical applications, for example, processing spin-crossover materials in the form of thin films, enhancement of spin-transition signals, switching and sensing in different temperature regimes, or achievement of photo- and thermochromism in metal-containing liquid crystals. The change of color is certainly a phenomenon which is of interest in the field of material sciences. The interest lies in the necessity for color in a number of applications such as passive blocking filters, laser addressed devices, polarizers based on dichroic effects, or the utility of thermochromism [39, 40].

The development of spin-crossover systems with liquid crystalline properties is particularly interesting because of the possibility of the alteration of the spin-crossover properties through the phase transition (Figure 1). The merging of spin-crossover and mesogenic properties is expected to allow the control of spin-crossover properties by the melting and liquid crystalline properties of the compound which in turn are defined by the structure of the mesogenic groups.

## 1.2 Motivation and objectives

It is known that spin-crossover compounds are greatly influenced by their structural properties. This, for instance, becomes obvious when significant changes in the magnetic response are observed when the same material exhibits the phenomenon of polymorphism. An approach to employ this dependence in a rational predictable way is the implementation of functional groups that can assist the transition between two phases with different magnetic or optical behaviors. Therefore, the primary goal of the present work is the synthesis of the low melting compounds of iron(II) with spin-crossover and mesogenic properties.

Depending on the initial properties of the complexes, two approaches can be anticipated. The first one focuses on mononuclear systems where the weak intermolecular contacts between separate spin-crossover complex molecules and anions are of primary importance for the defining the bulk properties of materials. The second concerns polymeric systems where covalent bonds are expected to play a decisive role in the manifestation of the desired response, and, for instance, can provide strong short-range interactions between spin-crossover centers, while the intermolecular contacts are less important. Domination of intermolecular or covalent interactions, in other words the dimensionality of the compound, can be controlled by appropriate selection of the ligands and substituents. If necessary, further tuning of the properties can be achieved by minor chemical modifications of the donor groups which influence the ligand field strength. Additionally, variation of the mesogenic substituents could allow subtle systematic variation of the melting temperature of the materials which would reveal the basic relationship between the structure and the related spin-crossover properties. To achieve sufficient control over the pertinent parameters of a system, an understanding of the structure-property relations is required. Since only limited data about this new type of functional materials are available in literature, new results from extensive systematic studies could expand the knowledge about spin-crossover metallomesogens and allow eventually a generalization of the observed facts in a consistent way.

The main objectives of the study can be summarized as follows:

1.    Synthesis of new mononuclear systems, where interactions between spin-crossover centers can be controlled by weak intermolecular contacts;

2.    Synthesis of polymeric systems, where interactions between spin-crossover centers can be controlled by strong short-range covalent bonds;

3.    Investigation of the crystal structures and spin-crossover properties of the parent complexes based on the tripodand and triazole ligands;

4.   Tuning of spin-crossover properties by variation of the counterions or chemical modification of the ligation groups;

5.   Selection of suitable complexes on the basis of the observed properties and comparative structural analysis for father grafting of the mesogenic groups;

6.   Analysis of crystal structure of the modified systems grafted with short alkyl chains and confirmation of the similar structure for the long-chain homologues using structural and spectroscopic methods;

7.   Investigation of the influence of the substituents, mesogenic groups and representative series of the counterions on the spin-crossover properties;

8.   Investigation of the mesogenic properties of the long-chain homologues;

9.   Investigation of the interplay between mesogenic and spin-crossover properties in the synthesized systems on the basis of magnetic, thermodynamical and variable-temperature structural data;

10.   Correlation of the observed dependence of the spin-crossover properties on the structural modification of the compounds due to the crystal $\rightarrow$ mesophase transition;

11.   Conclusions about the decisive operative factors governing the interplay of the spin-crossover and phase transitions by comparison with solid functional materials from adjacent research areas.

## 1.3 Spin-crossover phenomenon and LIESST effect

### 1.3.1 Background of spin-crossover phenomenon

For transition metal ions with $d^4$–$d^7$ electron configuration in the environment of octahedral symmetry the inequality $10Dq^{LS} > \pi > 10Dq^{HS}$ determines the ground state, where $\pi$ is the spin-pairing energy. It expresses the condition for finding the particular transition metal complex with either high-spin behavior (complexes with weak ligand fields $\pi > 10Dq^{HS}$) or low-spin behavior (complexes with strong ligand fields $\pi < 10Dq^{LS}$). Most chromium(II), manganese(II), manganese(III), iron(II), iron(III), cobalt(II) and cobalt(III) complexes can be classified in one of these families.

In the case of iron(II) complexes, weak ligands like $H_2O$, favor the high-spin $^5T_2$ state as ground state, whereas with increasing ligand field strength the low-spin $^1A_1$ state is quickly lowered in energy; consequently, from a critical ligand field strength $\Delta_C$ (where $\pi$ and $10Dq$ are of similar magnitude), onward, it becomes the ground state of the complex. This is the case for the iron(II) complex with six $CN^-$ ligands.
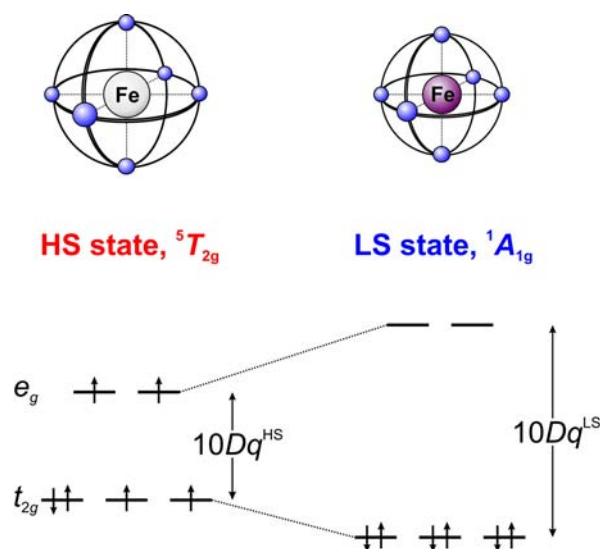


**Figure 2.** Modification of the coordination polyhedron (top) and distribution of the electrons over *d*-orbitals in high-spin (HS) and low-spin (LS) states (bottom) of iron(II) ion.
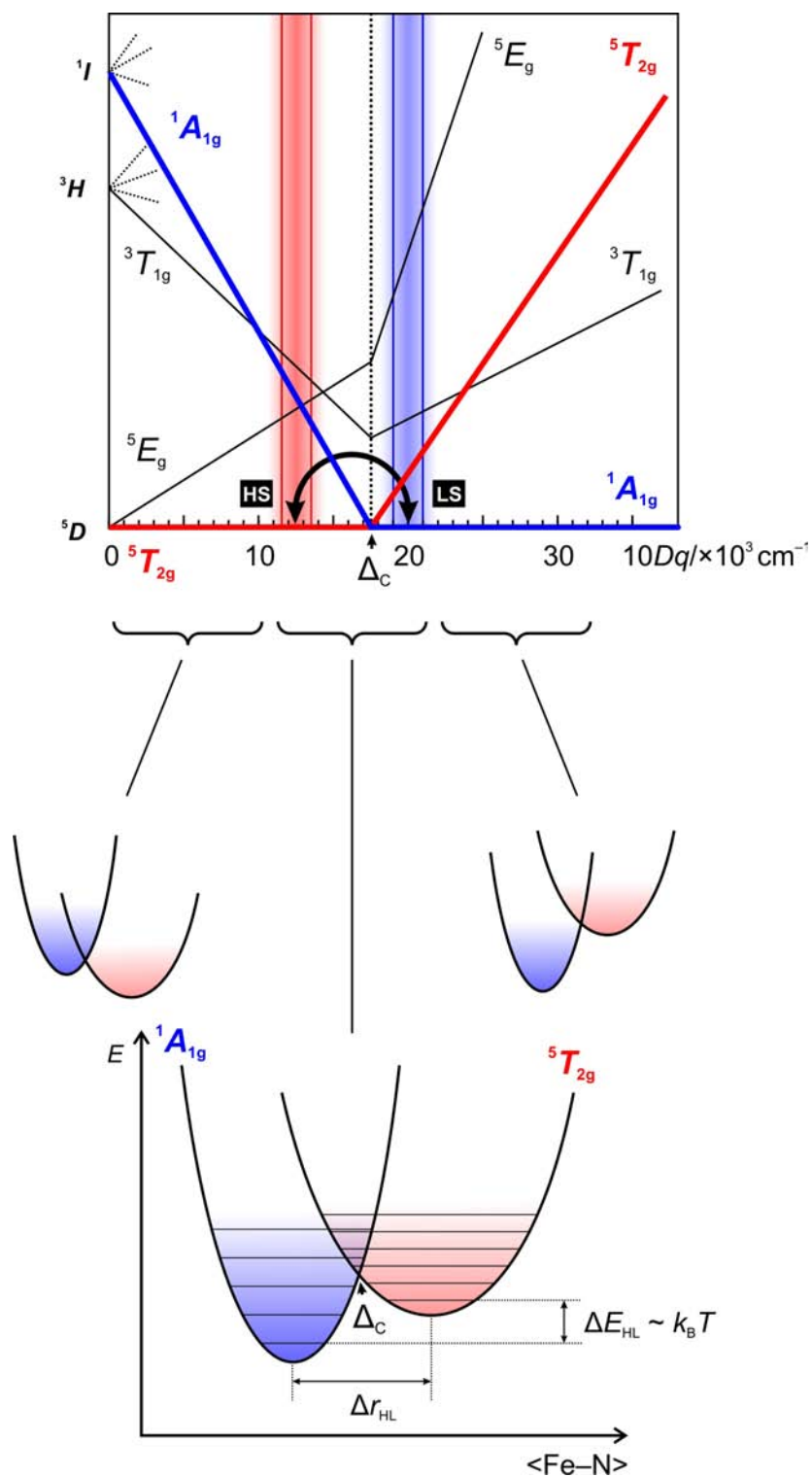
**Figure 3.** On the top a simplified Tanabe-Sugano diagram for an octahedral $d^6$-system is depicted. Colored areas show approximate ranges of the ligand field strength known for spin-crossover complexes in high-spin and low-spin states. The black arrow illustrates the transition between two states with the values of the ligand field strength related to $10Dq^{LS}/10Dq^{HS} \sim 1.75$. On the bottom, potential wells of the low-spin and high-spin species in complexes with different ligand field strength are schematized. The case of a spin-crossover complex is met under the condition $\Delta E_{HL} \sim k_B T$ ($k_B$ = Boltzmann constant).

Transition metal compounds which have ligand field strengths in the close proximity of the mean spin pairing energy can exhibit thermally induced spin-crossover. The phenomenon can be considered to be an intra-ionic electron transfer, where the electrons move between the $e_g$ and $t_{2g}$ orbitals. For iron(II) complexes with six $3d$ electrons in the valence shell of the metal center, thermal spin-transition is denoted, in the "strong field approach" of ligand field theory, as $(t_{2g})^6$, low-spin $\leftrightarrow$ $(t_{2g})^4(e_g)^2$, high-spin (Figure 2, bottom). Within the "weak field approach" of ligand field theory, preferentially used to interpret optical spectra, low-spin $\leftrightarrow$ high-spin transition in iron(II) complexes is denoted as $^1A_{1g}$ $(O_h)$, $S = 0 \leftrightarrow {}^5T_{2g}$ $(O_h)$, $S = 2$, where $^1A_{1g}$ and $^5T_{2g}$ refer to the Mulliken ligand field terms under $O_h$ symmetry, and $S$ to the total spin quantum number. The evolution of the energies of the terms with the increase of the ligand field strength is shown in the Tanabe-Sugano diagram (Figure 3, top).

In the high-spin state, the population of the $e_g$ orbitals with an antibonding character leads to elongation of the metal-to-ligand bond distances. On the other hand, a depopulation of the $t_{2g}$ orbitals affects the electron back-donation between the metal ion and the vacant $\pi^*$ orbitals of the ligands. Both $\sigma$ and $\pi$ factors contribute to the change of the metal–ligand bond length. The typical metal-to-ligand bond length change $\Delta r_{HL}$ is around 0.2, 0.15 and 0.10 Å for iron(II), iron(III) and cobalt(II), respectively [41]. Hence, a remarkable change of the coordination polyhedron (and molecular shape) takes place during the spin-state conversion (Figure 2, top).

The ligand field strength is not only determined by the properties of the ligand, but is also a strong function of the metal–ligand distance. For neutral ligands the approximation $10Dq \sim \mu/<\text{Fe–N}>^6$ holds, where $\mu$ is the dipole moment of the ligand and $<\text{Fe–N}>$ is the averaged metal–ligand distance. Averaged values for low-spin and high-spin complexes of iron(II) can be evaluated from the Cambridge Structural Data Base being *ca.* 1.97 and 2.17 Å, respectively (Figure 4). The experimentally determined range of the ligand field strength for the complexes which exhibit spin-crossover is *ca.* 19 000–21 000 cm$^{-1}$ in the low-spin state and 11 500–12 500 cm$^{-1}$ in the high-spin state (see Figure 3, top). If the $10Dq$ value is less than for the high-spin limit, then complex remains in the high-spin state down to the liquid helium temperature, if above, then the complex will be low-spin, at least up to 400 K. The data above 400 K is usually unavailable, which mainly due to the limited interest of the researchers in the high-temperature spin-crossover phenomenon on one hand and due to moderate thermal stability of the metal-organic compounds on the other hand. However, some

of the known low-spin complexes, supposedly, can show spin-crossover at higher temperatures.
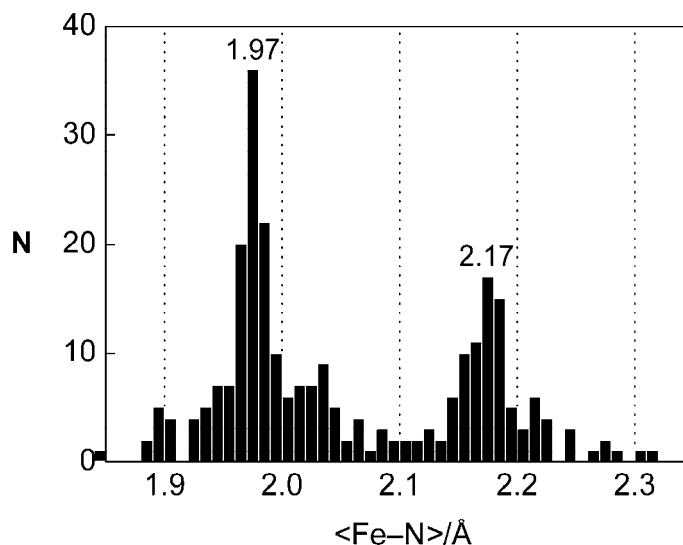


**Figure 4.** Histogram of <Fe–N> bond lengths in iron(II) complexes collected at the Cambridge Structural Data Base [42]. The peak at 1.97 Å refers to low-spin complexes, the peak at 2.17 Å to high-spin complexes.

The correlation between the cubic ligand field strength and the averaged metal–ligand bond distances is expresses as follows [21]:

$$\frac{10Dq^{\mathrm{LS}}}{10Dq^{\mathrm{HS}}} = \left(\frac{<\mathrm{Fe-N}>^{\mathrm{HS}}}{<\mathrm{Fe-N}>^{\mathrm{LS}}}\right)^6 \approx 1.75 \tag{1}$$

The metal-to-ligand bond change affects significantly the bond order and consequently the force constant of vibrations ($f$) and the low-frequency vibrational spectrum of the high-spin and low-spin forms [43]. An instructive and simple way to represent the spin-crossover centre is to consider the totally symmetric breathing mode $A_{1g}$ of the octahedron, as the most representative structural change, in a configurational coordinate diagram. The potential energy of the spin-crossover centre may be expressed as $E_{\mathrm{pi}} = 1/2[f_i<\mathrm{Fe-N}>_i^2]$, where i = HS, LS. If we consider typical <Fe–N> values for the Fe(II) complex (see Figure 4), the $E_{\mathrm{pi}}$ *vs* <Fe–N> plot gives the two parabolas represented in Figure 3, bottom. The horizontal displacement corresponds to $\Delta r_{\mathrm{HL}} \sim 0.2$ Å whereas the vertical displacement indicates that for an isolated spin-crossover molecule the low-spin state is stabilized with respect to the high-spin state by an energy $\Delta E_{\mathrm{HL}}$. The vibrational energy levels, $E_{\mathrm{vibr,i}}(n) = h\omega_i(n + 1/2)$, are represented by horizontal lines. Given that $\omega_i = \frac{1}{2}(\pi c)^{-1}(f_i/m^*)^{1/2}$ ($m^*$ is the reduced mass) and $f_{\mathrm{LS}} > f_{\mathrm{HS}}$, the density of vibrational levels per unit of energy is larger for the high-spin state than for the low-spin state (experimental value for $\omega_{\mathrm{HS}}$ is *ca.* 250 cm$^{-1}$, for

$\omega_{LS}$ is *ca.* 400 cm$^{-1}$ [44]). Similarly, the spin multiplicity of the high-spin state is larger than that of the low-spin state. At very low temperatures the spin-crossover centre is in the low-spin (n = 0) state. As the temperature increases, the spin-crossover centre transforms the thermal energy into vibrational energy, populating the excited vibrational levels up to the crossing point of the adiabatic potentials, $\Delta_c$, where the spread of vibrations Fe–N of the precursor (low-spin) overlaps with that of the successor (high-spin). At this point the low-spin $\rightarrow$ high-spin transition takes place. It is worth noting that this singular point corresponds to the crossing point $\Delta_c$ of the terms $^5T_{2g}$ and $^1A_{1g}$ in the Tanabe-Sugano diagram (Figure 3, top) and represents an unstable region where the transient species changes the spin-state. In summary, the energy cost to clear the enthalpy gap between the low-spin and high-spin states is compensated by the entropy difference between both states, which favors the population of the high-spin state at higher temperatures [21, 43].

The mechanism of the spin-crossover phenomenon at the molecular level can be understood in terms of an equilibrium fashion between the two electronic states, *i.e.*, Le Châtelier-Braun's principle [45]. Under external perturbations like temperature, pressure or irradiation a spin-crossover system responds in a way that partially neutralizes the imposed perturbation.

In order to discuss the stability of a given phase on thermodynamical grounds, one should examine the Gibbs energy consisting of both the entropy $S$ and the enthalpy $H$ terms: $\Delta G = \Delta H - T\Delta S$. The enthalpy change $\Delta H = H_{HS} - H_{LS}$ is typically 10 to 20 kJ mol$^{-1}$, and the entropy change $\Delta S = S_{HS} - S_{LS}$ is of the order of 50 to 80 J mol$^{-1}$ K$^{-1}$ [41]. The thermally induced spin-crossover is an entropy driven process, as was already mentioned; the degree of freedom is much higher in the high-spin state than in the low-spin state. According to recent data [46, 47], approximately 27 % of the total entropy gain during spin-transition in iron(II) complexes arises from the change in spin multiplicity

$$\Delta S_{el} = R \ln \left[ \frac{(2S+1)_{HS}}{(2S+1)_{LS}} \right] \tag{2}$$

Nearly 40 % is the contribution of the vibration-related entropy change mainly due to the metal-ligand skeletal vibrational modes [48]

$$\Delta S_{vib} = R \ln \left[ \frac{\prod (1 - \exp(-\omega_{LS}/RT))}{\prod (1 - \exp(-\omega_{HS}/RT))} \right] \tag{3}$$

The rest of 33 % in the entropy change is attributed to the change in the lattice vibrations perturbed by intermolecular interactions [46, 47].

While thermal spin-transitions in liquids are always gradual (obey a simple Boltzmann law), and spin-transition curves of that type do exist in solids as well, the $\gamma_{HS}(T)$ curves generally look very different because of long-range cooperative interactions. According to the shape of $\gamma_{HS}(T)$ curves, spin-transition in solids can be classified as gradual, abrupt with or without hysteresis and, finally, two-step transitions.

One should also mention, that despite by far most of the reported spin-crossover complexes are octahedral, it was recently reported the first tetrahedral $d^6$ spin-crossover complex of cobalt(III) [49, 50], whereas low-spin tetrahedral complexes have already been known for decades [51, 52].

### 1.3.2    Nomenclature

The term *spin-crossover* originates from the crossover of the energy *vs* field strength curves to reach the possible ground state terms for ions of particular $d^n$ configurations in the Tanabe-Sugano and related diagrams (Figure 3). The term *spin-transition* is used almost synonymously with *spin-crossover*, but the latter has the broader connotation, incorporating the associated effects and tending to refer to the actual physical event. Thus for a simple complete change in spin state, the spin-transition temperature $T_{1/2}$ is defined as the temperature at which the two states of different spin multiplicity are present in the ratio 1:1 ($\gamma_{HS} = \gamma_{LS} = 0.5$).

In liquid solution, spin-transition is a simple thermal equilibrium based on a Boltzmann-like distribution of the energy states. In these cases the term *spin-equilibrium* is most commonly used.

*Spin-change* or *spin-state change* is the result of change of the adopted spin state due to the external or internal factors, like ligand isomerization (Ligand-Driven Light-Induced Spin-Change, LD-LISC) [53-56], loss of the crystal solvent [57, 58] or an independent phase transition [59].

### 1.3.3    Physical response

Types of techniques used for characterization of spin-crossover materials can be separated into two main groups according to the type of the response. The first group of methods is used to probe electronic configurations of the spin-crossover center, *i.e.* UV/VIS, IR spectroscopy, Mössbauer spectroscopy, and magnetic methods. The second group belongs

to structural methods, which are used to characterize structural changes in the coordination shells surrounding the spin-crossover centers as well as lattice changes, for example, X-ray diffraction (XRD), X-ray single crystal analysis, EXAFS *etc*. The technical and theoretical backgrounds of the methods are reviewed in Chapter 6.5 and 6.6.

Perhaps the most impressive property of spin-crossover materials is the ability to display a bistability of macroscopic properties that might be used in memory devices [60], for "intelligent" contrast agents for biomedical imaging [61], temperature threshold indicators [60], or optical elements in display devices [60]. Besides thermal addressing, switching of spin-states by magnetic pulses [62, 63], light [64] or pressure [65] in the thermal hysteresis interval have been reported recently [66]. Concerning the reading process, for academic purposes the most convenient way to detect spin-transition is the magnetic method; however, for practical purposes the most suitable method is detecting the optical or dielectric responses. The reason for the observed dielectric response is a change of the local electrical dipoles and density of the material upon spin-crossover [65]. For most of the complexes, a higher value of $\varepsilon'$ (dielectric constant) in the high-spin state was found [65, 67-71].
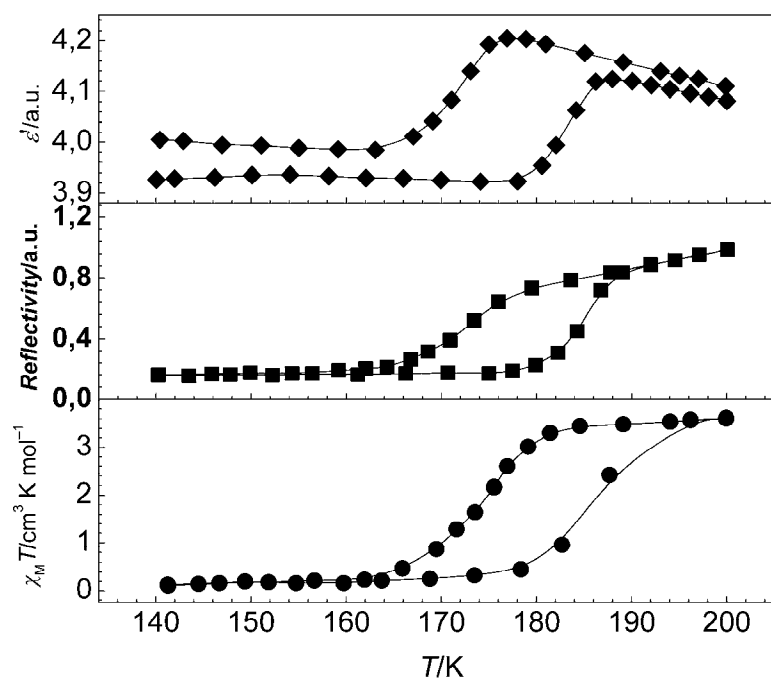


**Figure 5.** Thermal hysteresis loop for dielectric, optical, and magnetic properties in the same spin-crossover complex [Fe(DAPP)(abpt)]$(ClO_4)_2$. Adopted from [68].

As an example of bistability, three types of response of the same compound (dielectric, optical and magnetic) are shown in Figure 5 (compound = [Fe(DAPP)(abpt)]$(ClO_4)_2$, where DAPP is [bis(3-ami-nopropyl)(2-pyridylmethyl)amine], abpt

is 4-amino-3,5-bis(pyridin-2-yl)-1,2,4-triazole}) [68]. The changes in all three physical channels occur as first-order phase transitions with 10 K wide hysteresis loops centered around 176 K. The dielectric constant shows a similar variation of the absolute value as observed for magnetic and optical responses. The memory effect operates around 176 K by the storage of a high or low capacitance state.

### 1.3.4   Influence on spin-crossover behavior

The spin-transition behavior can be influenced by various factors, most important among these are:

*Nature of ligand and anion.* Substitution of one ligand by another can generate, or alter, the spin-crossover characteristics.

Empirically, for mixed complexes $[FeA_nB_{6-n}]$ the rule of "averaged environment" holds [72] which states that $10Dq$ values of complexes can be found approximately through linear interpolation between $10Dq$ values for $[FeA_6]$ and $[FeB_6]$:

$$10Dq([FeA_nB_{6-n}]) \approx \tfrac{n}{6} 10Dq([FeA_6]) + \tfrac{6-n}{6} 10Dq([FeB_6]) \qquad (4)$$

For example, the system $[Fe(py)_4(NCS)_2]$ is high-spin at room temperature and does not undergo a thermal spin-transition. Substitution of two of the pyridine molecules by a strong field 1,10-phenanthroline molecule gives $[Fe(phen)(py)_2(NCS)_2]$ which does undergo a thermal transition [73, 74], as does the species in which the remaining two pyridines are substituted $[Fe(phen)_2(NCS)_2]$ [75-77]. As would be expected, $T_{1/2}$ for the former complex (106 K) is lower than that for the latter (176 K). Replacement of the two thiocyanato groups by phenanthroline produces the totally low-spin complex cation $[Fe(phen)_3]^{2+}$. Their replacement by the strong field cyanide ion or the weak field chloride ion produces purely low-spin $[Fe(phen)_2(CN)_2]$ or purely high-spin $[Fe(phen)_2Cl_2]$, respectively [75].

*Intraligand substitution.* Substitution within a ligand may alter drastically the spin state of a system. This is illustrated by the effects of substitution within low-spin $[Fe(phen)_3]^{2+}$. Incorporation of a substituent into the 2-position of phenanthroline results in spin-crossover or high-spin behavior. The order of substituents with decreasing ligand field strengths (and thus increasing tendency towards paramagnetic behavior) of the $[Fe(2-R-phen)_3]^{2+}$ cation is as follows: $R = H > CH_3O > CH_3 > Cl$ [20]. In the substituted complexes, the close approach of the N-methyl donor to the metal atom is hindered by the substituent. The effect de-stabilizes the singlet state of the complex. An additional effect is the donating or

withdrawing properties of the substituent, which also perturb the electronic structure of the ligand.

*Nature of crystal solvent* can dramatically influence the spin-crossover properties of the complex compound. For the ethanol, methanol and water solvates of $[Fe(pic)_3]Cl_2$ spin-crossover is observed but there is an increasing stabilization of the singlet state in the order given [78]. There are also other numerous examples in which loss of crystal water dramatically modified the spin-crossover properties [66, 79-84]. The effects of solvation is not always consistent from one system to another and is not readily predictable [41].

The factor of *intermolecular contacts* between spin-crossover centers is also related to the nature of the crystal solvent. In the crystal lattice between components of mononuclear systems usually hydrogen or $\pi$–$\pi$ interactions are detected which are believed to play a decisive role in defining the character of the spin-transition. The importance of hydrogen bonding for the spin-crossover behavior of the $[Fe(pic)_3]Cl_2$ system was investigated through the effect of isotopic exchange (H/D and $^{14}N/^{15}N$) in various positions of the ligand and the solvent molecules [85]. In the polymeric triazole systems the crystal water was found to influence substantially the abruptness of the spin-transition, whereas the loss of it resulted into gradual transition [60, 81]. The most illustrative example of the systems with $\pi$–$\pi$ interactions are represented by the series of compounds $[Fe(L)_2(NCS)_2]$, where L = 1,10-phenanthroline (phen) [86] and dipyrido[3,2-*a*:2'3'-*c*]phenazine (dppz) [87]. The crystal packing analysis shows that in these complexes an important number of C···C contacts are observed. This situation is especially accentuated in the dppz derivative leading to abrupt transition with huge hysteresis (~ 40 K). Therefore, for these materials the magnetic response is correlated with the extent of their intermolecular interactions.

*Dimensionality*. The observation of cooperativity associated with the spin-crossover phenomenon in monomeric complexes and its rationalization in terms of effective intermolecular interactions, has led to the realization that enhancement of abruptness could be achieved by the use of bridging ligands capable of linking covalently the spin-crossover centers. The increase of the dimensionality, for example, from trinuclear [88-90] to polymeric structure [19, 89, 91-94], leads to improved spin-transition properties in triazole complexes, for example, shifts the transition to higher temperature and increases the abruptness of the transition up to appearance of large hysteresis (*ca.* 60 K) [60]. Another example is $[\{Fe_2(NCS)_2(\mu\text{-bpypz})_2\}X_n$, where X can be monodentate pyridine molecules, n = 2 [95], or bridging 4,4'-bipyridine, n = 1 [96] ($\mu$-bpypz = 3,5-bis(pyridin-2-yl)pyrazolato). Increase of the dimensionality of the system leads to appearance of the magnetic hysteresis loop in the

latter compound. Condensation of two 1,2,4-triazole rings gives the bis-monodentate ligand 4,4'-bis-1,2,4-triazole (btr). Self-assembly of btr, $NCS^-$ and iron(II) afforded $[Fe(btr)_2(NCS)_2] \cdot H_2O$, the first two-dimensional spin-crossover coordination polymer. The compound displays a strong cooperative spin-transition centered at around 134 K with a broad hysteresis loop of *ca*. 21 K width. Finally, the reported spin-crossover compound $[Fe(btr)_3](ClO_4)_2$ with the three-dimensional network of the covalent bonds between spin-crossover centers shows two-step transition with a hysteresis loop of 3 K [97]. In general, it is assumed, that the hysteresis effect and abruptness in the spin-crossover polymers are connected to dimensionality and follows the 1D > 2D > 3D [77, 98].

*Polymorphism*. The effect of polymorphism on the spin-crossover behavior is known since the first studies on the classical system $[Fe(L)_2(NCX)_2]$ where L = phen (X = S, Se) or 2,2'-bipy (X = S) by König and co-workers [99, 100]. Later numerous other systems were reported and structurally characterized [101-108]. Comparison of the crystal structures of the polymorphs showed that the differences in the spin-crossover behavior are due to crystal packing effects and crystal structure-induced modification of the complex geometry.

*Metal dilution*. The effect of dilution of spin-transition complexes into the lattice of isostructural species of zinc(II) or cobalt(II) and others has proved to be very diagnostic in influencing the nature of spin-crossover in solids [41]. If the transition curve is abrupt for the neat compound, it becomes more gradual with increasing dilution, approaching that indicative of a Boltzmann distribution over all spin states, as is generally found for thermal spin-transition in liquid solutions. The origin of such influence lies in the increase of the distances between spin-crossover centers with the decrease of their interactions.

*Lattice defects*. Mechanical treatment of samples or different synthetic procedures have been shown to influence strongly the spin-crossover behavior [76, 92, 109-112]. The origin of these effects stems from crystal quality considerations, in particular crystal defects introduced during sample preparation either by milling (sheared deformations) or rapid precipitation, the size of the particles playing a minor role.

### 1.3.5   Slichter-Drickamer Model

For the description of the conversion low-spin $\leftrightarrow$ high-spin in solid spin-crossover materials several theoretical approaches have been developed (see ref. [21]). One of them was proposed by Slichter and Drickamer for accounting deviations of spin-crossover behavior from the Boltzmann law [113]. We shall discuss the model in detail.

For an assembly of $N$ spin-crossover molecules, each of which can exist either in the low-spin state or high-spin state, we can define the molar fraction of high-spin molecules as $\gamma_{HS}$ and that of low-spin as $1 - \gamma_{HS}$. Assuming now that there is no interaction between the molecules we have to introduce a mixing entropy term to the Gibbs free energy $G$. This term accounts for the fact that there are many ways of distributing $\gamma_{HS}N$ high-spin molecules and $(1 - \gamma_{HS})N$ low-spin molecules within the assembly of $N$ molecules. This mixing entropy is given by

$$S_{mix} = k[N\ln N - \gamma_{HS}N\ln\gamma_{HS}N - (1 - \gamma_{HS})N\ln(1 - \gamma_{HS})N] \tag{5}$$

which may be rewritten as

$$S_{mix} = -R[\gamma_{HS}\ln\gamma_{HS} - (1 - \gamma_{HS})\ln(1 - \gamma_{HS})] \tag{6}$$

where $R$ is the gas constant. $S_{mix}$ is maximum for $\gamma_{HS} = 0.5$ and vanishes for $\gamma_{HS} = 0$ and 1. Taking into account $S_{mix}$, the molar Gibbs free energy is

$$G = \gamma_{HS}G_{HS} + (1 - \gamma_{HS})G_{LS} - TS_{mix} \tag{7}$$

where $G_{HS}$ and $G_{LS}$ are the molar Gibbs free energies for the high-spin and low-spin species, respectively. The partial derivative of $G$ with respect to $\gamma_{HS}$ is

$$\frac{\partial G}{\partial \gamma_{HS}} = \Delta G + RT \ln\left(\frac{\gamma_{HS}}{1 - \gamma_{HS}}\right) \tag{8}$$

and at any temperature and pressure the equilibrium condition for the transformation low-spin $\rightarrow$ high-spin is defined by

$$\left(\frac{\partial G}{\partial \gamma_{HS}}\right)_{T,p} = 0 \tag{9}$$

hence

$$\ln\left(\frac{1 - \gamma_{HS}}{\gamma_{HS}}\right) = \frac{\Delta G}{RT} = \frac{\Delta H}{RT} - \frac{\Delta S}{R} \tag{10}$$

Taking into account that $\Delta G = 0$ when $\gamma_{HS} = \gamma_{LS} = 0.5$ and thus $T_{1/2} = \Delta H/\Delta S$, we obtain:

$$\gamma_{HS} = \frac{1}{1 + \exp\left[\frac{\Delta H}{R}\left(\frac{1}{T} - \frac{1}{T_{1/2}}\right)\right]} \tag{11}$$

In the model proposed by Slichter and Drickamer the intermolecular interactions are accounted by an interaction term $G_{int}(\gamma_{HS},T,p) = \Gamma\gamma_{HS}(1 - \gamma_{HS})$, where $\Gamma$ is an interaction parameter assumed not to depend on $T$ to first approximation.

Taking $G_{LS}$ as the origin of the energies, we can write

$$G = \gamma_{HS}\Delta H + \Gamma\gamma_{HS}(1 - \gamma_{HS}) + T[R\gamma_{HS}\ln\gamma_{HS} + R(1 - \gamma_{HS})\ln(1 - \gamma_{HS}) - \gamma_{HS}\Delta S] \qquad (12)$$

which allows to plot the $G = f(\gamma_{HS})$ curves for various values $\Delta H$, $\Delta S$, and $\Gamma$, and at different temperatures. The $\gamma_{HS}$ value of extrema are defined by Equation (9), which leads to the implicit equation

$$\ln\left(\frac{1 - \gamma_{HS}}{\gamma_{HS}}\right) = \frac{\Delta H + \Gamma(1 - 2\gamma_{HS})}{RT} - \frac{\Delta S}{R} \qquad (13)$$

The critical temperature $T_{1/2}$ for which $\gamma_{HS} = 0.5$ corresponds to $\Delta G = 0$, *i.e.*, $T_{1/2} = \Delta H/\Delta S$, and the condition for observing hysteresis is: $\Gamma > 2RT_{1/2}$.

### 1.3.6   LIESST effect

This effect was first observed on a single crystal of the spin-crossover complex [Fe(ptz)$_6$](BF$_4$)$_2$ [114] (Figure 6). Irradiating the compound with green light into the $^1A_1 \rightarrow$ $^1T_{1,2}$ absorption bands at 20 K, *i.e.* in the low-spin region, resulted in the population of a metastable high-spin state with a long lifetime at this temperature. This phenomenon has become known as the LIESST effect (Light-Induced Excited Spin State Trapping). Thermal relaxation to the thermodynamically stable low-spin state was observed by warming the compound up to *ca*. 50 K. This relaxation occurs by tunneling through the energy barrier between the potential wells of the two states, whereby the observed temperature dependence of the relaxation rate is due to thermal population of the vibronic levels of the $^5T_2$ manifold [115]. It was also possible to return to the low-spin state by irradiating into the $^5T_2 \rightarrow {}^5E$ absorption band with red light for the initial excitation followed by two intersystem crossing processes $^5T_2 \rightarrow {}^3T_{1,2} \rightarrow {}^1A_1$. This back switching has been termed "reverse-LIESST" [116]. The mechanism of these photo-switching processes is depicted in Figure 6. It was found, that the lifetime of the light induced state is longer, the smaller $\Delta E_{HL}$ ("reduced energy gap law") and the larger $\Delta r_{HL}$ [117].
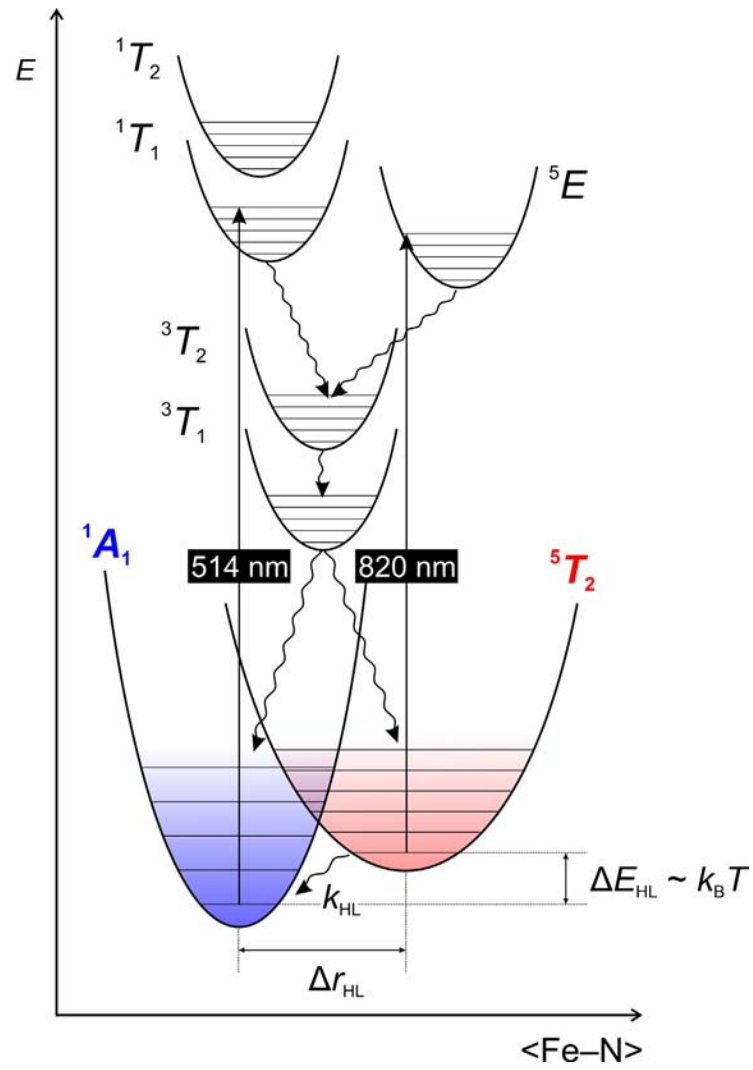
**Figure 6.** Mechanisms of LIESST (514 nm) and reverse-LIESST (820 nm) effects.

## 1.4  Liquid crystallinity phenomenon

### 1.4.1  Organic liquid crystals

The *liquid crystal* phase is a state of matter, which lies between the solid and the isotropic liquid phases. The terms *mesomorph* (from Gk. μέσος μορφή, between two states, forms) and *mesophase* are also used; a mesogen is the molecule which gives rise to a mesophase. In the crystal phase the molecules have a high degree of order, occupying fixed positions in the lattice and, conversely, in the isotropic liquid phase only a short-range order dominates, the molecules are mobile and have no orientation with respect to each other (Figure 7). The liquid crystal phase shares properties of both the crystal and liquid phases, possessing an intermediate molecular order between the perfect three-dimensional long range positional and orientational order found in crystals, and the absence of long-range order found in the isotropic liquids. The liquid crystal state is characterized by having a long-range orientational order and possible partial positional order (Figure 7). In this phase, the materials exhibit on one hand properties of a liquid (easily deformable) and on the other hand features typical for crystals (optical and electrical anisotropy).
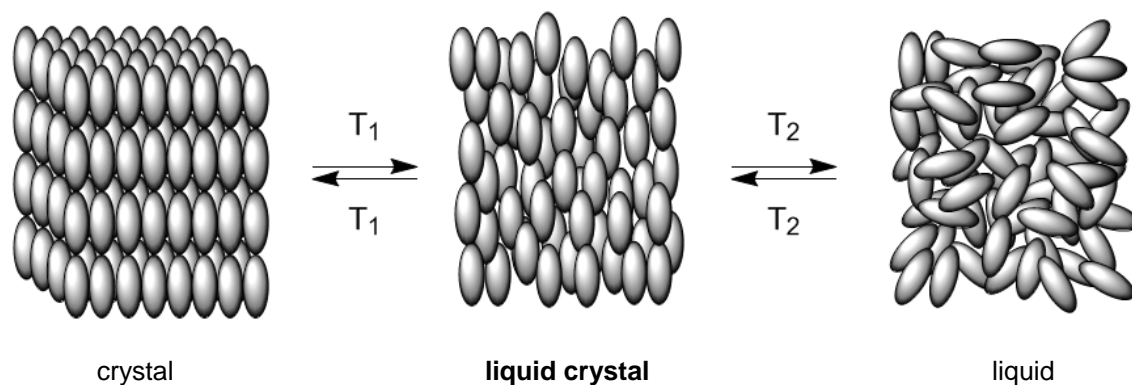


**Figure 7**. Schematic representation of crystal, liquid crystal and liquid phases.

The discovery of liquid crystals in 1888 is commonly attributed to the Austrian botanist Friedrich Reinitzer, who observed that a material known as cholesteryl benzoate has two distinct melting points [118, 119]. The crystals of this material melt at 145.5 °C into a cloudy liquid, which upon further heating to 178.5 °C becomes clear. Since then, immense efforts in research and development have pushed this field to further development.

According to classical definition, liquid crystals are divided into two main classes: *thermotropic*, whose mesophase formation is temperature dependent, and *lyotropic*, whose

mesophase formation is concentration-, solvent- and temperature dependent (Figure 8). It is noteworthy that a significant number of *amphotropic* liquid crystals (showing both lyotropic and thermotropic properties) exists [120]. The essential requirement for molecules to form a thermotropic liquid crystal is a structure consisting of a central rigid core (often aromatic) and a flexible peripheral moiety (generally aliphatic groups). The shape of the molecules is an important criterion for determining the liquid crystalline behavior. This structural requirement leads to several classes of liquid crystals: *calamitic*, characterized by the rod-like shape of molecules (Figure 9a), *discotic*, characterized by the disc-like core of the molecule (Figure 9b), *sanidic*, characterized by molecules with board-like shapes (Figure 9c) and *phasmidic*, characterized by molecules with a long rod-like rigid core ending in two half-disc groups (Figure 9d) (see also Figure 8).
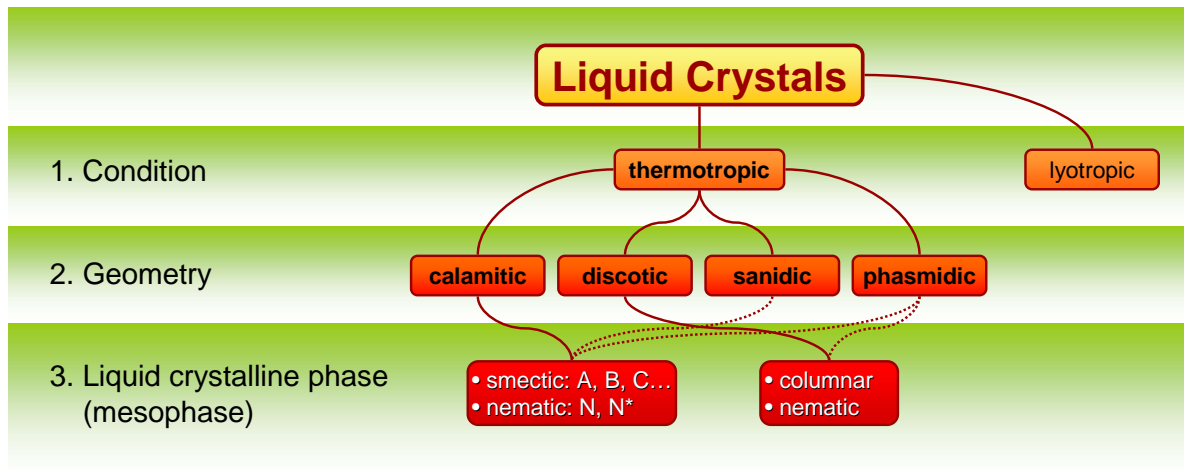


**Figure 8.** Classifications of liquid crystals.

Considering the structure of mesophases, several organizations can be distinguished (Figure 8). If calamitics arrange themselves in a way that they are in a fluid state, with one-dimensional orientational order and no positional order, then they form a *nematic* phase (N) (Figure 10). The orientational order in the phase is an averaged order and the degree of correlation, known as the order parameter (S), between the average direction (defined by the director, $\vec{n}$, see Figure 9a) and the actual orientational directions of all the molecules is given by the function below

$$S = \tfrac{1}{2}\left\langle 3\cos^2\theta - 1 \right\rangle \tag{14}$$

where $\theta$ is the angle between the long molecular axis and the director. Typically, $0.4 < S < 0.7$ for a nematic phase. The nematic phase is the most disordered type of mesophase and is the one used in most display applications [121, 122].
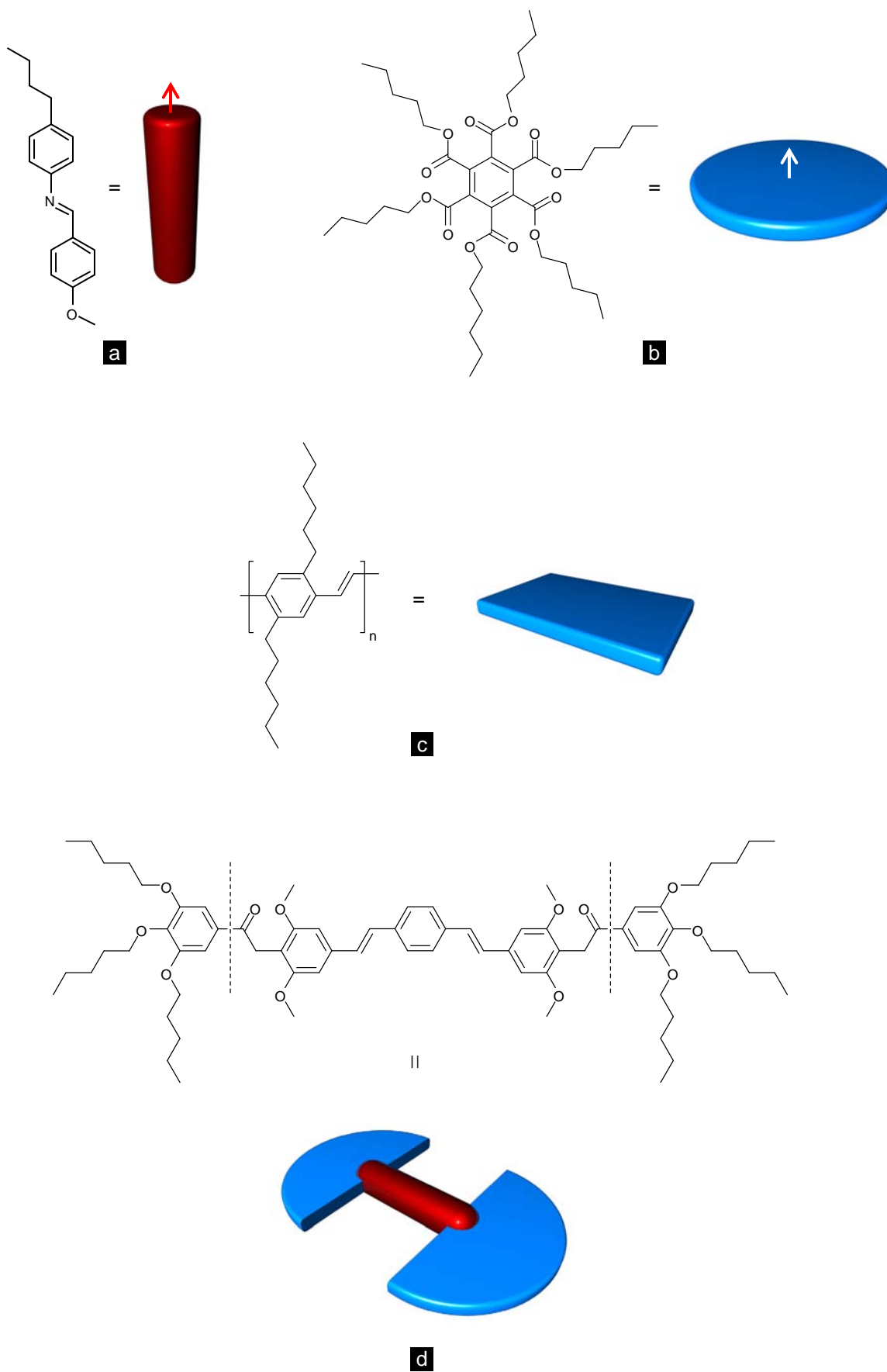
**Figure 9.** Examples of the thermotropic liquid crystals: a) calamitic; b) discotic; c) sanidic; d) phasmidic. For the calamitic and discotic red arrows show directors $\vec{n}$ of the molecules.

If in addition to the orientational order some partial positional order is introduced, a family of smectic phases can be generated, which are characterized by having some layering of the molecules. For example, in the *smectic A* ($S_A$) phase (Figure 10) the molecules are loosely associated within layers and, on average, all point in a direction parallel to the layer normal. The situation in the *smectic C* phase ($S_C$) is similar (Figure 10), except that the director now makes some angle, θ, to the layer normal. There is, however, no positional correlation between molecules within the $S_A$ or $S_C$ layers and indeed, in each case, there is considerable fluidity within and easy diffusion between the layers [123].

*Smectic B*, *F* and *I* phases can be generated by introducing some symmetry into the layers. The $S_B$ phase has molecules arranged in a hexagonal fashion within the layers with a director perpendicular to the layer normal (Figure 10). The $S_F$ and $S_I$ phases are tilted variations of this phase, with the tilt lying across a hexagonal edge or along a hexagonal vertex, respectively. Chiral variants of the N, $S_A$, $S_C$, $S_F$ and $S_I$ phases are also known [123].
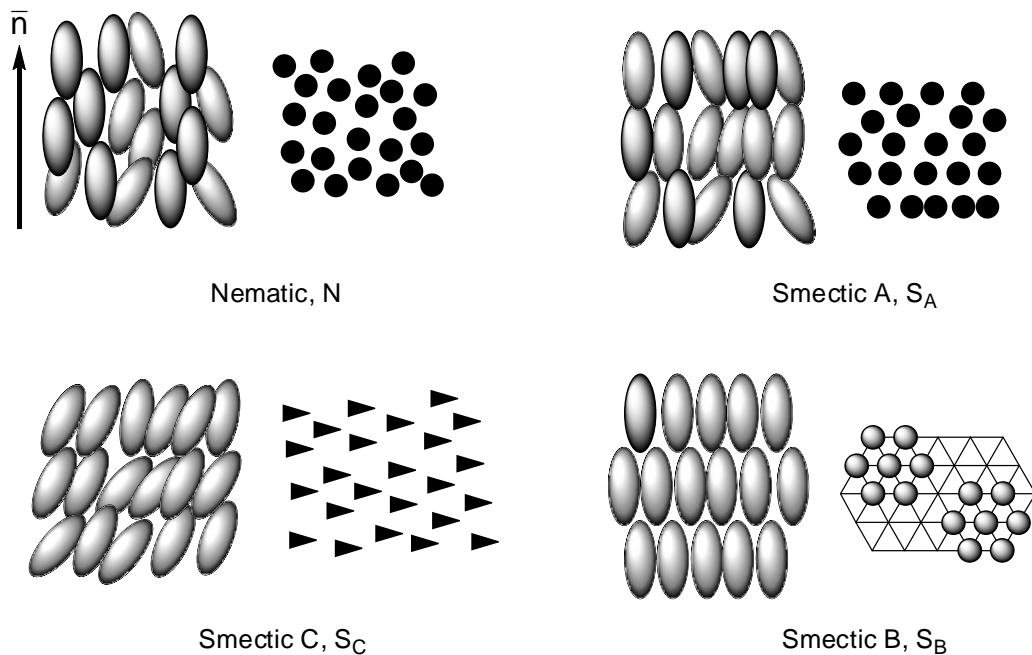


**Figure 10.** Schematic representation of the N, $S_A$, $S_C$ and $S_B$ phases [123].

We can also consider the formation of discotic phases by disc-like molecules and in such cases it is the correlation of the unique, short molecular axis which is in question (see Figure 9b). Thus, it is possible to have a *discotic nematic phase* ($N_D$) in which there is orientational correlation of the short molecular axis in the absence of any positional ordering (Figure 11a). In addition, there is a whole family of *columnar phases* in which the molecules

are stacked in columns which are then arranged with respect to one another. A further classification describes the packing of the columns with respect to one another: *columnar nematic* ($N_{Col}$) with disordered axes of columns (Figure 11b) *hexagonal* ($Col_h$) (Figure 11c), *rectangular* ($Col_r$) (Figure 11d) and *lamellar* ($Col_L$) (Figure 11e). These phases are distinguished as *ordered* (additional subscript "o") (Figure 12a) or *disordered* (subscript "d") (Figure 12b), according to the absence or presence, respectively, of liquid-like order within the columns [124].
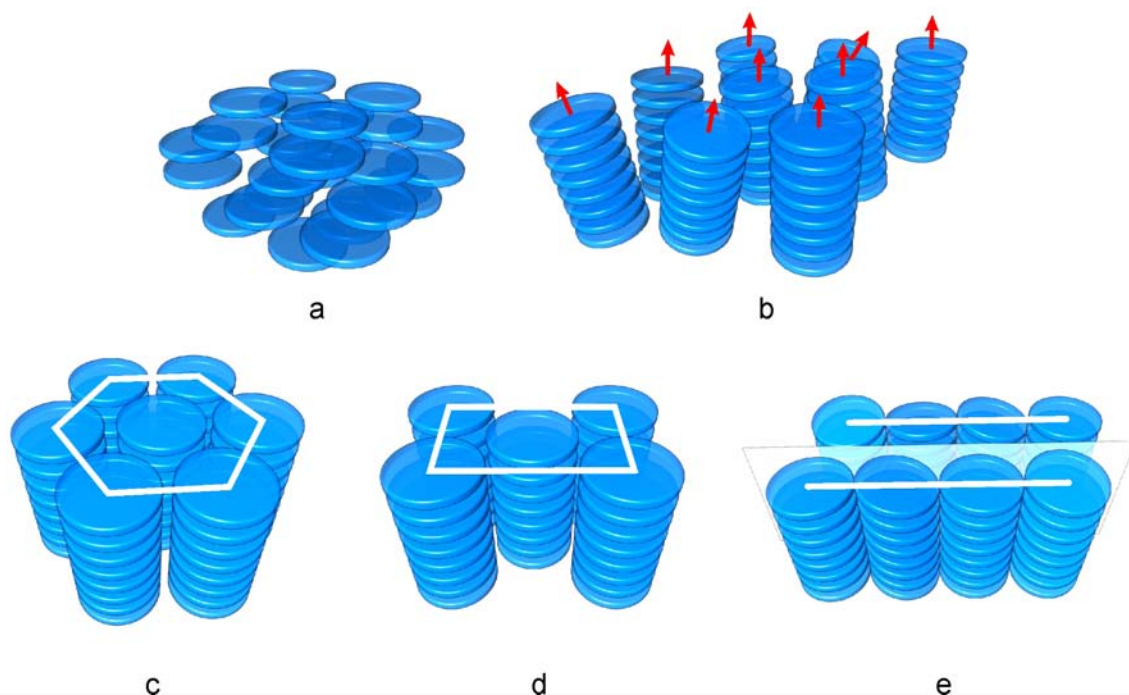


**Figure 11.** Schematic representation of a) discotic nematic ($N_D$); b) nematic columnar phase ($N_{Col}$); c) hexagonal columnar phase ($Col_h$); d) rectangular columnar phase ($Col_r$) and e) columnar lamellar phase ($Col_L$).
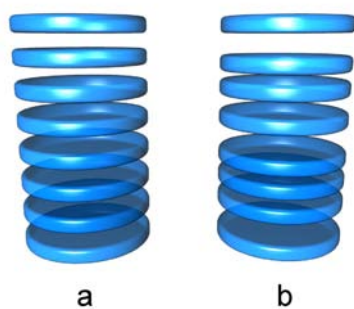


**Figure 12.** Intracolumnar stacking ordered (a) and disordered (b).

The characterization of thermotropic mesophases relies initially on optical microscopy; as the temperature is changed the different phases show characteristic textures when viewed between crossed polarizers. Mixing with a known mesophase will often confirm the assignment, since two identical mesophases are normally miscible. Further confirmation and assignment require differential scanning calorimetry (DSC), and low-angle X-ray scattering in the mesophase (for details see Chapters 6.5.2, 6.5.6 and 6.5.8).

### 1.4.2   Metallomesogens

The first report on metallomesogens, *i.e.* metal-containing liquid crystals, was by Vorländer who reported, in 1923, a number of mercury-based mesomorphic materials, such as the Schiff-base complexes of diarylmercury(II), which showed smectic phases [125]. The next sixty years, reports describing metallomesogens were sporadically published until the "explosion" in metallomesogen research started in 1986. An overview of the publications concerning metal-containing liquid crystals reveals that the majority of authors, using quite similar words, enclose in their texts an attractive and promising leitmotif: "... liquid crystalline materials in which a metal atom is incorporated into the molecular skeleton are of interest because such new materials are expected to have not only the intrinsic properties of organic mesogens but also the unique properties based on metal atoms..." [126].
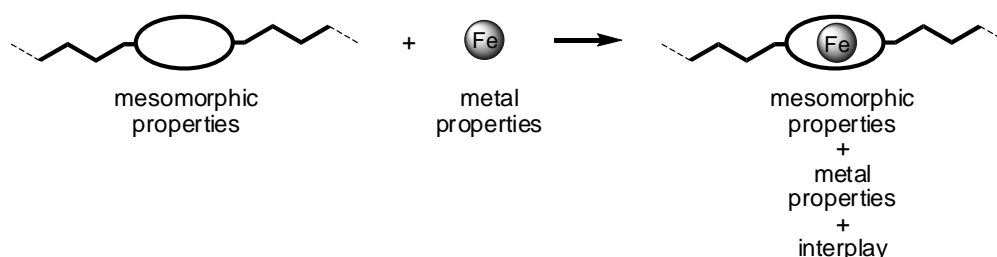


**Figure 13.** Combining properties of a liquid crystal and of an iron(II) ion in a metallomesogen.

The possibility of combining the properties of liquid crystals (fluidity, ease of processability, one- or two-dimensional order, *etc*.) with the properties associated with metal atoms (color, paramagnetism, an electron-rich environment, *etc*.) is the main origin of the progress in this field (Figure 13). In addition, the possibility of tuning the physical (mesomorphic, optical, magnetic, *etc*.) properties of metallomesogens is significantly extended, since the organic ligand can be varied. A particular metal ion [*e.g.* iron(II)] can be complexed to numerous mesomorphic ligands which differ in nature or mesomorphic

properties. Alternatively, the well-documented effects of structural modifications found for organic liquid crystals can also be applied to the organic ligand in a metallomesogen [126].

Similarly to organic liquid crystals, the classification of metallomesogens can be done within the two groups regarding the nature of the mesophases formed: lyotropic or thermotropic. The next subdivision of thermotropic metallomesogens can be made due to the generally different molecular geometries of compounds showing calamitic and discotic mesophases. Further, taking into account the electronic character of the thermotropic complexes, two different types of compound can be distinguished: neutral and ionic. In neutral complexes the metal is very often joined to an organic ligand, which normally leads to a system with a molecular geometry very similar to that of organic liquid crystals. In contrast, in ionic compounds, two parts of the molecule need to be considered: the promesogenic organic ligand and the non-promesogenic counterion. The promesogenic ligand is mainly responsible for the molecular order observed in the mesophase. The (non-mesogenic) counterion is normally a small mobile molecule which is situated near to the charge on the promesogenic unit. However, in some cases the counterion plays an important role in the formation of the mesophase (*e.g.* alkyl sulfate or 4-(alkoxy)benzenesulfonate derivatives) [127]. The classification of metallomesogens is represented in Figure 14.
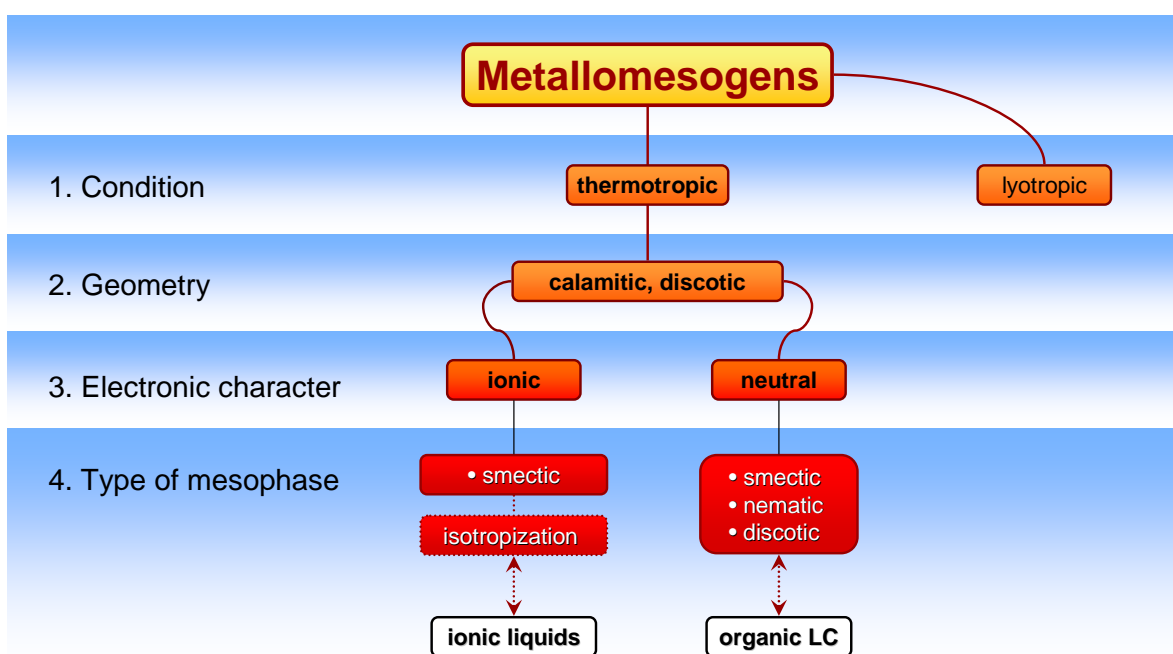


**Figure 14**. Classification of metallomesogens.

The ionic character means that some of the properties of the ionic liquid crystals differ significantly from those of conventional liquid crystals. Typical for ionic liquid crystals

is the ionic conductivity. The ionic interactions tend to stabilize lamellar mesophases, for example, typical is a modified form of a smectic phase – a bilayer smectic A phase. In this phase, the molecules are in repeating bilayer motif. Ionic liquid crystals can be considered as materials which combine the properties of liquid crystals and ionic liquids [128].

### 1.4.3 Melting point of alkyl derivatives

Figure 15 shows the melting point, $T_m$, as a function of the number of carbon atoms for several homologous series of alkyl derivatives. In each series the melting points fall on a smooth curve (or two curves due to the odd-even effect). As the number of carbon atoms $n$ increases, the melting point increases as well and tends to a fixed limit – the melting point of polyethylene [129]. The variation of the melting point in mesogens is very similar, as shown by the example of di-n-alkyl 4-(4-n-octyloxycinnamoyloxy)benzylidene malonates ($C_n$-CBM) [130] (Figure 15), but sometimes has a more complicate character. There is a general rule in homologous series of organic mesogens: Lower members often exhibit relatively high melting temperatures, the medium-sized members ($n \sim 4$–$8$ carbon atoms) have the lowest $T_m$, and in higher members $T_m$ again increases in a smooth way [131]. This provides a platform for the fine-tuning of the phase transition temperature in metallomesogens, too [127, 132], and also served as a starting point for the present work.
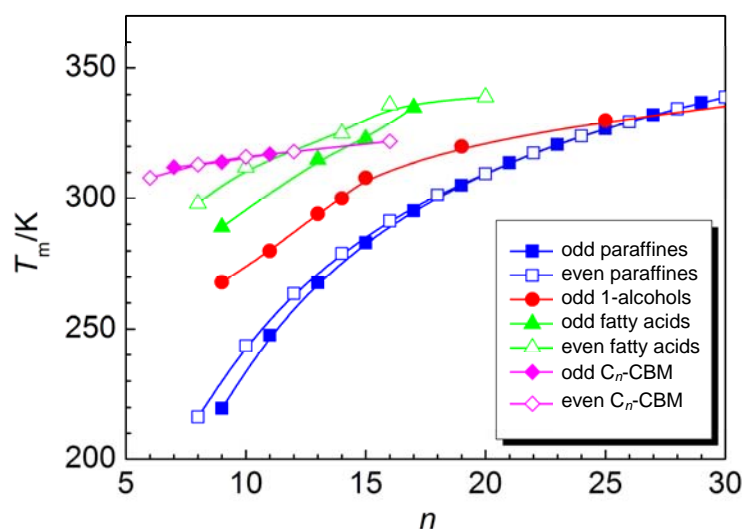


**Figure 15.** Temperature variation of the melting point $T_m$ for homologous series of alkyl derivatives.

# 2 Mononuclear iron(II) systems

## 2.1 Parent systems

### 2.1.1 Introductory remarks

Chapter 2 is organized in the following way. In the first section parent systems, their characterization and properties are described. The second section is devoted to modified systems obtained by introducing mesogenic alkyl moieties into parent complex molecules.

Prior to the work carried out, a search of appropriate parent systems, which after modification would possess liquid crystalline and spin-crossover properties and allow their interplay, was performed.

Selection of parent systems was accomplished according to the two criteria:

▪ The system should show spin-transition or to be low-spin at ambient temperature. This requirement is based on the known fact that introduction of substituents into an organic ligand generally alter the character of the spin-transition [93, 133-135];

▪ The structure of the complex molecule should be of the type, that on substitution with alkoxy groups it would be possible to obtain asymmetric molecules with separated coordination polar heads and alkyl parts, capable to form a microsegregated structure.

It was realized that the required criteria could be satisfied by the class of the polypodand-based complexes. In the following a short overview of the reported data (1957–2008) is presented concerning the structure and magnetic properties of such systems containing iron(II) or iron(III) ions.

### 2.1.2 Overview of the literature on iron(II)- and iron(III)-based polypodand complexes

**System *a*.** The first report on tripodand complexes of 3*d*-metals was published in 1957 by Lions and Martin [136]. It was a class of *tach*-based systems synthesized by condensation of the trifurcated triamine with three equivalents of picolinaldehyde in the presence of a metal salt (*tach* = *cis,cis*-1,3,5-cyclohexanetriamine). The authors pointed out the diamagnetism of the iron(II) perchlorate complex at room temperature. Later the series of the complexes was investigated by spectroscopic methods (Gillum *et al.* [137]). The aim of the work was to find a correlation between spectroscopic properties and molecular structure.

Progress was achieved by Reiff [138] who used Mössbauer spectroscopy for the same purpose and could predict a rather pronounced twist of the coordination polyhedron on the basis of the magnitude and sign of the quadrupole splitting. Later the structures of zinc(II) and cobalt(II) complexes were reported and on the basis of the XRD data the conclusion was made about the peculiarities of distortion in iron(II) system; the corresponding structure was not reported [139]. At the same time 3$d$-metal systems based on triamine *tame* with the same set of pyridine substituents attracted considerable interest of chemists, particularly regarding structural studies [*tame* = 2,2,2-tris(aminomethyl)ethane] [140]. In the case of the iron(II) compound the coordination polyhedron was found to be rather distorted toward trigonal prism but less than for other 3$d$-metal ions, thus following the order Zn(II) ~ Mn(II, high-spin) < Co(II, high-spin) < Ni(II) < Fe(II, low-spin). It was suggested that the observed dependence resulted from ligand field stabilization energies, which are higher for octahedral fields compared to trigonal prismatic fields, and this represented the "driving force" leading away from the trigonal prismatic geometry. The first description of the low-spin iron(II) complex based on the ligand *tren(py)*₃ (= tris[3-aza-4-(2-pyridyl)but-3-enyl]amine) was reported by Mealli and Lingfelter [141] (Figure 16a). However, these reports concerned mostly stereochemical aspects and were an attempt to rationalize the factors which led to the trigonal distortion of the coordination polyhedron.
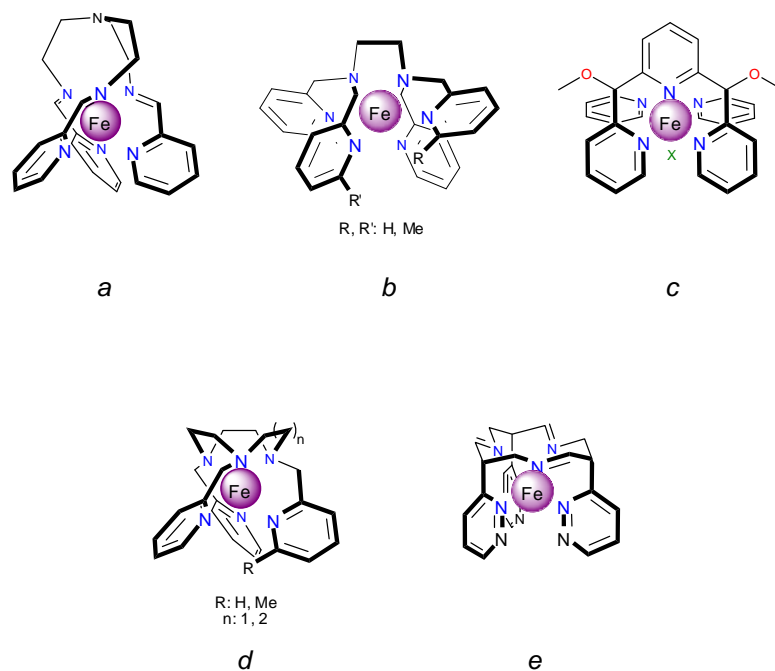


**Figure 16**. Candidate complexes *a–e* for the mononuclear systems.

Subsequently a comprehensive series of papers appeared describing spin-transition (in solid state) and spin-equilibrium effects (in solution) in methylated *tren*-based systems [*tren* = tris(2-aminoethyl)amine] [142-146]. It was found that the $PF_6^-$ salt of triply methylated ligand *tren*(6-*Mepy*)$_3$ (= tris[3-aza-4-(6-methyl-2-pyridyl)but-3-enyl]amine) shows gradual spin-transition centered at 214 K [142, 143]. Some selected structural data were published, in particular Fe–N bond distances and the twist angle of the distorted octahedron. Later this system, as well as asymmetric *tren*(6-*Mepy*)$_2$(*py*)- and *tren*(6-*Mepy*)(*py*)$_2$-based systems, were used as model compounds in a series of studies [147-151]. Recently performed quantitative mass spectroscopic reinvestigation of these two systems prepared according to the procedure proposed in ref. [142], became doubtful regarding the purity of the samples [152]. Another iron(II)-based system obtained by a redox-reaction of iron(III) with the reduced ligand $H_6$-*tren*(*py*)$_3$ (= tris{2-[(2-pyridylmethyl)amino]ethyl}amine) shows gradual incomplete spin-crossover centered at 140 K [153].

During the last years several explicit studies of imidazole-containing spin-crossover systems with a variety of counterions and substituents in imidazole units were published [154-161]. Depending on structural variables and on their deprotonation level, in iron(II)-based compounds one step or two step gradual or abrupt spin-transitions with a concomitant pronounced thermochromism from orange (high-spin) to deep red (low-spin) were detected. Low temperature irradiation with green/red laser successfully afforded an increase/decrease (after excitation) in the susceptibility, which was attributed to the LIESST/reverse-LIESST effect [154]. Contrary to *tren*(*py*)$_3$ which forms exclusively iron(II) low-spin complexes, imidazole analogues may form iron(III) spin-crossover and low-spin complexes as well, depending, among other factors, on the deprotonation of the ligand [156]. Reported protonated pyrazole based *tren* systems of iron(II) can be high-spin down to 100 K [162] or show low temperature spin-transition [163], analogously to the partially deprotonated mixed-valence iron(II)–iron(III) pseudo-dimer [164].

The mononuclear chelate complex of iron(III) with trianionic Schiff base ligand, prepared by condensation of 1*H*-pyrrole-2-carbaldehyde with *tren*, shows low-spin behavior [165]. The ligand field is very strong which prompted to prepare the complex with manganese(III) ion known to have a relatively high crossover point [166]. The magnetic measurements revealed spin-crossover behavior with an abrupt spin-transition from $S = 2$ to $S = 1$ at $T_{1/2} = 44$ K.

**System *b***, the general structure of which is shown in Figure 16b, combines two aliphatic and four pyridine nitrogen atoms creating together a ligand field at the crossover

point [167]. Depending on the number and the type of substituents, exclusively low-spin or high-spin or spin-equilibrium complexes can be prepared [168]. The most remarkable feature of the mono-methylated spin-crossover system derived from X-ray diffraction data is a pronounced distortion toward trigonal prismatic environment of iron(II) with twist angle $\theta$ between two opposite trigonal faces of the polyhedron being 37° [169]. The non-methylated compound is the first iron(II) spin-crossover complex possessing a spin-state interconversion rate in the solid state higher than *ca.* $10^7$ s$^{-1}$, the reciprocal lifetime of 14.4 keV nuclear state of $^{57}$Fe [170].

**System c.** The magnetic behavior of iron(II)-based systems with the ligand 2,6-bis(methoxydipyridin-2-ylmethyl)pyridine (PY5) (Figure 16c) was reported recently. The behavior of the complexes strongly depends on the nature of the group X. With strong field ligands like acetonitrile and pyridine the system is low-spin [171, 172], with azide anion and methanol generate spin-crossover complexes while benzoic acid and chloride anion form high-spin complexes [172]. The structures at different temperatures as well as EXAFS and XANES data have been reported.

**System d.** Compared to linear triamine ligands, the macrocycle 1,4,7-triazacyclononane provides a surprisingly strong ligand field (Figure 16d). Extending the system to a hexadentate ligand by introduction of 2-pyridylmethyl groups on all of three nitrogen atoms results in the formation of very stable low-spin complexes with iron(II) [173]. Expansion of the macrocycle by one CH$_2$ group to a 10-membered tri-aza macrocycle allowed to prepare a spin-crossover complex with $T_{1/2}$ at 282 K in solution [167]. Introduction of a methyl group in one of three pendant arms of the ligand turned out to be sufficient to transform the parent low-spin system into a spin-crossover one [167]. The perchlorate salt has a $T_{1/2}$ at 380 K.

**System e** (Figure 16e) was not reported, but is supposed to be low-spin.

Concluding, one can say that all low-spin and spin-crossover systems are suitable for further modification experiments. The choice was done for the system based on the class of tripodand Schiff bases *a* (Figure 16a). The structure of such complexes is formed by aliphatic triamine condensed with three heterocyclic aldehydes. The relative disposition of nitrogens within the formed strands is efficient for chelating of an iron(II) ion. The chosen type of trifurcated ligands provide six N-donor atoms in coordination sphere of the central atom combining three imine and three aromatic nitrogens, which, depending on the type of further structural modification, might create ligand field from strong to moderate [174].

### 2.1.3 Synthesis

Except triamine *tren*, other *fac*-chelating triamines shown in Figure 17 are also suitable for the preparation of the tripodand complexes [175].
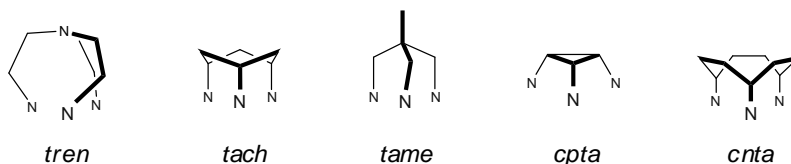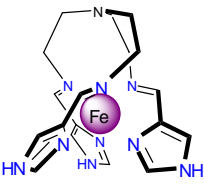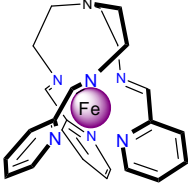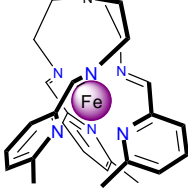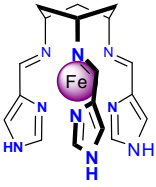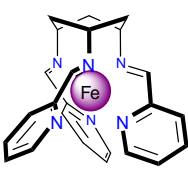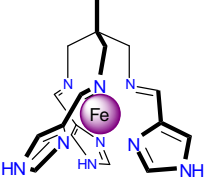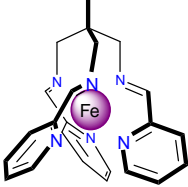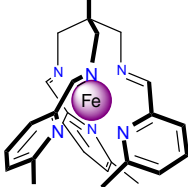


**Figure 17**. *fac*-Chelating triamines (*cpta* = 1,2,3-*cis*,*cis*-triaminocyclopropane; *cnta* = 1,4,7-triaminocyclononane).

For the present work the triamines *tren*, *tach* and *tame* along with picolinaldehyde [introduces pyridin-2-yl group (*py*)], 6-methyl-picolinaldehyde [introduces 6-methyl-pyridin-2-yl group (6-*Mepy*)] and 1(3)*H*-imidazole-5-carbaldehyde [introduces 1(3)*H*-imidazol-5-yl group (*imd*)] were selected. Possible combinations of the precursors are presented in Table 1. For comparison, the completely characterized complexes {Fe[*tren*(*imd*)$_3$]}(BF$_4$)$_2$ [155] and {Fe[*tren*(*py*)$_3$]}(ClO$_4$)$_2$ [160] denoted as **A** and **B** are included in the discussion, but the structures of them are not analyzed in details. Tetrahedral perchlorate and tetrafluoroborate were chosen as the anions in the present work.

All precursors for the synthesis of mononuclear complexes are commercially available, except the triamine *tach*. It was prepared according to the method based on Curcius rearrangement [176]. The Experimental section contains all synthetic details (Chapter 6.7).

The synthetic route for the family of the complexes **1**–**6** is depicted in Figure 18. The tripodal hexadentate ligand can be prepared *in situ* by condensation of the corresponding triamine and one of the selected aldehydes in a 1:3 molar ratio in aqueous or alcoholic medium in the presence of the iron(II) salt. Each complex has a molecular $C_3$ axis and can form a mixture of *L* and *D* optical antipodes. The chirality of the coordination species is known for **A** [155] and **B** [160]; thus it may also occur in other tripod-based complexes due to screw arrangement of symmetrical achiral tripod ligands.

**Table 1**. Molecular structure of parent compounds **A**, **B**, **1**–**6**. Used anion is shown in brackets.

| Triamine | Aldehyde | | |
|---|---|---|---|
| | 1(3)*H*-imidazole-5-carbaldehyde | picolinaldehyde | 6-methyl-picolinaldehyde |
| *tren* | **A** (BF$_4$) | **B** (ClO$_4$) | **1**, **1-Zn**[a] (ClO$_4$) |
| *tach* | **2** (BF$_4$), **2-ClO$_4$**[b] | **3** (ClO$_4$) | – [c] |
| *tame* | **4** (ClO$_4$) | **5** (ClO$_4$) | **6** (ClO$_4$) |

[a] **1-Zn** is zinc-based analogue of **1**;

[b] **2-ClO$_4$** is ClO$_4$-based analogue of **2**;

[c] Does not exist, see explanation in Chapter 2.3.6.
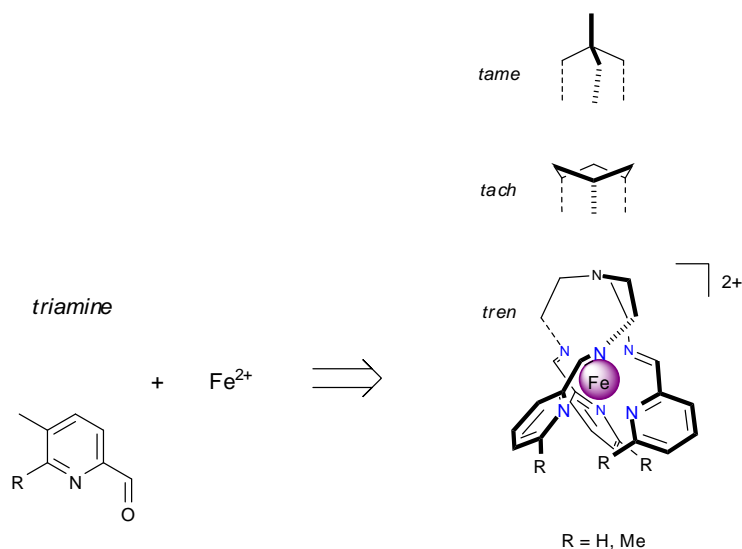
**Figure 18**. Schematic synthetic route for the compounds **1–6.**

Crystallization of all compounds occurred immediately after mixing of the components and was finished by cooling of the reaction mixtures overnight. Cherish-red crystals of the complex **1** were obtained by recrystallization of the crude product from hot water during slow cooling in a thermostat, the compound **2** was grown as yellow needle-like crystals by the same procedure, while slow recrystallization of the compounds **3–6** resulted in dark block-shaped crystalline material with metallic glance. The CHN microanalyses agreed with the formula proposed for each substance. Field desorption (FD) or electrospray ionization (ESI) mass spectroscopic studies confirmed the identity of the molecular structures. For X-ray single crystal measurements small single crystals of good quality were selected under a polarization microscope. All synthetic and characterization details are presented in the Experimental section (Chapter 6.7) and Chapters 2.2 and 2.3.

## 2.2 Structural and physical characterization
##     of compounds 1 and 1-Zn

### 2.2.1 Introductory remarks

The occurrence of spin-crossover and its characteristics ($T_{1/2}$, hysteresis, chromism, *etc*.) are governed by subtle structural and electronic modifications tuned by the crystal packing, which determines the ligand field strength and the transition type (abrupt, gradual *etc*.). These modifications depend essentially on the nature of the ligands, the non-coordinating anions, the solvent molecules and the crystal packing. The complete control of these variables is a rather difficult task to accomplish. In addition, their effects are not always consistent from one system to another and in general are not predictable. This is particularly accentuated for mononuclear complexes as the communication between the spin-crossover centers is achieved exclusively through intermolecular interactions, such as hydrogen bonding [88], π–π interactions between aromatic ligand constituents [77, 87, 177], S···S interactions [77]. Despite this, in some cases, it is possible to find correlations between the structure and the nature of the spin-crossover [21, 41]. One of the key problems in this kind of rationalization is the lack of systematic experimental studies. In polymeric compounds, partial or total substitution of these intermolecular interactions by covalent linkage of the metal centers leads to a more predictable control of the cooperative behavior.

Determination of the crystal structure in low- and high-spin states and subsequent analysis of the structural transformations within the complex molecules and the crystal lattice can give answers to some of the actual questions and help in understanding the effects responsible for specific magnetic and spectroscopic features of the solid spin-crossover materials. A series of precise structural studies was published providing crystal data of spin-transition complexes in both spin states. The goal of those studies was clarifying the nature of the cooperativity and the role of the structural phase transitions in the thermally, light and pressure induced spin-transitions [22, 23, 104, 163, 177-189].

Crystal data evidenced the role of the intermolecular contacts or intra-polymer contacts in determining the strength and nature of the cooperativity associated to the spin-transition process. It was found that a comparison of the structural properties of the spin-crossover material with an isostructural and isomorphous material which does not undergo spin-change can give additional valuable information. Such studies allow precise determination of the effects induced in the lattice by the spin state conversion and lead to

assumptions about the role of the deformations of the coordination sphere alone [178, 190, 191].

The present chapter is devoted to the structural, magnetic and Mössbauer spectroscopic studies of the isomorphous and isostructural complexes **1** and **1-Zn** formed by tris[3-aza-4-(6-methyl-2-pyridyl)but-3-enyl]amine [*tren*(6-*Mepy*)$_3$] and perchlorate anions (Figure 19).
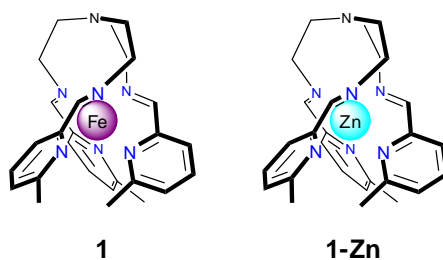


**Figure 19.** Schematic molecular structures of **1** and **1-Zn**. Perchlorate anions are not shown.

### 2.2.2 Variable-temperature X-ray single crystal diffraction of 1 and 1-Zn

The single crystal X-ray experiments for **1** were performed at different temperatures: 80 K, 130 K, 150 K, 170 K, 190 K, 210 K, 230 K, 250 K, 270 K, 290 K, 310 K and 330 K. For the measurements a dark red small single crystal (0.10 × 0.29 × 0.43 mm$^3$) of good quality was pre-selected under a polarization microscope. For comparison the measurements of **1-Zn** compound were performed at ten different temperatures: 80 K, 130 K, 170 K, 210 K, 230 K, 250 K, 270 K, 290 K, 310 K and 330 K. For these measurements a yellow small single crystal (0.12 × 0.26 × 0.32 mm$^3$) of good quality was chosen. Crystallographic, experimental and computational details are collected in Table 2 and Table 3.

Both samples are monoclinic and retained at all measured temperatures the space group $P2_1/c$. The molecular structures of **1** (C$_{27}$H$_{33}$Cl$_2$FeN$_7$O$_8$, $M_w$ = 710.35 g mol$^{-1}$) and **1-Zn** (ZnC$_{27}$H$_{33}$Cl$_2$N$_7$O$_8$, $M_w$ = 719.87 g mol$^{-1}$) together with the numbering scheme are presented in Figure 20a–d. Each iron and zinc atoms adopt a pseudo-octahedral symmetry and are surrounded by six nitrogen atoms belonging to imino groups and pyridine moieties of the trifurcated ligand [*tren*(6-*Mepy*)$_3$]. It can be noticed that the complex molecules are chiral and that each cell contains two molecules of opposite chirality ($Z$ = 4), both are equivalent by the *c* glide plane.

The volume of the unit cell increases by heating from 80 K up to 330 K. On the other hand, while the cell parameters *a*, *b* and *c* increase as well the behavior of the *β* value

for both compounds has a complicate character. The bond lengths M–N and cell parameters related to **1** and **1-Zn** are compared in Figure 22 and Figure 23 and listed in Table 2, Table 3 and Table 4.



a



b
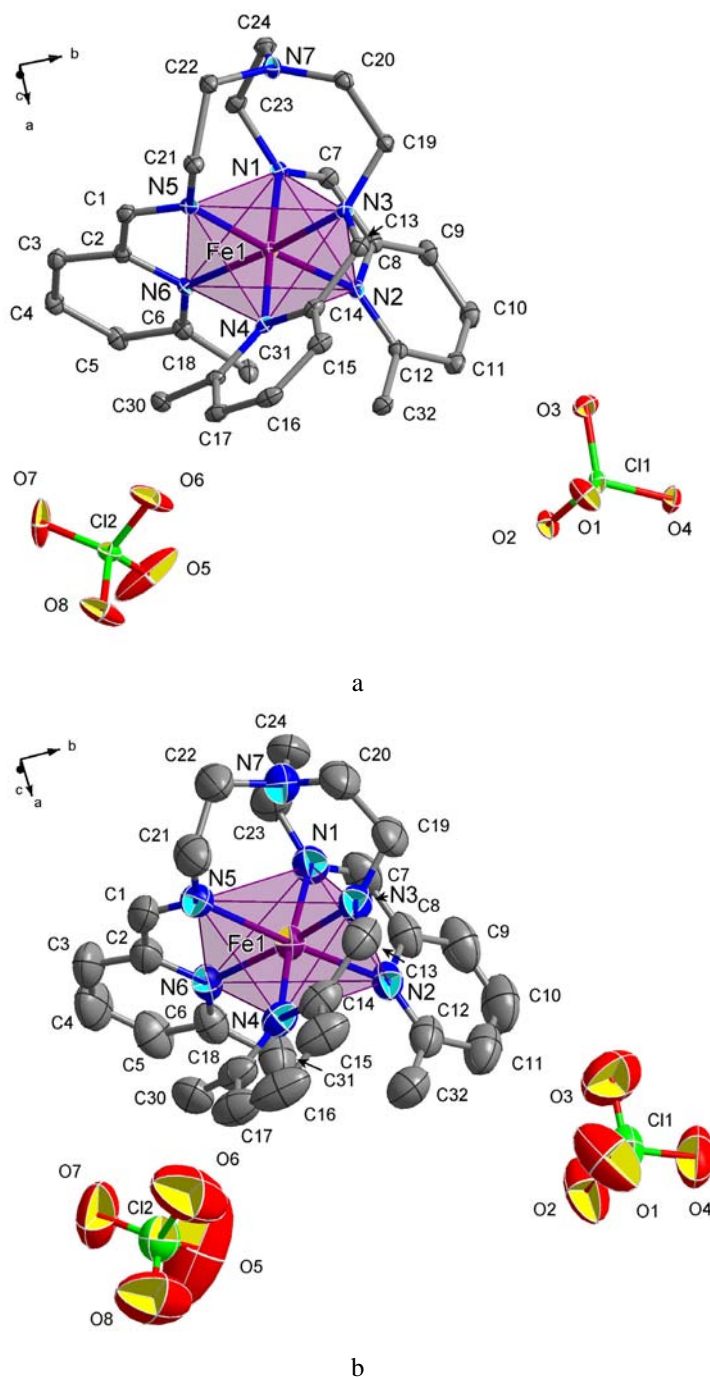
**Figure 20.** The molecular structure of **1** at 80 K (a) and at 330 K (b). The molecular structure of **1-Zn** at 80 K (c) and at 330 K (d). Displacement ellipsoids are drawn at the 50 % probability level.

c



d
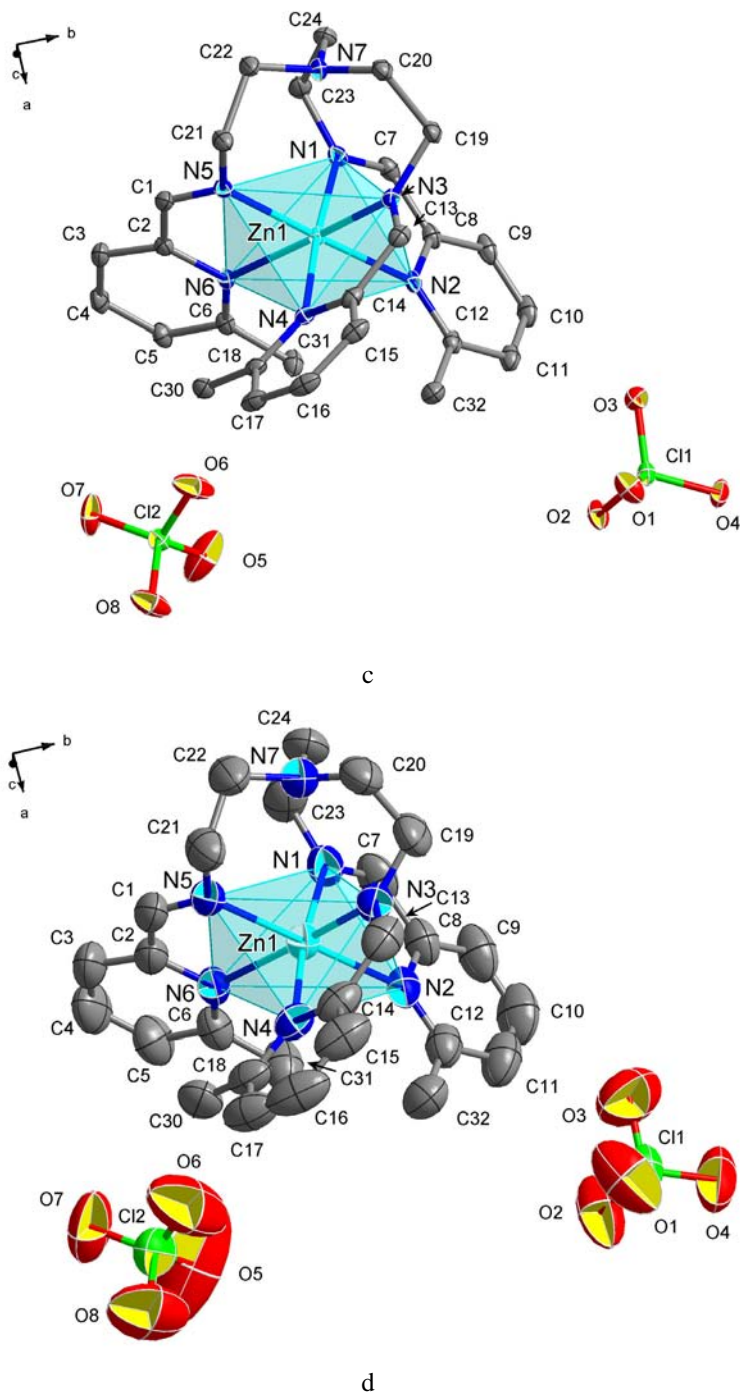
**Figure 20.** (*continued*)

**Table 2.** Crystallographic data and refinement details for **1**.

| $T$ [K] | 80 | 130 | 150 | 170 | 190 | 210 | 230 | 250 | 270 | 290 | 310 | 330 |
|---|---|---|---|---|---|---|---|---|---|---|---|---|
| $a$ [Å] | 10.1545 (3) | 10.1834 (3) | 10.1952 (4) | 10.2122 (3) | 10.2327 (4) | 10.2747 (4) | 10.3663 (4) | 10.4678 (4) | 10.5290 (4) | 10.5677 (5) | 10.6005 (7) | 10.6286 (7) |
| $b$ [Å] | 19.0923 (6) | 19.0720 (5) | 19.0901 (7) | 19.1179 (6) | 19.1464 (7) | 19.2019 (6) | 19.2603 (6) | 19.3228 (7) | 19.3683 (7) | 19.4022 (7) | 19.4289 (11) | 19.4535 (11) |
| $c$ [Å] | 15.0033 (5) | 15.0304 (4) | 15.0429 (6) | 15.0573 (5) | 15.0753 (6) | 15.1011 (5) | 15.1373 (5) | 15.1695 (6) | 15.1933 (6) | 15.2137 (6) | 15.2382 (10) | 15.2589 (10) |
| $\beta$ [°] | 91.566 (3) | 91.467 (3) | 91.451 (4) | 91.420 (3) | 91.402 (4) | 91.399 (3) | 91.432 (3) | 91.501 (3) | 91.541 (3) | 91.564 (4) | 91.595 (6) | 91.626 (6) |
| Volume [Å³] | 2907.65 (16) | 2918.21 (14) | 2926.8 (2) | 2938.82 (16) | 2952.7 (2) | 2978.46 (18) | 3021.34 (18) | 3067.2 (2) | 3097.2 (2) | 3118.2 (2) | 3137.2 (3) | 3153.7 (3) |
| $\rho$ [g cm⁻³] | 1.623 | 1.617 | 1.612 | 1.606 | 1.598 | 1.584 | 1.562 | 1.538 | 1.523 | 1.513 | 1.504 | 1.496 |
| Absorption coefficient [mm⁻¹] | 0.77 | 0.76 | 0.76 | 0.76 | 0.76 | 0.75 | 0.74 | 0.73 | 0.72 | 0.72 | 0.71 | 0.71 |
| $F(000)$ | 1472 | 1472 | 1472 | 1472 | 1472 | 1472 | 1472 | 1472 | 1472 | 1472 | 1472 | 1472 |
| $\theta$ range for data collection [°] | 2.92 to 32.76 | 2.93 to 32.84 | 2.91 to 32.84 | 2.92 to 32.90 | 2.91 to 32.90 | 2.90 to 32.90 | 2.89 to 32.84 | 2.87 to 32.82 | 2.86 to 32.82 | 3.13 to 32.79 | 2.87 to 32.82 | 2.87 to 32.77 |
| Index ranges | $-14 \leq h \leq 15$ $-28 \leq k \leq 19$ $-20 \leq l \leq 22$ | $-15 \leq h \leq 15$ $-28 \leq k \leq 21$ $-22 \leq l \leq 21$ | $-15 \leq h \leq 14$ $-29 \leq k \leq 21$ $-22 \leq l \leq 20$ | $-15 \leq h \leq 15$ $-28 \leq k \leq 21$ $-22 \leq l \leq 21$ | $-14 \leq h \leq 15$ $-29 \leq k \leq 19$ $-20 \leq l \leq 22$ | $-15 \leq h \leq 15$ $-28 \leq k \leq 21$ $-22 \leq l \leq 21$ | $-15 \leq h \leq 15$ $-28 \leq k \leq 21$ $-22 \leq l \leq 21$ | $-15 \leq h \leq 15$ $-29 \leq k \leq 21$ $-22 \leq l \leq 21$ | $-15 \leq h \leq 15$ $-29 \leq k \leq 21$ $-22 \leq l \leq 22$ | $-15 \leq h \leq 15$ $-29 \leq k \leq 21$ $-22 \leq l \leq 22$ | $-15 \leq h \leq 15$ $-29 \leq k \leq 20$ $-22 \leq l \leq 20$ | $-15 \leq h \leq 15$ $-29 \leq k \leq 20$ $-22 \leq l \leq 20$ |
| Reflections collected | 27924 | 28510 | 27839 | 28521 | 27639 | 28574 | 28711 | 29034 | 29143 | 29041 | 27567 | 27325 |
| Independent reflections | 9683 [$R_{int}$ = 0.0187] | 9866 [$R_{int}$ = 0.0191] | 9709 [$R_{int}$ = 0.0190] | 9889 [$R_{int}$ = 0.0199] | 9686 [$R_{int}$ = 0.0187] | 9941 [$R_{int}$ = 0.0198] | 10014 [$R_{int}$ = 0.0204] | 10160 [$R_{int}$ = 0.0206] | 10242 [$R_{int}$ = 0.0206] | 10248 [$R_{int}$ = 0.0206] | 9909 [$R_{int}$ = 0.0217] | 9826 [$R_{int}$ = 0.0213] |
| Data/restraints/ parameters | 9683/0/409 | 9866/0/409 | 9709/0/409 | 9889/0/409 | 9686/0/409 | 9941/0/409 | 10014/0/409 | 10160/0/409 | 10242/0/409 | 10248/0/409 | 9909/0/409 | 9826/0/409 |
| Goodness-of-fit, $F^2$ | 1.006 | 1.003 | 1.007 | 1.005 | 0.999 | 1.006 | 1.000 | 1.004 | 1.003 | 1.007 | 1.005 | 1.003 |
| Final $R$ indices [$I > 2\sigma(I)$] | R1 = 0.0327, wR2 = 0.0993 | R1 = 0.0338, wR2 = 0.1032 | R1 = 0.0380, wR2 = 0.1153 | R1 = 0.0398, wR2 = 0.1228 | R1 = 0.0452, wR2 = 0.1433 | R1 = 0.0466, wR2 = 0.1441 | R1 = 0.0467, wR2 = 0.1394 | R1 = 0.0440, wR2 = 0.1252 | R1 = 0.0448, wR2 = 0.1262 | R1 = 0.0467, wR2 = 0.1321 | R1 = 0.0488, wR2 = 0.1407 | R1 = 0.0509, wR2 = 0.1489 |
| $R$ indices (all data) | R1 = 0.0454, wR2 = 0.1042 | R1 = 0.0471, wR2 = 0.1079 | R1 = 0.0569, wR2 = 0.1229 | R1 = 0.0572, wR2 = 0.1301 | R1 = 0.0662, wR2 = 0.1555 | R1 = 0.0711, wR2 = 0.1546 | R1 = 0.0771, wR2 = 0.1494 | R1 = 0.0804, wR2 = 0.1338 | R1 = 0.0859, wR2 = 0.1354 | R1 = 0.0934, wR2 = 0.1417 | R1 = 0.1047, wR2 = 0.1523 | R1 = 0.1073, wR2 = 0.1619 |
| $\rho_{min}$, $\rho_{max}$ [e Å⁻³] | 1.169, −0.922 | 0.962, −0.896 | 1.140, −1.087 | 1.411, −1.274 | 1.572, −1.438 | 1.285, −1.444 | 1.027, −1.162 | 0.893, −0.902 | 0.840, −0.822 | 0.815, −0.831 | 0.874, −0.761 | 0.904, −0.760 |

**Table 3.** Crystallographic data and refinement details for **1-Zn**.

| $T$ [K] | 80 | 130 | 170 | 210 | 230 | 250 | 270 | 290 | 310 | 330 |
|---|---|---|---|---|---|---|---|---|---|---|
| $a$ [Å] | 10.3736 (3) | 10.4189 (3) | 10.4611 (3) | 10.5070 (4) | 10.5321 (4) | 10.5561 (4) | 10.5813 (4) | 10.625 (2) | 10.6308 (5) | 10.6541 (5) |
| $b$ [Å] | 19.1884 (5) | 19.2284 (5) | 19.2701 (6) | 19.3169 (7) | 19.3391 (7) | 19.3641 (7) | 19.3933 (7) | 19.456 (4) | 19.4519 (8) | 19.4812 (8) |
| $c$ [Å] | 15.1122 (4) | 15.1216 (4) | 15.1320 (4) | 15.1467 (6) | 15.1543 (5) | 15.1621 (5) | 15.1756 (5) | 15.220 (3) | 15.2130 (6) | 15.2306 (6) |
| $\beta$ [°] | 91.885 (2) | 91.726 (2) | 91.596 (3) | 91.492 (3) | 91.468 (3) | 91.441 (3) | 91.429 (3) | 91.50 (3) | 91.451 (4) | 91.478 (4) |
| Volume [Å³] | 3006.50 (14) | 3028.07 (14) | 3049.22 (15) | 3073.2 (2) | 3085.64 (19) | 3098.29 (19) | 3113.16 (19) | 3145.2 (11) | 3144.9 (2) | 3160.1 (2) |
| $\rho$ [g cm⁻³] | 1.590 | 1.579 | 1.568 | 1.556 | 1.550 | 1.543 | 1.536 | 1.520 | 1.520 | 1.513 |
| Absorption coefficient [mm⁻¹] | 1.06 | 1.05 | 1.04 | 1.03 | 1.03 | 1.03 | 1.02 | 1.01 | 1.01 | 1.01 |
| $F(000)$ | 1488 | 1488 | 1488 | 1488 | 1488 | 1488 | 1488 | 1488 | 1488 | 1488 |
| $\theta$ range for data collection [°] | 2.89 to 32.86 | 2.88 to 32.89 | 2.87 to 32.97 | 2.87 to 32.92 | 2.86 to 32.90 | 2.86 to 32.88 | 2.85 to 32.96 | 2.84 to 32.85 | 2.84 to 32.93 | 2.83 to 32.94 |
| Index ranges | $-15 \leq h \leq 15$ $-27 \leq k \leq 28$ $-13 \leq l \leq 22$ | $-15 \leq h \leq 15$ $-27 \leq k \leq 28$ $-12 \leq l \leq 22$ | $-15 \leq h \leq 15$ $-27 \leq k \leq 28$ $-12 \leq l \leq 22$ | $-15 \leq h \leq 15$ $-27 \leq k \leq 28$ $-13 \leq l \leq 22$ | $-15 \leq h \leq 15$ $-28 \leq k \leq 28$ $-13 \leq l \leq 22$ | $-15 \leq h \leq 15$ $-28 \leq k \leq 28$ $-12 \leq l \leq 22$ | $-15 \leq h \leq 15$ $-28 \leq k \leq 28$ $-12 \leq l \leq 23$ | $-15 \leq h \leq 15$ $-28 \leq k \leq 29$ $-12 \leq l \leq 23$ | $-15 \leq h \leq 15$ $-28 \leq k \leq 29$ $-12 \leq l \leq 23$ | $-15 \leq h \leq 15$ $-28 \leq k \leq 29$ $-13 \leq l \leq 23$ |
| Reflections collected | 29446 | 29476 | 29485 | 29488 | 29403 | 29330 | 29239 | 29203 | 29149 | 29045 |
| Independent reflections | 10191 [$R_{int} = 0.0224$] | 10213 [$R_{int} = 0.0225$] | 10256 [$R_{int} = 0.0235$] | 10298 [$R_{int} = 0.0239$] | 10304 [$R_{int} = 0.0239$] | 10295 [$R_{int} = 0.0248$] | 10314 [$R_{int} = 0.0252$] | 10329 [$R_{int} = 0.0255$] | 10367 [$R_{int} = 0.0266$] | 10348 [$R_{int} = 0.0270$] |
| Data/restraints/ parameters | 10191/0/409 | 10213/0/409 | 10256/0/409 | 10298/0/409 | 10304/0/409 | 10295/0/409 | 10314/0/409 | 10329/0/409 | 10367/0/409 | 10348/0/409 |
| Goodness-of-fit, $F^2$ | 1.001 | 1.000 | 1.005 | 1.001 | 1.000 | 1.000 | 1.009 | 1.001 | 1.004 | 1.021 |
| Final $R$ indices [$I > 2\sigma(I)$] | $R1 = 0.0271$, $wR2 = 0.0731$ | $R1 = 0.0290$, $wR2 = 0.0758$ | $R1 = 0.0313$, $wR2 = 0.0796$ | $R1 = 0.0338$, $wR2 = 0.0863$ | $R1 = 0.0367$, $wR2 = 0.944$ | $R1 = 0.0381$, $wR2 = 0.0991$ | $R1 = 0.0406$, $wR2 = 0.1071$ | $R1 = 0.0424$, $wR2 = 0.1145$ | $R1 = 0.0447$, $wR2 = 0.1199$ | $R1 = 0.0466$, $wR2 = 0.1258$ |
| $R$ indices (all data) | $R1 = 0.0389$, $wR2 = 0.0754$ | $R1 = 0.0458$, $wR2 = 0.0787$ | $R1 = 0.0533$, $wR2 = 0.0831$ | $R1 = 0.0627$, $wR2 = 0.0904$ | $R1 = 0.0701$, $wR2 = 0.995$ | $R1 = 0.0768$, $wR2 = 0.1045$ | $R1 = 0.0860$, $wR2 = 0.1136$ | $R1 = 0.0933$, $wR2 = 0.1220$ | $R1 = 0.1027$, $wR2 = 0.1274$ | $R1 = 0.1131$, $wR2 = 0.1335$ |
| $\rho_{min}, \rho_{max}$ [e Å⁻³] | 0.820, −0.582 | 0.720, −0.577 | 0.655, −0.508 | 0.695, −0.533 | 0.738, −0.582 | 0.797, −0.600 | 0.844, −0.575 | 0.866, −0.600 | 0.901, −0.566 | 0.926, −0.540 |

**Table 4.** Intramolecular parameters of **1** and **1-Zn** at different temperatures.

| $T$ [K] | $\langle$Fe–N$\rangle$ [Å] | $\langle$Zn–N$\rangle$ [Å] | $\langle$C=N$\rangle$, **1** [Å] | $\langle$C=N$\rangle$, **1-Zn** [Å] | Fe$\cdots$N7 [Å] | Zn$\cdots$N7 [Å] | $\Sigma$, **1** [°] | $\Sigma$, **1-Zn** [°] | $\theta$, **1** [°] | $\theta$, **1-Zn** [°] |
|---|---|---|---|---|---|---|---|---|---|---|
| 80 | 2.013(1) | 2.210(1) | 1.285(2) | 1.270(2) | 3.572(1) | 3.215(1) | 83.82(51) | 104.12(48) | 57.22(5) | 52.48(4) |
| 130 | 2.013(1) | 2.211(1) | 1.282(2) | 1.268(2) | 3.567(1) | 3.207(1) | 83.29(55) | 104.39(49) | 57.24(5) | 52.35(5) |
| 150 | 2.015(1) | – | 1.281(2) | – | 3.564(2) | – | 83.59(63) | – | 57.21(6) | – |
| 170 | 2.015(1) | 2.213(1) | 1.280(2) | 1.264(2) | 3.559(2) | 3.200(2) | 84.03(67) | 104.94(53) | 57.16(6) | 52.20(5) |
| 190 | 2.018(2) | – | 1.280(3) | – | 3.551(2) | – | 84.67(74) | – | 57.04(7) | – |
| 210 | 2.035(2) | 2.215(1) | 1.279(3) | 1.261(2) | 3.525(2) | 3.191(2) | 86.81(83) | 105.27(59) | 56.64(8) | 52.05(6) |
| 230 | 2.090(2) | 2.215(1) | 1.268(3) | 1.260(3) | 3.418(3) | 3.187(2) | 93.71(87) | 105.46(65) | 55.08(8) | 51.98(6) |
| 250 | 2.158(2) | 2.216(1) | 1.264(3) | 1.257(3) | 3.293(2) | 3.184(2) | 102.09(78) | 105.81(70) | 53.37(8) | 51.94(6) |
| 270 | 2.189(2) | 2.217(2) | 1.263(3) | 1.255(3) | 3.246(2) | 3.179(2) | 106.83(78) | 106.25(77) | 52.59(7) | 51.91(7) |
| 290 | 2.203(2) | 2.223(2) | 1.260(3) | 1.255(8) | 3.224(3) | 3.180(12) | 108.79(84) | 106.72(86) | 52.30(7) | 51.83(8) |
| 310 | 2.211(2) | 2.219(2) | 1.258(3) | 1.251(4) | 3.216(4) | 3.168(3) | 109.99(90) | 107.34(88) | 52.15(8) | 51.75(8) |
| 330 | 2.216(2) | 2.221(2) | 1.257(4) | 1.248(4) | 3.210(3) | 3.166(3) | 110.98(97) | 107.72(94) | 52.14(9) | 51.70(9) |
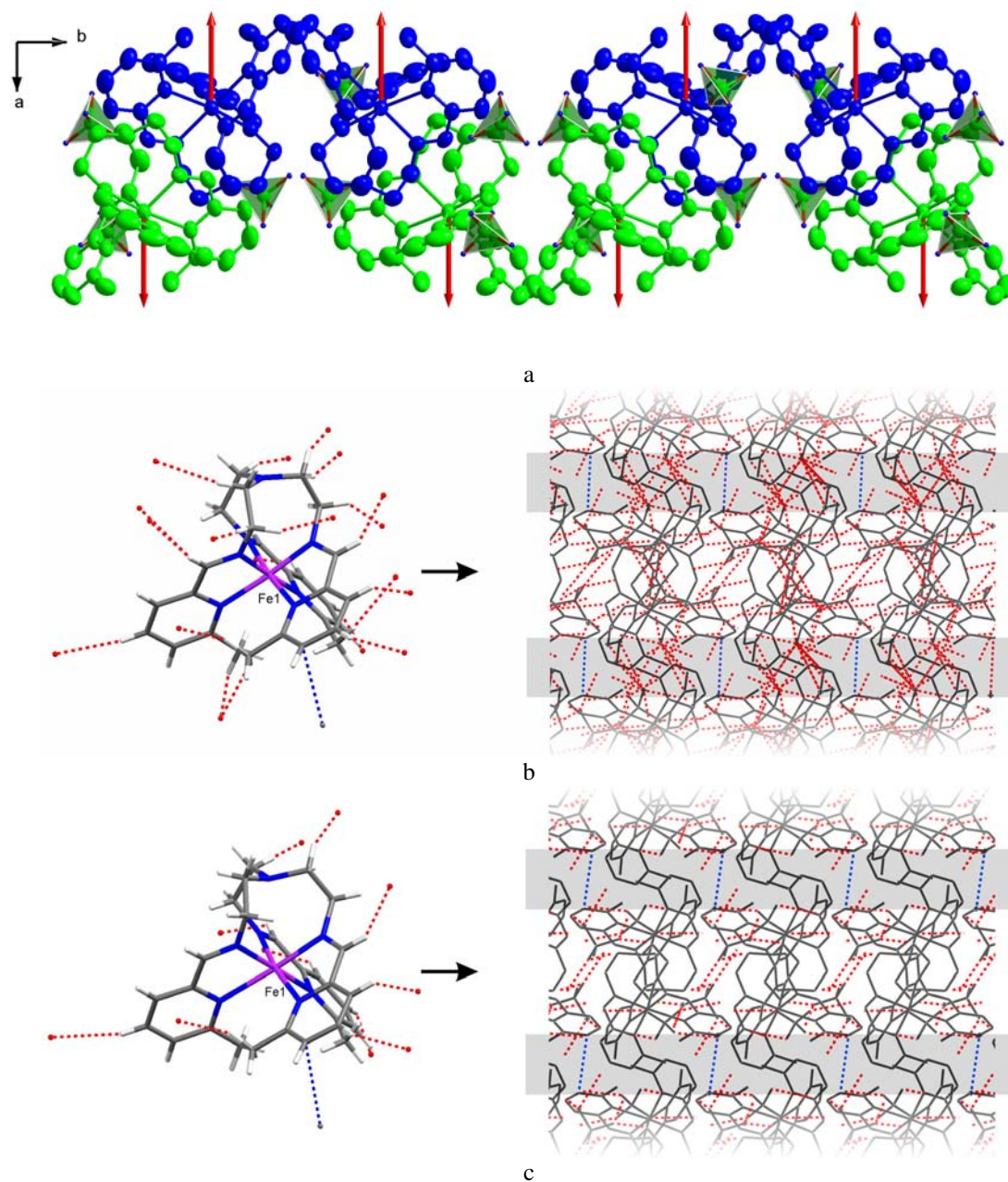
**Figure 21.** a) A bilayer composed of oppositely directed complex molecules {Fe[*tren*(6-*Mepy*)]}²⁺
and perchlorate anions (tetrahedra) residing in the voids. Red arrows show an approximate direction of the
vectors through N7···Fe1; b) On the left is projection of the complex cation of **1** (low-spin, 80 K) and on the
right projection of the crystal structure along the direction *b* both emphasizing the intermolecular interactions
and c) the same for **1** (high-spin, 330 K). In the projection of the crystal packing hydrogen atoms are omitted for
simplicity, complex molecules and anions are shaded grey whereas red dashed lines correspond to CH···O
hydrogen bonds, blue dashed lines correspond to π-π contacts of pyridine rings. Shaded areas highlight inter-
bilayer space with intermolecular contacts.

**Low-spin crystal structure of 1 (80 K).** A pseudo-octahedral environment of the
iron(II) ion is shaped by nitrogen atoms belonging to two different groups. Three of them in
the upper part (see projection shown in Figure 20a) belong to the imino groups of the tripodal

arms and form shorter bonds than the other three on the bottom, which belong to pyridine rings. The average distances for both types of the contacts differ by 0.13 Å and <Fe–N> is 2.013(1) Å. The tertiary amine nitrogen atom N7 is not coordinated, the Fe···N7 distance being 3.572(1) Å. Interestingly, the geometry around this nitrogen atom is almost planar, similar to cases reported earlier for the low-spin complexes of similar structure [153, 160]. Another characteristic distance is that of the methyl group and the nearest nitrogen atom of the neighboring pyridine ring. The value averaged over three separations is 3.013(3) Å. The trigonal distortion of the iron(II) octahedron can be quantitatively estimated by two characteristic values. The first is that of the twist angle $\theta$ which reflects the rotation of a triangular face of the octahedron relatively to the opposite one [104]. For **1** two faces composed by similar imino and pyridine nitrogen atoms were selected. Averaging over three angles gave a value of 57.22(5)° which is rather close to that of perfect $O_h$ symmetry (60°). Note, in the low-spin analogue lacking methyl substituents {Fe[*tren(py)*$_3$]}(ClO$_4$)$_2$ (**B**) [160] this angle approaches a value of 53.86(6)°. Another characteristic value $\Sigma$ represents octahedron distortion defined as the sum of deviations from 90° of the 12 *cis*-N–Fe–N angles in the coordination sphere $\Sigma_{i=1}^{12}(|\phi_i - 90|)$ [192]. In **1** at 80 K $\Sigma$ is equal to 83.52(51)°, and for the unmethylated analogue at 100 K it is 61.37(5)°, while for the perfect octahedron it is 0°.

The molecular packing in **1** at 80 K can be described as a set of bilayers composed of oppositely directed complex cations where voids are occupied by ClO$_4^-$ anions. The bilayers extend in the *bc* plane. Most of the numerous CH···O contacts are detected between the complex cations and the perchlorate anions within these bilayers. The first type of the contacts involves the CH$_2$ groups of the triamine part, the second comprises the CH moiety of an imine group with the separations CH···O for both types of contacts falling within 2.423(1)–2.707(1) Å. There is a π–π interaction between pyridine cycles of complex molecules belonging to adjacent bilayers [3.327(2) Å] (Figure 21b, c).

**High-spin crystal structure of 1 (330 K).** The structure of **1** determined at 330 K is quite similar to that at 80 K. There are, however, several principal changes. First of all, large thermal coefficients associated with the oxygen atoms of the perchlorate anions reflect partial delocalization (Figure 20b). This feature already indicates that these anions are not maintained by significant molecular contacts within the crystal lattice.

In general, a change of the spin state affects mostly the geometry of the FeN$_6$ core. The Fe–N bonds average [2.216(2) Å] in the high-spin state is about 0.2 Å longer than that in the low-spin state, which corresponds to 10 % of their initial value (Table 4, Figure 22). This result is typical for iron(II)-based complexes [41, 193]. The decrease of the length observed

for the bonds of iron with nitrogen atoms of pyridine units is larger than that of the bonds with imine groups, which is opposite to results observed earlier in similar compounds [177]. A reason for this might be the influence of the methyl groups of pyridines which create repulsion between pyridine pendants [41]. The distances between methyl substituents and the closest nitrogen atoms of the adjacent heterocyclic ring increase upon heating; in the high-spin species it is 0.2 Å longer than in the low-spin species. The octahedron becomes more irregular in the high-spin state as probed by the angular distortion $\theta$ and the parameter $\Sigma$ which are found to be 52.14(9)° and 110.98(97)°, respectively, *i.e.* the distortion of the $FeN_6$ core follows the spin-transition of the iron(II) ion and it is more distorted in the high-spin state than in the low-spin state. The same conclusion about the distortion of the coordination sphere is inferred from the twist angle $\theta$.
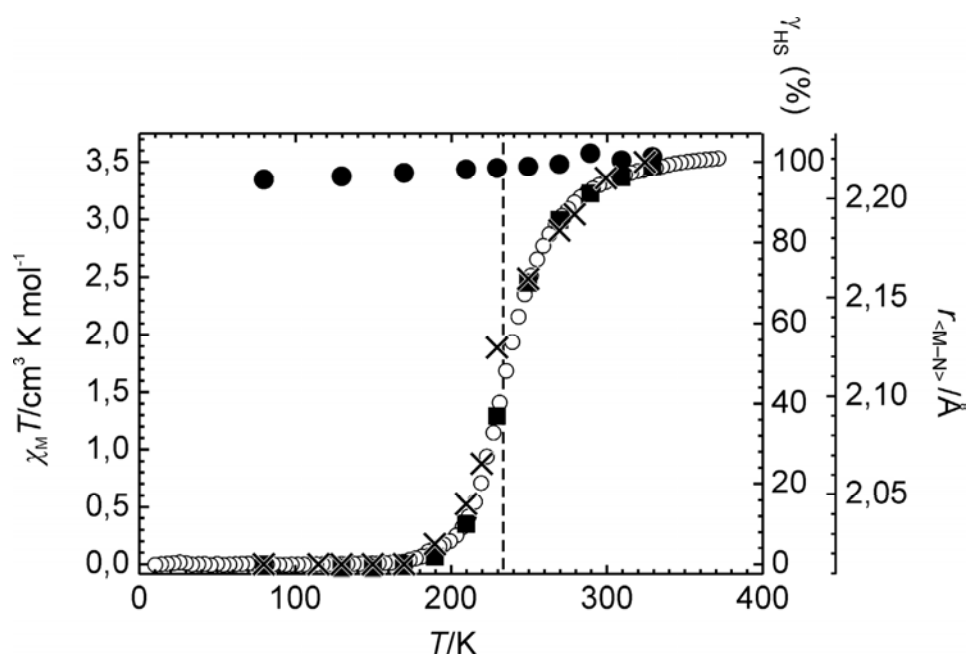


**Figure 22.** Plot of $\chi_M T$ *vs* $T$ for **1** (○) and concomitant variation of the M–N distances for **1** (■) and **1-Zn** (●). $\gamma_{HS}$ value (×) is the molar fraction of high-spin molecules derived from the Mössbauer experiment. The transition temperature $T_{1/2} = 233$ K is marked by the vertical dashed line.

Although the character of the packing in the low-spin and high-spin structures is almost identical, upon spin-crossover the range of CH···O contacts converges to 2.489(2)–2.709(2) Å and a $\pi$–$\pi$ contact somewhat elongates [3.372(2) Å].
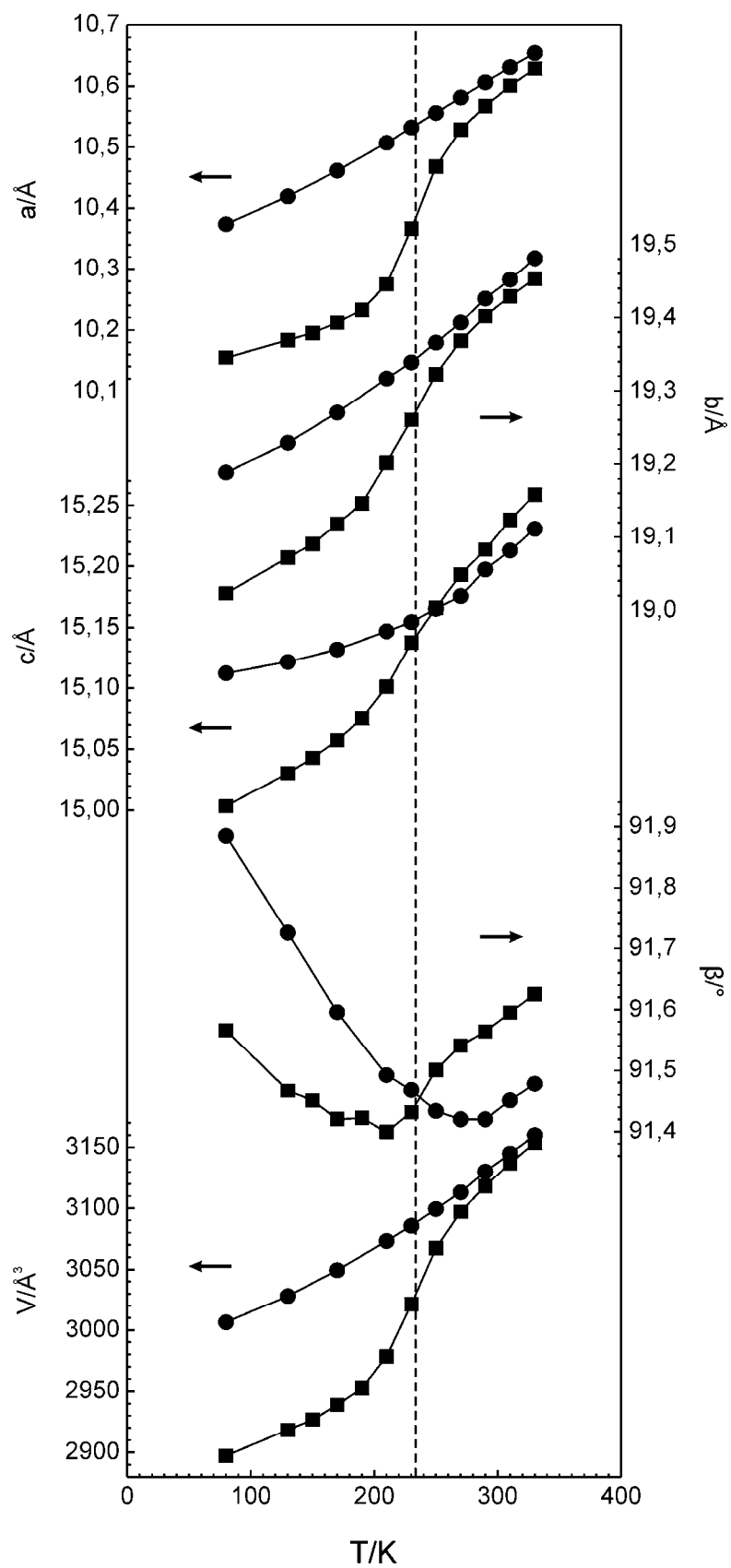
**Figure 23**. Temperature dependence of the cell parameters for **1** (■) and **1-Zn** (●). The transition temperature $T_{1/2}$ = 233 K is marked by the vertical dashed line. Error bars are smaller than the symbols on the graph.
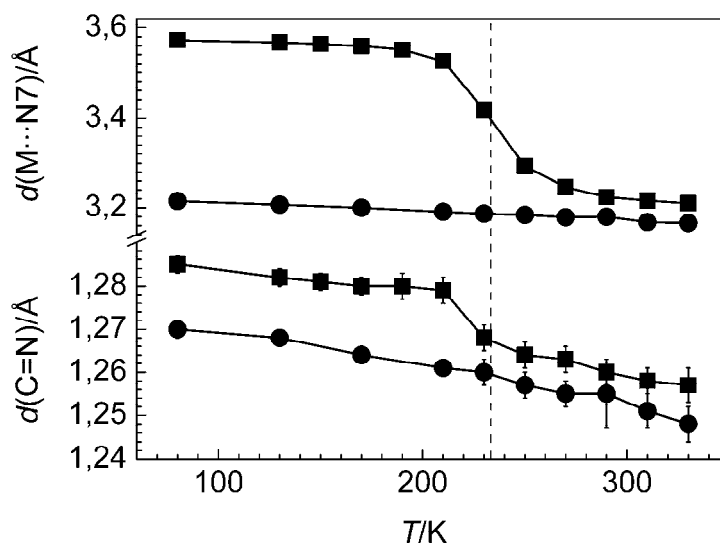
**Figure 24**. Variation of the M···N7 distance and of the C=N bond length with temperature in **1** (■) and **1-Zn** (●). The transition temperature $T_{1/2}$ = 233 K is marked by the vertical dashed line. On the upper graph, error bars are smaller than the symbols.

**Crystal structure of 1-Zn.** In contrast to **1** and as expected, the structures of the zinc complex at low and high temperatures are similar. They repeat structural features of the high-spin structure of **1**. Projections of both are presented in Figure 20c, d. The changes of the unit cell parameters (Figure 23) and of the intramolecular distances have monotonic character (Figure 22 and Figure 24). The parameters $\theta$ and $\Sigma$ at 80 K are found to be 52.48(4)° and 104.12(48)°, respectively, while at 330 K they are 51.70(9)° and 107.72(94)° (see Table 4). The crystal packing of **1-Zn** is observed to be similar to **1** both in the high-spin and the low-spin states with intermolecular CH···O contacts at 330 K embracing a range of 2.479(5)–2.706(5) Å [2.449(1)–2.678(1) Å at 80 K] and the π–π contact being 3.364(3) Å [3.201(1) Å at 80 K].

The spin-crossover in **1** modifies not only the bond lengths of the coordination shell but also the distance Fe···N7 (Figure 24). This distance is 3.210(3) Å in the high-spin state and clearly higher than 2.80 Å, which is the sum of the covalent radius of iron (1.25 Å) and the van der Waals radius of nitrogen (1.55 Å), hence indicating the absence of a possible bonding. Nevertheless, this nonbonding distance between ternary amine and central atom decreases by about 0.35 Å as the temperature increases from 80 up to 330 K. As discussed in literature [156, 194] this might be attributed to the different repulsive interactions between the $d$-electrons of the iron ion and the lone pair of electrons of the N7 nitrogen atom. Depending on the number of electrons occupying the $t_{2g}$ level, which differs in the low-spin and high-spin states, the

apical nitrogen N7 might be more or less repelled from the central atom. According to this explanation it is, however, difficult to understand why in **1-Zn** with six $t_{2g}$ electrons the distance Zn⋯N7 is even shorter than in **1** in the high-spin state with only four $t_{2g}$ electrons (Figure 24). To our opinion the variation of this distance comes from the variation of the length Fe–N$^{im}$ as a consequence of spin-crossover. Because of the relatively rigid backbone of the *tren* moiety, the rather flexible geometry around N7 is modified (distorted-$sp^3$ to almost-$sp^2$) and thus its distance to the central atom. This allows to avoid a congestion of nitrogens atoms around the small low-spin iron(II) ion. A structural investigation of the [*tren*(*py*)$_3$]-based complexes of $3d$ metals confirms this suggestion (Cambridge Structural Data Base [42]). There is a clear linear dependence of the $M^{II,III}$⋯N7 distance on the length of the bond $M^{II,III}$–N$^{im}$ and absence of an obvious dependence on the number of the $t_{2g}$ electrons (Figure 25).
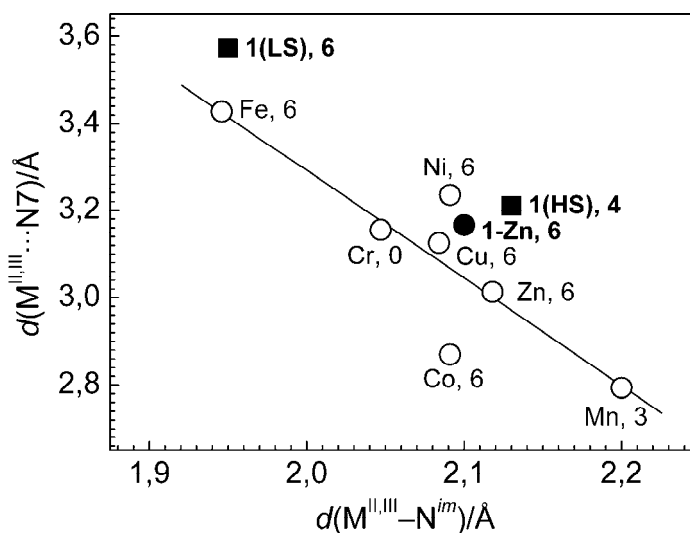


**Figure 25**. Dependence of the $M^{II,III}$⋯N7 distance on the $M^{II,III}$–N$^{im}$ length. The metal ions and (after the comma) number of $t_{2g}$ electrons are shown next to the corresponding point. From a Cambridge Structural Data Base investigation [42].

Monitoring of the imino C=N lengths, groups which directly interact with orbitals of the central atoms, shows significant change in temperature which coincides with spin-crossover (Figure 24). On heating, such a change of the C=N distance is not detected in **1-Zn**, but as expected, only a change with monotonic character. This anomaly in the length of C=N bond in **1** is consistent with increasing strength of back-bonding between the low-spin iron(II) and the ligand. Transfer of electron density from the $t_{2g}^6$-subset of low-spin iron(II) to the ligand places electron density in the π*-orbitals of the imine functionality, which results in an increase in this bond distance as observed in the present data. An investigation of the

structural parameters of the analogous unmethylated complex, for which low and high temperature data has been published, reveals minor shortening of the C=N bond length as well. For **B** this value is 1.287(2) Å at 100 K and goes down to 1.275(3) Å at 298 K [160].

Modifications of the coordination sphere of **1** due to spin-transition are directly reflected on the conformation of the ligand, which is illustrated by the distinguishable divergence of the overlapped high-spin and low-spin structures (Figure 26a). The overlapped low-temperature and high-temperature complex molecules of the zinc analogue are also shown for comparison (Figure 26b).



a                                                          b
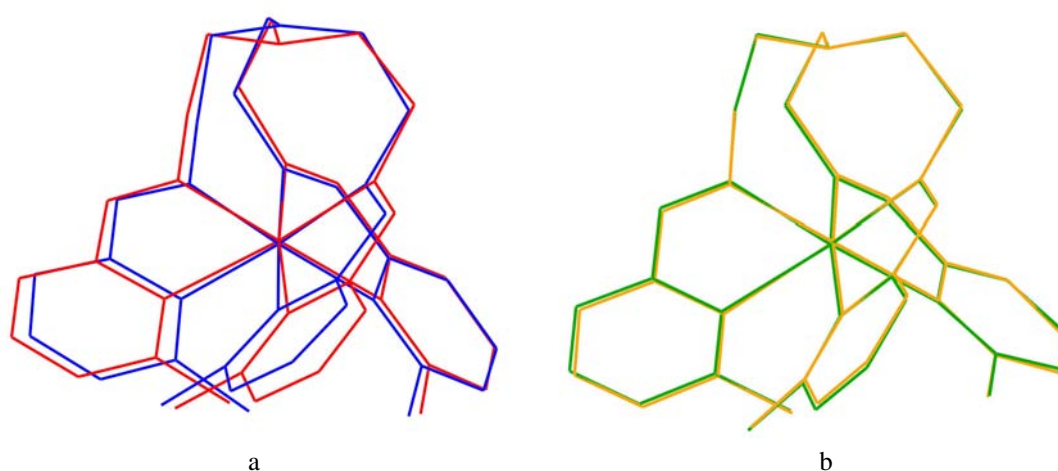
**Figure 26**. a) Projection of the minimized overlay of the cation **1** in low-spin state at 80 K (blue) and in high-spin state at 330 K (red); b) Projection of the minimized overlay of the **1-Zn** cation at 80 K (orange) and at 330 K (green).

The temperature dependence of the cell parameters of **1** reveals that the largest change, 4.7 %, is undergone by the *a* axis, which is almost collinear with the pseudo-$C_3$ axis of the complex cations. The changes in the *b* and *c* axes are smaller (being 1.8 and 1.3 % respectively) on increase in temperature to 330 K. Changes of the coordination sphere arising from spin-transition are the driving force of the changes in the unit cell which is clearly seen by comparing analogous parameters for the iron and zinc compounds. The variation of the Fe–N bond upon spin-transition is reflected on the behavior of the cell parameters, whereas parameters of the zinc compound have monotonic character (Figure 23). After correction of the total volume change by the effect of thermal expansion the value of the volume change attributed only to the spin-transition in **1** is equal to ~3.5 %, which is typical for iron(II) compounds [41, 195]. The variation of the unit cell volume with temperature recalculated per

iron atom, shows a change of $\Delta V = 27.16$ Å$^3$ during the spin-crossover process while for other spin-crossover systems of iron(II) this value is about 25 Å$^3$ [41, 195-198].

### 2.2.3 UV/VIS spectroscopy

The UV/VIS spectrum of **1** has been measured in acetonitrile solution (Figure 27). It consists of one weak band attributed to $^5T_2 \rightarrow {}^5E$ transition (720 nm) and two intensive bands, a MLCT band (492 nm) and a $\pi$–$\pi$* absorption band of the organic ligand (250 nm), respectively. The ligand field strength $10Dq^{HS}$ can be determined from the maximum of the obscured spin-allowed $^5T_2 \rightarrow {}^5E$ $d$–$d$ transition [72] being 13 800 cm$^{-1}$. This $10Dq$ value is at the upper limit expected for iron(II) complexes [199], however has a precedent [200]. Due to an intensive MLCT band, $10Dq^{LS}$ cannot be directly determined from the UV/VIS spectrum of the low-spin complex of the tris(diimino) type [174]. It is possible, however, to evaluate an approximate value of the splitting parameter from the dependence of $10Dq$ on the variation of the distance Fe–N deduced from the X-ray crystal data [21]. Solving the Equation (1) (Chapter 1.3.1) with <Fe–N>$^{HS}$ and <Fe–N>$^{LS}$ parameters derived from the crystal data, $10Dq^{LS}$ is estimated as 24 000 cm$^{-1}$.
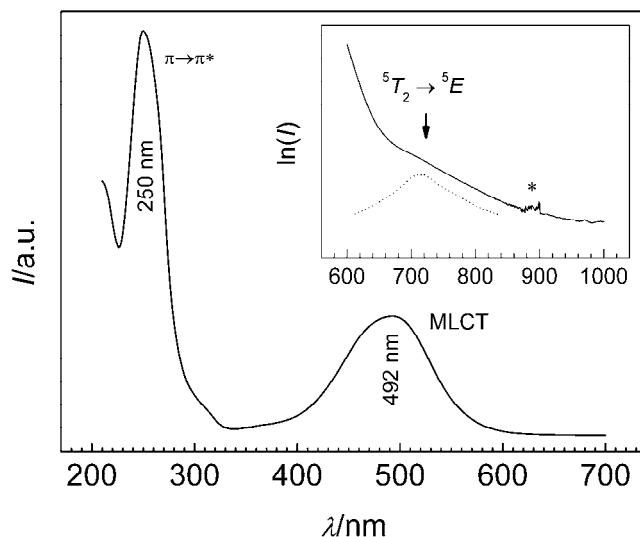


**Figure 27**. UV/VIS spectrum of **1** at room temperature in acetonitrile solution. * – an artifact due to the mirror switch.

### 2.2.4   Magnetic properties of 1

The magnetic behavior of **1** is shown in Figure 22 in the form of the $\chi_M T$ *vs* $T$ plot. At 300 K, the $\chi_M T$ value is 3.32 cm$^3$ K mol$^{-1}$ which is consistent with an high-spin configuration of the iron(II) ions. Upon cooling, the $\chi_M T$ value decreases gradually down to 160 K. The $\chi_M T$ value at 80 K corresponds to a diamagnetic signal confirming complete transformation into the low-spin state. The inversion temperature, $T_{1/2}$, where the molar fractions of low-spin and high-spin sites are both equal to 0.5, was found to be 233 K. This value is slightly higher than that of the PF$_6^-$ salt where $T_{1/2}$ is 214 K [142, 193]. The transition does not show hysteresis since the $\chi_M T$ *vs* $T$ curves recorded at decreasing and increasing temperatures are identical. Also, upon irradiation with a green laser at 4 K (514 nm, 25 mW/cm$^2$), **1** does not show LIESST effect similarly to the PF$_6^-$ analogue, which is expected due to the relatively high spin-transition temperature $T_{1/2}$ [21, 201].

The least squares fitting of the magnetic curve was simulated using Equation (13) (Chapter 1.3.5) which leads to $\Delta H^{SCO}$ = 11.5 kJ mol$^{-1}$, $\Delta S^{SCO}$ = 49 J K$^{-1}$ mol$^{-1}$, and $\Gamma$ = 2.8 kJ mol$^{-1}$. According to the classification given by comparison with $2RT_{1/2}$ the spin-transition can be considered as being moderately cooperative [3, 113].

### 2.2.5   Mössbauer spectroscopy study of 1

Mössbauer spectra of **1** were recorded as a function of temperature from 80 K up to 325 K. They are displayed in Figure 28, detailed values of the Mössbauer parameters deduced from least-square fitting procedures are listed in Table 5. At 80 K, the spectrum consists of an asymmetrical doublet indicating iron(II) ions in low-spin state. A small bump observed in the low temperature spectra refer to a component of the high-spin fraction. As the corresponding doublet was evaluated to be about 1 % in area fraction, it was neglected in the final fitting procedure. Upon heating, an additional doublet characteristic of the high-spin state of iron(II) ions appears at *ca*. 190 K (see Figure 28). At 330 K the high-spin doublet is the only signal present; no Mössbauer signal is detected referring to the low-spin state. This result is in contrast to previously reported Mössbauer measurements for the compound under study, where an incomplete low-spin → high-spin transition even at 380 K was found [149]. Most probably this discrepancy is due impurities in the sample used. In the present case, a sample consisting of micro-crystals was used. It is worth noting, that despite the low-spin component is strongly asymmetric the high-spin doublet is symmetric in intensities and the fitting

procedure provided satisfactory results. The asymmetry observed in the low-spin doublet is due to the texture effect. At high temperatures this texture effect in the high-spin doublet is compensated by Goldanskii-Karyagin effect [202]. Comparison of the transition curves deduced from $^{57}$Fe Mössbauer spectra on the one hand and of the magnetic susceptibility measurements on the other hand reveals close resemblance (Figure 22).

**Table 5.** $^{57}$Fe Mössbauer parameters of isomer shift ($\delta$, relative to α-iron), quadrupole splitting $\Delta E_Q$, half-width of the lines ($\Gamma_{1/2}$) and percentage of the multiplet populations in the high-spin (HS) and low-spin (LS) states ($A$) for **1** at different temperatures.

| $T$ [K] | Spin state | $\delta$ [mm s$^{-1}$] | $\Delta E_Q$ [mm s$^{-1}$] | $\Gamma_{1/2}$ [mm s$^{-1}$] | $A$ [ %] |
|---|---|---|---|---|---|
| 80 | LS | 0.47(1) | 0.32(0) | 0.16(0) | 100 |
| 115 | LS | 0.46(0) | 0.31(1) | 0.15(0) | 100 |
| 130 | LS | 0.46(1) | 0.31(0) | 0.15(0) | 100 |
| 150 | LS | 0.45(0) | 0.31(0) | 0.15(1) | 100 |
| 170 | LS | 0.45(1) | 0.30(0) | 0.15(1) | 100 |
| 190 | LS | 0.44(1) | 0.30(1) | 0.15(1) | 93.0(7) |
|  | HS | 1.05(0) | 1.76(0) | 0.20(4) | 7.0(13) |
| 210 | LS | 0.43(0) | 0.28(0) | 0.15(0) | 84.6(11) |
|  | HS | 1.01(0) | 1.70(0) | 0.18(1) | 15.4(17) |
| 220 | LS | 0.42(0) | 0.27(1) | 0.16(1) | 75.0(11) |
|  | HS | 1.01(0) | 1.67(1) | 0.18(0) | 25.0(16) |
| 230 | LS | 0.41(0) | 0.22(0) | 0.20(1) | 45.9(20) |
|  | HS | 1.00(1) | 1.57(1) | 0.19(1) | 54.1(23) |
| 250 | LS | 0.44(1) | 0.21(1) | *0.2* | 29.5(12) |
|  | HS | 0.99(1) | 1.53(0) | 0.20(0) | 70.5(22) |
| 270 | LS | 0.38(1) | 0.20(0) | *0.2* | 17.0(27) |
|  | HS | 0.97(0) | 1.44(1) | 0.20(0) | 83.0(15) |
| 280 | LS | 0.32(1) | 0.19(0) | *0.2* | 12.7(39) |
|  | HS | 0.96(0) | 1.41(0) | 0.20(1) | 87.3(39) |
| 300 | LS | 0.33(0) | 0.18(0) | *0.2* | 4.0(26) |
|  | HS | 0.93(0) | 1.35(0) | 0.19(0) | 96.0(44) |
| 325 | HS | 0.90(0) | 1.31(1) | 0.16(0) | 100 |

The values given in italics were fixed during the fitting.
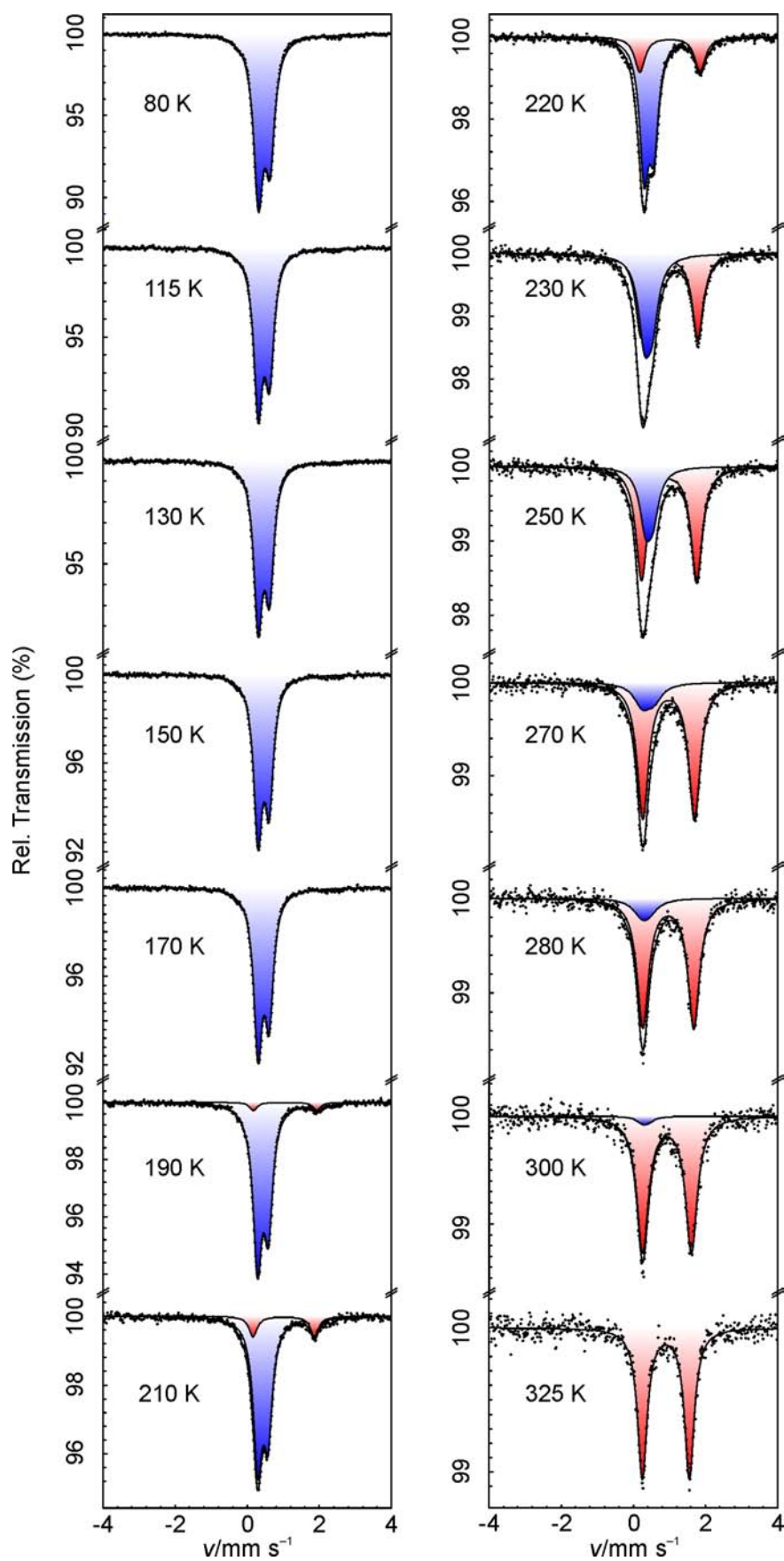
**Figure 28**. Mössbauer spectra of **1** at different temperatures. Low-spin doublet is blue and high-spin doublet is red.

### 2.2.6 Discussion

The crystal structure of the hexafluorophosphate salt of {Fe[*tren*(6-*Mepy*)$_3$]} above and below the transition temperature was reported more than thirty years ago presenting selected structural data based on a preliminary study [142]. Subsequently was published a projection of a high-spin structure of the complex cation together with the dependence of the lattice parameters on temperature [193]. Despite this system was later on often used as a model compound for a variety of studies [143-151] it was never reinvestigated more precisely with complete characterization of both low- and high-spin structures. Among other goals the present work covers the lack of structural information for the system under discussion.

From the structural study it is clear that the spin-transition in **1** is neither associated with a change of the crystal symmetry nor is it triggered by a structural order-disorder transition of perchlorate anions that would occupy different positions in the high and low temperature phases. The arrangement of units in **1** is quite the same in the low-spin and high-spin structures, the most remarkable differences being observed in the intramolecular geometry of the complex. The main structural change related to the spin-transition is a reorganization of the coordination environment of the iron ion toward a more regular octahedron when transforming into the low-spin form. The nonbonding nitrogen atom N7 is also shifted to the iron ion on low-spin to high-spin conversion. The fact that the FeN$_6$ core is less distorted in the low-spin state than in the high-spin state is distinctive [190, 203] and is in line with values of the parameter $\Sigma$ and of the twin angle $\theta$. In particular, the geometry of the low temperature low-spin molecule of **1** approaches that of the unmethylated **B** with a rather undistorted FeN$_6$ polyhedron. On heating, the variation in metal-ligand bond lengths as well as the distortion parameters are very close to the character of the magnetic curve and the curve of $\gamma_{HS}(T)$ derived from the Mössbauer data which shows their connection (Figure 22). A similar statement is valid also for the unit-cell parameters which change proportionally to the fraction of molecules in the high-spin state, such that the lattice deforms smoothly with increasing temperature and going to the high-spin form (Figure 23).

The dependence of the lattice parameters on temperature shows a slope which was interpreted by a superposition of a normal temperature dependence of the lattice, for which the isostructural zinc compound served as a reference, and a part proportional to the fraction of molecules in the high-spin state [178]. The spin state conversion of the iron atom from the low-spin to the high-spin state is accompanied by an increase of the unit-cell volume, which is

typical for spin-transition in iron(II) compounds, whereby the metal-ligand bond length increases by 0.2 Å.

Analysis of the intermolecular interactions suggests a significant role of the weak hydrogen bonds between the perchlorate anions and the CH moieties of the complex cations. A simple approach for a qualitative estimation of the preferable directions in which the hydrogen bonds network extend takes into account the interatomic contacts with a threshold below the sum of the van der Waals radii. For a complex molecule in the low-spin structure (80 K) 4 O$\cdots$H contacts and one $\pi$–$\pi$ contact contribute to inter-bilayer bonding (along axis *a*) and 14 O$\cdots$H contacts are essentially intra-bilayer (plane *bc*) (see description of the low-spin structure). This suggests a preferably two-dimensional character of interactions between spin-crossover molecules. In the high-spin structure (330 K) all inter-bilayer O$\cdots$H contacts are broken except the $\pi$–$\pi$ contact as opposite to the preserved 10 intra-bilayer ones (see Figure 21b, c). This fact correlates the variation with temperature of the parameter *a*, the change of which is the most pronounced one. According to a previous study [77] the main factors governing the cooperativity of the spin-crossover would be the strength and number of intermolecular interactions and their anisotropy. Despite noticeable anisotropic variation of intermolecular contacts is evident in **1** on going from the low-spin to the high-spin structures the relatively weak intermolecular contacts are responsible for the crossover character of the spin-transition. In contrast to the discontinuous transitions observed in [Fe(phen)$_2$(NCS)$_2$] [77] [Fe(bt)$_2$(NCS)$_2$] polymorph A [77] and [Fe(PM-BiA)$_2$(NCS)$_2$] [177] the crossover transition in **1** is supposedly attributable to intermolecular contacts taking the form of weak hydrogen bonds for **1**, while in those three spin-crossover compounds it is due to strong $\pi$–$\pi$ or S$\cdots$S interactions.

### 2.2.7   Summary

1. Complexes **1** and **1-Zn** crystallize in the same space group $P2_1/c$ allowing direct comparison of their structural parameters. Comparison of the data of **1** and **1-Zn** allowed precise determination of the effects induced in the lattice by the spin state conversion in **1**;

2. The variation in metal-ligand bond lengths, the distortion parameters, as well as the cell parameters of **1** are very close to the character of the magnetic curve and the curve of $\gamma_{HS}$ derived from the Mössbauer data which shows the correlation between structural and physical properties;

3. The thermodynamic parameters associated with the spin-transition were estimated by fitting the magnetic curve of **1** using Slichter-Drickamer model. The presence of moderate cooperativity in **1** has been concluded from the fitting results;

4. The absence of the strong cooperative effects is attributed to the relatively weak intermolecular contacts which are represented mostly by CH···O hydrogen bonds.

## 2.3 Characterization and physical properties of compounds 2–6

### 2.3.1 Introductory remarks

The iron(II) complex compounds under study are displayed in Figure 29. The compound **2** is formed by 1,3,5-*cis,cis*-tris[1-aza-2-(imidazol-4-yl)vinyl]cyclohexane [*tach*(*imd*)₃] and BF₄⁻ anions, **3** by 1,3,5-*cis,cis*-tris[1-aza-2-(2-pyridyl)vinyl]cyclohexane [*tach*(*py*)₃] and ClO₄⁻ anions, **4** by 2,2,2-tris[2-aza-3-(imidazol-4-yl)prop-2-enyl]ethane [*tame*(*imd*)₃] and ClO₄⁻ anions, **5** by 2,2,2-tris[2-aza-3-(2-pyridyl)prop-2-enyl]ethane [*tame*(*py*)₃] and ClO₄⁻ anions, **6** by 2,2,2-tris{2-aza-3-[(6-methyl)(2-pyridyl)]prop-2-enyl}ethane [*tame*(6-*Mepy*)₃] and ClO₄⁻ anions.
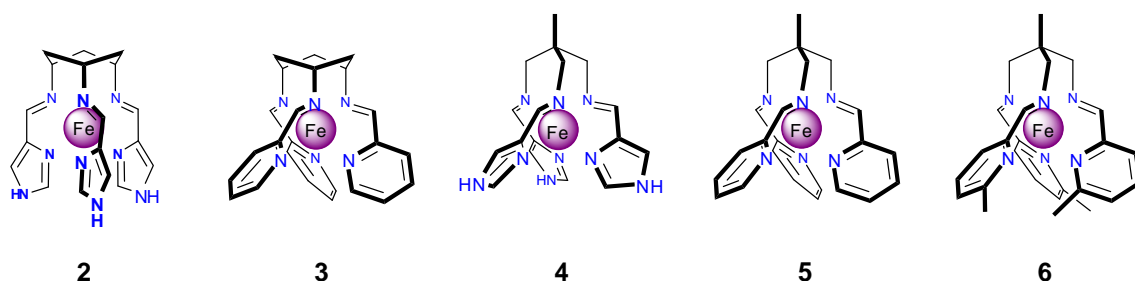


**Figure 29.** Schematic molecular structures of the compounds **2**–**6**.

From literature is known that minor changes in the structure of the ligand can result in modification of the spin-crossover properties of the complexes [20, 174]. Therefore the background idea was to synthesize a group of complexes possessing a similar structure, where the central iron(II) ion is octahedrally surrounded by imine nitrogen atoms and nitrogen atoms of heterocycles. The difference between the complexes would originate from the type of the capping triamine and the type of the heterocycle. In the present chapter the structural and spectroscopic properties of iron(II) tripod-based complexes are analyzed.

### 2.3.2 Crystal structures of 2–6

Crystallographic, experimental and computational details for **2**, **3**, **4** and **6** are presented in Table 6.

**Table 6.** Crystallographic data and refinement details for **2**, **3**, **4** and **6**.

| | **2** | **3** | **4** | **6** |
|---|---|---|---|---|
| Empirical formula | $C_{18}H_{21}B_2F_8FeN_9$ | $C_{24}H_{24}Cl_2FeN_6O_8$ | $C_{17}H_{22}Cl_2FeN_9O_{8.5}$ | $C_{26}H_{30}N_6FeCl_2O_8$ |
| Formula weight | 592.83 | 651.24 | 1230.32 | 681.31 |
| Temperature [K] | 298(2) | 298(2) | 298(2) | 298(2) |
| Wavelength [Å] | 0.71073 | 0.71073 | 0.71073 | 0.71073 |
| Crystal system | orthorhombic | monoclinic | triclinic | monoclinic |
| Space group | $Pnma$ | $Cc$ | $P\bar{1}$ | $P2/c$ |
| a [Å] | 9.523(2) | 17.497(1) | 10.229(2) | 11.055(2) |
| b [Å] | 15.262(3) | 9.865(1) | 12.868(3) | 18.234(4) |
| c [Å] | 16.850(3) | 16.262(1) | 19.274(4) | 14.656(3) |
| α [°] | 90 | 90 | 80.20(3) | 90 |
| β [°] | 90 | 105.12 | 79.71(3) | 90.58(3) |
| γ [°] | 90 | 90 | 80.20(3) | 90 |
| Volume [Å³] | 2448.98(83) | 2709.78(733) | 2434.04(1939) | 2954.16(137) |
| Z | 4 | 4 | 2 | 4 |
| $\rho$ [g cm⁻³] | 1.614 | 1.596 | 1.677 | 1.526 |
| Absorption coefficient [mm⁻¹] | 5.759 | 0.814 | 0.905 | 0.749 |
| $F(000)$ | 1208 | 1336 | 1258 | 1403 |
| $\theta$ range for data collection [°] | 7.86 to 89.84 | 3.75 to 32.88 | 3.25 to 32.90 | 3.22 to 32.97 |
| Index ranges | $-12 \leq h \leq 6$ $-19 \leq k \leq 19$ $-21 \leq l \leq 21$ | $-25 \leq h \leq 25$ $-14 \leq k \leq 14$ $-18 \leq l \leq 24$ | $-14 \leq h \leq 15$ $-19 \leq k \leq 17$ $-26 \leq l \leq 29$ | $-16 \leq h \leq 16$ $-26 \leq k \leq 26$ $-13 \leq l \leq 22$ |
| Reflections collected | 18053 | 13116 | 25136 | 29848 |
| Independent reflections | 2865 [$R_{int}$ = 0.0375] | 6314 [$R_{int}$ = 0.0725] | 15799[$R_{int}$ = 0.0544] | 10209[$R_{int}$ = 0.0589] |
| Data/restraints/parameters | 2865/106/240 | 6314/14/371 | 15799/12/678 | 10209/12/392 |
| Goodness-of-fit, $F^2$ | 1.059 | 1.126 | 0.932 | 1.055 |
| Final $R$ indices [$I > 2\sigma(I)$] | $R1$ = 0.0580, $wR2$ = 0.1718 | $R1$ = 0.0907, $wR2$ = 0.2396 | $R1$ = 0.0676, $wR2$ = 0.1733 | $R1$ = 0.0758, $wR2$ = 0.2228 |
| $R$ indices (all data) | $R1$ = 0.0828, $wR2$ = 0.1967 | $R1$ = 0.1575, $wR2$ = 0.0.2396 | $R1$ = 0.1482, $wR2$ = 0.2087 | $R1$ = 0.1251, $wR2$ = 0.2228 |
| $\rho_{min}, \rho_{max}$ [e Å⁻³] | 1.063, −0.371 | 1.133, −1.352 | 1.572, −0.851 | 1.566, −0.992 |

**Table 7.** The intramolecular parameters of **A**, **B**, **1**–**6**.

| Compound | Spin state | $\theta$ [°] | $\Sigma$ [°] | $\langle$Fe–N$^{het}\rangle$ [Å] | $\langle$Fe–N$^{im}\rangle$ [Å] | $\Delta r$ [Å] | $s^{het}$ [Å] | $s^{im}$ [Å] | $\Delta s$ [Å] | $h$ [Å] | $\alpha$ [°] | $\langle$N=C$\rangle$ [Å] | $\varphi^{tor}$ [°] |
|---|---|---|---|---|---|---|---|---|---|---|---|---|---|
| **A** [155] | LS | 51.10(2) | 56.19(1) | 1.993(1) | 2.013(0) | 0.020(1) | 2.809(1) | 3.207(1) | −0.398(1) | 2.156(1) | 81.06(1) | 1.307(0) | 176.41(2) |
| **B** [160] | LS | 53.86(6) | 61.37(5) | 1.975(2) | 1.952(2) | 0.020(2) | 2.889(2) | 2.901(3) | −0.012(3) | 2.050(0) | 81.22(7) | 1.276(3) | 178.81(19) |
| **1** | LS (80 K) | 57.22(5) | 83.82(51) | 2.079(2) | 1.950(2) | 0.130(2) | 3.195(2) | 2.839(2) | 0.356(2) | 2.015(1) | 81.15(4) | 1.285(2) | 175.75(11) |
|  | HS (330 K) | 52.14(9) | 110.98(97) | 2.303(4) | 2.129(4) | 0.174(4) | 3.568(4) | 3.190(3) | 0.378(4) | 2.097(2) | 75.42(8) | 1.257(4) | 174.03(26) |
| **2** | HS | 0 | – | 2.196(4) | 2.213(4) | −0.170(4) | 3.165(6) | 2.888(5) | 0.277(6) | 2.671(0) | 74.75(15) | 1.270(6) | 178.74(38) |
| **3** | LS | 42.22(43) | 65.40(35) | 1.999(22) | 1.920(21) | 0.079(22) | 2.837(27) | 2.697(30) | 0.140(30) | 2.270(8) | 81.00(35) | 1.293(19) | 155.74(96) |
| **4** | LS (Fe1) | 43.18(17) | 73.01(14) | 1.982(22) | 1.932(24) | 0.050(24) | 2.858(34) | 2.673(36) | 0.185(36) | 2.259(38) | 81.23(14) | 1.282(16) | 167.03(16) |
|  | LS (Fe2) | 42.86(18) | 78.48(15) | 1.984(24) | 1.941(25) | 0.043(25) | 2.888(41) | 2.668(37) | 0.220(41) | 2.257(24) | 80.86(15) | 1.277(19) | 167.48(36) |
| **5** [140] | LS | 43.41(3) | 76.35(2) | 2.002(1) | 1.908(1) | 0.094(1) | 2.913(2) | 2.625(1) | 0.288(2) | 2.245(2) | 81.05(2) | 1.275(1) | 166.90(4) |
| **6** | LS | 50.46(14) | 75.84(12) | 2.087(11) | 1.919(14) | 0.168(14) | 3.197(10) | 2.624(9) | 0.573(10) | 2.154(8) | 80.93(12) | 1.271(8) | 161.48(35) |

Structures of **A** and **B** are already known from [155] and [160], respectively. Their structures are essentially similar to those discussed below.



a



b
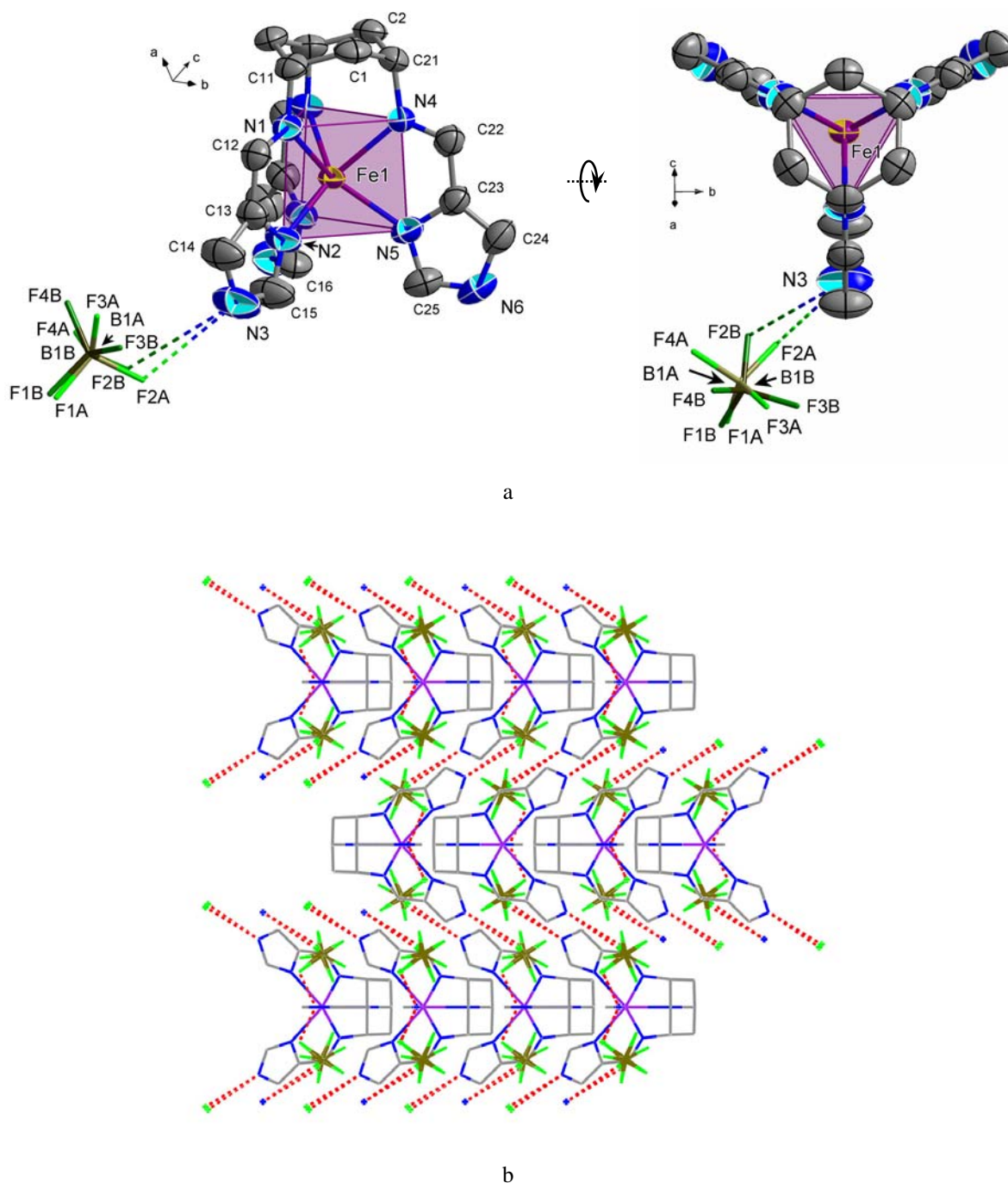
**Figure 30.** a) On the left is the molecular structure of **2** with numbering scheme showing hydrogen bonding with the disordered anion, on the right is projection along the pseudo-$C_3$ axis displaying trigonal prismatic environment of the central iron(II) ion; b) Projection of a layer in the *ab* plane formed by the complex cations {Fe[*tach*(*imd*)$_3$]}$^{2+}$ with disordered BF$_4^-$ anions connected by hydrogen bonds NH$\cdots$F (dashed red lines).

**Structure of 2.** A projection of the molecular structure of **2** with the atom numbering scheme is shown in Figure 30. The crystallographically disordered tetrafluoroborate anion (A:B ≈ 40:60) completes elementary unit. A mirror plane goes through the complex cation making it symmetry related as well as doubling the anion. The iron(II) ion is located in a coordination environment with the $N_6$ donor set of the tripod ligand, which includes three imidazole and three imine nitrogen atoms. The lengths of six Fe–N bonds fall in the expected range for this coordination number and donor set [2.196(6)–2.225(3) Å]. Geometric constraints of bidentate units with five-membered hererocycles cause significant reduction of the $N^{im}$–Fe–$N^{imd}$ bite angle $\alpha$ compared to the ideal 90° value (Table 7). Average coordination geometry within $\{Fe[tach(imd)_3]\}^{2+}$ may be represented as unprecedented for $FeN_6$ chromophore, slightly tapered trigonal prism (Figure 30a). Previously only near trigonal prismatic low-spin iron(II) with twist angle $\theta = 8.1°$ [204] and trigonal prismatic high-spin iron(II) in $O_6$ environment were reported [205]. The alignment of donor nitrogen atoms in trigonal prismatic manner is possible by virtue of planar imidazole-5-carboxaldimino chelate arms and due to the reduced $M_d$–$L_{\pi*}$ back-bonding of iron(II) ion in high-spin state (see UV/VIS spectrum, Figure 35a). The disordered $BF_4^-$ anion is engaged into strong hydrogen bonding with NH groups of imidazole moieties [F···N is 2.892(21)−3.155(15) Å], and additionally into weak CH···F interaction with ligand moieties. The separations of carbon and fluorine atoms lie in the range 2.906(13)−3.640(25) Å. Molecules of the complex are arranged in layers forming *ab* planes of the crystal, which are consequently packed in a three-dimensional framework linked by numerous intermolecular hydrogen bonds (Figure 30b).

**Structure of 3.** The molecular structure of **3** at 293 K is shown in Figure 31a. The complex is chiral, with either right-hand (*D*) or left-hand (*L*) configuration due to the screw arrangement of the achiral tripod ligand around the central iron(II) ion. The unit cell contains two pairs of complex molecules with opposite chirality. Like in the previous case the iron(II) ion is surrounded by three imine nitrogen and three pyridine nitrogen atoms in pseudo-octahedral fashion. The Fe–N bond lengths at 293 K are typical for low-spin iron(II): 1.920(21) Å (Fe–$N^{im}$) and 1.999(22) Å (Fe–$N^{py}$). The $FeN_6$ octahedron is rather distorted, with parametrer $\Sigma$ equal to 65.40(35)°. Compared to **B** [160], the polyhedron is more twisted towards trigonal prism. In fact, it is almost halfway between two idealized geometries with $\theta$ parameter equal to 42.22(43)°, thus being closer to octahedron (Table 7). Detailed analysis of the conformation of the ligand in the complex reveals significant deviation of imine-pyridine fragments from planarity. According to Gillum *et al.* [137] pronounced $M_d$–$L_{\pi*}$-back-bonding (confirmed by IR and UV/VIS spectroscopy, *vide infra*) can decrease the bond order of the

C=N group by decreasing the rotational barrier of the bond, which explains the observed deviation. This is caused by the strong tendency of low-spin iron(II) to form energetically favorable pseudo-octahedral arrangement of donor atoms [206], but this competes with the rigidity of the ligand, which prefers trigonal prismatic conformation.
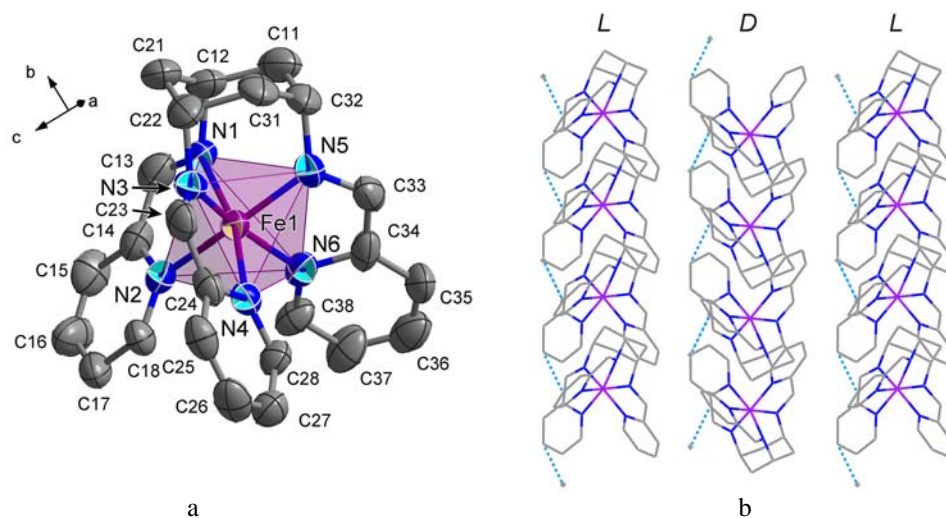


**Figure 31**. a) The molecular structure of **3** with numbering scheme. Hydrogen atoms and anion are omitted for clarity. Displacement ellipsoids are drawn at 50 % probability level; b) Projection of the molecular packing along the *a* axis shows segregation of the complex molecules with the same chirality into layers extending in the *ab* plane. Blue dashed lines correspond to π–π stacking contacts between neighbouring complex cations.

The packing of the molecules in the unit cell along the *a* axis is shown in Figure 31b. There is weak slipped π-stacking interaction between two adjacent and co-planar pyridine rings along the *c* axis with the distance being about 3.75 Å. The molecules of the same chirality are spread in layers alternating along the *c* axis with the change of chirality.

**Structure of 4.** The unit cell of **4** consists of two independent mononuclear cations $\{Fe[tame(imd)_3]\}^{2+}$, four perchlorate anions and one water molecule. The complex molecules possess internal symmetry close to $C_3$ (Figure 32a). Pseudo-octahedral coordination polyhedrons are twisted from trigonal antiprism toward trigonal prism (average $\theta$ approximates the value of 43°, Table 7). For the two species Fe−N$^{im}$ and Fe−N$^{imd}$ bond distances evidence low-spin state of iron(II) ions. All imidazole moieties are protonated and involved in hydrogen bonding with oxygen atoms of perchlorate anions or of bridging water molecules. Numerous NH···O intermolecular contacts are formed with separations 2.903(48) Å and more. Each complex molecule is connected by three hydrogen bonds to oxygen atoms of anions or water molecule (Figure 32b), which participate in the construction

of a two dimensional hydrogen bond network. The system is optically inactive with balanced quantity of *L* and *D* molecules in the unit cell for both independent cations.



a



b
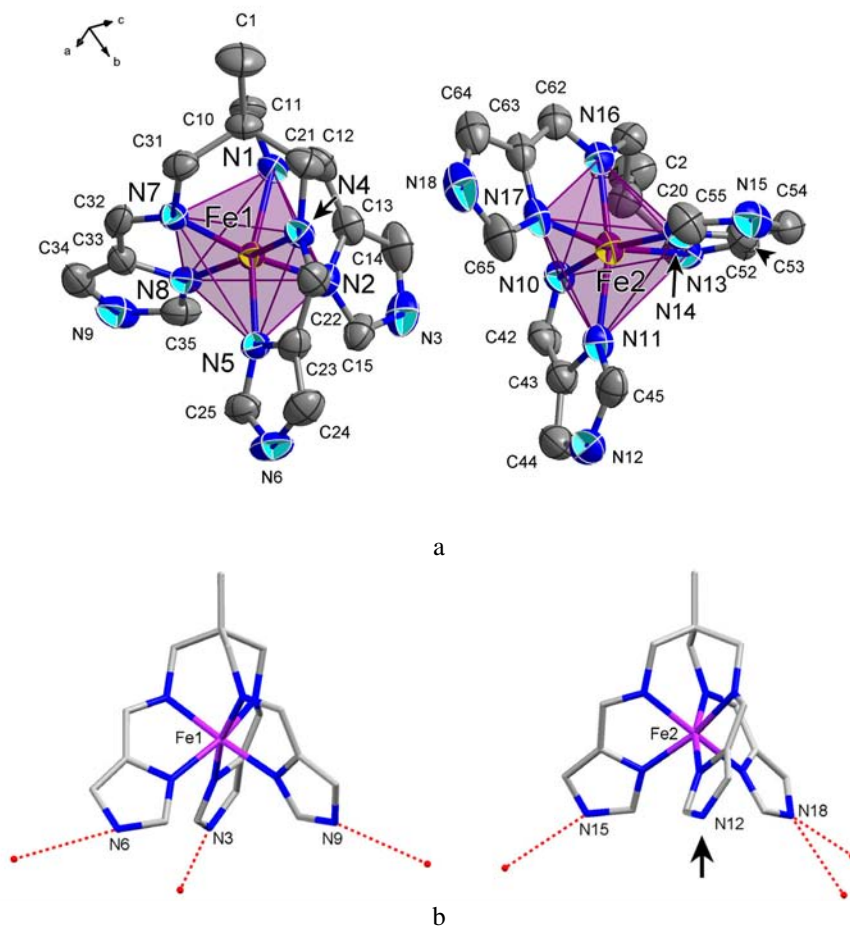
**Figure 32**. a) Two independent complex molecules of **4** with numbering scheme. Hydrogen atoms, water molecule and anions are omitted for clarity. Displacement ellipsoids are drawn at 50 % probability level; b) Projection of the complex cations with Fe1 and Fe2 with the different patterns of strong hydrogen bonding. The black arrow points at the "idle" NH imidazole function of the Fe2-based cation.

**Structure of 5** is already known. The identity of the compound **5** with reported one was confirmed by comparison of the unit cell parameters with those reported in ref. [140]. They were found to be identical.

**Structure of 6.** A projection of the complex cation of **6** is shown in Figure 33a. Like in compounds **1**, **3**, **4**, **5**, the central iron(II) ion possesses pseudo-octahedral coordination environment with a $N_6$ donor set consisting of three imine nitrogen atoms and three pyridine nitrogen atoms. The spin state can be assigned on the basis of the bond lengths; the average value for the six bonds is very close to 2 Å indicating low-spin state of the iron(II) ion.
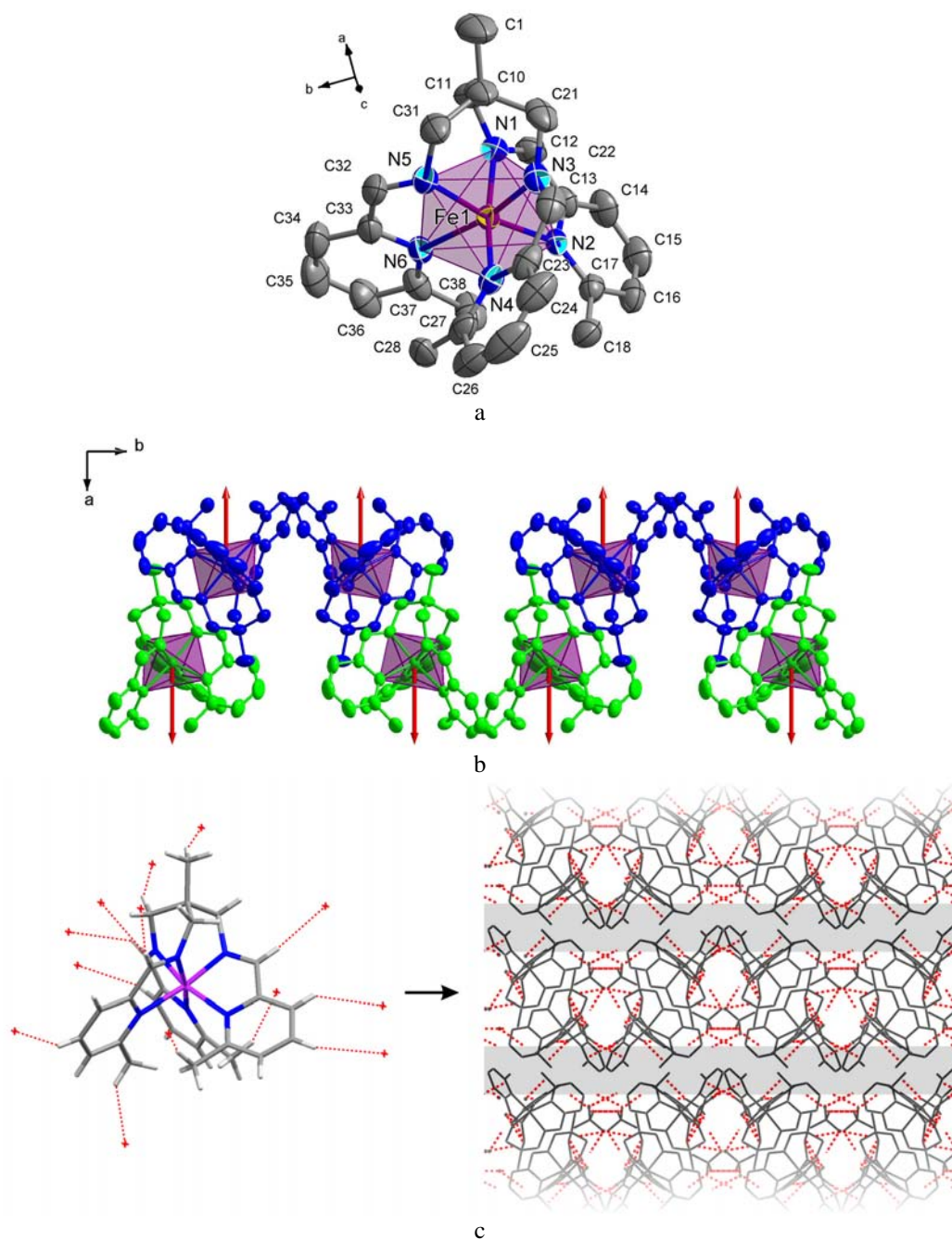
**Figure 33**. a) The molecular structure of **6** with numbering scheme. Hydrogen atoms and anions are omitted for clarity. Displacement ellipsoids are drawn at 50 % probability level; b) Projection along the *c* axis displays a bilayer composed of oppositely directed complex molecules {Fe[*tame*(6-*Mepy*)]}$^{2+}$. Red arrows show an approximate direction of C10···Fe1 vector; c) On the left projection of the complex cation of **6** and on the right projection of the crystal structure along the *b* direction are shown, both emphasizing weak intermolecular contacts. In the projection of the crystal packing hydrogen atoms are omitted for simplicity, complex molecules and anions are shaded grey whereas red dashed lines correspond to CH···O hydrogen bonds. Shaded areas highlight inter-bilayer space**.**

Interestingly, the difference between bonds Fe−N$^{py}$ and Fe−N$^{im}$ is the largest among the compounds under discussion (*ca*. 0.168 Å) and is similar to the corresponding value of

low-spin **1** (Table 7). The *cis*-N−Fe−N bond angles are evidence for distorted octahedral geometry, but the magnitude of the prismatic distortion expressed by the value $\Sigma$ is smaller compared to the similar non-methylated compound **5** [140] (Table 7). The distance from the methyl carbon to the nearest nitrogen of the adjacent pyridine ring is similar to the value found in the structure of **1** in low-spin state; it is equal to 3.035 Å. As in the previous cases, the crystal of **6** appears to be a racemic mixture of two optical isomers equally represented in the structure.

Projection along the *c* axis (Figure 33b) reveals bilayer arrangement similar to **1** (Figure 21a). Each bilayer consists of arrays of molecules **6** ordered in up-and-down fashion. The complex molecule has no groups allowing the formation of any type of strong hydrogen bonds, on the other hand the structure possesses numerous contacts of perchlorate anions with CH moieties of the ligand attributable to weak hydrogen bonds [2.380(11)–2.719(10) Å)] (Figure 33c). Contrary to **1**, there are no inter-bilayer contacts between complex cations.

### 2.3.3   IR spectroscopy and mass spectroscopy

The IR spectra of **2**–**6** are shown in Figure 34, for comparison spectra of compounds **1** and **1-Zn** are also plotted. The most informative region in the spectra is that covering the imine absorption band and the bands assigned to polyatomic anions, *i.e.* perchlorate or tetrafluoroborate. It is known [207] that the position of C=N band in the complexes depends on the type and spin state of the chelated metal ion [156, 208]. A shift of the band can also be caused by the ligand conformation [137], but usually it results from redistribution of electronic density between molecular orbitals of the ligands and *d*-orbitals of the metal ion. Enhanced $M_d \rightarrow L_{\pi*}$ back-bonding in the low-spin state influences the order or bond strength of C=N groups. Thus the method of IR spectroscopy is a sensitive tool to follow spin-transition [209-211].

*C=N group.* The imidazole-based complex **2** exhibits a split band with two maxima at 1634 and 1637 cm$^{-1}$ assigned to the C=N stretching vibration. The positions of the bands call for the high-spin state of the chelated iron(II) ion. The positions of C=N bands in the low-spin complexes **3**, **5** and **6** are shifted towards lower wavenumbers compared to the pyridine-based high-spin complex **1**. For instance, the corresponding value in **3** is 1597 cm$^{-1}$ whereas for **5** it is 1607 cm$^{-1}$ and for **6** 1623 cm$^{-1}$. Note, a shoulder at 1614 cm$^{-1}$ in **5** is suggested to be due to the poor ratio of noise/signal. For **6** the bands in the region of 3000–2875 cm$^{-1}$ are also observed (not shown) corresponding to symmetric and asymmetric absorption bands of C–H

bonds belonging to methyl substituents of pyridine rings. The imidazole-based complex **4** shows a split band with maxima at 1605 and 1615 cm$^{-1}$. They may be assigned to C=N stretching vibrations of two different sets of C=N groups, which might be an additional evidence for two inequivalent complex cations found in the crystal structure (Figure 32a). The positions of C=N bands for **2–6** appear to be consistent with the data obtained by other techniques.
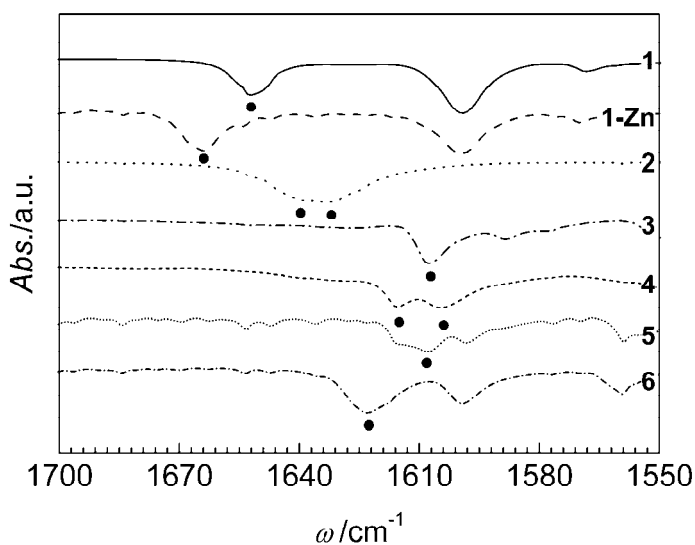


**Figure 34.** IR spectra of **1–6** in the region of C=N stretching vibrations. The symbol ● shows absorption bands assigned to $v$(C=N).

***Anion***. Absorption bands of the $BF_4^-$ anion in **2** are at 1070 cm$^{-1}$ and of the perchlorate anions in **3–6** are at 622 and 1090 cm$^{-1}$, which may be used to confirm the chemical composition of the compounds.

Mass spectroscopic (MS) characterization of the complexes was performed by electrospray ionization (ESI) or field desorption (FD) methods. The observed *m/z* values of ions and their assigning are given in Table 8. The main feature observed in the ESI mass spectra of these complexes is little fragmentation, which allows simple identification of the molecular ion. Ionization pathways for **2** and **4** involve loss of imidazole proton or pairing with an anion. For the perchlorate-based **3–6** the main peak corresponds to molecular ion plus perchlorate anion.

**Table 8.** ESI MS data for **2–6**.

| Compound | 2 | 3 | 4 | 5 | 6 |
|---|---|---|---|---|---|
| **MS [*m/z*]** | 418 [M–H]$^{+ a}$ | 226 [M]$^{++}$, 551 [M+ClO$_4$]$^+$ | 406 [M–H]$^+$, 506 [M+ClO$_4$]$^+$ | 539 [M+ClO$_4$]$^+$ | 581 [M+ClO$_4$]$^+$ |

[a] Field desorption ionization.

### 2.3.4   UV/VIS spectroscopy of 2–6

Electronic absorption spectra of the complexes **2–6** were measured in solution and in solid state in absorption mode at room temperature.

The spectrum of **2** in methanol is shown in Figure 35a. It consists of two bands located in the UV region which were assigned to absorptions of the groups in the organic ligand. A weak broad peak at 977 nm (10 230 cm$^{-1}$) was assigned to crystal field transition $^5A_1 \rightarrow ^5E$ of iron(II) in trigonal prismatic environment (see Figure 38c).



a



b



c
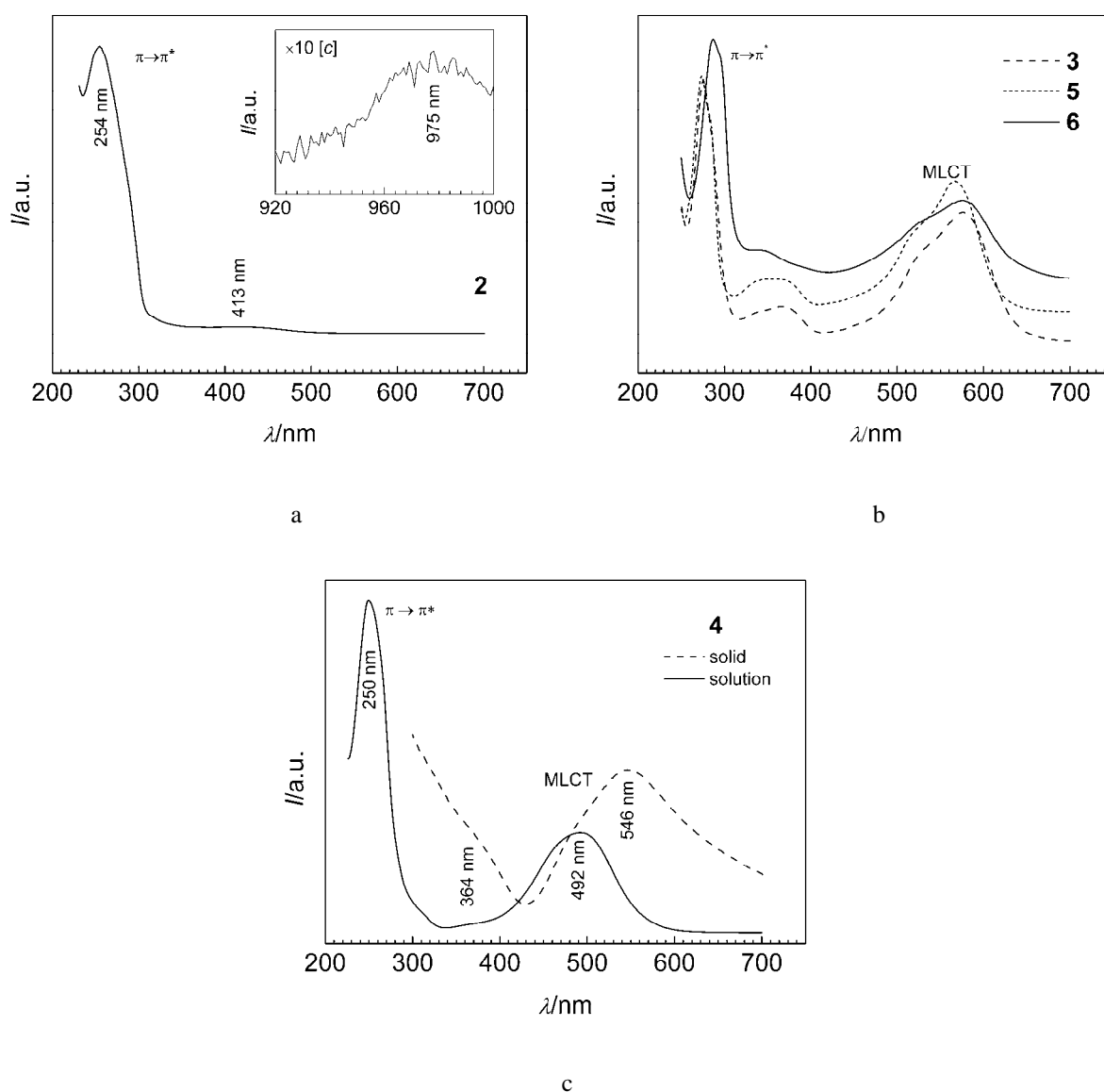
**Figure 35.** a) UV/VIS spectrum of **2** in methanol. Inset shows an absorption band at ×10 concentration; b) UV/VIS spectra of **3**, **5** and **6** (all in acetonitrile) and c) of **4** in acetonitrile and solid at room temperature.

The spectra of **3**, **5** and **6** in acetonitrile solution are shown in Figure 35b. In general, three spectra appear to have similar band structures. An intense absorption observed in the UV region at 280 nm is due to the ligand $\pi$–$\pi$* transitions while MLCT bands are observed in the visible region of the spectrum at about 570 nm. The ligand field bands $^1A_{1g} \rightarrow {}^1T_{1g}$ and $^1A_{1g} \rightarrow {}^1T_{2g}$ (log $\varepsilon$ ~ 0–2) are masked by intense MLCT (log $\varepsilon$ ~ 4–5) [72]. This prevents evaluation of the ligand field parameters from the electronic spectra of **3**, **5** and **6**. The discrepancies between the spectrum of **6** and the spectra of **3** and **5** in the positions of the band maxima and their intensities have to be assigned to distortions of the coordination sphere in **6** which arise from methyl pendants of pyridine moieties.

The spectrum of **4** in acetonitrile (Figure 35c) is very similar to that of complex **1** (Figure 27). It is rather unexpected since X-ray data indicate the low-spin state of the complex species in crystalline state. Nevertheless, two most intensive peaks are recognized as $\pi$–$\pi$* absorption of the ligand (250 nm) and intense MLCT band (492 nm), respectively, while the $^5T_{2g} \rightarrow {}^5E_g$ band is strongly obscured and is not observed. The main band in the UV/VIS spectrum of solid **4** consists of intraligand $\pi$–$\pi$* transitions (sh 364 nm) and low-spin asymmetric $^1A_{1g} \rightarrow {}^1$MLCT transition (546 nm) although it is apparent that other bands are also present. Shorter Fe–N bonds in the low-spin state lead to much larger overlaps between metal and ligand centered orbitals and consequently intensification of charge transfer absorptions. As a result, the bands associated with weak $^1A_{1g} \rightarrow {}^1T_{2g}$ and $^1A_{1g} \rightarrow {}^1T_{1g}$ transitions of the low-spin state are masked and their positions cannot be determined. According to this the conclusion was made that the low-spin state in solid **4** seems to be stabilized by hydrogen bonding with anions and water molecule, which is common for heterocycle-based spin-crossover materials [30, 57, 167, 212].

### 2.3.5   Magnetic properties and Mössbauer spectroscopy

Magnetic properties of **2** were determined in the range 10–300 K. Figure 36 shows a plot of $\chi_M T$ *vs* $T$ for **2**, where $\chi_M T$ is the product of molar magnetic susceptibility $\chi_M$ and temperature $T$. Complex **2** shows paramagnetic behavior retaining high susceptibility of 3.40 cm$^3$ K mol$^{-1}$ down to 40 K. A slight drop of the susceptibility at lower temperatures results from zero-field splitting of the $S = 2$ ground state. In contrast, **3–6** are diamagnetic up to 400 K confirming the low-spin character of the compounds.
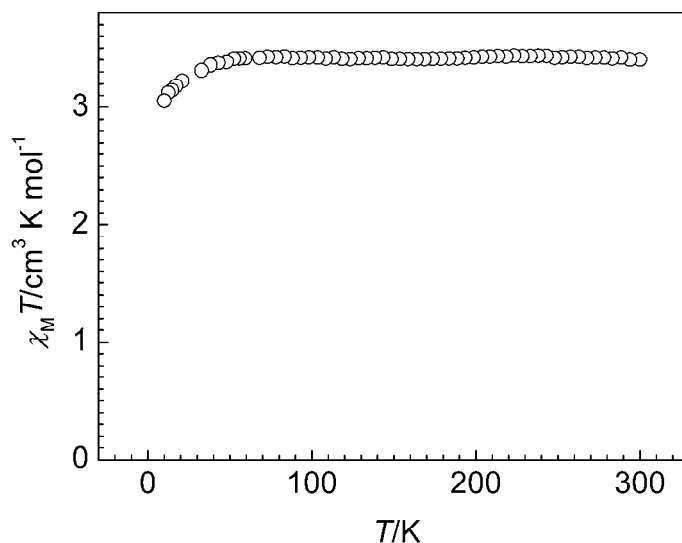
**Figure 36.** Plot of the magnetic susceptibility of **2** in coordinates $\chi_M T$ *vs T*.

**Table 9**. $^{57}$Fe Mössbauer parameters of isomer shift ($\delta$, relative to α-iron), quadrupole splitting $\Delta E_Q$ (for doublets), half-width of the lines ($\Gamma_{1/2}$) and percentage of the multiplet populations $A$ at different temperatures for **2–6**.

| Compound | $T$ [K] | Multiplet, spin state | $\delta$ [mm s$^{-1}$] | $\Delta E_Q$ [mm s$^{-1}$] | $\Gamma_{1/2}$ [mm s$^{-1}$] | $A$ [ %] |
|---|---|---|---|---|---|---|
| **2** | 6 | d, HS(A) | 1.11(1) | 3.95(0) | 0.16(1) | 35.4(52) |
| | | d, HS(B) | 1.10(0) | 3.52(0) | 0.16(1) | 64.6(52) |
| | 80 | d, HS(A) | 1.10(0) | 3.86(0) | 0.15(1) | 32.5(51) |
| | | d, HS(B) | 1.09(0) | 3.49(1) | 0.15(1) | 67.5(52) |
| | 130 | d, HS(A) | 1.09(1) | 3.70(0) | 0.16(1) | 39.7(41) |
| | | d, HS(B) | 1.07(0) | 3.28(1) | 0.16(1) | 70.3(40) |
| | 170 | d, HS(A) | 1.07(1) | 3.54(0) | 0.16(1) | 27.9(47) |
| | | d, HS(B) | 1.05(0) | 3.04(1) | 0.17(1) | 72.1(46) |
| | 210 | d, HS(A) | 1.06(0) | 3.37(1) | 0.17(1) | 25.7(1) |
| | | d, HS(B) | 1.04(0) | 2.85(0) | 0.16(1) | 74.3(0) |
| | 250 | d, HS(A) | 1.03(0) | 3.11(0) | *0.16* | 22.0(18) |
| | | d, HS(B) | 1.01(1) | 2.56(0) | *0.16* | 78.0(18) |
| | 290 | d, HS(A) | 1.02(0) | 2.86(1) | *0.16* | 22.8(19) |
| | | d, HS(B) | 0.99(0) | 2.35(1) | *0.16* | 77.2(19) |
| | 345 | d, HS(A) | 0.99(0) | 2.53(0) | *0.15* | 25.7(43) |
| | | d, HS(B) | 0.94(0) | 2.10(0) | *0.15* | 74.3(43) |
| **3** | 290 | d, LS | 0.21(1) | 0.28(0) | 0.13(0) | 100 |
| **4** | 290 | s, LS | 0.34(0) | – | 0.14(0) | *50* |
| | | s, LS | 0.24(0) | – | 0.14(1) | *50* |
| **5** | 290 | d, LS | 0.21(1) | 0.39(0) | 0.13(0) | 100 |
| **6** | 290 | d, LS | 0.34(1) | 0.42(0) | 0.24(2) | 100 |

The values given in italics were fixed during the fitting.
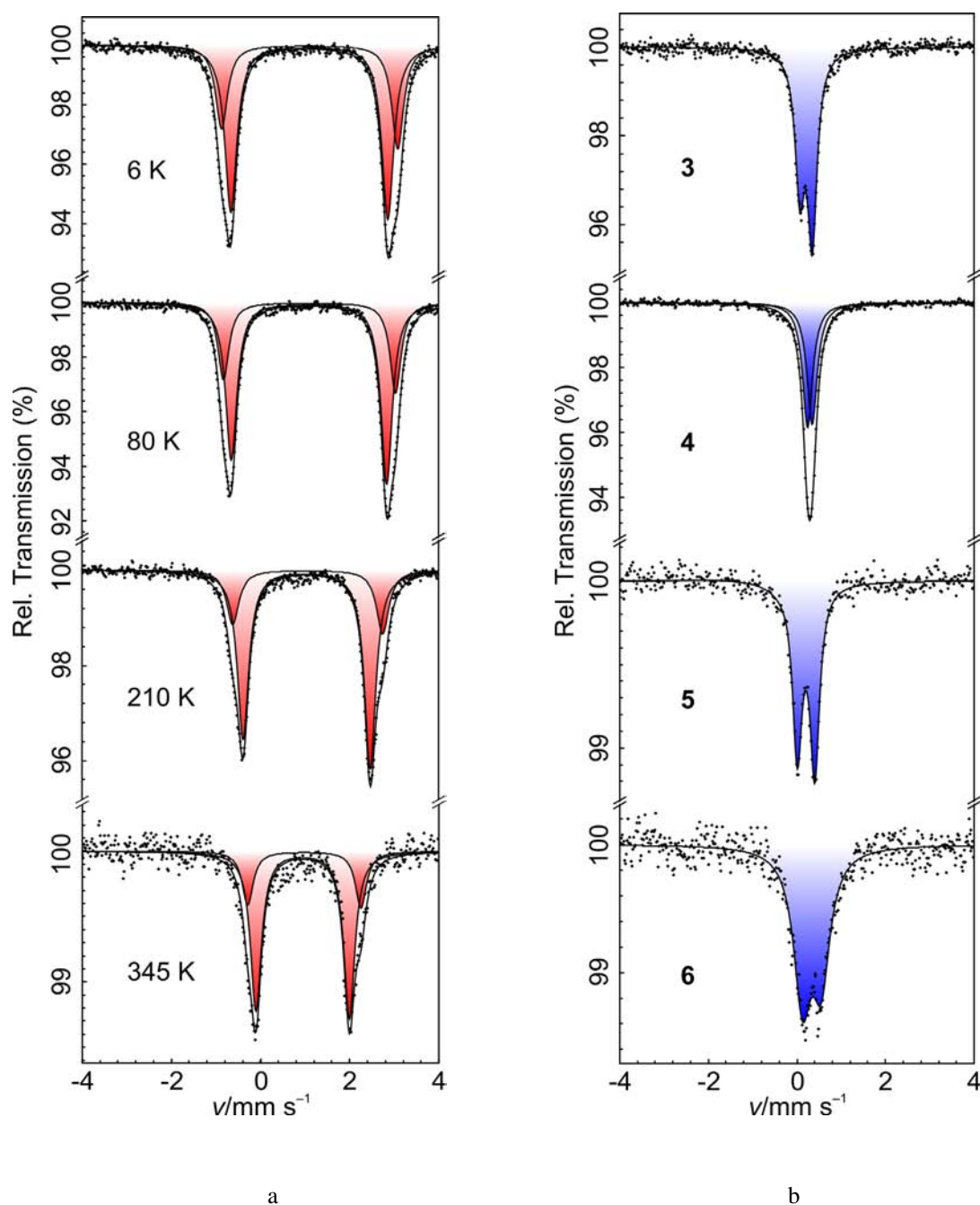
**Figure 37**. a) $^{57}$Fe Mössbauer spectra of **2** obtained at indicated temperatures and b) of **3–6** at 290 K. Solid lines represent fitting of experimental curves. Red doublets correspond to high-spin, blue to low-spin doublets.

Representative measured Mössbauer spectra of **2–6** are shown in Figure 37; the corresponding parameters derived from the fitting procedure are listed in Table 9. Mössbauer spectra of **3**, **5** and **6** consist of one low-spin doublet. Minor asymmetry of the quadrupole doublets is assigned to texture in the absorber resulting from the form of the crystals (plates or needles).
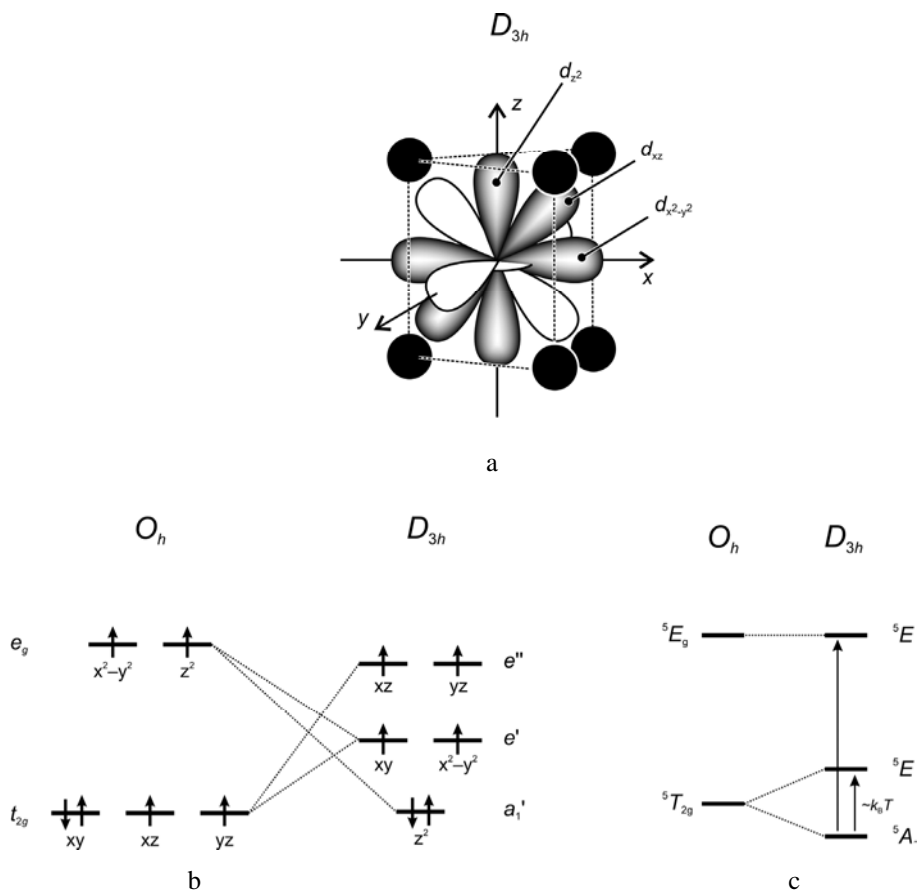
**Figure 38**. a) Schematic drawing visualizing the interactions of *d*-orbitals with a ligand field of $D_{3h}$ symmetry. For simplicity orbitals $d_{xy}$ and $d_{yz}$ are ommited; b) Splitting of the five *d*–orbitals of the iron(II) ion in ligand fields of $O_h$ and $D_{3h}$ symmetries; c) The diagram of term levels for $D_{3h}$ showing two possible transitions.
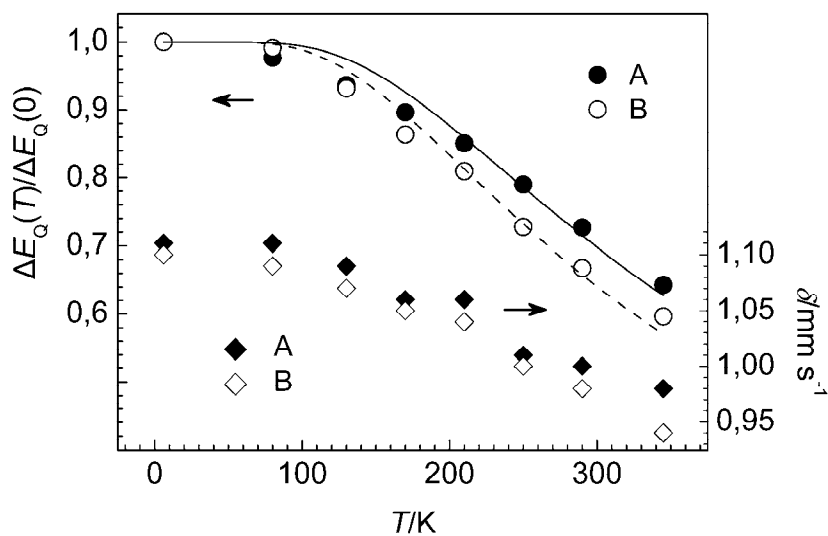


**Figure 39**. The plot in coordinates $\Delta E_Q(T)/\Delta E_Q(0)$ *vs T* for **2** (top). The lines represent fitting of the experimental data [solid for HS(A) and dashed for HS(B)]. On the bottom plot in coordinates $\delta$ *vs T*.

Selected Mössbauer spectra of **2** at different temperatures are shown in Figure 37a; more temperature data are given in Table 9. At all temperatures the spectra clearly include two high-spin doublets probably arising from the disorder over two positions A and B of $BF_4^-$ anions which are connected through hydrogen bonds to complex cations of **2** (Figure 30a). The chemical shifts $\delta$ and the quadrupole splitting values are characteristic of iron(II) in high-spin state. In view of the fact that the largest quadrupole splittings observed for high-spin iron(II) compounds are ~4.0 mm s$^{-1}$ [213], the value of the splitting in **2** is one of the highest reported [88, 205, 214-216]. This quadrupole splitting is the result of almost ideal trigonal prismatic geometry $D_{3h}$ of the coordination polyhedron (Figure 38a). In this symmetry electron energy levels are split into a$'_1$, e$'$ and e$''$ levels with a$'_1$ the lowest accepting the sixth electron [137, 138, 204, 205, 217] (Figure 38b), and with a gap between a$'_1$ and e$'$ levels (or between $^5A_1$ and $^5E$ terms) of the order of $k_BT$ (Figure 38c). The measurement of $\Delta E_Q$ *vs T* allows to determine a$'_1$–e$'$ gap according to the relation [218]:

$$\frac{\Delta E_Q(T)}{\Delta E_Q(0)} = \frac{1 - \exp(-\dfrac{E_0}{k_BT})}{1 + 2\exp(-\dfrac{E_0}{k_BT})} \tag{15}$$

where $\Delta E_Q(0)$ is the quadrupole splitting due to single $3d$ electron in a$'_1$ state and $E_0$ is the gap between a$'_1$ and e$'$ levels in trigonaly surrounded iron(II). As shown in Figure 39, the variation of the quadrupole splitting from 6 up to 345 K obeys this relation with $E_0 = 385$ cm$^{-1}$ ($R = 0.98$) and 433 cm$^{-1}$ ($R = 0.97$) for the less split HS(B) and the more split HS(A) components, respectively. A minor deviation of the fitted curves from the experimental ones is due to a simplification of the model neglecting spin-orbital coupling and lattice contributions to quadrupole splitting [213]. In agreement with the 2$^{nd}$ order Doppler effect, the thermal variation of the isomer shift in the range of 80–345 K for both species is linear with the slope $d\delta/dT = -5.11 \cdot 10^{-4}$ mm s$^{-1}$ K$^{-1}$, which leads to an effective vibrating mass of 81 g mol$^{-1}$ calculated according equation $M_{eff} = -4.1602 \cdot 10^{-2}$ $(d\delta/dT)^{-1}$ [219]. The width of the Mössbauer resonance lines is essentially temperature-independent with a $\Gamma_{1/2}$ value of 0.16 mm s$^{-1}$. The ratio HS(A) : HS(B) varies in the range from 1:3 to 1:4 increasing with temperature which possibly reflects the temperature-dependent disorder of $BF_4^-$ anion over two positions. In contrast, the perchlorate analogue of **2** compound **2-ClO₄** displays only one high-spin doublet in Mössbauer spectrum, which reflects absence of the disorder of the perchlorate anions in the lattice of the compound (Chapter 6.1).

The best fit of the Mössbauer spectrum of **4** is shown in Figure 37b. It is worth to emphasize two points. First, the best fit of the experimental spectrum was obtained with two

resonance singlets which are assigned to two inequivalent lattice positions of iron(II) with the same occupancy factors (1:1). The second feature is the absence of the splitting of resonance lines. Despite the deviations of the geometry of the coordination polyhedron from $O_h$ symmetry and the fact that the environments of the two species differ, the absence of splitting can be explained by accidental mutual compensation of the valence contribution $q_{val}$ and the lattice contribution $q_{latt}$ to the electric field gradient, which are known to have opposite signs [202]. The analysis of X-ray structure of **4** reveals almost similar Fe–N$^{imd}$ bond lengths for both species but a slight increase of Fe–N$^{im}$ distances going from Fe1 to Fe2-based complex cation (Table 7). The increase in bond length by 0.09 Å reduces $\sigma$–electron density at iron(II) in Fe2-based cation relative to that in Fe1-based, and explains the more positive isomer shift [213, 215]. Another reason might be differences between the complex cations regarding the intermolecular contacts as shown in Figure 32b. Hydrogen bonds NH$\cdots$O could have also an influence on the distribution of the electron density within imidazole groups modifying bonding properties of the ligands in the two species.

### 2.3.6    Discussion

The compounds **2–6** are mononuclear tripodand-based complexes, the structures of which were determined by X-ray single crystal diffractometry. Two compounds of these have already been known and some of their spectroscopic properties reported. The characterization, however, was found to be insufficient regarding the objectives of our study. For example, some spectroscopic and room temperature magnetic data were already available for **3** [136, 138], while for **5** the structure as well as IR and UV/VIS spectroscopic data have been reported but no magnetic or Mössbauer data were known [140]. Therefore, we decided to repeat the synthesis of these compounds and to perform a complete characterization of all compounds in order to have sufficient and consistent information about their structures and physical properties.

The compounds **3** and **5** were known from the literature to be low-spin [136, 160]. In this case modification of the ligand backbone was indicated in order to decrease the ligand field strength of the constituent ligands. Two empirical "thumb rules" are often used to predict how a low-spin system should be modified to obtain a spin-crossover or a high-spin complex [174]. Both rules concern the chemical adjustment of the organic groups to tune the donor properties of the ligand. The first method implies the introduction of steric hindrance close to the donor atom coordinating to the central ion, for example, a methyl group or a chlorine atom

into the sixth position of the pyridine ring which rotates and requires more space than a hydrogen atom. As a consequence, the donor atom–central ion distance R lengthens and the ligand field strength weakens according to $10Dq \sim (1/R)^{5-6}$ [72]. The steric hindrance effect can substantially decrease the ligand field strength and destabilize the singlet ground state of iron(II) ion [174]. This synthetic approach is applied for the preparation of the complexes **1** and **6** containing 6-methylpyridin-2-yl (6-*Mepy*) groups. The second method implies the change of six-membered pyridine by five-membered imidazole, which creates weaker ligand field. This approach was implemented for the synthesis of **2** and **4**.



a



b
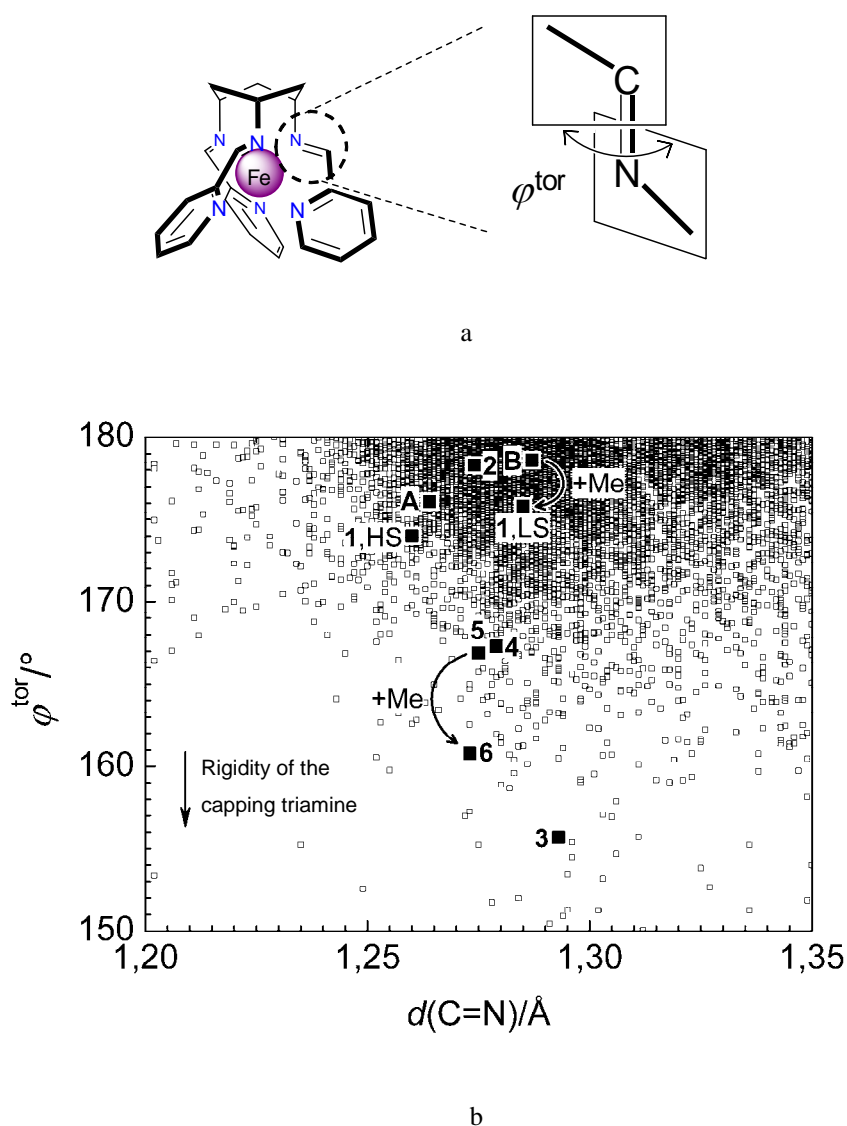
**Figure 40**. a) Definition of torsion angle $\varphi^{tor}$; b) Scatter plot of **A**, **B**, **1**–**6** in coordinates $\varphi^{tor}$ *vs* $d$(C=N). The points corresponding to the values of iron(II)-containing complexes from the Cambridge Structural Data Base [42] are shown on the background.

The combination of three capping triamines and three types of heterocyclic groups gives nine symmetrical tripod ligands. Eight isolated iron(II) complexes included in the work are shown in Table 1 (Chapter 2.1.3). The only structural fragment common for all those complexes is $C=N^{im}$ group directly coordinated to iron(II) ion. Therefore, it is reasonable to correlate the structural parameters of the group with the spin-state properties of the complexes. Actually, the torsion value $\varphi^{tor}$ of the free $C–C=N^{im}–C$ fragment is equal to 180°, but upon complexation it is one of the mostly affected structural elements (Figure 40a, b, Table 7). For a comparison of the complexes **A**, **B**, **1**–**6**, the structural data of iron(II) based-compounds from Cambridge Structural Data Base [42] are shown on the background in the form of a scatter plot $d(C=N)$ *vs* $\varphi^{tor}$ (Figure 40b). As is seen, the distance between the two atoms in the compounds under discussion varies slightly [1.257(4)–1.307(0) Å] contrary to the torsion angle. For the high-spin complexes **1** (330 K) and **2** the $\varphi^{tor}$ values almost coincide with the statistical maximum for the reported complexes (it corresponds to the darkest part on the background of the plot). The decrease of the rigidity of the capping triamine in the sequence *tach–tame–tren* [140] is mirrored by the increase of the angle $\varphi^{tor}$ in the low-spin complexes. The highest values are found in the *tren*-based compound **A**, **B** and the methylated analogue **1** (low-spin, 80 K) which corresponds to the most unaffected torsion angle $\varphi^{tor}$. It is then lower in the *tame*-based **4**, **5** and **6** and the lowest in **3** (see Table 7). A regular decrease of the torsion from non-methylated to methylated compounds (**B** → **1**(LS), **5** → **6**) is found as well (Figure 40b). According to this, the hypothetic methylated analogue of **3** should have a value $\varphi^{tor} < 155.7°$. An attempt to prepare this complex on the basis of the ligand *tach*(6-*Mepy*)$_3$[1] from 6-methylpicolinaldehyde and triamine *tach* gave no positive result. As it seen, in **3** the value of $\varphi^{tor}$ is one of the lowest reported, hence, the realization of a helical conformation of the ligand and low-spin state of the iron(II) ion with even more twisted $C–C=N^{im}–C$ fragment is supposed to be unlikely. On the other hand, the high-spin configuration preserving untwisted fragment, like the one found in **2** (Figure 30a), is also impossible. Molecular modeling shows that the formation of a complex with acceptable $Fe–N^{py}$ distances can be anticipated only with the helical wrapping of the ligand. Trigonal prismatic arrangement of nitrogen atoms does not allow unstrained arrangement of three methyl groups and simultaneous approaching of the iron(II) ion by the triangle of pyridine nitrogen atoms $N^{py}$ at distances sufficient for tight bonding (Figure 41). In this case, strong deviation of the angles in the fragments ($C=N^{im}–C$) should be expected as well. The same effect, but less pronounced, was found in the trigonal prismatic Zn-based derivative of *tach*(*py*)$_3$ [140]. Similarly to the

---

[1] 1,3,5-*cis,cis*-tris[1-aza-2-[(6-methyl)(2-pyridyl)]vinyl]cyclohexane

ligand  *tach*(6-*Mepy*)$_3$  ligands  2,9-dimethyl-1,10-phenanthroline  and  6,6'-dimethyl-2,2'-bipyridine were reported to be unable to form tris(ligand) complexes with iron(II) ion because of the crowding of the methyl groups [174, 220, 221].
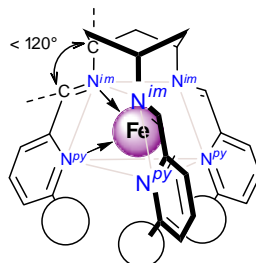


**Figure 41**. Unrealistic model of the iron(II) high-spin complex molecule based on the ligand *tach*(6-*Mepy*)$_3$.

In order to rationalize the structural features in **A**, **B** and **1**–**6**, several factors affecting the overall energy of the complex cation should be considered [140], notably: a) the energy of ligand strain; b) intraligand atom repulsion energy, and c) ligand field stabilization energies. Since these structures are determined in the solid state, crystal packing energies and intermolecular forces may contribute to the overall geometry of the cations, but they are probably small compared to these other effects [140]. Ligand field stabilization energies are higher for octahedral field than for trigonal prismatic fields [206] and it has been suggested that this represents a driving force leading away from trigonal prismatic geometry in **A**, **B**, **1** and **3**–**6**, but not in **2**. For the latter the rigidity of *tach* and the absence of back-bonding, which can decrease the rigidity of carboxaldimino chelate arms, play decisive roles. Intraligand repulsion energy is of primary importance in the methylated **1** and **6**.

Distortions from the ideal case of a perfect octahedron are described by a set of parameters [192, 222-224] (Figure 42) calculated from the structural data, namely:

- averaged distances <Fe–N$^{im}$> and <Fe–N$^{het}$> and their difference $\Delta r$;

- averaged distances between imine nitrogen atoms and nitrogen atoms of heterocycles, $s^{im}$ and $s^{het}$, respectively, and their difference $\Delta s$;

- distance $h$ between centroids of two opposite triangles formed by imine nitrogen atoms and nitrogen atoms of the heterocycles;

- twist angle $\theta$ (definition in Chapter 2.2.2);

- deviation parameter $\Sigma$ (definition in Chapter 2.2.2) and

- bite angle $\alpha$.

Derived parameters are presented in Table 7.
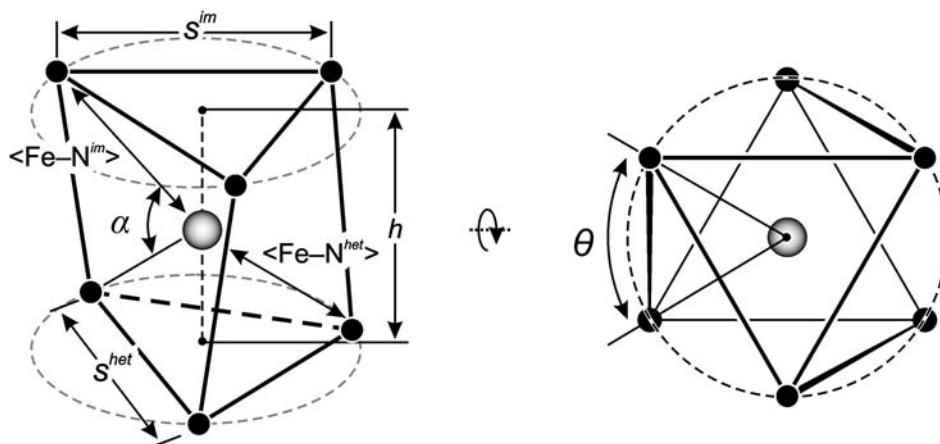


**Figure 42**. Definition of the distortion parameters of the pseudo-octahedron (side view and the projection along the threefold axis).
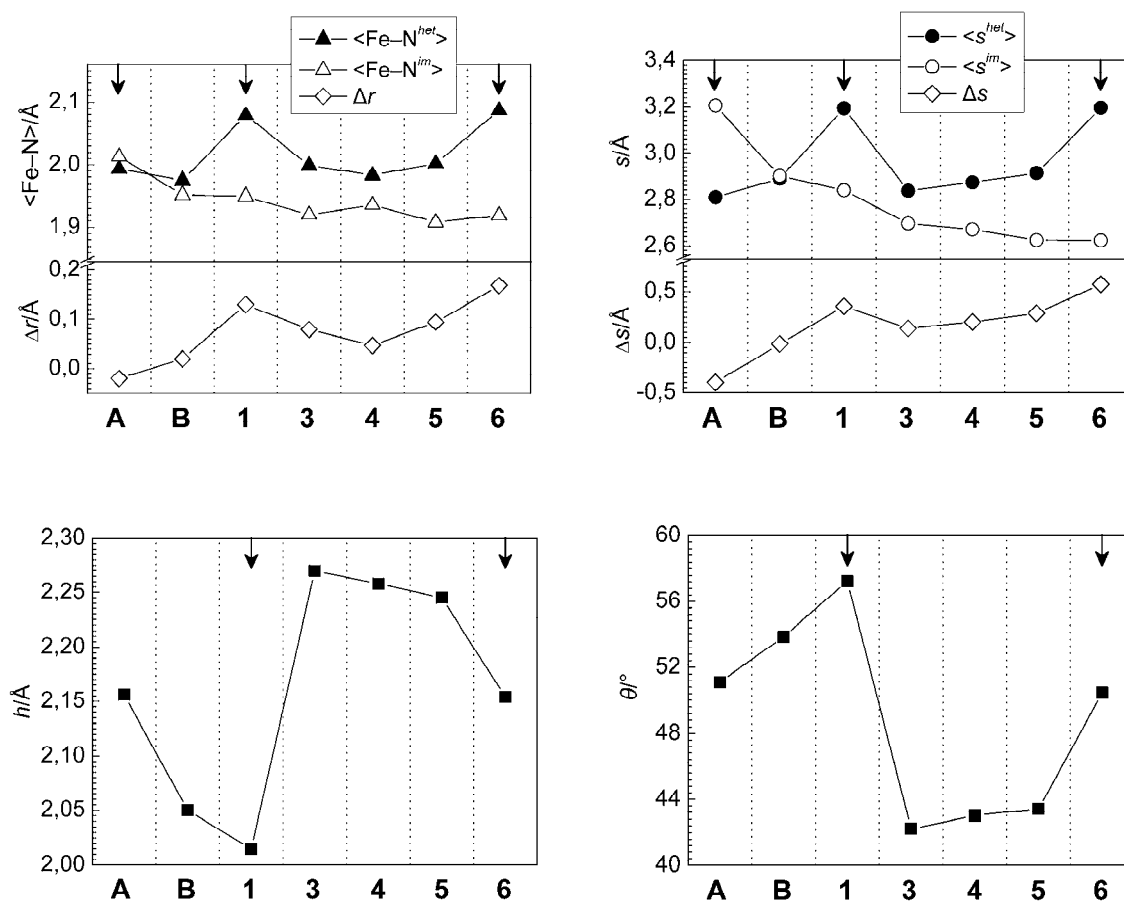


**Figure 43**. Plots of selected structural parameters of pseudo-octahedral **A**, **B**, **1**, **3–6** in low-spin state. Arrows point extremes in the series of structurally similar parameters.

Selected plots of derived structural parameters are shown in Figure 43. System **2** is excluded from the comparison because of the specificity of the coordination polyhedron and of the spin-state. In general, all of the systems show similar parameters with three exceptions, namely **A**, **1** and **6**. Since the donor atoms within the first coordination shell and their separations from the central atom directly influence the ligand field strength [72], some correlations regarding the spin-state properties can be drawn from these data. On the basis of structural analysis (Figure 43), spin-crossover properties might be expected for **6** similarly to **1** and **A**. Despite this and the close resemblance of the main structural parameters and of the space groups in which the compounds **1** and **6** crystallize, the latter is low-spin up to 400 K. This most likely results from the high rigidity of the capping triamine *tame* constituting the organic part of the complex. It prevents the transformation of the iron(II) ion from the compact low-spin state into more voluminous high-spin state. Nevertheless, it may be supposed that the ligand field strength in **6** is very close to the critical value and a minor alternation of the organic core can lead to formation of a compound with spin-crossover below 400 K. This suggestion was later confirmed by the study of the alkylated derivatives which show spin-transition with $T_{1/2}$ being *ca.* 360 K (Chapter 2.8).

### 2.3.7   Summary

1. Compound **2** is a high-spin iron(II) complex retaining a high magnetic susceptibly value down to 10 K. Structural insight reveals an unprecedented trigonal prismatic geometry of the $N_6$ polyhedron. The specific splitting of *d*-orbitals in $D_{3h}$ geometry is the reason for the observed huge quadrupole splitting of the doublets in the Mössbauer spectra of the compound.

2. Compounds **3**, **4**, **6** possess a pseudo-octahedral environment of the central iron(II) ions with different degree of the deviation from $O_h$ symmetry which was described by a set of structural parameters. The crystals of the compounds are a mixture of optical antipodes. Magnetic measurements up to 400 K demonstrate the diamagnetic nature of the compounds which is in agreement with the structural data.

3. The crystal lattice of **4** possesses two inequivalent low-spin complex cations which is confirmed by IR and Mössbauer spectroscopy. In contrast, the UV/VIS spectrum in acetonitrile solution corresponds to the high-spin state which led to the conclusion that hydrogen bonds are responsible for the stabilization of the low-spin state in the solid.

4. Comparison of the derived structural data of **A**, **B**, **1**, **3**–**6** shows close resemblance of the parameters for the pair **1** and **6** which suggests the occurrence of spin-crossover transition in **6** above 400 K. Chemical modification of the ligand is assumed to decrease the ligand filed strength sufficiently to shift spin-transition to the lower temperature region.

## 2.4  Mononuclear metallomesogenic systems of iron(II)

### 2.4.1  Introductory remarks

On the basis of the results described in the previous chapters, the complexes **B**, **1**, **3**, **5** and **6** were found to satisfy the condition for manipulating the spin state. They show spin-transition (**1**) or are low-spin (**B**, **3**, **5**, **6**) and can be used for further modification experiments (Figure 44). The complexes **A** and **4** were omitted from the further study because of the evident strong dependence of the spin state on hydration. Anhydrous imidazole-based complexes are usually high-spin [167]. The complex **2** was also not subject to chemical modification due to its high-spin nature.
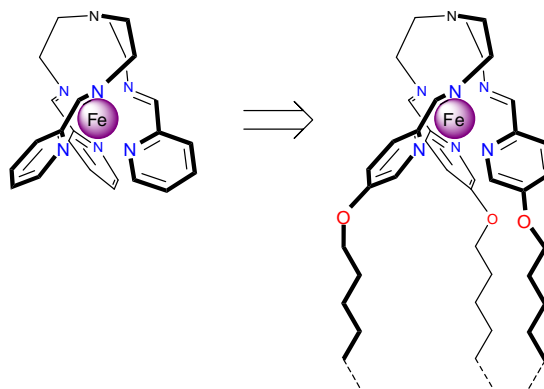


**Figure 44.** Schematic illustration of the chemical modification of the spin-crossover and low-spin compounds **B**, **1**, **3**, **5** and **6**.

In the following a short overview of reported data (1988–2008) is presented concerning the spin-crossover properties of mononuclear mesogenic iron(II) systems.

### 2.4.2  Overview of the literature on iron(II)-based mononuclear metallomesogens with spin-crossover properties

Perhaps, the first spin-crossover systems with unrecognized liquid crystalline properties are those used for the preparation of the Langmuir-Blodgett films. In 1988 the first article was published which described the neutral complex formed by two phenanthroline moieties with three grafted aliphatic alkyl chains and two thioacynite anions (Figure 45a) [225]. This system and similar one (Figure 45b) [134, 226, 227] show a temperature-induced

gradual spin-transition and at low temperature could be excited into a metastable high-spin state (LIESST effect) [228]. It was found that heating above 340 K caused melting of the alkyl chains which affected the spin-crossover properties, but the mesogenic properties of the systems were not investigated [226].
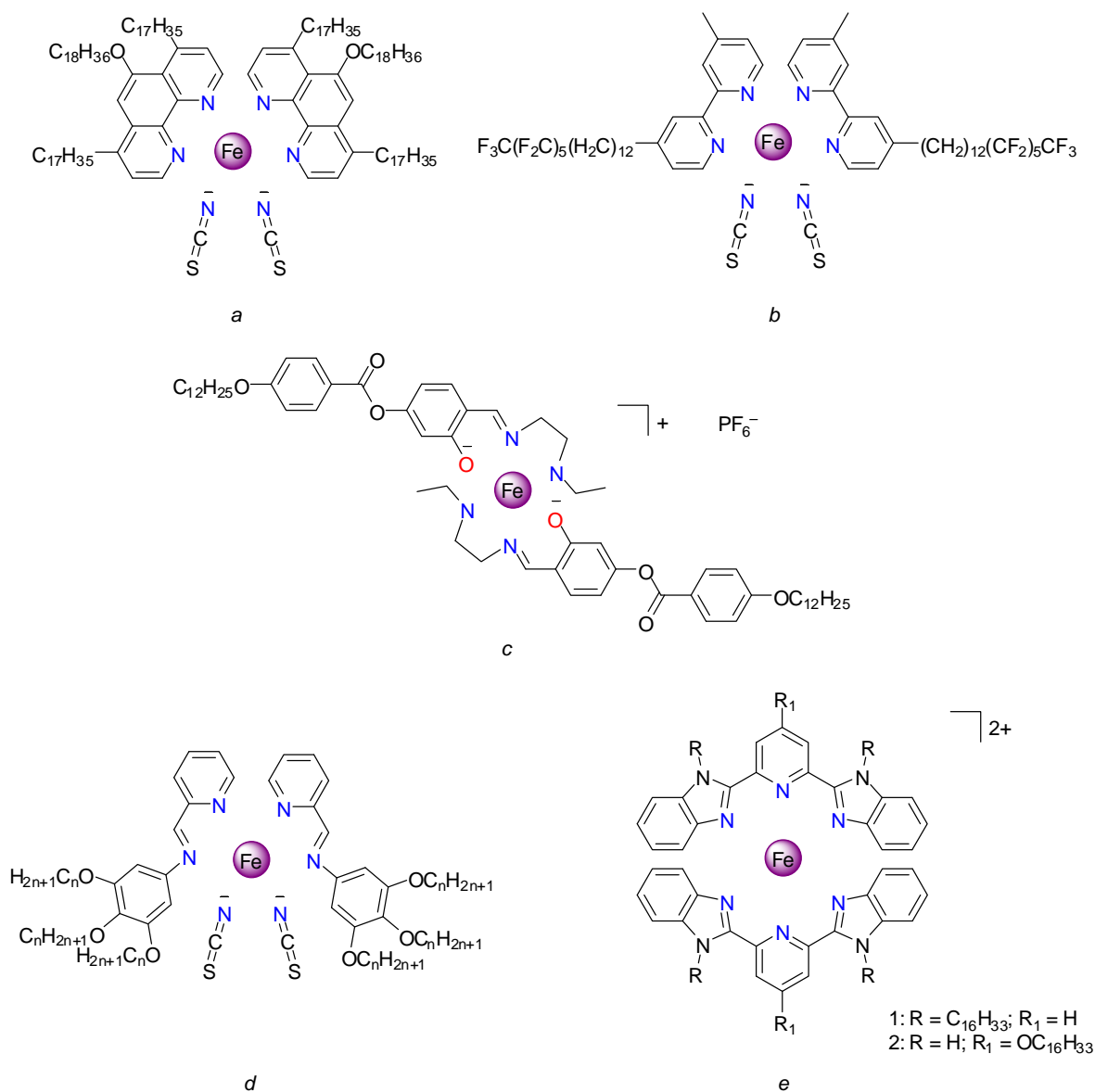


**Figure 45.** Molecular structures of the iron(II, III) complexes used for preparation of Langmuir-Blodgett films (a, b) and metallomesogens (c, d, e).

The first metallomesogen with spin-crossover properties was reported by Galyametdinov *et al.* (Figure 45c) [229]. The molecules of the compound are composed of two anionic Schiff-base ligands chelating an iron(III) ion. The excessive positive charge is compensated by a single $PF_6^-$ anion. During the cooling, the susceptibility of the compound gradually decreases resulting in an incomplete spin-transition confirmed also by Mössbauer

spectroscopy. On heating, at 375 K the susceptibility experiences a sudden jump corresponding to the transition from crystalline state into smectic A mesophase. The reason for the discontinuity suggested by the authors is the decrease of the viscosity due to the phase transition with subsequent alignment of the anisotropic complex molecules in the magnetic field [229]. Later, Hayami *et al.* reported on the iron(II)-based metallomesogen with incomplete gradual spin-crossover centered at $T_{1/2}$ = 217 K (Figure 45d) [230]. At low temperature the system shows the LIESST effect. The transition from crystalline state into smectic phase takes place at 345 K hence excluding the possibility for the two transitions to interact. Modified systems were reported later [231, 232]. The variation of the number of the alkyl substituents allowed to control the melting temperature; this, however, did not improve the interconnectivity of the two phenomena. Recently, the same group reported on new spin-crossover systems based on the alkylated 2,6-bis(benzimidazol-2-yl)pyridine ligands (Figure 45e). Depending on the number of substituents and their position they obtained low-spin and spin-crossover systems with mesogenic properties (1 and 2 in Figure 45e). As in the previous cases, the $T_{1/2}$ of the spin-transition is well below room temperature which is too low to be influenced by the phase transition taking place above 320 K.

Concluding, one can say that research of the mononuclear iron(II)-based metallomesogens is only starting. Today only three systems are known, whereas, for example, dozens of copper(II)-based metallomesogens have been described [233]. The development of metallomesogens exhibiting spin-crossover is primarily aimed to perform the co-occurrence of spin-transition and mesomorphism in the same temperature region. The next chapters describe the first examples of mononuclear iron(II) systems in which spin-crossover and liquid crystallinity phenomena are coupled.

### 2.4.3   Synthesis

The synthesis of the alkylated complexes was accomplished according to the procedure similar to that used for the parent complexes, *i.e.* by condensation of the stoichomertic amounts of a triamine and of an aldehyde in presence of an iron(II) salt (Figure 46). The precursors 5-(alkoxy)picolinaldehyde and 6-methyl-5-(alkoxy)picolinaldehyde were obtained by modified methods [234-237]. The stoichiometry of the obtained complexes is consistent with the proposed formula. The CHN analysis data of the complexes together with the synthetic details are collected in the Experimental section (Chapter 6.7). The mass

spectroscopic, IR and TGA data are presented in Chapters 2.5.4, 2.6.3, 2.7.2, 2.8.3. A summary of the iron(II) complexes included in the present study can be found in Table 10.
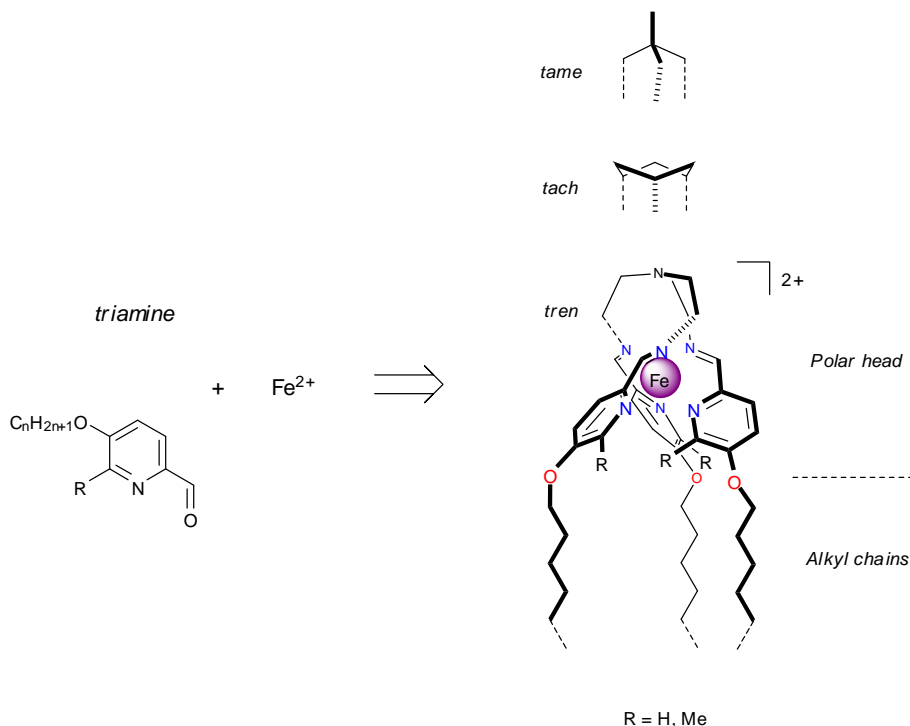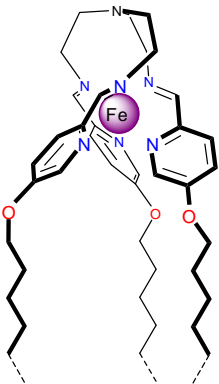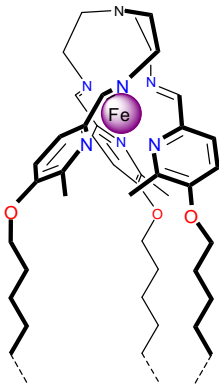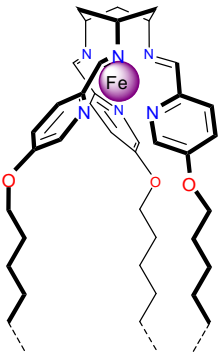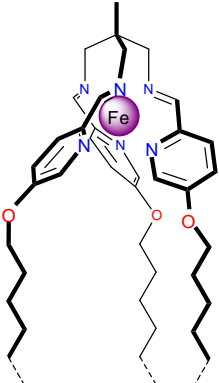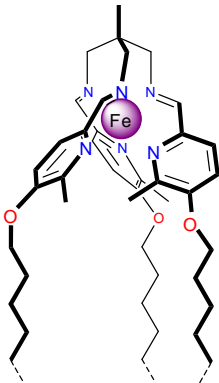


**Figure 46.** Synthesis of the mesogenic systems.

### 2.4.4   Nomenclature

The nomenclature $C_n$-**N** was adopted to label the alkylated complexes, where $C_n$ represents the alkyl substituents with $n$ carbon atoms ($C_nH_{2n+1}$), **N** corresponds to the type of the coordination core together with the anions and water molecules. Complexes $C_n$-**7**–$C_n$-**18** are derivates of the triamine *tren* and 5-(alkoxy)picolinaldehyde, $C_n$-**19**–$C_n$-**23** of *tren* and 6-methyl-5-(alkoxy)picolinaldehyde, $C_n$-**24** of *tach* and 5-(alkoxy)picolinaldehyde, $C_n$-**25** of *tame* and 5-(alkoxy)picolinaldehyde, $C_n$-**26**–$C_n$-**29** of *tame* and 6-methyl-5-(alkoxy)picolinaldehyde. In Table 10 are shown the schematic structure of the corresponding complex cations.

**Table 10.** Schematic molecular structures of the complex cations in compounds $C_n$-**7**–$C_n$-**29**.

| Triamine | Aldehyde | |
|---|---|---|
| | 5-(alkoxy)picolinaldehyde | 6-methyl-5-(alkoxy)picolinaldehyde |
| *tren* |  $C_n$-**7**–$C_n$-**18** |  $C_n$-**19**–$C_n$-**23** |
| *tach* |  $C_n$-**24** | – |
| *tame* |  $C_n$-**25** |  $C_n$-**26**–$C_n$-**29** |

### 2.4.5    The role of the constituents in compounds $C_n$-7–$C_n$-29

The structure of the ligand plays perhaps the most important role in the determination of the spin state of the compounds. The particular role of each constituent of the compounds $C_n$-7–$C_n$-29 is the following:

*Triamine* has direct influence on the rigidity of the ligand (Chapter 2.1.2) and its response to the change of the small low-spin iron(II) ion to the more voluminous high-spin form;

*Methyl substituents* influence the ligand field strength due to the steric hindrance and donation effects [174, 238];

*Alkyl chains* define the separation distance of the ionic bilayers, type of the packing and melting temperature of the compound, and modify the ligand field strength of the ligands;

*Anions* modulate through the electrostatic pressure and hydrogen bonding the ligand field strength and determine the structure of the ionic bilayers along with patterns of the intermolecular contacts.

### 2.4.6    The packing of compounds $C_n$-7–$C_n$-29

If the length of the alkyl chains exceeds some limit, which depends on the nature of the particular compound, the chains can form a definite paraffinic sublattice. The type of the packing of the mesogenic molecules in solid and in mesophase is governed by the interface curvature which is a measure of the cross-sections of the two incompatible molecular parts, of the charged head-group and of the alkyl chains [239]. In Figure 47a, b, c are shown schematically three possible types of the organization of the metallomesogens [240, 241]. The mostly realized is the type with the flat interface leading to smectic mesomorphism (Figure 47a) [128]. If the total cross-section of alkyl chains determined by their number exceeds that of the polar head then the columnar type of the packing is formed (Figure 47b) [242]. In strongly alkylated compounds the cubic type of the packing can be observed with spheric-like aggregates (Figure 47c) [242-244]. In the compounds $C_n$-7–$C_n$-29 an approximate ratio between the cross-sections of a polar head (evaluated from the crystallographic data of **B**, **1**, **3**, **5** and **6**) and the attached three alkyl chains is about 1.3:1 (see Figure 48a, b) which might favor the formation of the flat interface with the smectic mesomorphism (Figure 47a).

*interface curvature*

0

**layers**                    **cylinders**                    **spheroids**

*Polar heads*   *Alkyl chains*

Smectic          Columnar          Cubic
mesomorphism     mesomorphism      mesomorphism

a                    b                    c
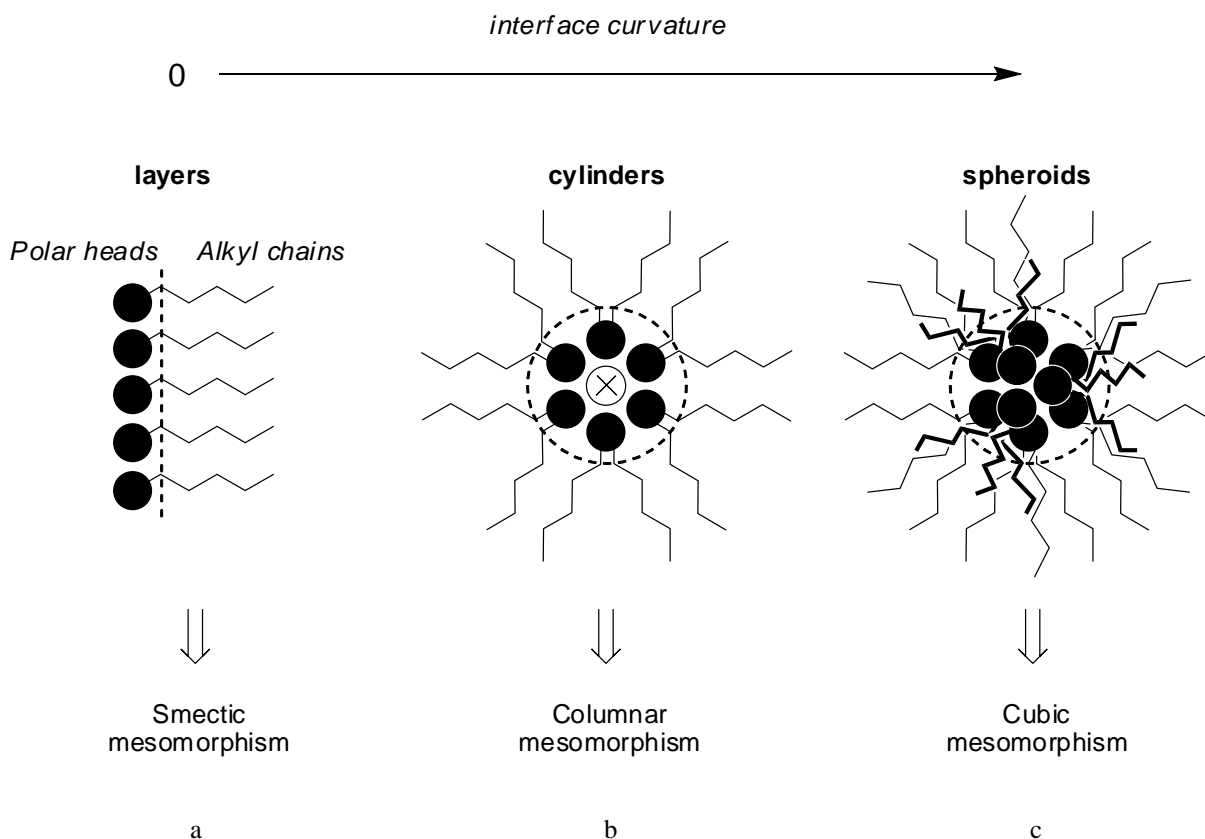
**Figure 47.** Schematic drawings show the interface curvature as a function of the cross-sections of a head-group and the attached alkyl chains in micro-segregated mesogens which leads to a) smectic, b) columnar and c) cubic mesomorphism. The dashed lines show the border between the two incompatible molecular parts.



Cross-section ≈ 70 Å$^2$              Cross-section ≈ 18 Å$^2$

a                                        b
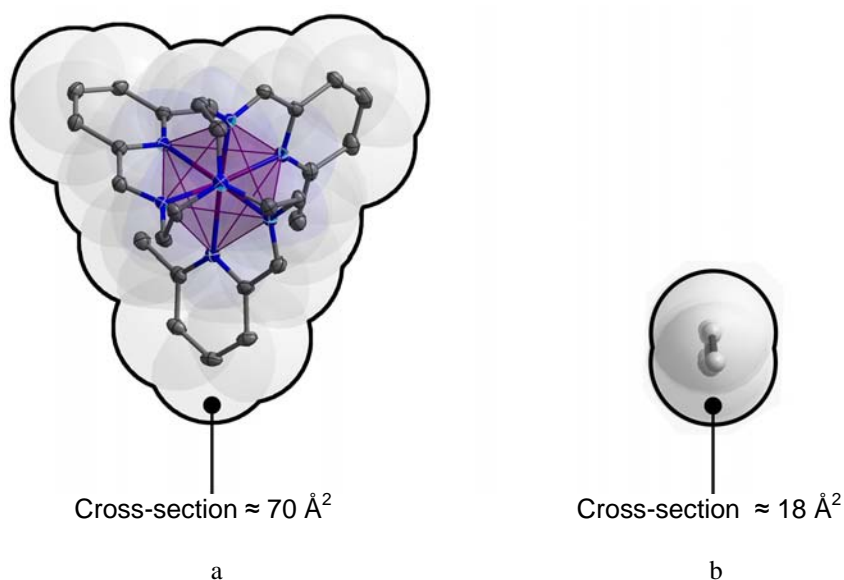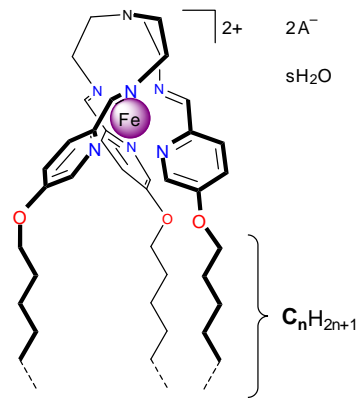
**Figure 48.** a) Projection of the complex cation of **1** (80 K, low-spin) along the direction N7···Fe1; b) Projection of an *all-trans* alkyl chain along the main axis.

## 2.5 Characterization and physical properties of compounds $C_n$-7–$C_n$-18

### 2.5.1 Introductory remarks

This chapter concerns the characterization and study of the derivatives of the parent system **B** formed by the ligand tris[3-aza-4-((5-alkoxy)(2-pyridyl))but-3-enyl]amine [*tren*($C_n$-*py*)$_3$]. The codes and the composition of compounds under study are shown in Table 11.

**Table 11.** Schematic structure and composition of $C_n$-**7**–$C_n$-**18.**

| Anion A$^-$ | s | Compound |
|---|---|---|
| ClO$_4^-$ | 0 | **C$_6$-7, C$_{18}$-7** |
| BF$_4^-$ | 0 | **C$_{12}$-8** |
| | 0.5 | **C$_{18}$-9** |
| SO$_4^{2-}$ | 4.0 | **C$_{18}$-10** |
| F$^-$ | 3.5 | **C$_{18}$-11** |
| | 0 | **C$_{18}$-12** |
| Cl$^-$ | 3.5 | **C$_{16}$-13, C$_{18}$-13, C$_{20}$-13** |
| | 0.5 | **C$_{16}$-14, C$_{18}$-14, C$_{20}$-14** |
| | 0 | **C$_{16}$-15, C$_{18}$-15, C$_{20}$-15** |
| Br$^-$ | 3 | **C$_{18}$-16** |
| I$^-$ | 0 | **C$_{18}$-17** |
| C$_{18}$TOS$^-$ | 1 | **C$_{18}$-18** |

### 2.5.2 Crystal structure of C$_6$-7

Dark red plate-like crystals of **C$_6$-7** were obtained from a hot saturated ethanolic solution of the compound by slow cooling in a thermostat. Projection of the independent *L* and *D* optical isomers is shown in Figure 49a, the unit cell parameters and refinement details are presented in Table 12, whereas Table 13 contains the characteristic intramolecular parameters. The amphiphilic nature of the alkylated molecules results in a self-assembly into the bilayered composite with one layer being made of the polar head-groups along with the perchlorate anions. Non-polar chains from oppositely directed molecules meet together to form the hydrocarbone layer. Almost completely stretched alkyl chains are distorted by *gauche* conformation of some of the methylene groups (Figure 49a) and tilted toward the *ac* plane, but do not intertwine with those of the adjacent layer (Figure 49b). Compared to the non-alkylated complex **B** [160], the introduction of alkyl chains into the complex molecule affects the crystal packing and leads to segregation into a layered structure (Figure 49b).

Whereas the hydrogen bond network has a three-dimensional character in **B**, all CH⋯O contacts in **$C_6$-7** belong to the two-dimensional hydrogen bond network formed within the ionic bilayers [2.428(2)–2.719(2) Å].



a



b
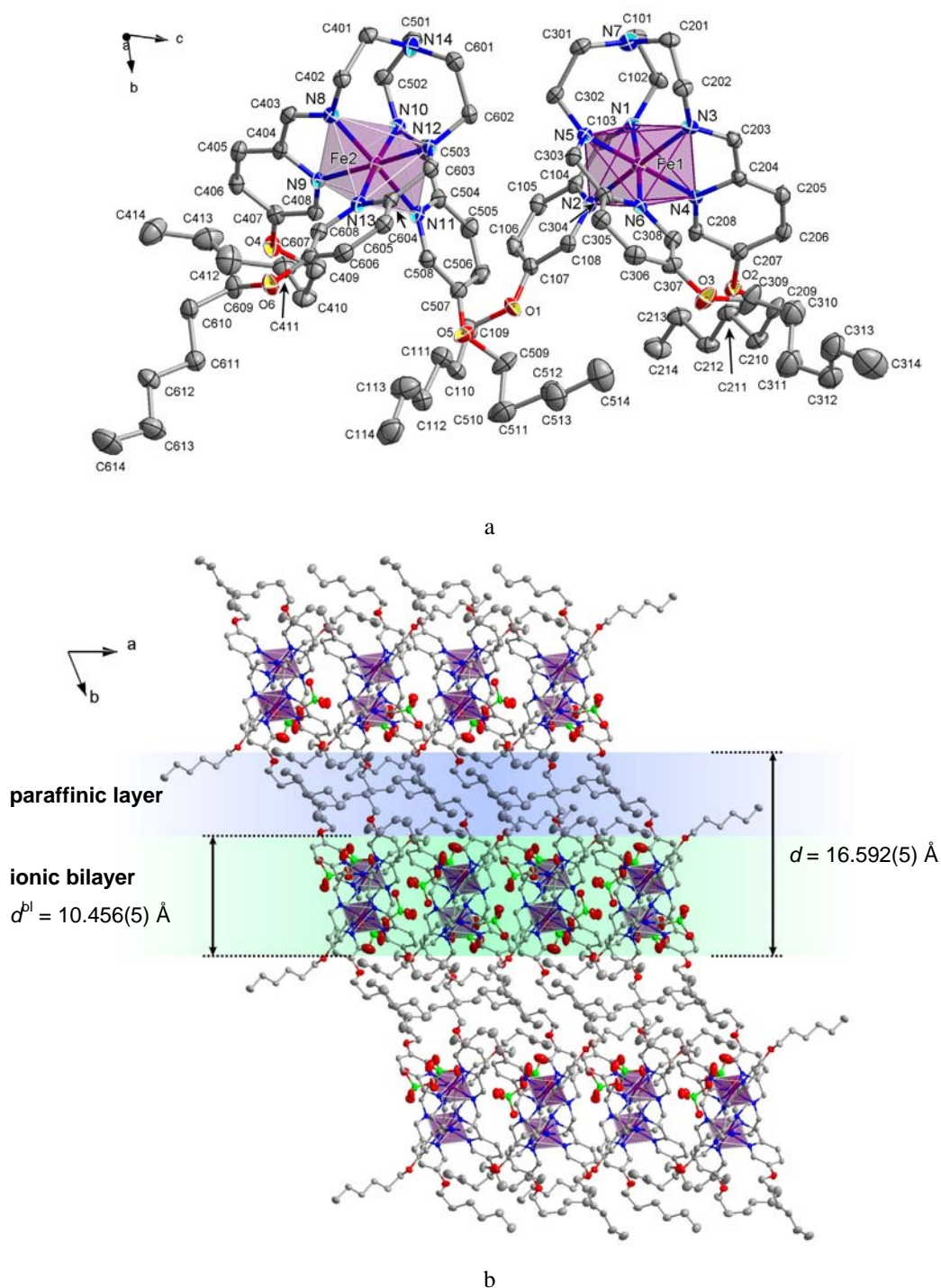
**Figure 49.** a) Projection of two independent cations of **$C_6$-7**. Hydrogen atoms and perchlorate anions are omitted for clarity; b) Projection of molecular packing along the *c* axis. The colored areas denote the paraffinic layer and the ionic bilayer. Paraffinic layers are formed by disordered alkyl chains, whereas ionic bilayers are formed by polar head-groups and perchlorate anions in between. Displacement ellipsoids are shown at 50 % probability level.

**Table 12.** Crystallographic data and refinement details for $C_6$-7 and $C_{12}$-8.

| | $C_6$-7 | $C_{12}$-8 |
|---|---|---|
| Empirical formula | $C_{42}H_{63}Cl_2FeN_7O_{11}$ | $C_{60}H_{99}B_2F_8FeN_7O_3$ |
| Formula weight | 968.74 | 1195.93 |
| Temperature [K] | 150(2) | 193(2) |
| Wavelength [Å] | 0.71073 | 1.54178 |
| Crystal system | triclinic | triclinic |
| Space group | $P\bar{1}$ | $P\bar{1}$ |
| a [Å] | 14.541(3) | 14.050(6) |
| b [Å] | 18.514(4) | 19.347(6) |
| c [Å] | 19.462(4) | 24.16(2) |
| α [°] | 74.96(3) | 102.26(6) |
| β [°] | 88.13(3) | 96.01(6) |
| γ [°] | 68.18(3) | 94.42(3) |
| Volume [Å$^3$] | 4685.50(7351) | 6348(7) |
| Z | 4 | 4 |
| $\rho$ [g cm$^{-3}$] | 1.373 | 1.251 |
| Absorption coefficient [mm$^{-1}$] | 0.501 | 98 |
| $F(000)$ | 2048 | 2560 |
| $\theta$ range for data collection [°] | 2.83 to 32.90 | 1.89 to 69.99 |
| Index ranges | $-14 \le h \le 22$ | $-17 \le h \le 17$ |
| | $-27 \le k \le 26$ | $0 \le k \le 23$ |
| | $-29 \le l \le 27$ | $-29 \le l \le 28$ |
| Reflections collected | 43465 | 24734 |
| Independent reflections | 27353 [$R_{int} = 0.0276$] | 23960 [$R_{int} = 0.1249$] |
| Data/restraints/parameters | 27353/0/1141 | 23960/943/1460 |
| Goodness-of-fit, $F^2$ | 1.031 | 1.068 |
| Final $R$ indices [$I > 2\sigma(I)$] | $R1 = 0.0470$, | $R1 = 0.2000$, |
| | $wR2 = 0.1288$ | $wR2 = 0.4641$ |
| $R$ indices (all data) | $R1 = 0.0907$, | $R1 = 0.3317$, |
| | $wR2 = 0.1454$ | $wR2 = 0.5227$ |
| $\rho_{min}, \rho_{max}$ [e Å$^{-3}$] | 1.457, 0.952 | 0.656, 0.658 |

**Table 13.** Intramolecular parameters [a] of $C_6$-7 and $C_{12}$-8.

| | $C_6$-7 | $C_{12}$-8 |
|---|---|---|
| $<$Fe–N$^{im}>$ [Å] | 1.954(2) | 1.935(54) |
| $<$Fe–N$^{py}>$ [Å] | 1.973(2) | 1.941(55) |
| $\theta$ [°] | 55.10(4) | 52.90(71) |
| $\Sigma$ [°] | 67.56(8) | 61.22(7) |
| Fe···N7(N14) [Å] | 3.420(2) | 3.450(58) |

[a] Values are averaged over two independent cations

### 2.5.3 Crystal structure of $C_{12}$-8

Dark red plate-like crystals of **$C_{12}$-8** were obtained by keeping a saturated chloroform/ethanol solution of the compound at –40° C over two weeks. A projection of the two independent molecules with numbering scheme is shown in Figure 50a, the unit cell

parameters and refinement details are presented in Table 12, whereas Table 13 contains the characteristic intramolecular parameters. The temperature factors of alkyl chains are relatively high due to a pronounced disorder. The relatively high *R* value of the structure can be explained by the fact that it is very difficult to obtain good quality crystals of layered structures with long alkyl chains [245].



a
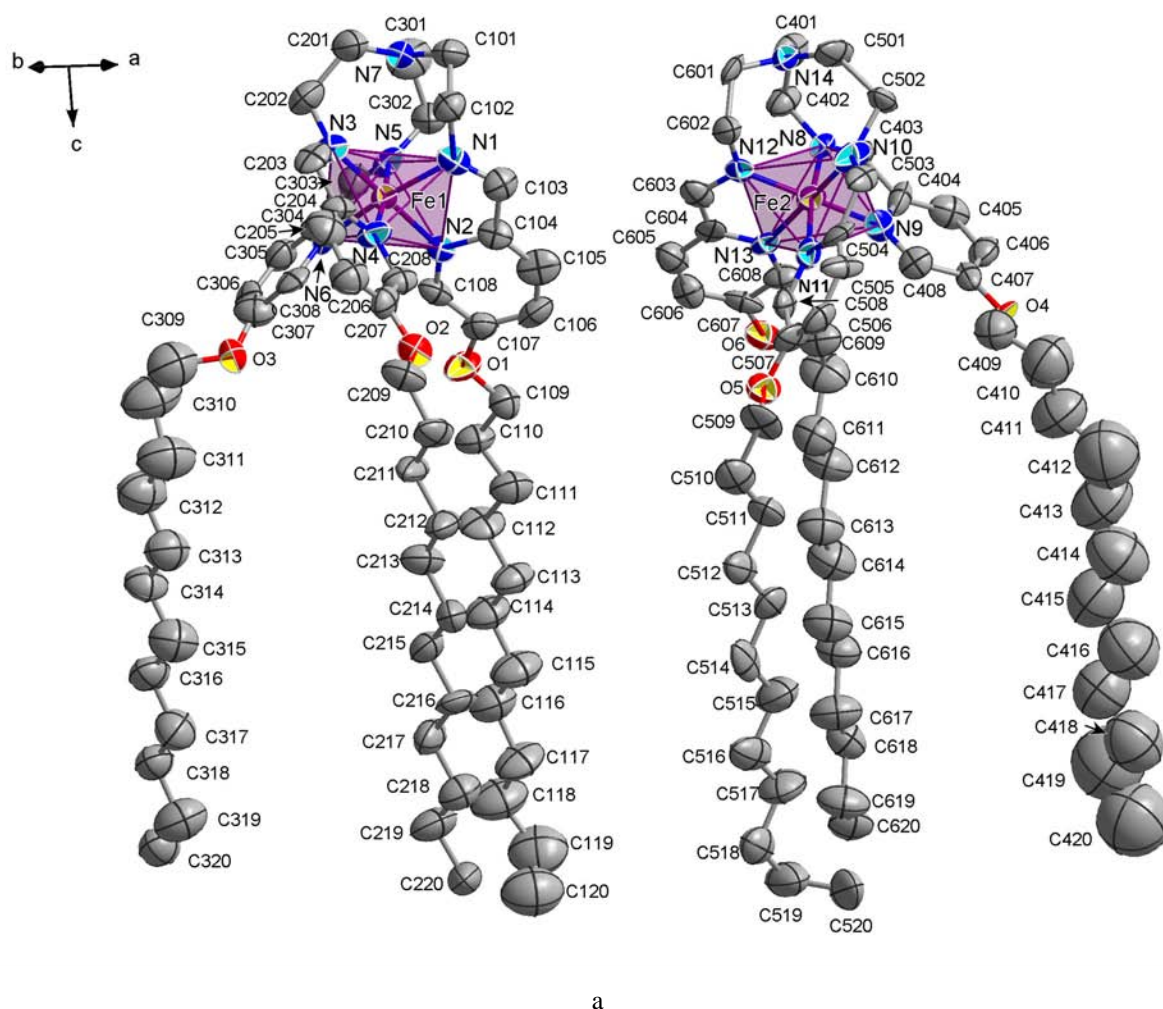
**Figure 50.** a) Projection of the two independent complex cations of **$C_{12}$-8**. Anions and hydrogen atoms are omitted for clarity; b) Projection of the crystal packing along the *a* axis. The colored areas denote the paraffinic layer and the ionic bilayer. Paraffinic layers are formed by ordered almost *all-trans* alkyl chains, whereas ionic bilayers are formed by polar head-groups and tetrafluoroborate anions in between; c) Projection showing rotationally distorted hexagonal packing of the alkyl chains in the paraffinic layer. Displacement ellipsoids are shown at 50 % probability level.

**paraffinic layer**

**ionic bilayer**
$d^{bl}$ = 10.55(35) Å

$d$ = 23.45(35) Å

b



~ 4.8 Å
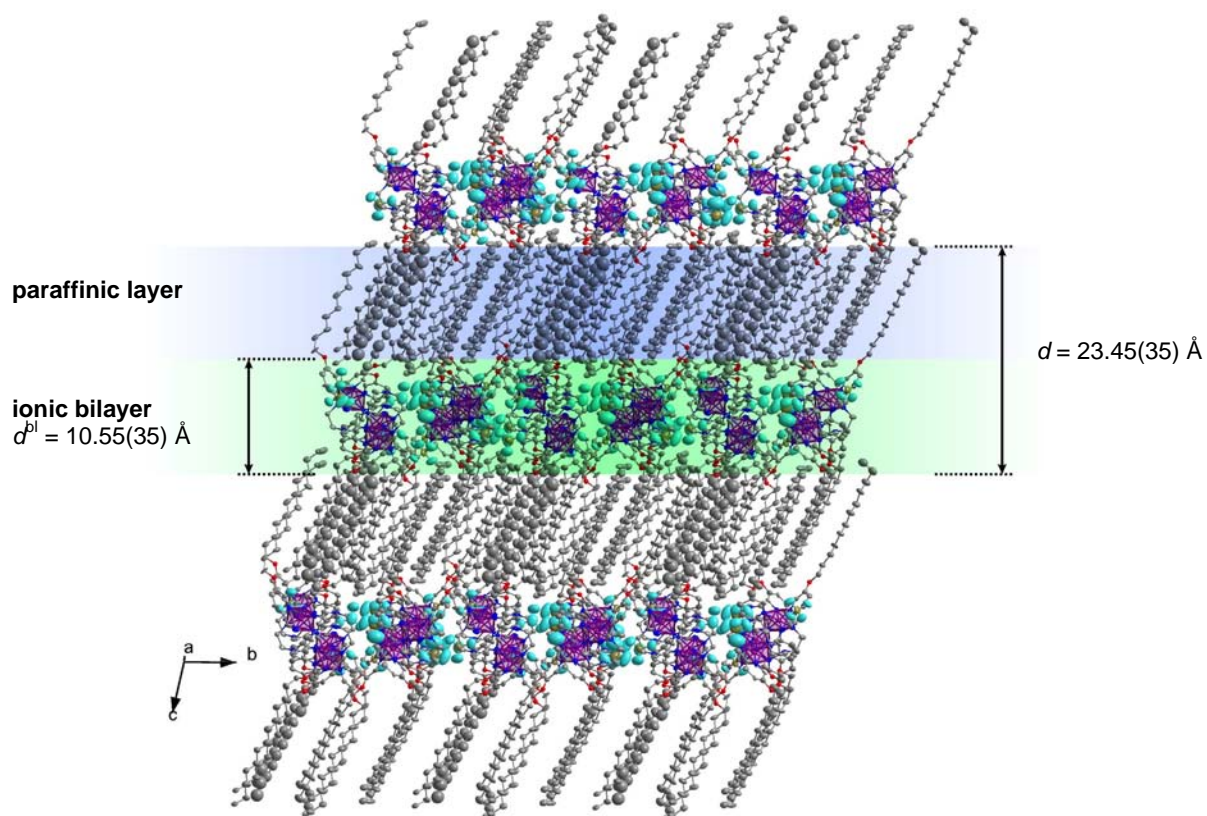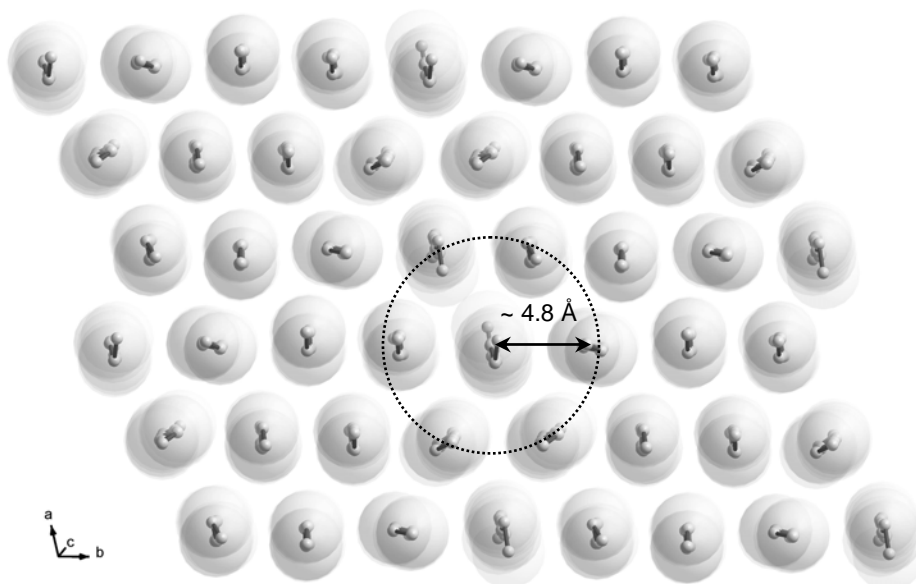
c

**Figure 50.** (*continued*)

As in the previous case, the unit cell contains two dyads of opposite chiralities, thus forming an optically inactive structure. The triple-strands ligand is wrapped around a pseudo-$C_3$ axis defined by the central atom and the capping nitrogen N7 (or N14), leading to helical complex species. The *L* and *D* optical isomers shown in Figure 50a are independent. The charged polar heads together with the anions and, on the other hand, the alkyl chains adopt the neighborhood of similar groups with the change of two lamellar substructures along the *c* crystal axis (Figure 50b). In other words, ionic head-groups are located in the galleries between paraffinic layers and tethered to them via covalent bonding. The difference between the space filling of one ionic head and its three pendant terminal chains is compensated by tilt *τ* of the alkyl chains with respect to the normal of the ionic bilayer by the value of about 31°. Contrary to $C_6$-**7**, the alkyl chains of $C_{12}$-**8** are long enough to force themselves to a parallel alignment in the intertwined layers. The separation between packed alkyl chains is about 4.8 Å (Figure 50c). Numerous weak hydrogen bonds [2.216(12)–2.669(12) Å] occur between tetraflurorborate anions and CH moieties of the complex cations, interlinking the ionic bilayer. Supposedly, these intermolecular contacts along with ionic interactions play a significant role in the mesomorphic properties preserving isotropization of the ionic bilayers due to transition of alkyl chains into quasi-liquid state.

### 2.5.4   Mass spectroscopic, TGA and IR data

Mass spectroscopic characterization of the complexes was performed by field desorption ionization method (FD). In all cases positive ions corresponding to the desired species were observed as the base peaks. In cases where the FD method failed to provide identifiable spectra the characterization was repeated by electrospray ionization (ESI) or Matrix Assisted Laser Desorption/Ionization (MALDI) methods. For all complexes the most intensive peaks correspond to the molecular cation without anion(s) or the molecular cation plus anion or its fragments (Table 14). TGA measurements allowed to determine the water content in the pristine and thermally treated compounds (Table 14).

The analysis of the IR spectra included the regions with characteristic bands of alkyl chains and C=N vibrations since they can provide information about the type of packing within the paraffinic sublattice and the spin-state of the complex species.

*Alkyl chains.* The packing of alkyl chains in paraffinic layers and the adopted conformations are of interest. The relevant frequencies in the vibration spectra are observed at 2600–3000 cm$^{-1}$ and 700–1600 cm$^{-1}$.

**Table 14.** MS, TGA and IR spectroscopic data for the compounds $C_n$-7–$C_n$-18.

| Compound | MS [*m/z*] | TGA, w/w [ %] (*T*)[d] | $v$(O–H) | $v_s$(CH$_2$), $v_{as}$(CH$_2$) | $v$(C=N) | $\delta$(CH$_2$) | $\rho$(CH$_2$) | $v$(Anion) |
|---|---|---|---|---|---|---|---|---|
| | | | IR [cm$^{-1}$][f] | | | | | |
| $C_6$-7 | 868 [M+ClO$_4$]$^+$ 385 [M]$^{++}$ | 0 | – | 2928, 2851 | 1616 | 1466 | 727 | 1089, 622 |
| $C_{18}$-7 | 1373 [M+ClO$_4$]$^+$ 637 [M]$^{++}$ | 0 | – | 2918, 2850 | 1616 | 1468 | 721 | 1095, 623 |
| $C_{12}$-8 | 1196 [M+BF$_4$]$^{+ a}$ | 0 | – | 2920, 2851 | 1616 | 1467 | 721 | 1059 |
| $C_{18}$-9 | 1361 [M+BF$_4$]$^+$ 637 [M]$^{++}$ | 0.8 (325 K) | 3400 br | 2918, 2850 | 1616 | 1468 | 721 | 1058 |
| $C_{18}$-10 | 637 [M]$^{++ b}$ | 5.3 (340 K) | 3400 br | 2918, 2850 | 1615 | 1468 | 720 | 1119 |
| $C_{18}$-11 | 1293 [M+F]$^{+ b, c}$ 637 [M]$^{++}$ | 4.5 (340 K) | 3400 br | 2917, 2850 | 1613 | 1467 | 720 | – |
| $C_{16}$-13 | 1225 [M+Cl]$^+$ | 4.2 (355 K) | 3400 br | 2917, 2850 | 1616 | 1467 | 720 | – |
| $C_{16}$-14 | | 0.6 (360 K) | – | – | – | – | – | – |
| $C_{16}$-15 | | 0.2 (380 K$^e$) | – | – | – | – | – | – |
| $C_{18}$-13 | 1309 [M+Cl]$^+$ 637 [M]$^{++}$ | 4.5 (345 K) | 3400 br | 2918, 2850 | 1616 | 1467 | 720 | – |
| $C_{18}$-14 | | 0.8 (360 K) | – | – | – | – | – | – |
| $C_{18}$-15 | | 0.1 (390 K$^e$) | 3400 br | 2918, 2851 | 1616 1649 | 1467 | 721 | – |
| $C_{20}$-13 | 1393 [M+Cl]$^+$ 679 [M]$^{++}$ | 4.0 (340 K) | 3400 br | 2917, 2850 | 1616 | 1467 | 720 | – |
| $C_{20}$-14 | | 0.5 (345 K) | – | – | – | – | – | – |
| $C_{20}$-15 | | 0.1 (360 K$^e$) | – | – | – | – | – | – |
| $C_{18}$-16 | 1353 [M+Br]$^{+ c}$ 637 [M]$^{++}$ | 6.0 (380 K) | 3400 br | 2917, 2850 | 1616 | 1467 | 720 | – |
| $C_{18}$-17 | 1400 [M+I]$^+$ 637 [M]$^{++}$ | 0 | – | 2917, 2850 | 1613 | 1468 | 720 | – |
| $C_{18}$-18 | 1699 [M+C$_{18}$TOS]$^+$ 637 [M]$^{++ c}$ | 0.9 (321 K) | 3400 br | 2917, 2850 | 1628 | 1467 | 721 | 1190 |

$^a$ MALDI MS; $^b$ ESI MS; $^c$ Trace; $^d$ Value is given at the point where the plateau is reached. *T* is the temperature at which the dehydration process is centered; $^e$ Evaluated approximately; $^f$ $v$, stretching; $\delta$, bending; $\rho$, rocking; as, asymmetric, s, symmetric.

*High-frequency region.* It has been well-established that the $v_s$(CH$_2$) and $v_{as}$(CH$_2$) absorptions are strong indicators of the chain conformation [246, 247]. The characteristic values lie in the regions 2846–2850 and 2915–2920 cm$^{-1}$, respectively, for *all-trans* extended chains and in the regions 2854–2856 and 2924–2928 cm$^{-1}$ for disordered chains characterized by significant presence of *gauche* conformers [248]. On this basis, the observed peak frequencies at 2850–2951 cm$^{-1}$ and 2916–2920 cm$^{-1}$ for the C–H stretching modes of the methylene groups suggested that the majority of methylene units of alkyl chains in $C_n$-7– $C_n$-18 (except $C_6$-7) are in the *trans* conformation with a little significant or absent *gauche*

population. On the other hand, the $v_{as}(CH_2)$ in $C_6$-7 is 2928 cm$^{-1}$, which suggested significant *gauche* population and is consistent with the structural data.

*Low-frequency region.* The scissoring band $\delta(CH_2)$ at ~1467 cm$^{-1}$ provides a sensitive measure of the packing arrangement of alkyl chains. The splitting of this peak or the absence of the splitting depends on the type of subcell packing. The singlet can be attributed to hexagonal or triclinic subcell with weak interchain interactions, and a split band is characteristic for orthorhombic subcell with lateral interchain interactions between contiguous $CH_2$ groups [246, 249, 250]. For the whole $C_n$-13 series the occurrence of a single narrow peak at ~1467 cm$^{-1}$ was attributed to one type of chains. The crystal structure of $C_{12}$-8 can serve as the model of the packing of alkyl chains in higher homologues (Figure 50b, c).

Regarding the chain packing, the *rocking mode* (~720 cm$^{-1}$) of the methylene groups can provide additional confirmation of the packing type [247]. The band appears for crystalline compounds with more than four consecutive $CH_2$ groups and in close analogy to the scissoring mode at ~1467 cm$^{-1}$ its shape is strongly dependent on alkyl chain packing geometry for aliphatic compounds [246]. Orthorhombic packing is known to split the rocking mode into two components of comparable intensities, but the vibration levels are not split when the packing is hexagonal containing only one chain per subcell. On these grounds, the occurrence of a single narrow peak at ~720 cm$^{-1}$ confirms the proposed hexagonal packing with stretched *trans* chains.

*C=N group.* The IR spectra of $C_n$-7–$C_n$-18 provide clues both to spin state of the complexes and to some of their structural features. The bands at about 1615 cm$^{-1}$ are observed in the $v(C=N)$ region and may be assigned to the low-spin state of iron(II) ion in all complexes. For $C_{18}$-15, the IR spectrum was also obtained in dehydrated form which showed the occurrence of an additional broad band assigned to high-spin complex molecules.

*Anions.* For the compounds $C_6$-7, $C_{18}$-7, $C_{12}$-8, $C_{18}$-9, $C_{18}$-10, $C_{18}$-18 with multiatomic anions $BF_4^-$, $ClO_4^-$, $SO_4^{2-}$, $C_{18}TOS^-$, serially, the corresponding absorption bands confirmed the expected composition. The positions (in cm$^{-1}$) of the discussed absorption bands are presented in Table 14.

### 2.5.5   UV/VIS and $^1$H NMR spectroscopy

Since the compound $C_{18}$-13 is the derivative of the parent compound **B**, the UV/VIS spectra of both compounds are very similar (cf. ref. [143]). The spectrum of the low-spin compound $C_{18}$-13 in dichloromethane (Figure 51a) features several $\pi \rightarrow \pi^*$ ligand bands in

the UV region and rather intensive and broad Laporte-allowed metal-to-ligand charge transfer ($^1A_{1g} \rightarrow$ $^1$MLCT) in the visible region that is typical for the tris(α-diimine) complexes of iron(II) [251]. The MLCT band completely obscures the weak parity forbidden $d$–$d$ transitions $^1A_{1g} \rightarrow$ $^1T_{1g}$ and $^1A_{1g} \rightarrow$ $^1T_{2g}$ and does not allow to evaluate the ligand field strength $10Dq^{LS}$ of the compound. Despite compound $C_{18}$-15 (completely dehydrated derivative of $C_{18}$-13) is partially high-spin in solid state and possesses comparatively lighter coloration, upon dissolving in dichloromethane the color is recovered and the spectra of both solutions are undistinguishable.
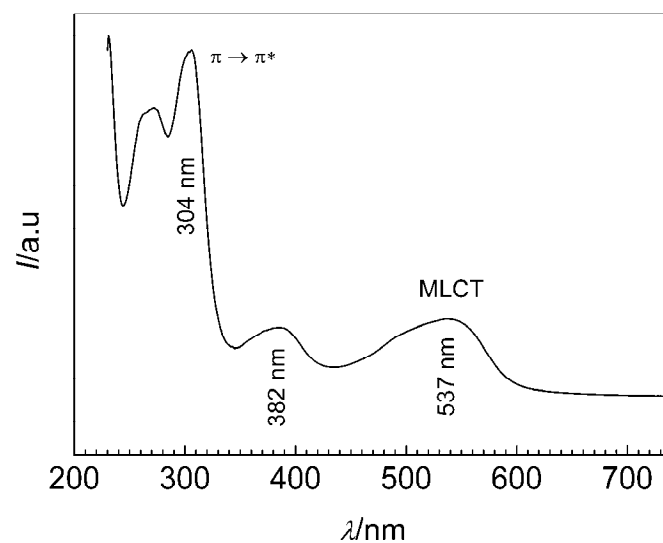


a
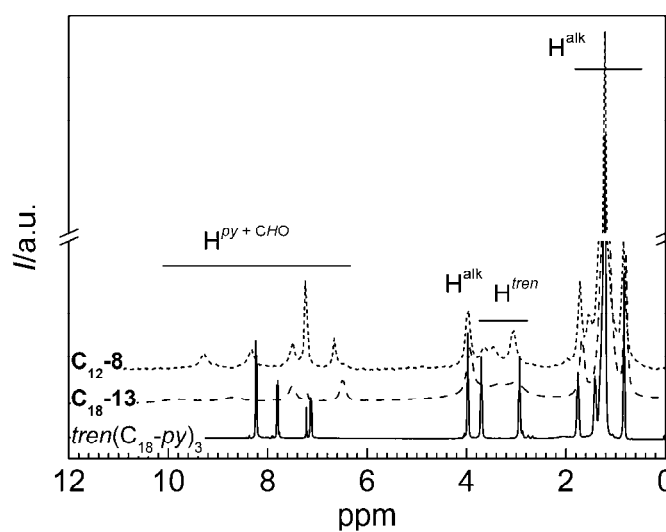


b

**Figure 51.** a) The UV/VIS spectrum of $C_{18}$-13 in dichloromethane solution; b) $^1$H NMR spectra of $tren$($C_{18}$-$py$)$_3$, $C_{12}$-8 and $C_{18}$-13 at 298 K (400 MHz).

The $^1$H NMR spectra of **C$_{12}$-8** and **C$_{18}$-13** and the precursor ligand of the later compound tris(3-aza-4-((5-octadecyloxy)(2-pyridyl))but-3-enyl)amine [*tren*(C$_{18}$-*py*)$_3$] in chloroform-*d* are shown in Figure 51b. They are consistent with the molecular structure of the compound **C$_{12}$-8** as found in the solid state (Figure 50a). Downfield from internal TMS, proton resonance lines appear as a complicated pattern with broadened peaks. The small number of resonances confirms that the complex molecules have a threefold symmetry. The line broadening for the pseudo-octahedral chiral complex molecules results from the dynamic interconversion of *L* and *D* antipodes through the trigonal twisting mechanism (Bailar twist) [199, 252]. Sharper peaks in **C$_{12}$-8** reflect the decrease of the racemization rate, presumably due to the presence of a BF$_4^-$ anion in the pockets of the [Fe{*tren*(C$_{12}$-*py*)$_3$}]$^{2+}$ which exert the configuration locking effect on the complex cation. A similar effect was observed earlier for the tris(1,10-phenanthroline) complex cation of iron(II) [Fe(phen)$_3$]$^{2+}$ [253]. For **C$_{18}$-13**, the observed minute shift of the peaks in the 6–10 ppm region comparatively to **C$_{12}$-8** might indicate the onset of the spin-transition. The pronounced broadening does not allow evaluation of the coupling constants for the pyridine protons and direct unambiguous assigning of the resonance lines. Only qualitative analysis is possible which is sufficient. For **C$_{12}$-8** and **C$_{18}$-13** the proton patterns in the range 6–10 ppm consist of four separated resonance signals and can be analyzed in terms of the three ring protons and one carboxaldimine proton chemical shifts. The pattern in the 0–4 ppm range is confidently attributed to chemical shifts of CH$_2$-groups of the capping triamine *tren* and of the CH$_2$- and CH$_3$-groups of the alkyl chains.

### 2.5.6    Magnetic properties

Compounds **C$_{18}$-10**, **C$_{18}$-11**, **C$_{16}$-13**, **C$_{18}$-13**, **C$_{20}$-13** show a very particular spin-state change (Figure 52a–e), while **C$_6$-7**, **C$_{18}$-7**, **C$_{12}$-8**, **C$_{18}$-9**, **C$_{18}$-16** together with **C$_{18}$-17** and **C$_{18}$-18** are in the low-spin state (10–400 K). Figure 52c illustrates the $\chi_M T$ *vs* $T$ plots for **C$_{16}$-13** (s = 3.5), a partial hydrate **C$_{16}$-14** (s = 0.5) and for the dehydrated complex **C$_{16}$-15** (s = 0). Compound **C$_{16}$-13** is in the low-spin state at 300 K as confirmed by the $\chi_M T$ value of 0.2 cm$^3$ K mol$^{-1}$ as well as by the Mössbauer spectrum (*vide infra*). Upon heating $\chi_M T$ increases abruptly, attaining the value of 1.75 cm$^3$ K mol$^{-1}$ at 400 K, where around 50 % of the Fe(II) ions have converted to the high-spin state. TGA experiments have shown that the gradual dehydration takes place in the same temperature region where the spin-state change occurs (Table 14); note, that the temperature of the dehydration (~340 K) and that of the magnetic

anomaly (~370 K) do not coincide. This points out some threshold loss of crystal water after which the spin-state change sets in.

The DSC data and the XRD data of **C$_{16}$-13** show that the melting occurs at 340 K. In order to clarify the role of the melting we have performed dehydration experiments on **C$_{16}$-13** monitoring the temperature dependence of the magnetic susceptibility (Figure 52g, h) and have recorded temperature dependent XRD patterns following the sequence 310–410–230–410 K (Figure 54f). The sample was heated and subsequently cooled during several cycles between 300 K (low-spin state) and 350 K (still low-spin state). In addition, the temperature variation of *d* derived from the XRD patterns (Figure 52c, right scale) presents an abrupt increase as a consequence of the melting between 340 and 350 K, but the increase in the $\chi_M T$ value begins at 360 K. Consequently, the hypothesis that the phase transition to the mesophase drives the spin-state change can be ruled out, at least in the present compound **C$_{16}$-13**. Contrary, it is clearly seen in the dehydration experiments that the magnetic susceptibility increases upon losing water, which matches with reported TGA data, and is completely accomplished upon continuous heating (*ca.* 12 h) at 400 K (Figure 52h). For compound **C$_{16}$-13** 50 % of the iron(II) ions undergo spin-state change at $T_{1/2} = 375$ K induced by releasing water. Synergy between dehydration and spin-state change as observed in **C$_{16}$-13** has been reported in several cases [21, 166, 197].

The $\chi_M T$ *vs* *T* plot for **C$_{16}$-15** is characteristic of iron(II) ions in the high-spin state (Figure 52c). The magnetic properties of a partially dehydrated **C$_{16}$-14** have also been investigated, which discloses interesting synergy between the spin-transition and the change of the aggregate state of matter (solid ↔ liquid crystal). Figure 52c displays the $\chi_M T$ *vs* *T* plot for **C$_{16}$-14**. The partial dehydration of **C$_{16}$-13** was monitored by recording $\chi_M T$ *vs* *T* during two cycles of warming-cooling following the sequence 300–400–10–400 K and proved by TGA analysis to generate **C$_{16}$-14** (Table 14). For **C$_{16}$-14** the $\chi_M T$ *vs* *T* between 400–296 K presents a variation accompanied by a narrow hysteresis. Bellow 296 K $\chi_M T$ remains almost constant until 30 K where it sharply decreases as a consequence of the zero-field splitting of the iron(II) ions remaining in the high-spin state (near 18 %, from the Mössbauer data). The thermally induced spin-transition in **C$_{16}$-14** starts right after the onset of the first order phase transition solid → liquid crystal. Since the spin-transition is blocked below the temperature at which the compound solidifies one can conclude that the melting process drives the spin-transition in this compound. The fact that the spin-transition inside the smectic A mesophase (S$_A$) is accompanied by hysteresis is not surprising since in the present state of the material

the spin-transition is not expected to follow a Boltzmann distribution of spin states as observed in the liquid state [41].

One remarkable fact is that the compounds $\mathbf{C_{18}}$-13 and $\mathbf{C_{20}}$-13 behave similarly as $\mathbf{C_{16}}$-13. The magnetic susceptibility plots of these materials are presented in Figure 52d, e and the TGA data in Table 14. For a comparative analysis Figure 53 shows the $\chi_M T$ *vs* $T$ plots for $\mathbf{C}_n$-14 with $n$ = 16, 18, 20. It is worth mentioning that the spin-transition temperature is determined by the melting temperature which is higher for the derivatives with longer alkyl chains. In the case of $\mathbf{C_{20}}$-14 the melting and solidification processes are evidently reflected as the minor anomalies in the heating and cooling curves (Figure 52f). Contrary to $\mathbf{C}_n$-13, for compounds $\mathbf{C_{18}}$-10 and $\mathbf{C_{18}}$-11 no partial hydrates can be obtained. The full dehydration provokes the spin-state change of nearly 50 % of the iron(II) ions (Figure 52a, b).
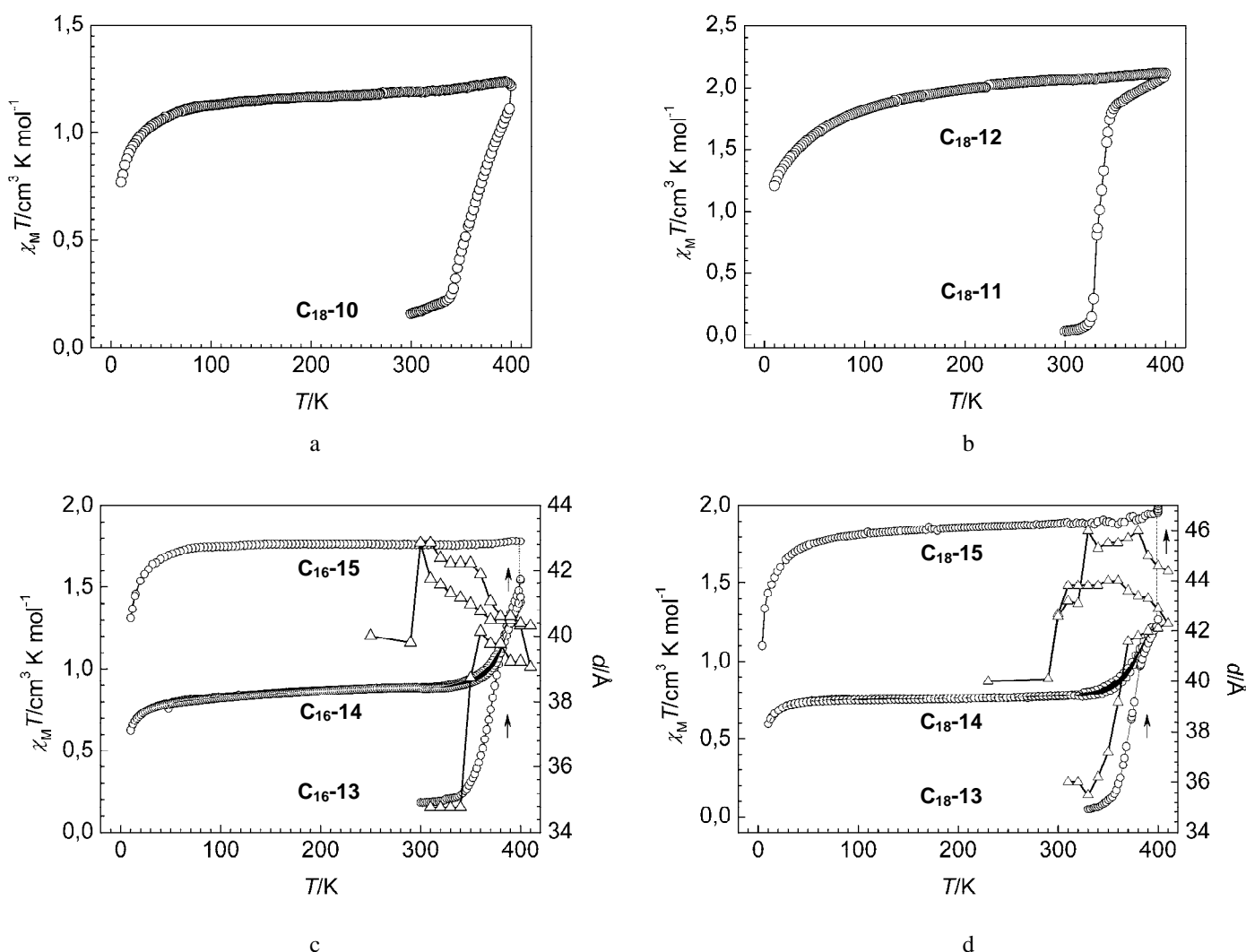


**Figure 52.** Magnetic susceptibility plot in the coordinates $\chi_M T$ *vs* $T$ for a) $\mathbf{C_{18}}$-10; b) $\mathbf{C_{18}}$-11 and $\mathbf{C_{18}}$-12; c) $\mathbf{C_{16}}$-13, $\mathbf{C_{16}}$-14 and $\mathbf{C_{16}}$-15; d) $\mathbf{C_{18}}$-13, $\mathbf{C_{18}}$-14 and $\mathbf{C_{18}}$-15; e) $\mathbf{C_{20}}$-13, $\mathbf{C_{20}}$-14 and $\mathbf{C_{20}}$-15. Black area shows the hysteresis loop in $\mathbf{C}_n$-14. The symbol $\triangle$ corresponds to the interlayer distance $d$; f) The anomalies in the magnetic curves of $\mathbf{C_{20}}$-14 due to melting/solidification in the two successive measurements; g) The plot in the coordinates $\chi_M T$ *vs* $T$ illustrates the role of the dehydration in governing the spin-crossover properties in $\mathbf{C_{16}}$-13 upon its transformation in $\mathbf{C_{16}}$-14 and $\mathbf{C_{16}}$-15; h) The same in the coordinates $\chi_M T$ *vs* Time.

e



f



g



h
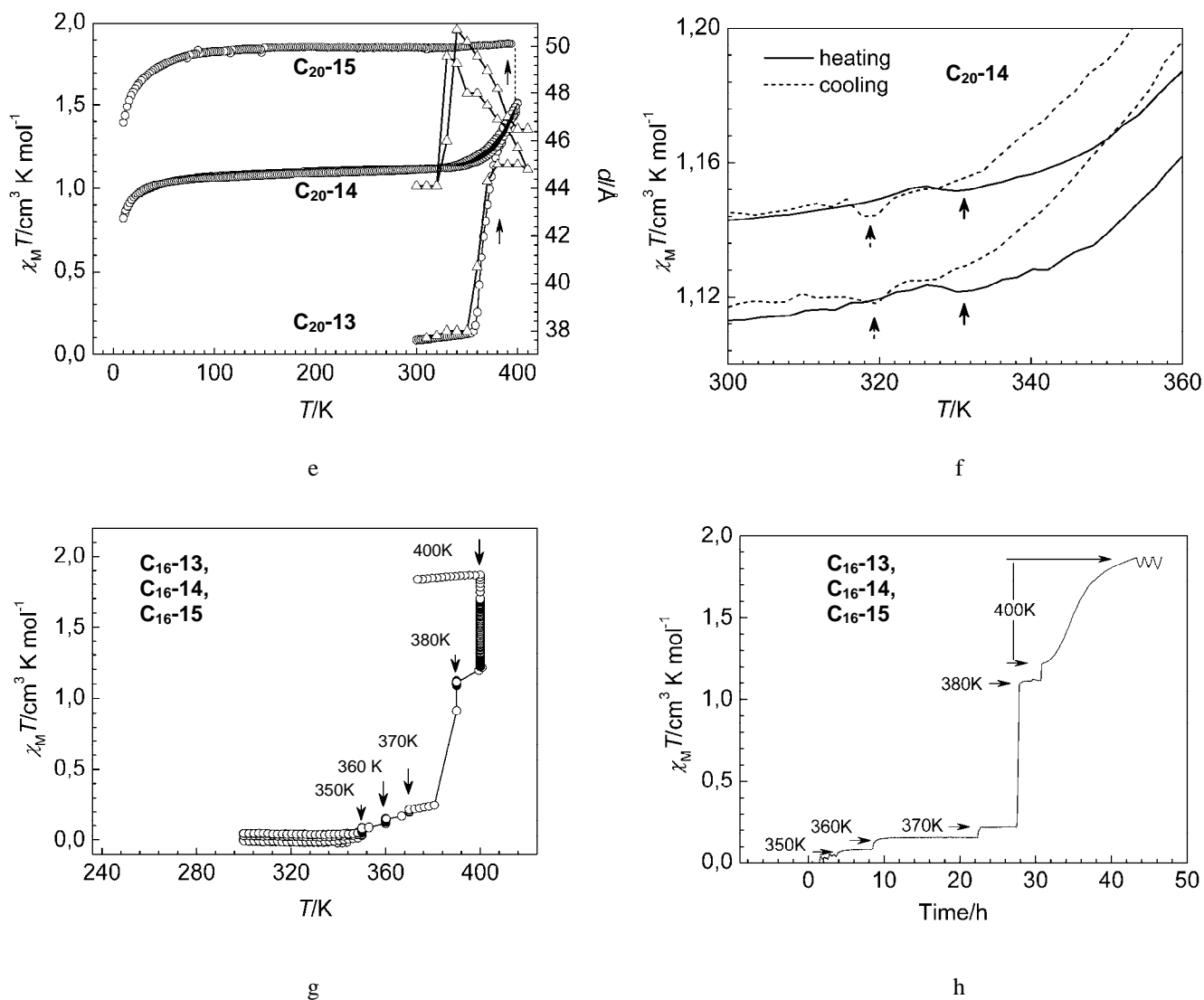
**Figure 52.** (*continued*)
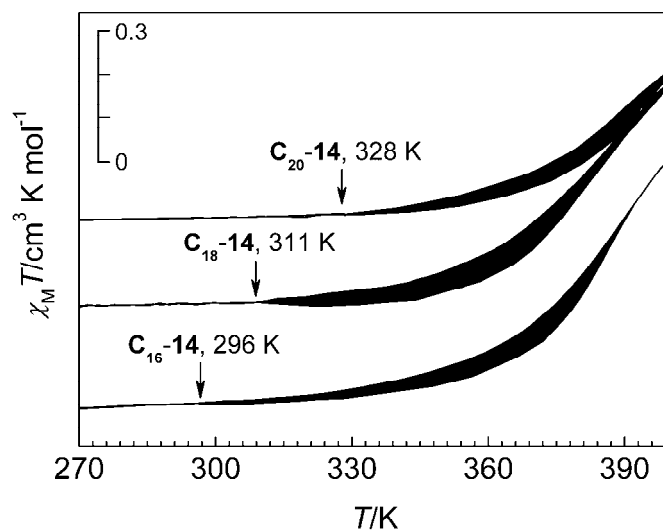


**Figure 53.** Magnetic susceptibility plots in the form $\chi_M T$ *vs* $T$ for **C$_{16}$-14**, **C$_{18}$-14** and **C$_{20}$-14** emphasizing the low temperature edge of the hysteresis loops where the heating and cooling curves diverge.

### 2.5.7 XRD data

X-ray diffraction experiments were performed in the range of $2\theta = 1$–$30°$. In each case, the XRD experiment was done on the pristine sample at 300 K, then in the liquid crystalline state at 410 K and then again at 300 K. For compounds $C_n$-13 and $C_n$-14 precise measurements were performed with 10 K steps in the range 300–400 K and additionally at 230 K well below the phase transition.

For compounds $C_n$-7–$C_n$-18 (Figure 54a–k) the halo in the wide angle region corresponds to an approximate distance between planes formed by alkyl chains. This value in solid state is about 4.2 Å. Assuming hexagonal packing of alkyl chains, the recalculation[2] gives an approximate distance between *trans* (from IR) alkyl chains being near 4.8 Å which agrees well with the interchain distance found in $C_{12}$-8 (Figure 50c). Despite the fact that the XRD profiles after the phase transition resemble the ones of the crystalline phase, there are two principal differences. Indeed, at higher temperature the alkyl signal is shifted to about 4.6 Å and becomes more diffuse confirming the transition of alkyl chains into quasi-liquid state. The X-ray data for the high-temperature phase are consistent with the existence of the regions where alkyl chains form a "melt" alternated with "crystalline" ionic bilayers [128]. On cooling the reversed shift is observed. In the small-angle region, for all samples the single strong reflection with Miller indices $hk = (10)$ corresponds to the periodicity of the layered structure. For some samples it is accompanied by the second-order reflection (20), both confirming the layer-like structure of the compounds. In general, the first melting in compounds $C_n$-7–$C_n$-18 is accompanied by disappearance or lowering of the intensity of the weak reflections. This indicates some decrease of the crystallinity upon consequent melting-solidification. A particularly pronounced effect on melting is observed in the water containing complexes $C_{18}$-10, $C_n$-13 ($n = 16, 18, 20$) and $C_{18}$-16 (Figure 54d, f, g, h and i) but not in $C_{18}$-11 which showed only minor differences in the profiles compared to its anhydrous derivative $C_{18}$-12 (Figure 54e).

Except for $C_{18}$-17 (Figure 54j), upon heating the main reflection with $hk = (10)$ of the thermally treated samples is shifted to lower $2\theta$ values with a decrease of its intensity and in the case of $C_{18}$-18 with disappearance of the second-order reflection (Figure 54k). Upon cooling the reverse shift to a higher value is observed. The type of the observed diffraction patterns and the changes they undergo upon heating and cooling were attributed to the smectic mesomorphism. The XRD measurements performed on three homologues $C_n$-14 indicated the

---

[2] see Equation 21, Chapter 6.5.2

formation of the mesophase of the same nature and of the similar temperature behavior. The decrease of the distance $d$ in the mesophase upon heating (Figure 52c, d, e; right scale) implies formation of the smectic A ($S_A$) mesophase that is in good accordance with the polarization optical microscopy (POM) (Figure 57, Table 15).

For $C_{18}$-18 disappearance of the texture on heating near 420 K is observed by POM, which agrees with the DSC data (*vide infra*). The XRD profile measured at 475 K (Figure 54k) showed the presence of a weak broad reflection in the small angle region and a broad alkyl signal at higher angles. The data point out possible mesophase randomization with the preserving of local ordered domains randomly distributed in the sample [254]. No birefrignance is observed for the structure with random domains and the total random phase because of their isotropy.

It is supposed that the polar coordination head-groups and anions in $C_n$-7–$C_n$-18 are arranged in ionic bilayers in a way, where each half of a bilayer is electrically neutral. A bilayer can be imagined as being formed by head-groups with one or two anions which organized in a manner where the positive charge of the head-group is shielded by the negatively charged anion and vise versa, *i.e.* similarly to that observed in crystal structures of $C_6$-7 and $C_{12}$-8 (Figure 49b, Figure 50b). Possible variables which can influence the packing within ionic bilayers and their thickness are the relative disposition of head-groups from each half of an ionic bilayer, the size of the anions and their charge which defines their number. The distance between the centroid of the three oxygen atoms O1, O2 and O3 on the bottom and the apical nitrogen N7 on the top of the polar head-group of the complex cation $C_{12}$-8 based on Fe1-ion (see Figure 50a), is 7.29(15) Å which with the radius of a methylen group on the top gives an approximate height of the head-group being *ca.* 9 Å (Figure 55a). Assuming further two border cases of the organization shown in Figure 55b and c, the thickness of ionic bilayer $d^{bl}$ can vary in the range from *ca.* 9 Å up to *ca.* 20 Å, where the later case is determined by the size of intercalated anions and solvate molecules (*e.g.* water) and their number.

The analysis of the interlayer distances $d$ as a function of the alkyl chain length $n$ in the series of homologues with similar structure allows to evaluate approximate thickness of the ionic bilayers $d^{bl}$. For the pair $C_{12}$-8 and $C_{18}$-9 (both are $BF_4^-$ salts) extrapolation of the interlayer distance $d$ to $n = 0$ gives the value $d^{n=0} = 8.6$ Å which is less than the thickness of ionic bilayer directly determined from the crystal structure of $C_{12}$-8 (*ca.* 10.6 Å). The discrepancy is possibly due to the hydration of $C_{18}$-9. According to the IR data, for both

compounds is confidently assumed a similar chain packing, however, the tilt of alkyl chains, which affects the interlayer spacing $d$, can vary and give rise to different structures.

　　　Figure 56 displays the trend of the $d$ spacing for compounds **$C_n$-13** and **$C_n$-14** as a function of the alkyl chain length $n$. As is apparent from the figure, a regular increase of the parameter $d$ with increasing $n$ is found. For **$C_n$-13** the value $d^{n=0}$ is equal to 22.6 Å, which after subtracting two radii of the terminal methyl groups ($d^{C-H}$ = 1.09 Å) gives value $d^{bl}$ = 20.4 Å that is almost twice larger than that found in **$C_{12}$-8** (Figure 50b). The result is explained in terms of the different anions and number of water molecules, and therefore different organization of the bilayers (see Figure 55b, c). For samples **$C_n$-14** ($n$ = 16, 18, 20) extrapolation was done in liquid-crystalline state giving the value $d^{n=0}$ of 10.2 Å and in solid state the value of 16.9 Å (Figure 56). The difference of $ca$. 6 Å cannot be explained by the experimental error. A possible reason for the decrease of the $d^{n=0}$ value might be a longitudinal change at the level of the coordination head-groups, *i.e.* there might be some reorganization of the ionic bilayers upon melting which leads to the observed variation of the value. Solidification of the alkyl chains might induce the mechanical strain and is probably the cause of the detected variation of the thickness of the bilayer.

　　　The values of the interlayer distances $d$ derived from the XRD data of **$C_n$-7**–**$C_n$-18** are collected in Table 15.
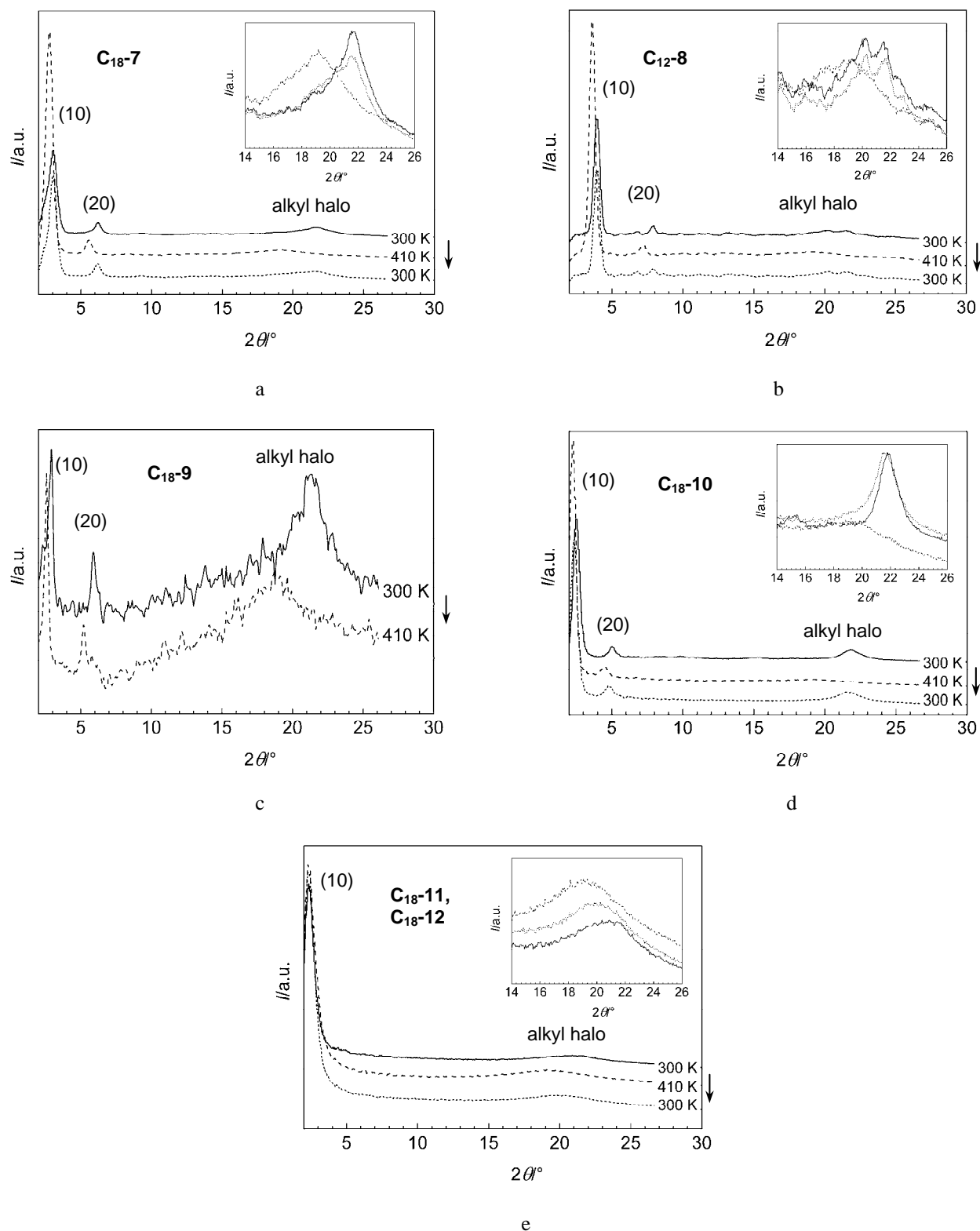
**Figure 54.** XRD patterns at different temperatures of a) $C_{18}$-7; b) $C_{12}$-8; c) $C_{18}$-9; d) $C_{18}$-10; e) $C_{18}$-11, $C_{18}$-12; f) $C_{16}$-13, $C_{16}$-14; g) $C_{18}$-13, $C_{18}$-14; h) $C_{20}$-13, $C_{20}$-14; i) $C_{18}$-16; j) $C_{18}$-17; k) $C_{18}$-18. Insets show enlarged region of the alkyl halo.

f



g



h

**Figure 54.** (*continued*)

i



j



k

**Figure 54.** (*continued*)



a                                          b                                          c
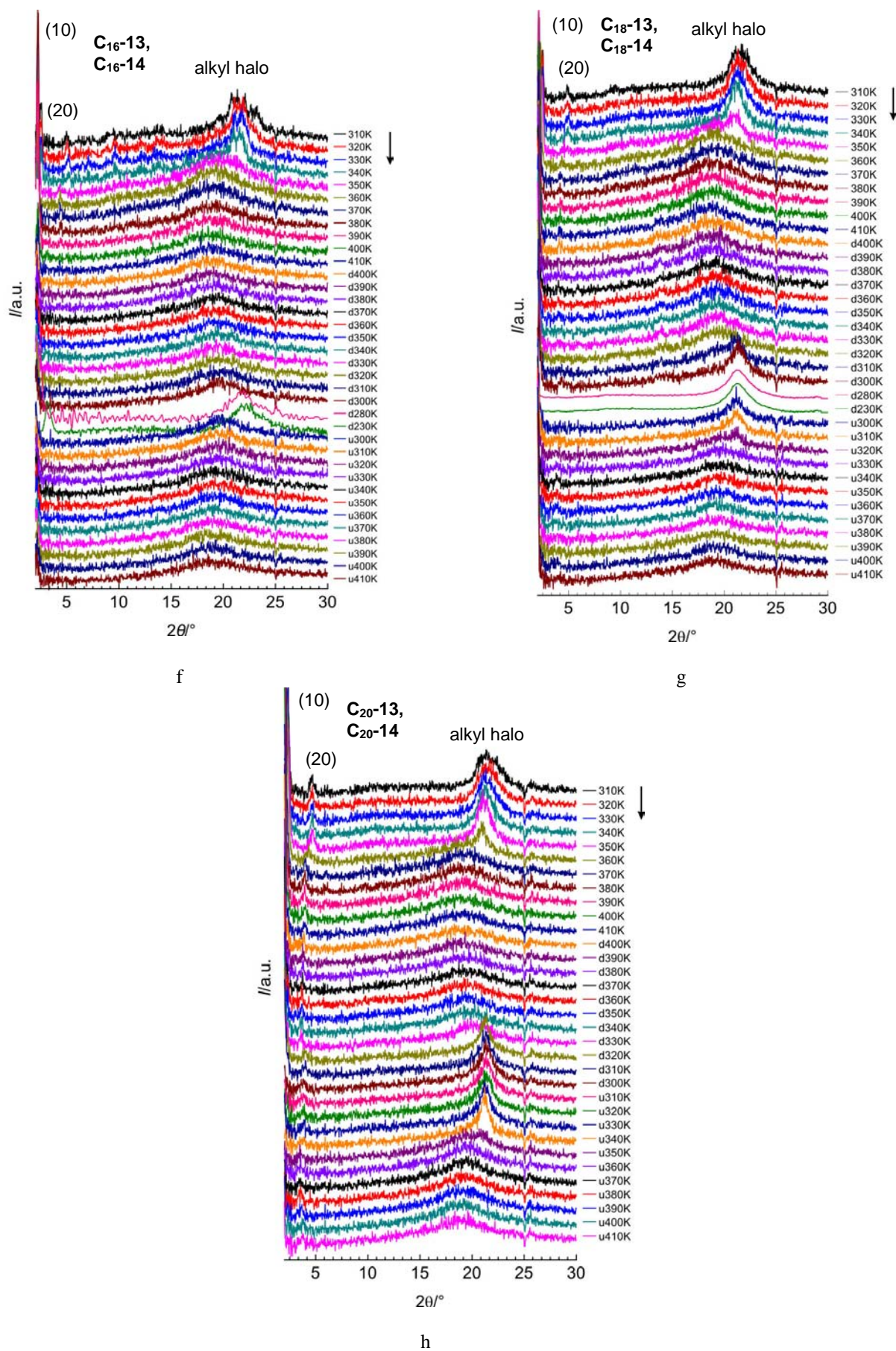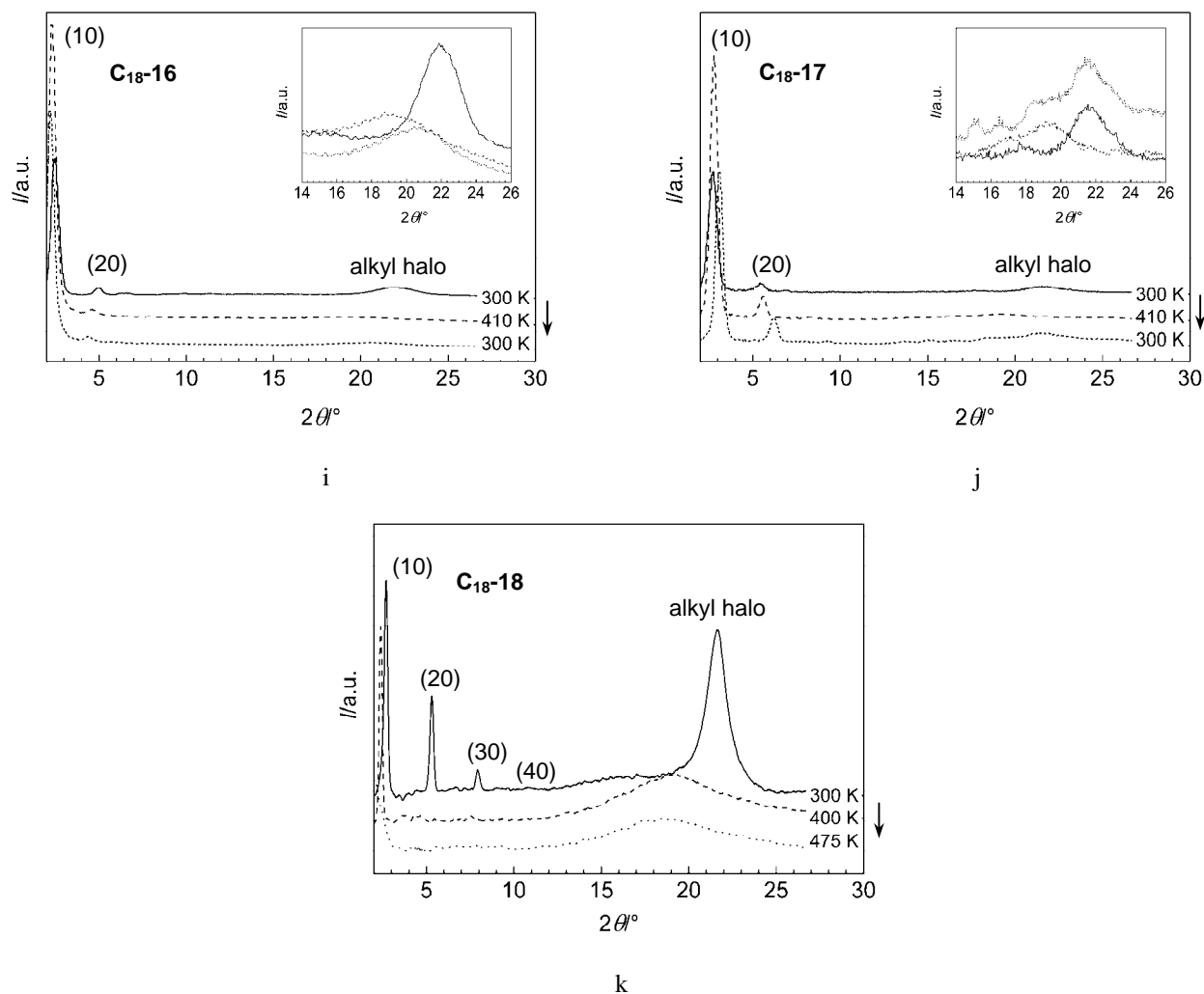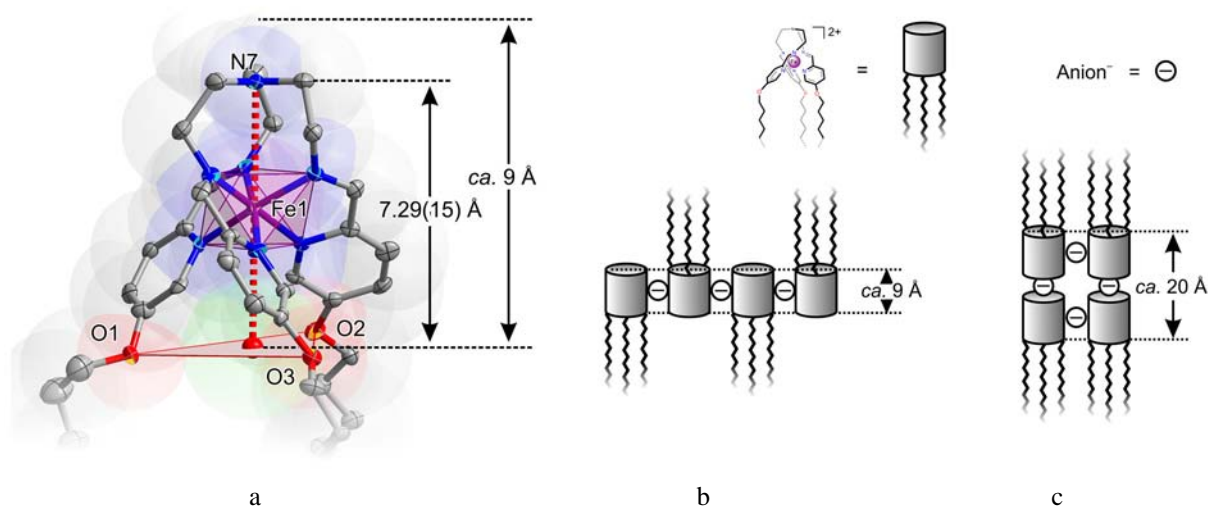
**Figure 55.** a) Approximate height of the coordination head-group of $C_{12}$-**8**. The ball-and-stick model is overlapped with the space-filling model; b) and c) are the two border cases of the organization of ionic bilayers in $C_n$-**7**–$C_n$-**18** with the smallest possible and the largest possible thickness of the ionic bilayer, respectively.
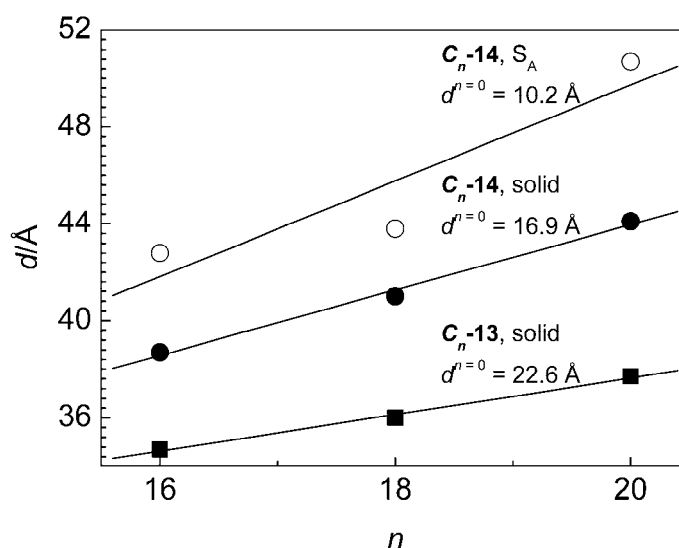
**Figure 56.** Trend of the *d* spacing as a function of *n* in solid $C_n$-13 at room temperature (■), molten $C_n$-14 in $S_A$ phase (*d* value just above the melting point) (○) and in solid $C_n$-14 (●), where *n* = 16, 18, 20. The solid lines are the linear fit of the experimental data.

**Table 15.** Interlayer distances *d* at different temperatures, thermal transitions and mesomorphism, enthalpy $\Delta H^{Cr \to S_x}$ and entropy $\Delta S^{Cr \to S_x}$ of phase transition solid → liquid crystalline and thermal stability determined by XRD, DSC, TGA and POM for $C_n$-7–$C_n$-18.

| Com-pound | *d* [Å] | | | Thermal transitions [K][b] | $\Delta H^{Cr \to S_x}$ [kJ mol$^{-1}$][b] | $\Delta S^{Cr \to S_x}$ [J K$^{-1}$ mol$^{-1}$][b] |
|---|---|---|---|---|---|---|
| | 300 K (pristine) | 410 K | 300 K | | | |
| $C_6$-7 | 16.592(5)[a] | – | – | – | – | – |
| $C_{18}$-7 | 29.1 | 31.05 | 29.1 | Cr $\underset{355}{\overset{380}{\rightleftarrows}}$ $S_X$ 473 d | 49.6 | 134.0 |
| $C_{12}$-8 | 22.8 [23.45(35)[a]] | 24.1 | 22.1 | Cr $\overset{363}{\rightarrow}$ $S_X$ 520 i | 31.3 | 86.2 |
| $C_{18}$-9, $C_{18}$-8 | 29.9 | 33.7 | – | Cr $\underset{335}{\overset{383}{\rightleftarrows}}$ $S_X$ 500 i(d) | 51.0 | 152.2 |
| $C_{18}$-10 | 35.9 | 39.0 | 38.1 | Cr $\underset{307}{\overset{315}{\rightleftarrows}}$ $S_X$ 464 i(d) | 30.8 | 99.3 |
| $C_{18}$-11, $C_{18}$-12 | 37.8 | 38.6 | 37.8 | Cr $\underset{313}{\overset{327}{\rightleftarrows}}$ $S_X$ 439 i(d) | 53.5 | 167.2 |
| $C_{16}$-13, $C_{16}$-14 | 34.7 | 39.1 | 38.7 | Cr $\underset{270}{\overset{287}{\rightleftarrows}}$ $S_A$ 456 i(d) | 28.1 | 97.9 |
| $C_{18}$-13, $C_{18}$-14 | 36.0 | 42.3 | 40.1 | Cr $\underset{287}{\overset{301}{\rightleftarrows}}$ $S_A$ 463 i(d) | 38.5 | 127.9 |
| $C_{20}$-13, $C_{20}$-14 | 37.7 | 45.0 | 44.1 | Cr $\underset{320}{\overset{330}{\rightleftarrows}}$ $S_A$ 449 i | 63.8 | 193.3 |
| $C_{18}$-16 | 35.8 | 39.1 | 39.7 | Cr $\underset{325}{\overset{350}{\rightleftarrows}}$ $S_X$ 451 i(d) | 62.4 | 192.0 |
| $C_{18}$-17 | 32.5 | 31.3 | 31.3 | Cr $\underset{365}{\overset{393}{\rightleftarrows}}$ $S_X$ 456 i(d) | 65.7 | 167.1 |
| $C_{18}$-18 | 32.7 | 36.9 | – | Cr $\underset{327}{\overset{330}{\rightleftarrows}}$ $S_X$ 427 i 510 d | 95.7 | 290.0 |

[a] From the monocrystal X-ray data; [b] Measured by the DSC on the second heating-cooling cycle. The values correspond to the maxima of the enthalpy peaks. The identification of the mesophase was done on the basis of the POM and the XRD data. [c] The value was measured on the first heating run.

### 2.5.8   DSC and POM data

On heating, the compounds $C_n$-7–$C_n$-18 undergo a transition from the solid to birefringent viscous fluid, and exhibit an anisotropic texture (Figure 57). The dark coloration of the low-spin compounds (due to the MLCT) complicated observation of the characteristic textures by hot-stage polarized-light optical microscopy (POM). We can note that the observation of the texture was done well above the temperature where according to the DSC data the phase transition is expected to occur. This fact is explained as follows. On the one hand, with increasing temperature the spin-transition took place with the concomitant decrease in the intensity of the coloration, therefore at higher temperatures the samples were lighter. On the other hand, in general, the ionic layered metallomesogens with the smectic mesomorphism have strong tendency to show a homeotropic texture [128]. In this case, the smectic planes are parallel to the microscope glass slide and the optic axis is perpendicular to it. The homeotropic texture in the layered $C_n$-7–$C_n$-18 was observed as a dark field between crossed polarizers. By pressing with a needle on the cover glass, this alignment could be destroyed, and the optical birefringence was noticed. However, it was possible only at high temperatures due to the decrease of the viscosity of the samples upon heating. The textures obtained can be assigned to the smectic type.
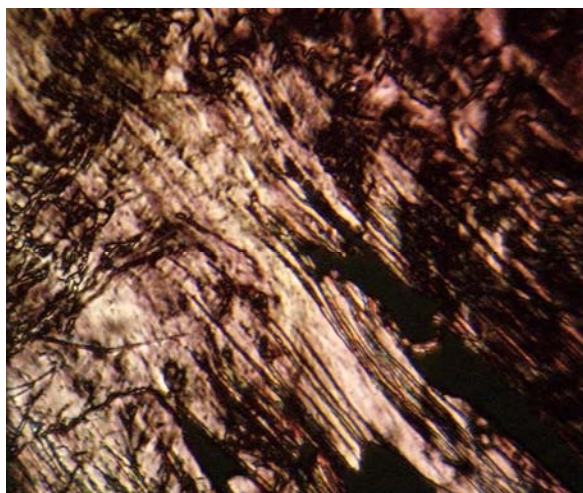


**Figure 57.** The texture of compound $C_{16}$-14 under crossed polarizers. The dark fields are due to homeotropic alignment of the smectic layers parallel to the microscope glass slides.

In the water containing compounds $C_{18}$-9, $C_{18}$-10, $C_{18}$-11, $C_n$-13 ($n$ = 16, 18, 20), $C_{18}$-16 and $C_{18}$-18 the first melting is accompanied by the dehydration and in the cases of $C_{18}$-10, $C_{18}$-11, $C_n$-13 the dehydration process is also accompanied by a partial spin-state

change (Figure 58c–i, k). For these compounds, the change in the heat flow corresponds to three processes taking place almost simultaneously. The second and further measurement runs provide practically identical DSC curves. Integration of peaks on the second heating scan gave the enthalpy values of the transition solid → liquid crystal (Table 15). In the DSC profiles of $C_{18}$-7, $C_{12}$-8, $C_{18}$-9 and $C_{18}$-17 (Figure 58a, b, c, j) the minor heat flow peaks observed at the temperatures below the main peak might be tentatively attributed to solid-solid transitions and pre-transition phenomena [255] and were not studied in details. For compound $C_{18}$-18 the broad peak observed at about 430 K (Figure 58k) corresponds to randomization of the mesophase as it was discussed above.
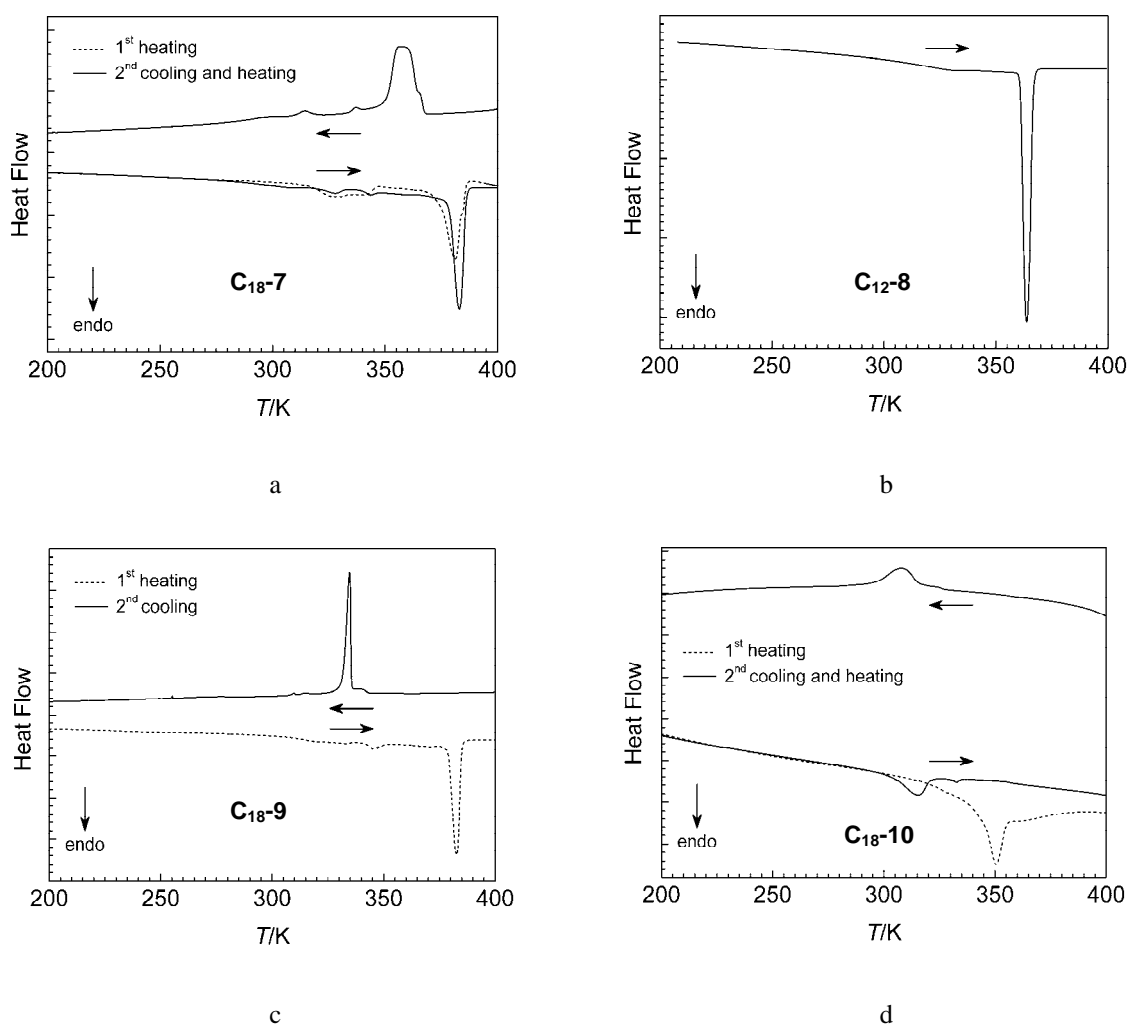


Figure 58. DSC profiles in heating and cooling modes for a) $C_{18}$-7; b) $C_{12}$-8; c) $C_{18}$-9; d) $C_{18}$-10; e) $C_{18}$-11, $C_{18}$-12; f) $C_{16}$-13, $C_{16}$-14; g) $C_{18}$-13, $C_{18}$-14; h) $C_{20}$-13, $C_{20}$-14; i) $C_{18}$-16; j) $C_{18}$-17; k) $C_{18}$-18. Arrows show the direction of scanning runs.

e



f



g



h



i



j
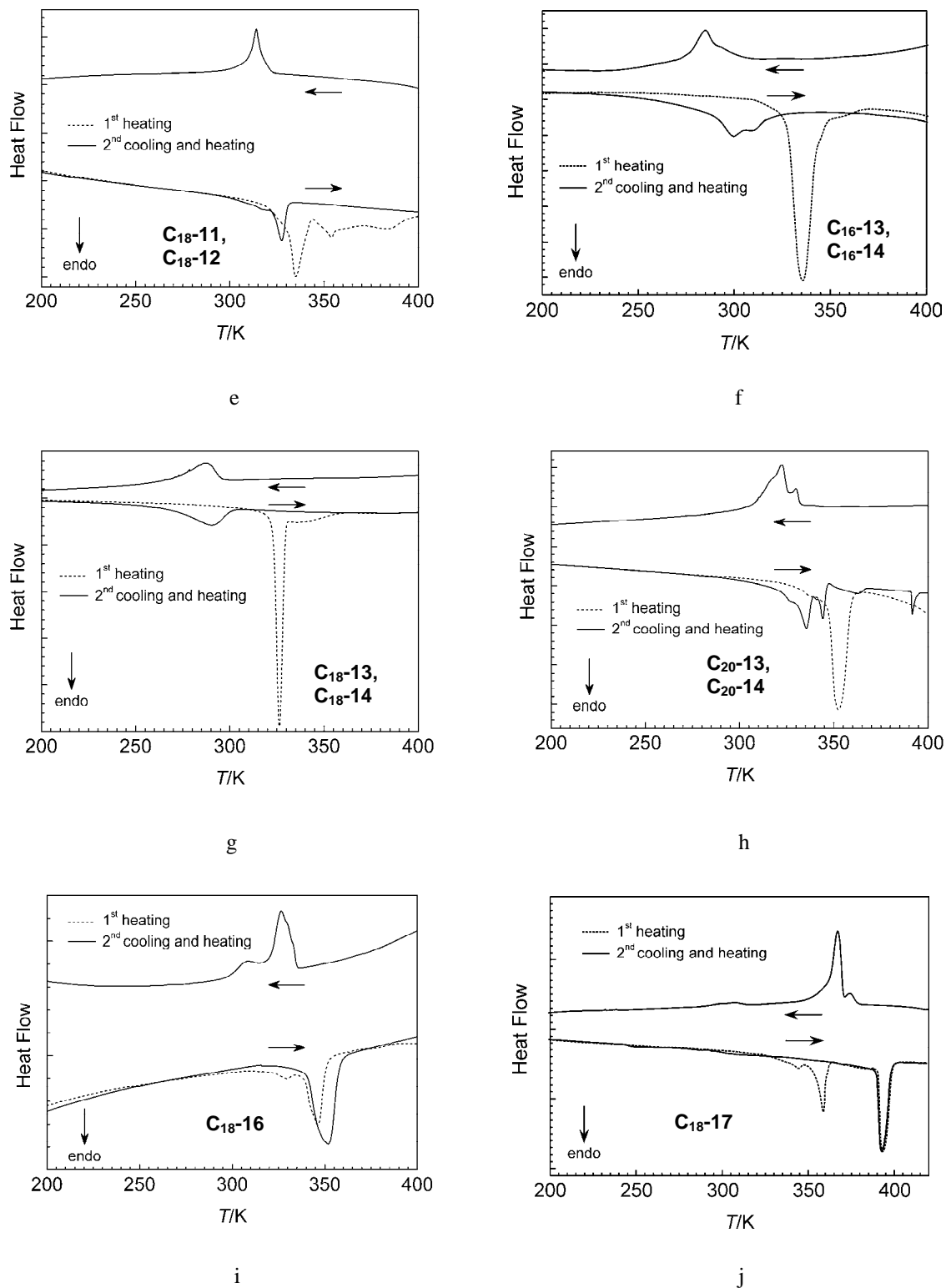
**Figure 58.** (*continued*)
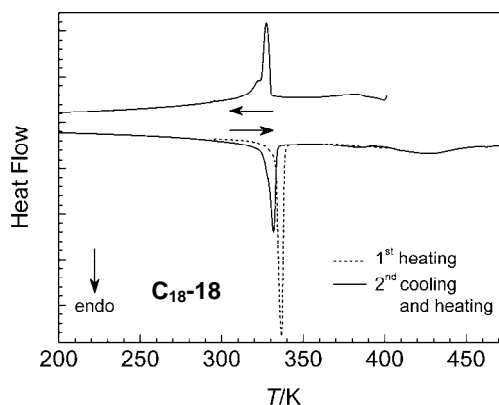
k

**Figure 58.** (*continued*)

The entropy analysis proposed by Sorai *et al.* for phase transitions in liquid crystals is based on the assumption that the entropy is an extensive quantity with a clear microscopic meaning expressed in the mathematical form by the Boltzmann equation: $S = k_B \ln W$, where W is the number of microscopic states [256, 257]. This is a thermodynamic method which allows to deduce the contributions of the molecular counterparts into the total entropy gain. If the compound consists of two covalently tethered groups with different nature, these groups will behave differently with temperature due to their different inherent properties. The comprehensive study of the series of mesogenic compounds possessing the rigid aromatic core and flexible alkyl chains confirmed the general applicability of the method [256]. The fitting of the data of homologous compounds to a linear equation gives the sign of the slope which represents the disordering (+) or ordering (–) upon the phase transition, whereas the slope itself is the difference in entropy per methylene group in two phases. The enthalpy analysis follows the same logic and was successfully applied by Burrows *et al.* for the analysis of a homologous series of cerium carboxylates to elucidate the type of the transformation of the ionic head-groups during the phase transitions [258].

Both methods were applied for the transition solid → liquid crystal in the homologues $C_n$-14 yielding the results shown in Figure 59. The entropy change per one methylene group is 23.9 J K$^{-1}$ mol$^{-1}$ which is less than expected for completely molten three alkyl chains (3×9.8 = 29.4 J K$^{-1}$ (mol CH$_2$)$^{-1}$) and indicates preserving in part the crystalline order. Extrapolation to zero carbon atoms gives a negative enthalpy contribution $\Delta H^{n=0} = -117.2$ kJ mol$^{-1}$. Despite possible overestimation of the value because of insufficient statistics (only three points are available) the results allowed to qualitatively elucidate what

kind of transformation the polar heads experience during the melting of alkyl chains. The net stabilization of the electrostatic interactions which appears to occur is probably due to favoring the equilibrated displacement of the polar heads and anions unconstrained by the partially molten alkyl chains. Melting might be accompanied by a longitudinal change at the level of the head-groups, *i.e.* some fusion of the polar region can take place leading to a perturbation of the electrostatic and intermolecular contacts. From the XRD analysis it is known that the change of the thickness of the ionic bilayers indeed takes place.
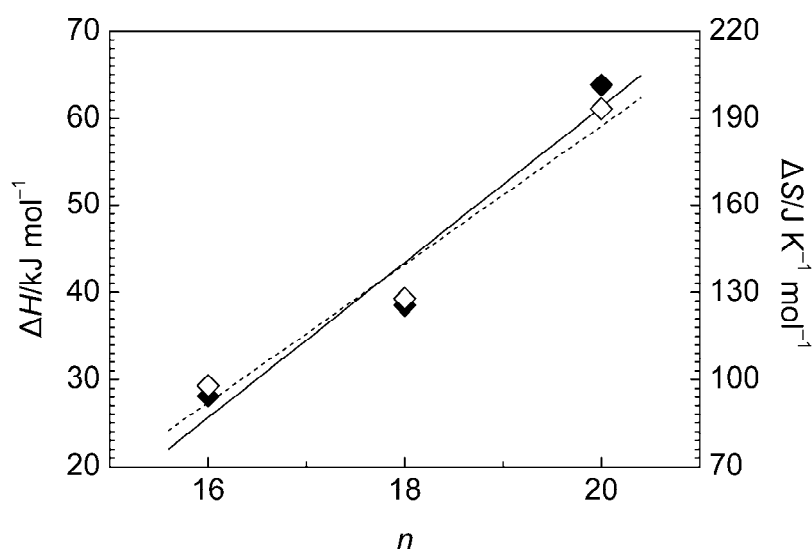


**Figure 59.** The enthalpy (◆) and entropy (◇) change during transition Cr → $S_A$ for $C_n$-**14** as a function of the chain length *n*. The solid line represents the linear fit for enthalpy values and the dashed line for entropy values.

The TGA data were used to determine the decomposition temperatures of the compounds.

All derived parameters are collected in Table 15.

### 2.5.9    Mössbauer spectroscopy

$^{57}$Fe Mössbauer spectra of compounds $C_n$-**7**–$C_n$-**18** were recorded at 80 K (Figure 60a–l). Detailed values of the Mössbauer parameters deduced from least-squares fitting are presented in Table 16.

The Mössbauer spectrum of $C_6$-**7** points out two inequivalent iron(II) ions, both in low-spin state (Figure 60a). The asymmetry of the doublets results from the texture effect due to the plate-like form of the crystalline sample. The Mössbauer spectrum of $C_{18}$-**7**, however,

could be satisfactorily fitted with only one low-spin doublet (Figure 60b). For **C$_{12}$-8** in complete agreement with the single crystal data (Figure 50a) the fitting with two low-spin doublets provides acceptable result (Figure 60c). The similar is valid for the higher homologue **C$_{18}$-9** and the sulfate **C$_{18}$-10** (Figure 60d, e). For the halogenides **C$_n$-11**–**C$_n$-15** the recorded spectra were used as a confirmation of the dehydration and of the spin-state change (Figure 60f–i). For example, compound **C$_{16}$-13** is in the low-spin state at 80 K as confirmed by the magnetic measurements. The Mössbauer spectrum of the compound contains two doublets corresponding to two inequivalent iron(II) positions in the lattice (Figure 60g). The partial dehydration of the compound led to a new compound **C$_{16}$-14** the spectrum of which consists of two equally populated low-spin and two equally populated high-spin doublets. The relative total population $A$ of the high-spin fraction is 18 % (Table 16). The full dehydration gave compound **C$_{16}$-15**. The Mössbauer spectrum of it recorded at 80 K has the equal relative populations for the two inequivalent iron sites (1,2) in high-spin and low-spin spin states: Fe(1): 25 % (HS), 25 % (LS); Fe(2): 25 % (HS), 25 % (LS) (Table 16, Figure 60g). The $\chi_M T$ value of **C$_{16}$-14** and **C$_{16}$-15** agrees well with the Mössbauer spectra (cf. Figure 52c). Very similar spectra were obtained also for the pairs **C$_{18}$-13**, **C$_{18}$-15** (Figure 60h), **C$_{20}$-13**, **C$_{20}$-15** (Figure 60i) and the fluorides **C$_{18}$-11**, **C$_{18}$-12** (Figure 60f). Mössbauer spectra of the compounds **C$_{18}$-16**, **C$_{18}$-17**, **C$_{18}$-18** contain a single low-spin doublet (Figure 60j, k, l).

We note the overall broadening of the Mössbauer doublets in the spectra of the completely dehydrated derivatives **C$_n$-15** in comparison to the pristine compounds **C$_n$-13** (Table 16). A Mössbauer line broadening can have several origins, for example: i) the excessive thickness of the absorber; ii) an inhomogeneous distribution of hyperfine fields and unresolved hyperfine interactions in the absorber; iii) diffusion broadening of Mössbauer lines; iv) the presence of structurally similar species in slightly different environments and v) rate of the low-spin ↔ high-spin conversion. While the first three reasons for the observed line broadening in samples **C$_n$-13**–**C$_n$-15** are invalid, the cases iv) and v) might be the acceptable explanations. On other hand, the XRD data show a decrease of the crystallinity of samples **C$_n$-15** in comparison to **C$_n$-13** which call for explanation iv).

**j**
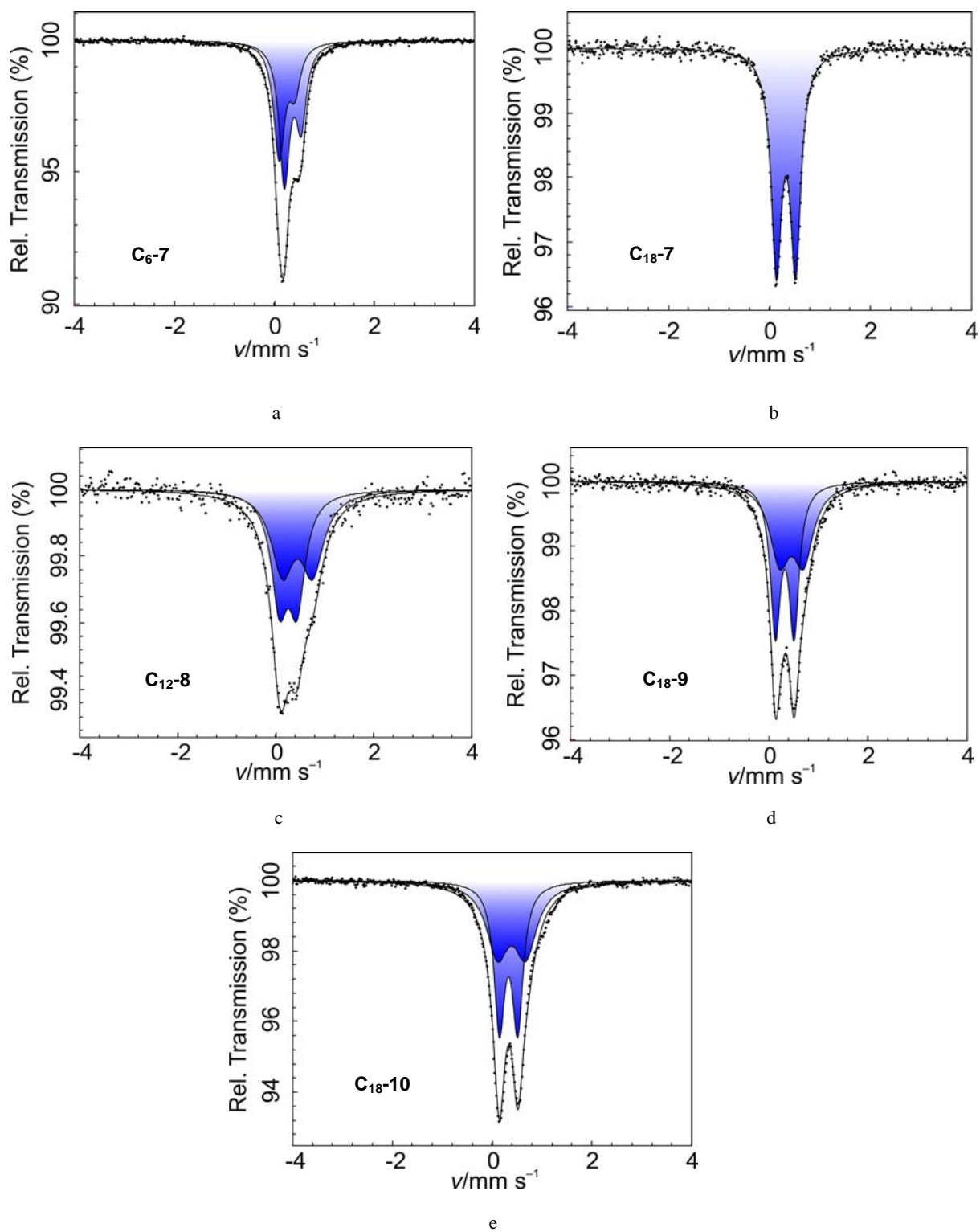
**Figure 60.** Mössbauer spectra at 80 K of a) $C_6$-**7**; b) $C_{18}$-**7**; c) $C_{12}$-**8**; d) $C_{18}$-**9**; e) $C_{18}$-**10**; f) $C_{18}$-**11**, $C_{18}$-**12**; g) $C_{16}$-**13**, $C_{16}$-**14**, $C_{16}$-**15**; h) $C_{18}$-**13**, $C_{18}$-**15**; i) $C_{20}$-**13**, $C_{20}$-**15**; j) $C_{18}$-**16**; k) $C_{18}$-**17**; l) $C_{18}$-**18**.

**Figure 60.** (*continued*)

h



i



j



k
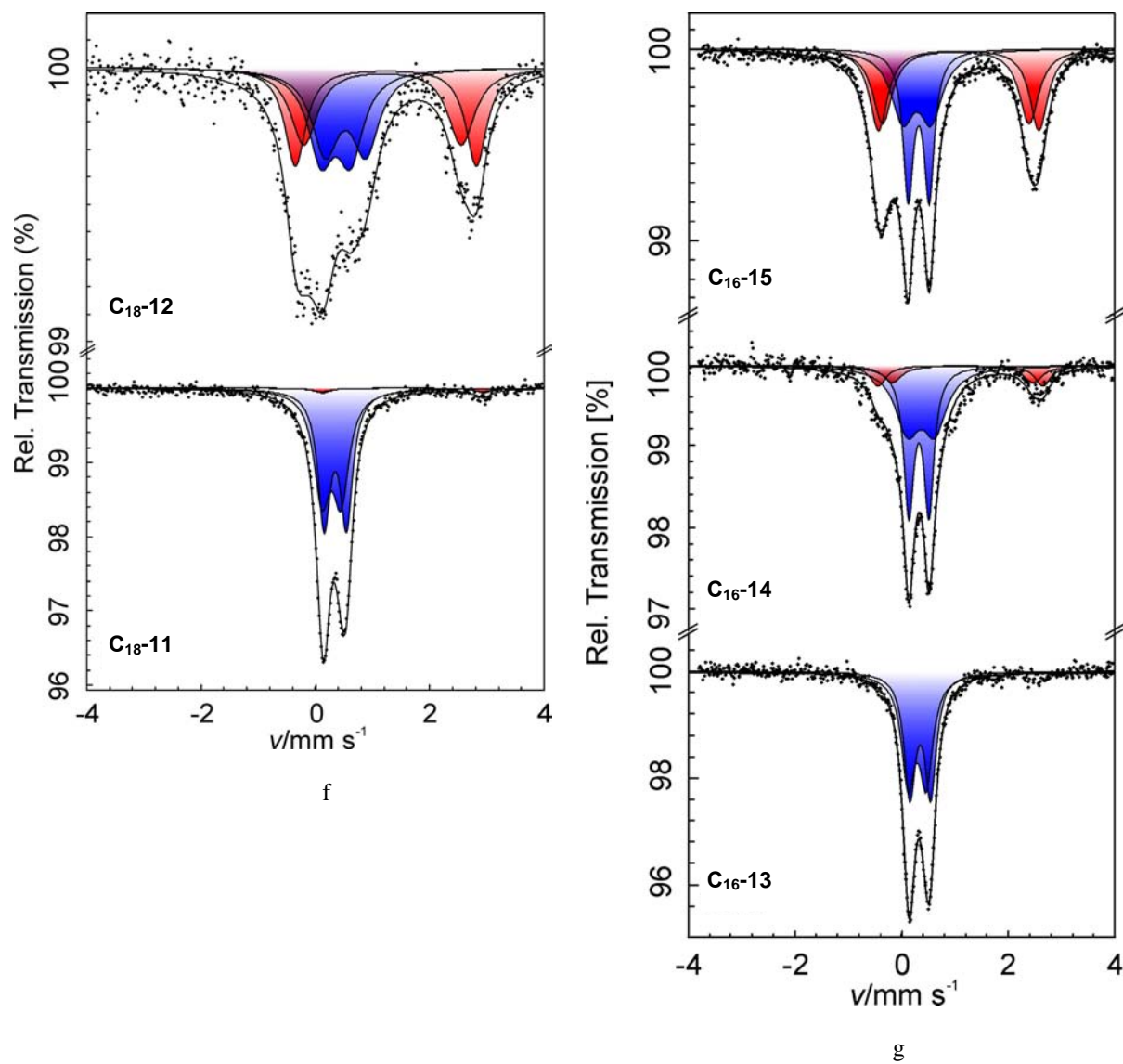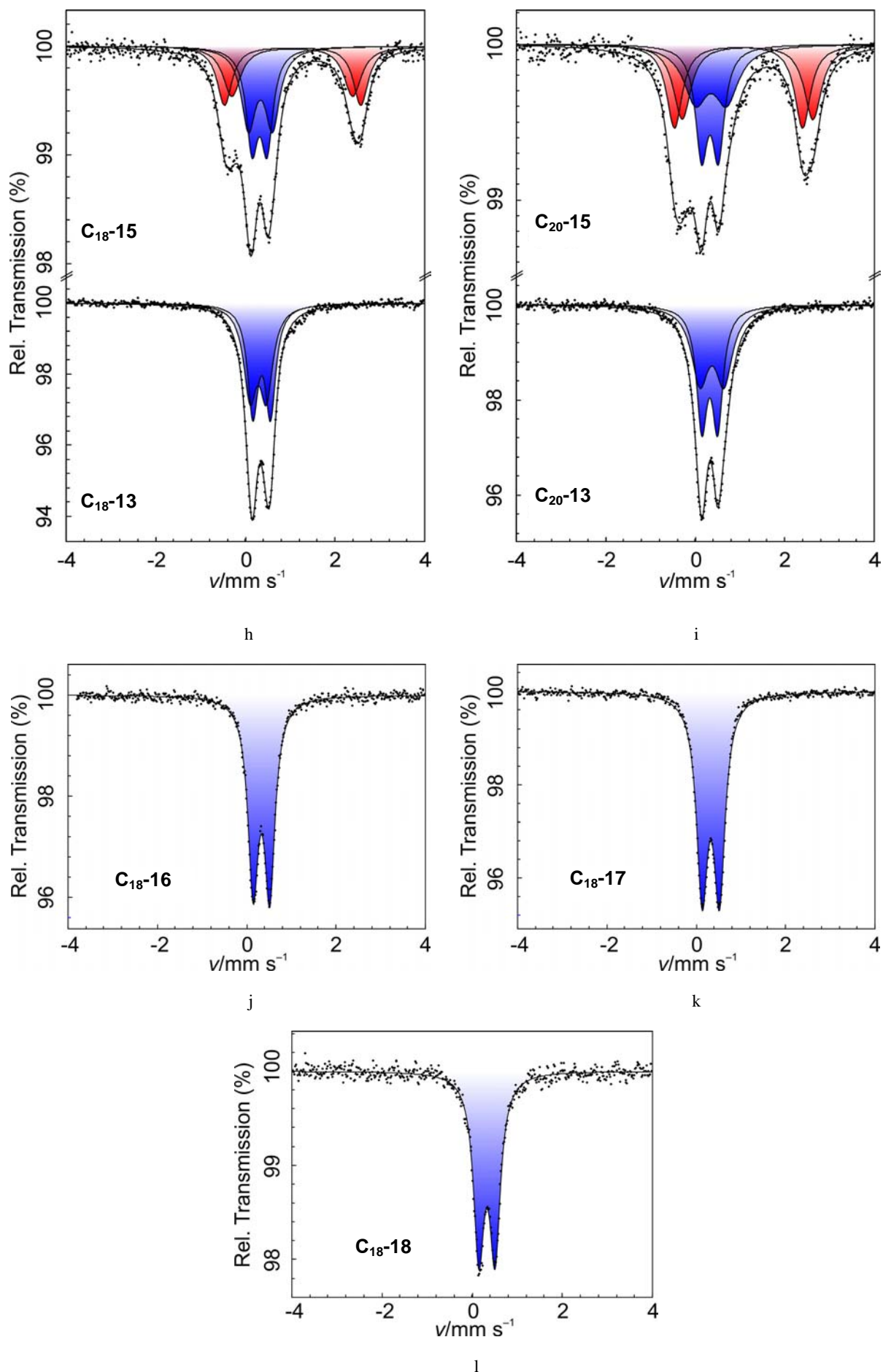


l

**Figure 60.** (*continued*)

**Table 16.** Mössbauer parameters, isomer shift ($\delta$, relative to α-iron), quadrupole splitting ($\Delta E_Q$), half-width of the lines ($\Gamma_{1/2}$) and percentage of the multiplet populations in the high-spin (HS) and low-spin (LS) states ($A$) at different temperatures for $C_n$-7–$C_n$-18.

| Compound | Spin state | $\delta$ [mm s$^{-1}$] | $\Delta E_Q$ [mm s$^{-1}$] | $\Gamma_{1/2}$ [mm s$^{-1}$] | $A$ [ %] |
|---|---|---|---|---|---|
| $C_6$-7 | LS1 | 0.25(0) | 0.31(0) | 0.14(1) | 44(12) |
| | LS2 | 0.37(1) | 0.33(0) | 0.13(1) | 56(12) |
| $C_{18}$-7 | LS | 0.33(1) | 0.38(0) | 0.13(1) | 100 |
| $C_{12}$-8 | LS1 | 0.26(1) | 0.36(1) | 0.20(0) | 49.9(70) |
| | LS2 | 0.45(1) | 0.61(0) | 0.28(1) | 50.1(76) |
| $C_{18}$-9 | LS1 | 0.32(0) | 0.38(1) | 0.12(0) | *50* |
| | LS2 | 0.46(1) | 0.48(1) | 0.25(0) | *50* |
| $C_{18}$-10 | LS1 | 0.33(1) | 0.37(1) | 0.13(1) | *50* |
| | LS2 | 0.39(1) | 0.57(1) | 0.27(0) | *50* |
| $C_{18}$-11 | LS1 | 0.35(1) | 0.39(0) | 0.13(0) | *48* |
| | LS2 | 0.28(0) | 0.34(0) | 0.17(1) | *48* |
| | HS1 | 1.50(0) | 2.80(0) | 0.20(1) | *2* |
| | HS2 | 1.51(1) | 2.81(1) | *0.16* | *2* |
| $C_{18}$-12 | LS1 | 0.53(1) | 0.71(1) | 0.29(1) | *26* |
| | LS2 | 0.35(0) | 0.51(1) | 0.29(1) | *26* |
| | HS1 | 1.18(1) | 2.75(1) | 0.23(1) | *24* |
| | HS2 | 1.23(0) | 3.17(1) | 0.28(1) | *24* |
| $C_{16}$-13 | LS1 | 0.29(1) | 0.36(0) | 0.17(0) | *50* |
| | LS2 | 0.36(0) | 0.39(0) | 0.14(0) | *50* |
| $C_{16}$-14 | LS1 | 0.37(1) | 0.51(0) | 0.26(0) | *41* |
| | LS2 | 0.33(1) | 0.39(1) | 0.12(1) | *41* |
| | HS1 | 1.15(1) | 2.64(1) | 0.23(1) | *9* |
| | HS2 | 1.11(1) | 3.08(0) | 0.21(1) | *9* |
| $C_{16}$-15 | LS1 | 0.34(1) | 0.54(1) | 0.20(1) | *28* |
| | LS2 | 0.32(1) | 0.33(0) | 0.16(1) | *28* |
| | HS1 | 1.05(0) | 3.04(0) | 0.20(1) | *22* |
| | HS2 | 1.05(1) | 2.70(1) | 0.24(1) | *22* |
| $C_{18}$-13 | LS1 | 0.30(1) | 0.34(0) | 0.15(0) | *50* |
| | LS2 | 0.35(0) | 0.39(0) | 0.13(0) | *50* |
| $C_{18}$-15 | LS1 | 0.29(0) | 0.53(0) | 0.26(0) | *25* |
| | LS2 | 0.33(1) | 0.39(0) | 0.12(1) | *25* |
| | HS1 | 1.02(0) | 2.75(0) | 0.23(1) | *25* |
| | HS2 | 1.08(1) | 3.00(0) | 0.21(1) | *25* |
| $C_{20}$-13 | LS1 | 0.32(0) | 0.35(0) | 0.15(1) | *50* |
| | LS2 | 0.37(0) | 0.54(0) | 0.23(0) | *50* |
| $C_{20}$-15 | LS1 | 0.33(1) | 0.38(1) | 0.17(2) | *25* |
| | LS2 | 0.35(1) | 0.69(0) | 0.32(0) | *25* |
| | HS1 | 0.96(0) | 2.86(0) | 0.24(1) | *25* |
| | HS2 | 1.17(1) | 2.92(0) | 0.21(2) | *25* |
| $C_{18}$-16 | LS | 0.33(0) | 0.37(0) | 0.14(0) | 100 |
| $C_{18}$-17 | LS | 0.32(0) | 0.38(1) | 0.15(1) | 100 |
| $C_{18}$-18 | LS | 0.33(1) | 0.36(1) | 0.14(0) | 100 |

The values given in italics were fixed during the fitting.

### 2.5.10  Discussion

Compounds $C_6$-7, $C_{18}$-7, $C_{12}$-8 and $C_{18}$-9 do not present spin-crossover behavior in the temperatures region under investigation (10–400 K) but exhibit mesomorphic behavior (except $C_6$-7). Compounds $C_{18}$-10, $C_{18}$-11 and $C_n$-13 ($n$ = 16, 18, 20) are new examples of materials in which the phase transition (melting) and the spin-state change coexist in the same temperature region but are not coupled. These very interesting materials present a change of the aggregate state of matter and spin-state change upon dehydration in a narrow temperature interval. The compounds $C_n$-14 ($n$ = 16, 18, 20) represent the first examples of systems in which the solid ↔ liquid crystal transition drives the spin state transition.

Complete control of the variables that affect the spin-crossover behavior in solid state is a rather difficult task to accomplish, since it depends essentially on the nature of the ligands, the non-coordinating anions, the solvent molecules, and the crystal packing (Chapter 1.3.4). This is particularly accentuated for mononuclear complexes as the communication between the spin-crossover centers is achieved exclusively through intermolecular interactions, such as hydrogen bonding or π–π interactions between aromatic ligand, anions and solvent molecules. In polymeric compounds, partial or total substitution of these intermolecular interactions by covalent linkage of the metal centers leads to a more predictable control of the spin-transition behavior.
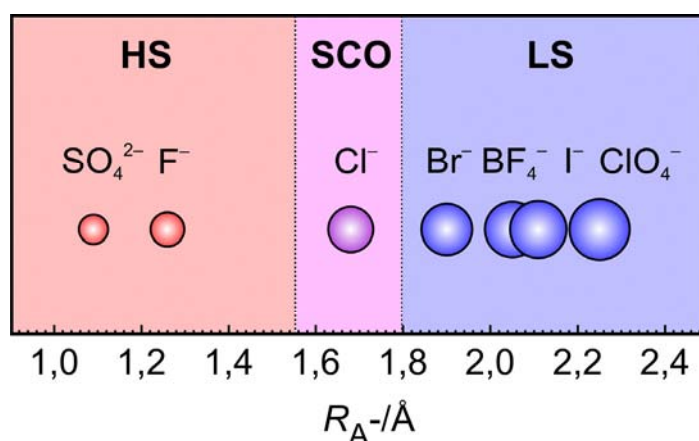


**Figure 61.** Change of spin-transition properties with the radius $R_A$- of the spherical anion A⁻ for compounds $C_{18}$-7, $C_{18}$-9, $C_{18}$-10 (anhydrous), $C_{18}$-12, $C_{18}$-14, $C_{18}$-16 and $C_{18}$-17. For the double charged anion $SO_4^{2-}$ the radius is one half of the actual value.

The general observation in the metallomesogens $C_{18}$-10, $C_{18}$-11, $C_{18}$-13, $C_{18}$-16 and $C_{18}$-17 with anions $SO_4^{2-}$, F⁻, Cl⁻, Br⁻ and I⁻, serially, is that the spin state depends mainly on

the degree of hydration of the compounds. In contrast, no solvates were isolated in the case of perchlorate derivatives $C_6$-7 and $C_{18}$-7 where the low-spin state is the preferred spin state. In fact, if the complexes under discussion are ordered according to the radius of the anion $A^-$ (from ref. [259]), the chloride complex $C_{18}$-13 occupies the unique position between the two classes of compounds with fixed high-spin and low-spin behavior (Figure 61). Compounds with the fluoride and sulfate anions transform on heating directly into spin-crossover inactive form, whereas the bulkier bromide, iodide, tetrafluoroborate and perchlorate anions show no spin-state change upon heating despite dehydration (of bromide). In some instances correlations between anion size and spin-transition temperature have been proposed [260-267], but the generality of this association has not been established.

Replacement of the anion or solvent molecule is expected to modify the lattice as a result of different crystal packing geometry or strength of the intermolecular forces. In addition, changes in the chemical composition of the lattice could impose different degrees of "chemical pressure" (also known as "image pressure") on the spin-transition centers and thereby influence the transition temperature. Hydrogen bonding can be a major influence on both the transition temperature (in part at least through a relayed effect on the ligand field strength) and the nature of the transition, providing the structural links for communication between the spin-crossover centers. Thus the extent to which an anion or solvate molecule can hydrogen bond with the spin-crossover centre will likely influence the nature of the transition [20, 21, 43, 197].

It has been proposed that hydration will generally result in a stabilization of the low-spin state, through hydrogen bonding of the water with the ligand [20, 21, 43, 197]. This does indeed seem to be the case for most hydrates, but in a cationic spin-crossover system where the ligand is hydrogen bonded to the associated anion only and this in turn is bonded to the water the effect can be reverse, *i.e.* loss of water can also result in stabilization of the low-spin state [66, 268]. Whatever the rationale for the effects, it is clear that variation in the anion or the solvatation is a very readily accessible, if not entirely predictable, means of potentially modulating the transition temperature or the nature of the transition.

Extrapolation of the interlayer distances $d$ to $n = 0$ for compounds $C_n$-14 ($n = 16, 18, 20$) and the entropy analysis can suggest the reason for the observed change of the magnetic properties at the melting temperature. Supposedly it is the consequence of the structural reorganization of the ionic bilayers that results from different pattern of the intermolecular contact in two phases. The realized situation is shown in Figure 62, top, with two different organizations of the ionic bilyers in solid and liquid crystalline phases. During the phase

transition one type of the structure is changed by another one. The "switch on" of the spin-transition can be imagined as the crossing of the curve corresponding to the magnetic behavior in the solid crystalline phase (Cr) and the curve corresponding to the magnetic behavior in the liquid crystalline phase ($S_A$) in the point $T_m$ where the phase transition takes place (Figure 62, bottom). The magnetic hysteresis inside the mesophase is the result of the delay of the structural reorganization which is confirmed by the XRD data, namely by the variation of the interlayer distance $d$ in cooling and heating modes (Figure 52c, d, e, right scale).

In this chapter we have shown that synchronization of spin-state and liquid crystal transitions is achieved by the modification of the parent spin-crossover system **B** suitable after attaching the alkyl moieties to possess low-spin state and spin-transition properties at the temperature at which the solid ↔ liquid crystal transition occurs.
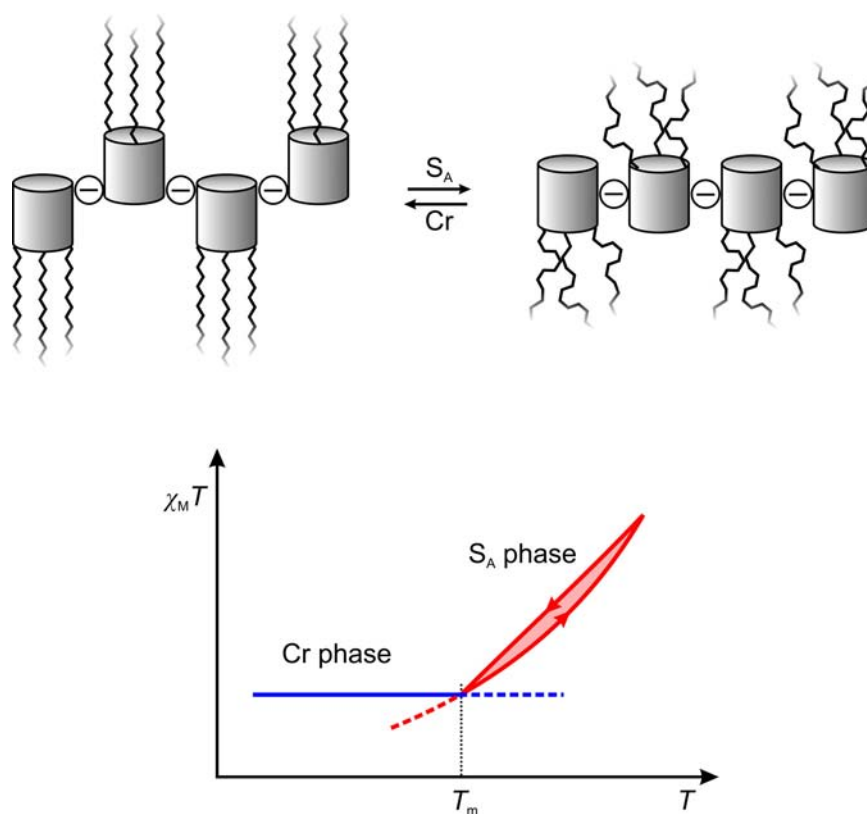


**Figure 62.** On the top is schematically shown the change of the bilayer thickness on melting/solidification in $C_n$-**14** ($n$ = 16, 18, 20) as deduced from the XRD data and confirmed by the DSC data. On the bottom are shown schematic magnetic curves in coordinates $\chi_M T$ $vs$ $T$ in the solid (Cr) and liquid crystalline smectic A ($S_A$) phases. Dashed lines show imaginary magnetic behavior without melting (for Cr) and without solidification (for $S_A$).

### 2.5.11 Summary

1. The chemical modification of the parent system **B** led to the mesogenic compounds **C$_n$-7–C$_n$-18**;

2. The crystal structures of alkylated compounds **C$_6$-7** and **C$_{12}$-8** have been determined. The crystal packing is segregated into the ionic bilayers formed by polar heads with anions, and the paraffinic layers formed by alkyl chains. Depending on the length, the alkyl chains could adopt disordered conformation with high *gauche* population or ordered *trans* conformation.

3. The crystal data explained the occurrence of two low-spin doublets in the Mössbauer spectra of the higher homologues. The reason is the differentiation of the complex cations by packing of covalently tethered alkyl chains;

4. For water containing complexes particular spin-state change is observed, which is associated with solvent molecules loss;

5. Compounds **C$_n$-14** (*n* = 16, 18, 20) are the first examples of the iron(II) mononuclear systems in which interplay between structural transformation and magnetic behavior is observed. In crystalline state complexes showed constant susceptibility value while on melting spin-transition was observed. This behavior is explained by the structural modifications of the ionic bilayers caused by melting of alkyl chains;

6. Heating and cooling magnetic curves inside mesophase do not coincide, forming a hysteresis loop;

7. The temperature of the phase transition solid ↔ liquid crystal in **C$_n$-14** depends on *n* and increases with the increase of *n*;

8. Complete dehydration transforms **C$_n$-14** into spin-crossover inactive **C$_n$-15** with equal LS:HS ratio.

## 2.6 Characterization and physical properties of compounds $C_n$-19–$C_n$-23

### 2.6.1 Introductory remarks

This chapter deals with derivatives of the parent system **1** formed by the ligand tris[3-aza-4-((5-alkoxy)(6-methyl)(2-pyridyl))but-3-enyl]amine    [*tren*($C_n$-6-*Mepy*)$_3$].    The codes and the composition of the compounds under study are listed in Table 17.

**Table 17.** Schematic molecular structure and the composition of **$C_n$-19–$C_n$-23.**
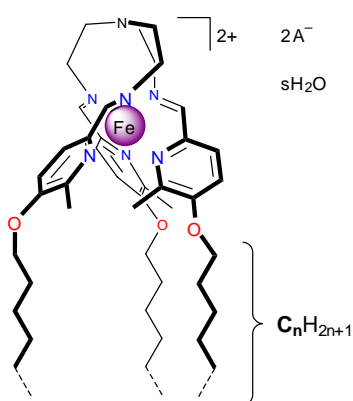


| Anion $A^-$ | s | Compound |
|---|---|---|
| $ClO_4^-$ | 0 | **$C_6$-19, $C_{12}$-19, $C_{18}$-19** |
| $BF_4^-$ | 0 | **$C_{18}$-20** |
| $PF_6^-$ | 0 | **$C_{20}$-21** |
| $SiF_6^{2-}$ | 0 | **$C_{18}$-22** |
| $SO_4^{2-}$ | 3 | **$C_{20}$-23** |

### 2.6.2 Crystal structure of $C_6$-19

Orange-red plate-like crystals of **$C_6$-19** were obtained by slow cooling of a hot saturated ethanolic solution of the compound in a thermostat. The lattice adopted by the compound is monoclinic and retains the space group $P2_1$/c at low and high temperatures. The complex molecule is chiral, hence the unit cell contains two dyads of opposite chirality ($Z = 4$) (Figure 63a, b). One of the perchlorate anions is disordered over two positions with approximately equal occupancies of both sites which differ only slightly for the low and high temperature structures. The amphiphilic nature of the alkylated molecules results in self-assembly into a layered structure, where an ionic bilayer is made up of polar head-groups along with perchlorate anions. Non-polar chains from oppositely directed molecules meet together to form a hydrocarbon layer. Alkyl chains in paraffinic layers, mainly in planar zig-zag conformation, are tilted toward ionic bilayers and show double layered packing, without chain intertwining from the adjacent layers (Figure 63c). The cell parameters and refinement details are presented in Table 18.
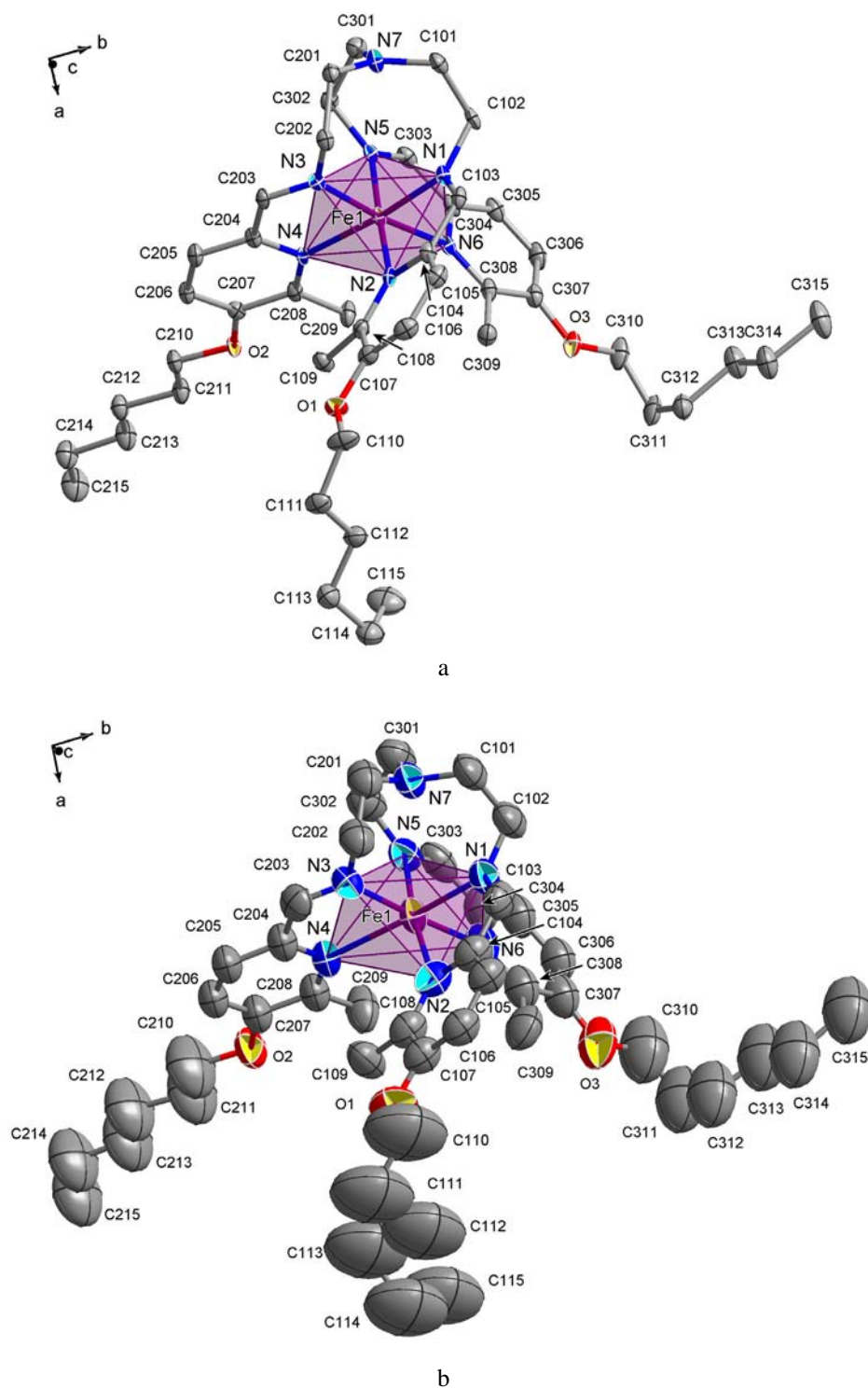
**Figure 63.** a) Projection of the molecular structure of $C_6$-19 with atom numbering scheme at 90 K and b) at 298 K. Hydrogen atoms and perchlorate anions are omitted for clarity. Displacement ellipsoids are shown at 50 % probability level; c) Projection of molecular packing of $C_6$-19 (298 K) along the $c$ axis; d) Projection along the Fe···N7 axis of the minimized overlay of the low-spin (90 K, blue) and the high-spin (298 K, red) molecules of $C_6$-19.

**paraffinic layer**

**ionic bilayer**
$d^{bl} = 10.470(11)$ Å

$d = 17.870(9)$ Å
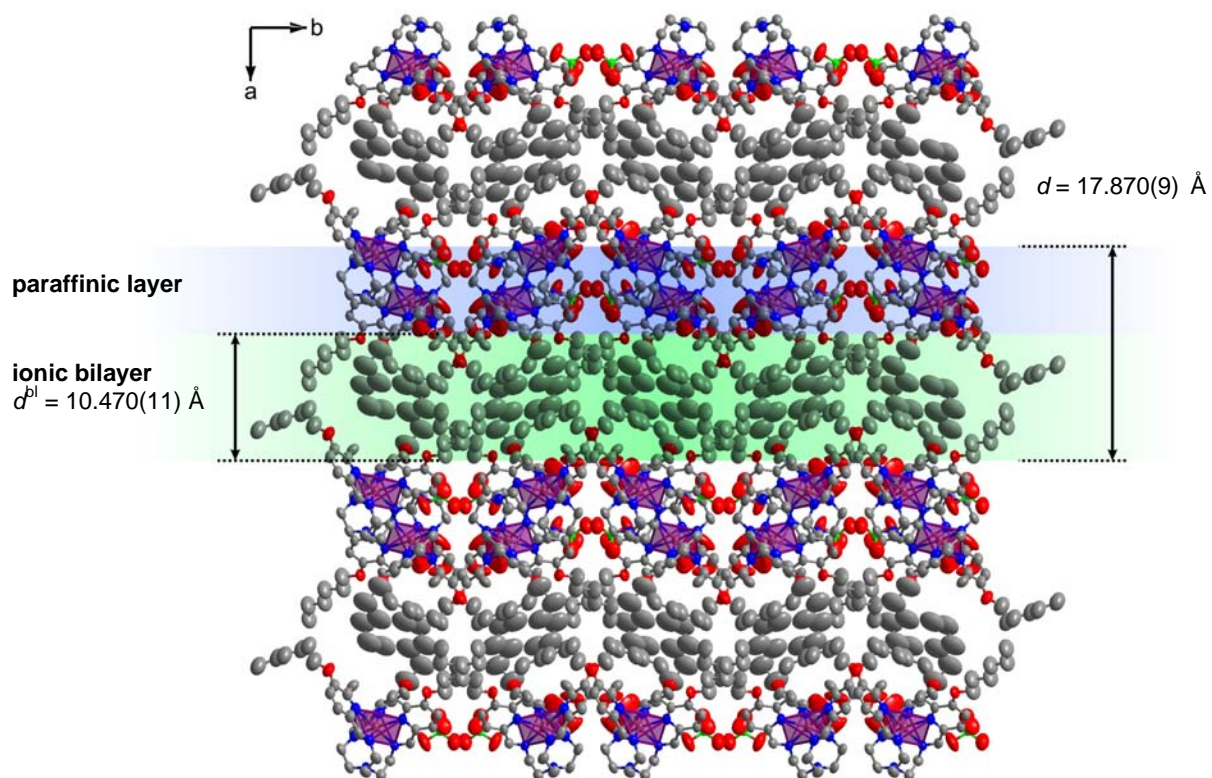
c
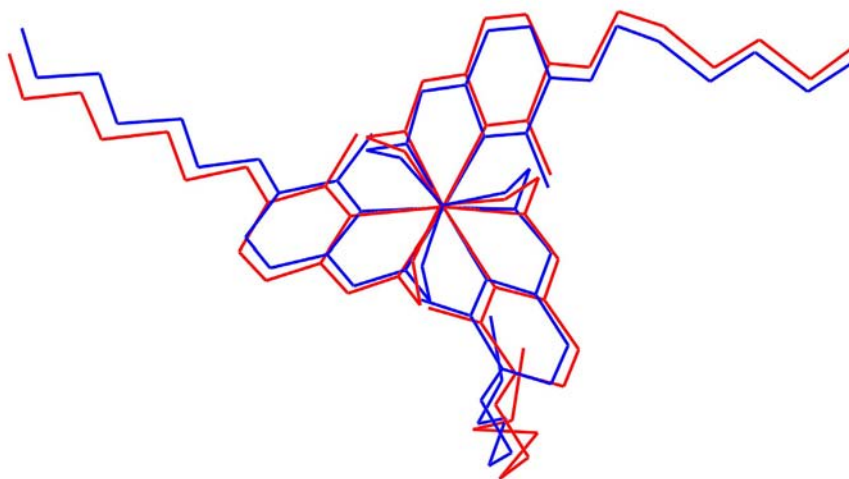


d

**Figure 63.** (*continued*)

**Table 18.** Crystallographic data and refinement details of $C_6$-19 at 90 and 298 K.

| $T$ [K] | 90 | 298 |
|---|---|---|
| Empirical formula | $C_{45}H_{69}Cl_2FeN_7O_{11}$ | |
| Formula weight | 1010.82 | |
| Wavelength [Å] | 0.71073 | |
| Crystal system | monoclinic | |
| Space group | $P2_1/c$ | |
| Z | 4 | |
| $a$ [Å] | 18.713(5) | 18.836(4) |
| $b$ [Å] | 19.072(5) | 19.926(4) |
| $c$ [Å] | 14.697(5) | 15.216(3) |
| $\beta$ [°] | 111.175(5) | 108.56(3) |
| Volume [Å$^3$] | 4891.12 | 5413.9(19) |
| $\rho$ [g cm$^{-3}$] | 1.373 | 1.240 |
| Absorption coefficient [mm$^{-1}$] | 0.483 | 0.436 |
| $F(000)$ | 2144 | 2144 |
| $\theta$ range for data collection [°] | 2.97 to 33.10 | 2.82 to 32.76 |
| Index ranges | $-27 \leq h \leq 28$ | $-27 \leq h \leq 27$ |
| | $-28 \leq k \leq 28$ | $-28 \leq k \leq 28$ |
| | $-10 \leq l \leq 22$ | $-23 \leq l \leq 11$ |
| Reflections collected | 37657 | 46936 |
| Independent reflections | 15781 [$R_{int} = 0.0623$] | 17578 [$R_{int} = 0.0894$] |
| Data/restraints/parameters | 15781/0/622 | 17578/43/440 |
| Goodness-of-fit, $F^2$ | 0.921 | 0.820 |
| Final $R$ indices [$I > 2\sigma(I)$] | $R1 = 0.0647$, | $R1 = 0.0902$, |
| | $wR2 = 0.1741$ | $wR2 = 0.2473$ |
| $R$ indices (all data) | $R1 = 0.1283$, | $R1 = 0.3220$, |
| | $wR2 = 0.1945$ | $wR2 = 0.2926$ |
| $\rho_{min}$, $\rho_{max}$ [e Å$^{-3}$] | 1.027, 1.383 | 1.282, 0.927 |

The structural evolution of the complex molecule $C_6$-19 with temperature resembles that of the parent **1** (Chapter 2.2.2) and is discussed in a similar manner.

**Low-spin structure (90 K).** A pseudo-octahedral environment of the iron(II) ion is formed by nitrogen atoms belonging to two different moieties (Figure 63a). The bonds Fe–N$^{im}$ are shorter than the bonds Fe–N$^{py}$ formed by nitrogen atoms of the pyridine units. The averaged distances for the two types of Fe–N bonds differ by 0.13 Å and the averaged value of both is 2.007(1) Å. The tertiary amine nitrogen atom N7 is not coordinated, the Fe···N7 distance is 3.519(2) Å. The geometry around N7 atom is almost planar, similarly to the one in **1**. Another characteristic distance is the separation of the methyl group and the nitrogen atom of the neighboring pyridine unit. The value averaged over three separations is 3.015(8) Å. The trigonal distortion of the N$_6$ pseudo-octahedron is quantitatively described by the parameters $\theta$ and $\Sigma$ (Table 19). The first has a value of 57.70(2)° which is rather close to that of the perfect $O_h$ symmetry (60°). In the low-spin non-methylated analogue $C_6$-7 this value is slightly lower [55.10(4)°, Table 13, Chapter 2.5.2]. The parameter $\Sigma$ is equal to 85.54(7)° and for the non-methylated analogue is lower by about 20° [67.56(8)°, Table 13]. The last value corresponds

to a more distorted octahedron in close analogy to the pair of the non-alkylated parent complexes **B** and **1** (Chapter 2.2.2; see also Table 7).

**Table 19.** Intramolecular parameters of $C_6$-19 at 90 and 298 K.

|                              | **90 K,** LS | **298 K,** HS |
|------------------------------|--------------|---------------|
| $<Fe–N^{im}>$ [Å]            | 1.939(1)     | 2.130(3)      |
| $<Fe–N^{py}>$ [Å]            | 2.075(1)     | 2.339(3)      |
| $<Fe–N>$ [Å]                 | 2.007(1)     | 2.234(3)      |
| $\theta$ [°]                 | 57.70(2)     | 52.53(1)      |
| $\Sigma$ [°]                 | 85.54(7)     | 116.59(11)    |
| Fe⋯N7 [Å]                    | 3.519(2)     | 3.162(3)      |

**High-spin structure (298 K).** The structure of $C_6$-19 determined at 298 K is quite similar to the structure determined at 90 K, however, there are several principal changes. First of all, large thermal coefficients associated with the oxygen atoms of the perchlorate anions (not shown) and of the alkyl carbon atoms reflect their partial delocalization (Figure 63b). This feature already indicates that these anions and moieties are not maintained by significant intermolecular contacts within the crystal lattice. The change of the molecular shape on going up in temperature is obvious (Figure 63d) and stems from the expansion of the $FeN_6$ coordination core due to the spin-transition. The value of $<Fe–N>$ in high-spin state (2.234(3) Å) is about 0.23 Å larger than that in low-spin state. The difference corresponds to 12 % of its initial value. This value is slightly larger than 10 % typically reported for iron(II) compounds [21] that presumably is due to the unaccounted thermal expansion of the crystal lattice. The increase of the length observed for Fe–$N^{py}$ bonds is higher than that for Fe–$N^{im}$ bonds which does not contradict with the sterical hindrance imposed by the methyl groups which complicate approximation of the central atom by the pyridine moieties. The average distance between methyl substituents and the closest nitrogen atoms of the adjacent pyridine ring increases upon heating with attaining the value of 3.263 Å. In the high-spin molecule it is by 0.26 Å larger than in low-spin molecule. In the parent compound **1** the variation of the intramolecular parameters is less pronounced (Chapter 2.2.2; Table 7). The octahedron becomes more irregular in high-spin state as probed by the angular distortion $\theta$ and the parameter $\Sigma$ which are found to be 52.53(1)° and 116.59(11)°, respectively, *i.e.* the distortion of the $FeN_6$ core follows the spin-transition of iron(II) ion and it is more distorted in high-spin state than in low-spin state. The same conclusion about the distortion of the coordination sphere can be made from the twist angle $\theta$. A comparison of the low-spin and high-spin structures of $C_6$-19 (Figure 63d) demonstrates that, in addition to the expansion of the

coordination sphere and concomitant motion of the $C_2H_4$ groups linking N7 to the three chelating arms of the ligand, the alkyl chains are also significantly affected, although their geometry does not change and the same conformation is preserved in both spin states. The pronounced variation of the intramolecular parameters is reflected in the character of the intermolecular contact, primarily in the weak hydrogen bonds CH···O of the numerous CH groups with the oxygen atoms of the perchlorate anions. A simple visual comparison of the hydrogen bond networks in projections of the low-spin and high-spin structures (Figure 64) shows that in the high-spin structure their number is reduced. Despite this, the character of the packing in both low-spin and high-spin structures is essentially identical. The range of distances of the CH···O contacts is the same in both [2.302–2.718 Å].

All derived intramolecular parameters are listed in Table 19.



a



b
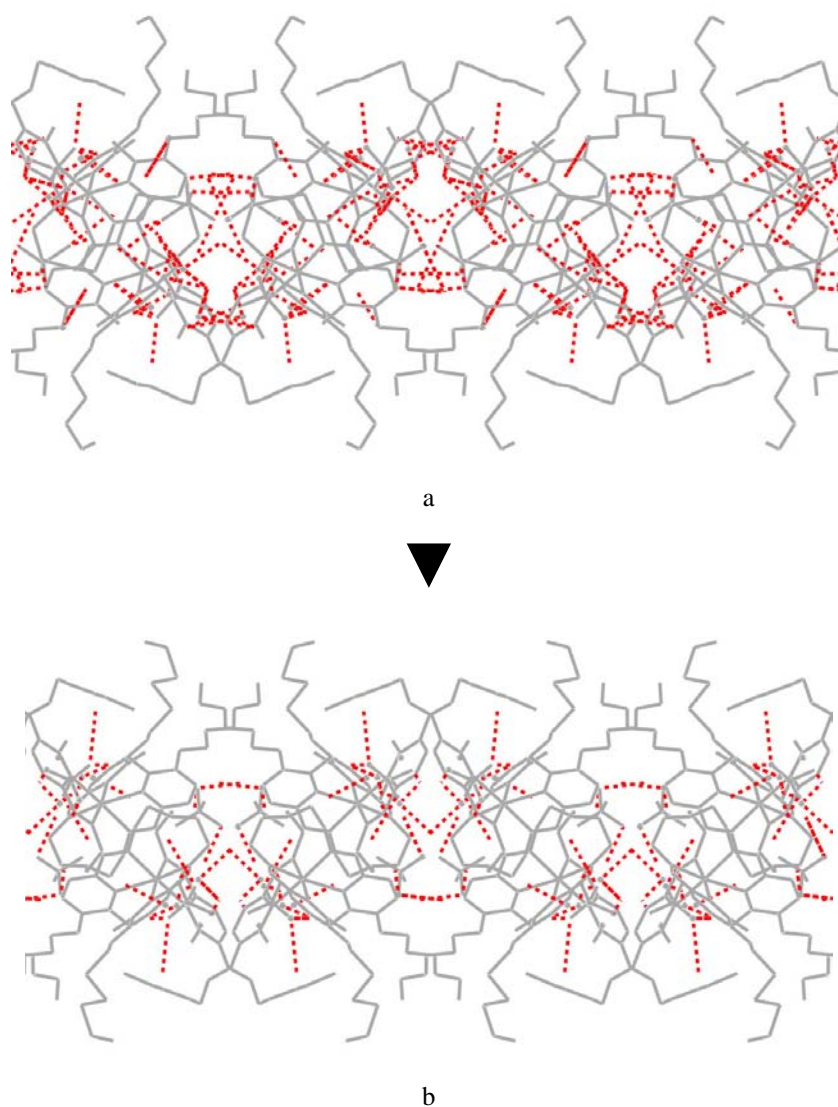
**Figure 64.** Projection of the bilayer of $C_6$-19 at 90 K (a) and at 298 K (b) along the *c* axis denoting decrease the number of hydrogen bonds CH···O (red dashed lines) upon spin-transition.

### 2.6.3  Mass spectroscopic, TGA and IR data

Mass spectroscopic characterization of the complexes was accomplished by electrospray ionization (ESI) or field desorption ionization (FD) methods. In all cases positive ions corresponding to the desired species were observed as the base peaks along with the identifiable fragmentation. For all the complexes the most intensive peaks correspond to the molecular cation without anion or to the molecular cation plus anion or its fragment (Table 20).

TGA measurements confirmed the anhydrous nature of all compounds except **$C_{20}$-23**, which contains about 3 molecules of water per complex cation.

The analysis of the IR spectra of **$C_n$-19**–**$C_n$-23** (Table 20) included the separate analysis of the regions with the characteristic bands of C=N groups and alkyl chains. The latter can provide the structural information about the type of the packing within the paraffinic sublattice and the adopted conformation by the alkyl chains.

**Table 20.** MS, TGA and IR spectroscopic data for the compounds **$C_n$-19**–**$C_n$-23**.

| Compound | MS [m/z] | TGA, w/w [ % ] $(T)^{a}$ | IR [cm$^{-1}$]$^{b}$ | | | | |
|---|---|---|---|---|---|---|---|
| | | | $v_s(CH_2)$, $v_{as}(CH_2)$ | $\delta(CH_2)$ | $\rho(CH_2)$ | $v(N=C)$ | $v(Anion)$ |
| $C_6$-19 | 910 [M+ClO$_4$]$^{+}$ | 0 | 2931, 2858 | 1458 | 726 | 1650 | 1092, 623 |
| $C_{12}$-19 | 1163 [M+ClO$_4$]$^{+}$ | 0 | 2919, 2850 | 1469 | 721 | 1651 | 1087, 623 |
| $C_{18}$-19 | 1415 [M+ClO$_4$]$^{+}$ | 0 | 2918, 2850 | 1469 | 720 | 1652 | 1088, 623 |
| $C_{18}$-20 | 1403 [M+BF$_4$]$^{+}$ | 0 | 2918, 2850 | 1467 | 721 | 1650 | 1054 |
| $C_{20}$-21 | 1446 [M+PF$_6$]$^{+}$ 1420 [M+F]$^{+}$ | 0 | 2919, 2850 | 1466 | 720 | 1653 | 839 |
| $C_{18}$-22 | 1335 [M+F]$^{+}$ 658 [M]$^{++}$ | 0 | 2919, 2851 | 1467 | 723 | 1648 | 740 |
| $C_{20}$-23 | 700 [M]$^{++}$ | 3 (340 K) | 2918, 2850 | 1467 | 720 | 1648 | 1145, 647 |

$^{a}$ Value is given at the point where the plateau is reached. *T* is the temperature at which the dehydration process is centered; $^{b}$ *v*, stretching; *δ*, bending; *ρ*, rocking; as, asymmetric, s, symmetric.

***N=C group.*** The absorption band of the carboxaldimino group C=N provided information about the spin state of the complexes. The band at about 1650 cm$^{-1}$ assigned to $v$(N=C) vibrations were confidently attributed to the high-spin state of the iron(II) ion in all complexes of the series.

***Alkyl chains.*** In the IR spectra, the symmetric and asymmetric stretching modes $v_s(CH_2)$ and $v_{as}(CH_2)$, the scissoring band $\delta(CH_2)$, the wagging progression and the rocking mode $\rho(CH_2)$ are observed in the regions of 2600–3000 cm$^{-1}$ and 700–1600 cm$^{-1}$. The

analyses of the IR data in these regions did not differ from the previous family of compounds described in Chapter 2.5.4 that led to the conclusion about the hexagonal ordering of *trans* configurated alkyl chains.

It is worth noting, that the $CH_2$ vibration bands of **C$_6$-19** are different from those of higher homologues of the family. This allowed to conclude that the packing of alkyl chains found in the former compound is not retained in compounds with longer alkyl chains.

***Anions.*** All compounds of the series contain multiatomic anions ($BF_4^-$, $ClO_4^-$, $SO_4^{2-}$, $SiF_6^{2-}$) the absorption bands of which confirm the expected composition.

In addition, for compound **C$_{20}$-23** a broad peak was observed in the region of 3400 $cm^{-1}$ attributable to $\nu$(O–H) of the solvate water molecules.

The values of all discussed absorption bands are presented in Table 20.

### 2.6.4   UV/VIS spectroscopy

The UV/VIS absorption spectra of three **C$_n$-19** ($n$ = 6, 12, 18) homologues in dichloromethane are shown in Figure 65.
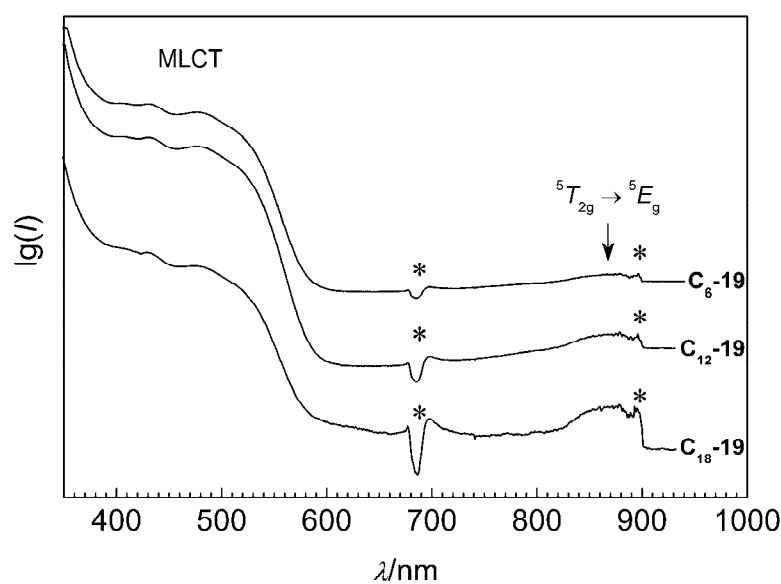


**Figure 65.** UV/VIS spectra of **C$_n$-19** compounds in dichloromethane. The artifacts in the absorption curves (symbol *) are features of the spectrometer.

The spectra are very similar and show the same band structure, therefore we shall discuss only the spectrum of the compound **C$_{18}$-19**. It shows the onset of an intense $\pi$–$\pi^*$ ligand centered peak at $\lambda$ > 350 nm. An intense multicomponent metal-to-ligand charge

transfer (MLCT) band is located at $\lambda$ = 450 nm. The origin of the band is a Laporte-allowed transition from the $d$-orbitals to the $\pi^*$ orbitals of the pyridine moieties, since no other ligand orbitals are of the appropriate symmetry to mix with the metal orbital [150, 194]. The MLCT band supposedly is the superposition of several bands that most probably points out the split of the ligand $\pi^*$ state in the relatively low symmetry of the complex molecule [150].

The metal centered parity forbidden and therefore weak $^5T_{2g} \rightarrow {}^5E_g$ transition is visible as a broad bump at $\lambda$ = 870 nm. This value provides directly the ligand field strength $10Dq^{HS}$ equal to *ca.* 11 500 cm$^{-1}$. The empirical Equation 1 (Chapter 1.3.1) connects the variation of the Fe–N distances with the strength of the ligand field spitting in the spin-crossover compounds [21]. Using the structural data from Table 19 the value $10Dq^{LS}$ = 21 900 cm$^{-1}$ was obtained. In comparison with the parent compound **1** the ligand field strength is somewhat reduced. This can originate from the chemical substitution of the pyridine moieties and the consequent modification of the donating properties of the ligand and/or may be the result of the mechanical hindrance imposed by the alkoxy substituents.

### 2.6.5   Magnetic properties

The magnetic behavior of compounds **$C_n$-19–$C_n$-23** was characterized by the measurements of the molar magnetic susceptibility $\chi_M T$ as a function of temperature $T$.

Among other compounds of the series, the magnetic behavior of the perchlorate systems is the most prominent. Compounds **$C_6$-19**, **$C_{12}$-19** and **$C_{18}$-19** exhibit spin-crossover with $T_{1/2}$ centered at 146 K, 120 K and 133 K, respectively (Figure 66a, b, c). Spin-transition is almost complete and relatively continuous with $\Delta T_{80}$ = 40 K. The $\gamma_{HS}$ values derived from the Mössbauer spectra are consistent with the reported magnetic and structural data. The spin-transition is accompanied by pronounced thermochromism from the high-spin orange-red colored **$C_6$-19** or orange colored **$C_{12}$-19** and **$C_{18}$-19** to the dark red low-spin compounds. The irradiation of the compounds with a laser beam (514 nm) at 4 K for two hours resulted into an increase of the susceptibility till saturation evidencing the LIESST effect. The highest percentage of molecules which was photo-converted into the high-spin state was inferred from the $\chi_M T$ values at 42 K, 25 K and 42 K for **$C_6$-19**, **$C_{12}$-19** and **$C_{18}$-19** as 80 %, 54 %, 50 %, respectively. The critical temperature of relaxation of the high-spin metastable state known as $T_{1/2}^{LIESST}$ is 56 K, 48 K and 56 K, respectively. No obvious dependence of $T_{1/2}$ or $T_{1/2}^{LIESST}$ on the length of alkyl chains was found. In fact, the highest value of this parameter is observed for the **$C_6$-19** homologue and the lowest for **$C_{12}$-19**, while the **$C_{18}$-19** homologue

shows intermediate values. In the cooling and heating modes, compound $C_{12}$-19 shows a discontinuity in the magnetic curve at about 380 K which was attributed to solid → mesophase transition (Figure 66b, Figure 69a).

For the rest of the series with anions other than perchlorate magnetic susceptibility measurements revealed several remarkable features (Figure 66d–g). In the high temperature region, compounds $C_{20}$-21, $C_{18}$-22 and $C_{20}$-23 show anomalies in the magnetic susceptibility curve, which coincide in temperature with the melting point of the pristine compounds determined from the DSC data (for two latter compounds, *vide infra*). These anomalies can be explained by the molecular reorientation due to phase transition [232] or "annealing" of lattice strains. The subsequent cooling and heating do not show any more discontinuity with melting. For the pristine compounds $C_{18}$-20, $C_{20}$-21, $C_{18}$-22 and $C_{20}$-23 a partial decrease of the susceptibility is observed with $T_{1/2}$ located in the range of 100–120 K. This variation is attributed to the gradual and incomplete spin-transition resulting in high percentage of the residual high-spin molecules. The decrease of $\chi_M T$ below 50 K is attributed to zero-field splitting. It is worth noting that the first melting influences the low temperature behavior as well (Figure 66c, f, g). After thermal treatment compounds $C_{18}$-22 and $C_{20}$-23 show even more gradual spin-transition.



a



b
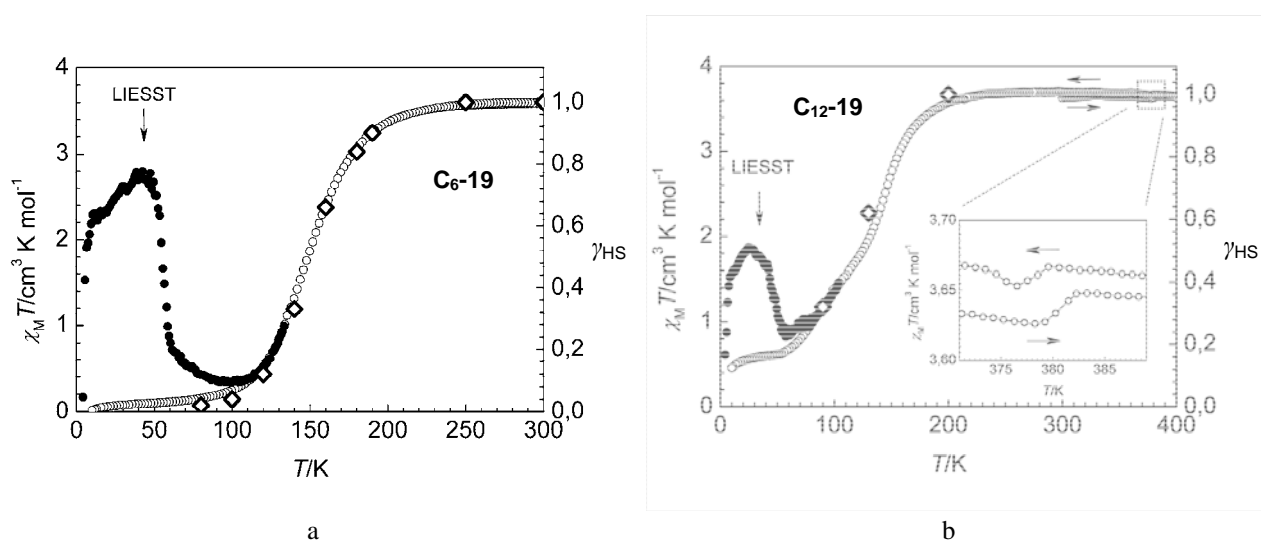
**Figure 66**. Magnetic susceptibility curves for a) $C_6$-19, b) $C_{12}$-19, c) $C_{18}$-19, d) $C_{18}$-20, e) $C_{20}$-21, f) $C_{18}$-22, g) $C_{20}$-23 in the form $\chi_M T$ *vs* $T$ (○). The symbol ● for $C_n$-19 corresponds to magnetic susceptibility curves measured after irradiation with green laser light (514 nm, 4 K, 2 h). Arrows indicate heating and cooling runs. Symbol ◇ corresponds to $\gamma_{HS}$ value derived from variable temperature Mössbauer spectra (Table 22).
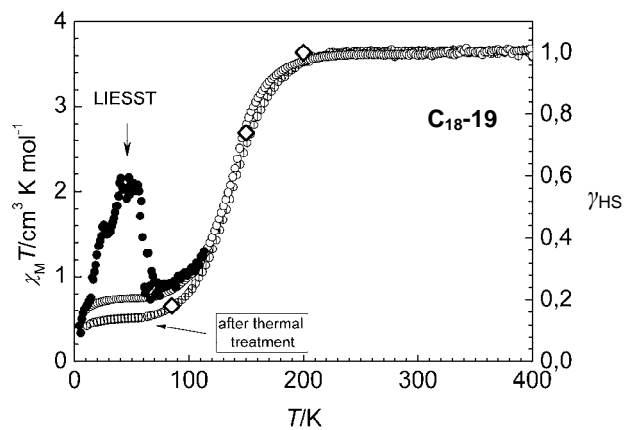
c
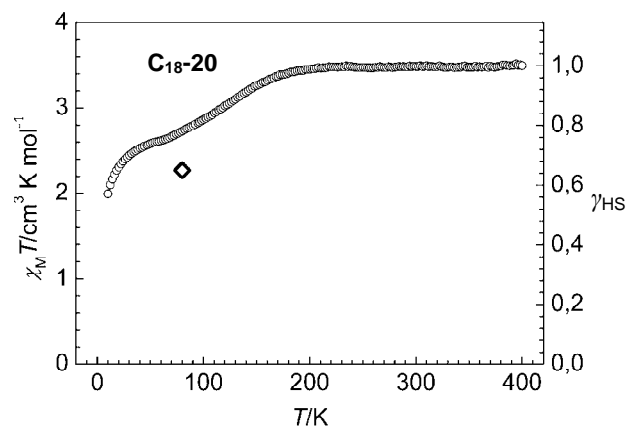


d
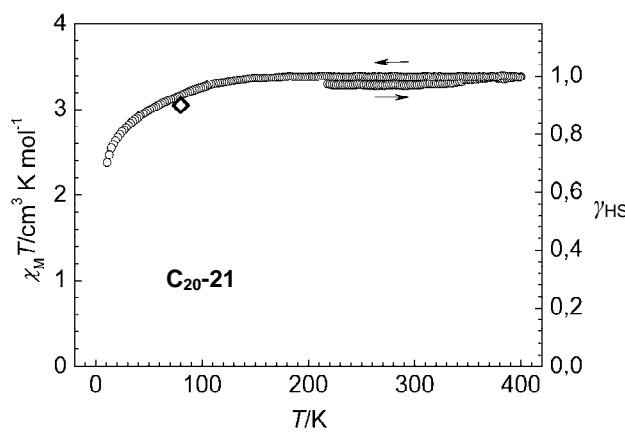


e
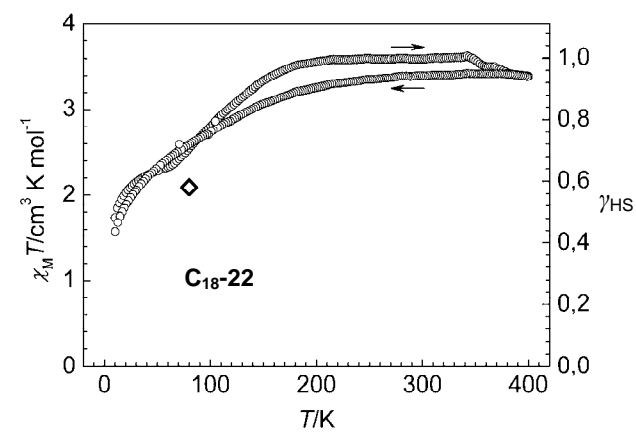


f
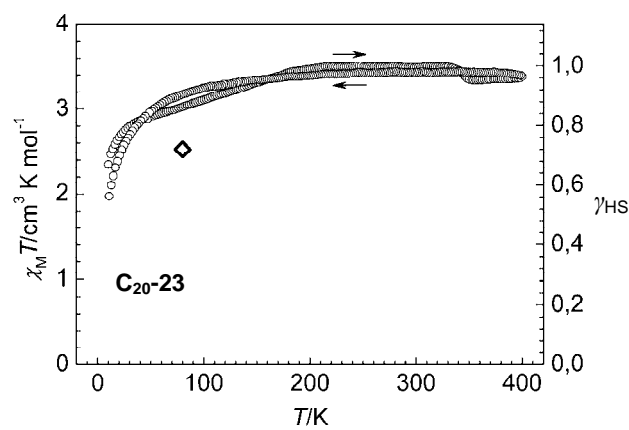


g

**Figure 66.** (*continued*)

### 2.6.6   XRD measurements

The diffractograms of compounds $C_n$-19–$C_n$-23 in the range $2\theta = 2$–$30°$ at temperatures 300, 410 and 300 K are shown in Figure 67a–f. At all temperatures, they include a single low-angle reflection (10), indicative of the layered structure. In general, on phase transition a shift of low and high angle reflections to lower values with a change of intensity of higher reflections and broadening of the alkyl reflection is observed. For the $C_{20}$-23 derivative a complete disappearance of the low-intensity reflections (20) is detected that is caused by the transition into mesophase. The weaker the (20) reflection is with respect to the (10) reflection, the worse the layers are defined [269].
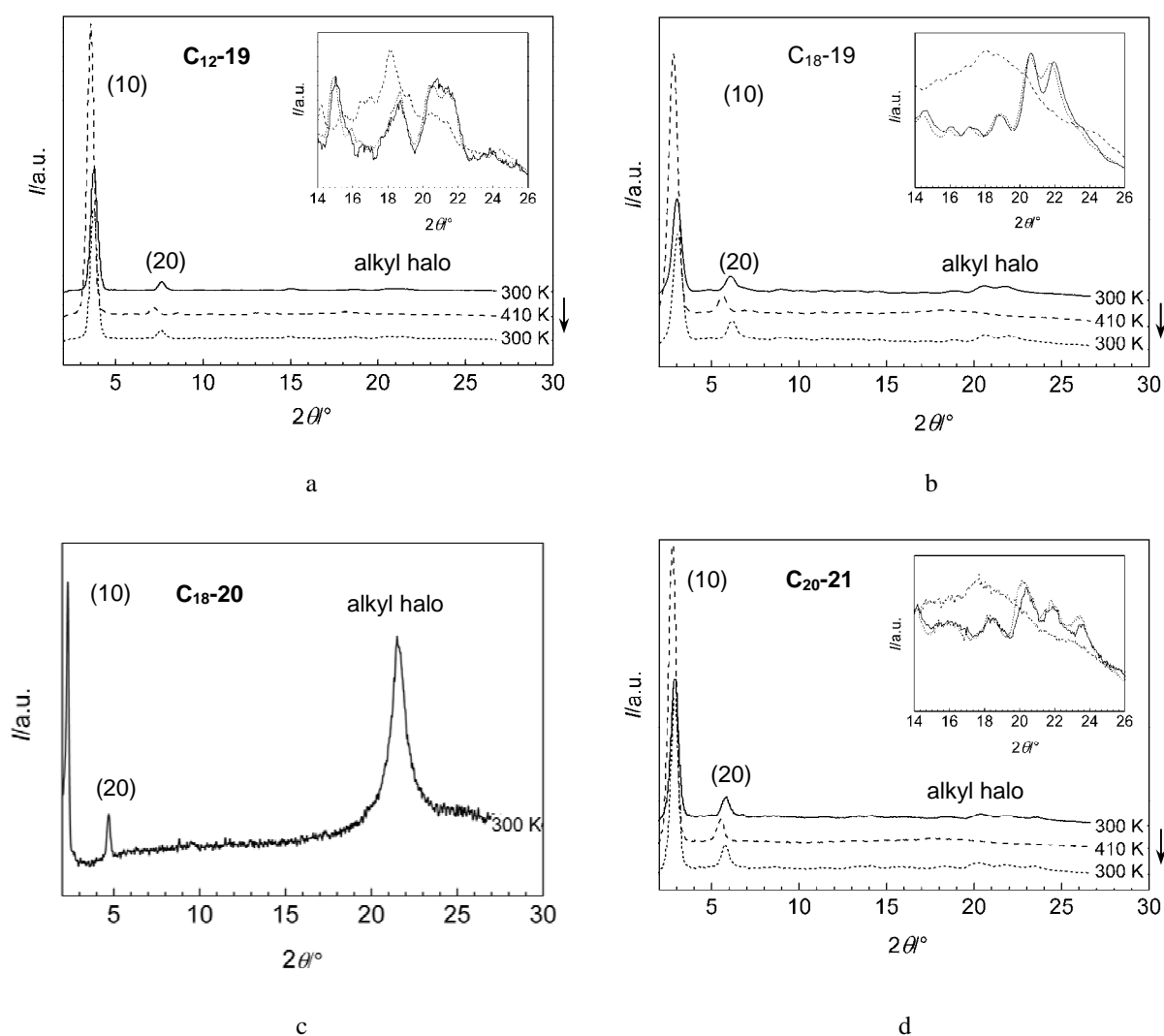


**Figure 67.** XRD diffractograms of a) $C_{12}$-19, b) $C_{18}$-19, c) $C_{18}$-20, d) $C_{20}$-21, e) $C_{18}$-22, f) $C_{20}$-23 at different temperatures. Insets show enlarged region of the alkyl halo.

e                                        f
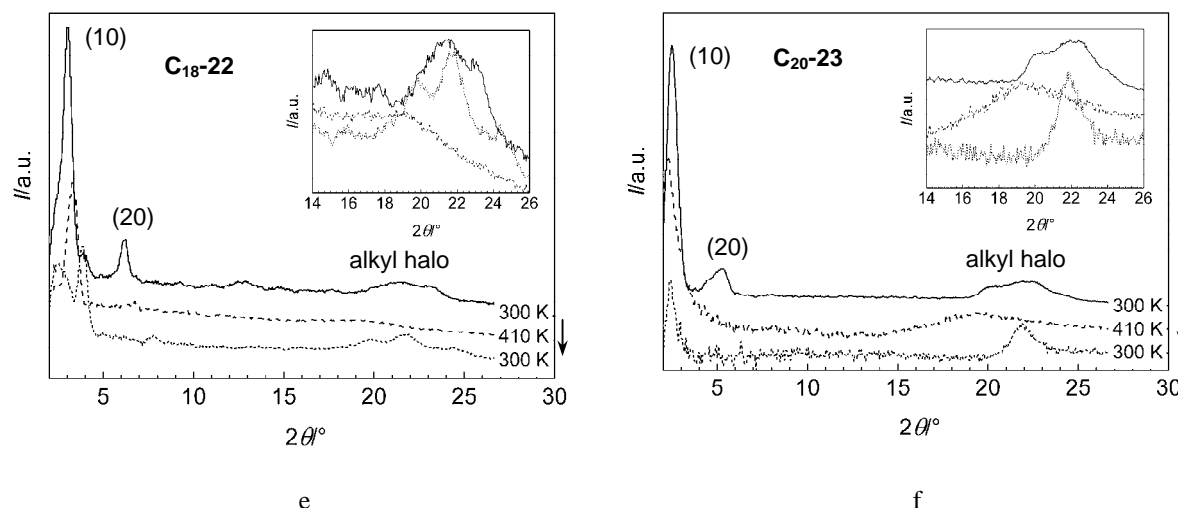
**Figure 67.** (*continued*)

Additional low-intensity reflections in the diffractograms of $C_{12}$-19, $C_{18}$-19, $C_{20}$-21 and $C_{18}$-22 indicate a relatively high crystallinity of these compounds (Figure 67a, b, d, e). Some of the weak crystalline reflections are preserved even in the mesophase pointing out partial retaining of the solid structure which in general is typical for layered ionic metallomesogens [128, 258]. However, poor resolution of the reflections and their low intensity does not allow reliable indexing of the XRD profiles. The interlayer spacing $d$ of compounds $C_n$-19–$C_n$-23 was calculated from the maxima of the reflections (10) in both solid and liquid crystalline phases according to the Bragg's law (Table 21).

**Table 21**. Interlayer distances $d$ at different temperatures, thermal transitions and mesomorphism, enthalpy $\Delta H^{Cr \to S_x}$ and entropy $\Delta S^{Cr \to S_x}$ of phase transition solid → liquid crystalline and thermal stability determined by XRD, DSC, TGA and POM for $C_n$-19–$C_n$-23.

| Compound | $d$ [Å] 300 K (pristine) | 410 K | 300 K | Thermal transitions [K] | $\Delta H^{Cr \to S_x}$ [kJ mol$^{-1}$][c] | $\Delta S^{Cr \to S_x}$ [J K$^{-1}$ mol$^{-1}$] |
|---|---|---|---|---|---|---|
| $C_6$-19 | 17.461(6) (90 K) 17.870(9) (298 K) [a] | – | – | – | – | – |
| $C_{12}$-19 | 24.0 | 24.8 | 24.0 | Cr $\underset{360}{\overset{370}{\rightleftarrows}}$ $S_X$ 500 d | 31.3 | 82.8 |
| $C_{18}$-19 | 29.6 | 31.3 | 29.5 | Cr $\underset{367}{\overset{382}{\rightleftarrows}}$ $S_X$ 470 d | 54.9 | 146.4 |
| $C_{18}$-20 | 29.6 | 31.2 | 29.6 | – | – | |
| $C_{20}$-21 | 32.0 | 30.4 | 30.4 | – | – | |
| $C_{18}$-22 | 28.9 | 26.4 | 23.0 | Cr $\underset{300}{\overset{310}{\rightleftarrows}}$ M[b] $\underset{375}{\overset{390}{\rightleftarrows}}$ $S_X$ 477 d | 61.2 (Cr → M), 5.1 | 200.0, 13.2 |
| $C_{20}$-23 | 35.9 | 39.4 | 36.8 | Cr $\underset{305}{\overset{320}{\rightleftarrows}}$ $S_X$ 490 d | 112.3 | 359.9 |

[a] From the monocrystal X-ray data; [b] An intermediate mesophase. See explanation in text; [c] Measured by DSC on the second heating-cooling cycle. The values correspond to the maxima of the enthalpy peaks. The identification of the mesophase was done on the basis of the POM data.

It is known, that for homologues the increment in the *d*-spacing due to addition of one methylene group is a constant value only if the chain packing and the tilt angle are retained. From the IR data it is known that disordered alkyl chains in **C₆-19** are not retained by two higher homologues which adopt packing with the straight *trans* or *all-trans* alkyl chains similarly to **C₁₂-8** (Figure 50a, b, c). In spite of this fact, the plot of the interlayer spacing *vs* number of carbon atoms *n* shows that the *d* values of three compounds fit on a straight line (Figure 68). To our opinion the fit of the spacing for the lower homologue is fortuitous. Extrapolation to $n = 0$ gave the distance $d^{n=0}$ equal to 12.8 Å. After correction for the radii of the two terminal methyl groups ($2 \times 1.09$ Å) the extrapolated thickness of the ionic bilayer $d^{bl}$ was calculated to be 10.6 Å. It agrees well with the value $d^{bl} = 10.470(11)$ Å directly obtained from the high-spin crystal structure of **C₆-19** at 290 K (see Figure 63c).
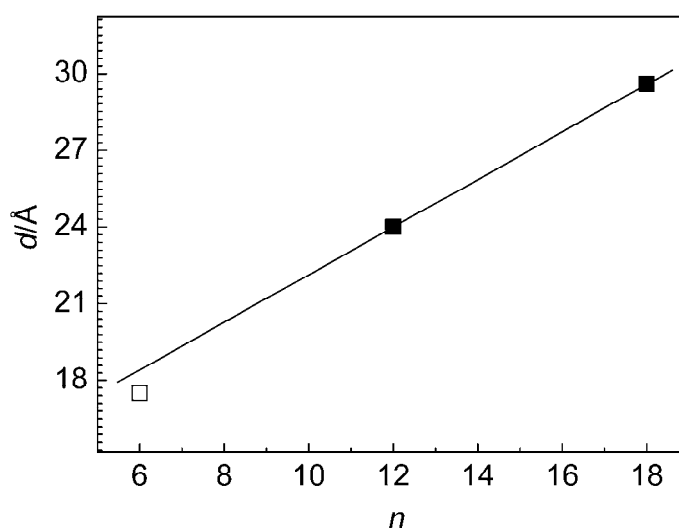


**Figure 68**. Interlayer spacing *d* of the room-temperature crystal phase of $C_n$-19, $n = 6$, 12, 18 as a function of the number of carbon atoms in the alkyl chains. The solid line was drawn through points of the two higher homologues.

### 2.6.7    DSC and POM data

The DSC profiles of compounds **C₁₂-19**, **C₁₈-19**, **C₁₈-22** and **C₂₀-23** obtained in heating and cooling modes are shown in Figure 69a–d. The enthalpies of the transition from solid state to smectic ($S_X$) mesophase in the first two compounds increased with the lengthening of the alkyl substituents. For **C₁₈-19** a hysteresis of phase transition is detected with a width of 25 K (Figure 69b). For the compounds **C₁₈-22** and **C₂₀-23** the first heating scan did not coincide with the second one being reminiscent of the magnetic behavior, where

the artifact on the magnetic curve is probably due to annealing of the pristine structure or loss of solvent molecules (Figure 69c, d; Figure 66f, g). Once heated, compound $C_{18}$-22 undergoes a phase transition at 375 K as is confirmed by a low energy peak (5.1 kJ mol$^{-1}$) and on further cooling a second high energy peak (61.2 kJ mol$^{-1}$) at 310 K (Figure 69c). The subsequent heating run repeats the features, but with a slight shift in temperature because of the structural hysteresis. This behavior was tentatively ascribed to an intermediate mesophase denoted as M in Table 21.
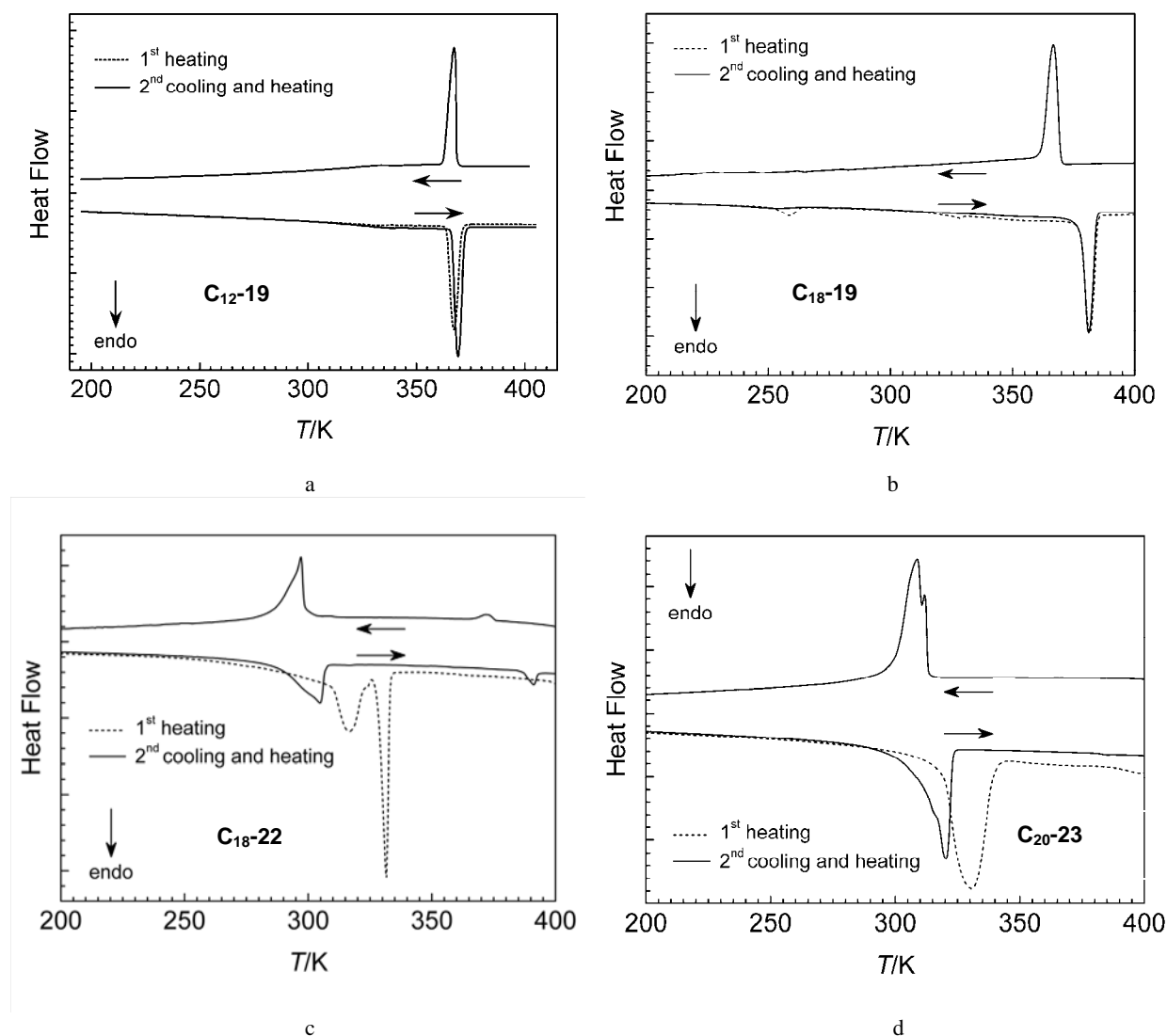


**Figure 69.** DSC profiles of a) $C_{12}$-19, b) $C_{18}$-19, c) $C_{18}$-22 and d) $C_{20}$-23 in heating and cooling modes. Arrows show the direction of the scanning runs.

Contrary to the intensively colored low-spin compounds of $C_n$-7–$C_n$-18 which are derivatives of the low-spin parent compound **B**, the intensity of the coloration in $C_n$-19–$C_n$-23 is significantly less being typical of the high-spin iron(II) compounds. This simplified

observation of the anisotropic textures by polarizing optical microscopy (POM), however, only at relatively high temperature because of the strong tendency of the compounds to show homeotropic texture. The textures observed were assigned to smectic type ($S_X$).

TGA measurements allowed to determine precisely the decomposition temperature of the compounds. Surprisingly, the perchlorate compounds $C_n$-19 ($n$ = 12, 18) are stable on heating up to about 470–500 K, the temperature at which the compounds with other anions also start to decompose. Derived values of the transition temperature, *viz.* the enthalpy and entropy calculated by the integration of the DSC peaks, and the POM data are collected in Table 21.

### 2.6.8 Mössbauer spectroscopy

Representative Mössbauer spectra of the compounds $C_n$-19–$C_n$-23 recorded in cooling mode are shown in Figure 70a–g; the values of Mössbauer parameters obtained by least-square fitting of the spectra are presented in Table 22.

The Mössbauer spectra of $C_6$-19 recorded below and above $T_{1/2}$ are consistent with the magnetic and structural data reported (Figure 70a). Above 250 K the Mössbauer spectra of the compound contains a single high-spin doublet. Its asymmetry is caused by texture since for the measurement a polycrystalline sample with thin plate-like crystals was used. Upon cooling, a low-spin doublet appeared which intensified at the expense of the high-spin doublet. At each measured temperature the high-spin molar fraction $\gamma_{HS}$ was deduced from the total area determined from the fitting procedure (Table 22). In agreement with the magnetic data, the plot of $\gamma_{HS}$ *vs* $T$ closely coincides with the corresponding magnetic curve (Figure 66a). For the two higher homologues $C_{12}$-19 and $C_{18}$-19 the Mössbauer spectra were better fitted with two doublets for each the high-spin and low-spin fractions (Figure 70b, c). Still the better fitting for the Mössbauer spectrum of $C_{12}$-19 at 90 K was obtained with one low-spin and one high-spin doublet. The reason for this is perhaps a phase transition which the compound undergoes near 120 K. In the magnetic curve it is manifested as a change of the slope (Figure 66b). The spectra of both compounds measured at low temperature confirmed the incompleteness of the spin-transition as they can be fitted with the presence of low-spin and high-spin doublets.

For the compounds $C_{18}$-20, $C_{18}$-22 and $C_{20}$-23 the comparison of the magnetic data with the $\gamma_{HS}$ values derived from the Mössbauer spectra, shows relatively high overestimation of the low-spin molar fraction (Figure 70d, f, g; Figure 66d, f, g). In a rough approximation, a

correlation is found between the incompleteness of the spin-transition and the degree of the overestimation. The differences observed between the intensities of low-spin and high-spin doublets in comparison with the magnetic measurements may be attributed to the known difference of the Debye-Waller factors for the two species. For "classical" crystalline compounds Debye-Waller factor *f* for the low-spin state is generally larger by *ca*. 20 % than for the high-spin state and shows different temperature dependence for the two states [88, 270]. As a consequence, some inconsistency between the derived values of $\gamma_{HS}$ from Mössbauer spectra and the magnetic data is detected. The low-spin fraction is overestimated due to the higher tightness of binding of the iron(II) ions in the low-spin iron(II) complex molecules as compared to the high-spin complex molecules. For the alkylated compounds this effect should be even more pronounced because of the two-dimensional character of packing of the iron-containing head-groups (see the packing in Figure 63c and Figure 71a).

A pronounced broadening of the resonance doublets might point out a variety of small structural differences in the surroundings of the complex molecules which produces a distribution of unresolved isomeric shifts and quadrupole splittings. The low crystallinity of the compounds inferred from XRD data supports this suggestion.
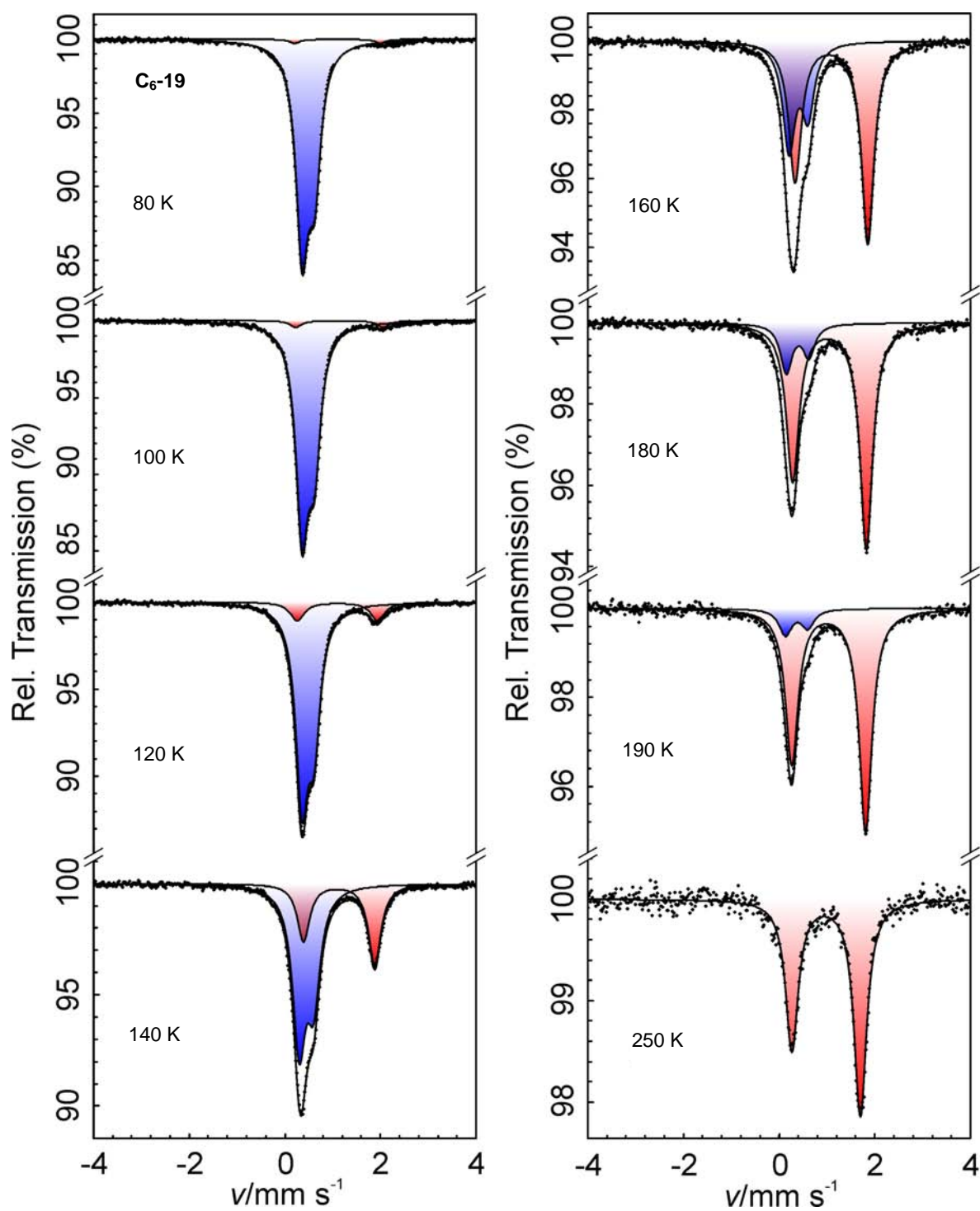
a

**Figure 70.** Mössbauer spectra of a) $C_6$-**19**, b) $C_{12}$-**19**, c) $C_{18}$-**19**, d) $C_{18}$-**20**, e) $C_{20}$-**21**; f) $C_{18}$-**22**, g) $C_{20}$-**23** at different temperatures.
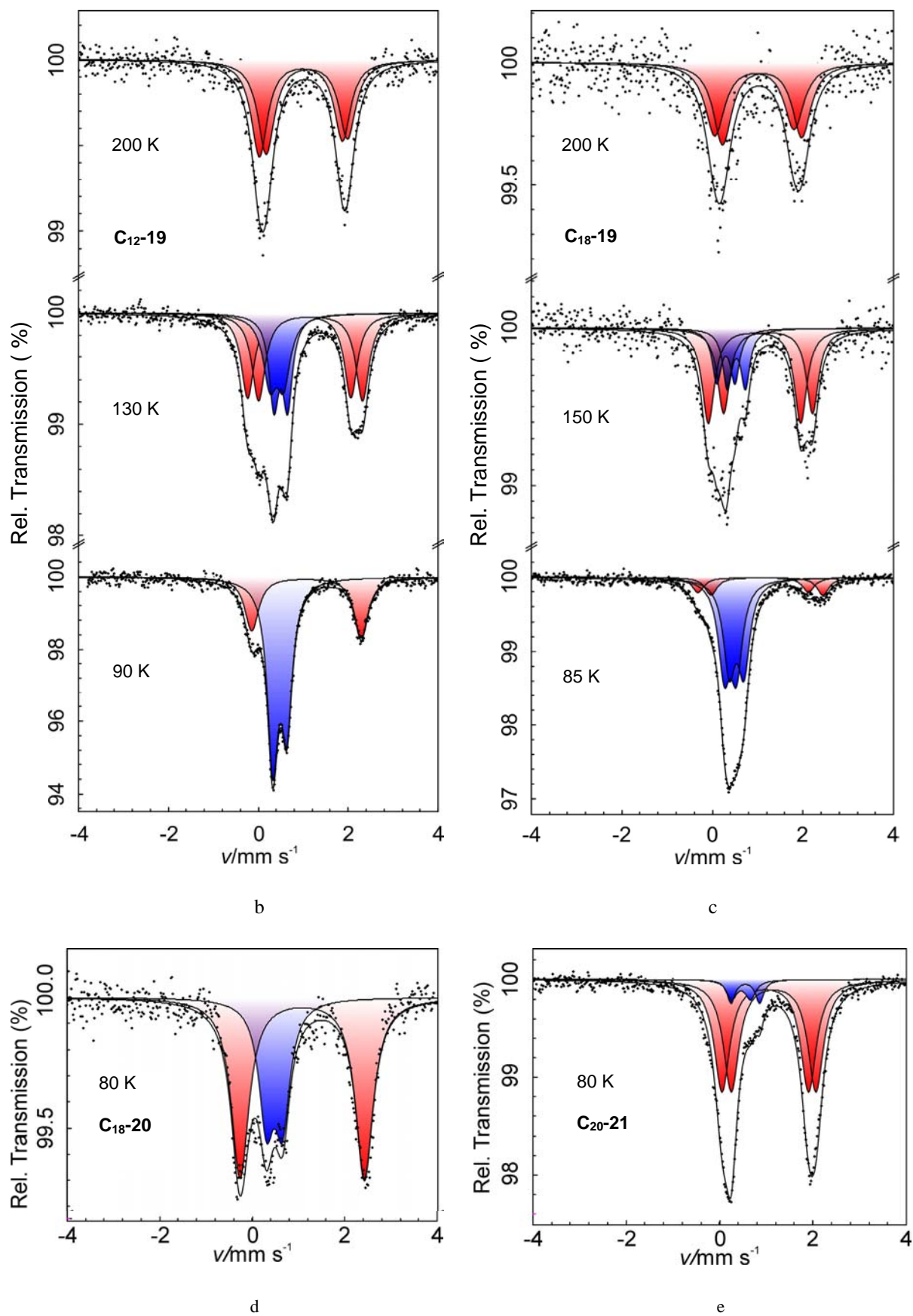
Figure 70. (*continued*)

f            g
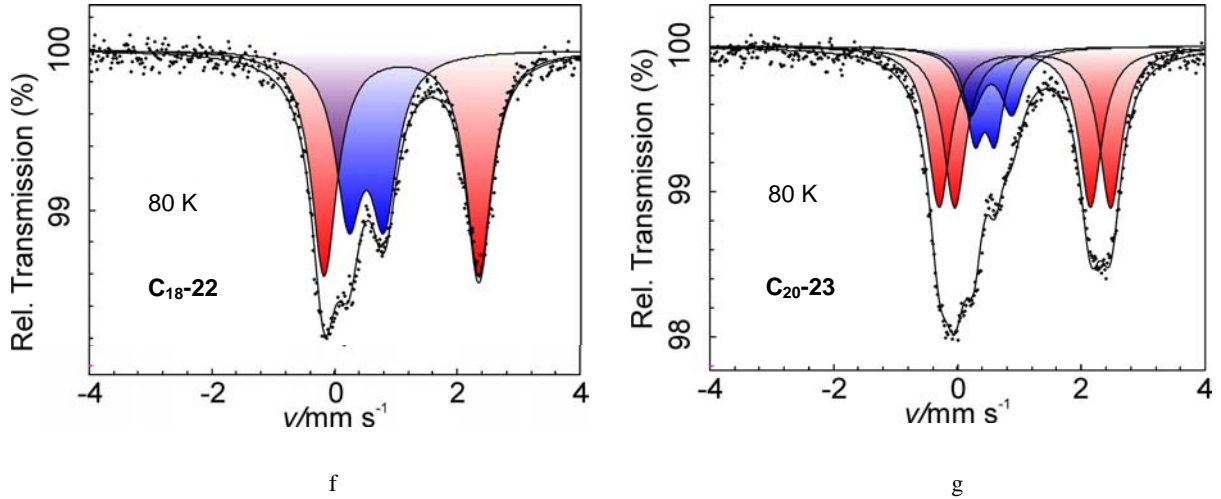
**Figure 70.** (*continued*)

**Table 22.** Mössbauer parameters, isomeric shift ($\delta$, relative to α-iron), quadrupole splitting ($\Delta E_Q$), half-width of the lines ($\Gamma_{1/2}$) and percentage of the multiplet populations in the high-spin (HS) and low-spin (LS) states (*A*) at different temperatures for $C_n$-19–$C_n$-23.

| Compound | *T* [K] | Spin state | $\delta$ [mm s$^{-1}$] | $\Delta E_Q$ [mm s$^{-1}$] | $\Gamma_{1/2}$ [mm s$^{-1}$] | *A* [ %] |
|---|---|---|---|---|---|---|
| **$C_6$-19** | 80 | LS | 0.49(0) | 0.26(0) | 0.16(1) | 98.0(5) |
| | | HS | 1.10(0) | 1.79(0) | 0.13(1) | 2.0(5) |
| | 100 | LS | 0.49(0) | 0.26(1) | 0.16(1) | 96.4(5) |
| | | HS | 1.14(0) | 1.83(0) | 0.14(0) | 3.6(6) |
| | 120 | LS | 0.48(0) | 0.26(1) | 0.16(1) | 87.9(5) |
| | | HS | 1.10(0) | 1.68(0) | 0.18(1) | 12.1(7) |
| | 140 | LS | 0.45(1) | 0.30(0) | 0.17(0) | 66.5(5) |
| | | HS | 1.13(0) | 1.49(1) | 0.16(0) | 33.5(7) |
| | 160 | LS | 0.40(0) | 0.40(1) | 0.16(0) | 33.8(6) |
| | | HS | 1.09(0) | 1.52(0) | 0.16(0) | 66.1(8) |
| | 180 | LS | 0.38(0) | 0.47(0) | 0.15(1) | 16.4(8) |
| | | HS | 1.05(0) | 1.54(0) | 0.16(0) | 83.6(11) |
| | 190 | LS | 0.37(0) | 0.47(0) | 0.16(0) | 10.6(9) |
| | | HS | 1.04(1) | 1.54(0) | 0.16(0) | 89.4(13) |
| | 250 | HS | 0.98(0) | 1.43(0) | 0.16(0) | 100 |
| | 300 | HS | 0.95(1) | 1.32(1) | 0.17(0) | 100 |
| **$C_{12}$-19** | 90 | LS | 0.48(1) | 0.31(0) | 0.15(1) | 68.4(14) |
| | | HS | 1.07(0) | 2.43(0) | 0.19(1) | 31.6(21) |
| | 130 | LS1 | 0.41(1) | 0.31(1) | 0.18(0) | 21.7(0) |
| | | LS2 | 0.50(0) | 0.31(1) | 0.13(1) | 21.6(14) |
| | | HS1 | 0.91(0) | 2.30(1) | 0.18(1) | 27.6(60) |
| | | HS2 | 1.16(0) | 2.31(1) | 0.18(0) | 29.1(62) |
| | 200 | HS1 | 0.95(1) | 1.85(1) | 0.22(1) | *50* |
| | | HS2 | 1.08(1) | 1.81(1) | 0.23(1) | *50* |
| **$C_{18}$-19** | 85 | LS1 | 0.39(0) | 0.27(0) | *0.16* | *42* |
| | | LS2 | 0.53(0) | 0.32(0) | *0.16* | *42* |
| | | HS1 | 0.90(0) | 2.44(0) | *0.16* | *7* |
| | | HS2 | 1.21(1) | 2.48(1) | *0.16* | *9* |
| | 150 | LS1 | 0.29(1) | *0.35* | 0.15(0) | *15* |
| | | LS2 | 0.53(1) | *0.35* | 0.14(1) | *16* |
| | | HS1 | 0.93(1) | 2.04(1) | 0.17(1) | *32* |
| | | HS2 | 1.23(0) | 1.96(0) | 0.16(0) | *37* |

**Table 22.** (*continued*)

| Compound | $T$ [K] | Spin state | $\delta$ [mm s⁻¹] | $\Delta E_Q$ [mm s⁻¹] | $\Gamma_{1/2}$ [mm s⁻¹] | $A$ [ % ] |
|---|---|---|---|---|---|---|
| $C_{18}$-19 | 200 | HS1 | 0.93(1) | *1.75* | 0.26(0) | *48* |
|  |  | HS2 | 1.10(1) | *1.75* | 0.25(0) | *51* |
| $C_{18}$-20 | 80 | LS | 0.47(0) | 0.35(1) | 0.20(1) | 35.4(25) |
|  |  | HS | 1.07(1) | 2.68(1) | 0.23(1) | 64.6(38) |
| $C_{20}$-21 | 80 | LS1 | 0.46(0) | 0.40(0) | 0.11(1) | *5* |
|  |  | LS2 | 0.55(0) | 0.61(0) | 0.13(1) | *5* |
|  |  | HS1 | 0.98(1) | 1.85(0) | 0.20(0) | *45* |
|  |  | HS2 | 1.16(1) | 1.81(0) | 0.20(0) | *45* |
| $C_{18}$-22 | 80 | LS | 0.51(1) | 0.58(1) | 0.26(1) | 41.8(15) |
|  |  | HS | 1.08(1) | 2.52(1) | 0.25(1) | 58.2(20) |
| $C_{20}$-23 | 80 | LS1 | 0.45(0) | 0.28(1) | 0.16(1) | *14* |
|  |  | LS2 | 0.52(0) | 0.70 (0) | 0.16(0) | *14* |
|  |  | HS1 | 0.93(1) | 2.44(0) | 0.22(0) | *36* |
|  |  | HS2 | 1.21(0) | 2.52(1) | 0.22(1) | *36* |

The values given in italics were fixed during the fitting.

## 2.6.9    Discussion

By introducing an alkoxy substituent into each pyridine unit of the ligand of the parent compound **1**, the distribution of the electronic density within the ligation moieties is modified resulting in a weaker ligand field strength. The UV/VIS spectra of the alkylated derivatives $C_n$-**19** ($n$ = 6, 12, 18) confirms the reduced $10Dq^{HS}$ value in comparison to that of the parent compound **1**. The values of the parent system and the alkylated derivatives are 13 800 and 11 500 cm⁻¹, respectively.

Intermolecular contacts within the crystal lattice are an additional factor which influences the magnetic properties of the spin-crossover compounds in solid state [20, 21, 271]. We shall show this by the comparison of the projections of the structures **1** and its derivative $C_6$-**19** and their magnetic properties. In solid state, both compounds form layered structures. Preserving the same space group $P2_1$/c, they show the same topology of the ionic bilayers (Figure 71a). The parameters $b$ and $c$ of the unit cells are very similar in both compounds (compare data in Table 2 and Table 18). Hence, the main change in the arrangement has to be observed along the $a$ axis which is perpendicular to the plane of the layers. In compound $C_6$-**19** the increase of the parameter $a$ arises from the alkyl substituents attached to the coordination head-groups (Figure 63a, Figure 71b). The paraffinic layer moves ionic bilayers apart by nearly 7.5 Å, breaking all hydrogen bonds and π–π stacking interactions between coordination heads of the adjacent bilayers. In contrast, in **1** the bilayers are close enough to show inter-bilayer intermolecular contacts (Figure 71b). The disorder of

one of the perchlorate anions is not observed in **1**, but found in system **$C_6$-19** in the low- and high-spin structures. It has no obvious influence on the character of the spin-transition in the alkylated compound, since the ratio between occupancy factors for two positions of the anion do not change substantially with temperature and is similar in both structures. Perhaps, a change in the anion(s) disorder is observed in **$C_{12}$-19** which is responsible for a step detected near 120 K in the magnetic susceptibility curve (Figure 66b).



a



b
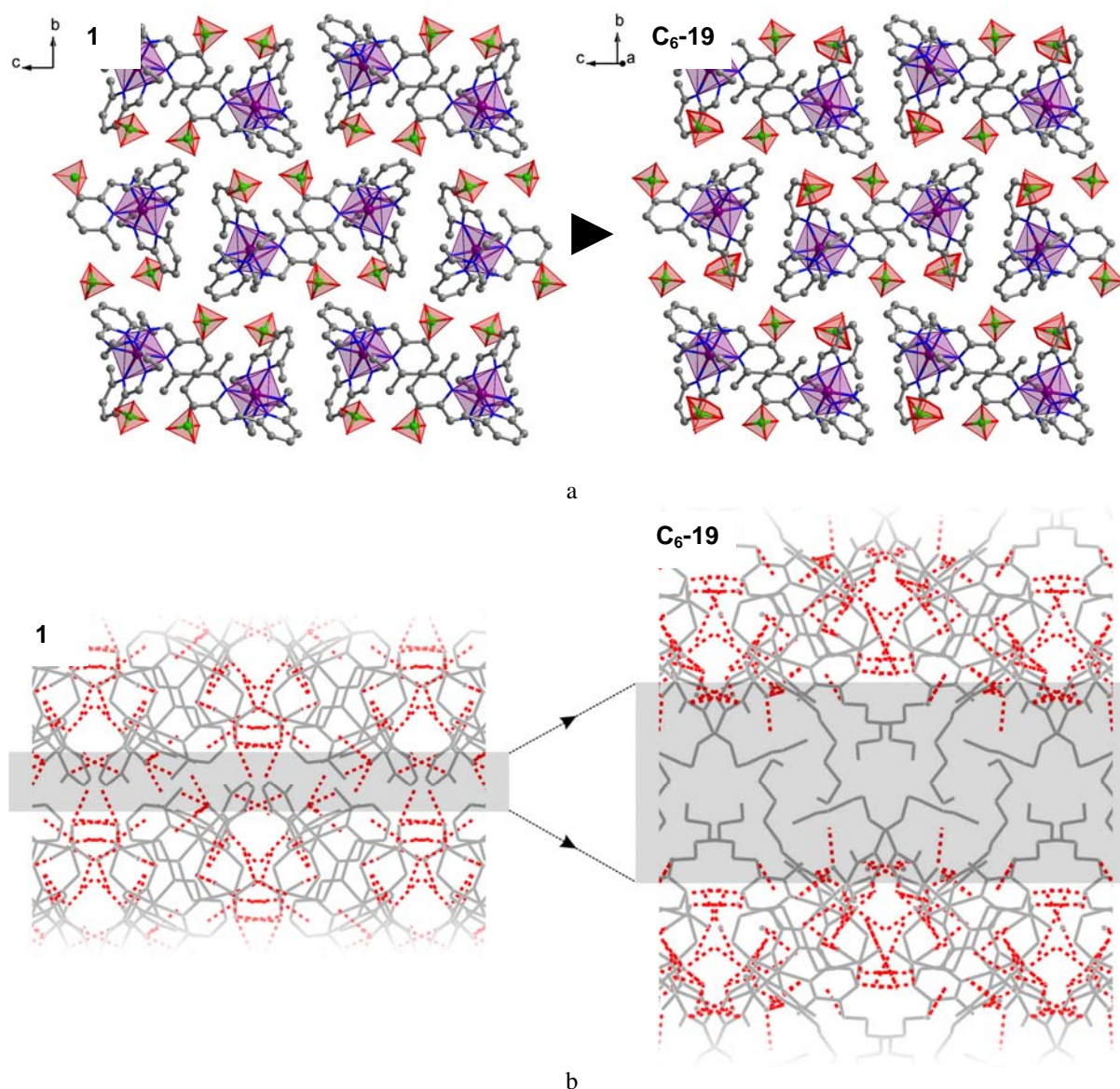
**Figure 71.** a) A comparison of ionic bilayers in **1** (low-spin, 80 K) (left) and in **$C_6$-19** (low-spin, 90 K; without alkoxy chains) (right); b) A comparison of hydrogen bonding networks (projection along the *c* axis) of the ionic bilayers formed by **1** (low-spin, 80K) (left) and **$C_6$-19** (low-spin, 90 K) (right). Red dashed lines denote weak hydrogen bonds CH···O. Shaded area shows inter-bilayer space in both projections.

The least squares fitting of the magnetic susceptibility curve of **$C_6$-19** by the equation derived from the regular solution model (Equation 13, Chapter 1.3.5) [113] leads to

$\Delta H = 8.1$ kJ mol$^{-1}$, $\Delta S = 56$ J K$^{-1}$ mol$^{-1}$, which are comparable to the parameters of the parent system **1** (Chapter 2.2.4). At the same time, the parameter of the cooperativeness $\Gamma$ is equal to 0.9 kJ mol$^{-1}$ which is about three times less than that of **1**. According to the classification given by comparison with $2RT_{1/2}$, the spin-transition can be considered as being almost non-cooperative [3, 113]. The absence of the inter-bilayer interaction in the alkylalted system is assumed to be responsible for the decrease of the cooperativity in **C$_6$-19**. However, an additional factor could be also the disordered perchlorate anion, which modifies somewhat the character of the intermolecular contacts (see Figure 71b).

As is seen from the IR data, the packing of alkyl chains in the two higher members of the perchlorate family is not similar to the **C$_6$-19** homologue nevertheless the arrangement of ionic bilayers seems to be preserved. This is evident from the similar magnetic behavior of all **C$_n$-19** compounds ($n = 6, 12, 18$). For example, the $T_{1/2}$ parameter for three compounds is *ca*. 140 K whereas the $\Delta T_{80}$ value is *ca*. 40 K. This may confirm the same character of intermolecular contacts regardless of the length of alkyl substituents and the state of their disorder. The same conclusion can be made from the XRD analysis of the interlayer distances *d vs n*, which gives very similar $d^{bl}$ values as determined directly form the high-spin crystal structure of **C$_6$-19**. The incompleteness of the transition in **C$_{12}$-19** and **C$_{18}$-19** homologues at low temperature is caused by structural strains of the pristine samples, which were used for the magnetic experiment. The residual high-spin fraction in **C$_{18}$-19** was reduced upon annealing (Figure 66c).

If the shift of $T_{1/2}$ of **C$_6$-19** in comparison with the non-alkylated compound **1** can be explained by the decrease of the ligand field strength due to chemical substitution, the shift of $T_{1/2}$ in **C$_{12}$-19** and **C$_{18}$-19** in comparison with **C$_6$-19** may be caused by the ordering of *trans* alkyl chains in the paraffinic sublattice. In fact, compounds **C$_n$-19** were obtained at ambient temperature in the high-spin form and they adopt packing of molecular substituents favoring bulkier high-spin polar head-groups. This could play a role in the shift of spin-transition to lower temperature since the fixed distances between packed alkyl chains to some extent may prevent contraction of the cavity within the trifurcated ligand with an encapsulated iron(II) ion. The effect is rather weak causing the shift to lower temperature by only about 15 K.

The fact of pronounced incompleteness of spin-transition in the rest of the complexes can find an explanation in poorly arranged ionic layers of the compounds with a substantial number of packing defects, which in an indirect way was confirmed by the relatively large width $\Gamma_{1/2}$ of the Mössbauer doublets and by the XRD data.

The temperature of the phase transition solid → liquid crystal is precisely known from the DSC data for all compounds except $C_{18}$-20 and $C_{20}$-21. Nevertheless, from the XRD measurements it is known that in these two samples the transition temperature is lower than 410 K and presumably does not strongly deviate from the temperature found for other compounds with the same length of alkyl chains. In any case, the phase transition is too far up in temperature (~ 320–390 K) to have a direct influence on the spin-transition taking place in the low temperature region ($T_{1/2}$ = 100–150 K). As it was found from the magnetic data, the character of the spin-transition is affected only by the first melting accompanied by the annealing of structure strains or loss of the crystal water. The susceptibility of the samples after the first heating up to 400 K can be decreased or increased depending on the compound, but the magnitude of this change is rather small. The liquid crystalline compounds with spin-crossover properties described by Hayami *et al.* in [232] show similar behavior. Some of those exhibit a decrease or an increase of the susceptibility on first heating due to solid → liquid crystal transition which was attributed to the reorganization of the pristine materials.

To conclude, the compounds $C_n$-19–$C_n$-23 are multifunctional materials which combine spin-crossover and liquid crystalline properties. The spin-transition and the phase transition occurring in these materials take place in very different temperature regions. Therefore, any interplay between the two physical phenomena, spin-transition and change of aggregate state of matter (solid → liquid crystal), cannot be anticipated.

### 2.6.10  Summary

1. Chemical modification of the parent system **1** provided the liquid crystalline systems which show spin-transition at $T_{1/2}$ = 100–150 K;

2. The crystal structure of the alkylated spin-crossover compound $C_6$-19 was determined in the low-spin and the high-spin states. Overlapping of the low-spin and high-spin structures shows substantial divergence of both originating from the increase of the distances Fe–N due to spin-transition;

3. As evidenced by the structural analysis, in $C_6$-19 on spin-crossover the hydrogen bond network within the ionic bilayers is significantly modified with decrease of the number of the intermolecular contacts, while the inter-bilayer contacts are completely removed due to the alkyl substituents. In the alkylated $C_n$-19 the decrease of the cooperativity in comparison with parent **1** was attributed to a decrease of intermolecular contacts CH⋯O;

4. The higher homologues **C$_{12}$-19** and **C$_{18}$-19** preserved spin-crossover behavior, but with a slight decrease of $T_{1/2}$ which was attributed to the influence of alkyl chain packing. At 4 K irradiation of **C$_n$-19** ($n$ = 6, 12, 18) with green laser resulted in excitation of the system into the metastable high-spin state (LIESST effect);

5. Change of the perchlorate anion by another anion caused incomplete gradual spin-transition;

6. Upon heating the higher homologues can form smectic (S$_X$) mesophase. The phase transition of the pristine samples was reflected in the magnetic curve and modified the low temperature behavior of the compounds making it more gradual.

## 2.7 Characterization and physical properties of compounds $C_{18}$-24 and $C_{18}$-25

### 2.7.1 Introductory remarks

This chapter is devoted to the description of the derivatives of the parent systems **3** and **5**, compounds **$C_{18}$-24** and **$C_{18}$-25**, respectively, formed by the ligands 1,3,5-*cis,cis*-tris[1-aza-2-((5-octadecyloxy)(2-pyridyl))vinyl]cyclohexane [*tach*($C_{18}$-*py*)$_3$] and 2,2,2-tris(2-aza-3-((5-octadecyloxy)(2-pyridyl))prop-2-enyl)ethane [*tame*($C_{18}$-*py*)$_3$], respectively, with the counterion 4-(octadecyloxy)benzenesulfonate ($C_{18}TOS^-$). The codes and composition of compounds under study are shown in Table 23.

**Table 23.** Schematic molecular structures and the composition of compounds $C_{18}$-24 and $C_{18}$-25.
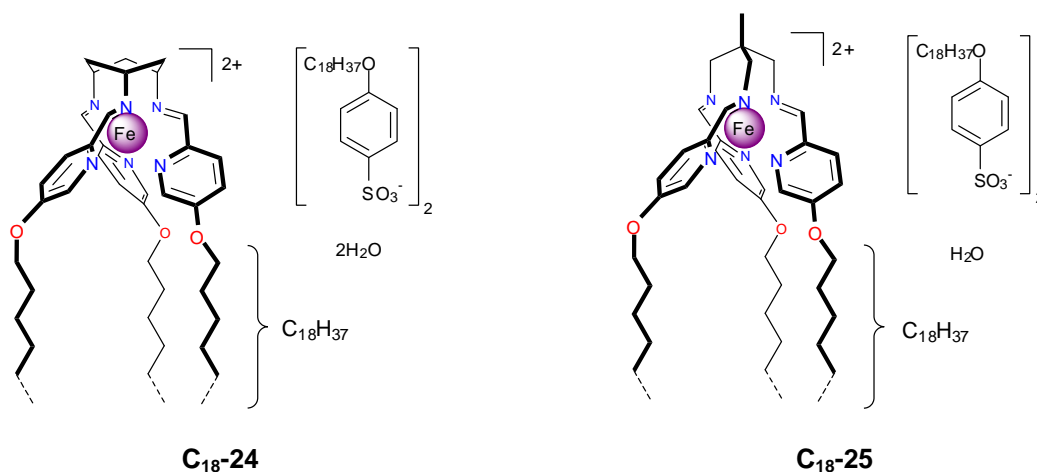


| Compound | Anion $A^-$ | s |
|----------|-------------|---|
| $C_{18}$-24 | $C_{18}TOS^-$ | 2 |
| $C_{18}$-25 | $C_{18}TOS^-$ | 1 |

### 2.7.2 Mass spectroscopic, TGA and IR data

Mass spectroscopic characterization of the complexes was performed by the field desorption method (FD MS). For both complexes the most intensive peaks correspond to the molecular cation without and with anion (Table 24). TGA measurements determined the water content in the pristine compounds (Table 24).

The analysis of the IR spectra included the regions with characteristic bands for N=C group, alkyl chains and anions.

**Table 24.** MS, TGA and IR data for the compounds $C_{18}$-24 and $C_{18}$-25.

| Compound | MS [$e/z$] | TGA, w/w [ %] $(T)^a$ | IR [cm$^{-1}$]$^b$ | | | | | |
|---|---|---|---|---|---|---|---|---|
| | | | $v$(O–H) | $v_s$(CH$_2$), $v_{as}$(CH$_2$) | $v$(C=N) | $\delta$(CH$_2$) | $\rho$(CH$_2$) | $v$(Anion) |
| $C_{18}$-24 | 1683 [M+C$_{18}$TOS]$^+$ 628 [M]$^{++}$ | 1.6 (327 K) | 3440br | 2917, 2850 | 1599 | 1467 | 721 | 1123, 1031 |
| $C_{18}$-25 | 1671 [M+C$_{18}$TOS]$^+$ 623 [M]$^{++}$ | 1.0 (328 K) | 3440br | 2917, 2850 | 1598 | 1469 | 721 | 1125, 1031 |

$^a$ Value is given at the point where the plateau is reached. $T$ is the temperature at which the dehydration process is centered; $^b$ $v$, stretching; $\delta$, bending; $\rho$, rocking; as, asymmetric, s, symmetric.

***N=C group.*** The vibrational spectra of the compounds $C_{18}$-24 and $C_{18}$-25 in the region of 1600 cm$^{-1}$ provide confirmation of the low-spin spin state of the coordinated iron(II) ion.

***Alkyl chains.*** In the IR spectra, the symmetric and asymmetric stretching modes $v_s$(CH$_2$) and $v_{as}$(CH$_2$), the scissoring band $\delta$(CH$_2$), the wagging progression and the rocking mode $\rho$(CH$_2$) range from 2600–3000 cm$^{-1}$ and 700–1600 cm$^{-1}$. The analyses of the IR data in these regions did not differ from the previous two families of compounds that led to the conclusion about the hexagonal ordering of *trans* configured alkyl chains.

***Anions.*** For the complexes with the multiatomic anion $C_{18}$TOS$^-$ the strong absorption bands of the SO$_3$-group confirmed the composition of the compounds.

Values of the discussed absorption bands are presented in Table 24.

### 2.7.3 UV/VIS spectroscopy

The spectral features of the iron(II) compounds $C_{18}$-24 and $C_{18}$-25 are very similar to each other, and clearly indicate the presence of the octahedral low-spin iron(II) chromophores (Figure 72). The UV/VIS spectra in dichloromethane exhibit a strong broad peak with a shoulder centered at 550 nm, assigned to the Laporte allowed $^1A_{1g} \rightarrow$ $^1$MLCT (metal-to-ligand charge-transfer) band. Two very intense peaks are observed at 296 and 269 nm ascribed to $\pi \rightarrow \pi^*$ transitions of the ligands. According to the literature data [272, 273], the parity forbidden $^1A_{1g} \rightarrow$ $^1T_{1g}$ and $^1A_{1g} \rightarrow$ $^1T_{2g}$ transitions associated to the low-spin Fe$^{II}$N$_6$ chromophore would be expected at *ca.* 380 and 550 nm, respectively, with molar extinction coefficients much weaker than that of the MLCT [72].
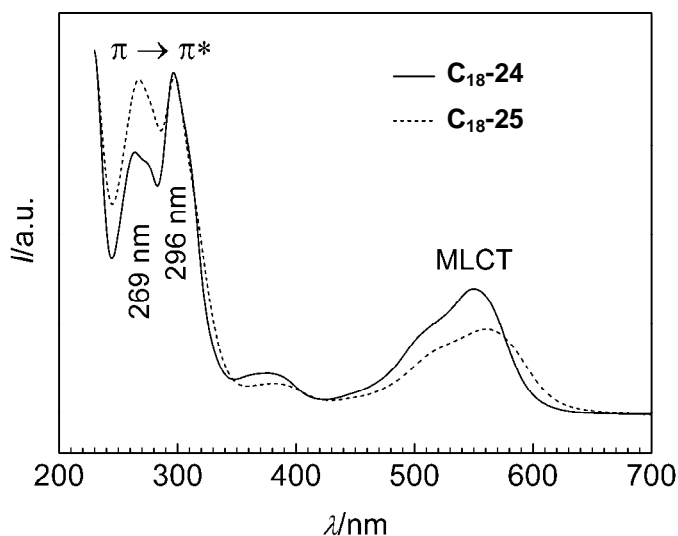
**Figure 72.** Normalized UV/VIS spectra of $C_{18}$-24 and $C_{18}$-25 in dichloromethane at room temperature.

### 2.7.4  Magnetic properties and Mössbauer spectroscopy
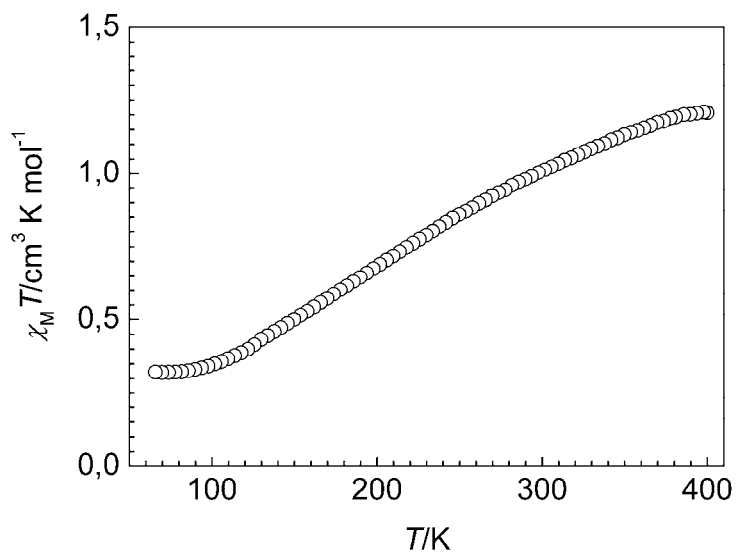


**Figure 73.** Magnetic susceptibility plot of $C_{18}$-24 in coordinates $\chi_M T$ *vs* T.

The measurements of the temperature dependence of the magnetic susceptibility on the samples $C_{18}$-24 and $C_{18}$-25 were performed over the 60–400 K temperature range. Compound $C_{18}$-25 is low-spin up to 400 K whereas $C_{18}$-24 shows a very gradual incomplete thermally driven spin-transition (Figure 73). At 400 K the susceptibility value is

1.20 cm$^3$ K mol$^{-1}$. The magnetic curve does not show anomalies at temperatures of the phase transition or loss of the crystal water determined by DSC and TGA measurements.

The Mössbauer spectrum of **C₁₈-24** measured at 80 K was fitted with the low-spin and high-spin doublets (Figure 74a, Table 25). The population found for the high-spin fraction is in good agreement with the magnetic data at 80 K (Figure 73). The better fit for the low-spin compound **C₁₈-25** was obtained with two almost equally populated low-spin doublets (Figure 74b, Table 25). This points at the likely presence of the two inequivalent positions in the crystal lattice similarly to that found in compound **C₁₂-8** (Figure 50a).



a                                                                 b
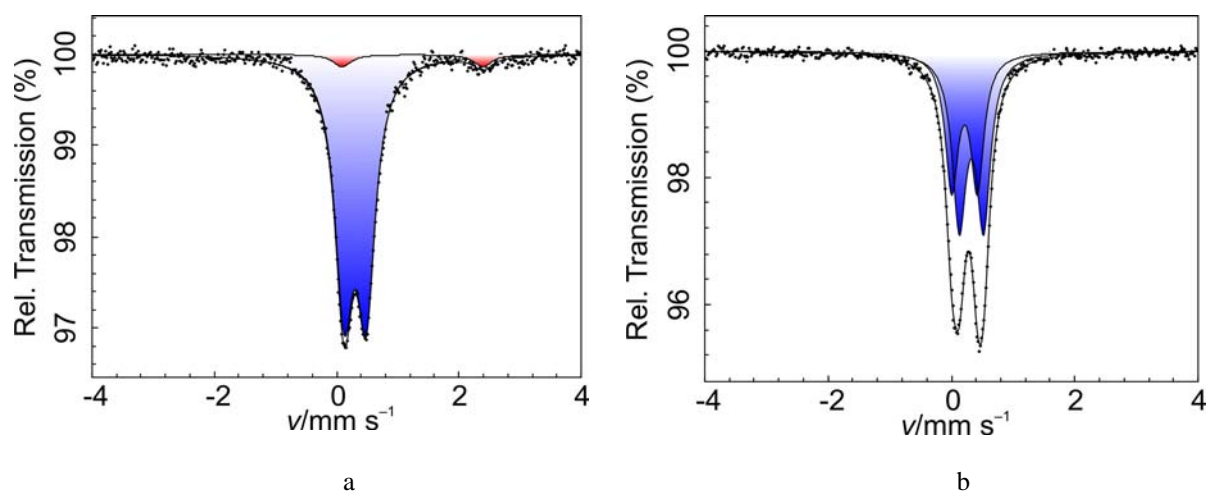
**Figure 74.** Mössbauer spectra of the compounds **C₁₈-24** (a) and **C₁₈-25** (b) at 80 K.

**Table 25.** Mössbauer parameters, isomer shift ($\delta$, relative to α-iron), quadrupole splitting ($\Delta E_Q$), half-width of the lines ($\Gamma_{1/2}$) and percentage of the multiplet populations in the high-spin (HS) and low-spin (LS) states (*A*) for **C₁₈-24** and **C₁₈-25** at 80 K.

| Compound | Spin state | $\delta$ [mm s$^{-1}$] | $\Delta E_Q$ [mm s$^{-1}$] | $\Gamma_{1/2}$ [mm s$^{-1}$] | *A* [ %] |
|---|---|---|---|---|---|
| **C₁₈-24** | LS | 0.30(0) | 0.36(1) | 0.18(0) | 95.0(14) |
| | HS | 1.24(14) | 2.31(28) | 0.18(8) | 5.0(19) |
| **C₁₈-25** | LS1 | 0.21(1) | 0.42(1) | 0.13(1) | 57(12) |
| | LS2 | 0.32(1) | 0.39(0) | 0.14(1) | 43(12) |

### 2.7.5   XRD, DSC and POM data

The X-ray diffraction experiments were performed in the range of $2\theta = 2$–30°. In each case, the XRD experiment was done on the pristine sample at 300 K, then in the liquid crystalline state at 410 K, and then again at 300 K. The obtained XRD pattern of **C₁₈-24** and **C₁₈-25** are typical for layered structures whose reflections are indexed as (10) and (20) [and

(30)] in the patterns of both compounds (Figure 75a, b). A broad alkyl halo in the solid state located at $2\theta \sim 22°$ on melting becomes even broader and shifts to $\sim 19°$ due to the transition of the alkyl chains into quasi-liquid state. The values of the interlayer distances $d$ derived from the XRD data of $C_{18}$-24 and $C_{18}$-25 are collected in Table 26.
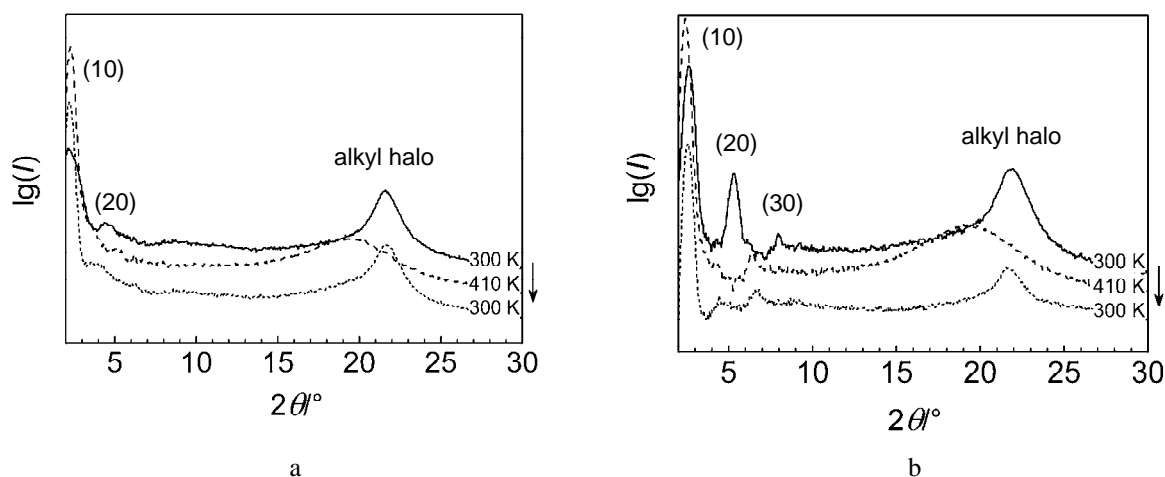


**Figure 75.** XRD patterns of $C_{18}$-24 (a) and $C_{18}$-25 (b) at different temperatures.

Figure 76 shows the DSC thermograms for both compounds. The first heating run was accompanied by the dehydration, therefore the first trace does not coincide neither by the form nor by the temperature of the transition with the second one measured on the dehydrated compounds. The surface under the peak in the second measurement run is a measure for the transition enthalpy $\Delta H^{Cr \rightarrow S_x}$ (Table 26).
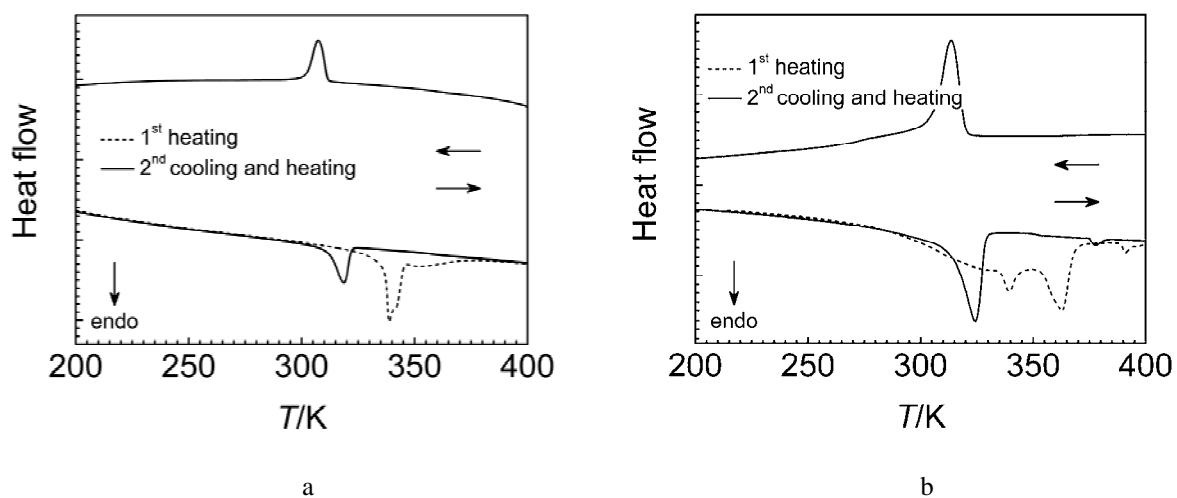


**Figure 76.** DSC profiles in heating and cooling modes of $C_{18}$-24 (a) and $C_{18}$-25 (b). Arrows show the direction of scanning runs.

The clearing point for compound **C$_{18}$-25** was determined by polarizing optical microscopy (POM) in the heating and cooling runs. The anisotropic texture observed with crossed polarizers is typical for the smectic mesophase. The same is valid also for compound **C$_{18}$-24**. The compounds have a large thermal range of the mesophase, approaching 200 K. This high stability can be attributed to the strong van der Waals interactions between the alkyl chain and to the ionic interactions between the charged head-groups and sulfoxo-groups of the anions.

The derived thermodynamic parameters are collected in Table 26.

**Table 26.** Interlayer distances *d* at different temperatures, thermal transitions and mesomorphism, enthalpy $\Delta H^{\mathrm{Cr}\rightarrow \mathrm{S}_X}$ and entropy $\Delta S^{\mathrm{Cr}\rightarrow \mathrm{S}_X}$ of phase transition solid $\rightarrow$ liquid crystal and thermal stability determined by XRD, DSC, TGA and POM for **C$_{18}$-24** and **C$_{18}$-25**.

| Compound | *d* [Å] 300 K (pristine) | 410 K | 300 K | Thermal transitions [K] [a] | $\Delta H^{\mathrm{Cr}\rightarrow \mathrm{S}_x}$ [kJ mol$^{-1}$] [a] | $\Delta S^{\mathrm{Cr}\rightarrow \mathrm{S}_x}$ [J mol$^{-1}$ K$^{-1}$] |
|---|---|---|---|---|---|---|
| **C$_{18}$-24** | 39.4 | 39.5 | 39.4 | Cr $\underset{314}{\overset{325}{\rightleftharpoons}}$ S$_X$ 523 d | 116.1 | 357.2 |
| **C$_{18}$-25** | 36.8 | 33.6 | 34.3 | Cr $\underset{307}{\overset{325}{\rightleftharpoons}}$ S$_X$ $\underset{487}{\overset{516}{\rightleftharpoons}}$ i [b] 526 d | 75.7 | 237.3 |

[a] Measured by DSC in the second heating/cooling cycle. The values correspond to the maxima of the enthalpy peaks. The identification of the mesophase was done on the basis of the POM and XRD data; [b] From the POM data.

### 2.7.6 Discussion

The ligand field strength in compound **C$_{18}$-25** is too strong to allow spin-transition below 400 K. The loss of the lattice solvent and melting of the alkyl chains also do not modify sufficiently the structure of the compound or the intermolecular contacts to provoke the appearance of the magnetic anomaly observed for the mononuclear compounds discussed above. In contrast, compound **C$_{18}$-24** contains a minor fraction of the high-spin iron(II) species already at low temperature which increases upon heating, but in a gradual and incomplete way. The magnetic moment of the compound at 400 K does not reach the saturation (expected value is near to 3.50 cm$^3$ K mol$^{-1}$ [41]). This compound is also insensitive to the dehydration or the melting into the mesophase which have no effect on the magnetic properties. Both compounds by virtue of the alkyl substituents exhibit on melting anisotropic textures observed by POM. The low and high temperature XRD experiments confirmed the formation of the mesophase with the lamellar organization similar to that found in the two previous series of compounds (Chapters 2.5.7, 2.6.6).

The reason for the failure in observing of a spin state change driven by the phase transition might be the insignificance of the structural reorganization inside of the ionic bilayers regardless of the fact that alkyl chains undergo transition into the liquid-like state. Thereby, compounds $C_{18}$-24 and $C_{18}$-25 are examples of the systems in which despite evident structural modifications the magnetic properties remain unaffected.

### 2.7.7 Summary
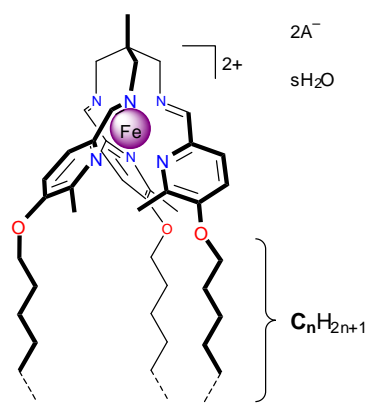
1.      The chemical modification of the parent systems **3** and **5** and change of the anion led to compounds $C_{18}$-24 and $C_{18}$-25, respectively;

2.      Compound $C_{18}$-24 on heating exhibits very gradual and incomplete spin-transition without saturation. The dehydration and melting of the compound do not modify magnetic properties;

3.      In contrast, compound $C_{18}$-25 is low-spin up to 400 K and is also insensitive to modification of the structure on melting or dehydration;

4.      The reason of the insensitivity of both compounds is seemingly the insignificance of the structural reorganization inside of the ionic bilayers during phase transition solid $\rightarrow$ liquid crystal.

## 2.8 Characterization and physical properties of compounds $C_n$-26–$C_n$-29

### 2.8.1 Introductory remarks

This chapter deals with the derivatives of the parent system **6** formed by the ligand 2,2,2-tris(2-aza-3-((5-akloxy)(6-methyl)(2-pyridyl))prop-2-enyl)ethane [*tame*($C_n$-6-*Mepy*)₃]. The codes and the composition of the compounds under discussion are shown in Table 27.

**Table 27.** Schematic molecular structure and composition of $C_n$-26–$C_n$-29.



| Anion A⁻ | s | Compound |
|---|---|---|
| $ClO_4^-$ | 0 | **C₆-26, C₁₈-26** |
| $BF_4^-$ | 0 | **C₁₀-27, C₁₂-27, C₁₄-27, C₁₆-27, C₁₇-27, C₁₈-27, C₂₀-27** |
| | 1 | **C₂₀-28** [a] |
| C₁₈TOS⁻ | 2 | **C₁₈-29** |

[a] Upon heating **C₂₀-28** looses water and transforms into **C₂₀-27**.

### 2.8.2 Crystal structure of C₆-26

Figure 77a displays the molecular structure of **C₆-26** at 100 K together with the atom numbering. The crystal structure possesses one independent complex cation along with two non-bonded perchlorate anions. The iron(II) ion is in a distorted octahedral environment formed by three imine and three pyridine nitrogen atoms. Average <Fe–N$^{im}$> bond distance is 1.918(2) Å and 2.084(2) Å for <Fe–N$^{py}$>, pointing out low-spin state of the iron(II) ion. The average distance between a methyl group and the adjacent nitrogen atom of the pyridine ring is 3.040(3) Å. The neighboring molecules are packed in head-to-head fashion forming microsegregated layered structure (Figure 77b). The ionic bilayers are built by the ionic head-groups and perchlorate anion, whereas alkyl tails are arranged into non-polar paraffinic layers. Within the ionic bilayers short CH···O(Cl) contacts are present [2.444(2)–2.711(2) Å] (Figure 77c). Each alkyl chain introduces single *gauche* kink next to the bridging oxygen atom, which allows tilt alignment, whereas remaining bonds are in *trans* configuration (Figure 77a). The

poorly aligned short alkyl chains of the adjacent layers interpenetrate (Figure 77b, c) defining a kind of paraffinic sublattice with distorted hexagonal ordering. The distance between neighboring layers is 18.087(7) Å.

Table 28 contains the parameters of the unit cell and refinement details, whereas Table 29 contains selected intramolecular parameters.



a
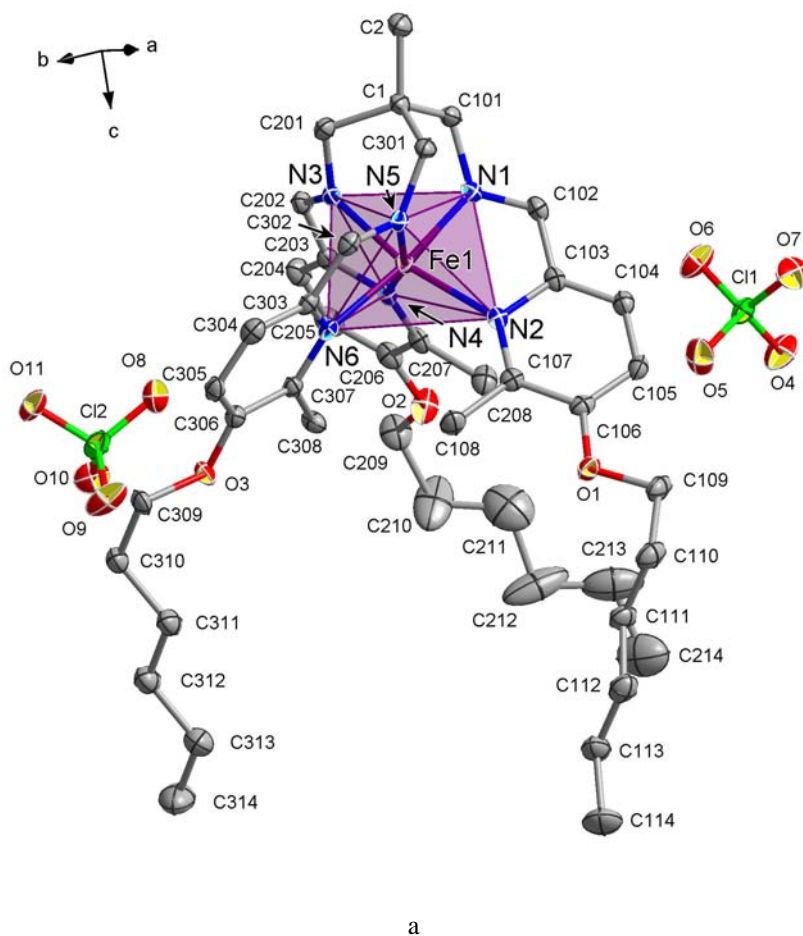
**Figure 77.** a) Projection of molecular structure of **C$_6$-26** with the numbering scheme; b) Projection of the molecular packing along the *a* axis. Hydrogen atoms are omitted for clarity. Displacement ellipsoids are shown at 50 % probability level; c) On the left projection of **C$_6$-26** and on the right projection of the crystal structure along the *b* direction both emphasizing intermolecular hydrogen bonds. In the projection of the crystal packing hydrogen atoms are omitted for clarity, complex molecules and anions are shaded grey whereas dashed red lines correspond to CH···O hydrogen bonds.

b



c
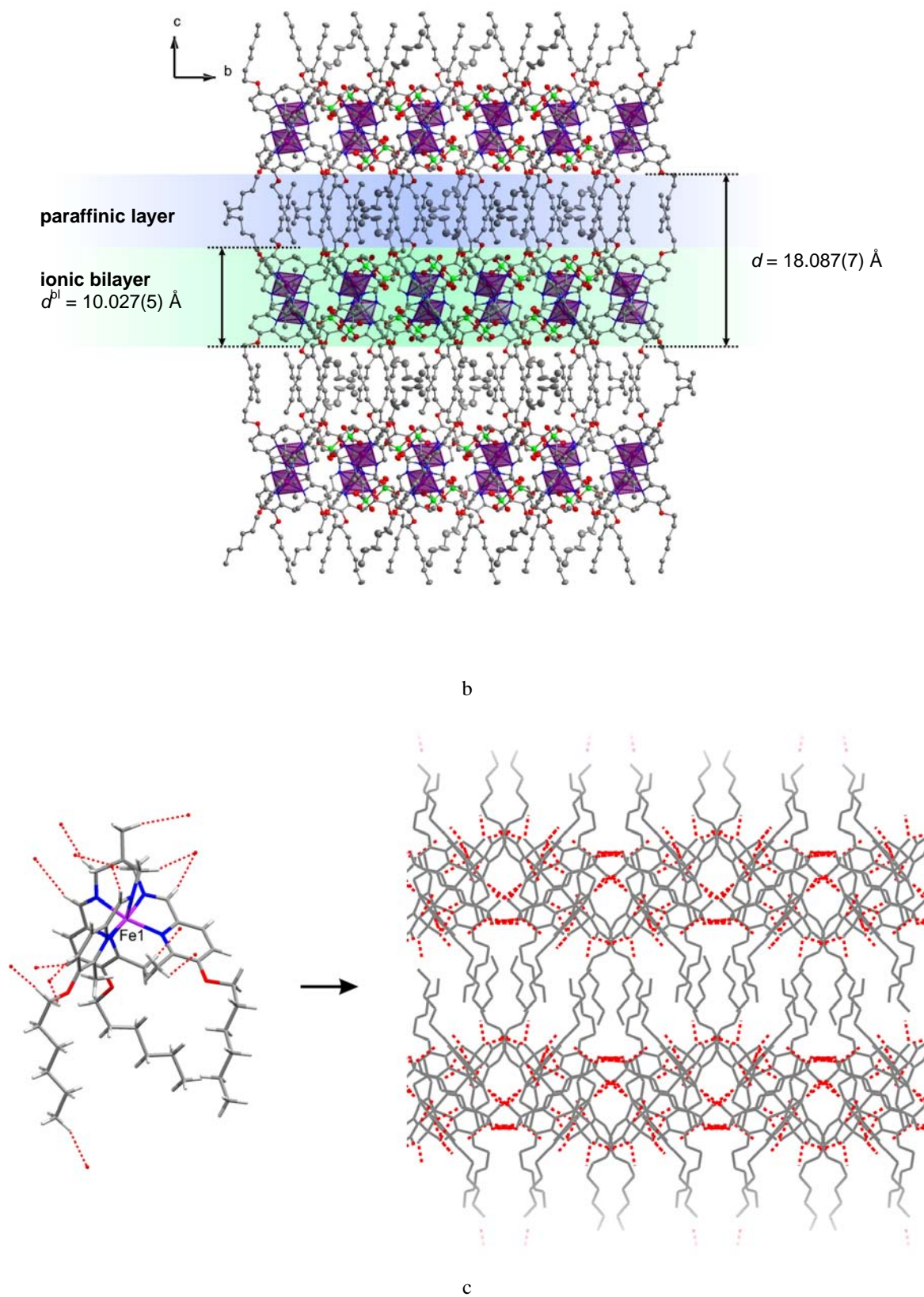
**Figure 77.** (*continued*)

**Table 28.** Crystallographic data and refinement details of $\mathbf{C_6\text{-26}}$.

| | |
|---|---|
| Empirical formula | $C_{44}H_{66}Cl_2FeN_6O_{11}$ |
| Formula weight | 956.48 |
| Temperature [K] | 100 |
| Wavelength [Å] | 0.71073 |
| Crystal system | orthorhombic |
| Space group | $Pbca$ |
| a [Å] | 18.746(4) |
| b [Å] | 14.398(3) |
| c [Å] | 36.174(7) |
| Volume [Å$^3$] | 9763.54(347) |
| Z | 8 |
| $\rho$ [g cm$^{-3}$] | 1.335 |
| Absorption coefficient [mm$^{-1}$] | 0.481 |
| $F(000)$ | 4159 |
| $\theta$ range for data collection [°] | 2.88 to 32.88 |
| Index ranges | $-27 \le h \le 28$ |
| | $-9 \le k \le 21$ |
| | $-53 \le l \le 53$ |
| Reflections collected | 16690 |
| Independent reflections | 7834 |
| Data/restraints/parameters | 16690/0/584 |
| Goodness-of-fit, $F^2$ | 0.827 |
| Final $R$ indices [$I > 2\sigma(I)$] | $R1 = 0.0456$, |
| | $wR2 = 0.1050$ |
| $R$ indices (all data) | $R1 = 0.1173$, |
| | $wR2 = 0.1158$ |
| $\rho_{min}$, $\rho_{max}$ [e Å$^{-3}$] | 1.938, $-0.692$ |

**Table 29.** Selected intramolecular parameters of $\mathbf{C_6\text{-26}}$.

| | |
|---|---|
| $<\text{Fe–N}^{im}>$ [Å] | 1.918(2) |
| $<\text{Fe–N}^{py}>$ [Å] | 2.084(2) |
| $\theta$ [°] | 50.81(7) |
| $\Sigma$ [°] | 74.26(6) |

### 2.8.3 Mass spectroscopy, TGA and IR spectroscopy

Mass spectroscopic characterization of the complexes was performed by electrospray ionization MS (ESI). In all cases positive ions corresponding to desired species were observed as the base peaks along with the identifiable fragmentation. For all complexes the most intensive peaks correspond to the cation without anion or with the anion or its fragments (Table 30). The termogravimetry analysis (TGA) confirmed the anhydrous nature of all compounds except $\mathbf{C_{20}\text{-28}}$ and $\mathbf{C_{18}\text{-29}}$. The calculated number of water molecules per one complex molecule is about 1 and 2, respectively (Table 30).

The analysis of the IR spectra included the regions with characteristic bands for N=C group, alkyl chains and anions.

**Table 30.** MS, TGA and IR spectroscopic data for the compounds $C_n$-26–$C_n$-29.

| Compound | MS | TGA, w/w [ %] $(T)^c$ | IR [cm$^{-1}$]$^d$ | | | | | |
|---|---|---|---|---|---|---|---|---|
| | | | $v$(O–H) | $v_s$(CH$_2$), $v_{as}$(CH$_2$) | $v$(N=C) | $\delta$(CH$_2$) | $\rho$(CH$_2$) | $v$(Anion) |
| $C_6$-26 | 391 [M]$^{++\,b}$ 728 [M+H]$^+$ 881 [M+ClO$_4$]$^+$ | 0 | – | 2932, 2854 | 1626 | 1461 | – | 1084, 622 |
| $C_{18}$-26 | 1387 [M+ClO$_4$]$^+$ | 0 | – | 2920, 2851 | 1630 | 1463 | 721 | 1087, 622 |
| $C_{10}$-27 | 970 [(M+F]$^+$ | 0 | – | 2921, 2852 | 1647 | 1464 | 722 | 1069 |
| $C_{12}$-27 | 1054 [M+F]$^+$ | 0 | – | 2921, 2852 | 1648, 1698 | 1467 | 721 | 1066 |
| $C_{14}$-27 | 1206 [M+BF$_4$]$^+$ | 0 | – | 2919, 2851 | 1630, 1698 | 1466 | 721 | 1081 |
| $C_{16}$-27 | 1289 [M+BF$_4$]$^+$ | | – | 2918, 2850 | 1650 | 1468 | 721 | 1072 |
| $C_{16}$-27$^a$ | | 0 | – | 2919, 2851 | 1650 | 1468 | 721 | 1072 |
| $C_{17}$-27 | 1264 [M+F]$^+$ 1332 [M+BF$_4$]$^+$ | 0 | – | 2921, 2852 | 1648, 1699 | 1463 | 721 | 1081 |
| $C_{18}$-27 | 644 [M]$^{++}$ 1375 [M+BF$_4$]$^+$ | 0 | – | 2918, 2850 | 1654, 1698 | 1467 | 721 | 1071 |
| $C_{20}$-28 | 1458 [M+BF$_4$]$^+$ 686 [M]$^{++}$ | 1.3 (350 K) | 3410 br | 2919, 2851 | 1645, 1697 | 1464 | 721 | 1076 |
| $C_{20}$-29 | 2138 [M+C$_{18}$TOS]$^{+\,b}$ 1713 [M]$^+$ | 1.9 (334 K) | 3450 br | 2917, 2850 | 1650, 1697 | 1468 | 721 | 1252, 607 |

$^a$ After heating up to 400 K; $^b$ Trace; $^c$ Value is given at the point where the plateau is reached. $T$ is the temperature at which the dehydration process is centered; $^d$ $v$, stretching; $\delta$, bending; $\rho$, rocking; as, asymmetric, s, symmetric.

***N=C group.*** The vibrational spectra of compounds $C_n$-26–$C_n$-29 in the region of 1600–1700 cm$^{-1}$ provide confirmation of the spin state of the constituting iron(II) ion. In the two perchlorate complexes $C_6$-26 and $C_{18}$-26 the bands at about 1630 cm$^{-1}$ are observed in the region of $v$(N=C) vibrations, which were assigned to the low-spin state of the complex species. For the rest of the compounds a shift to higher wavenumbers and occurrence of an additional band at ~1698 cm$^{-1}$ is detected, which is associated with the coexistence of low-spin and high-spin species at room temperature.

***Alkyl chains.*** The packing of the chains in the paraffinic layers and their conformation are of interest. In the IR spectra, the relevant frequencies embrace regions of 2600–3000 cm$^{-1}$ and 700–1600 cm$^{-1}$ including symmetric and asymmetric stretching modes $v_s$(CH$_2$) and $v_{as}$(CH$_2$), the scissoring band $\delta$(CH$_2$), the wagging progression and the rocking mode $\rho$(CH$_2$). The treatment of the IR data in these regions did not differ from the three

previous families of compounds that led to the conclusion about the hexagonal ordering of (almost) *trans* configurated alkyl chains similarly to $C_{12}$-8 (Figure 50a, b, c).

Practically all bands of CH$_2$-vibrations in $C_6$-26 show values which differ from those of higher members of the family. This allowed us to conclude that the packing of alkyl chains found in the former compound is not retained in the homologues with longer alkyl chains.

***Anions.*** For the complexes with multiatomic anions (ClO$_4^-$, BF$_4^-$, C$_{18}$TOS$^-$) the corresponding absorption bands confirmed the composition of the compounds.

Values of the discussed absorption bands are presented in Table 30.

### 2.8.4 UV/VIS spectroscopy

Complexes $C_n$-26–$C_n$-29 are derivatives of the parent compound **6** which explains the similarities in the position of the absorption bands (Figure 78). For example, for $C_{10}$-27 an intensive and broad $^1A_{1g} \rightarrow {}^1$MLCT (537 nm) and several $\pi \rightarrow \pi^*$ ligand bands in the UV region are observed. Compound $C_{20}$-28 has a very similar spectrum. From these data the dominating low-spin state of the compounds in solution has been identified. The comparison of both spectra with the spectrum of the parent compound **6** shows a shift of the MLCT band which seems to be caused by the chemical substitution of the pyridine units, whereas the deceased intensity of it might be assigned to the onset of spin-crossover in solution. The band $^5T_{2g} \rightarrow {}^5E_g$ however, was not observed, presumably because of its forbidden nature and the comparatively weak intensity.
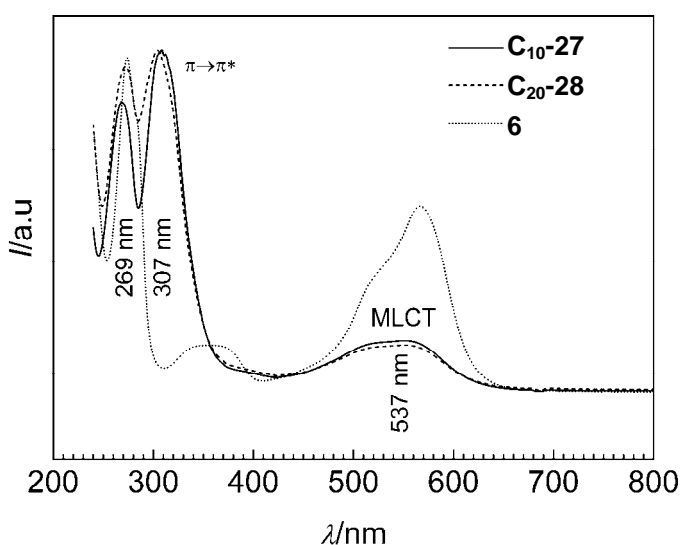


**Figure 78.** Normalized UV/VIS spectra of $C_{10}$-27 and $C_{20}$-28 in dichloromethane at room temperature. For comparison the spectrum of **6** in acetonitrile is shown.

### 2.8.5    Magnetic properties

The measurements of the temperature dependence of the magnetic susceptibility of $C_n$-26–$C_n$-29 were performed over the 10–400 K range. $\chi_M T$ *vs T* plots of the series are shown in Figure 79a–j. At 300 K, the $\chi_M T$ value of **C$_6$-26** (Figure 79a) is 0.05 cm$^3$ K mol$^{-1}$ which corresponds to the value characteristic for the low-spin iron(II) ions. Upon heating the susceptibility gradually increases reaching the value of 0.25 cm$^3$ K mol$^{-1}$ at 400 K. At low temperature the behavior of the substance is also low-spin as it is evidenced by Mössbauer spectroscopy (*vide infra*). For the higher homologue **C$_{18}$-26** the variation of the susceptibility is modulated by the mesomorphic properties of the compound (Figure 79b). At low temperature the compound shows low-spin behavior and upon heating exhibits thermally driven gradual spin-crossover. At 400 K about 25 % of iron(II) ions transform into high-spin state. In contrast to the short chain compound **C$_6$-26**, for the higher homologue the heating and cooling susceptibility curves diverge at 380 K showing occurrence of the magnetic hysteresis. This behavior is reminiscent of compounds $C_n$-14 (*n* = 16, 18, 20) which show similar properties (Chapter 2.5.6).

Detailed magnetic studies of compounds $C_n$-27 (*n* = 10, 12, 14, 16, 17, 18, 20) reveal the influence of the phase transition solid ↔ liquid crystal which takes place on heating and causes the anomaly of the magnetic susceptibility (Figure 79c–i). The first compound in the series, **C$_{10}$-27**, is low-spin up to 250 K where the susceptibility starts to increase until 400 K attaining the value of 2.30 cm$^3$ K mol$^{-1}$ (Figure 79c). This corresponds to about 70 % of high-spin and 30 % of low-spin iron(II) ions. The heating and cooling curves coincide revealing no anomalies in gradual increase or decrease of the susceptibility. The next three homologues $C_n$-27 with *n* = 12, 14, 16 show discontinuities in the heating and cooling curves with hysteresis centered at 356, 368 and 375 K, respectively (Figure 79d, e, f). The next even homologues with *n* = 18, 20 reveal a change of the type of hysteresis loop and abruptness of the anomaly (Figure 79h, i). The hysteresis of the **C$_{16}$-27** homologue is of 10 K width ($\Delta T_{hys}$) and is rate dependent (Figure 80a). Increasing the heating/cooling rate from 0.1 up to 10 K min$^{-1}$ almost doubles the width of the loop (Figure 80b). Successive thermal cycles did not modify the shape of it. It was also checked that the loop does not depend on the magnitude of the field up to 7 T (Figure 80c). The decrease of magnetic susceptibility upon heating is in contrast to the normally observed behavior of spin-crossover compounds suggesting to be a structural reorganization of the compounds through the phase transition [59]. In fact, *d vs T*

plots demonstrate that the discontinuity in $d$ takes place in the same temperature interval where the magnetic change occurs (Figure 79f, right scale).

The magnetic curves of the annealed sample $C_{12}$-27 before and after melting was simulated using the equation derived from regular solution model by Slichter and Drickamer (Equation 13, Chapter 1.3.5) (Figure 81) [113] (this compound was selected because it provides the largest high temperature range available for the fitting procedure and the smallest anomalous decrease of the susceptibility in the premelting region, before phase transition). The least squares fitting leads to similar thermodynamical parameters $\Delta H$ = 22.3 kJ mol$^{-1}$, 21.9 kJ mol$^{-1}$, and $\Delta S$ = 63.5 J K$^{-1}$ mol$^{-1}$ and 59.3 J K$^{-1}$ mol$^{-1}$ before and after melting, respectively. This corresponds to $T_{1/2}{}^{\text{solid}}$ = 351 K and $T_{1/2}{}^{\text{mesophase}}$ = 369 K. The interaction parameters $\Gamma$ is 2.2 kJ mol$^{-1}$ in solid state and 1.9 kJ mol$^{-1}$ in the mesophase. As is seen, in the solid state interactions between molecules are more cooperative and become less cooperative after melting of the alkyl chains. However, the transition is still rather cooperative that means preserving in part the crystal ordering within the ionic bilayers. According to the classification given by comparison with $2RT_{1/2}$, the spin-transition in both phases can be considered as being moderately cooperative [3, 113].

Compounds $C_n$-27 with $n$ = 18, 20 show rather high residual high-spin fractions at low temperatures with gradual increase of the susceptibility on heating from 225 K (Figure 79h, i). Anomalies in the magnetic curves are also observed, but the shape of the hysteresis loops is not similar to that of the lower homologues. The spin-transition in $C_{20}$-27 is more gradual without any discontinuities in the region of the phase transition (Figure 79i). The center of the loop in $C_{18}$-27 is lower than in $C_{20}$-27, being 353 and 367 K, respectively. The compound $C_{17}$-27 with odd-numbered carbon chains behaves similarly to the higher homologues and shows the largest magnetic hysteresis loop with $\Delta T_{\text{hys}}$ = 30 K, but with rather gradual character of the transitions (Figure 79g).

Compound $C_{18}$-29 is partially high-spin in the pristine state, but on heating shows two step spin-change (Figure 79j). Both steps are irreversible.

a

b

c

d
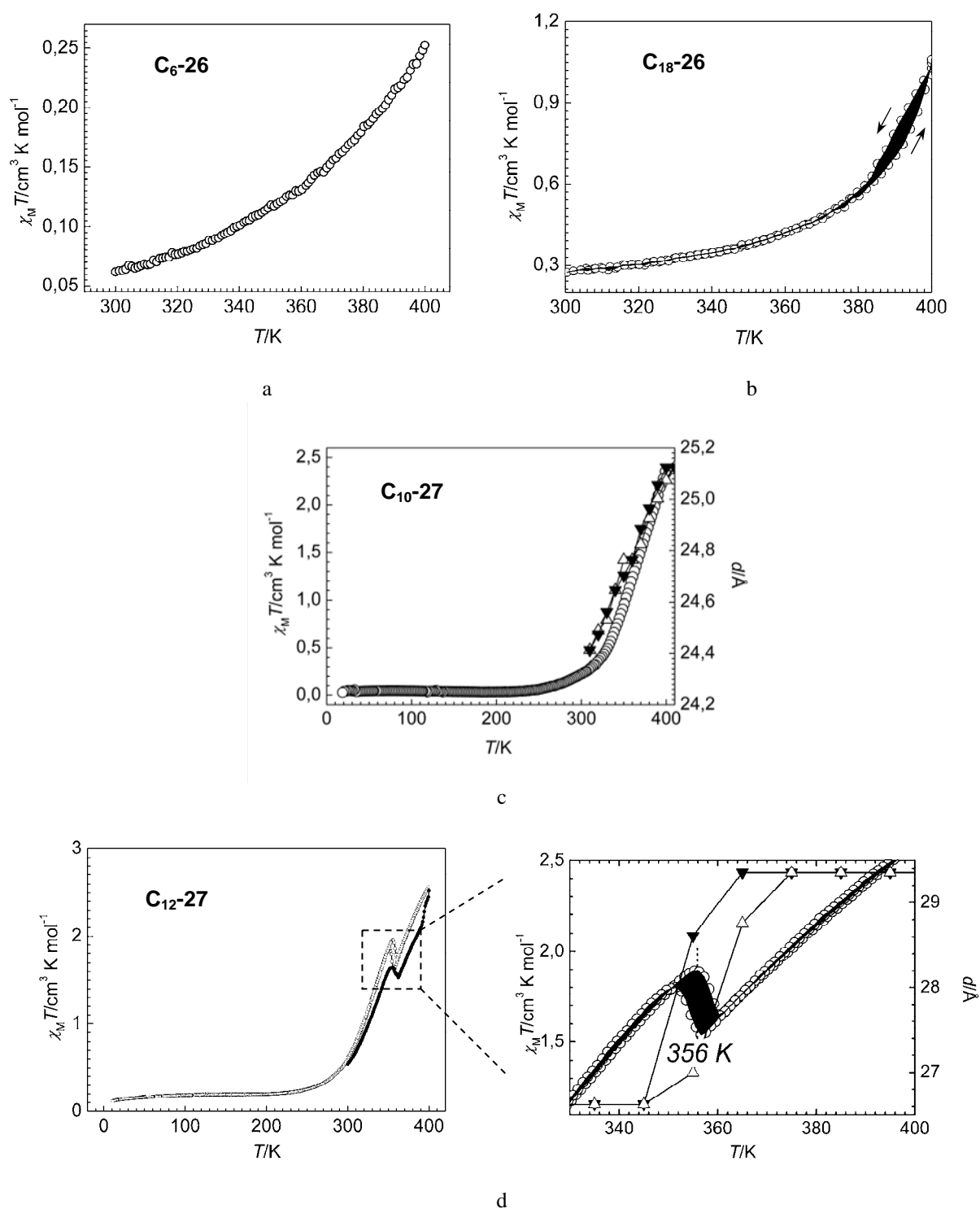
**Figure 79.** Magnetic susceptibility plots $\chi_M T$ *vs* $T$ of compound a) $C_6$-26, b) $C_{18}$-26, c) $C_{10}$-27, d) $C_{12}$-27, e) $C_{14}$-27, f) $C_{16}$-27, g) $C_{17}$-27, h) $C_{18}$-27, i) $C_{20}$-27 and $C_{20}$-28, j) $C_{18}$-29. The symbol ● corresponds to the first heating run, the symbol ○ to the second heating-cooling cycle, the symbol ▼ corresponds to the interlayer distance $d$ measured during the first cooling, symbol △ – during the second heating.

e



f



g

**Figure 79.** (*continued*)

h



i



j

**Figure 79.** (*continued*)

a

b



c
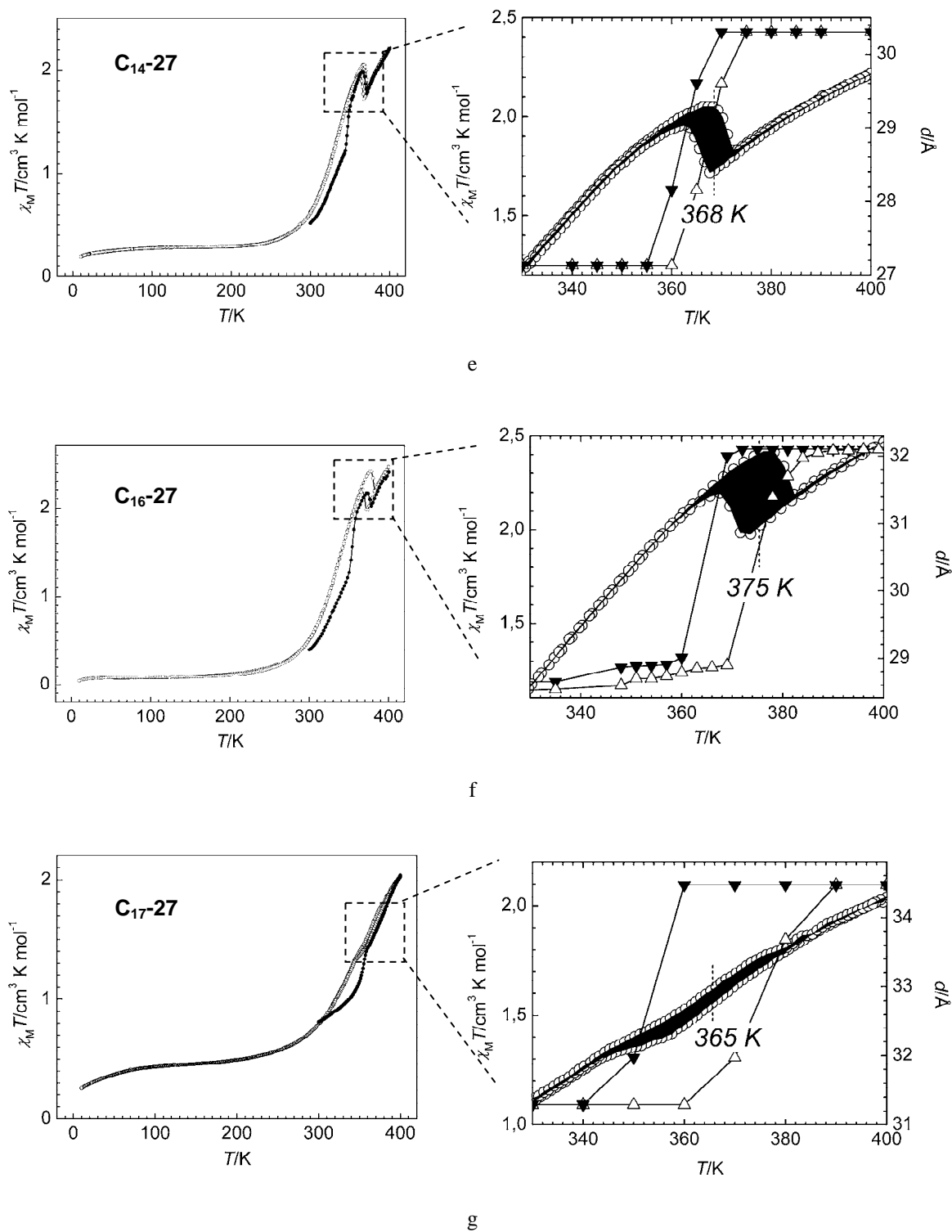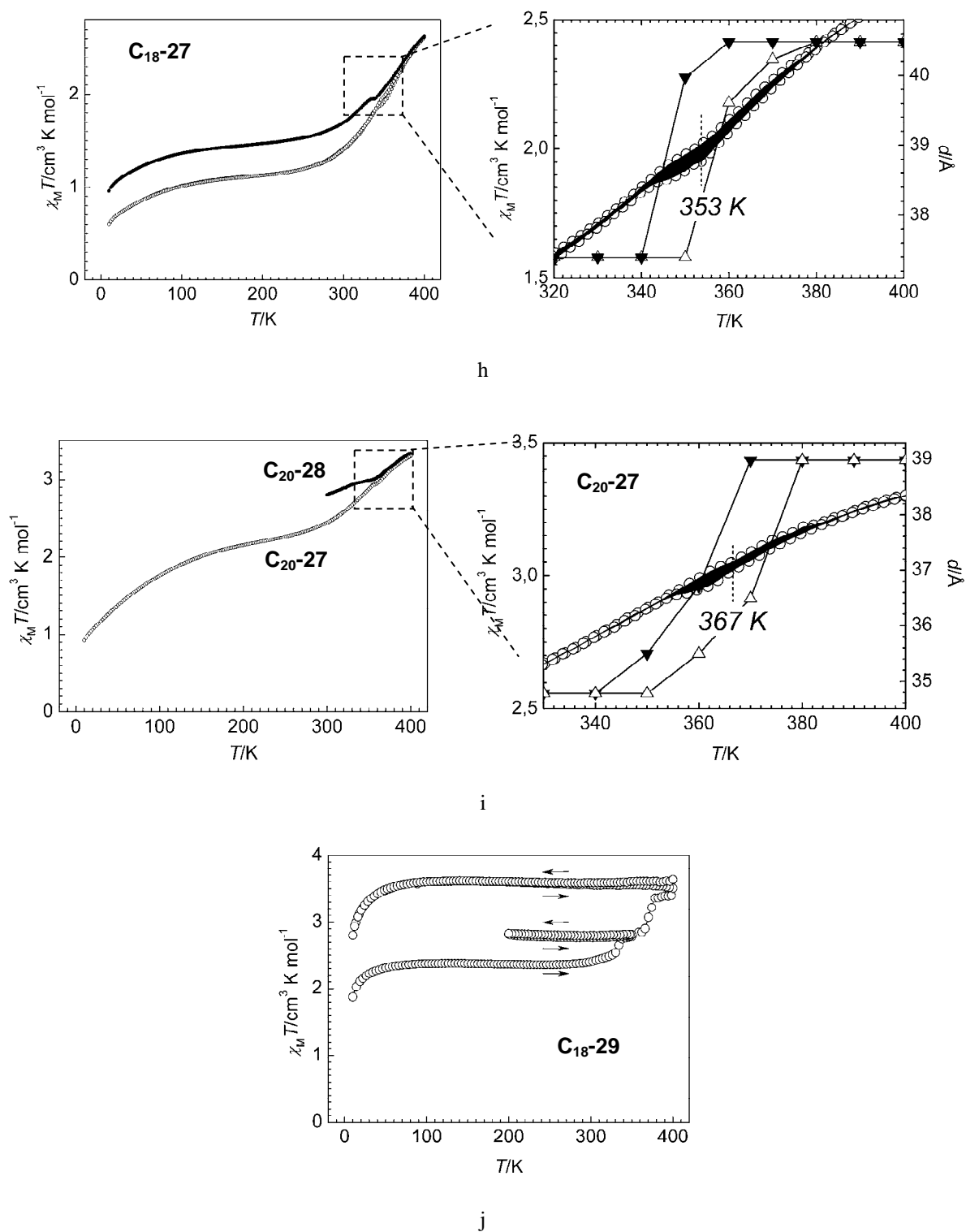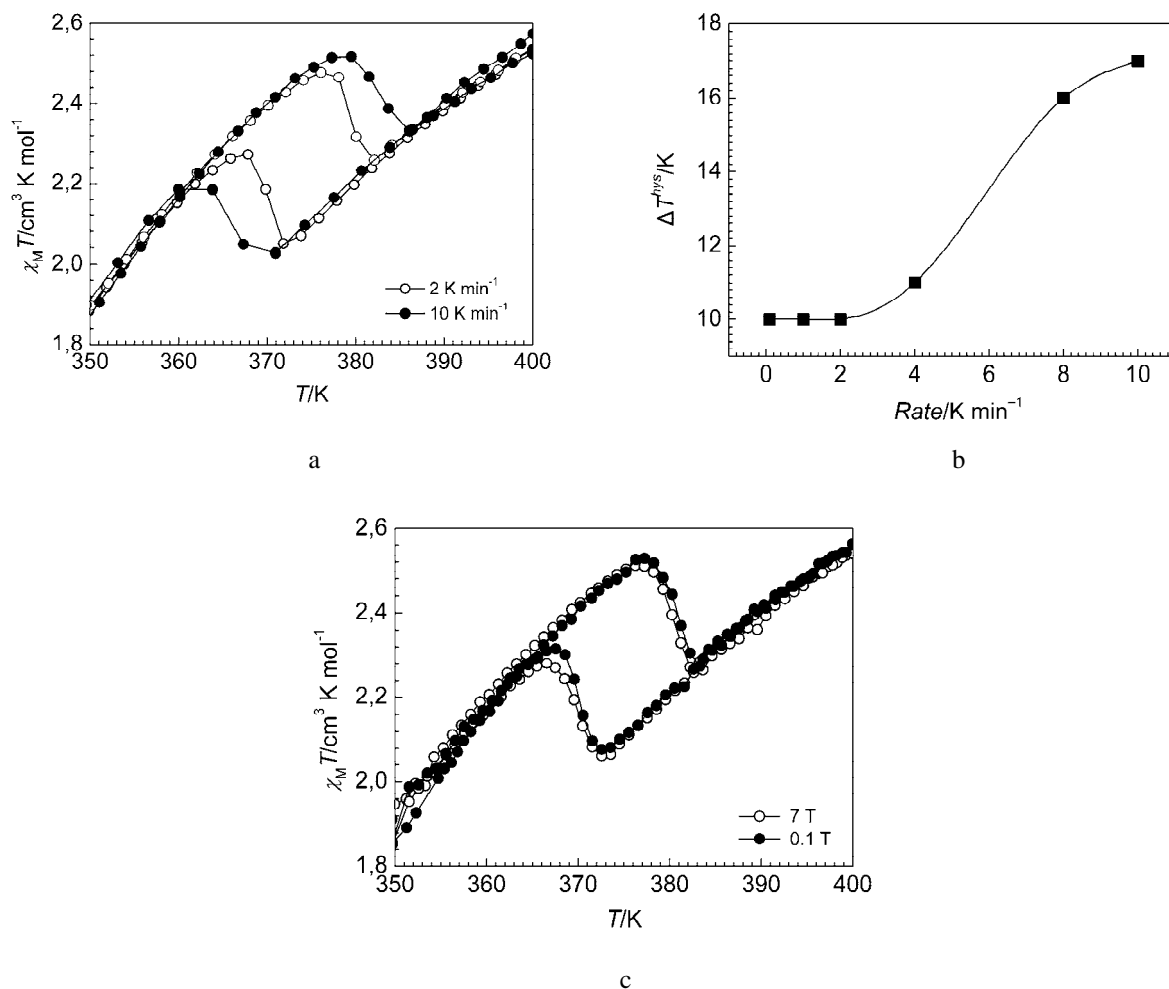
**Figure 80.** a) Hysteresis loop of the magnetic susceptibility for $C_{16}$-27 in the form $\chi_M T$ *vs* $T$ at rates of 2 K min$^{-1}$ and 10 K min$^{-1}$ under magnetic field of 1 T; b) Dependence of the width of the hysteresis loop $\Delta T_{hys}$ on the heating-cooling rate; c) Hysteresis loop measured under magnetic filed of 0.1 T and 7 T at 2 K min$^{-1}$.
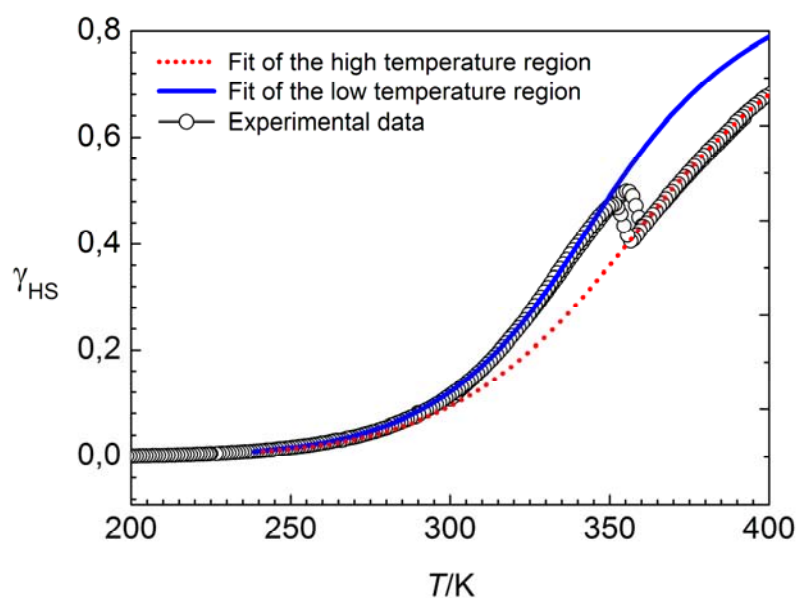


**Figure 81.** The solid and dashed lines represent the simulation of the transition curve of $C_{12}$-27 using Slichter-Drickamer model in the regions before and after melting.

### 2.8.6   XRD measurements

The XRD patterns of the pristine compounds $C_n$-27 at ambient temperature are shown in Figure 82a, whereas the variable temperature patterns of $C_n$-26, $C_n$-27 and $C_{18}$-29 are shown in Figure 83a–i.



a                                          b
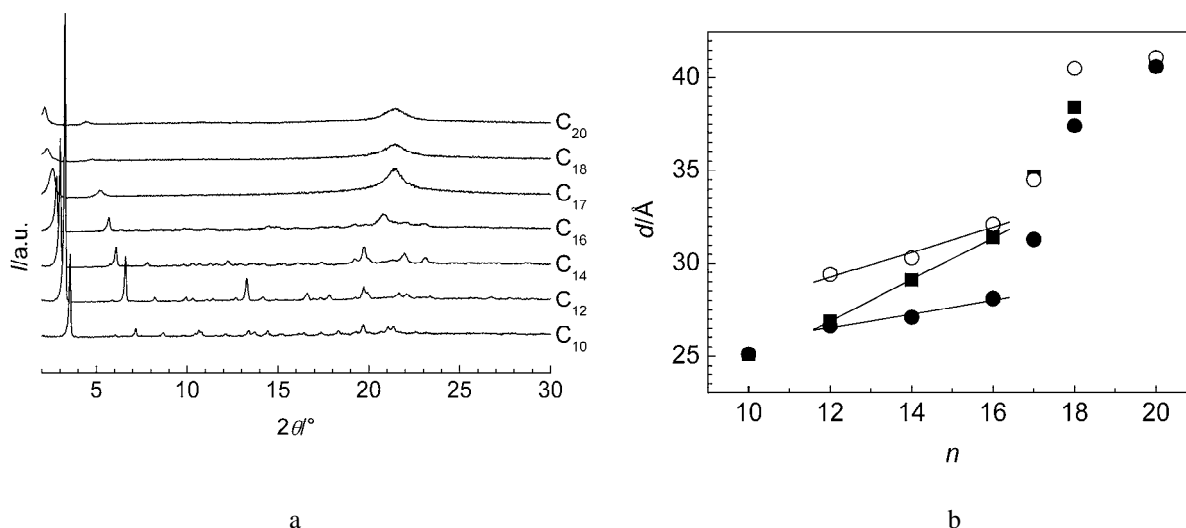
**Figure 82.** a) The XRD diffraction patterns of $C_n$-27 ($n$ = 10, 12, 14, 16, 17, 18, 20), and b) Dependence of the interlayer distance $d$ on the length of alkyl chains defined by $n$ in $C_n$-27 in solid state (pristine) (■), molten state just above melting point (○) and solid state (●). The solid lines correspond to the linear fit of values $d$ belonging to $C_n$-27 with $n$ = 12, 14, 16.

The diffractograms measured on sample $C_{18}$-26 in the sequence 300–410–300 K show a single low-angle reflection at all temperatures, indicative of the layered structure (Figure 83a). Upon heating a shift of low and high angle reflections to lower values with the change of their intensity and broadening of the alkyl reflection was observed. Compound $C_{18}$-29 also exhibits similar behavior (Figure 83i).

The compounds $C_n$-27 exhibit lamellar structure, as evidenced by the powder XRD patterns. They display intense low angle reflection $hk$ = (10) and another one (20) and higher concomitant reflections, all corresponding to the stacking periodicity of the layers (Figure 83b-h). Other reflections are much weaker, which is characteristic of long-chain materials because of extremely high degree of the preferred orientation [255]. Compound $C_{17}$-27 and two higher homologues $C_{18}$-27 and $C_{20}$-27 exhibit only two reflections in the low-angle region and one intense broad halo in the region of high angles (Figure 82a and Figure 83f, g, h). Upon the first heating the crystallinity of the short chain homologues ($n$ = 12, 14, 16) decreases, which is confirmed by attenuation of the number of orders of lamellar reflections. The most intense reflection (10) is preserved despite some broadening (Figure 83c, d, e).
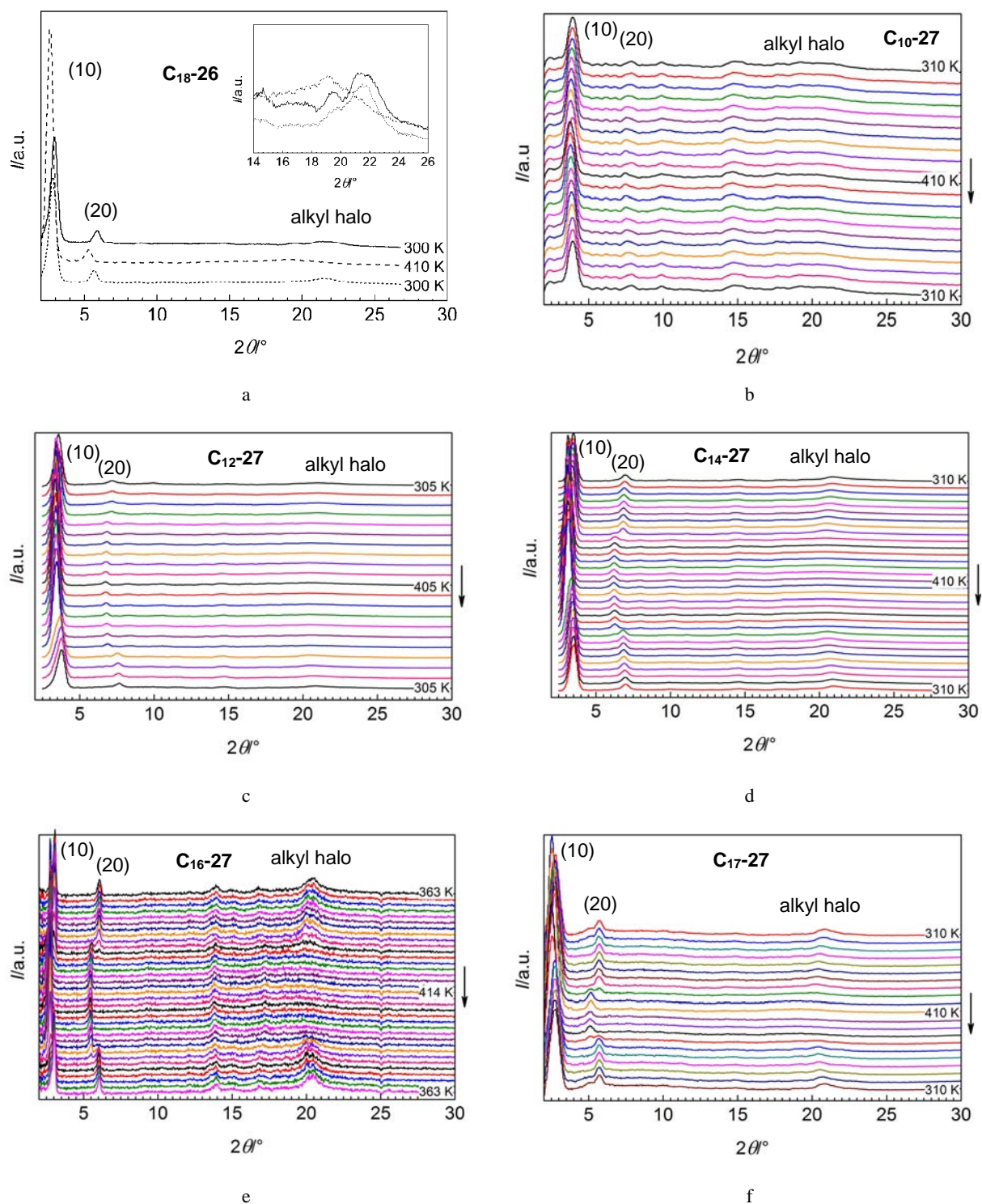
**Figure 83.** Variable temperature XRD patterns of a) $C_{18}$-26, b) $C_{10}$-27, c) $C_{12}$-27, d) $C_{14}$-27, e) $C_{16}$-27, f) $C_{17}$-27, g) $C_{18}$-27, h) $C_{20}$-27 and i) $C_{18}$-29. Inset shows enlarged region of the alkyl halo.

g



h



i
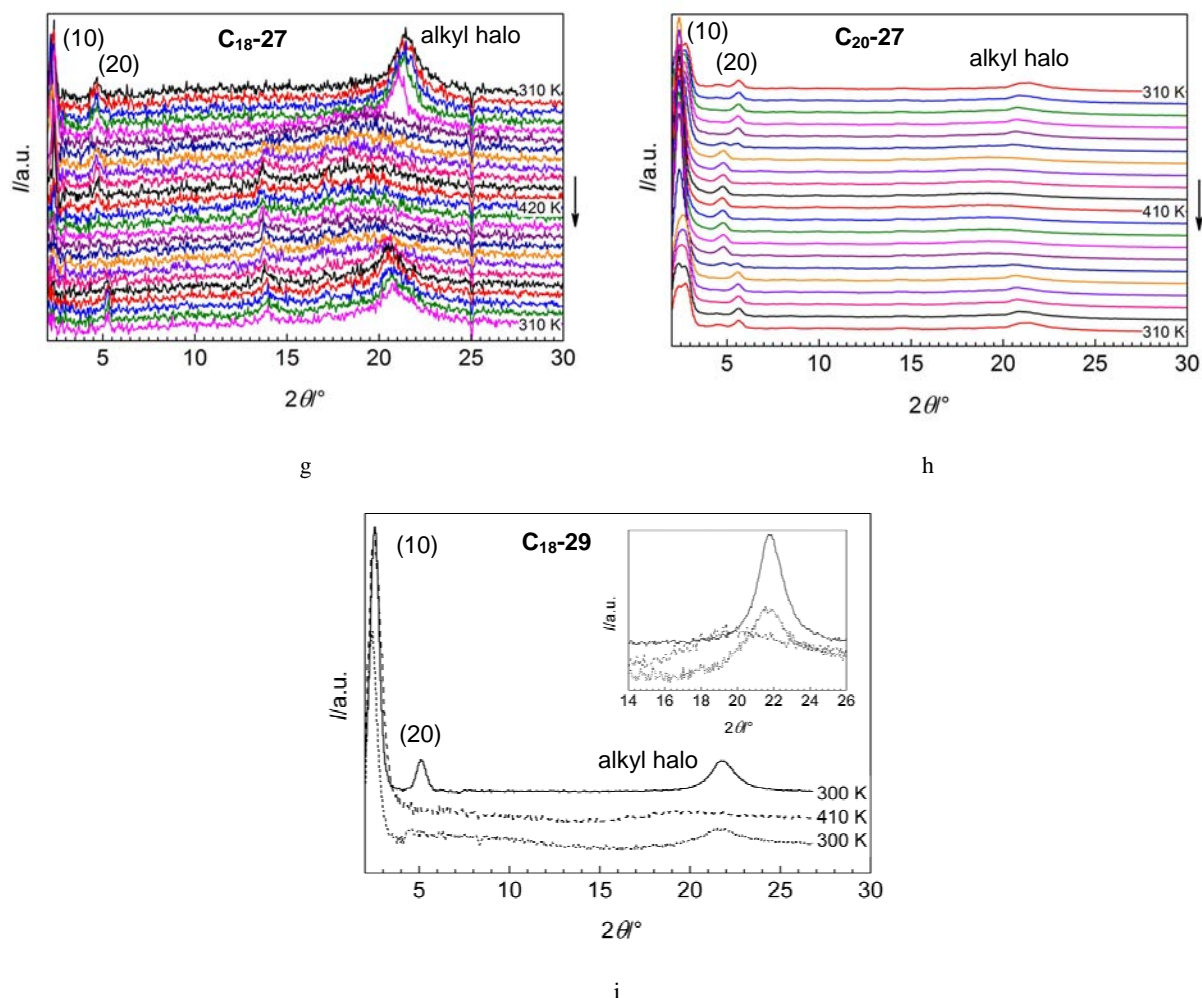
**Figure 83.** (*continued*)

The chain packing in compounds $C_n$-27 can be understood by the analysis of the spacing $d$ as a function of chain length $n$. As was established in the previous studies [247, 255, 258], for a system with intertwined alkyl chains the interlayer spacing $d$ is related to the carbon chain length $n$ through the relationship

$$d(\text{Å}) = d^{n=0} + 1.27 n \cos\tau \tag{16}$$

where $d^{n=0}$ is the intercept value which takes into account the radii of two methyl groups ($2d^{C-H}$) and of an ionic bilayer ($d^{bl}$) composed of the polar heads and anions: $d^{n=0} = d^{bl} + 2d^{C-H}$, $d^{C-H} = 1.09$ Å [258]; $\tau$ is the tilt angle of the chains and the coefficient 1.27 is the distance C–C in Å in *all-trans* alkyl chains orthogonal to the ionic bilayers. For a homogeneous series, a variation of $d$ can point out the change of the packing of the alkyl chains, because of the independence of the molecular area of the chains on $n$ value.

For the $C_n$-27 series ($n$ is even) (Figure 82b) a discontinuity in the interlayer spacing with the lengthening of chains is found. Therefore, the compounds $C_n$-27 were divided into two groups by the length of alkyl chains: shorter with $n = 12, 14, 16$ (group I) and longer with $n = 18, 20$ (group II). The variation of the interlayer spacing as a function of chain length is described by the formula $d = 13.75 + 1.27n\cos30.4$ for group I. For group II the line drawn through the $d$ points of the two members $C_{18}$-27 and $C_{20}$-27 led to the formula $d = 16.80 + 1.27n\cos19.0$. The change in spacing $d$ with each added carbon atom is thus a measure of chain packing. The intercept of the plot of spacing $d$ *vs* carbon atom number $n$ allows to calculate the value of bilayers $d^{bl}$, which is equal to 11.75 Å, while the same value for $C_6$-26 is 10.027(5) Å. The difference might be associated with some disorder of ionic and alkyl groups. After thermal treatment the interlayer distances $d$ decrease (Figure 82b). However, as is seen, the organization of the bilayers upon thermal treatment is changed as well. For the successive members of group I the $d^{bl} = 19.8$ Å in solid state and $d^{bl} = 18.9$ Å in molten state.

For group II a tilt of the chains by 19° for the pristine samples means that alkyl chains are located closer to perpendicular to the layer. The intercept of spacing $d$ provided the value $d^{bl}$ of 14.8 Å. As is seen, the intercept for groups I and II gives different values suggesting different kind of organization or different degree of disorder of the polar heads and anions within the ionic bilayers.

In $C_n$-27 ($n = 12, 14, 16, 18, 20$) the change of the high-angle lamellar reflection upon heating with concomitant increase of interlayer distance is deduced from the XRD data above the corresponding melting points (Figure 82b). The variation of the interlayer distance $d$ as a function of temperature is shown in Figure 79c–i, right scale, along with the magnetic data, left scale. The anomalous change of the magnetic susceptibility is synchronous with the phase transition and the change of the interlayer distance $d$. In compound $C_{10}$-27 the change of the $d$ value has monotonic character opposite to higher homologues, for which the transition from low-temperature to high-temperature phase coincides with the magnetic hysteresis loop. With temperature decrease, the transition is reversible but shows supercooling. Depending on the value $n$ the width of the hysteresis loop can vary in the range of 10–30 K. It is worth noting, upon cooling for $C_{20}$-27 an additional low-angle reflection appears along with the respective second order reflection. The transition is still incomplete at 230 K and two low-angle reflections are present.

In accordance with the XRD data the mesophases observed for $n = 12, 14, 16, 18, 20$ may be assigned to the smectic type [274].

A summary of reflections and calculated distances $d$ for compounds $C_n$-26–$C_n$-29 are presented in Table 31.

**Table 31.** Interlayer distances $d$ at different temperatures, thermal transitions and mesomorphism, thermal stability, enthalpy $\Delta H^{Cr\to S_x}$ and entropy $\Delta S^{Cr\to S_x}$ of phase transition determined by XRD, DSC, TGA and POM for $C_n$-26–$C_n$-29. The values $\Delta H^{est}$ and $\Delta S^{est}$ are estimated enthalpy and entropy, respectively. For details see explanation in text.

| Compound | $d$ [Å] 300 K (pristine) | 410 K | 300 K | Thermal transitions [K][b] | $\Delta H^{Cr\to S_x}$ [kJ mol⁻¹] [b] | $\Delta H^{est}$ [kJ mol⁻¹] | $\Delta S^{Cr\to S_x}$ [J K⁻¹ mol⁻¹] | $\Delta S^{est}$ [J K⁻¹ mol⁻¹] |
|---|---|---|---|---|---|---|---|---|
| **C₆-26** | 18.087(7)[a] | – | – | – | – | – | – | – |
| **C₁₈-26** | 31.8 | 35.7 | 33.3 | Cr ⇌(397/383) S$_X$ 506 d | 34.2 | 255 | 86.1 | 503 |
| **C₁₀-27** | 24.8 | 24.4 | 25.1 | Cr ⇌(395/380) S$_X$ 523 d | 19.3 | 135 | 48.7 | 267 |
| **C₁₂-27** | 26.9 | 29.4 | 26.6 | Cr ⇌(361/349) S$_X$ 500 d | 22.2 | 165 | 62.7 | 326 |
| **C₁₄-27** | 29.1 | 30.3 | 27.1 | Cr ⇌(369/360) S$_X$ 490 d | 30.0 | 195 | 81.3 | 385 |
| **C₁₆-27** | 31.4 | 32.1 | 28.1 | Cr ⇌(377/365) S$_X$ 510 d | 35.0 | 225 | 92.8 | 445 |
| **C₁₇-27** | 34.7 | 34.5 | 31.3 | Cr ⇌(375/342) S$_X$ 464 d | 40.3 | 240 | 116.1 | 474 |
| **C₁₈-27** | 38.4 | 40.5 | 37.4 | Cr ⇌(375/345) S$_X$ 460 d | 30.1 | 255 | 85.5 | 503 |
| **C₂₀-28, C₂₀-27** | 40.9 | 41.1 | 40.6 | Cr₁ ⇌(327/310) Cr₂ ⇌(380/350) S$_X$ 450 d | 36.4 | 285 | 101.1 | 563 |
| **C₁₈-29** | 36.5 | 36.4 | 38.1 | Cr ⇌(305/299) S$_X$ 510 d | 44.9 | 425 | 150.1 | 838 |

[a] From the X-ray single crystal data at 100 K; [b] Measured by DSC in the second heating-cooling cycle. The values correspond to the maxima of the enthalpy peaks. The identification of the mesophase was done on the basis of POM and XRD data.

### 2.8.7    POM and DSC data

Polarizing optical microscopy measurements (POM) detected the occurrence of anisotropic textures in **C₁₈-26**, **C$_n$-27** ($n$ = 12, 14, 16, 17, 18, 20) and **C$_n$-29** upon heating. The textures of compounds **C₁₆-27** and **C₂₀-27** are shown in Figure 84a, b. The textures observed can be assigned to the smectic (S$_X$) type.

To clarify the thermotropic behavior, compounds **C$_n$-26–C$_n$-29** were studied by DSC over the range of 250–500 K at a heating rate of 10 K min⁻¹. A summary of the thermodynamic parameters calculated by integration of the major endothermic peak in the second heating run are collected in Table 31 and graphically displayed in Figure 85a–i.

a                                                                b
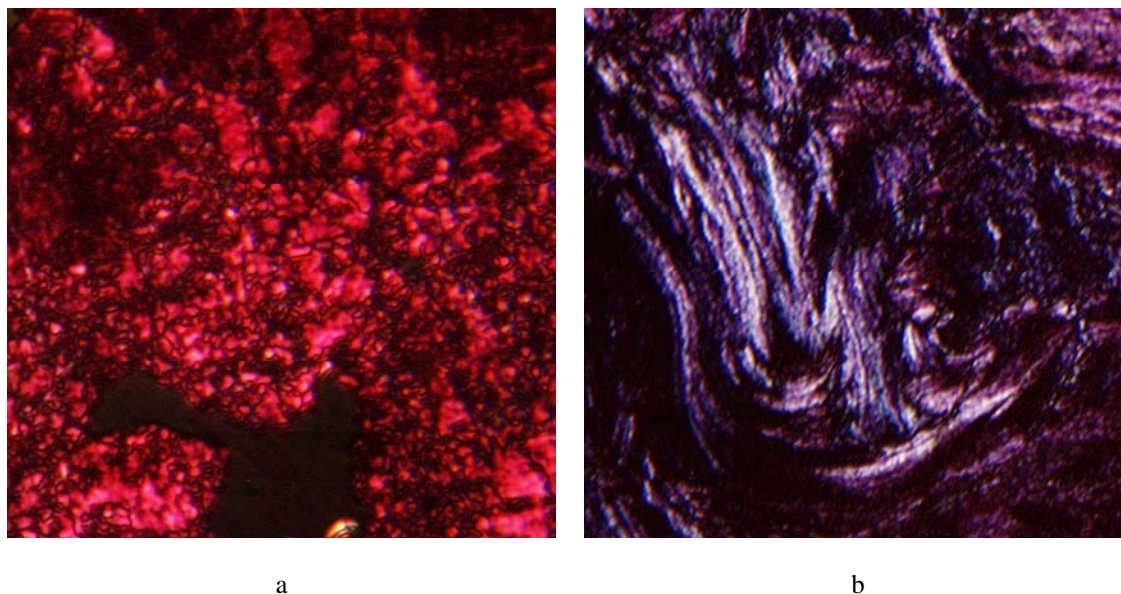
**Figure 84.** The anisotropic texture of compound **C$_{16}$-27** (a) and vertex texture of **C$_{20}$-27** (b) under crossed polarizers.

Compound **C$_{18}$-26** shows an endothermic peak at 397 K corresponding to melting of the substance into a smectic mesophase and exothermic peak at 380 K on cooling (Figure 85a). At this temperature, the cooling and heating magnetic curves start to diverge (Figure 79b), which confirms the correlation of the magnetic and structural properties. As it was detected by TGA, the first heating of **C$_{18}$-29** is accompanied by water loss, thus the total enthalpy measured in the first heating run is the sum of the melting enthalpy and the enthalpy of the change of spin multiplicity and the enthalpy of the concomitant dehydration process. The second and the third measurement cycles correspond to the anhydrous compound and reveal broad melting peaks centered at 299 K (Figure 85i). This is due to the transition into the smectic mesophase, which is supported by POM (Table 31).
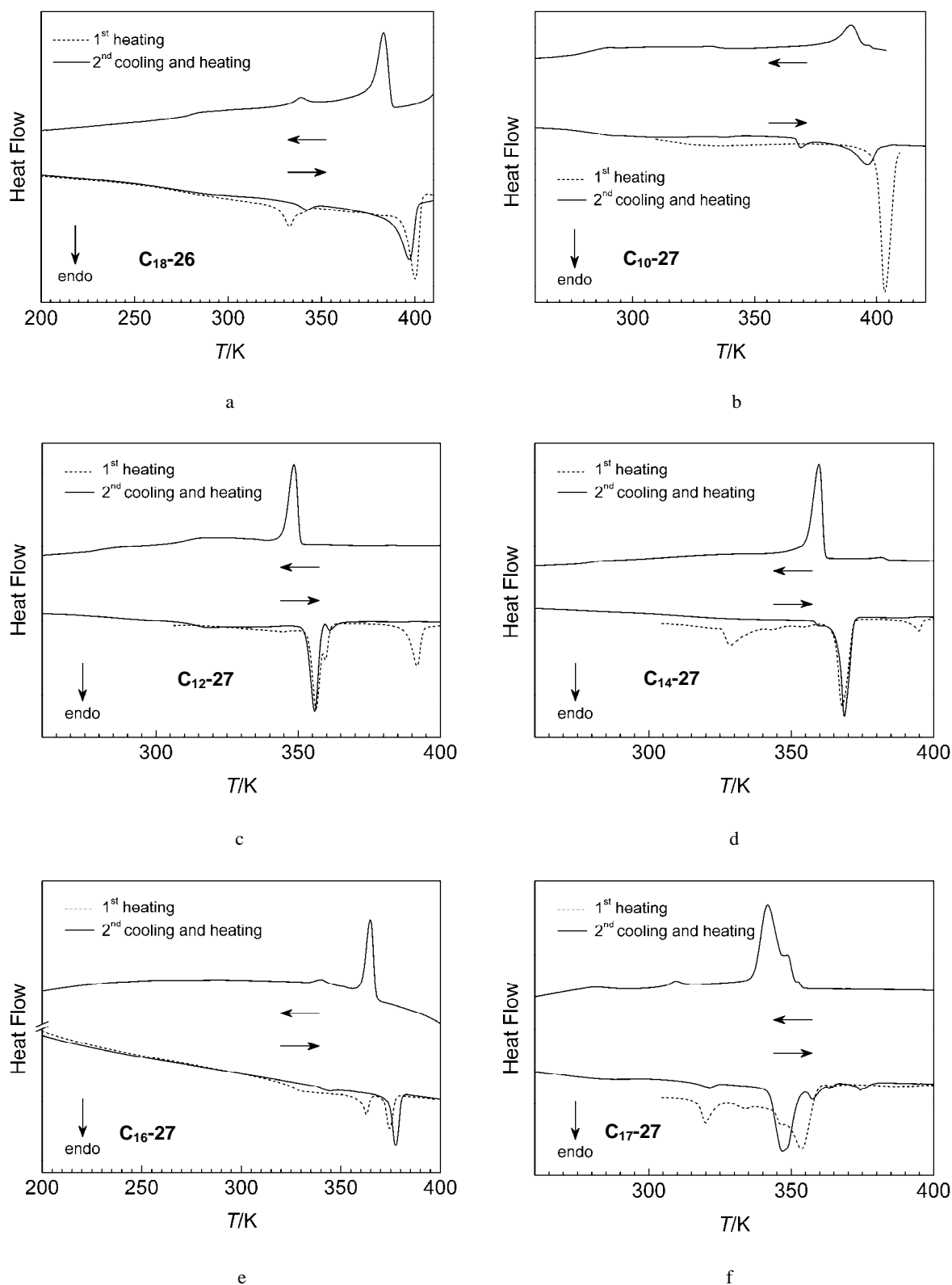
**Figure 85.** DSC profiles for a) $C_{18}$-26, b) $C_{10}$-27, c) $C_{12}$-27, d) $C_{14}$-27, e) $C_{16}$-27, f) $C_{17}$-27, g) $C_{18}$-27, h) $C_{20}$-28, $C_{20}$-27, and i) $C_{18}$-29, in heating and cooling modes. Arrows show the direction of the scanning runs.

g



h



i
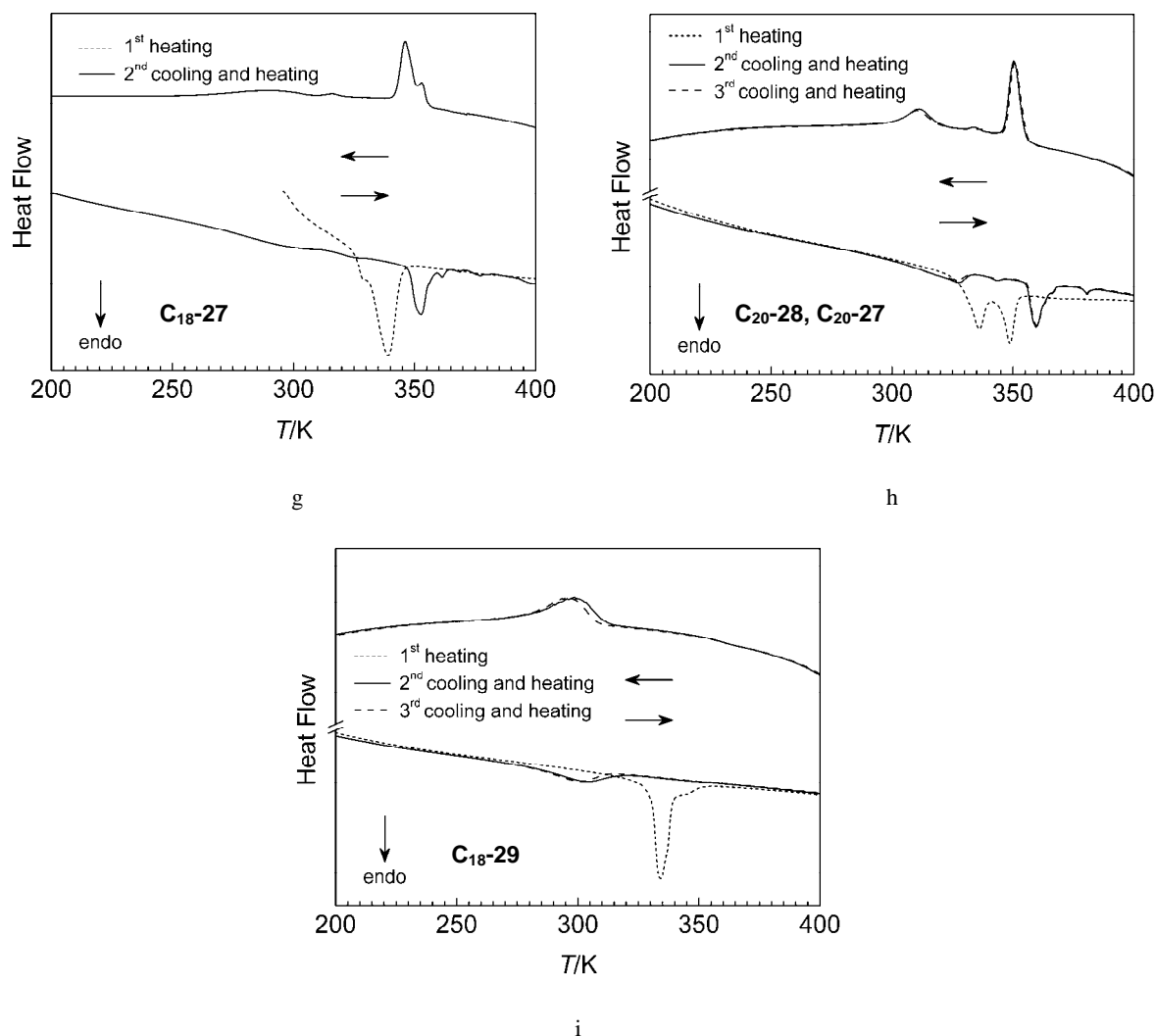
**Figure 85.** (*continued*)

Among the $C_n$-27 series, the marked difference in thermal behavior is clearly apparent for the compounds with $n = 10$, then $n = 12$, 14, 16 (group I) and $n = 18$, 20 (group II) (Figure 85b–e, g, h). Firstly, $C_{10}$-27 presents a higher melting temperature and a broader endothermic peak than is observed for $C_{12}$-27 (Figure 85b, c). For the three compounds $C_n$-27 with $n = 12$, 14, 16 a gradual increase of the transition temperature is observed with a lengthening of the alkyl substituents (Figure 85c, d, e). In contrast, for $C_{18}$-27 a decrease of the melting temperature with the following increase for homologue $C_{20}$-27 is found (Figure 85g, h). These data agree with the XRD and the magnetic data, where the dependence of the anomaly of the magnetic susceptibility and the phase transitions on the length of alkyl chains is observed in the order similar to that found from the DSC data. Compound $C_{17}$-27 with odd-numbered carbon chains behaves similarly to the higher homologues (Figure 85f).

The presence of structural water in pristine $C_{20}$-28 has the expected influence on the thermal behavior of the compound. The initial heating removes water molecules and as a consequence several peaks are observed in the DSC trace (Figure 85h). The coinciding DSC traces of the second and the third runs confirm the completeness of the dehydration. In general, the first heating run also differs from the next runs for anhydrous materials with $n$ = 12, 14, 16, 17, 18, and is reminiscent of the initial annealing of the structure confirmed also by the magnetic and XRD data (Figure 79d–h; compare XRD profiles in Figure 82a and Figure 83b–g).

For derivatives with $n$ = 12, 14, 16 the main transition precedes the minor transitions tentatively attributed to solid-solid and order-disorder pre-transitions [255, 275]. It is well known that melting of metallomesogens, such as $n$-alkylammonium tetrachlorometalate(II) and metal carboxylates, is often a stepwise process in which one or more intermediate solid phases form before the transition into the melt [257, 276, 277]. The compounds $C_n$-27 do not show any noticeable changes in the XRD profiles on passing through the corresponding temperature points. For $n$ = 18, 20 the situation is also complicated by the low enthalpy transition after the main peak, which according to the XRD data is associated with the transition into the mesophase. For anhydrous $C_{20}$-27 solid-solid transition is detected by the XRD measurement which is confirmed by a high-enthalpy broad peak centered at 305 K. Supercooling during the transition from the mesophase into the solid is observed for all $C_n$-27 compounds and confirmed by the XRD data. It is more pronounced for $n$ = 18, 20 ($\Delta T_{hys}$ ~20 K) than for $n$ = 12, 14, 16 ($\Delta T_{hys}$ ~10 K). This observation indicates that the mesophases possess some degree of crystalline order [258, 278].

In Figure 86 the experimentally deduced values for the enthalpy and entropy of the transition solid $\leftrightarrow$ mesophase are plotted $vs$ the chain length $n$ for $C_n$-27. A linear dependence of $\Delta H$ and $\Delta S$ is observed for both group I and group II. A way to interpret and rationalize the phase transitions in alkylated compounds is to separate the total enthalpy and entropy into their main contributions and then to compare theoretical estimates with the experimental results. A modified equation [279] for the enthalpy change associated with the fusion process in ionic spin-crossover metallomesogens can be written as:

$$\Delta H^{\text{solid} \rightarrow \text{liquid crystal}} = \Delta H_{\text{conf}} + \Delta H_{\text{vdW}} + \Delta H_{\text{es}} + p\Delta V + \Delta H_{\text{SCO}} \qquad (17)$$

where $\Delta H_{\text{conf}}$ and $\Delta H_{\text{vdW}}$ are enthalpy variations associated with the intramolecular conformational disorder (introduction of *gauche* kinks into the chains) and intermolecular van der Waals interactions, respectively, and $\Delta H_{\text{es}}$ incorporates electrostatic term. The $p\Delta V$ term is of minor importance compared to other terms and can be neglected [279]. The term $\Delta H_{\text{SCO}}$ is

responsible for the enthalpy change due to spin-change observed in $C_n$-**27** with $n = 12, 14, 16$ during melting/solidification. Taking into account a value of $\Delta H_{SCO} = 22$ kJ mol$^{-1}$ evaluated by the fit of the magnetic data, and considering the fact that only about 14 % of iron(II) ions transform back to low-spin state due to melting, the value of *ca.* 3 kJ mol$^{-1}$ is obtained. The value is relatively small compared to the total enthalpy gain deduced from the DSC data (Table 31).
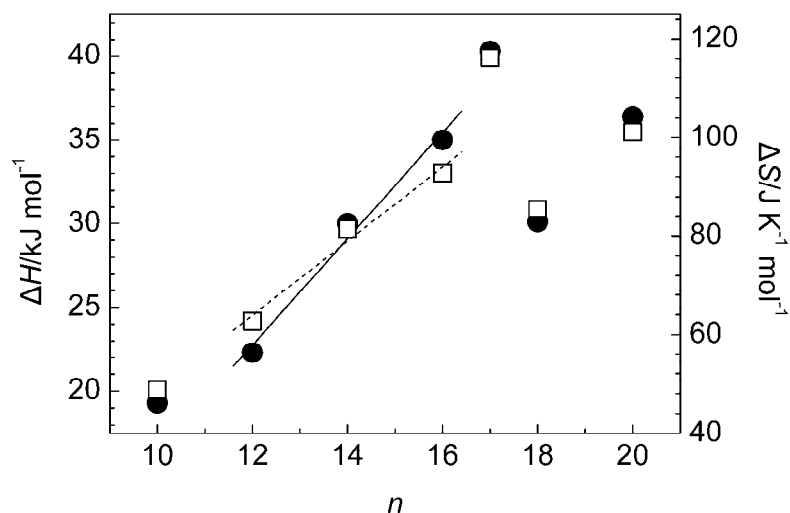


**Figure 86.** Enthalpy (●) and entropy (□) change for the phase transition solid → liquid crystal for the compounds $C_n$-**27** as a function of chain length $n$. The solid line is the fit of the enthalpy value whereas dashed line is the fit of the entropy value for group I ($n = 12, 14, 16$).

The enthalpy of chain-melting transition $\Delta H_{conf}$ in layered systems can be evaluated using Flory's value for the enthalpy of a *gauche* bond relative to a *trans* bond, and it comes out to be 2.1 kJ/mol [280]. The changes in van der Waals interactions were estimated [281] using Salem's treatment of the interaction between parallel alkyl chains and the experimental data for the cohesive energy in polyethylene [282]. Ignoring repulsive terms, the energy $\Delta H_{vdW}$ is estimated to be in the range 2.8–3.0 kJ (mol CH$_2$)$^{-1}$. For simplicity, the average was used for the calculation of the expected enthalpy change in $C_n$-**27**. The obtained data are presented in Table 31 as $\Delta H^{est}$. In general, as seen, the experimental values are much lower than estimated for entirely molten alkyl chains confirming an incomplete transformation into liquid-like form on phase transition [258]. The observed linear growth of melting enthalpy with increase of the chain length is associated both with decreasing van der Waals interactions and introduction of some degree of conformational disorder with increasing $n$. The fit for the $\Delta H$ plot ("enthalpy analysis", Figure 86) for $n = 12, 14, 16$ (group I) gives a slope of 3.18 kJ mol$^{-1}$, which is smaller than the 15 kJ (mol CH$_2$)$^{-1}$ associated with the sum of the terms

$\Delta H_{conf}$ and $\Delta H_{vdW}$ for three alkyl chains of one complex molecule. Extrapolation to zero methylene groups gives an intercept $\Delta H^{n=0} = -15.35$ kJ mol$^{-1}$ which might imply that electrostatic interactions give a negative contribution to the melting enthalpy. The stabilization of the electrostatic interactions which appears to occur with the fusion is probably due to lateral stress of the ionic bilayers. This might be accompanied by a tilt of the coordination head-groups or a longitudinal change at the level like it was found in $C_n$-14 (Chapter 2.5.7). For $n = 18, 20$ (group II) the difference between the enthalpy gain on melting for two related homologues is 3.15 kJ mol$^{-1}$.

The entropy change on melting is supposed to originate mostly from the disorder of flexible alkyl chains. The evaluation of the entropy change for group I ("entropy analysis" [256], Figure 86) gives a slope of 7.5 J K$^{-1}$ mol$^{-1}$ which is much lower than that expected for the complete fusion of three alkyl chains (3×9.8 J K$^{-1}$ (mol CH$_2$)$^{-1}$ [278]). From these data a kind of mesophase can be predicted which retains some crystalline arrangement. This assumption is in agreement with the structural and microscopic data. For group II the difference between the entropy gain on melting for two related homologues is 7.8 J K$^{-1}$ mol$^{-1}$ and is similar to that of group I.

### 2.8.8    Mössbauer spectroscopy

In order to confirm the low-spin character of the complexes $C_n$-26–$C_n$-29 at low temperature, Mössbauer spectra were measured (Figure 87a–j). For compound $C_6$-26 as well as for $C_n$-27 with $n = 10, 12, 14, 16$ the spectra were fitted with a single doublet with isomer shift $\delta$ and quadrupole splittings $\Delta E_Q$ attributable to the low-spin state of iron(II)-containing species and being consistent with the magnetic data (Figure 87a, c–f). The spectrum of $C_{18}$-26 was fitted with two inequivalent doublets for each the major low-spin and the minor high-spin fractions (Figure 87b). The spectrum is reminiscent of the spectra of $C_n$-14 compounds (Figure 60g, h, i). In fact, the magnetic behaviors of both types of compounds are quite similar, showing acceleration of spin-transition due to melting and hysteresis of the magnetic susceptibility.

For $C_{17}$-27 and two higher homologues $C_{18}$-27 and $C_{20}$-28 (*i.e.* pristine hydrated form of $C_{20}$-27, see Table 27), least square-fit routine analysis of the Mössbauer spectrum indicates that nearly 10 % of iron(II) ions comprise the high-spin fraction (Figure 87g, h, i). This corresponds to the residual paramagnetism at low temperature elucidated from the magnetic data. The considerable broadening of both low-spin and high-spin fractions is the

result of the poorly structured compounds and is similar to that found in the previous series. This also might be responsible for the underestimation of the high-spin fraction that would correspond to lower magnetic value of $\chi_M T$ than is found in the susceptibility measurements. For the compounds $C_{18}$-27 and $C_{20}$-27, the high-spin fraction found has the same population, however, the magnetic data unequivocally show an increase of the residual high-spin fraction with lengthening of the alkyl chains. The different values derived for the two spin states from the Mössbauer spectra on the one hand and the magnetic susceptibility measurements on the other hand attributed to known difference of Debye-Waller factors for the two species. The low-spin fraction is somewhat overestimated due to higher tightness of binding of iron(II) ions in low-spin complex molecules compared to high-spin complex molecules. For alkylated compounds this effect might be more pronounced because of the lamellar organization of the crystals (see Figure 77b) and because of poor crystallinity of the solid compounds revealed by the XRD data (Figure 82a).

The Mössbauer spectrum of $C_{18}$-29 was fitted with two sites for both almost equally populated and broadened low-spin and high-spin fractions (Figure 87j). The value of $\gamma_{HS}$, which was found, is in fairly good agreement with the magnetic data at *ca.* 80 K (Figure 79j).

The values of Mössbauer parameters are collected in Table 32.
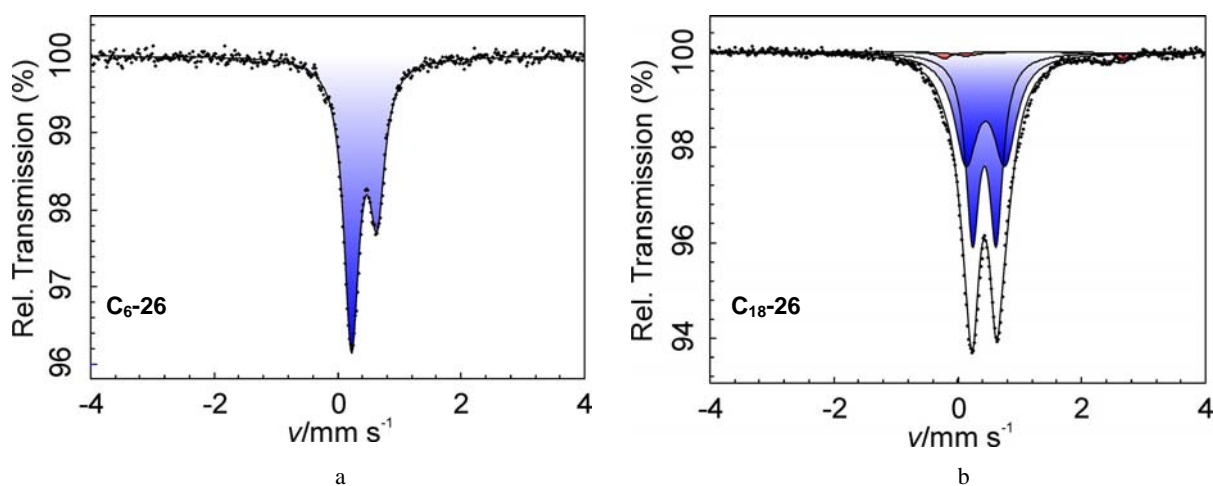


**Figure 87.** Mössbauer spectra of compounds a) $C_6$-26, b) $C_{18}$-26, c) $C_{10}$-27, d) $C_{12}$-27, e) $C_{14}$-27, f) $C_{16}$-27, g) $C_{17}$-27, h) $C_{18}$-27, i) $C_{20}$-28, j) $C_{18}$-29 at 80 K.

c



d



e



f



g



h
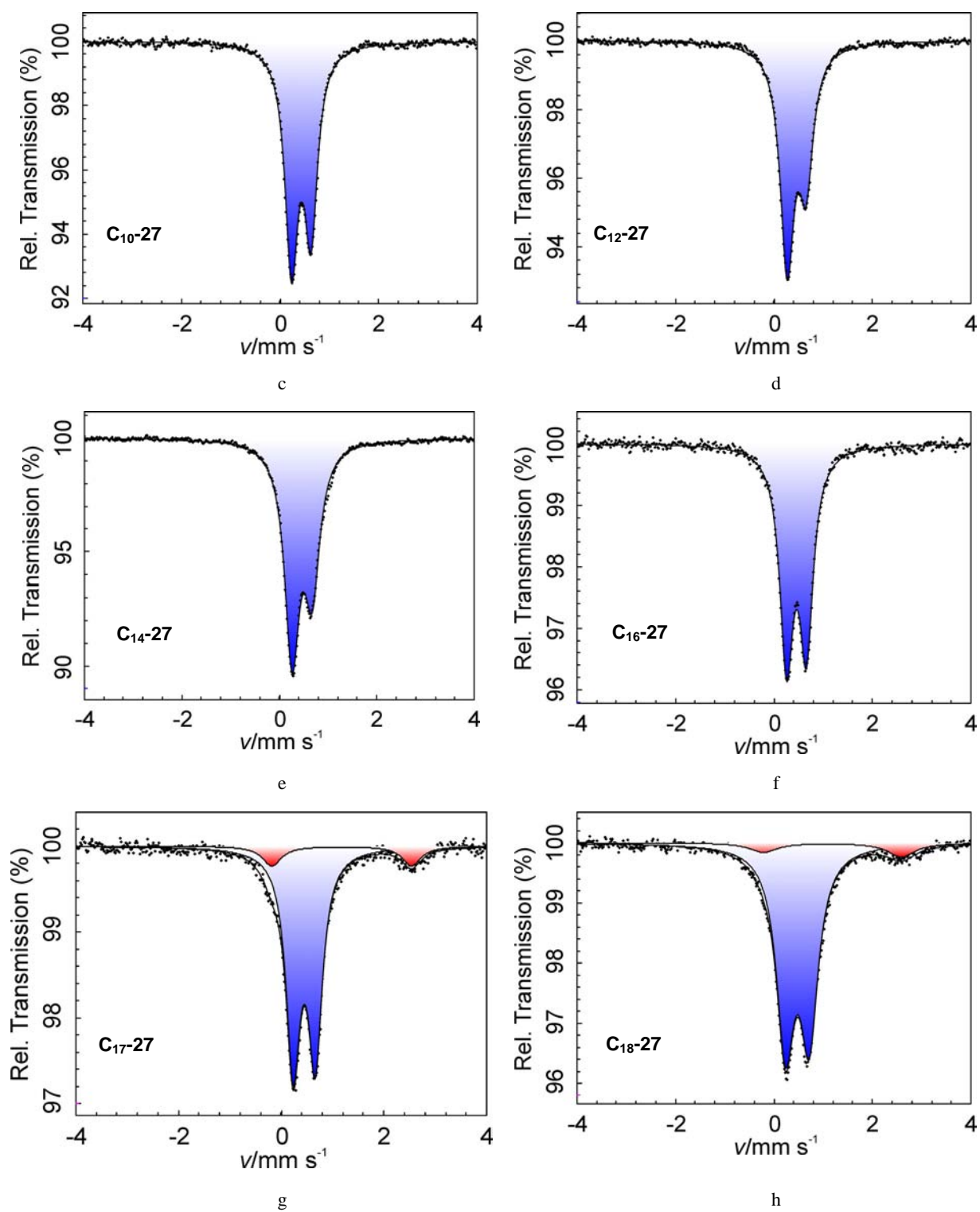
**Figure 87.** (*continued*)
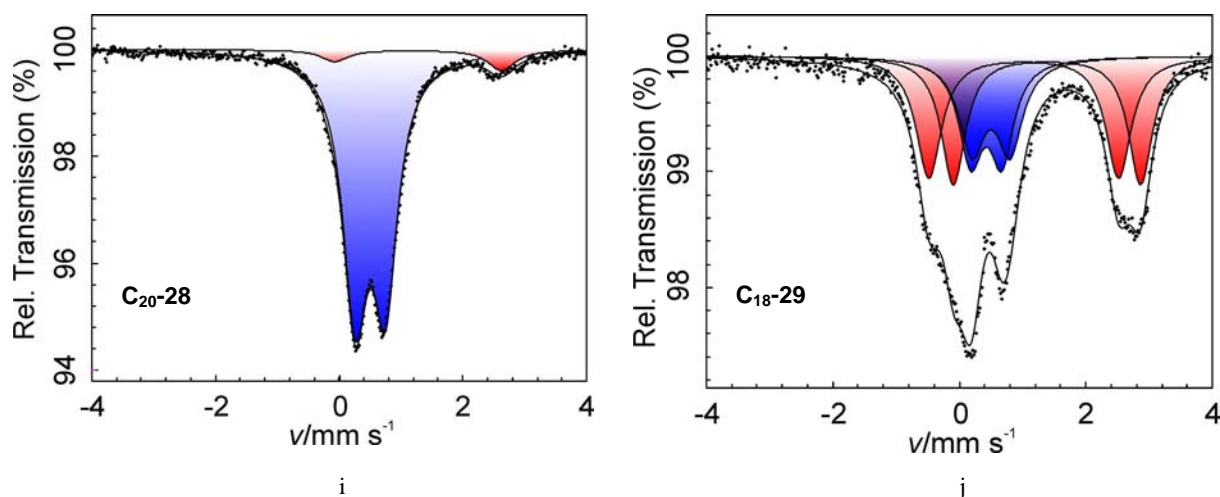
**Figure 87.** (*continued*)

**Table 32.** Mössbauer parameters, isomer shift ($\delta$, relative to $\alpha$-iron), quadrupole splitting ($\Delta E_Q$), half-width of the lines ($\Gamma_{1/2}$) and percentage of the multiplet populations in the low-spin (LS) and high-spin (HS) states (*A*) for **C$_n$-26–C$_n$-29** at 80 K.

| Compound | Spin state | $\delta$ [mm s$^{-1}$] | $\Delta E_Q$ [mm s$^{-1}$] | $\Gamma_{1/2}$ [mm s$^{-1}$] | A [ %] |
|---|---|---|---|---|---|
| **C$_6$-26** | LS | 0.43(2) | 0.41(0) | 0.15(1) | 100 |
| **C$_{18}$-26** | LS1 | 0.45(1) | 0.38(1) | 0.13(0) | *47* |
| | LS2 | 0.45(1) | 0.64(0) | 0.22(0) | *47* |
| | HS1 | 1.05(3) | 2.58(7) | 0.13(0) | *3* |
| | HS2 | 1.26(3) | 2.91(1) | 0.22(0) | *3* |
| **C$_{10}$-27** | LS | 0.43(0) | 0.39(0) | 0.16(0) | 100 |
| **C$_{12}$-27** | LS | 0.46(0) | 0.38(0) | 0.17(0) | 100 |
| **C$_{14}$-27** | LS | 0.43(1) | 0.40(0) | 0.17(1) | 100 |
| **C$_{16}$-27** | LS | 0.46(1) | 0.40(0) | 0.17(1) | 100 |
| **C$_{17}$-27** | LS | 0.45(1) | 0.43(1) | 0.17(0) | 88.5(16) |
| | HS | 1.18(1) | 2.72(1) | 0.23(5) | 11.5(24) |
| **C$_{18}$-27** | LS | 0.48(1) | 0.48(0) | 0.22(0) | 89.5(11) |
| | HS | 1.22(5) | 2.81(10) | 0.37(8) | 10.5(22) |
| **C$_{20}$-28** | LS | 0.50(0) | 0.49(1) | 0.24(0) | 90.7(7) |
| | HS | 1.32(0) | 2.61(5) | 0.29(4) | 9.3(12) |
| **C$_{18}$-29** | LS1 | 0.43(1) | 0.49(1) | 0.23(0) | *22* |
| | LS2 | 0.50(0) | 0.60(0) | 0.25(0) | *22* |
| | HS1 | 1.02(1) | 2.99(0) | 0.24(0) | *28* |
| | HS2 | 1.38(0) | 2.96(1) | 0.23(0) | *28* |

The values given in italics were fixed during the fitting.

### 2.8.9   Discussion

Contrary to the parent complex **6**, which is low-spin up to 400 K (Chapter 2.3.5), introducing the alkoxy substituents into the pyridine units of the ligand *tame*(6-*Mepy*)$_3$ reduced the ligand field strength. Compounds **$C_n$-26**–**$C_n$-29** based on the ligand *tame*($C_n$-6-*Mepy*)$_3$ show onset of spin-crossover below 400 K.

The thermal behavior of the compounds **$C_n$-27** depends on the chain length defined by *n*. This parameter is reflected on the position of the magnetic anomaly caused by the melting/solidification process and changes with lengthening of alkyl chains. A common structural feature of all homologues of the series is a similar layered structure and adoption of the a smectic mesophase $S_X$ on melting. Formation of the mesophase originates from melting of alkyl chains rather than a rearrangement of the ionic bilayers. The changes in the structure of the ionic bilayers are rather small, however, they play a central role in governing the magnetic properties during the transition solid ↔ liquid crystal.

Before discussing the structure-property correlations in **$C_n$-27** (*n* = 10, 12, 14, 16, 17, 18, 20), a short overview of the published data of the magnetic measurements of organic and metal containing liquid crystals will be given, which describe the change in the magnetic properties caused by a phase transition.

The magnetic properties of classical organic liquid crystals have a complicated character. The diamagnetic response in these materials results from the magnetic anisotropy of the liquid crystal molecules which governs their orientation in the applied magnetic field [283]. The orientational behavior is a consequence of cooperativity within domains in the mesophase [284]. In a particular system the molecular anisotropy is mainly produced by the phenyl groups by the induction of the ring currents which gives a large negative contribution to the diamagnetic susceptibility in the direction perpendicular to the plane of the aromatic rings. The liquid crystalline molecules adjust themselves in a way that minimizes this effect. It can be achieved by the orientation of the phenyl rings with planes parallel to the vector of the field [285], but the degree of the adjustment depends on the inherent characteristics of the mesophase [283]. While in the isotropic (i) and the crystalline (Cr) phases the susceptibility values are rather similar [283], in fluid but structured mesophases (nematic (N) or smectic (S)) the diamagnetic response is efficiently modulated by the magnetic field and is usually reduced [286]. This explains the increase of susceptibility upon cooling, for example, in the sequence i → N → S → Cr in the applied field [283]. For the organic liquid crystals the magnitude of the magnetic anisotropy is approximately 6 % of the total diamagnetic contribution determined in

the isotropic melt [287] and therefore is small. For diamagnetic metal containing liquid crystals like square-planar Ni(II) complexes, the orientational effect and its influence on the magnetic properties is the same as found in the organic liquid crystals [233].

Molecular paramagnetism is mostly related to the spins of unpaired electrons. The majority of studied paramagnetic liquid crystals are metallomesogens in which spins originate from the transition metal centers. Many such compounds exhibit significant paramagnetic anisotropy due to the spin-orbit coupling, especially mesogenic complexes of some lanthanides [287, 288]. The anisotropy results in response similar to that observed for pure organic liquid crystals with the only difference in the type (sign) of the magnetic response. The alignment of these materials is induced by the orientation of the molecules with the axis of highest susceptibility $\chi_{max}$ parallel to magnetic field and is mostly observed on cooling from the isotropic phase, but is less pronounced or not observed on heating of the solid compounds [287]. The alignment of the complex molecules in mesophase with subsequent freezing of the molecular orientation in the crystalline phase is the main reason for the increase of magnetic susceptibility on cooling of the isotropic melt [288]. The value of $\chi_{max}$ can sporadically exceed the isotropic value of $\chi_{iso}$ by 30 % but mostly in lanthanide compounds it does not exceed a 5 % threshold [287]. The same orientation effect is known for some of the oxovanadium and planar copper(II)-based metallomesogens [233, 289-292]. In iron(III)-containing metallomesogen reported by Galyametdinov *et al.* [229] a jump in the magnetic susceptibility was detected which was associated to the crystal → liquid crystal phase transition and which was reversible on cooling in zero filed. The explanation proposed by the authors was also based on the anisotropy effect resulting from the increased orientation of microcrystalline aggregates in pre-transition regions with attaining the highest alignment of the magnetic vectors during the transition into the mesophase. The authors could also not exclude the assumption that the increase of the magnetic susceptibility in the vicinity of the phase transition was accompanied by the change in HS:LS ratio of iron(III) ions due to the changes of the elastic properties of the sample through the phase transition.

Another mechanism was assumed to be responsible for the change of magnetic susceptibility in dicopper(II) and dirhuthenium(II) tetracarboxylates [293, 294]. During the transition from the crystalline state into the discotic mesophase the copper compound revealed a decrease of the susceptibility, which could not be explained by the intramolecular structural changes as it was confirmed by the EXAFS measurements [233, 295-297]. Later it was ascribed to a decrease of the intermolecular ferromagnetic interaction upon melting into the mesophase [233, 298]. The reversible character of the transition was confirmed by the

recovery of initial magnetic properties over a period of several weeks by the copper-containing samples [293].

Several years ago the synthesis and the magnetic properties of a new class of paramagnetic organic liquid crystals bearing radical moieties were reported [299-301]. Due to transition from solid into mesophase, an irreversible discontinuity in the magnetic susceptibility was observed. It was assumed that increasing strength of intermolecular antiferromagnetic interactions was abruptly released by the phase transition due to a structural change in the surrounding of the radical moieties [302].

To conclude, two types of interplay between phase transition and magnetic properties are known. The first one includes the orientation effect of the liquid crystalline phase dependent on the strength of the external magnetic field and heating/cooling runs. The second type of interplay originates from intermolecular contacts and their modification through the phase transition.

Returning back to the discussion of compounds $C_n$-27 and the anomaly of the magnetic susceptibility due to the phase transition, we can suppose that the first effect, namely the possibility that the complex molecules align under the magnetic field, can be excluded. The reason is the high viscosity of the samples in the mesophase (from POM), which would give rise to a dependence of the anomaly on the strength of the field. A higher field should result in a larger amplitude of the anomaly. The magnetic measurements in weak and strong fields, however, show only a minor negligible shift of the hysteresis loop (Figure 80c). On the other hand, the influence of the heating rate on the width of the hysteresis loop, observed for $C_{16}$-27, is reminiscent of the superheating and supercooling of the solid or the mesophase, respectively, caused by the delay of the structural rearrangements. From these hints and the firm support by the XRD data, we can assume that the structural transformation has a direct influence on the magnetic properties.

As was shown, the separation of the compounds $C_n$-27 ($n$ = 12, 14, 16, 18, 20) into two groups is based on the visual examination of the XRD profiles and is confirmed by the comparison of the interlayer distances $d$. Along with the DSC and the Mössbauer data, these findings explain the dependence of the magnetic properties on the different structures adopted by the compounds.

The first melting modifies the magnetic properties of the compounds $C_n$-27 ($n$ = 12, 14, 16; group I) and concomitantly reduces the overall crystallinity of pristine compounds as it is seen in the XRD profiles from the reduced number of weak reflections and broadening of preserved ones (compare Figure 82a and Figure 83c, d, e). Only some of these are retained

with the main one at $2\theta \sim 14.0°$ which is observed in all homologues. This reflection is tentatively attributed to one of the reflection of the ionic bilayers. Its position and the intensity are changed only slightly on melting. In contrast, for group II ($n = 18, 20$) the overall improvement of the crystallinity after the first melting is strongly reflected in the residual paramagnetism. The residual high-spin fraction decreases with crystallinity improvement as seen from the comparison of the magnetic curves for the first and the second heating runs (Figure 79h, i) and the XRD profiles before and after thermal treatment (Figure 82a and Figure 83g, h). On the basis of the obtained data, we can assume that in the pristine samples of group II the strains are realized on melting (and dehydration for $n = 20$) and thereafter the ionic head-groups adopt a more equilibrated ordered structure.

The analysis of the interlayer distance $d$ vs $n$ in the homologous compounds of group I showed a change in the thickness of the ionic bilayers. In our opinion, the weak longitudial perturbation or the agitation of the ionic head-groups or some tilt might occur that plays a crucial role in governing the anomalous magnetic properties in the compounds $C_n$-27. The fitting of the magnetic curves indicated a decrease of the cooperativity on going from the solid to the liquid crystalline state which can be expected if a change of the intermolecular contacts such as weak hydrogen bonds occurs. As it was discussed in Chapter 1.3.4, intermolecular contacts between molecules are important for defining the gradual or abrupt character of the spin-transition. In fact, the behavior of the compounds $C_n$-27 of group I in liquid crystalline state approaches the behavior of systems with reduced or absent cooperative interactions such as metal diluted spin-crossover systems [303-309] or spin-equilibrium systems in solution [21, 310-313], the magnetic properties of which obey the simple Boltzmann distribution. Also some triazole systems were reported to show an abrupt spin-transition in hydrated form and rather gradual in dehydrated [81, 314] (see also Chapter 3.1.2). The role of water was assigned to the creation of hydrogen bonds favoring the cooperativity. In addition, an analogy can be drawn with the pair of compounds **1** and $C_6$-**19** presented in this work where the change of the structure from the three-dimensional to the lamellar two-dimensional one decreased the number of the hydrogen bonds which was attributed to a reason for the observed decrease of the cooperativity. But we emphasize that the reason for the decrease of the cooperativity in compounds $C_n$-**27** is the reversible change of the structure on melting/solidification.

Figure 88 illustrates the proposed arrangement of the compounds $C_n$-**27** with $n = 12$, 14, 16 in crystalline state (Cr) and mesophase (S) and the resulting magnetic behavior.
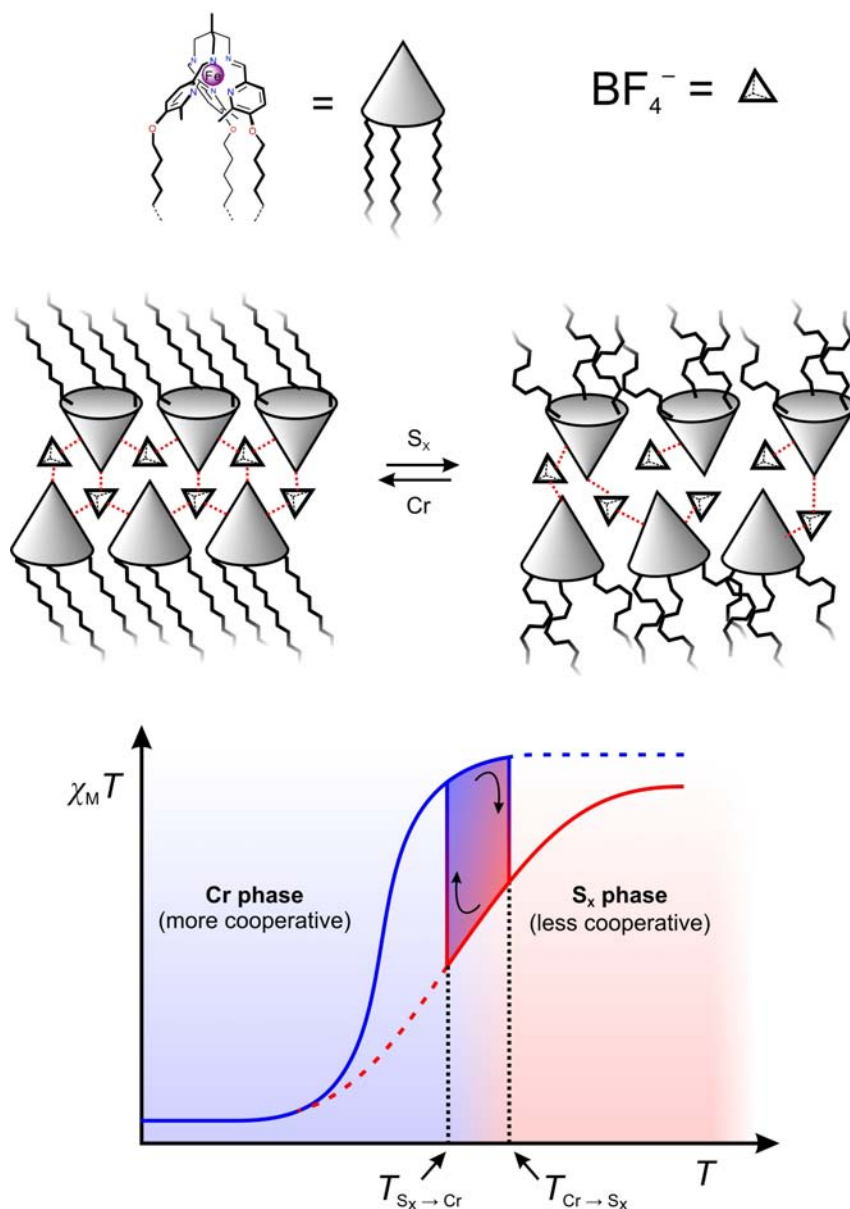
**Figure 88.** On the top, proposed organization of the ionic bilayers of $C_n$-27 ($n$ = 12, 14, 16) in crystalline state (Cr) and mesophase ($S_X$) with intermolecular contacts represented by red dashed lines. On the bottom is the schematic plot of the transition at temperature of the phase transition between curves corresponding to the behavior in the crystalline phase and mesophase. Dashed curves show hypothetical behavior in absence of the phase transition.

The composition of $C_{18}$-26 differs from the analogous compound $C_{18}$-27 only by the anion ($ClO_4^-$ instead of $BF_4^-$), however, its properties are more similar to those of $C_n$-14. The striking difference can be the result of different degree of intermolecular contacts, in particular, of the weak hydrogen bonds. Lack of the homologous compounds did not allow us to determine the kind of the transformation the compound undergoes upon melting, but we can expect very similar structural features like those found for compounds $C_n$-14 and $C_n$-27.

### 2.8.10  Summary

1.  The chemical modification of the parent system **6** provided liquid crystalline systems which show spin-transition at $T_{1/2} \sim 360$ K;

2.  The crystal structure of the alkylated complex **C$_6$-26** was determined. The crystal packing is segregated into ionic bilayers and paraffinic layers;

3.  The segregated structure is preserved in the higher homologues as indicated by the XRD data;

4.  For compounds **C$_n$-27** ($n = 12, 14, 16, 18, 20$) a dependence of the packing on the length of alkyl chains is found. Accordingly, the compounds are separated into group I ($n = 12, 14, 16$) and group II ($n = 18, 20$);

5.  For compounds **C$_n$-27** ($n = 12, 14, 16, 17, 18, 20$) a magnetic anomaly is detected which coincides with the solid $\leftrightarrow$ liquid crystal phase transition. Cooling and heating curves do not coincide, but result in a hysteresis loop. Its width increases on going from group I to group II but with a change in the abruptness;

6.  The width of the hysteresis loop is dependent on the heating/cooling rate and is insensitive to the strength of the external magnetic field;

7.  The reason for the magnetic anomaly was ascribed to the reversible modification of the intermolecular contacts through the phase transition.

## 2.9 Cumulative table of the mononuclear systems

| Parent compound | | ▶ | Mesogenic compound | | | |
|---|---|---|---|---|---|---|
| *Code* | *Ligand* | *A⁻* | *Code* | *Ligand* | *A⁻* | *s* |
| **A** [155] | *tren(imd)₃* | $BF_4^-$ | – | – | – | – |
| **B** [160] | *tren(py)₃* | $ClO_4^-$ | **C₆-7** | *tren(C₆-py)₃* | $ClO_4^-$ | 0 |
| | | | **C₁₈-7** | *tren(C₁₈-py)₃* | $ClO_4^-$ | 0 |
| | | | **C₁₂-8** | *tren(C₁₂-py)₃* | $BF_4^-$ | 0 |
| | | | **C₁₈-9** | *tren(C₁₈-py)₃* | $BF_4^-$ | 0.5 |
| | | | **C₁₈-10** | *tren(C₁₈-py)₃* | $SO_4^{2-}$ | 4 |
| | | | **C₁₈-11** | *tren(C₁₈-py)₃* | $F^-$ | 3.5 |
| | | | **C₁₈-12** | | | 0 |
| | | | **C₁₆-13** | *tren(C₁₆-py)₃* | $Cl^-$ | 3.5 |
| | | | **C₁₆-14** | | | 0.5 |
| | | | **C₁₆-15** | | | 0 |
| | | | **C₁₈-13** | *tren(C₁₈-py)₃* | $Cl^-$ | 3.5 |
| | | | **C₁₈-14** | | | 0.5 |
| | | | **C₁₈-15** | | | 0 |
| | | | **C₂₀-13** | *tren(C₂₀-py)₃* | $Cl^-$ | 3.5 |
| | | | **C₂₀-14** | | | 0.5 |
| | | | **C₂₀-15** | | | 0 |
| | | | **C₁₈-16** | *tren(C₁₈-py)₃* | $Br^-$ | 3 |
| | | | **C₁₈-17** | *tren(C₁₈-py)₃* | $I^-$ | 0 |
| | | | **C₁₈-18** | *tren(C₁₈-py)₃* | $C_{18}TOS^-$ | 1 |
| **1** | *tren(6-Mepy)₃* | $ClO_4^-$ | **C₆-19** | *tren(C₆-6-Mepy)₃* | $ClO_4^-$ | 0 |
| | | | **C₁₂-19** | *tren(C₁₂-6-Mepy)₃* | | 0 |
| | | | **C₁₈-19** | *tren(C₁₈-6-Mepy)₃* | | 0 |
| | | | **C₁₈-20** | *tren(C₁₈-6-Mepy)₃* | $BF_4^-$ | 0 |
| **1-Zn** | | | **C₂₀-21** | *tren(C₂₀-6-Mepy)₃* | $PF_6^-$ | 0 |
| | | | **C₁₈-22** | *tren(C₁₈-6-Mepy)₃* | $SiF_6^-$ | 0 |
| | | | **C₂₀-23** | *tren(C₂₀-6-Mepy)₃* | $SO_4^{2-}$ | 3 |
| **2** | *tach(imd)₃* | $BF_4^-$, $ClO_4^-$ | – | – | – | – |
| **3** | *tach(py)₃* | $ClO_4^-$ | **C₁₈-24** | *tach(C₁₈-py)₃* | $C_{18}TOS^-$ | 2 |
| **4** | *tame(imd)₃* | $ClO_4^-$ | – | – | – | – |
| **5** | *tame(py)₃* | $ClO_4^-$ | **C₁₈-25** | *tame(C₁₈-py)₃* | $C_{18}TOS^-$ | 1 |
| **6** | *tame(6-Mepy)₃* | $ClO_4^-$ | **C₆-26** | *tame(C₆-6-Mepy)₃* | $ClO_4^-$ | 0 |
| | | | **C₁₈-26** | *tame(C₁₈-6-Mepy)₃* | $ClO_4^-$ | 0 |
| | | | **C₁₀-27** | *tame(C₁₀-6-Mepy)₃* | $BF_4^-$ | 0 |
| | | | **C₁₂-27** | *tame(C₁₂-6-Mepy)₃* | $BF_4^-$ | 0 |
| | | | **C₁₄-27** | *tame(C₁₄-6-Mepy)₃* | $BF_4^-$ | 0 |
| | | | **C₁₆-27** | *tame(C₁₆-6-Mepy)₃* | $BF_4^-$ | 0 |
| | | | **C₁₇-27** | *tame(C₁₇-6-Mepy)₃* | $BF_4^-$ | 0 |
| | | | **C₁₈-27** | *tame(C₁₈-6-Mepy)₃* | $BF_4^-$ | 0 |
| | | | **C₂₀-27** | *tame(C₂₀-6-Mepy)₃* | $BF_4^-$ | 0 |
| | | | **C₂₀-28** | | | 1 |
| | | | **C₁₈-29** | *tame(C₁₈-6-Mepy)₃* | $C_{18}TOS^-$ | 2 |

# 3 One-dimensional iron(II) systems

## 3.1 Parent systems

### 3.1.1 Introductory remarks

Chapter 3 is organized similarly to Chapter 2. In the first section parent systems, their characterization and properties are described. The second section is devoted to modified systems obtained by introducing mesogenic alkyl moieties into the parent complex systems.

In the following a short overview is presented of the reported relevant data (1977–2008) concerning the triazole-based systems of iron(II).

### 3.1.2 Overview of the literature on 1,2,4-triazole-based iron(II) complexes

Among all iron(II) spin-crossover compounds known to date, the extensively studied polymeric triazole systems appeared to have the greatest potential for technological applications, for example in molecular electronics [3, 19, 60] or as temperature sensors [57, 60]. This is due to their near-ideal spin-crossover characteristics: pronounced thermochromism, transition temperatures near room temperature, large thermal hysteresis and relatively high stability [60, 315].
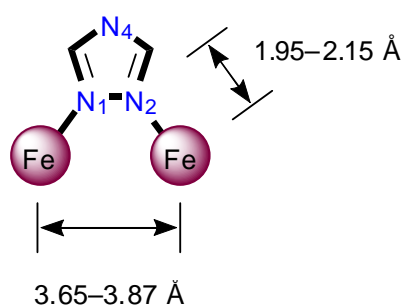
**Figure 89.** Geometry of the $N1,N2$ bridging mode of 1,2,4-triazole in polymeric complexes of iron(II).

Several types of the coordination can be realized with triazole ligands [315, 316], however, the bridging mode $N1,N2$ is the coordination mode usually found with triazoles where the $N4$-position is substituted (Figure 89) [317]. In this mode the two iron(II) ions are

brought together at distances of about 3.65–3.87 Å depending on the distance Fe–N determined by the spin state (1.95–2.15 Å) [94]. For the often encountered triple triazole *N*1,*N*2 bridge the metal ions are on a trigonal axis where the angles N–M–N around the metal ions are 90° and the M–N–N angles are ideally 125.26°. This angle is so close to the angle of the exocyclic free donor electron pair of a regular five-membered ring, 126°, that this triple bridge can be formed without appreciable strain. Almost all structurally characterized iron(II) complexes of triazoles show the triple *N*1,*N*2 bridge [88-90].

Work on triazole-based iron(II) systems exhibiting spin-transition, started in 1977 with the first report by Haasnoot *et al.* [318]. During the 1980's only the Novosibirsk group under guidance of Prof. L. Lavrenova investigated polymeric triazole systems [319, 320]. Renewal of the interest in these systems was associated with the French group of Prof. O. Kahn [19, 89, 91-94]. At the beginning of the 1990's his group reported on the successful tuning of the spin-transition properties in "molecular alloys" of the triazole complexes [321]. It was possible to synthesize materials, the transition temperature and the hysteresis width of which were suitable for use in devices operating at room temperature. Thereafter several groups were involved in the study of the iron(II)-based triazole systems (see ref. [317]).

Particularly, nowadays the interest in the triazole systems lies in the pronounced thermochromic properties. In general, the thermochromism of the iron(II) azole-type systems is due to absence of metal-to-ligand or ligand-to-metal absorption bands in the visible region [315]. Therefore, the coloration of the azole-complexes is determined mostly by the *d*–*d* transitions of the coordination chromophore $Fe^{II}N_6$. The high-spin form of the compounds is usually colorless with the absorption band located in the near infrared (NIR) region at 770–920 nm due to the transition $^5T_{2g} \rightarrow {}^5E_g$ [115, 315]. In the UV/VIS spectra of the low-spin compounds the band of the parity forbidden $^1A_{1g} \rightarrow {}^1T_{1g}$ *d*–*d* transition occurring at 520–550 nm is observed which determines the purple-pink coloration of the complexes. Since the triazole-based compounds are highly thermochromic, for some of them the thermal spin-transition was studied optically using a specially designed UV/VIS spectrometer [212, 322].

According to Kahn *et al.* [60], four different types of the spin-transition regime in triazole-based compounds of iron(II) may be distinguished:

1) The very abrupt transitions with a well-shaped thermal hysteresis loop and a perfect reproducibility of this loop over successive thermal cycles. It has been observed for $[Fe(NH_2trz)_3](NO_3)_2$ ($NH_2trz$ is 4*H*-1,2,4-triazol-4-amine) [306, 319] and $[Fe(Htrz)_2(trz)](BF_4)$ (Htrz is 4*H*-1,2,4-triazole, trz – 1,2,4-triazolato anion) [92, 323].

The abruptness of the transition is associated with the cooperativity of the interactions between the spin-crossover centers [28, 197, 271]. In the chain-like triazole-based systems the cooperativity is assumed to be due to the strong intrachain interactions [324]. For example, the spin-transition in $[Fe(Htrz)_2(trz)](BF_4)$ is exceptionally abrupt in both the warming and cooling modes which was ascribed to the bridging anionic triazolato ligands. On the other hand, long-range interactions seemingly also play an important role in defining the parameters of the transition [325].

2) The spin-transitions occurring over a range of at least 10 K, while the hysteresis width is in the range of 5 to 20 K. Many $[Fe(Rtrz)_3]Anion_2 \cdot sH_2O$ compounds exhibit such behavior [320, 326], for instance, $[Fe(NH_2trz)_3](BF_4)_2 \cdot H_2O$ with a hysteresis loop of 7 K centered at 255 K. In systems with less abrupt transitions the cooperativity was assumed to be mediated by water molecules or by anions with the sulfonate group ($-SO_3^-$) [81, 93, 133, 327].

3) The spin-state change is governed by the synergy with the dehydration-rehydration process. This happens, for instance, for $[Fe(NH_2trz)_3](p\text{-tol})_2 \cdot 2H_2O$ (*p*-tol is tosylate) [212]. At room temperature, the material is low-spin and has a violet color, however, as the temperature increases, the non-coordinated water molecules are removed, followed by an extremely abrupt transition at 361 K from the metastable low-spin state to the stable high-spin state of $[Fe(NH_2trz)_3](p\text{-tol})_2$. The high-spin ↔ low-spin transitions for the dehydrated compound $[Fe(NH_2trz)_3](p\text{-tol})_2$ are smoother. Usually, the dehydrated material is hygroscopic and spontaneously reverts to the starting material in a humid atmosphere at room temperature.

4) Some materials resemble those described in 3), with two important differences: the transitions for the dehydrated material occur at much lower temperature than for the hydrated one, and the dehydrated material is stable in normal conditions, that is, it does not reabsorb water. A typical example of such a behavior is offered by $[Fe(hyettrz)_3]Anion_2 \cdot 3H_2O$ with hyettrz = 4-(2′-hydroxy-ethyl)-1,2,4-triazole and Anion = 3-nitro-phenylsulfonate [57]. The low-spin → high-spin transition for this compound is detected optically at 370 K, whereas the transition temperature for the dehydrated material $[Fe(hyettrz)_3](Anion)_2$ is near 105 K. In other words, once the starting violet material has turned white by heating, it remains white being in the high-spin state when coming back to room temperature.

Extensive researches of the triazole-based systems allowed to determine the variables which have influence on the magnetic and thermochromic properties of the complexes. These we shall review separately.

*Structure.* For the first 1,2,4-traizole-based spin-crossover complex reported by Haasnoot *et al*. with the formula $[Fe(Htrz)_2(trz)](BF_4)$ the elemental analysis along with the IR data suggested the linear polymeric structure [318]. Almost twenty years later the system was reinvestigated by the Australian [323] and the French groups [92] along with systems with other anions ($ClO_4^-$, $PF_6^-$). In all cases an abrupt and almost complete spin-transition low-spin $\leftrightarrow$ high-spin was reported. In the following the EXAFS and WAXS studies of the compound $[Fe(Htrz)_2(trz)](BF_4)$ confirmed the chain-like polymeric structure of the compound with the bridging triazole and triazolato groups [328, 329] where each iron(II) ion adopts the $N_6$ coordination environment. It was also established that in the low-spin state the iron(II) ions are linearly aligned whereas in the high-spin state the polymeric chains have zig-zag conformation due to tetragonal distortion of the coordination sphere. Earlier [319, 320, 326] it was concluded on the basis of the IR and UV/VIS data that a similar organization of the iron(II) compounds exists as in the case of structurally characterized copper(II) analogues $[Cu(NH_2trz)_3](A)_2 \cdot sH_2O$ (A = $ClO_4^-$, $BF_4^-$, $SiF_6^{2-}$; s = 0.5, 1) [330, 331]. Despite numerous attempts it was impossible to grow crystals of the iron(II)-based coordination polymers. In many cases instead of polymeric compounds trinuclear species were obtained with the general formula $[Fe_3(Rtrz)_6(H_2O)_6](Anion)_6 \cdot sH_2O$ where only the central iron(II) ion is surrounded by six triazole units establishing the $Fe^{II}N_6$ chromophore. These triazole units are also bridged to the terminal iron(II) ions coordinated to water molecules. Each of the terminal iron(II) ions has the $Fe^{II}N_3O_3$ chromophore and therefore too weak ligand field strength for spin-transition. Only the central iron(II) ion undergoes spin-transition upon cooling [88-90, 317, 332].

*Water content.* Already the first reports on the triazole-based complexes emphasized the importance of the presence of water molecules in the propagation of the cooperative interactions which influence the temperature of the spin-transition, its abruptness and completeness. In general, insertion of non-coordinated solvent molecules in these systems stabilizes the low-spin state [333]. For instance, in compound $[Fe(Htrz)_{2.85}(NH_2trz)_{0.15}](ClO_4)_2 \cdot sH_2O$ to observe the abrupt spin-transition centered at *ca*. 305 K with 17 K hysteresis loop it was necessary to keep the compound in the humid atmosphere inside the hermetically closed glass tube. Otherwise at room temperature, under 1 atm, release of the non-coordinated water molecules favored smooth spin-transition centered at *ca*. 265 K with a weak thermal hysteresis of about 5 K [81]. Another example is provided by the systems $[Fe(hyettrz)_3]$(3-nitrophenylsulfonate)$_2 \cdot$Solv (hyettrz = 4-$HOC_2H_4$-trz, 2-(4*H*-1,2,4-triazol-4-yl)ethanol) whose properties depend dramatically on the nature of the solvent as follows: Solv = 0 ($T_{1/2} \sim$ 105 K) < DMA ($T_{1/2} \sim$ 145 K) < MeOH ($T_{1/2} \sim$ 175 K) < DMF

($T_{1/2}$ ~ 235 K) < $3H_2O$ (low-spin at room temperature) [333, 334]. The hydrate [Fe(hyettrz)$_3$](3-nitrophenylsulfonate)$_2 \cdot 3H_2O$ loses water when heated and this is accompanied by a spin-change to the high-spin state [57]. Several other examples of spin-state changes induced by water removal were identified for the 1D polymeric chain compounds [58, 92, 133, 212, 264, 314, 323, 335, 336].

   *Nature of anions and pressure effect.* Lavrenova *et al.* have analyzed the effect of the substituent of the triazole ligands and of the anion on the electronic structure of the central atom and the local symmetry of the $N_6$ polyhedron [265, 266, 337-339]. For example, within the [Fe(NH$_2$trz)$_3$](Anion)$_2 \cdot sH_2O$ series an increase of the transition temperatures with decreasing anion radii was observed along the series of anions: $ClO_4^-$, $I^-$, $Br^-$, $NO_3^-$, $Cl^-$ [266, 337, 338]. The EXAFS studies on the low-spin complexes showed that the Fe–N bond distances tend to decrease with the above mentioned series [266, 337, 339]. Furthermore, $^{57}$Fe Mössbauer spectroscopy [338] and X-ray fluorescence spectroscopic studies [265] confirmed that the decrease of interatomic distances correlates with the covalency of the Fe–N bond along the series of anions. Therefore, it was concluded that this increase of transition temperatures is associated with the increasing anion-cation interactions and thereby resulting increase of the electrostatic pressure [266, 337]. Garcia *et al.* confirmed the observed dependence and reported on the invariance of the hysteresis width (13±4 K) within the [Fe(hyetrz)$_3$](Anion)$_2$ series on the size of the anions ($Cl^-$, $NO_3^-$, $Br^-$, $I^-$, $BF_4^-$, $ClO_4^-$, $PF_6^-$). Furthermore, the hysteresis width was also not altered upon incorporation of the water molecules into the lattice. In addition, it was shown that for the compound [Fe(hyetrz)$_3$](3-nitrophenylsulfonate)$_2$ the applied external pressure leads to a shift of $T_{1/2}$ of the spin-transition to higher temperatures (from 105 K without applied external pressure up to 270 K for 8.9 kbar) without altering significantly the hysteresis width, which remained at a constant value of 10 K [334]. This fact was attributed to similar effects of the electrostatic pressure due to anion-cation interactions and of the applied external pressure. Both lead to considerable shifts of the transition temperature without significant influence on the hysteresis width.

   *Effect of the substituent R.* Despite rather elaborated and extensive work on the triazole-based systems, no dependence of the spin-transition parameters on the nature of the substituent in [Fe(Rtrz)$_3$](Anion)$_2 \cdot sH_2O$ was reported. Only in the case of the 4-alkyltriazoles-based systems with the tetrafluoroborate as anion, a gradual change of the parameters $T_{1/2}$ and $\Delta T_{80}$ with the length of the alkyl substituents was found [133]. Despite the lack of the correlation between the nature of the substituent R and the resulting magnetic properties in the pure compound, an approach was proposed, to synthesize mixed triazole-based compounds

with the desired magnetic properties. These are so-called molecular alloys which can be prepared from two types of triazole ligands, $R_1$trz and $R_2$trz. Consider, for example, an alloy of the formula $[Fe(R_1trz)_{3-3x}(R_2trz)_{3x}](Anion)_2 \cdot sH_2O$, where along each chain there is a proportion $1-x$ of $R_1$trz ligands and $x$ of $R_2$trz ligands. It was found that the alloy shows a unique spin-transition regime, with transition temperatures solely controlled by the composition defined by $x$. If the two ligands were chosen in such a way that the transition temperatures for one of the pure compound is above room temperature, and for the other pure compound below, for a particular composition of the alloy, for example, room temperature may fall in the middle of the hysteresis loop [81, 340]. Another kind of alloy involved mixed anions instead of mixed triazole ligands [60]. The spin-transition temperatures for a given type of cationic chains $[Fe(Rtrz)_3]_\infty$ have been found to depend on the nature of the anion (see above), which suggests that the spin-transition regime may be also fine-tuned through the composition of alloys of the formula $[Fe(Rtrz)_3](Anion_1)_{1-x}(Anion_2)_x \cdot sH_2O$ [60].

*Metal dilution* is another approach to control the temperature of the transition in the triazole-based iron(II) complexes. The effect of the dilution is manifested in the decrease of the transition temperature, however, it smears also the transition curve and makes the thermochromic properties less pronounced [306, 341-343].

### 3.1.3 Synthesis
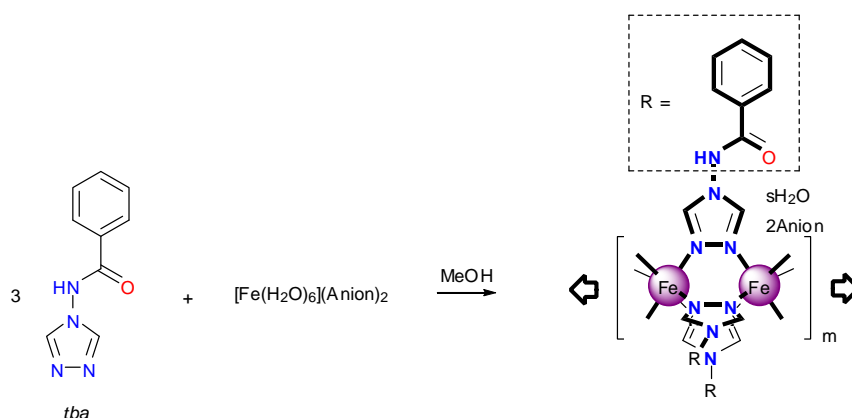


**Figure 90.** Synthetic route for compounds **30**, **32** and **34**.

The selection of the ligand system was done according to the analysis of the published works. It was suggested that the ligand *N*-4*H*-1,2,4-triazol-4-ylbenzamide (abbreviated to *tba*) could form polymeric spin-crossover complexes with iron(II) ions and also could possess the chemical modification for the synthesis of the metallomesogens [211].

The synthesis of the ligand was accomplished according to the literature source [344]. Due to the known dependence of the spin-transition properties on the type of the anion [264, 338], we chose for the synthesis of the complexes two derivatives of the sulfonic acid, namely, triflate ($CF_3SO_3^-$ compound **30**) and tosylate (*p*-tol$^-$, compound **34**), and the tetrafluroborate anion ($BF_4^-$, compound **32**) (Figure 90). The Experimental section contains all synthetic details and elemental analysis of the obtained compounds (Chapter 6.7).

## 3.2 Characterization and physical properties
## of compounds 30–35 and 30-Cu

### 3.2.1 Introductory remarks

This chapter concerns the characterization of the parent one-dimensional systems formed by the ligand *N*-4*H*-1,2,4-triazol-4-ylbenzamide (*tba*) along with the anions triflate ($CF_3SO_3^-$), tetrafluoroborate ($BF_4^-$) and tosylate (*p*-tol$^-$). The codes and the composition of the compounds included in this chapter are shown in Table 33.

**Table 33.** Schematic polymeric structure and composition of **30–35** and **30-Cu**.
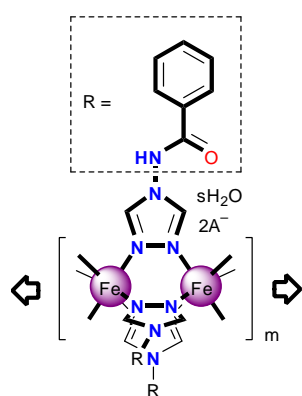
| Anion A$^-$ | s | Compound |
|---|---|---|
| $CF_3SO_3^-$ | 2 | **30** |
| | 0 | **31** |
| | 3 | **30-Cu**[a] |
| $BF_4^-$ | 3 | **32** |
| | 0 | **33** |
| *p*-tol$^-$ | 3 | **34** |
| | 0 | **35** |

[a] Compound **30-Cu** is the copper(II) analogue of compound **30**

### 3.2.2 X-ray single crystal diffraction of 30-Cu

All attempts to obtain single crystals of the iron containing compounds **30–35** were unsuccessful. This is the case up to now for all related tris(triazole) iron(II) chain systems [315, 317]. However, it was possible to obtain single crystals of the copper analogue **30-Cu** (Figure 91a, b, c). X-ray diffraction data were collected at 293 K. Due to the medium quality of the single crystals, it was not possible to decrease the *R* factor of the structure below 17.6 %. The X-ray powder diffraction pattern of **30-Cu** was collected at 293 K, where it matches that calculated from the single crystal data (Figure 92). Compound **30-Cu** crystallizes in the triclinic space group $P\bar{1}$. A selection of crystallographic data, bond distances and angles is given in Table 34 and Table 35. Figure 91a displays a fragment of the 1D polymer **30-Cu** together with the atom numbering scheme. The bis-dentate *N*-4*H*-1,2,4-triazole-4-ylbenzamide (*tba*) ligand bridges neighboring copper ions through the N1 and N2 nitrogen

atoms leading to a one-dimensional infinite polymer. Each copper(II) ion is coordinated to six N atoms belonging to six *tba* ligands defining a pseudo-octahedral symmetry. For the four independent copper ions the octahedral symmetry deviates from the ideal octahedron as indicated by the angles and bond distances (Table 35). The axial bond lengths are notably larger than the equatorial ones due to the Jahn-Teller distortion, those are in the range of 2.242(10)–2.351(10) Å for the four copper(II) ions. The average Cu–N bond length is 2.134(10), 2.154(10), 2.143(10) and 2.135(10) Å for Cu1, Cu2, Cu3 and Cu4, respectively. The intrachain Cu···Cu distance is 3.891(12) Å. These structural parameters are similar to those observed previously for other copper(II)-triazole systems [331, 345, 346]. The water molecules are located around the copper(II) ions at a distance ranging between 4.509(2)–4.951(2) Å. The three water molecules are involved into the intrachain hydrogen bonding with the CH moieties of the triazole units (Figure 91b). In Figure 91c is shown the crystal packing of **30-Cu** in the *ab* plane. The molecular crystal packing of **30-Cu** can be described as a hexagonal array of the $[Cu(tba)_3]^{2+}_\infty$ linear chains extended along the *c* direction, with water molecules and $CF_3SO_3^-$ counterions in vacancies. The distance between neighboring copper(II) linear chains is 17.816(2) Å. There are no interchain interactions neither through the phenyl group of the *tba* ligands, nor between the counterions. The shortest distance between the carbon atoms of two phenyl groups belonging to adjacent chains is 5.219(2) Å.



a
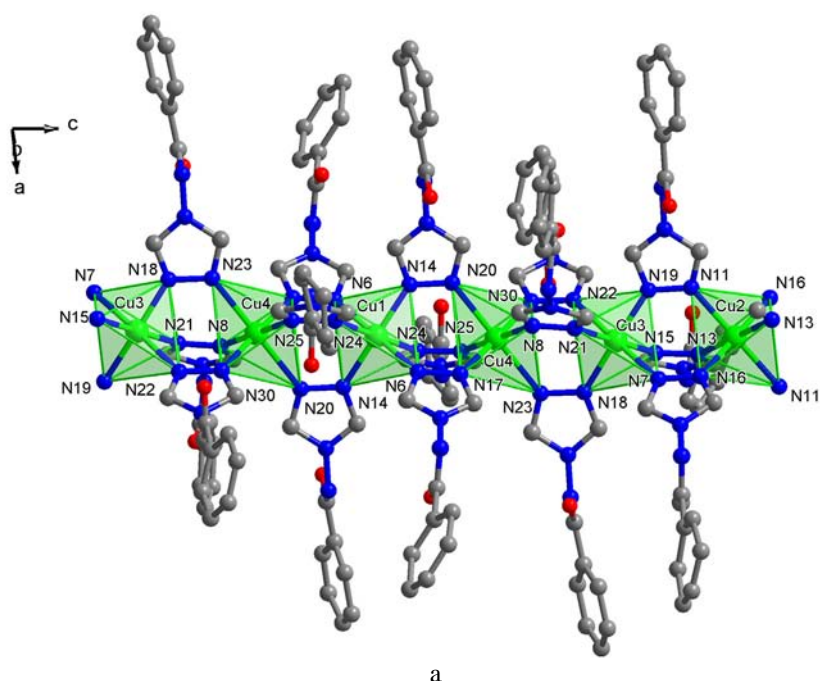
**Figure 91.** a) Crystal structure of a fragment of **30-Cu** and atom numbering scheme (shown partially for simplicity); b) Weak hydrogen bonds (dashed lines) between CH groups of the triazole units and of the water molecules (ligand molecules are shown partially for simplicity); c) Projection of the crystal structure of **30-Cu** in the *ab* plane. The anions $CF_3SO_3^-$ are shown as polyhedra whereas the water molecules as spheres.

b



c
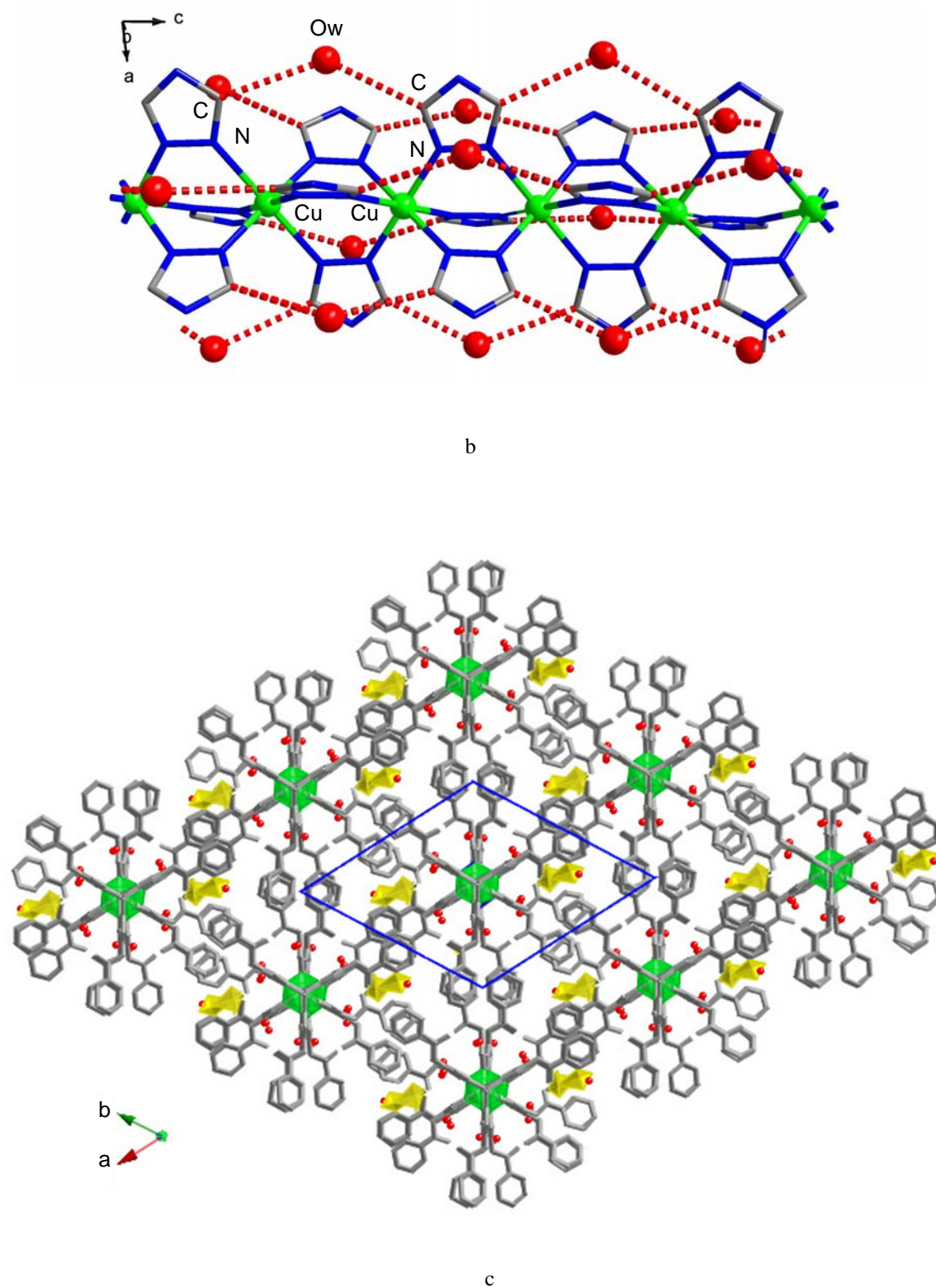
**Figure 91.** (*continued*)

**Table 34.** Crystal data and refinement details of **30-Cu**.

| | |
|---|---|
| Empirical formula | $C_{29}H_{32}CuF_6N_{12}O_{13}S_2$ |
| Formula weight | 980.31 |
| Temperature [K] | 293(2) |
| Wavelength [Å] | 0.71073 |
| Crystal system | triclinic |
| Space group | $P\bar{1}$ |
| $a$ [Å] | 17.8020(3) |
| $b$ [Å] | 17.8160(4) |
| $c$ [Å] | 23.2650(5) |
| $\alpha$ [°] | 89.2120(10) |
| $\beta$ [°] | 84.2040(10) |
| $\gamma$ [°] | 60.3130(10) |
| Volume [Å$^3$] | 6371.8(2) |
| $Z$ | 6 |
| $\rho$ [g cm$^{-3}$] | 1.533 |
| Absorption coefficient [mm$^{-1}$] | 0.709 |
| $F(000)$ | 2994 |
| $\theta$ range for data collection [°] | 1.51 to 22.75 |
| Index ranges | $-19 \leq h \leq 19$ |
| | $-19 \leq k \leq 19$ |
| | $-25 \leq l \leq 24$ |
| Reflections collected | 30807 |
| Independent reflections | 16999 |
| Data/restraints/parameters | 16999/38/715 |
| Goodness-of-fit, $F^2$ | 1.953 |
| Final $R$ indices [$I > 2\sigma(I)$] | $R1 = 0.1764,$ |
| | $wR2 = 0.4725$ |
| $R$ indices (all data) | $R1 = 0.2265,$ |
| | $wR2 = 0.5154$ |
| $\rho_{min}, \rho_{max}$ [e Å$^{-3}$] | $-1.225, 2.773$ |

**Table 35.** Selected bond lengths [Å], intermolecular contacts and angles [º] for **30-Cu**.

| | | | | | |
|---|---|---|---|---|---|
| Cu1 N14 | 2.011(9) | Cu3 N18 | 2.016(9) | Cu4 N30 | 2.008(10) |
| Cu1 N71 | 2.151(10) | Cu3 N19 | 2.029(10) | Cu4 N17 | 2.036(10) |
| Cu1 N24 | 2.242(10) | Cu3 N15 | 2.043(11) | Cu4 N25 | 2.035(11) |
| Cu2 N16 | 2.044(10) | Cu3 N21 | 2.080(10) | Cu4 N8 | 2.053(9) |
| Cu2 N11 | 2.159(10) | Cu3 N22 | 2.329(10) | Cu4 N23 | 2.329(10) |
| Cu2 N13 | 2.259(10) | Cu3 N7 | 2.365(10) | Cu4 N20 | 2.351(10) |
| | | | | | |
| N14–Cu1–N14$^a$ | 180.0(5) | N18 Cu3 N19 | 176.7(4) | N30 Cu4 N17 | 177.7(4) |
| N14–Cu1–N24 | 91.0(4) | N18 Cu3 N15 | 89.1(4) | N30 Cu4 N25 | 88.9(4) |
| N14–Cu1–N24$^a$ | 89.0(4) | N19 Cu3 N15 | 92.3(4) | N17 Cu4 N25 | 91.4(4) |
| N24–Cu1–N24$^a$ | 180.0(5) | N18 Cu3 N21 | 90.5(4) | N30 Cu4 N8 | 91.3(4) |
| N14–Cu1–N71 | 90.0(4) | N19 Cu3 N21 | 88.0(4) | N17 Cu4 N8 | 88.4(4) |
| N71–Cu1–N71$^a$ | 180.0(4) | N15 Cu3 N21 | 179.6(4) | N25 Cu4 N8 | 179.5(4) |
| N71–Cu1–N24 | 93.5(4) | N18 Cu3 N22 | 92.1(4) | N30 Cu4 N23 | 90.7(4) |
| N71$^a$–Cu1–N24 | 86.5(4) | N19 Cu3 N22 | 90.8(4) | N17 Cu4 N23 | 91.6(4) |
| N16–Cu2–N16$^a$ | 180.0(4) | N15 Cu3 N22 | 92.8(4) | N25 Cu4 N23 | 91.9(4) |
| N16–Cu2–N11 | 88.3(4) | N21 Cu3 N22 | 87.0(4) | N8 Cu4 N23 | 87.7(4) |
| N16–Cu2–N11$^a$ | 91.7(4) | N18 Cu3 N7 | 90.2(4) | N30 Cu4 N20 | 90.1(4) |
| N11–Cu2–N11$^a$ | 180.0(0) | N19 Cu3 N7 | 86.9(4) | N17 Cu4 N20 | 87.6(4) |
| N16–Cu2–N13 | 90.4(4) | N15 Cu3 N7 | 89.3(4) | N25 Cu4 N20 | 89.1(4) |
| N16–Cu2–N13$^a$ | 89.6(4) | N21 Cu3 N7 | 90.9(4) | N8 Cu4 N20 | 91.3(3) |
| N11–Cu2–N13 | 93.1(4) | N22 Cu3 N7 | 176.9(3) | N23 Cu4 N20 | 178.7(4) |
| N11–Cu2–N13$^a$ | 86.9(4) | | | | |
| N13–Cu2–N13$^a$ | 180.0(0) | | | | |

$^a$ $i = 1 - x, 1 - y, -z$

### 3.2.3   XRD data of 30, 32, 34 and 30-Cu

X-ray powder diffraction patterns of **30**, **32**, **34** and **30-Cu** were recorded at 293 K (Figure 92). Only two compounds have similar patterns, namely compounds **30** and **30-Cu**, where small discrepancies between weak reflections can be interpreted in relation with the hydration numbers of both compounds and position of the anions in the lattice. The patterns of compounds **32** and **34** are not similar and not isostructural with **30**. In all of them were found only two common intense reflections located at about the same values in the ranges of 5−6° and 23−24°. This shows, together with the fact of the comparable patterns for only the triflate complexes of iron(II) and copper(II), that although the chain structure seems to be present in all of these compounds, different packing and lattice arrangements are determined by the different nature of the anions and may yield completely different crystallographic patterns [314, 323].
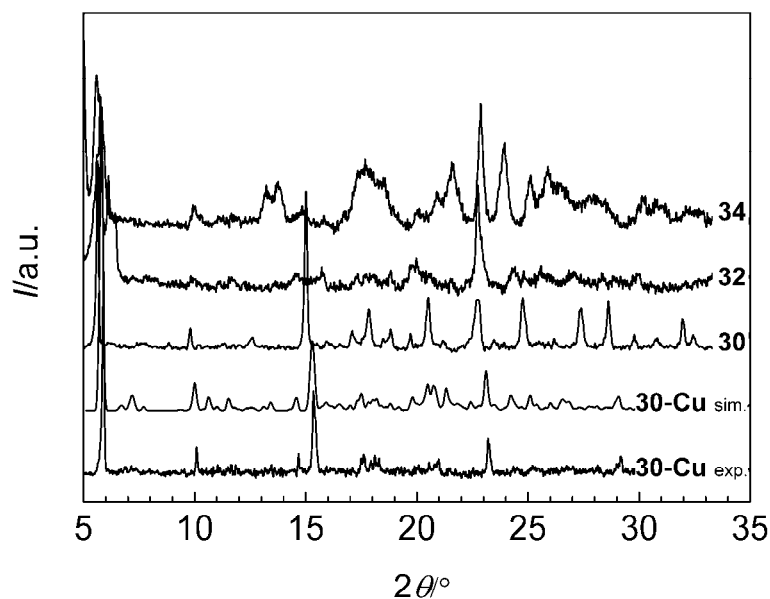


**Figure 92.** X-ray powder diffraction patterns of complexes **30**, **32**, **34** and **30-Cu** (exp.) at room temperature along with the simulated XRD pattern (sim.).

### 3.2.4   IR spectroscopic and TGA data of 30, 32, 34 and 30-Cu

Information about the *tba* coordination in complexes **30**, **32**, **34** and **30-Cu** can be derived from the IR spectra at room temperature. The intense peaks located in **30**, **32**, **34** and **30-Cu** at 627, 625, 625 and 628 cm$^{-1}$, respectively, correspond to torsion vibrations $\tau_2$ of the triazole rings bridging neighbor iron(II) or copper(II) ions (see schematic structure of the

monomeric unit in Table 33) [318]. This observation confirms the one-dimensional structure for **30** and **30-Cu** and strongly suggests the same for compounds **32** and **34**.
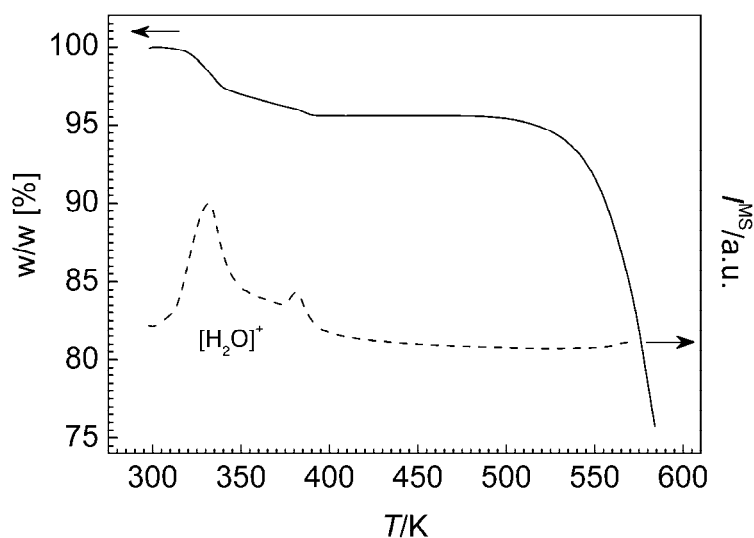


**Figure 93.** TGA data of compound **30** performed in tandem with mass spectroscopy (MS EI) following the signal of the cation $[H_2O]^+$ which emphasizes the two-step loss of crystal water.

On heating compounds **30**, **32** and **34** lose their solvate water and transform into compounds **31**, **33** and **35**, respectively. In **30** the water release takes place in two separate steps which was confirmed by thermogravimetry (TGA) in tandem with mass spectroscopy (Figure 93).

TGA and IR data for **30**, **32** and **34** are collected in Table 36.

**Table 36.** TGA and IR data for **30**, **32**, **34** and **30-Cu**.

| Compound | TGA, w/w [ %] $(T)^a$ | $v$(O–H) | $v$(C–H) | $v$(C=O) | $\tau_2$ | $v$(Anion) |
|---|---|---|---|---|---|---|
| | | IR$^b$ | | | | |
| **30** | 4.4 (330, 380 K) | 3440br | 3098 | 1694 | 627 | 1269, 1176, 1029 |
| **32** | 6.0 (337 K) | 3440br | 3129 | 1689 | 625 | 1084, 1060, 534, 522 |
| **34** | 6.1 (364 K) | 3440br | 3066 | 1686 | 625 | 1170, 1034 |
| **30-Cu** | 5.8 (350 K) | 3440br | 3071 | 1693 | 628 | 1270, 1179, 1028 |

$^a$ Value is given at the point where the plateau is reached. $T$ is the temperature at which the dehydration process is centered; $^b$ $v$, stretching; $\tau$, ring torsion vibration of triazole units.

### 3.2.5 EXAFS and XANES data of 30

The normalized XANES spectrum of **30** recorded at 80 K at the Fe $K$-edge is typical for an octahedral complex of iron(II) (Figure 94a). It includes absorption in the pre-edge

region P assigned to the symmetry-forbidden electronic dipolar transitions from $1s$ to $3d$ levels [347]. The first strong absorption (peak A) is located at 7130 eV and can be attributed to a metal $1s$ to $4p$ levels dipole-allowed transition [347]. Further, intense shoulders B and M with energies 7142 and 7154 eV, respectively, are due to multiple scattering processes [348]. Finally, absorption in the E region corresponds to the first EXAFS oscillations. The EXAFS oscillation at relatively high energy (7205 eV) evidences short Fe–N distances and the low-spin character of the iron(II) ion. The EXAFS spectrum measured at 80 K is shown in Figure 94b, whereas the Fourier transform of it is displayed in Figure 94c. The EXAFS signal provides direct information about the radial distribution of the neighboring atoms around the absorbing atom. Our data are very similar to previous EXAFS studies with similar materials (changing the triazole ligand and the counterions) demonstrating the linear local structure (Figure 95) [94, 339, 349-351]. It is composed of triazole moieties and iron(II) ions arranged in a one-dimensional fashion, where the $N1,N2$ groups of triazoles bridge adjacent metal centers. The Fourier transform at 80 K consists of five main peaks (Figure 94c). The first intense one appearing without phase correction at 1.53 Å (*i.e.* 1.96 Å after correction, see below) can be attributed to the first coordination shell $(N1)_6$ of the iron ion. The short distance clearly indicates the low-spin state. Also several peaks are distinguishable in the region of 2–4 Å, which correspond to several kinds of distances such as Fe–N2, Fe–C5 (Figure 95), and Fe1 with its two nearest Fe2 neighbors (Figure 95) [349]. Particularly important is the weak intensity peak at *ca.* 7.0 Å ascribed to the next-nearest iron neighbors Fe3 in the chain (Figure 95). Except for very special conditions, a shell at such a long distance is usually undetectable by EXAFS. In our case, as in the preceding ones by Yokohama *et al.* [349] and Michalowicz *et al.* [94], the intensity of the peak is strongly enhanced due to the well-documented focusing effect for the collinearly arranged iron ions in the chain: Fe3–Fe2–Fe1–Fe2–Fe3 (Figure 95). The presence of this peak provides a new confirmation of the polymeric structure of **30**. The curve-fitting analysis for the first coordination sphere of the iron was performed (Figure 94d). The fitting variables were the Fe–N distance, the Debye-Waller factor $\sigma$ and the edge energy shift $\Delta E_0$. The coordination number $N$ was fixed to 6. The obtained values were $d^{\text{Fe–N}} = 1.96$ Å, $\sigma = 0.068$ Å, $\Delta E_0 = 1.8$ eV with goodness of fit $\rho = 1.2$ %. The value of the Fe–N distance is in good agreement with previously reported data recorded on similar compounds [339, 349-351].
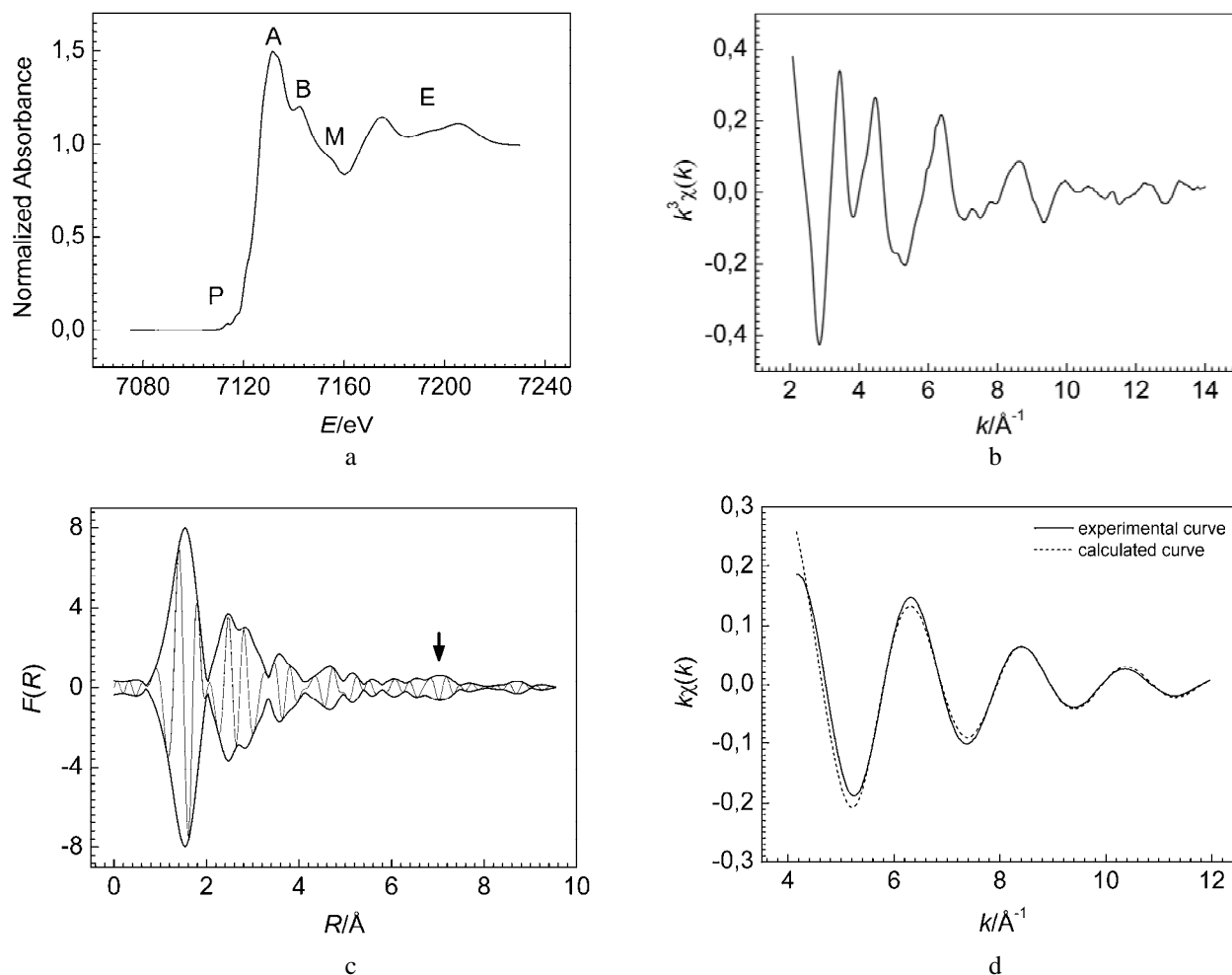
**Figure 94.** Complex **30**: a) Edge spectrum at 80 K. P, pre-edge; A, top of the edge; B and M, shoulders; E, EXAFS oscillations; b) Weighted EXAFS signal $k^3\chi(k)$; c) Modulus and imaginary parts of the Fourier transform of the EXAFS spectrum at 80 K. The arrow points at the peak at ~ 7 Å, which corresponds to the enhanced Fe1–Fe3 signal due to the multiple scattering path Fe1–Fe2–Fe3; d) Comparison of the experimental and calculated $k\chi(k)$ values for the first filtered shell.
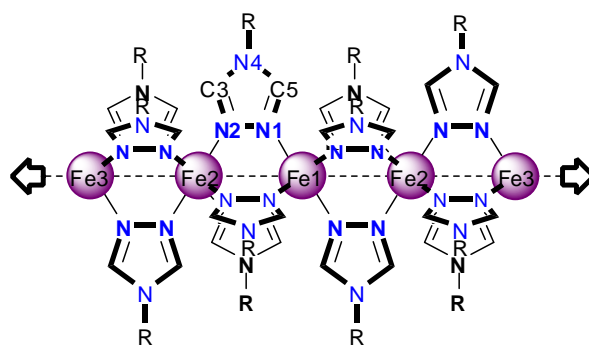


**Figure 95.** Schematic linear chain structure of the coordination core $[Fe(R\text{-}trz)_3]^{2+}_\infty$ in **30–35** with collinear iron(II) ions. R is the same as in Table 33.

### 3.2.6   Magnetic properties

The magnetic data of compounds **30**–**35** expressed in the form of $\chi_M T$ *vs T*, $\chi_M$ being the molar magnetic susceptibility and *T* the temperature, are shown in Figure 96a, b, c. Compound **30** is in the low-spin configuration at 290 K as shown by the low $\chi_M T$ value (Figure 96a). Upon heating $\chi_M T$ increases abruptly, attaining the value of 3.29 cm$^3$ K mol$^{-1}$ at 400 K. TGA experiments show that dehydration takes place in the same temperature region as the spin-state change (Figure 93). Both dehydration and spin-state change take place in two distinct steps. Synergy between dehydration and spin-state change as observed in this material has been reported in several other cases [19, 60, 335].

For compound **32**, the $\chi_M T$ value at 330 K is 3.41 cm$^3$ K mol$^{-1}$, which falls into the range of values expected for a high-spin iron(II) (Figure 96b). This value decreases abruptly at around 260 K reaching a value of 0.43 cm$^3$ K mol$^{-1}$ at 230 K ($T_{1/2}\downarrow$ = 250 K). This is a consequence of spin-transition. Then, the magnetic susceptibility further decreases very gradually down to 0.07 cm$^3$ K mol$^{-1}$ at 10 K, indicating that almost all the iron(II) ions are in the low-spin state and that the transition is complete. In the warming mode, the measurement reveals a hysteresis width of 8 K ($T_{1/2}\uparrow$ = 258 K). Like **32**, compound **34** undergoes an abrupt spin-transition, but at lower temperatures ($T_{1/2}\downarrow$ = 226 K and $T_{1/2}\uparrow$ = 238 K) (Figure 96c). The $\chi_M T$ value for **34** at 290 K is 3.30 cm$^3$ K mol$^{-1}$ and diminishes slightly on lowering the temperature down to 250 K (3.07 cm$^3$ K mol$^{-1}$). Then, upon further cooling, $\chi_M T$ falls down as a consequence of change of spin state of the iron(II) ions. At 145 K, the $\chi_M T$ value is 0.19 cm$^3$ K mol$^{-1}$ corresponding to about 95 % low-spin iron(II).

For the dehydration the pristine samples were heated up to 400 K and then kept at this temperature for 15 min in the SQUID magnetometer. Subsequently, the magnetic susceptibility of the dehydrated samples was recorded from 400 K down to 10 K and up to 400 K (Figure 96a, b, c). Compound **31** exhibits an abrupt spin-transition centered at room temperature (Figure 96a). At 400 K the $\chi_M T$ value is 3.28 cm$^3$ K mol$^{-1}$, which remains practically constant down to the vicinity of $T_{1/2}\downarrow$. At 300 K, $\chi_M T$ suddenly diminishes reaching a value of 0.39 cm$^3$ K mol$^{-1}$ at 250 K and 0.090 cm$^3$ K mol$^{-1}$ at 10 K. The critical temperatures in the cooling and warming mode, $T_{1/2}\downarrow$ and $T_{1/2}\uparrow$, are 284 K and 309 K, respectively. A relatively large 25 K width hysteresis ($\Delta T_{hys}$) accompanies the spin-transition. The hysteresis loop is perfectly reproducible after several cooling-warming cycles. The spin-transition in **31** (and also in **32** and **34**) is accompanied by a change of color from white (high-spin state) to violet (low-spin state). Compound **33** exhibits a very gradual and incomplete

spin-transition (Figure 96b). At around 400 K the $\chi_M T$ value shows that all molecules are in the high-spin state (3.41 cm$^3$ K mol$^{-1}$). It remains practically constant down to 250 K, where the high-spin to low-spin transition sets in. Further decrease of the temperature gives rise to a progressive decrease of $\chi_M T$ due to the transformation of approximately 50 % of the iron(II) ions from high-spin to low-spin. Below 70 K, $\chi_M T$ corresponding to 50 % of the remaining high-spin state iron(II) ions, continues to decrease (see below). The temperature dependence of the magnetic susceptibility of compound **35** shows high-spin behavior in the whole temperature range under study between 10 and 400 K (Figure 96c). At 400 K the $\chi_M T$ value is 3.38 cm$^3$ K mol$^{-1}$ and remains constant down to 100 K, where it diminishes.
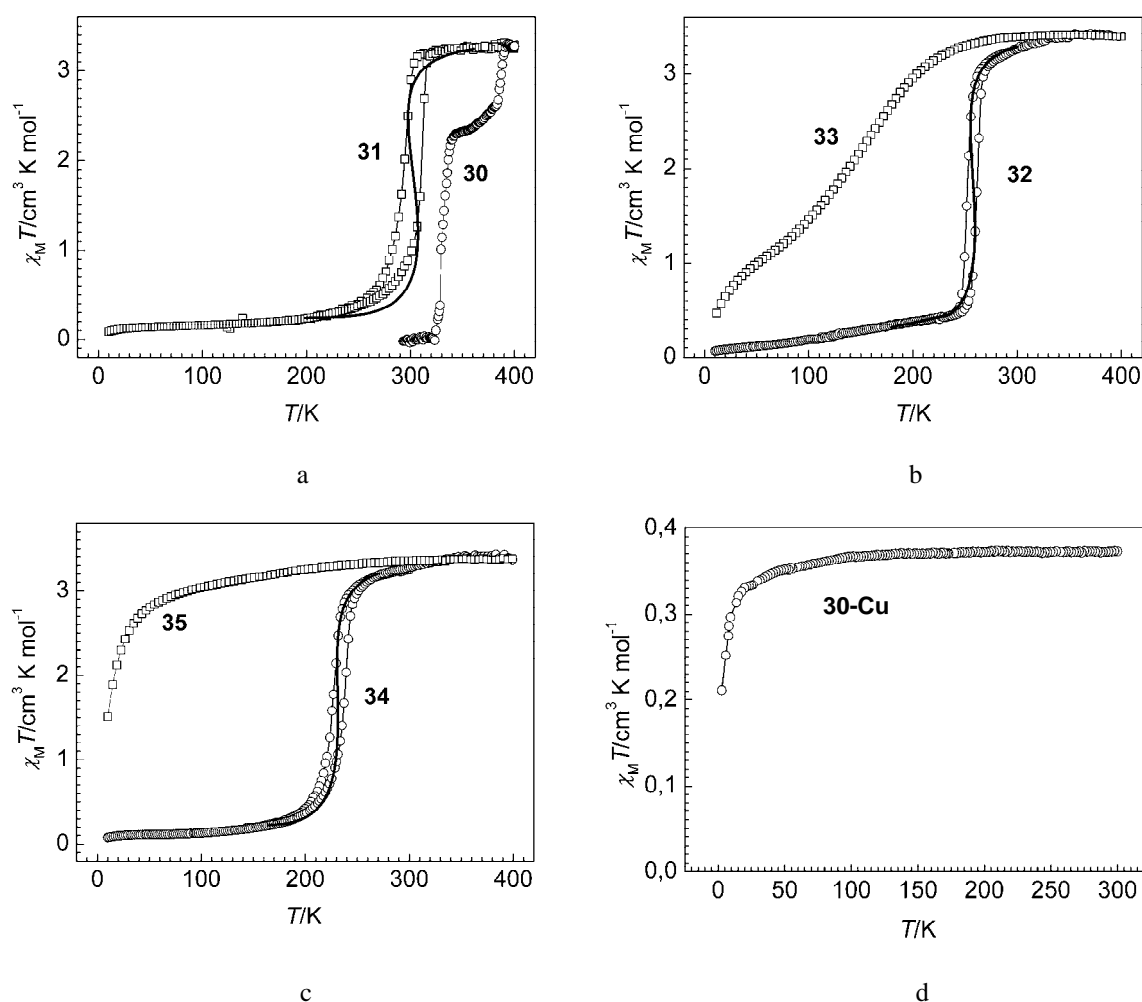


**Figure 96.** Thermal variation of the molar magnetic susceptibility $\chi_M T$ *vs T* of: a) **30**, **31**; b) **32**, **33**; c) **34**, **35** and d) **30-Cu**. Solid bold lines represent the fitting of the magnetic curves. See details in text.

The decrease of $\chi_M T$ when lowering of temperature for **33** and **35**, can be due either to zero-field splitting of the high-spin iron(II) ions or to a very weak antiferromagnetic

coupling between neighboring high-spin iron(II) ions in the polymeric chain. Such antiferromagnetic interaction is indeed observable in the copper(II) analogues **30-Cu** (Figure 96d) and the one of ref. [345].

### 3.2.7   DSC data of 31, 32, 34

The DSC measurements were carried out in the 175–400 K temperature range at a rate of 7 K min$^{-1}$. The temperature dependence of the heat flow in the heating and cooling modes for **31**, **32** and **34** is shown in Figure 97a, b, and c, respectively. Compounds **31** and **32** exhibit anomalies in the heat flow at $T_{1/2}\downarrow = 290$ K and $T_{1/2}\uparrow = 310$ K and $T_{1/2}\downarrow = 240$ K and $T_{1/2}\uparrow = 252$ K, respectively, which match reasonably well with the magnetic susceptibility data (Figure 96a, b). The small differences in the critical temperatures between the DSC and magnetic data have their origin in the different rate at which the experiments were done. For compound **34** the anomalies in the heat flow appears at $T_{1/2}\downarrow = 226$ K in the cooling mode and at $T_{1/2}\uparrow = 238$ K in the warming mode, indicating the occurrence of a $\Delta T_{hys} = 12$ K (Figure 97c). Given the experimental difference in the temperature change rates, these values agree reasonably well with the magnetic susceptibility data. Table 37 summarizes the derived thermodynamic parameters $\Delta H^{SCO}$ and $\Delta S^{SCO}$ for compounds **31**, **32** and **34**. The values are in the range expected for the spin-crossover from $S = 2$ to $S = 0$ in iron(II) compounds [105, 106, 198, 352, 353].
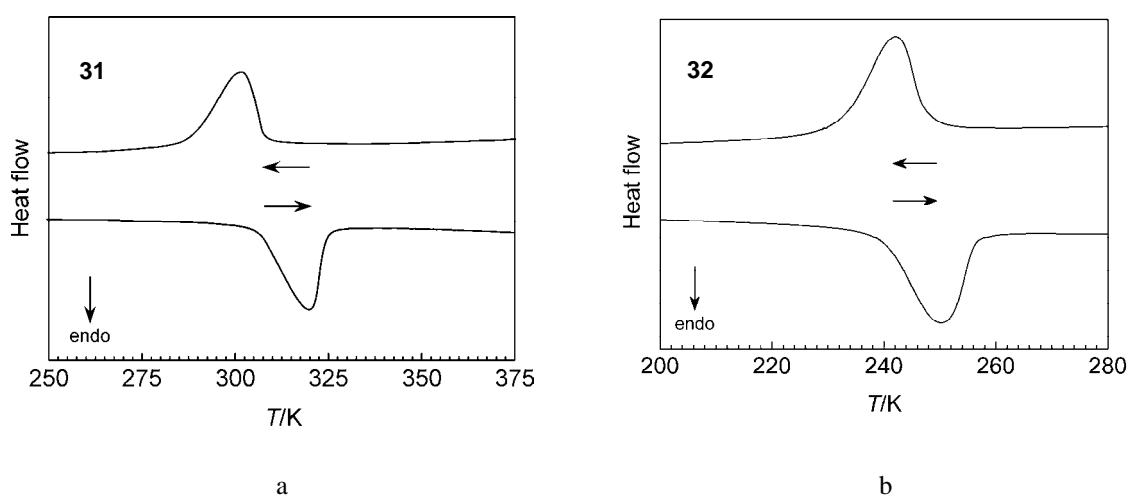


**Figure 97.** DSC data of: a) **31**; b) **32** and c) **34** in the warming and cooling modes. The run directions are shown by arrows.
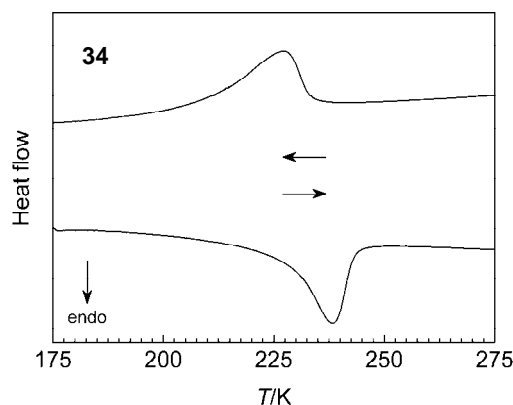
c

**Figure 97.** (*continued*)

The fitting of the magnetic curves was simulated using the equation derived from the regular solution model [Equation (13), Chapter 1.3.5] (Figure 96a, b, c). Using the parameters $\Delta H^{\mathrm{SCO}}$ and $\Delta S^{\mathrm{SCO}}$ from the DSC data the parameter $\Gamma$ corresponding to the cooperativity of the interaction was evaluated [113] (Table 37). Note, that in Figure 96a the discrepancy of the experimental magnetic data and the fitting curve is due to non-standard form of the hysteresis loop.

**Table 37.** Enthalpy $\Delta H^{\mathrm{SCO}}$ and entropy $\Delta S^{\mathrm{SCO}}$ of the spin-crossover process derived from the DSC data and parameter $\Gamma$ derived from the fitting of the magnetic curves for compounds **31**, **32** and **34**.

| Compound | $\Delta H^{\mathrm{SCO}}$ [kJ mol$^{-1}$] | $\Delta S^{\mathrm{SCO}}$ [J K$^{-1}$ mol$^{-1}$] | $\Gamma$ [kJ mol$^{-1}$] |
|---|---|---|---|
| **31** | 19.7 | 65.6 | 6.1 |
| **32** | 17.8 | 67.2 | 4.9 |
| **34** | 14.6 | 63.5 | 4.0 |

### 3.2.8 Mössbauer data of 30, 31, 32 and 34

Table 38 collects the Mössbauer parameter values and percentages of populations in the high-spin and low-spin states for compounds **30**, **31**, **32** and **34** at different temperatures. The Mössbauer spectrum of compound **30** was recorded at 80 K (Figure 98a). The spectrum clearly indicates the presence of only one slightly asymmetrical doublet with an isomer shift and a quadrupole splitting typical for low-spin iron(II), which matches with the magnetic data. For **31**, the Mössbauer spectrum at 80 K reveals a doublet typical for high-spin iron(II) (Figure 98b). Upon heating up to 330 K an increase in the intensity of the high-spin doublet is

observed. The spectrum reveals the presence of low-spin iron(II) ions, confirming the incomplete character of the spin-transition. For **32**, the Mössbauer spectra were recorded above and below $T_{1/2}$ (Figure 98c). At 290 K, the spectrum shows mainly a doublet characteristic of the high-spin state of iron(II). At 80 K, the spectrum clearly shows the change of spin state. After further cooling the high-spin doublet almost disappears whereas the low-spin fraction increases. The Mössbauer analysis confirms that almost 100 % of the iron(II) ions undergo spin-transition in **32**, as observed in magnetic measurements. For **34**, the Mössbauer spectra were recorded at 145, 230 and 290 K (Figure 98d; spectrum at 230 K is not shown). At 290 K, two doublets are observed corresponding to high-spin (92.3 %) and low-spin (7.7 %) states of the iron(II) ions. At 145 K, there is a clear inversion of the population distribution due to spin-transition, high-spin (5.0 %) and low-spin (95.0 %). The Mössbauer data of **30**, **31**, **32** and **34** agree well with their magnetic properties.

**Table 38.** Mössbauer parameters, isomer shift ($\delta$, relative to α-iron), quadrupole splitting ($\Delta E_Q$), half-width of the lines ($\Gamma_{1/2}$) and percentage of the multiplet populations in the high-spin (HS) and low-spin (LS) states at different temperatures ($A$) for **30**, **31**, **32** and **34**.

| Compound | T [K] | Spin state | $\delta$ [mm s$^{-1}$] | $\Delta E_Q$ [mm s$^{-1}$] | $\Gamma_{1/2}$ [mm s$^{-1}$] | $A$ [ %] |
|---|---|---|---|---|---|---|
| **30** | 80 | LS | 0.49(0) | 0.23(1) | 0.14(1) | 100 |
| **31** | 80 | LS | 0.51(1) | 0.25(0) | 0.15(1) | 95.4(13) |
| | | HS | 1.16(4) | 3.29(8) | *0.15* | 4.6(11) |
| | 330 | LS | 0.32(3) | *0.20* | *0.16* | 14.0(17) |
| | | HS | 1.02(0) | 2.71(1) | 0.17(1) | 86.0(40) |
| **32** | 80 | LS | 0.51(0) | 0.27(0) | 0.14(1) | 97.4(8) |
| | | HS | 1.23(8) | 3.40(18) | 0.14(15) | 2.6(16) |
| | 290 | LS | 0.29(10) | *0.15* | *0.15* | 2.5(10) |
| | | HS | 1.04(0) | 2.80(1) | 0.15(0) | 97.5(23) |
| **34** | 145 | LS | 0.52(1) | 0.28(1) | 0.14(1) | 95.0(10) |
| | | HS | 1.15(1) | 3.35(0) | *0.14* | 5.0(9) |
| | 230 | LS | 0.49(1) | 0.26(1) | 0.14(1) | 63.3(22) |
| | | HS | 1.08(0) | 3.08(1) | 0.16(1) | 36.7(34) |
| | 290 | LS | 0.40(1) | 0.14(0) | 0.14(0) | 7.7(18) |
| | | HS | 1.05(0) | 2.85(1) | 0.14(1) | 92.3(18) |

The values given in italics were fixed during the fitting.
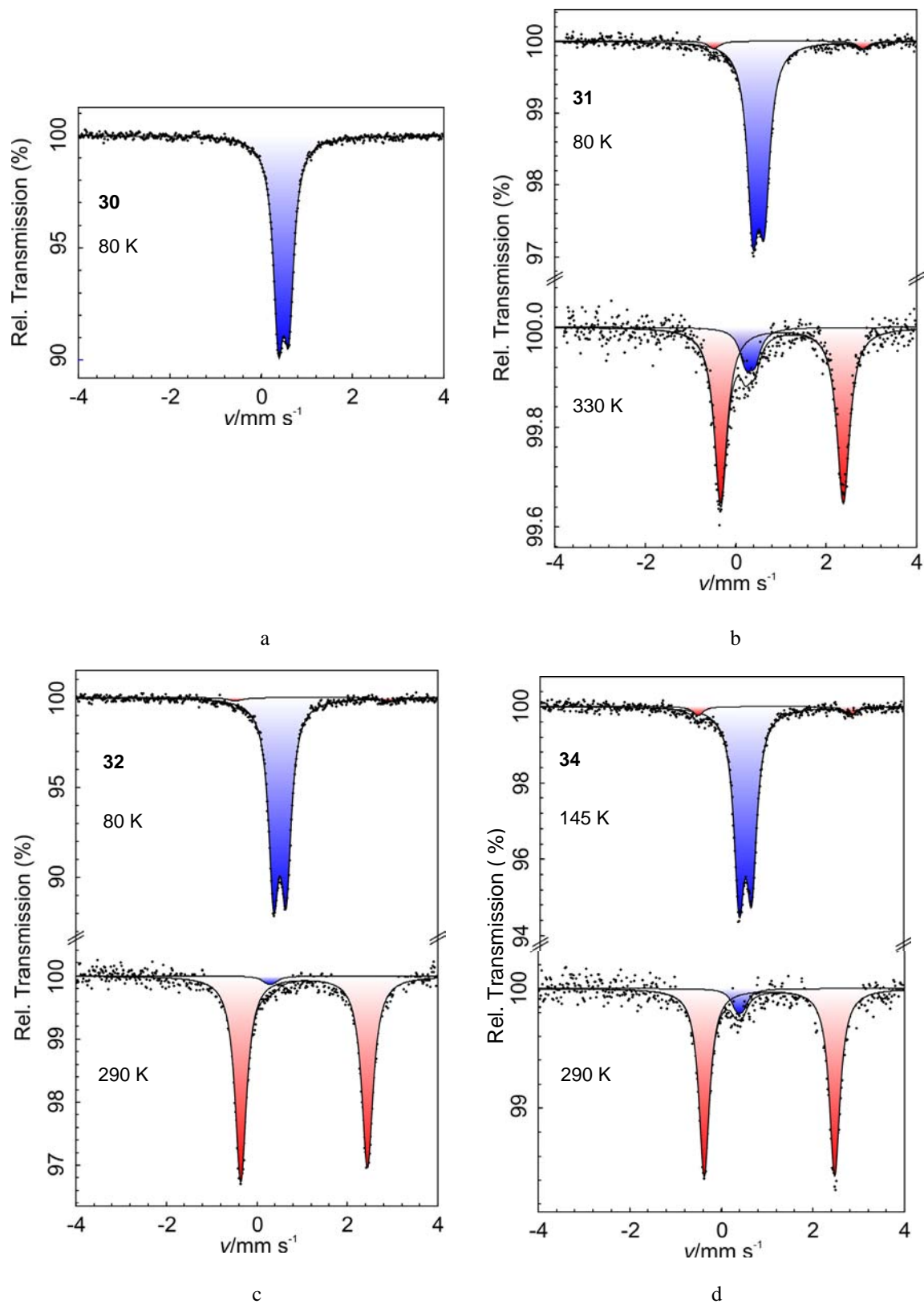
**Figure 98.** Mössbauer spectra of: a) **30**; b) **31**; c) **32**; d) **34** at indicated temperatures.

### 3.2.9   Discussion

The linear chain structure of compound **30** was convincingly derived from EXAFS data, which confirms the collinear alignment of the metal ions in the chain, bridged by triazole units. The crystal structure of **30-Cu** confirms the structural features of **30** by similar XRD patterns of the two complexes. For **32** and **34**, the demonstration of the chain structure is provided by IR spectroscopy, namely by the band assigned to the vibrations of the bridging triazole rings, featuring $C_{2v}$ symmetry. The fact that their powder X-ray patterns do not fit with the ones of **30** and **30-Cu** does not rule out a similar chain structure. The different crystallographic patterns reveal different packing and lattice arrangements.

The family of one-dimensional 4-substituted-1,2,4-triazole iron(II) compounds, **30**–**35**, presents spin-crossover behavior similar to the ones previously reported in analogous systems [19, 60, 92, 319, 354, 355]. Three main factors are supposed to influence the spin-transition and its characteristics in these compounds. These are the water content in the crystal lattice [21, 334], the chemical nature of 4-R substituted ligands [133] along with the size and the nature of anions [264], and, finally, the length of the polymeric chains [314, 316]. The stabilization of the low-spin state by interactions with lattice water molecules has frequently been observed for iron(II) spin-crossover compounds and particularly for those polymers which are based on the triazole bridge [315, 317, 352]. It is also the case for compound **30**. Upon heating, **30** loses its lattice water with an accompanying abrupt change from low-spin to high-spin state. When the obtained dehydrated material **31** is cooled, an abrupt high-spin to low-spin transition occurs at $T_{1/2}\downarrow$ = 284 K ($T_{1/2}\uparrow$= 309 K). Subsequent reheating reveals a hysteresis loop of 25 K width centered at room temperature. The length of the chains has been discussed to be critical for the observation of cooperative and complete spin-transition in such triazole polymers [19, 60, 92, 133, 264, 319, 334, 354, 355]. In a rough approximation, the longer the chains are, the lower the residual high-spin fraction is. The Mössbauer spectra of compound **31** at 80 K clearly denotes the completeness of the spin-transition, since almost all iron(II) ions are in the low-spin state. For compound **30**, the Mössbauer spectrum recorded at 80 K shows that 100 % population is in the low-spin state. These facts together with the observation that all water molecules are removed below 400 K (lattice water) rules out the possibility of having water coordinated to the outer iron(II) ions of the polymeric chains in **30** and **31** like it is observed in the trinuclear triazole-based complexes [88-90, 317, 332]. Therefore, it is probable that the length of the polymeric chains is large or the end groups are

mono-coordinated *tba* ligands like it was proposed for some of the triazole-based compounds [314].

Compounds **32** and **34** undergo abrupt spin-transitions at 258 and 238 K, respectively, both with a hysteresis width of *ca*. 10 K. Mössbauer spectra recorded for compounds **32** and **34** at liquid nitrogen temperature indicate that all iron(II) ions are in the low-spin state with a small residual high-spin fraction. For the corresponding dehydrated compounds, **33** and **35**, very different temperature dependent magnetic behavior is observed. Complex **33** presents a continuous and incomplete spin-transition at $T_{1/2}$ ~150 K, while **35** shows a paramagnetic behavior in the whole range of temperature under study, 10–400 K. These results demonstrate that the lattice water plays a dominant role in the spin-crossover behavior.

The present family of polymeric 4-substituted triazole-based iron(II) compounds add new examples to the richness of spin-transition properties of triazole bridged polymers. Since long, possible applications of these materials have been suggested as optical sensors by virtue of their thermochromic properties. Indeed, compound **30** represents a new example of material with potential applications as temperature threshold optical indicators. As compound **31** is stable at ambient atmosphere, **30** can only be used as a "single-shot" indicator. On the other hand, compound **31** fulfils the necessary conditions (abruptness, hysteresis, room temperature operation, change of color) and could be used for thermal displays or recording data. Compounds **32** and **34** could be appropriate for another temperature range of operation such as the freezing water region.

### 3.2.10  Summary

1. A new family of one-dimensional cooperative spin-crossover triazole-based polymers **30**, **32** and **34** were synthesized and characterized;

2. For the copper(II) analogue **30-Cu** of the compound **30** the crystal structure was solved at 293 K. It was found, that the bis-dentate *N*-4*H*-1,2,4-triazole-4-ylbenzamide ligand (*tba*) bridges the neighbor copper ions through the *N*1,*N*2 bridge leading to a one-dimensional structure;

3. The EXAFS data collected at 80 K for **30** agree with the linear chain structure as observed for **30-Cu**. IR spectroscopy confirmed the chain arrangement in **32** and **34** too;

4.  At room temperature, compound **30** is low-spin while **32** and **34** are high-spin. The latter two undergo cooperative thermal spin-transition at lower temperatures which is accompanied by a change of color from white (high-spin state) to violet (low-spin state);

5.  In contrast, the dehydrated compounds **31**, **33** and **35** show different behaviors. Complex **31** exhibits an abrupt spin-transition centered at room temperature with a 25 K width hysteresis loop, **33** shows a continuous and incomplete spin-transition, however, **35** is high-spin in the whole temperature range (10–400 K).

## 3.3 One-dimensional metallomesogenic systems of iron(II)

### 3.3.1 Introductory remarks

On the basis of the results described in the previous chapter, the complexes **30**, **32** and **34** were found to satisfy the condition of the spin state. They show spin-transition and were therefore used for further modification experiments towards metallomesogenic systems exhibiting spin-crossover (Figure 99).
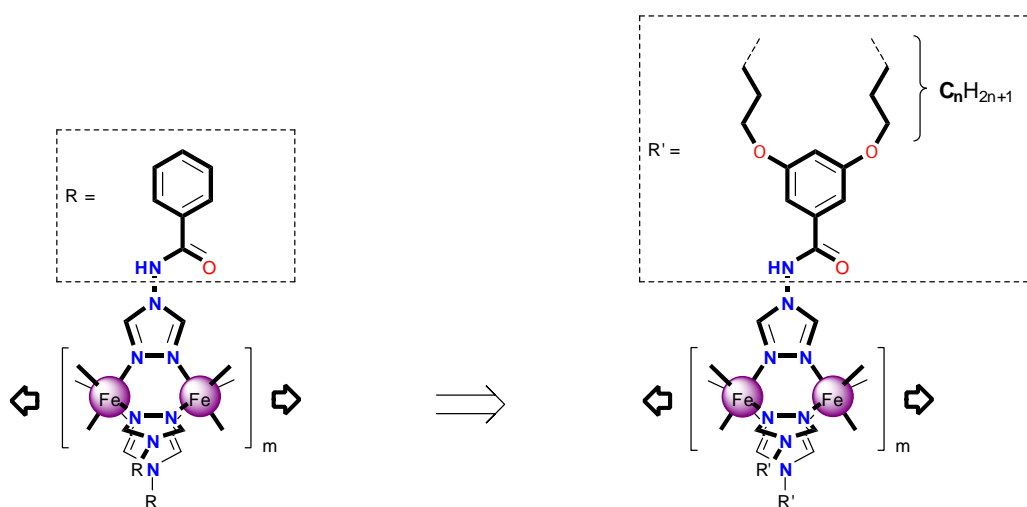


**Figure 99.** Schematic illustration of the chemical modification of the parent spin-crossover compounds **30**, **32** and **34**.

### 3.3.2 Overview of the literature on the one-dimensional iron(II) alkylated compounds with spin-crossover properties

The first reported triazole-based system with mesogenic groups was one used for the preparation of the Langmuir-Blodgett films [93]. The report by Armand *et al.* pointed out the importance of the intrachain interaction for the abrupt spin-transition in the triazole-based iron(II) polymers. This conclusion was done on the basis of the data collected on a series of compounds with the alkylated ligand 4-n-octadecyl-1,2,4-triazole (Figure 100a). The mesomorphic properties of the compounds were not reported. Later several studies were undertaken on similar compounds. The reports were focused mostly on the magnetic properties and cooperativity or gel-formation properties and therefore did not contain any information about the possible liquid crystalline properties of the systems [133, 316, 358-360]. Incorporation of such alkylated triazole complexes into a polymer matrix resulted into

preparation of hybrids consisting of poly(methyl metacrylate) and iron(II) complexes, which could be readily solution-cast into films. The composites demonstrate steep or abrupt spin-transitions preserving the hysteresis loop, which is centered at temperatures not far from the spin-transition of the pure complexes [361]. Blending of the iron(II)-based complex of 4-n-octadecyl-1,2,4-triazole with a liquid crystalline poly(oxetane) polymer gives composites which reveal a reversible spin-crossover from the low-spin to the high-spin state along with the glass transition and isotropization of the liquid crystalline polymer matrix, but without evident interplay of these transitions [362].
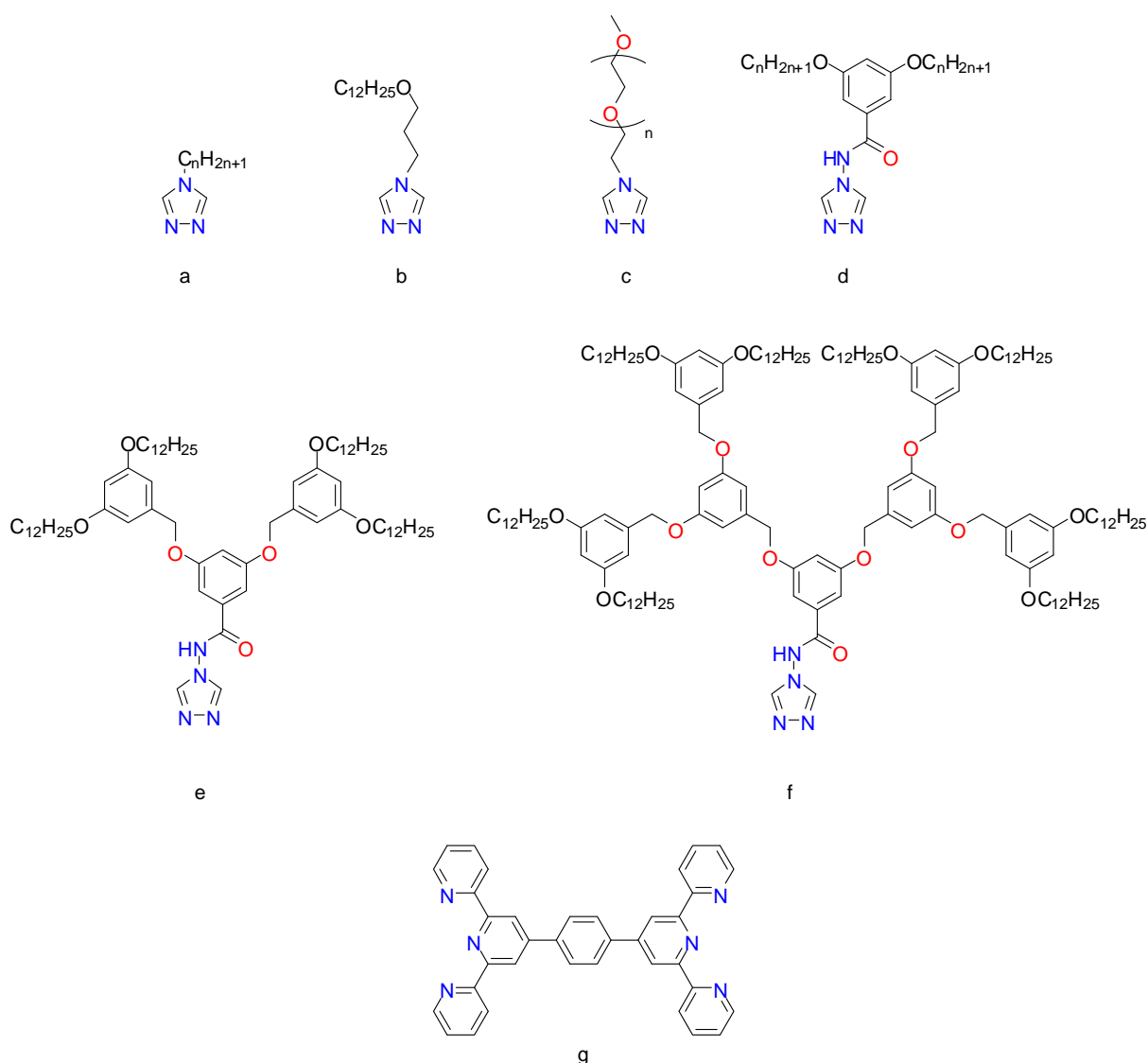


**Figure 100.** Molecular structures of the ligands with mesogenic groups (a–f) and of the bridging ligand (g) used for the preparation of one-dimensional iron(II) systems. For details see explanation in text.

Recently a study of the iron(II) spin-crossover systems based on the ligand 4-(3-dodecyloxy)propyl-1,2,4-triazole was reported (Figure 100b) [363]. As stated by the authors,

introducing the oxygen bridge into the alkyl chain allowed to decouple the packing preferences of tethered alkyl chains from those of the polymeric chains which leads to lamellar structure. The iron(II)-based derivatives doped with alcohol molecules exhibit thermal spin-transition. The appearance of the hysteresis is observed only at some chain length of the dopants. The observed bistability was ascribed to the dynamic structural transformations between the lamellar and hexagonal structures, however, as follows from the analysis of the reported DSC data, the structural transition is not coupled with the spin-transition [363]. By attaching poly(ethylene oxide) chains to the triazole units (Figure 100c) and subsequent complexation with the 3-nitrophenylsulfonate salt of iron(II) a liquid complex at ambient conditions can be obtained which exhibit spin-transition below room temperature [364].

Fujigaya *et al.* have reported on the coexistence of the spin-transition and liquid crystalline phenomena in iron(II) coordination polymers based on the ligand 3,5-bis(alkoxy)-*N*-(4*H*-1,2,4-triazol-4-yl)benzamide (Figure 100d) with perchlorate anions. However, the supposed mesomorphism of the complexes was not confirmed [211]. Later the iron(II)-based dendrimers formed by the ligands shown in Figure 100e, f were investigated. It was found, that the spin-state change in these systems is actually driven by the water release.

Another one-dimensional polymeric iron(II) system is based on the ditopic bis-terpyridine (Figure 100g) with promesogenic dihexadecyl phosphate anions [365, 366]. The compound was reported to show spin-state change in the molten state irreversible on cooling. The XRD data confirmed the reason for the observed magnetic properties which are induced by irreversible structural changes of the compound [367].

Concluding, one can say that achieving the interplay between the phase-transition and spin-transition in one-dimensional systems is still a challenge. The next chapters describe results in the field of triazole-based one-dimensional spin-crossover systems where the coexistence of the liquid crystallinity and spin-transition phenomena was found in the same temperature region with sporadic interplay between them.

### 3.3.3   Synthesis and nomenclature

The synthesis of the alkylated ligands 3,5-bis(alkoxy)-*N*-(4*H*-1,2,4-triazol-4-yl)benzamide (C$_n$-*tba*) was accomplished according to the published method [211]. The precursors DBOP and the alkylated organic acids were prepared as described in the literature [356, 357]. The synthesis of the alkylated complexes was accomplished according to a similar

procedure as used for the parent complexes, *i.e.* by the reaction of the stoichiometric amounts of the ligand and of an iron(II) salt in methanol (Figure 101). The stoichiometry of the obtained complexes is consistent with the proposed formula. The CHN analysis data of the complexes together with the synthetic details are collected in the Experimental section (Chapter 6.7), IR and TGA data are presented in Chapters 3.4.3 and 3.5.2.

The nomenclature $C_n$-**N** was adopted to label the alkylated complexes, where $C_n$ represents the alkyl substituents with $n$ carbon atoms ($C_nH_{2n+1}$), **N** corresponds to the type of the anion along with the water of crystallization. Compounds $C_n$-**36** and $C_n$-**37** are pristine and anhydrous derivatives, respectively, with the anion triflate ($CF_3SO_3^-$), $C_n$-**38** and $C_n$-**39** with the tetrafluoroborate ($BF_4^-$), $C_n$-**40** and $C_n$-**41** with the *p*-tolylsulfonate (*p*-tol$^-$). In Table 39 are collected the codes of the compounds.
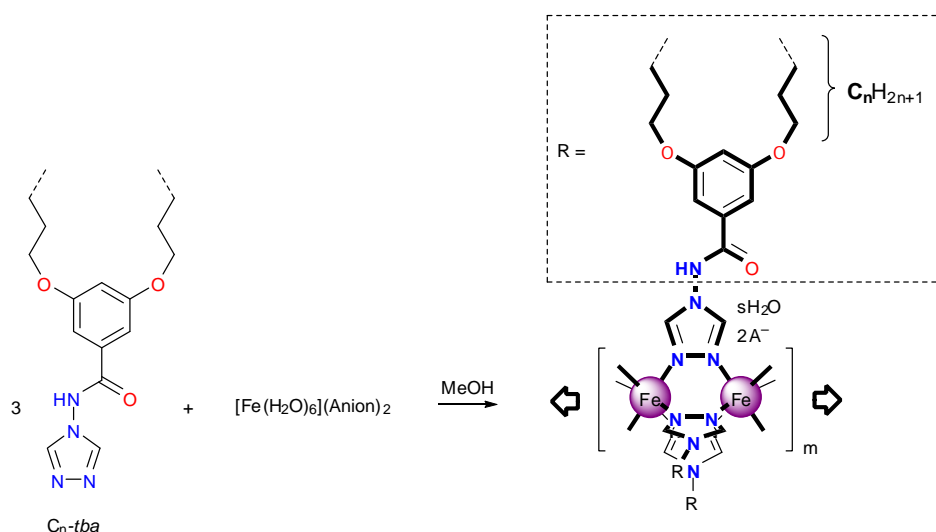


**Figure 101.** Synthetic route for compounds $C_n$-**36**, $C_n$-**38** and $C_n$-**40** ($n$ = 4, 6, 8, 10, 12).

**Table 39.** Codes of the alkylated triazole-based complexes in the pristine and the dehydrated forms separated by the comma.

| | Anion | | |
|---|---|---|---|
| $n$ | $CF_3SO_3^-$ | $BF_4^-$ | *p*-tol$^-$ |
| 4 | **C$_4$-36, C$_4$-37** | **C$_4$-38, C$_4$-39** | **C$_4$-40, C$_4$-41** |
| 6 | **C$_6$-36, C$_6$-37** | **C$_6$-38, C$_6$-39** | **C$_6$-40, C$_6$-41** |
| 8 | **C$_8$-36, C$_8$-37** | **C$_8$-38, C$_8$-39** | **C$_8$-40, C$_8$-41** |
| 10 | **C$_{10}$-36, C$_{10}$-37** | **C$_{10}$-38, C$_{10}$-39** | **C$_{10}$-40, C$_{10}$-41** |
| 12 | **C$_{12}$-36, C$_{12}$-37** | **C$_{12}$-38, C$_{12}$-39** | **C$_{12}$-40, C$_{12}$-41** |

## 3.4  Characterization and physical properties
## of compounds C*n*-36–C*n*-39

### 3.4.1  Introductory remarks

This chapter concerns the characterization and study of derivatives of the parent systems **30** and **32** formed by the ligand 3,5-bis(alkoxy)-*N*-(4*H*-1,2,4-triazol-4-yl)benzamide (C*n*-*tba*) with triflate (CF$_3$SO$_3^-$) and tetrafluoroborate (BF$_4^-$) anions. The codes and the composition of the compounds under discussion are shown in Table 40.

**Table 40**. Schematic polymeric structure and composition of **C*n*-36–C*n*-39** (*n* = 4, 6, 8, 10, 12).
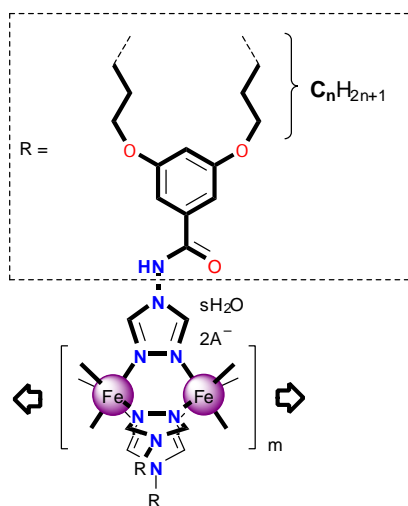


| Anion A$^-$ | s | Compound |
|---|---|---|
| CF$_3$SO$_3^-$ | 0.5 | **C$_4$-36, C$_6$-36, C$_8$-36, C$_{10}$-36, C$_{12}$-36** |
| | 0 | **C$_4$-37, C$_6$-37, C$_8$-37, C$_{10}$-37, C$_{12}$-37** |
| BF$_4^-$ | 1 | **C$_4$-38, C$_6$-38, C$_8$-38, C$_{10}$-38, C$_{12}$-38** |
| | 0 | **C$_4$-39, C$_6$-39, C$_8$-39, C$_{10}$-39, C$_{12}$-39** |

### 3.4.2  XANES and EXAFS data of C$_{12}$-36

The interpretation of the XANES and EXAFS spectra of **C$_{12}$-36** is very similar to that of the precursor complex **30** (Chapter 3.2.5).

The normalized XANES spectrum of **C$_{12}$-36** recorded at 80 K at the Fe *K*-edge is typical for an octahedral complex of iron(II) (Figure 102a). It includes absorption in the pre-edge region P assigned to the symmetry-forbidden electronic dipolar transitions from 1*s* to molecular levels implying 3*d* orbitals [347]. The first strong absorption (peak A) is located at 7130 eV and can be attributed to a metal 1*s* to molecular levels implying *4p* orbitals dipole-allowed transition [347]. Further, intense shoulders B and M with energies 7142 and 7154 eV, respectively, are due to multiple scattering processes [348]. Finally, absorption in the E region

corresponds to the first EXAFS oscillations. The EXAFS oscillation at relatively high energy (7205 eV) evidences short Fe–N distances and the low-spin character of the iron ion.
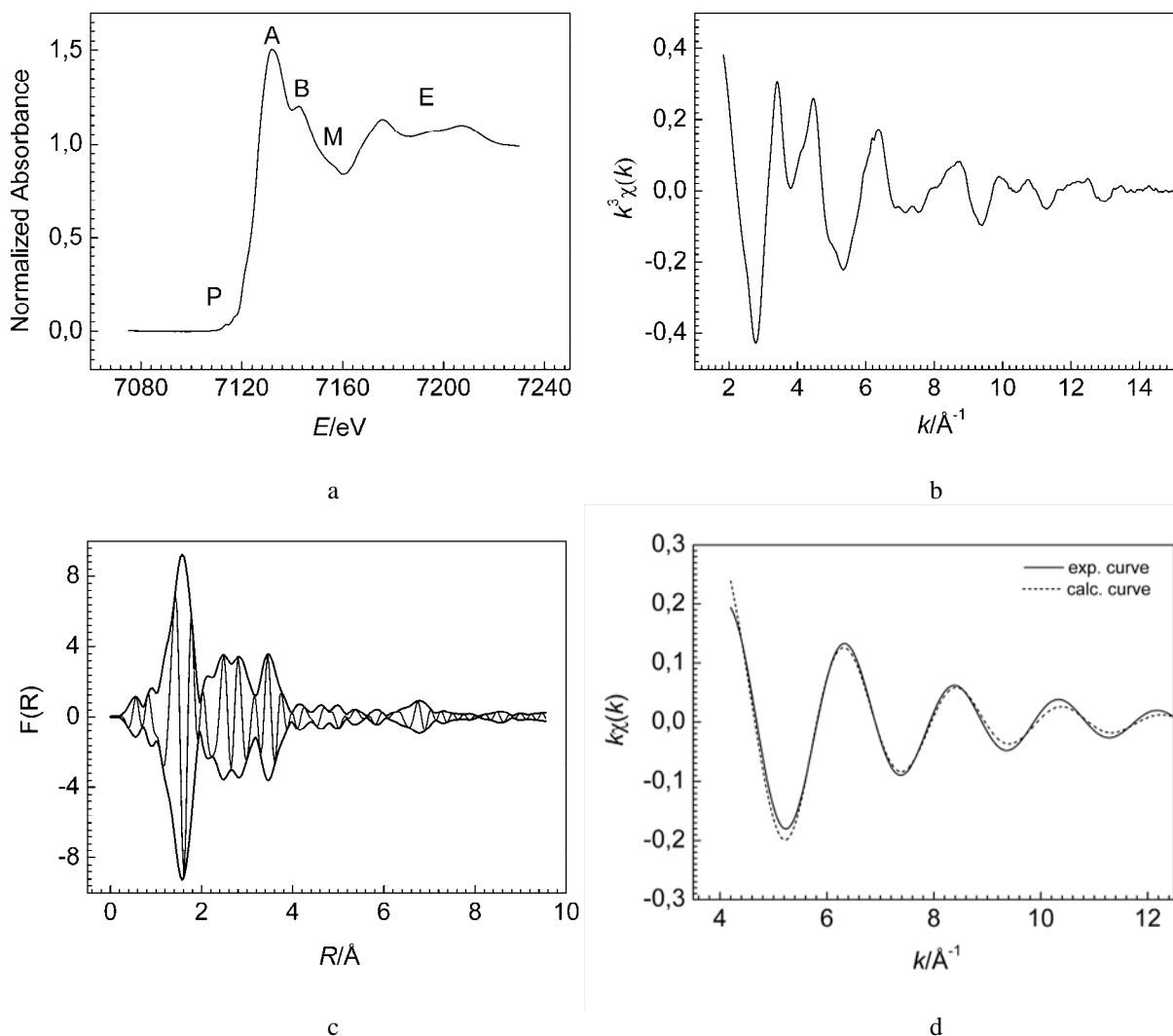


**Figure 102.** Complex $C_{12}$-36: a) Edge spectrum at 80 K. P, pre-edge; A, top of the edge; B and M, shoulders; E, EXAFS oscillations; b) weighted EXAFS signal $k^3\chi(k)$; c) Modulus and imaginary parts of the Fourier transform of the EXAFS signal at 80 K; d) Comparison of the experimental and calculated $k\chi(k)$ values for the first filtered shell.

The EXAFS spectrum measured at 80 K is shown in Figure 102b, and the Fourier transform of it is displayed in Figure 102c. The EXAFS signal provides direct information about the radial distribution of the neighboring atoms around the absorbing atom. The data are very similar to previous EXAFS studies with similar materials (changing the triazole ligand and the counterions) demonstrating the linear local structure [94, 339, 349-351]. The Fourier transform at 80 K consists of five main peaks (Figure 102c). The first intense one appearing without phase correction at 1.60 Å (*i.e.* 1.96 Å after correction, *vide infra*) can be attributed to

the first $N_6$ coordination shell of the iron ion. The short distance clearly indicates the low-spin state. Also several peaks are distinguishable in the region of 2–4 Å, which correspond to several kinds of distances such as Fe–N, Fe–C, and iron with its two nearest iron neighbors [349]. Particularly important is the weak intensity peak at ~ 7.0 Å ascribed to the next-nearest iron neighbors of an iron(II) ion in the chain. The presence of this peak is a clear demonstration the polymeric structure of **C$_{12}$-39**. The curve-fitting analysis for the first coordination sphere of the iron was performed (Figure 102d). The fitting variables were the distance Fe–N, the Debye-Waller factor $\sigma$ and the edge energy shift $\Delta E_0$. The coordination number $N$ was fixed to 6. The obtained values were $d^{\text{Fe–N}} = 1.96$ Å, $\sigma = 0.072$ Å, $\Delta E_0 = -4.8$ eV with goodness of fit $\rho = 1.8$ %. The value of the Fe–N distance is in good agreement with that of the parent low-spin compound **30** and with previously reported data recorded on iron(II) low-spin compounds [339, 349-351].

### 3.4.3   TGA and IR data

The analysis of the IR spectra included the regions with the characteristic bands of alkyl chains, triazole units and anions.

*Alkyl chains.* The packing of the chains in the alkyl layers and the adopted conformations are of interest. The relevant frequencies of the vibration spectra are observed at 2600–3000 cm$^{-1}$ and 700–1600 cm$^{-1}$.

*High-frequency region.* The stretching absorptions $v_s(\text{CH}_2)$ and $v_{as}(\text{CH}_2)$ are strong indicators of the chain conformation [246, 247]. The characteristic values lie in the ranges of 2846–2850 and 2915–2920 cm$^{-1}$, respectively, for *all-trans* extended chains and in the ranges of 2854–2861 and 2924–2935 cm$^{-1}$ for disordered chains characterized by a significant presence of *gauche* conformers [248]. On this basis, the observed peak frequencies for the C–H stretching modes of the methylene groups suggest that the majority of the methylene units of the alkyl chains in **C$_n$-36** and **C$_n$-38** are in disordered state with a significant *gauche* population. The population of *gauche* kinks decreases with increasing length of the chains which for the higher homologues results in a shift of the peak maximum closer to the region of *all-trans* extended chains.Two peaks (for shorter homologues with $n = 4, 6$) or shoulders (for higher homologues $n = 8, 10, 12$) at ~2872 and ~2958 cm$^{-1}$ were attributed to the symmetric $v_s(\text{CH}_3)$ and asymmetric $v_{as}(\text{CH}_3)$ stretching vibrations of the methyl groups, respectively (Table 41).

**Table 41.** TGA and IR data for complexes **C$_n$-36** and **C$_n$-38** ($n$ = 4, 6, 8, 10, 12).

| Compound | TGA, w/w [ %] ($T$)[a] | IR [cm$^{-1}$][b] | | | | | | |
|---|---|---|---|---|---|---|---|---|
| | | $v$(C–H$_{trz}$) | $v_s$(CH$_2$), $v_{as}$(CH$_2$) | $v$(C=O) | $\delta$(CH$_2$) | $\rho$(CH$_2$) | $\tau_2$ | $v$(Anion) |
| C$_4$-36 | 0.9 (322 K) | 3104 | 2936 | 1700 | 1466 | 720 | 624 | 1253, 1169, 1030 |
| C$_6$-36 | 1.2 (320 K) | 3102 | 2932, 2859 | 1700 | 1464 | 723 | 627 | 1256, 1169, 1030 |
| C$_8$-36 | 0.8 (327 K) | 3101 | 2927, 2856 | 1700 | 1466 | 723 | 628 | 1255, 1168, 1029 |
| C$_{10}$-36 | 0.3 (324 K) | 3110 | 2925, 2854 | 1701 | 1466 | 721 | 626 | 1256, 1169, 1029 |
| C$_{12}$-36 | 0.3 (320 K) | 3110 | 2924, 2853 | 1700 | 1469 | 721 | 625 | 1257, 1169, 1029 |
| C$_4$-38 | 1.6 (324 K) | 3124 | 2935 | 1699 | 1466 | 720 | 627 | 1092, 1070, 1051 |
| C$_6$-38 | 1.7 (320 K) | 3126 | 2934, 2861 | 1701 | 1458 | 725 | 626 | 1093, 1060 |
| C$_8$-38 | 1.4 (320 K) | 3126 | 2927, 2856 | 1703 | 1469 | 723 | 624 | 1093, 1060 |
| C$_{10}$-38 | 0.9 (320 K) | 3125 | 2925, 2854 | 1705 | 1465 | 721 | 623 | 1089, 1059 |
| C$_{12}$-38 | 0.6 (320 K) | 3125 | 2924, 2853 | 1704 | 1465 | 721 | 624 | 1082, 1059 |

[a] Value is given at the point where the plateau is reached. $T$ is the temperature at which the dehydration process is centered; [b] $v$, stretching; $\delta$, bending; $\rho$, rocking; $\tau$, ring torsion vibration of triazole groups; as, asymmetric, s, symmetric.

*Low-frequency region.* The scissoring band $\delta$(CH$_2$) at ~1467 cm$^{-1}$ provides a sensitive measure of the packing arrangement of the alkyl chains. The splitting of this peak or absence of the splitting depends on the type of the subcell packing. The singlet can be attributed to a hexagonal or a triclinic subcell with weak interchain interactions, whereas a split band is characteristic of an orthorhombic subcell with lateral interchain interactions between contiguous CH$_2$ groups [246, 249, 250]. For **C$_n$-36** and **C$_n$-38** with $n$ = 8, 10, 12 the appearance of a single narrow peak at ~1467 cm$^{-1}$ was attributed to the hexagonal ordering of the chains implying that the compounds possess only one type of chains. For the lower homologues the assigning cannot be unambiguous because of the number of overlapped peaks observed in the respective region.

Regarding the chain packing, *the rocking mode* (~722 cm$^{-1}$) of the methylene group can provide additional confirmation of the packing type [247]. The band appears for all homologues. In close analogy to the scissoring mode at ~ 1467 cm$^{-1}$ its shape is highly dependent on the packing geometry of alkyl chains [246]. Orthorhombic packing is known to split this rocking mode into two components of comparable intensities, but the vibration levels are not split when the packing is hexagonal containing only one chain per subcell. On these grounds, the appearance of a single narrow peak at ~722 cm$^{-1}$ might point out hexagonal packing of the chains.

However, the rocking and scissoring bands do not allow to distinguish between the liquid and solid states of the compounds [368].

*Ligand groups.* *N*1,*N*2-bidentate coordination mode of the triazole units is confirmed by the non-split absorption band $\tau_2$ at ~625 cm$^{-1}$ in both series [318]. For complexes $C_n$-38 the absorption band $v$(C–H$_{trz}$) is at ~3125 cm$^{-1}$ while for the $C_n$-36 at ~3105 cm$^{-1}$. Also a slight difference by 3 cm$^{-1}$ in the position of the $v$(C=O) band is found between the two series which are ~1703 and ~1700 cm$^{-1}$, respectively (Table 41). This was explained in terms of the adopted spin state and the consequent electronic and geometrical properties.

*Anions.* The intensive single peak at ~1170 cm$^{-1}$ for complexes $C_n$-36 is the absorption band $v_{as}$(S–O) [214] while the absorption band at 1030 cm$^{-1}$ is due to $v_s$(S–O). The strong multicomponent absorption band at 1255 cm$^{-1}$ was attributed to the absorption $v$(C–F) of the triflate anion. The observed absorption bands confirm the composition of the complexes.
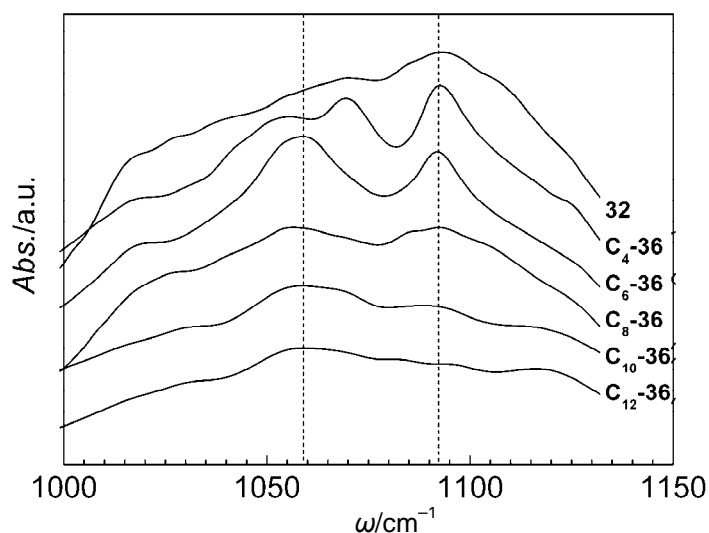


**Figure 103.** IR spectra of **32** and $C_n$-38 ($n$ = 4, 6, 8, 10, 12) in the region of $v$(B–F).

For the $C_n$-38 series the peak at ~1065 cm$^{-1}$ corresponds to the absorption band $v$(B–F). The observed splitting into two (or more) components with the main ones at ~1060 and ~1085 cm$^{-1}$ might be the result of the substantial distortion of the tetrafluoroborate anion (BF$_4^-$). A similar feature was reported for the anhydrous compound [Fe(NH$_2$trz)$_3$](BF$_4$)$_2$ (NH$_2$trz is 4*H*-1,2,4-triazol-4-amine) [320]. While for the homologues $C_4$-38 and $C_6$-38 the splitting is strongly apparent, for the higher homologues $C_{10}$-38 and $C_{12}$-38 the splitting of the components and their intensity is reduced (Figure 103). Compound $C_8$-38 shows a marginal difference between the two groups. For comparison the spectrum of the parent compound **32** with the stronger absorption component at 1085 cm$^{-1}$ is also shown (Figure 103).

In the region of 3460–3500 cm$^{-1}$ the spectra of all compounds exhibit a broad absorption peak of water.

Thermogravimetry (TGA) carried out with the pristine compounds at a rate of 10 K min$^{-1}$ in nitrogen atmosphere reveals a continuous loss of mass starting at 310 K. This decrease in mass proceeds rapidly in the temperature range 320–340 K, after which it stops. At 360 K the percentage mass loss is in agreement with the removal of half a molecule of water for the homologues $C_n$-36 and one molecule for the homologues $C_n$-38 (Table 41).

### 3.4.4   Magnetic properties

The magnetic properties of the compounds $C_n$-36 and $C_n$-38 ($n$ = 4, 6, 8, 10, 12) were measured in both cooling and heating modes in order to detect the influence of the temperature and dehydration on the magnetic properties of the compounds. The variation of the product of the molar magnetic susceptibility $\chi_M T$ *vs T* is shown in Figure 104a–j. At room temperature the compounds $C_n$-36 are almost diamagnetic. The absence of the residual paramagnetism at low temperature is confirmed by Mössbauer measurements (*vide infra*) as well as by the closeness of the experimental $\chi_M T$ to the expected value for a pure singlet spin state (zero). The homologue $C_4$-36 exhibits spin-transition centered near room temperature. Subsequent cooling and heating reveals a narrow hysteresis loop ($\Delta T_{hys}$ = 3 K) which disappears after heating of the sample up to 400 K. The thermal treatment of the complex was accompanied by the loss of half a molecule of water (from TGA) and the transformation into the anhydrous complex $C_4$-37 with spin-transition centered at 226 K. As is seen in Figure 104a, at low temperature the fraction of the residual paramagnetic iron(II) ions in the anhydrous compound  increases. For compound $C_n$-36 with $n$ = 6, 8, 10, 12 the hysteresis in the pristine samples is no more observable (Figure 104b–e). On the other hand, the temperature of the transition also increases (Figure 105). The influence of the water release is less pronounced for the higher homologues. In the anhydrous compound $C_{10}$-37 a narrow hysteresis loop is detected with $\Delta T_{hys}$ = 2 K (Figure 104d) while compound $C_{12}$-37 has a complicate form of the loop with a characteristic feature at lower temperatures (near 275 K) (Figure 104e). For $C_{12}$-37 the incompleteness of the transition at higher temperatures is confirmed by the value of 3.14 cm$^3$ K mol$^{-1}$ attained at 350 K. However, for the homologues with shorter alkyl chains $C_4$-37 and $C_6$-37, the transition is assumed to be complete as confirmed by the susceptibility value of 3.50 cm$^3$ K mol$^{-1}$ at 350 K.

All compounds $C_n$-**38** are high-spin at room temperature (Figure 104f–j). In $C_4$-**38** the transition is rather abrupt being reminiscent of the parent compound **32**, but $T_{1/2}$ is shifted by 30 K up to 270 K. The fit of the magnetic curves with the Slichter-Drickamer equation (Figure 104f) with the values of the enthalpy and entropy fixed to those from the DSC data, gave the value of the cooperativeness $\Gamma$ = 4.5 kJ which is similar to that of the parent compound **32** (cf. Table 37, Chapter 3.2.7). The dehydration took place on heating up to 350 K providing the anhydrous compound $C_4$-**39** with an incomplete gradual transition without hysteresis (Figure 104f). Despite the smoothing of the extremities of the transition, in compound $C_6$-**38** a narrow hysteresis is still observed ($\Delta T_{hys}$ = 4 K). The dehydration completely changes the magnetic behavior making the spin-transition gradual over the temperature range of 10–400 K (Figure 104g). In the three compounds $C_n$-**38** with $n$ = 8, 10, 12 the magnetic behavior is somewhat similar. The pristine samples exhibit an incomplete spin-transition with $T_{1/2}$ ~ 265 K. On cooling the transition is very gradual leading to a substantial residual high-spin fraction at low temperatures (Figure 104h, i and j). The decrease of the susceptibility below 40 K is due to zero-field splitting. The anhydrous compounds $C_n$-**39** with $n$ = 8, 10 and 12 obtained by heating of the pristine samples $C_n$-**38** up to 350 K or above are high-spin and display only very moderate variation of the $\chi_M T$ on cooling (Figure 104h, i and j). The value of $\chi_M T$ = 3.20 cm$^3$ K mol$^{-1}$ attained by compounds $C_n$-**39** in the high temperature region corresponds to the incomplete transition with a partially preserved low-spin fraction.

For comparison, Figure 105 displays the $T_{1/2}$ derived values plotted *vs* the length of alkyl chains $n$ for the compounds $C_n$-**36**, $C_n$-**37**, $C_n$-**38** and $C_n$-**39**.
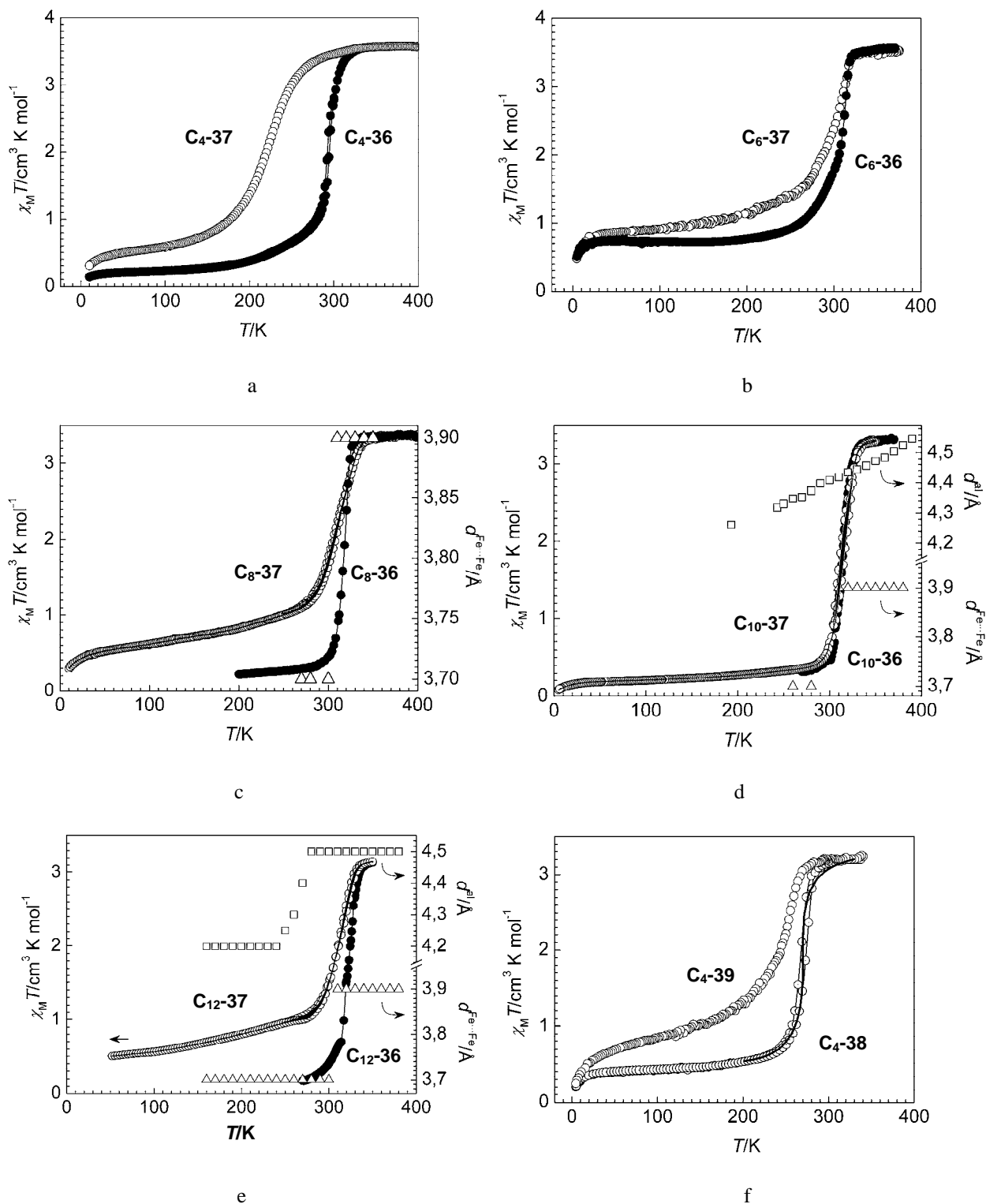
**Figure 104.** Plot of $\chi_M T$ *vs* $T$ for: a) **C₄-36**, **C₄-37**; b) **C₆-36**, **C₆-37**; c) **C₈-36**, **C₈-37**. The value $d^{Fe\cdots Fe}$ ($\triangle$) (distance between neighboring iron(II) ions in polymeric chains) corresponds to the compound **C₈-37**; d) **C₁₀-36**, **C₁₀-37**. The values $d^{alk}$ (of the alkyl halo) and $d^{Fe\cdots Fe}$ correspond to the compound **C₁₀-37**; e) **C₁₂-36**, **C₁₂-37**. The values $d^{alk}$ and $d^{Fe\cdots Fe}$ correspond to the compound **C₁₂-37**; f) **C₄-38**, **C₄-39**. The solid line represents the fit of the magnetic hysteresis; g) **C₆-38**, **C₆-39**; h) **C₈-38**, **C₈-39**; i) **C₁₀-38**, **C₁₀-39**; j) **C₁₂-38**, **C₁₂-39**.

g

h

i

j
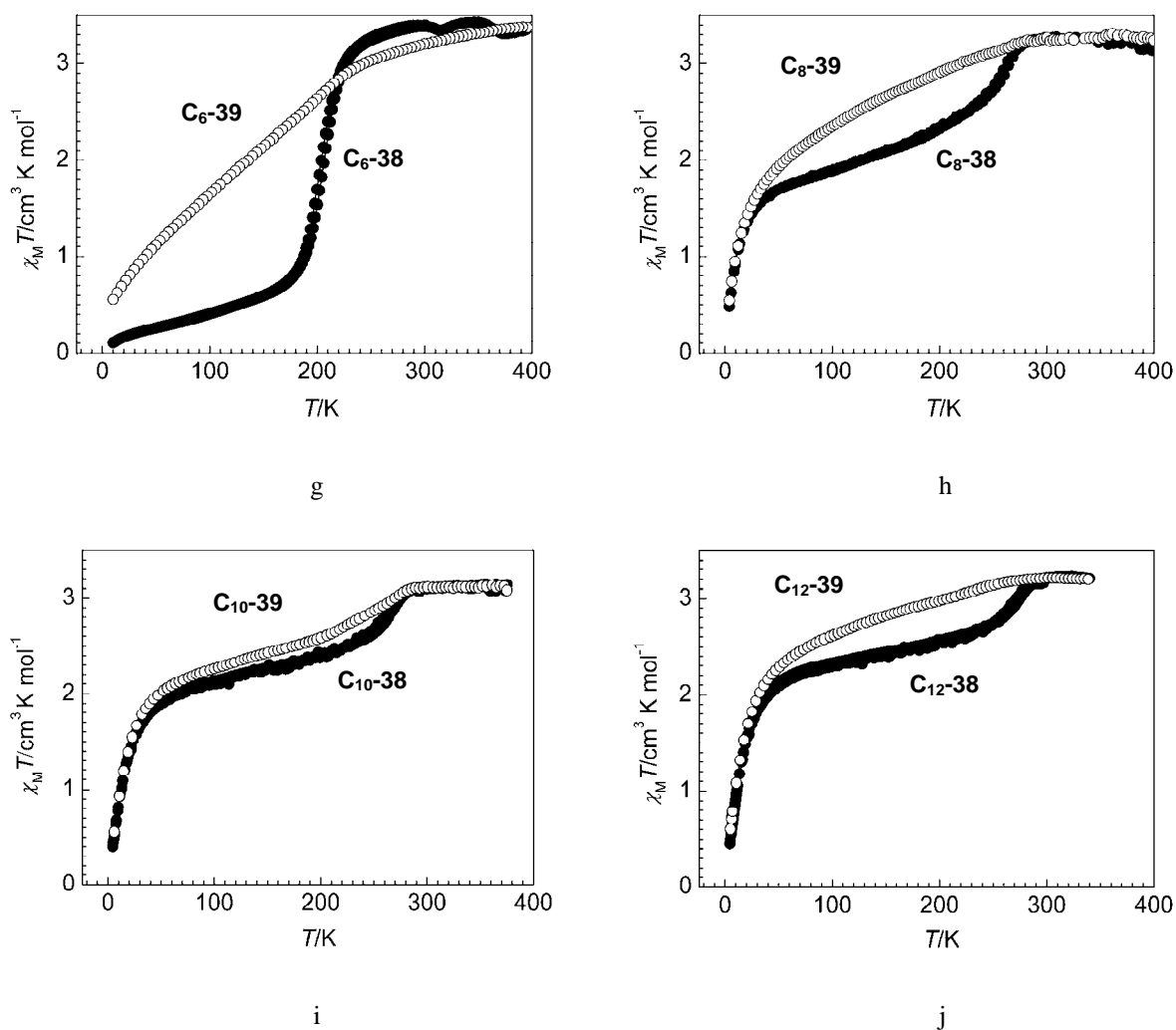
**Figure 104.** (*continued*)
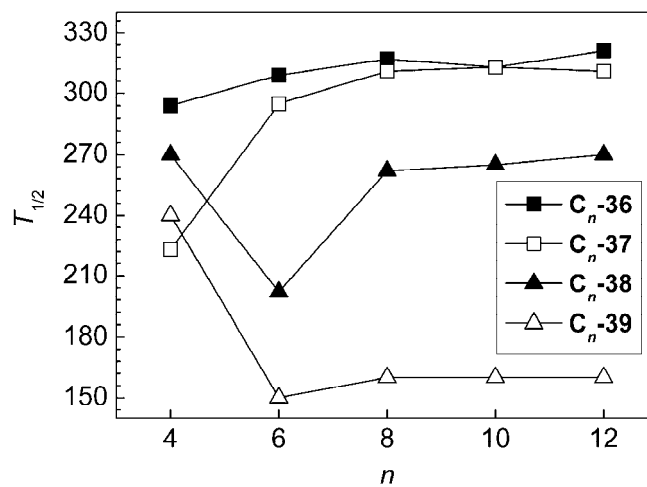


**Figure 105.** Plot $T_{1/2}$ as a function of the value $n$ for $C_n$-36, $C_n$-37, $C_n$-38 and $C_n$-39.

### 3.4.5   XRD data and dynamic light scattering data

The XRD patterns of the homologues **C$_n$-36** with $n$ = 4, 6, 8 are of poor quality reflecting the low crystallinity of the samples (Figure 106a, b, c). Only two reflections are observed in the low- and high-angle regions. The hexagonal columnar ordering is deduced for these samples from the intense reflection (10) and minor reflections with the reciprocal distances at $1/3^{1/2}$ (11), $1/4^{1/2}$ (20), $1/7^{1/2}$ (21) and $1/9^{1/2}$ (30). The first one with the Miller indices $(hk)$ = (10) provides the stacking periodicity $d$ of the layers. The halo in the wide angle regime at $2\theta \sim 19°$ with a spacing being 4.6 Å is assigned to the disordered alkyl chains. The lengthening of the alkyl substituent in the homologues with $n$ = 10, 12 results into some ordering of the structure which is seen from the number of reflections in the low-angle region (Figure 106d, e).

In **C$_8$-36** two other reflections are observed, the positions of which depend on temperature. In the pristine sample, one of the reflection at $2\theta \sim 24.0°$ corresponds to a spacing $\sim 3.70$ Å. The reflection is observable up to 300 K, but at 310 K it disappears. Instead, another reflection appears at $2\theta \sim 22.9°$ with a spacing $\sim 3.90$ Å. In compounds **C$_n$-36** with $n$ = 8, 10, 12, the behavior of these reflections perfectly coincides with the spin-transition as determined by the magnetic measurements (Figure 104c–e). Accordingly, these reflections can be ascribed to the Fe$\cdots$Fe separation representing the distances along the main axis of the polymeric chain. Since the coordination environment of the iron(II) ion is spin-state dependent and in low-spin state Fe–N distances are shorter, at lower temperatures this results into shorter Fe$\cdots$Fe spacing. In the high-spin state the increase of the Fe–N distances moves neighboring iron(II) ions apart. The precise value of the high-spin Fe$\cdots$Fe distance can be evaluated in the high-spin trinuclear iron(II)-based triazole complexes being equal to 3.84 Å [88, 90, 369, 370]. The distance of 3.89 Å between neighboring copper(II) ions in the 1D polymer **30-Cu** is also in agreement with values found for the compounds **C$_n$-36** at higher temperatures. For the samples in the low-spin state (below 300 K) the Fe$\cdots$Fe distance is roughly equal to the value found from the EXAFS measurement performed on the compound **C$_{12}$-36** (*vide supra*). The observed Fe$\cdots$Fe reflection of the compounds **C$_n$-36** is reminiscent of the stacking reflection observed in the XRD profiles of the discotic liquid crystals, the molecules of which can stack into one-dimensional columns with the regular periodicity defined by the nature of the material (3.5–3.8 Å) [371-373].
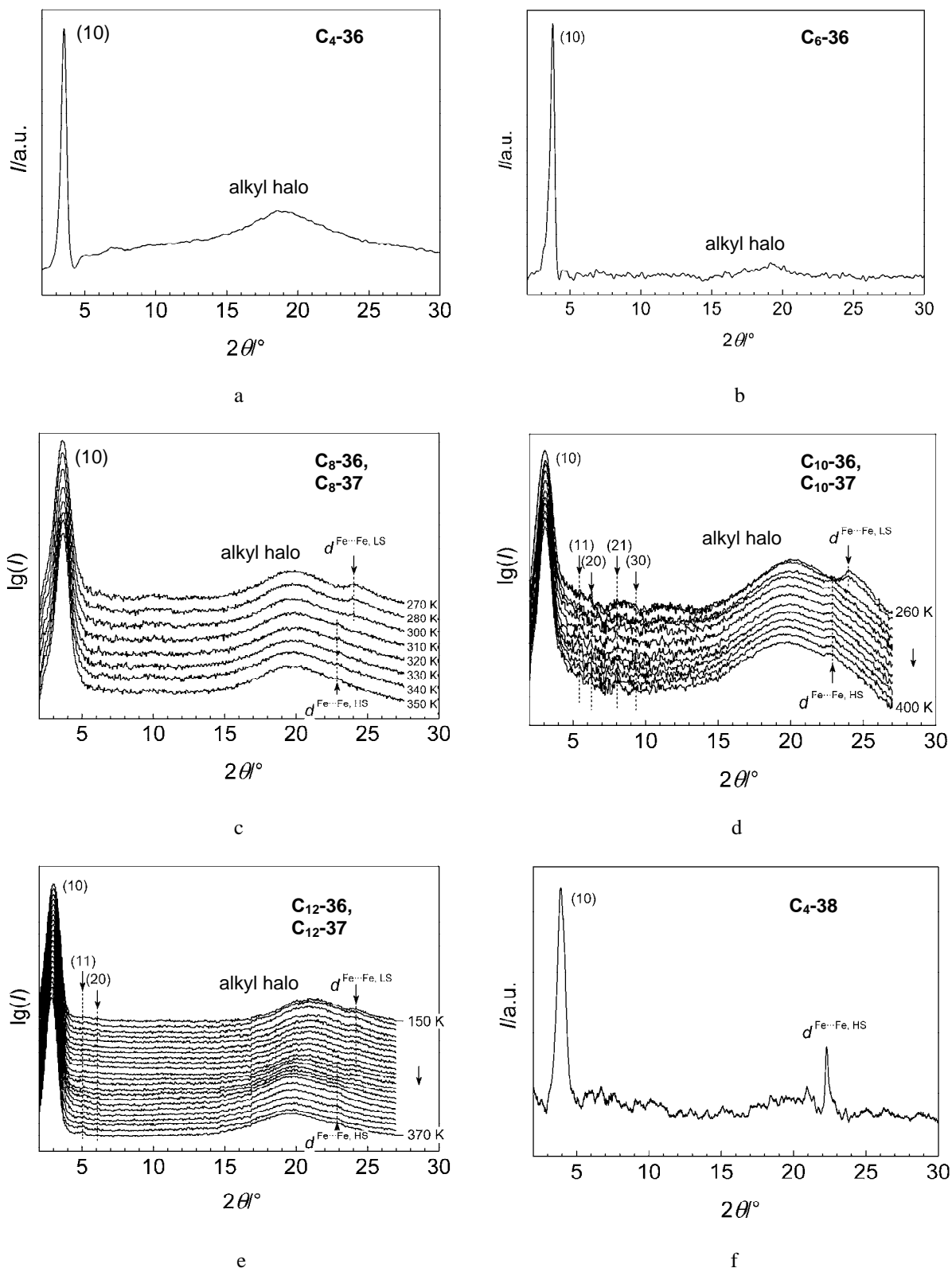
**Figure 106.** XRD profiles for: a) $C_4$-36; b) $C_6$-36; c) $C_8$-36, $C_8$-37; d) $C_{10}$-36, $C_{10}$-37; e) $C_{12}$-36, $C_{12}$-37; f) $C_4$-38; g) $C_6$-38; h) $C_8$-38; i) $C_{10}$-38; j) $C_{12}$-38, $C_{12}$-39 measured at room temperature (for single profiles) or at temperatures indicated next to the profiles.

g



h



i



j
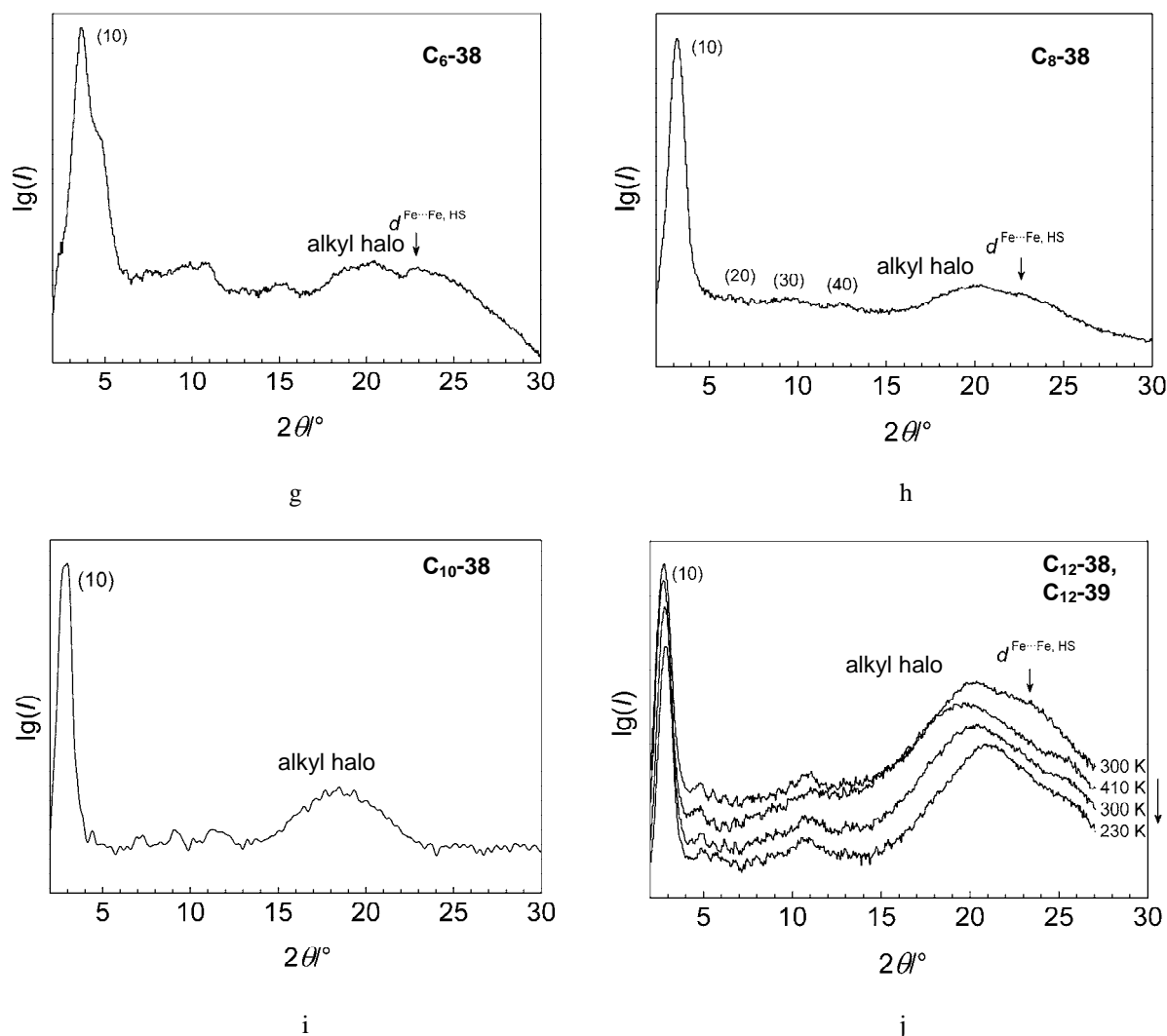
**Figure 106.** (*continued*)

The model of the bridging by a triazole unit of two neighboring iron(II) ions is illustrated in Figure 107. According to simple geometrical considerations the distance Fe–N ($d^{\text{Fe–N}}$) can be expressed through the spacing $d^{\text{Fe}\cdots\text{Fe}}$ by the equation

$$d^{\text{Fe–N}} = \frac{d^{\text{Fe}\cdots\text{Fe}} - 1.37}{2\cos 54°} \tag{18}$$

where 1.37 is the distance in angstrom between the bridging nitrogen atoms $N1$ and $N2$ of the triazole unit [42], the value 54° corresponds to the idealized mean angle Fe–Fe–N (see Figure 107). The spacing Fe$\cdots$Fe found at low temperature is 3.70 Å that gives a distance Fe–N equal to 1.98 Å. Above 300 K the spacing increases up to 3.90 Å which corresponds to 2.15 Å of the Fe–N distance. Both calculated values are in rather good coincidence with the EXAFS

data of the low-spin compound $C_{12}$-36 and the reported EXAFS data on high-spin iron(II)-based triazole complexes [339, 349-351].
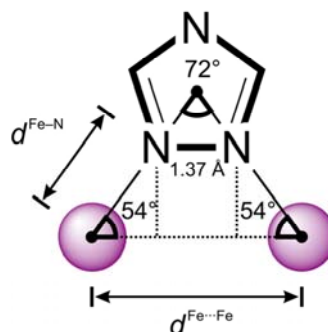


**Figure 107.** The simplified geometry of the triazole unit bridging two neighboring iron(II) ions.

Temperature dependent X-ray measurements were performed on the oriented sample of $C_{12}$-36 ($C_{12}$-37). The orientation was achieved by imposing the sample to mechanical stress. The 2D-WAXS patterns are similar at temperatures 150–390 K which implies that the structure of the pristine compound $C_{12}$-36 is also preserved in the anhydrous compound $C_{12}$-37. The diffractogram recorded at 390 K is shown in Figure 108 as a representative example. It consists of a pair of inner equatorial sharp reflections and a pair of meridional outer diffuse bands. The diffuse alkyl halo is situated in between. The analysis of these patterns confirms the columnar structure of the compound (see Figure 115c).
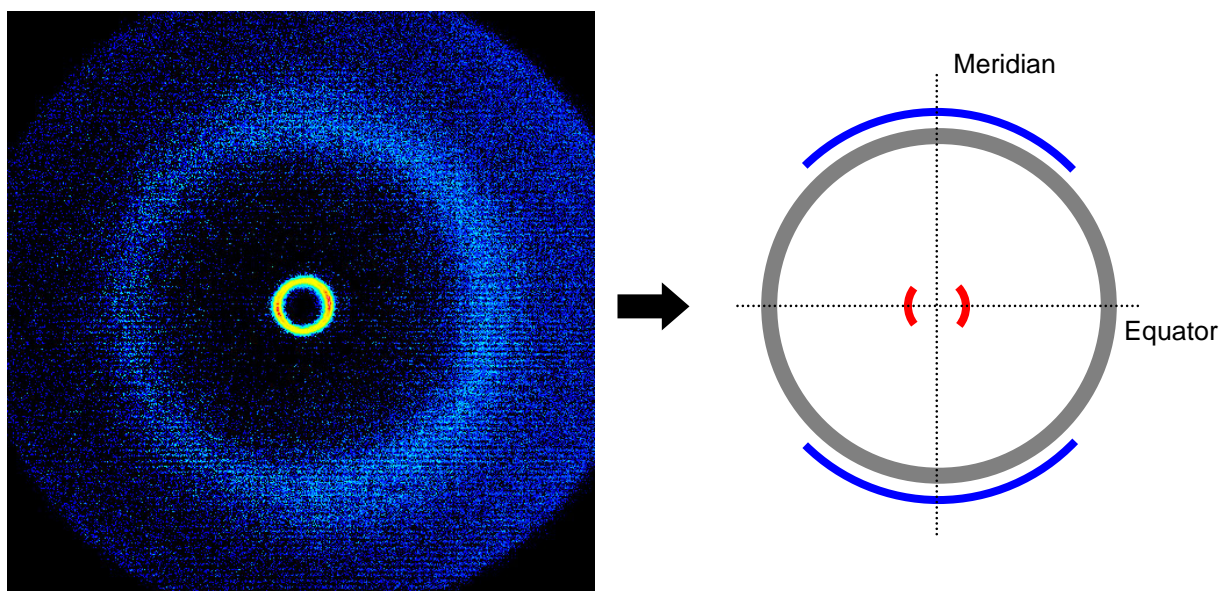


**Figure 108**. 2D-WAXS pattern of the oriented $C_{12}$-36 ($C_{12}$-37) at 370 K. A relatively sharp pair of equatorial reflections in the low-angle regime originates from the intercolumnar ordering, whereas a pair of weak meridional reflections is due to columnar organization of disk-like monomeric units. The diffuse circular reflection is attributable to the liquid-like alkyl chains.

The non-linear variation with temperature of the alkyl reflection was found only in compound $C_{12}$-36. The width of the reflection does not change on heating (Figure 106e), but the position of its maximum is temperature dependent. At low temperature the reflection gives a spacing $d^{alk}$ of *ca*. 4.2 Å whereas upon heating from 240 K up to 280 K it gradually increases with attaining the value of *ca*. 4.5 Å which is constant then up to 400 K. The phase transition influences the magnetic behavior and coincides in temperature with the magnetic hysteresis loop (Figure 104e, upper right scale). In compound $C_{10}$-36 the variation of the alkyl spacing has no evident discontinuity (200–400 K) being practically linear (Figure 104d, upper right scale). In $C_n$-36 with $n$ = 8, 10, 12, the variation of the main reflection (10) with temperature is negligible showing only a minor linear increase on heating. In the case of $C_{12}$-36 it is also insensitive to the variation of the alkyl reflection and does not show any features similar to those observed in mononuclear compounds, for example $C_n$-14 and $C_n$-27 (Chapters 2.5.7 and 2.8.6).

The XDR profiles of the compounds $C_n$-38 are similar to those discussed above (Figure 106f–j). The poor crystallinity of the substances complicates the observation of the weak high-order reflections. As in the previous cases, the broad halo at $2\theta \sim 19°$ is due to liquid-like alkyl chains. In compound $C_{12}$-38 like in the analogous $C_{12}$-36 the broadness of the alkyl reflection changes slightly on cooling, in addition to the shift of its maximum from $2\theta \sim 21°$ down to $\sim 19°$ (Figure 106j). The reflection at $2\theta \sim 23°$ detected in the four compounds with $n$ = 4, 6, 8, 12 (Figure 106f, g, h, j, respectively) is attributed to the spacing of iron(II) high-spin ions along the polymeric chains. In $C_{12}$-38 not all observed reflections were possible to index. The reason for this is the poor ratio of noise/signal due to the almost amorphous nature of the substance. The final proof of the similar packing in compounds $C_n$-38 was obtained on the basis of the interlayer distance $d$ plotted *vs* the length of alkyl substituents $n$ (Figure 109). As is seen, the dependence has a linear character which points out a similar organization of the compounds. The effective size of the coordination core in $C_n$-38 can be determined from the fit of the experimental data (Figure 109). A linear regression of this plot (R = 0.997) gives a slope of 1.16 Å per $n$ and an intercept of 17.9 Å which has to be near the size of the coordination core (the inner part of the polymeric chain without alkyl chains) in parent 32 (or 30-Cu), $n$ = 0. Assuming that the packing is hexagonal, calculation using the formula $d^{cc} = (2/3^{1/2})d^{n=0}$ provides the diameter of the coordination core $d^{cc}$ to be 20.6 Å. The value obtained directly from the structure of 30-Cu is 19.7 Å. Indeed, both values are rather similar and thus this confirms the validity of the proposed packing. The $d$ value of the compounds $C_n$-36 are plotted in the same Figure 109. For the higher homologues

the dependence of the interlayer distances $d$ *vs* $n$ does not have a linear character, but shows a discontinuity for **C$_6$-36** and **C$_8$-36** whereas the $d$ values of the compounds **C$_{10}$-36** and **C$_{12}$-36** lie near to the values of **C$_{10}$-38** and **C$_{12}$-38**, respectively (Figure 109). Extrapolation to zero of the straight line drawn through the experimental points of **C$_6$-39** and **C$_8$-39** gives the value of $d^{n=0}$ = 19.7 Å. It corresponds perfectly to the diameter of the polymeric chain in **30-Cu**. Accordingly, for these two homologues a lamellar packing of the polymeric chains is proposed [124]. On the other hand, compound **C$_4$-36** adopts a unique packing since its $d$ value fits neither the hexagonal nor the lamellar groups.
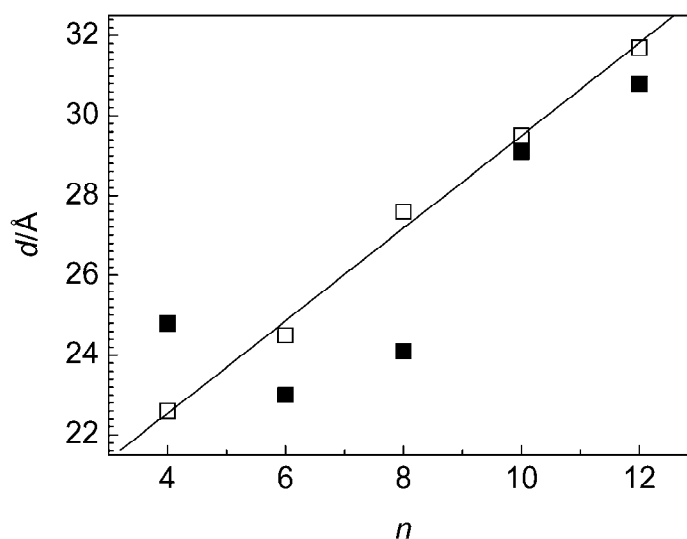


**Figure 109.** Dependence of interlayer distance $d$ on the length of alkyl chains $n$ in **C$_n$-36** (■) and **C$_n$-38** (□). The solid line represents the linear fit of the experimental points for compounds **C$_n$-38**.

The molecular modeling of the ligand molecule 3,5-bis(dodecyloxy)-*N*-(4*H*-1,2,4-triazol-4-yl)benzamide  (C$_{12}$-*tba*) gives a distance of *ca.* 25 Å between the ends of the molecule in the stretched configuration (Figure 110). A radial arrangement of the ligand molecules in the polymeric chain would imply at least a twice larger diameter of the polymeric chain (*ca.* 50 Å) which exceeds the experimentally observed one (for **C$_{12}$-38**: $31.7 \times 2/3^{1/2}$ = 36.6 Å). It can signify the tilt of the alkyl chains, for example, close to the axis of the polymeric chain. Taking also into account a possible interdigitation of the alkyl chains belonging to neighboring polymeric chains one can explain the observed decrease of the effective diameter of the single polymeric chain.

The length of the polymeric chains in solution was evaluated by dynamic light scattering. For both **C$_{12}$-36** and **C$_{12}$-38**, the averaged hydrodynamic radius of the polymeric species in chloroform is 780 Å. Assuming high-spin character of the iron(II) ions, which is

supported by the absence of coloration of the dissolved compounds, and taking into account an Fe···Fe distance equal to 3.9 Å, the approximate number or iron(II) ions per chain is near to 400.
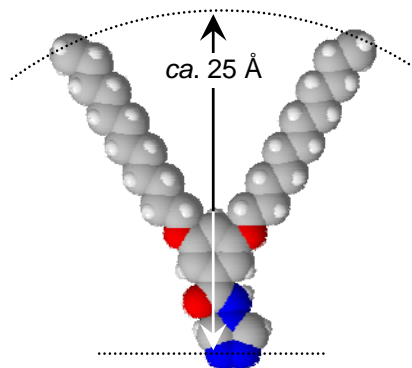


**Figure 110.** Molecular model of the ligand $C_{12}$-*tba* in the stretched configuration.

The derived structural parameters of compounds $C_n$-36 and $C_n$-38 at room temperature are presented in Table 42.

**Table 42.** Interlayer distances *d*, thermal transitions and mesomorphism, enthalpy $\Delta H^{SCO}$ and entropy $\Delta S^{SCO}$ of spin-transition and glass transition $\Delta H_g$ determined by XRD, DSC, TGA and POM for $C_n$-36–$C_n$-38.

| Compound | *d* [Å], RT | Transitions [K][a] | $\Delta H^{SCO}$ [kJ mol$^{-1}$][c] | $\Delta S^{SCO}$ [J K$^{-1}$ mol$^{-1}$] | $\Delta H_g$ [kJ mol$^{-1}$][c] |
|---|---|---|---|---|---|
| $C_4$-36, $C_4$-37 | 24.8 | Cr (LS $\underset{283}{\overset{291}{\rightleftarrows}}$ HS) $\xrightarrow{510}$ d | 14.3 | 49.2 | – |
| $C_6$-36, $C_6$-37 | 23.0 | Cr (LS $\underset{309}{\overset{312}{\rightleftarrows}}$ HS) $\xrightarrow{510}$ d | 14.6 | 46.6 | – |
| $C_8$-36, $C_8$-37 | 24.1 | Col$_L$ (LS $\underset{304}{\overset{312}{\rightleftarrows}}$ HS) $\xrightarrow{514}$ d | 15.3 | 49.4 | – |
| $C_{10}$-36, $C_{10}$-37 | 29.1 | g $\xrightarrow{271}$ Col$_h$ (LS $\underset{294}{\overset{299}{\rightleftarrows}}$ HS) $\xrightarrow{514}$ d | 14.9 | 48.2 | 5.0 |
| $C_{12}$-36, $C_{12}$-37 | 29.8 | g $\xrightarrow{273}$ Col$_h$ (LS $\underset{293}{\overset{297}{\rightleftarrows}}$ HS) $\xrightarrow{507}$ d | 14.2 | 48.1 | 6.2 |
| $C_4$-38, $C_4$-39 | 22.6 | Cr$_1$ (LS $\underset{255}{\overset{264}{\rightleftarrows}}$ HS) $\underset{370}{\overset{400}{\rightleftarrows}}$ Cr$_2$ $\xrightarrow{450}$ d | 17.8 | 68.7 | – |
| $C_6$-38, $C_6$-39 | 24.5 | Cr$_1$ (LS $\xrightarrow{191}$ HS[b]) $\xrightarrow{350}$ Cr$_2$ $\xrightarrow{456}$ d | 11.7[d] | 58.5[d] | – |
| $C_8$-38, $C_8$-39 | 27.6 | Col$_h$ (LS $\xrightarrow{256}$ HS[b]) $\xrightarrow{458}$ d | 4.6[d] | 17.8[d] | – |
| $C_{10}$-38, $C_{10}$-39 | 30.3 | g (LS $\underset{263}{\overset{270}{\rightleftarrows}}$ HS) $\xrightarrow{300}$ Col$_h$ $\xrightarrow{479}$ d | 5.2 | 19.8 | 7.1 |
| $C_{12}$-38, $C_{12}$-39 | 31.7 | g (LS $\underset{264}{\overset{273}{\rightleftarrows}}$ HS) $\xrightarrow{303}$ Col$_h$ $\xrightarrow{456}$ d | 7.1 | 26.5 | 8.5 |

[a] The values correspond to the maxima of the peaks. Decomposition temperatures from the TGA data; [b] No spin-transition peak was observed in the second heating run; [c] The value in the second heating run; [d] The value in the first heating run.

### 3.4.6   DSC and POM data

The spin and phase transitions in the compounds $C_n$-36 and $C_n$-38 were investigated using differential scanning calorimetry (DSC) (Figure 111a–j). The first heating run for these compounds does not coincide with the second one as expected from the transformations which undergo pristine samples upon heating above room temperature. For technical reasons, the DSC measurements were carried out with hermetically closed sample pans so that the results of the second cooling/heating run in most of the cases include the partial rehydration of the samples. One more reason for the rehydration or incomplete dehydration is the higher heating rate being 7 K min$^{-1}$ whereas, for example, the SQIUD experiments were done at 2 K min$^{-1}$. This means that the dynamic DSC measurements were less favorable for the equilibration of the systems which underwent dynamic dehydration process.

During the second measurement runs of the compounds $C_n$-36 ($n$ = 4, 6, 8, 10, 12) a heat capacity anomaly appeared around 300 K which corresponds to the spin-transition observed by the magnetic measurements (Figure 111a–e). Therefore, the heat capacity peaks obviously arise from the spin-crossover phenomenon. The enthalpy $\Delta H^{\mathrm{SCO}}$ deduced from the DSC data is about 15 kJ mol$^{-1}$ and the corresponding entropy $\Delta S^{\mathrm{SCO}}$ ~ 47 J K$^{-1}$ mol$^{-1}$ for the compounds $C_n$-36 (Table 42). The entropy gain is larger than the value expected for the change of the spin manifold of an iron(II) ion, *vis*. $R$ln5 (13.4 J K$^{-1}$ mol$^{-1}$), however somewhat smaller than the corresponding values of the dehydrated parent compound **31** (65.6 J K$^{-1}$ mol$^{-1}$, Table 37, Chapter 3.2.7). The difference arises from the incompleteness of the spin-transition (see Figure 104a–e) and may furthermore be due to weaker cooperativity of the spin-transition [92]. Compounds $C_4$-36, $C_6$-36 and $C_8$-36 do not show any additional peak which can be attributed to the phase transition of the alkyl chains (see Figure 111a, b, c). For the compounds $C_{10}$-36 and $C_{12}$-36 a heat anomaly at 270 K was ascribed to glass transition (Figure 111d, e; Table 42).

The first heating/cooling cycle for $C_4$-38 confirms the occurrence of an abrupt spin-transition which takes place just below room temperature (Figure 104f). A hysteresis loop with the width of 15 K was observed with transition temperatures $T_{1/2}\uparrow$ = 261 K and $T_{1/2}\downarrow$ = 255 K in the heating and cooling mode, respectively. When compared to the SQUID magnetic data, the DSC thermograms reveal transitions over broader temperature ranges and somewhat shifted relative to the value found from the magnetic data. We explain this by thermal conductivity of the materials which becomes more important with increasing scanning rate. In compound $C_6$-38 the spin-transition peak is observed only partially because of the low

temperature limit of the utilized DSC facility (175 K). In compounds $C_4$-38 and $C_6$-38, after the heating/cooling cycle the rehydration takes place leading to restoration of the spin-crossover properties (Figure 111f, g) (for $C_6$-38 is seen only the onset of the endothermic peak in cooling run). Additional peaks observable in the cooling runs near 370 K for both compounds were tentatively attributed to solid-solid transitions and were not investigated in details. For higher homologues with $n = 8, 10, 12$ the change of the magnetic properties, *i.e.* shift of the spin-transition to about 270 K and its incomplete character are reflected in the character of the anomalies detected by DSC (Figure 111h, i, j). Additionally, in the DSC traces of the compounds $C_{10}$-38 and $C_{12}$-38 a broad peak is found indicating minor structural changes which may be attributed to the vitrification of the samples ($T_g \sim 300$ K). The second heating run for these compounds shows the same behavior pointing out rehydration under the sealed conditions.

The examination of the anisotropic textures by polarized optical microscopy (POM) showed that the compounds $C_n$-36 and $C_n$-38 with $n = 8, 10, 12$ form a liquid crystal. For $C_n$-36 upon heating up to *ca.* 310 K the coloration of the samples changed from purple to colorless due to the spin-transition low-spin $\rightarrow$ high-spin. Despite high viscosity, the flow could nevertheless be induced by pressing the cover slip. On further heating the mesophase persisted up to 450 K, however, the viscosity was found to decrease greatly. No decomposition or clearing due to isotropization was observed at this temperature. On cooling, the viscosity gradually increased, and the mesophase could still be observed at room temperature. For the compounds $C_n$-36 ($C_n$-37) the purple coloration was recovered at about 300 K.

Derived parameters for the compounds $C_n$-36 and $C_n$-38 are collected in Table 42.
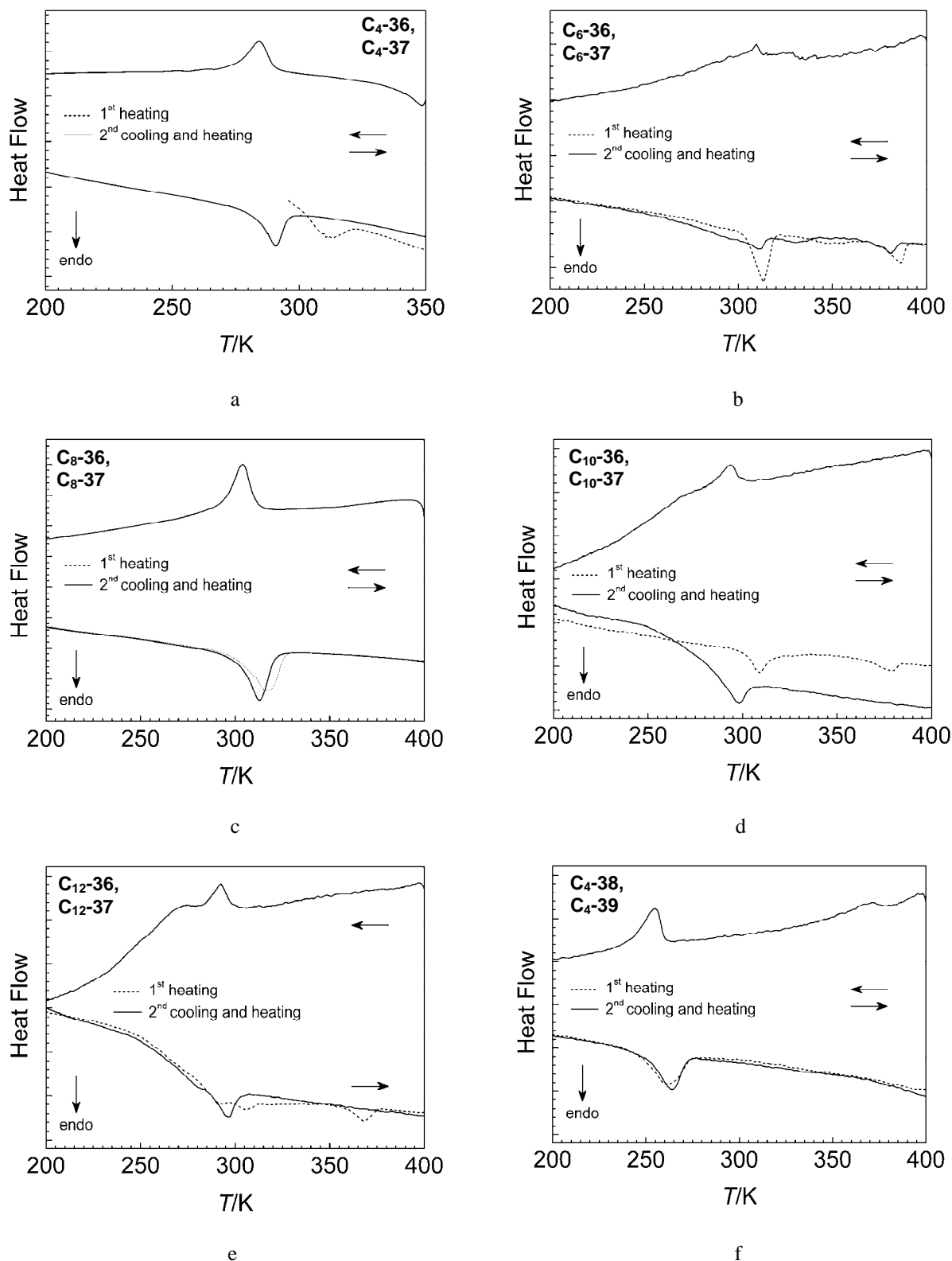
**Figure 111.** DSC profiles in heating and cooling modes for: a) **C$_4$-36, C$_4$-37** ; b) **C$_6$-36, C$_6$-37**; c) **C$_8$-36, C$_8$-37**; d) **C$_{10}$-36, C$_{10}$-37**; e) **C$_{12}$-36, C$_{12}$-37**; f) **C$_4$-38, C$_4$-39**; g) **C$_6$-38, C$_6$-39**; h) **C$_8$-38, C$_8$-39**; i) **C$_{10}$-38, C$_{10}$-39**; j) **C$_{12}$-38, C$_{12}$-39**. Arrows show direction of scanning runs.

g



h



i



j
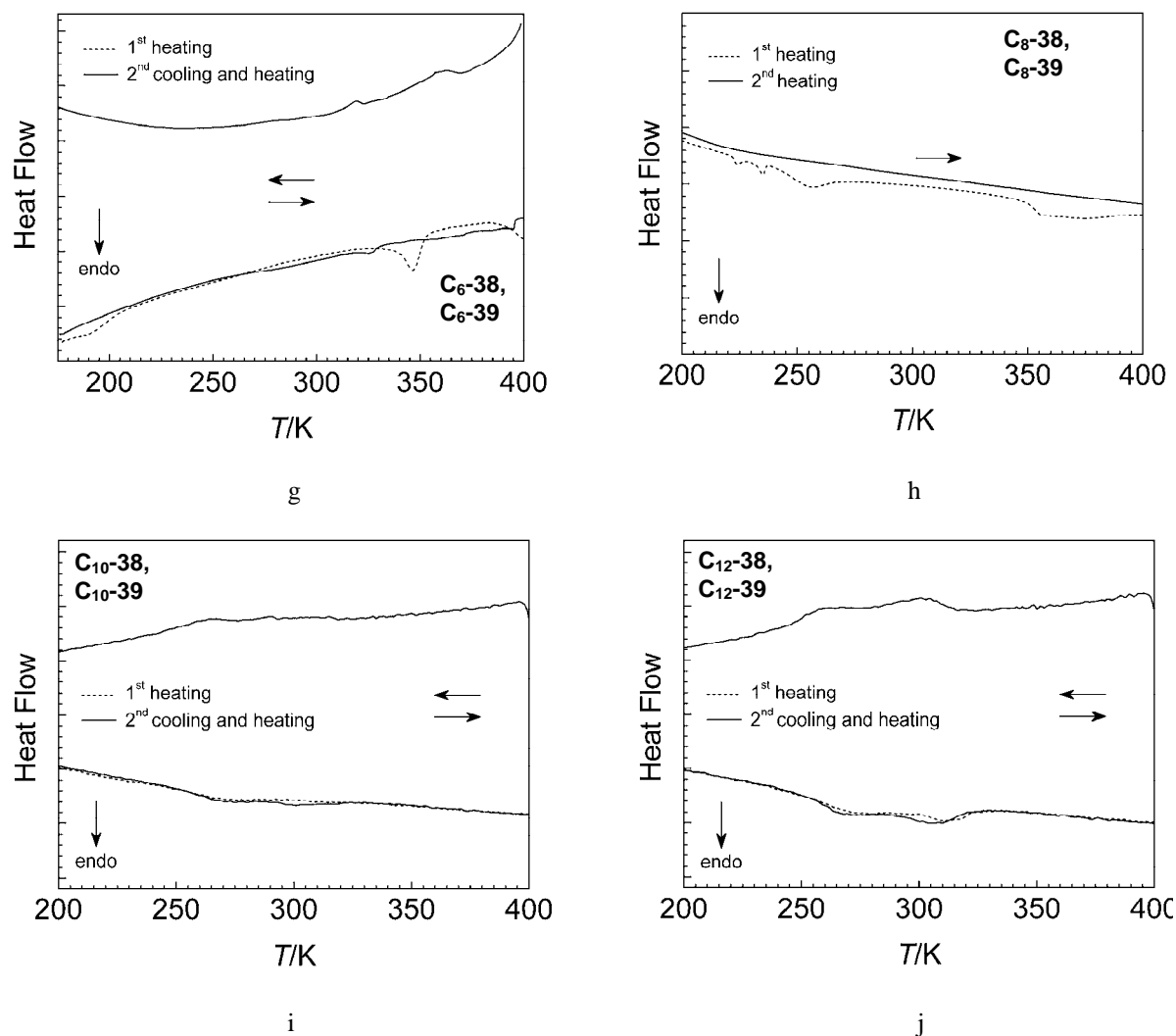
**Figure 111.** (*continued*)

### 3.4.7   Mössbauer spectroscopy

[57]Fe Mössbauer spectra of the compounds **$C_n$-36** and **$C_n$-38** ($n$ = 4, 6, 8, 10, 12) and **$C_{12}$-39** were recorded between 4.2 and 340 K (Figure 113a–k). The parameters derived from least-squares fitting are listed in Table 43. The observed spectra could be fitted considering low-spin and high-spin asymmetric doublets with area fractions in agreement with the magnetic data.

The large quadrupole splitting observed for the high-spin doublets of **$C_n$-36, $C_n$-38** and **$C_{12}$-39** (Table 43) can arise from a non-cubic valence electron distribution over the iron molecular orbitals. This can be the result of axial distortion for $d^6$ complex ions in the degenerate $^5T_{2g}$ ground state. For the electric quadrupole splitting to be observed for an iron(II)

high-spin complex, the octahedral distortion should be such that a splitting of the $t_{2g}$ orbital subset occurs on the order of a few hundred wavenumbers. The value calculated for **C$_4$-36** according to the Equation (15) (Chapter 2.3.5) is *ca.* 530 cm$^{-1}$. The large quadrupole splitting $\Delta E_Q$ can be observed for pseudo-octahedral iron(II) high-spin compounds in cases where the doubly occupied $d_{xy}$ orbital lies lowest. This corresponds to octahedral compression (Figure 112). The additional factor is the lattice contribution which, however, is relatively small and decreases the valence contribution.
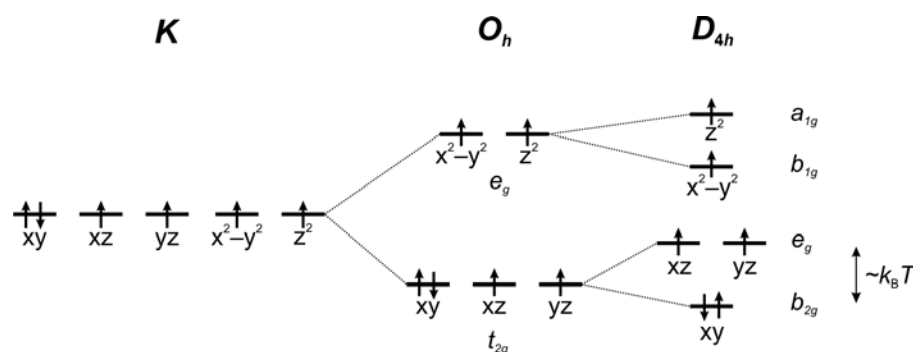


**Figure 112.** Splitting of the five *d*–orbitals of the iron(II) ion in the ligand fields of $O_h$ and $D_{4h}$ symmetries.

The rather pronounced residual high-spin fraction in the complexes **C$_8$-38**, **C$_{10}$-38** and **C$_{12}$-38** deduced from the magnetic data raises the question about its nature. Three explanations can be proposed: i) The complexes are actually trinuclear systems with only the central iron(II) ion undergoing spin-transition. Indeed, the ratio HS:LS is very near to that expected for the real trinuclear species. In this case the two terminal iron ions have the coordination environment $N_3O_3$ composed of three nitrogen atoms of the three triazole moieties and three oxygen atoms of water molecules and therefore should be in the high-spin state independently of temperature; ii) The compounds have polymeric structure but suffer from defects of coordination caused by the bulky alkyl substituents of the ligand (see Figure 114). Therefore, not all iron(II) ions are surrounded by six nitrogen atoms, but there is a substantial fraction having the $N_4O_2$ coordination environment; iii) An incomplete transition is the feature of the essentially polymeric compound because of, for example, imperfect packing of the polymeric chains. An analogy can be drawn with the magnetic properties of powdered spin-crossover crystalline systems which are affected by the defects in the crystal lattice which flattens the transition curve and increases the residual high-spin fraction at low temperature [76, 110, 111]. These three cases can be distinguished by the Mössbauer data

assuming that iron(II)-based species with different coordination environments should have different quadrupole splitting $\Delta E_Q$. Comparing the derived values of the quadrupole splitting for compounds $C_8$-38, $C_{10}$-38 and $C_{12}$-38 (3.31, 3.28 and 3.28 mm s$^{-1}$, respectively) with the corresponding value of the genuine spin-crossover compound $C_6$-38 (3.27 mm s$^{-1}$) one can find that all values are very similar. From the Mössbauer data of the structurally characterized trinuclear iron(II)-1,2,4-triazole compounds it is known, that the values of the quadrupole splitting attributed to the terminal iron(II) ions with the $Fe^{II}N_3O_3$ chromophore usually can be distinguished from that of the central spin-crossover iron(II) atom with the $Fe^{II}N_6$ chromophore [88-90]. The Mössbauer spectrum of the dehydrated compound $C_{12}$-38 (*i.e.* of $C_{12}$-39) did not reveal appearance of a new high-spin doublet since fitting with one high-spin doublet gave satisfactory results (see Figure 113k). The only observed change is the relative increase of the high-spin fraction at the expense of the low-spin fraction which is expected from the magnetic data (Figure 104j). Consequently, the conclusion was made about the polymeric nature of compound $C_{12}$-38 and its dehydrate $C_{12}$-39 where each iron(II) ion is connected to the neighboring iron(II) ions through three triazole bridges adopting $N_6$ coordination environment. This conclusion is supported by the CHN analysis, IR and dynamic light scattering data.

As was proposed in several reports, the averaged size of polymeric chains could be evaluated from the Mössbauer or magnetic data at low temperature by the assumption that the high-spin fraction under this condition originates exclusively from the terminal iron ions with $Fe^{II}N_3O_3$ chromophore with three oxygen atoms belonging to capping water molecules: $N = 2(100/\gamma_{HS\ low\ T})$ or $N = 2(\chi_M T_{high\ T}/\chi_M T_{low\ T})$ [335]. For example, for $C_{12}$-36 this gives only 26 iron(II) ions per one chain that is strongly underestimated in comparison with the light scattering data (400). This again implies the necessity to consider imperfections in the lattice which favors the high-spin state even by those iron(II) ions which are surrounded by nitrogen atoms of the triazole units.
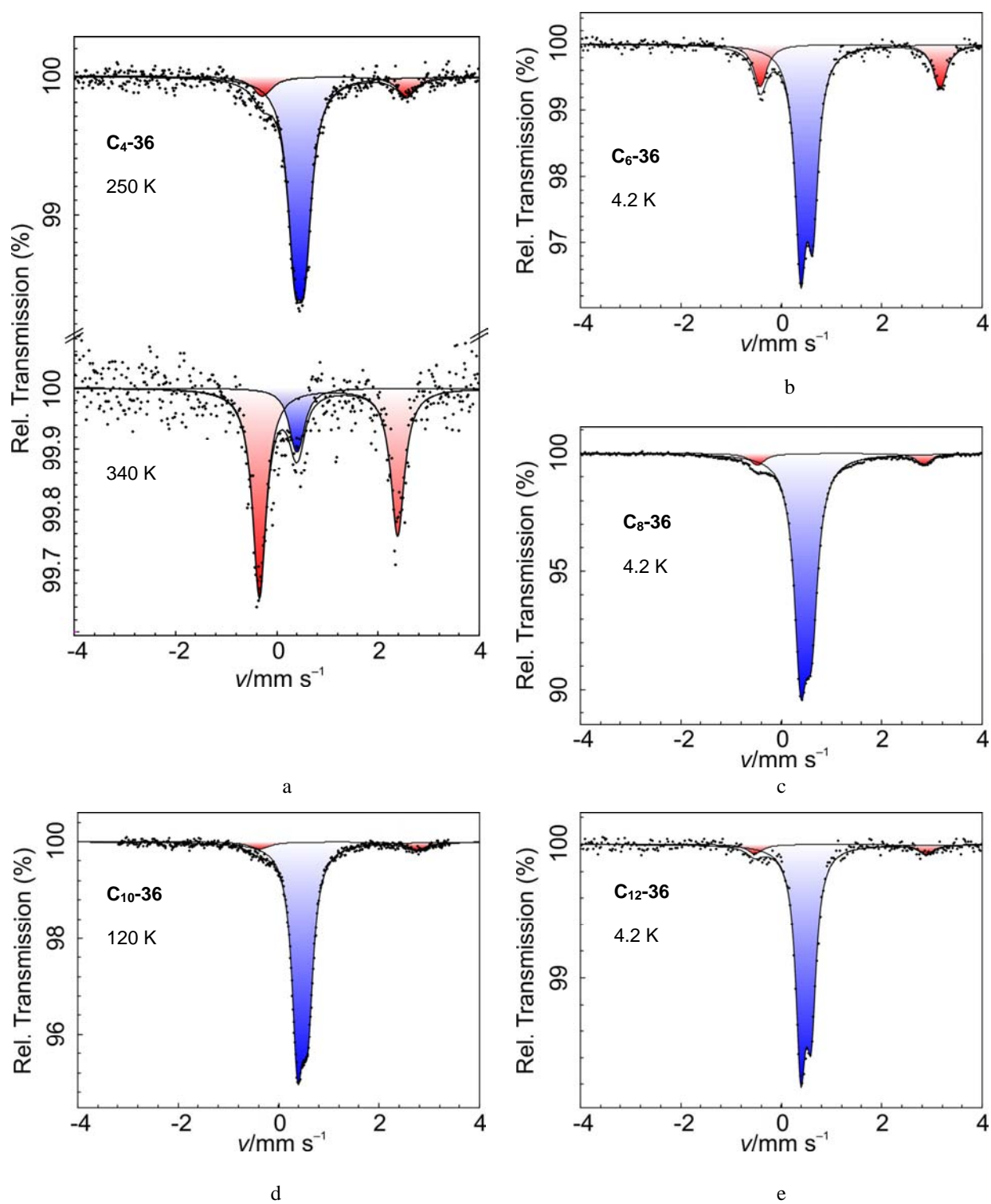
**Figure 113.** Mössbauer spectra of: a) **C$_4$-36** at 250 and 340 K; b) **C$_6$-36** at 4.2 K; c) **C$_8$-36** at 4.2 K; d) **C$_{10}$-36** at 120 K; e) **C$_{12}$-36** at 4.2 K; f) **C$_4$-38** at 200 and 300 K; g) **C$_6$-38** at 4.2 and 250 K; h) **C$_8$-38** at 80 K; i) **C$_{10}$-38** at 80 K; j) **C$_{12}$-38** at 80 K  and k) **C$_{12}$-39** at 80 K.
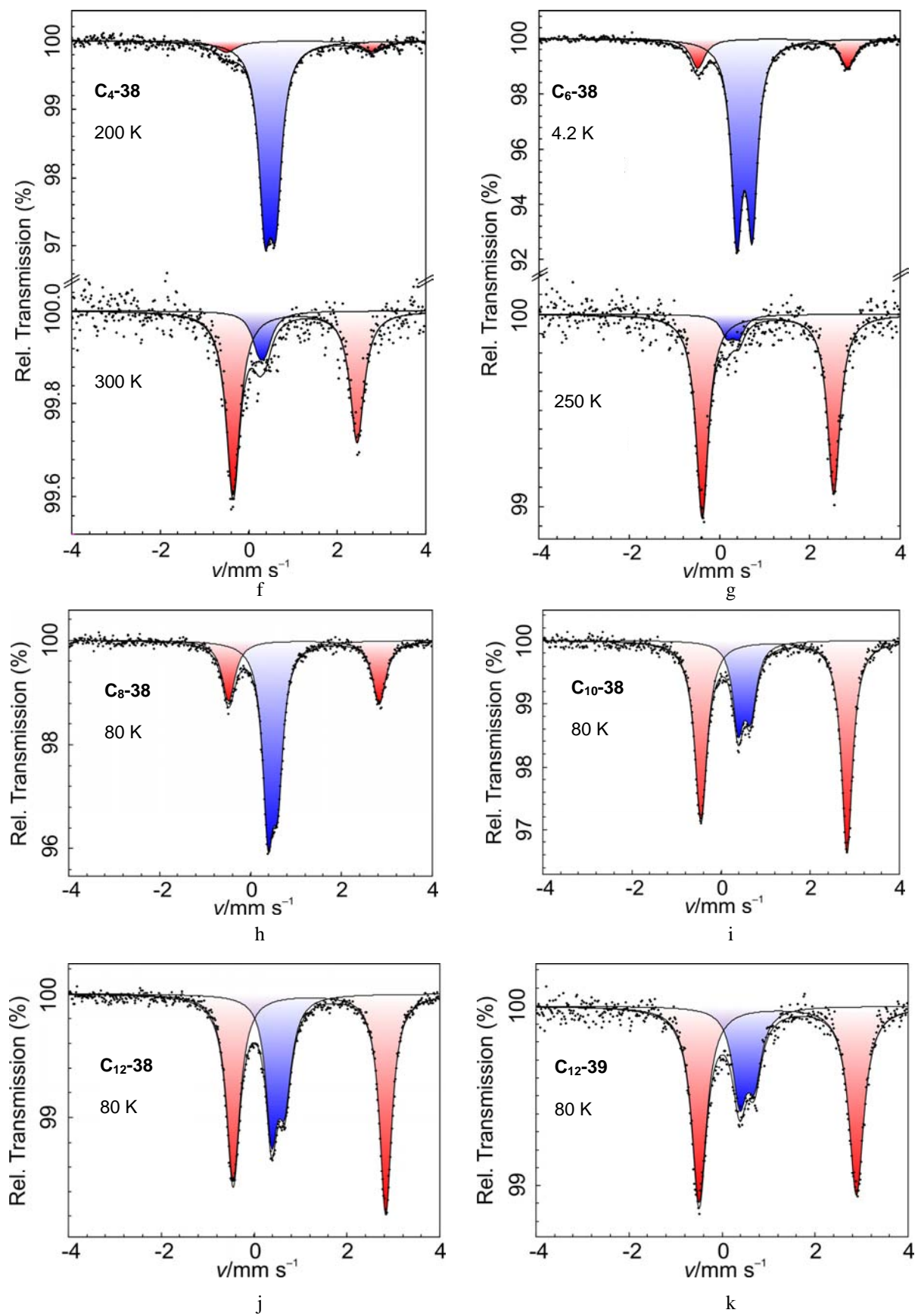
**Figure 113.** (*continued*)
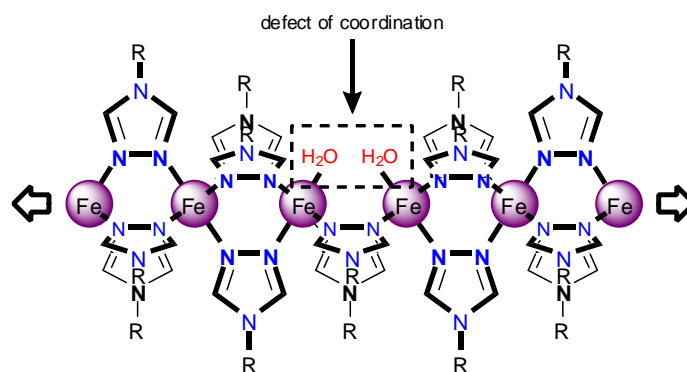
**Figure 114.** Proposed polymer structure of $C_{12}$-38 with the defect of coordination which could lead to the substantial residual high-spin fraction.

**Table 43.** Mössbauer parameters, isomer shift ($\delta$, relative to α-iron), quadrupole splitting ($\Delta E_Q$), half-width of the lines ($\Gamma_{1/2}$) and percentage of the multiplet populations in the high-spin (HS) and low-spin (LS) states at different temperatures ($A$) for $C_n$-36, $C_n$-38 ($n$ = 4, 6, 8, 10, 12) and $C_{12}$-39.

| Compound | $T$ [K] | Spin state | $\delta$ [mm s$^{-1}$] | $\Delta E_Q$ [mm s$^{-1}$] | $\Gamma_{1/2}$ [mm s$^{-1}$] | $A$ [ %] |
|---|---|---|---|---|---|---|
| $C_4$-36 | 80 | LS | 0.50(0) | 0.21(0) | 0.17(1) | 94.4(10) |
| | | HS | 1.11(0) | 3.18(1) | *0.17* | 5.6(8) |
| | 250 | LS | 0.45(1) | 0.20(1) | 0.17(0) | 87.3(17) |
| | | HS | 1.15(1) | 2.81(0) | *0.17* | 12.7(22) |
| | 340 | LS | 0.32(6) | 0.27(0) | 0.16(0) | 17.4(40) |
| | | HS | 1.02(1) | 2.73(2) | *0.16* | 82.6(54) |
| $C_6$-36 | 4.2 | LS | 0.51(1) | 0.24(0) | 0.13(5) | 77.5(17) |
| | | HS | 1.37(1) | 3.58(2) | 0.16(2) | 22.5(24) |
| $C_8$-36 | 4.2 | LS | 0.49(1) | 0.22(0) | 0.15(0) | 92.6(4) |
| | | HS | 1.18(1) | 3.30(2) | *0.18* | 7.4(4) |
| $C_{10}$-36 | 120 | LS | 0.48(2) | 0.20(0) | 0.13(0) | 92.5(8) |
| | | HS | 1.21(2) | 3.10(5) | *0.14* | 7.5(18) |
| $C_{12}$-36 | 4.2 | LS | 0.49(0) | 0.20(1) | 0.12(0) | 92.3(21) |
| | | HS | 1.18(0) | 3.42(2) | 0.19(0) | 7.7(35) |
| $C_4$-38 | 80 | LS | 0.51(0) | 0.25(0) | 0.16(1) | 91.2(4) |
| | | HS | 1.17(1) | 3.45(2) | 0.21(1) | 8.8(6) |
| | 200 | LS | 0.49(1) | 0.25(1) | 0.17(1) | 92.4(2) |
| | | HS | 1.14(3) | 3.29(6) | *0.16* | 7.6(1) |
| | 300 | LS | 0.35(1) | *0.2* | *0.22* | 16.8(29) |
| | | HS | 1.05(1) | 2.80(2) | 0.19(1) | 83.2(59) |
| $C_6$-38 | 4.2 | LS | 0.55(0) | 0.34(0) | 0.14(0) | 82.1(84) |
| | | HS | 1.18(1) | 3.32(2) | 0.19(1) | 17.9(13) |
| | 80 | LS | 0.55(0) | 0.35(0) | 0.15(0) | 69.4(11) |
| | | HS | 1.17(0) | 3.27(1) | 0.17(1) | 30.6(16) |
| | 190 | LS | 0.51(1) | 0.33(1) | 0.18(1) | 23.9(15) |
| | | HS | 1.11(0) | 3.13(0) | 0.17(1) | 76.1(20) |
| | 250 | LS | 0.32(0) | 0.26(1) | *0.16* | 8.3(25) |
| | | HS | 1.08(0) | 2.91(0) | 0.17(0) | 91.7(50) |

**Table 43**. (*continued*)

| Compound | $T$ [K] | Spin state | $\delta$ [mm s$^{-1}$] | $\Delta E_Q$ [mm s$^{-1}$] | $\Gamma_{1/2}$ [mm s$^{-1}$] | $A$ [ %] |
|---|---|---|---|---|---|---|
| **C$_8$-38** | 80 | LS | 0.49(0) | 0.22(1) | 0.14(3) | 65.8(9) |
| | | HS | 1.17(0) | 3.31(0) | 0.18(1) | 34.2(14) |
| **C$_{10}$-38** | 80 | LS | 0.52(0) | 0.28(1) | 0.16(2) | 26.5(9) |
| | | HS | 1.19(1) | 3.28(0) | 0.15(0) | 73.5(13) |
| **C$_{12}$-38** | 80 | LS | 0.52(1) | 0.28(1) | 0.18(1) | 34.7(7) |
| | | HS | 1.19(0) | 3.28(0) | 0.16(1) | 65.3(10) |
| **C$_{12}$-39** | 80 | LS | 0.54(1) | 0.32(0) | 0.19(1) | 27.6(18) |
| | | HS | 1.20(1) | 3.38(0) | 0.19(0) | 72.4(25) |

The values given in italics were fixed during the fitting.

### 3.4.8   Discussion

Before discussing the correlation between structure and magnetic properties in **C$_n$-36** and **C$_n$-38** ($n$ = 4, 6, 8, 10, 12) we shall clarify why the compounds under discussion can be considered as chain-like polymeric materials. The linear structure of the non-alkylated parent compound **30** was established unambiguously on the basis of the EXAFS data supported also by the crystal structure analysis of the linear triazole-based copper(II) polymer **30-Cu**. Support for the polymeric structure of the compound **32** comes from IR data along with Mössbauer and magnetic data. The alkylation of the parent systems **30** and **32** resulted in the formation of the compounds **C$_n$-36** and **C$_n$-38**. The EXAFS data of the compound **C$_{12}$-36** confirm the polymeric structure in close analogy with the parent system **30**. Furthermore, IR spectroscopic study carried out on the alkylated materials shows that the triazole units retain $C_{2v}$ symmetry disclosing the $N1,N2$-bridging coordination mode of the triazole units. For the compounds **C$_n$-36**, the small amount of remaining paramagnetism at low temperature indicates that most of the iron(II) ions undergo thermal spin-transition, which in turn points at the N$_6$ surroundings for most of the iron(II) ions. However, the incomplete spin-transition at low temperatures for compounds **C$_n$-38** with $n$ = 8, 10, 12 raises the question about its nature. Earlier several authors proposed the trinuclear structure for the alkylated triazole-based compounds with an incomplete transition [93, 133]. We have checked this hypothesis on our compounds with the dynamic light scattering technique and Mössbauer spectroscopy. The obtained results show that the polymeric structure is adopted by all compounds **C$_n$-38** independently of $n$. The incomplete spin-transition is rather a special feature of the compounds and probably arises from imperfections of the packing in these soft materials.

The higher homologues of the series $C_n$-36 and $C_n$-38 with $n$ = 8, 10, 12 exhibit the columnar mesomorphism. According to the XRD data of compound $C_8$-36 a columnar lamellar mesophase (Col$_L$) can be ascribed to this compound while two higher homologues possess hexagonal packing of the polymer chains with adopting the hexagonal columnar mesophase Col$_h$. In Figure 115a is shown the structure of the monomeric unit along with the spin-state dependent intrachain periodicity of the monomeric units (Figure 115b) and two packing motifs of the polymeric chains in the mesophase, Col$_h$ and Col$_L$ (Figure 115c, d).

On lengthening the alkyl chains, the magnetic properties of $C_n$-36 and $C_n$-38 change from those typical for crystalline spin-crossover compounds ($n$ = 4, 6) to those which coexist with the liquid crystalline properties ($n$ = 8, 10, 12). It was found that the pristine compounds are hydrates which lose solvate water on heating and generate new anhydrous compounds $C_n$-37 and $C_n$-39. Both forms differ in their spin-transition regime, however, the difference between the pristine and the dehydrated compounds depends on the type of the anion. For the triflate ($CF_3SO_3^-$) compounds $C_n$-36 and $C_n$-37 the magnetic properties of both forms are quite similar (Figure 104a–e), whereas for the tetrafluoroborate ($BF_4^-$) compounds $C_n$-38 the heating provokes the dehydration to yield $C_n$-39 which changes the character of the spin-transition to a very gradual one (Figure 104f–j).

In the following we shall discuss the role of the structural variables which have influence on the magnetic properties of the compounds, namely: 1) the type of the anion ($CF_3SO_3^-$ or $BF_4^-$) and the water content of the compound; 2) the length of alkyl chains and the role of the phase transition. One more factor which could influence the magnetic properties is the packing of polymeric polymeric chains, but it is apparently unimportant as follows from the practically similar magnetic data of compounds $C_8$-36 and $C_{10}$-36 which adopt lamellar and hexagonal packing, respectively.

***Anion and water content***. The role of the non-coordinated solvent molecules in most iron(II) spin-crossover complexes is well understood. The incorporation of the solvent molecules into the crystal lattice mostly influences the interlinking of the spin-crossover centers and leads to higher transition temperatures and abruptness of the spin-transition. An early example was provided by the compounds [Fe(2-pic)$_3$]Cl$_2$·Solv, where Solv = $C_2H_5OH$ or $CH_3OH$, or $H_2O$, or $2H_2O$ [78]. The spin-transition temperature was found to increase along the series, which was assigned to the nature of the solvent molecules [23, 85]. Specific hydrogen bonding of lattice water molecules was also noticed.
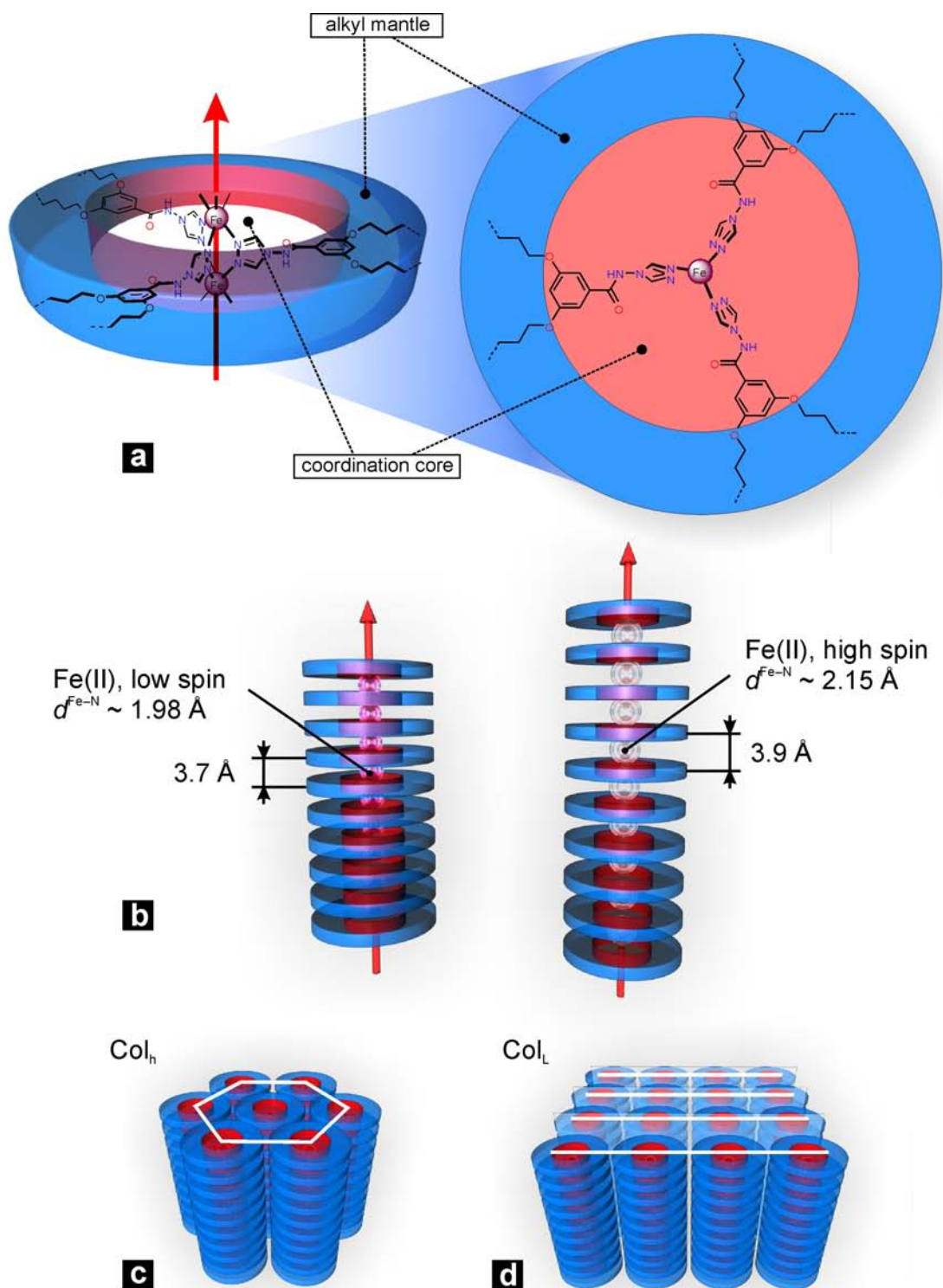
**Figure 115.** a) Schematic ideal structure of the monomeric unit in **C_n-36** and **C_n-38** (a neighbouring iron(II) ion is added for clarity). The inner part of the chain is the coordination core made by the linearly arranged iron(II) ions bridged by three triazole moieties (red). The coordination core is surrounded by the covalently tethered alkyl chains in the peripheral part (blue); b) Polymeric chains in the low-spin state (left) and high-spin state (right) with the Fe···Fe periodicity defined by the Fe–N bond length (larger for high-spin than for low-spin); c) Hexagonal packing Col_h of the polymeric chains in **C_n-36** and **C_n-38** except **C_6-36** and **C_8-36** and d) Lamellar packing Col_L of the polymeric chains in **C_6-36** and **C_8-36**.

As it was discussed by Garcia *et al.* in ref. [334], the explanation of the hydrogen bonding effect and its influence on the parameter $T_{1/2}$ implies formation of the strong hydrogen bonds N–H···OH$_2$, where the N atom belongs to the heterocycle or amine group directly bonded to the iron(II) ion. This interaction results in strengthening the metal-ligand interaction and then favoring the low-spin state at higher temperatures [167, 374]. In contrast, the N···H–OH interaction, where N is the imine nitrogen atom, favors the stabilization of the high-spin state. In this case $T_{1/2}$ is shifted toward lower temperatures in comparison to the anhydrous compound. Compounds $C_n$-36, $C_n$-38 possess no free imine group, they only have amide groups. However, as follows from the magnetic data, the nitrogen atom seems to be not involved in the hydrogen bonding with the water molecule. Therefore, the observed change in the magnetic properties on dehydration cannot be attributed to an electronic effect induced by the kinds of the hydrogen bonding discussed above.

In the particular case of the triazole complexes the role of water is assumed to be important as stated in numerous reports [81, 92, 94, 133, 314]. However, to the best of our knowledge the involvement of water molecules in the crystal lattice of the triazole-based iron(II) polymers was never analyzed despite available crystal structures of the copper(II) analogues. According to the crystal data, in **30-Cu** and [Cu(NH$_2$trz)$_3$](BF$_4$)$_2$·H$_2$O [331] the water molecules bridge CH groups of the neighboring triazole units reinforcing the polymeric chain by weak double hydrogen bonds CH···Ow···HC (Figure 116a). In the case where the number of water molecules per monomeric unit is less than three, the anion can be involved in the double hydrogen bonding with the CH-groups of the triazole rings (Figure 116b, c). It seems also to be the case for the parent compound **30** which has two molecules of water in the pristine form (Chapter 3.2.1). Comparison of the polymers [Cu(hyettrz)$_3$](CF$_3$SO$_3$)$_2$·H$_2$O (hyettrz = 4-(2′-hydroxy-ethyl)-1,2,4-triazole) [346] (Figure 116b) and [Cu(NH$_2$trz)$_3$](BF$_4$)$_2$·H$_2$O [331] (Figure 116c) does not show any differences between the involvement of the anions BF$_4^-$ and CF$_3$SO$_3^-$ in the weak hydrogen bonding. In both cases the anions bridge the neighboring triazole moieties through the oxygen atom or the fluorine atom as is depicted in Figure 116b, c. Since both types of the anions can be involved in the hydrogen bonding with the triazole units, the higher transition temperatures of the reported triflate-based compounds probably originate from a larger electrostatic pressure created by this type of anion [338]. The properties exhibited by the parent compounds **30** and **32** can be explained in a similar way.
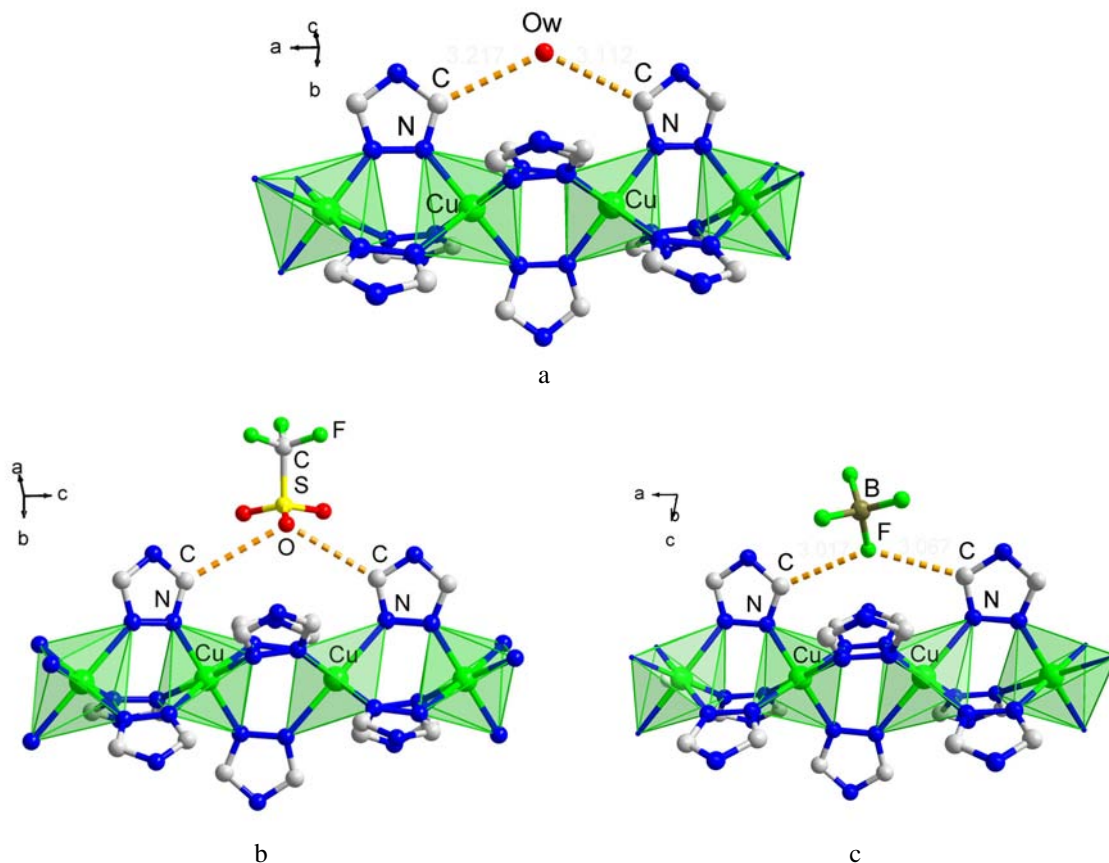
**Figure 116.** Types of the weak double hydrogen bonding CH···X···HC observed in one-dimensional polymers [Cu(trz)$_3$]$_\infty$, where X is: a) the oxygen atom of the water molecule (cf. Figure 91b); b) the oxygen atom of the triflate anion and c) the fluorine atom of the tetrafluoroborate anion. Substituents are omitted for clarity. Crystal structures were adopted from refs. [331] and [346].

The same explanation is also valid for the alkylated iron(II) derivatives. The TGA data show that the compounds $C_n$-36 contain only half a molecule of water per a monomeric unit which means also that the oxygen atoms of the triflate anions might be involved in the hydrogen bonding of the triazole units (Figure 116b) which can explain the observed abrupt spin-transition in the anhydrous compounds $C_n$-37 (and also in the parent 31) (see Figure 104a–e). On the other hand, for the BF$_4^-$ derivatives the loss of the lattice water molecules drastically decreases the cooperativity resulting in a very gradual incomplete spin-transition in 33 and $C_n$-39 which can imply that the hydrogen bridging of the triazole units through the BF$_4^-$ anions (like is shown in Figure 116c) is not so effective or not realized at all. The IR data in the region of the absorption band B–F (Figure 103) confirm the decrease of the symmetry of the tetrafluoroborate anions because of the interaction with the lattice surrounding that might indicate the involvement in the hydrogen bonding.

*Alkyl chains and phase transition.* By introducing alkyl substituents into the ligand *tba*, the separation between the neighboring polymeric chain was increased (Figure 109). The

resulting effect on the magnetic properties depends on the length of the substituents (Figure 104a–j and Figure 105). If we consider the three-dimensional character of the intermolecular contacts in the parent compounds **30** and **32**, the interactions in the derivatives **C$_n$-36** and **C$_n$-38** become a one-dimensional character; consequently, this should diminish the hysteresis or the steepness of the spin-transition [93]. Indeed, in comparison with the parent complexes, the $T_{1/2}$ changes slightly being *ca*. 300 K but, for example, in **C$_4$-36** and **C$_6$-36** the width of the hysteresis loop is reduced. Since the parent and alkylated derivatives differ from each other only by the alkyl substituent on the triazole ligands, this result tends to show that in the unalkylated polymers there is the interchain contribution to the overall cooperativity of the spin-transition which correlates with the conclusions of other researchers [93, 133]. Lengthening the alkyl chains influences the $T_{1/2}$ value in a rather gradual way for both the pristine and the dehydrated compounds as shown in Figure 105. With the triflate anion one can observe a monotonic increase of $T_{1/2}$ with *n*, whereas for the tetrafluoroborate compounds the dependence has a complicate character, but for the higher homologues the increase is apparent as well. In general, increase of *n* decreases the completeness of the spin-transition in both low- and high-temperature regions.

Roubeau *et al.* [133] reported on the absence of the general dependence of the magnetic properties on the length of the alkyl chain in the systems formed by 4-n-alkyl-triazoles. However, their report covered only part of the alkylated systems because of encountered synthesis problems [133]. Kojima *et al.* reported on the triazole systems with alkylated anion of the general formula [Fe(NH$_2$trz)$_3$](C$_i$H$_{2i+1}$SO$_3$)$_2 \cdot$2H$_2$O (*i* = 1–9) where a gradual dependence of the $T_{1/2}$ parameter on *i* was found [375]. From EXAFS measurements it was apparent that the distance Fe$\cdots$Fe within the polymeric chains decreases with increasing *i* which was supposed to be induced by the "fastener effect" of the alkyl chains [375]. In the case of compounds **C$_n$-36** and **C$_n$-38** where the coordination core is surrounded by the mantle of the covalently tethered alkyl chains (Figure 115a) the same effect can be called for the explanation of the observed increase of $T_{1/2}$ with *n*.

For the triflate-based anhydrous compounds **C$_n$-37** reappearance of the magnetic hysteresis loop in the homologues with *n* = 8, 10, 12 can by no means be attributed to the increase of the interchain cooperativity. The explanation should be looked for in the fact that those compounds down to 270 K are in the liquid crystalline state as was determined by XRD, DSC and POM measurements. The width of the loop is quite small ($\Delta T_{hys} = 2$ K) which points out that upon spin-transition the liquid crystalline compounds exhibit relatively small structural reorganization. Additionally, the complicate form of the loop for **C$_{12}$-37** shows an

influence of the glass transition on the magnetic properties. The feature detected at the low temperature edge near 275 K coincides with the anomaly detected by the XRD and DSC techniques.

As discussed in the literature [60, 133, 325], the interchain interactions in triazole-based spin-crossover polymers are important for defining the abruptness and hysteresis of the spin-transition. But as we have shown in this chapter, in the alkylated system upon passing some threshold of the chain length *n* a new effect comes into play which modifies the characteristics of the spin-transition. This effect is liquid crystallinity. The semi-fluid nature of the liquid crystalline materials is responsible for the delay effect in the restoring of the structural and magnetic properties upon subsequent heating/cooling.

### 3.4.9   Summary

1.  The chemical modification of the parent compounds **30** and **32** provided alkylated systems **C$_n$-36** and **C$_n$-38** (*n* = 4, 6, 8, 10, 12) which show modified spin-crossover properties;

2.  The polymeric structure of the parent compounds is preserved in the alkylated derivatives as determined by the EXAFS, IR, Mössbauer and dynamic light scattering data;

3.  Upon heating and consequent release of the crystal water anhydrous compounds **C$_n$-37** and **C$_n$-39** (*n* = 4, 6, 8, 10, 12) were obtained. The magnetic properties of the pristine and anhydrous compounds were found to be different. Seemingly, the preserved abruptness of the spin-transition in the anhydrous alkylated compounds is the result of the weak hydrogen bonding CH$\cdots$O$\cdots$HC between the anions and triazole units whereas in the pristine compounds the water of crystallization is an additional factor increasing the cooperativity of the spin-transition;

4.  Appearance of the narrow hysteresis loop in the higher homologues **C$_n$-37** with *n* = 8, 10, 12 is due to the liquid crystalline properties of the compounds which was supported by the DSC, XRD and POM data;

5.  For the compound **C$_{12}$-37** the phase transition almost coincides with the spin-transition and affects the shape of the hysteresis loop.

# 3.5   Characterization and physical properties
## of compounds $C_n$-40 and $C_n$-41

### 3.5.1   Introductory remarks

This chapter concerns the characterization and study of the derivatives of the parent system **34** formed by the ligand 3,5-bis(alkoxy)-*N*-(4*H*-1,2,4-triazol-4-yl)benzamide ($C_n$-*tba*) along with the anion tosylate (*p*-tol⁻). The codes and the composition of the compounds under discussion are shown in Table 44.

**Table 44.** Schematic molecular structure and composition of **$C_n$-40, $C_n$-41** (*n* = 4, 6, 8, 10, 12) and **$C_8$-40-Zn.**
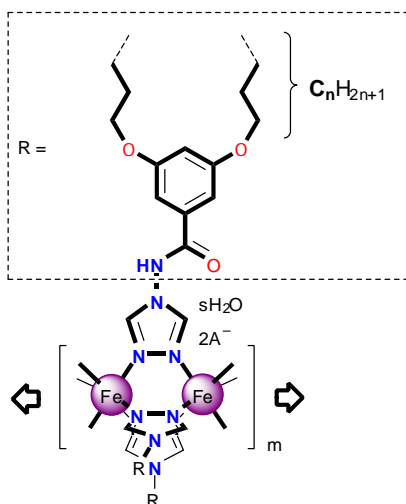


| Anion A⁻ | s | Compound |
|---|---|---|
| *p*-tol⁻ | 1 | **$C_4$-40, $C_6$-40, $C_8$-40, $C_{10}$-40, $C_{12}$-40** |
| | 0 | **$C_4$-41, $C_6$-41, $C_8$-41, $C_{10}$-41, $C_{12}$-41** |
| | 1 | **$C_8$-40-Zn** [a] |

[a] Compound **$C_8$-40-Zn** is the zinc(II) analogue of compound **$C_8$-40**

### 3.5.2   TGA and IR data

The analysis of the IR spectra included regions with the characteristic bands of alkyl chains, ligand groups and anions.

*Alkyl chains.* The packing of the chains in the paraffinic layers and their conformation are of interest. In the IR spectra, the relevant frequencies cover regions of 2600–3000 cm⁻¹ and 700–1600 cm⁻¹ including symmetric and asymmetric stretching modes $v_s(CH_2)$ and $v_{as}(CH_2)$, the scissoring band $\delta(CH_2)$, and the rocking mode $\rho(CH_2)$. The analysis of the IR data in these regions did not differ from the two previous families of compounds which led to the conclusion about the disordered state of the alkyl chains.

Practically all bands of the CH$_2$-vibrations in **C$_4$-40** and **C$_6$-40** show values which differ from those of higher members of the family. This means that the packing of alkyl chains found in the lower homologues differs from the higher homologues.

***Triazole units***. The N1,N2-Bidentate coordination mode of the triazole units is confirmed by the non-split absorption band $\tau_2$ at ~627 cm$^{-1}$ in both series [318]. For complexes **C$_n$-40** the absorption band $v$(C–H$_{trz}$) is at ~3095 cm$^{-1}$ like it was found in the series **C$_n$-36** (Chapter 3.4.3) with iron(II) ions in the low-spin state (Table 45) [330].

**Table 45.** TGA and IR data for complexes **C$_n$-40** (n = 4, 6, 8, 10, 12) and **C$_8$-40-Zn.**

| Compound | TGA, w/w [ %] $(T)^a$ | IR [cm$^{-1}$]$^b$ | | | | | | |
|---|---|---|---|---|---|---|---|---|
| | | $v$(C–H$_{tzr}$) | $v_s$(CH$_2$), $v_{as}$(CH$_2$) | $v$(C=O) | $\delta$(CH$_2$) | $\rho$(CH$_2$) | $\tau_2$ | $v$(Anion) |
| **C$_4$-40** | 1.7 (335 K) | 3095 | 2930, 2858 | 1698 | 1458 | 726 | 627 | 1166, 1034 |
| **C$_6$-40** | 1.6 (340 K) | 3096 | 2931, 2859 | 1699 | 1458 | 726 | 626 | 1165, 1034 |
| **C$_8$-40** | 1.6 (339 K) | 3094 | 2926, 2856 | 1697 | 1458 | 725 | 628 | 1165, 1034 |
| **C$_{10}$-40** | 1.4 (340 K) | 3095 | 2925, 2854 | 1696 | 1458 | 723 | 629 | 1166, 1034 |
| **C$_{12}$-40** | 0.9 (340 K) | 3092 | 2924, 2853 | 1697 | 1458 | 723 | 628 | 1164, 1034 |
| **C$_8$-40-Zn** | 1.6 (332 K) | 3093 | 2925, 2854 | 1698 | 1454 | 722 | 628 | 1168, 1034 |

$^a$ Value is given at the point where the plateau is reached. $T$ is the temperature at which the dehydration process is centered; $^b$ $v$, stretching; $\delta$, bending; $\rho$, rocking; $\tau$, ring torsion vibration of the triazole unit; as, asymmetric, s, symmetric.

***Anions***. For the anion *p*-tol$^-$ the corresponding absorption bands confirmed the composition of the compounds.

Additionally, in the region of 3460–3500 cm$^{-1}$ the spectra of all compounds exhibit a broad absorption peak of water.

Thermogravimetry (TGA) carried out with the pristine compounds at a rate of 10 K min$^{-1}$ in nitrogen atmosphere reveals a continuous loss of mass starting at 320 K. This decrease in mass proceeds rapidly centered near 340 K (Figure 117, Table 45). At 360 K the percentage mass loss is in agreement with the removal of one molecule for the homologues **C$_n$-40** (n = 4, 6, 8, 10, 12) and zinc(II) analogue **C$_8$-40-Zn**.

Values of the discussed absorption bands and the TGA data are presented in Table 45.
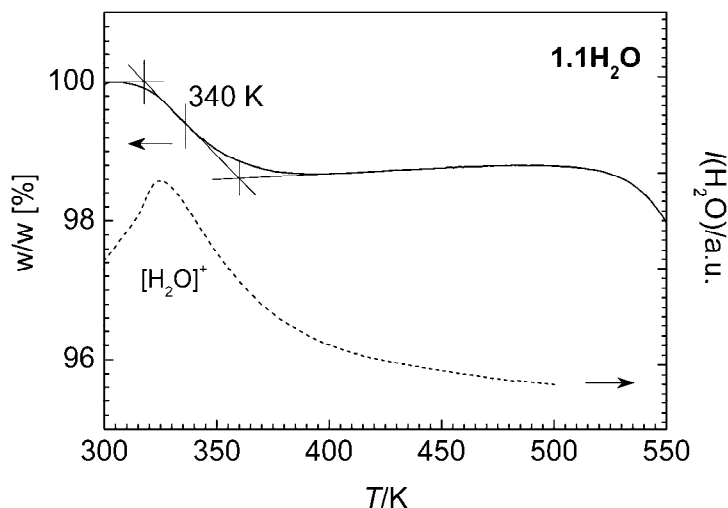
**Figure 117.** Thermogravimetric properties of $C_{10}$-40 recorded at a rate of 10 K min$^{-1}$ (solid line) measured in tandem with the electron impact mass spectroscopy (EI MS) which followed the signal of the cation $[H_2O]^+$ ($M_w$ = 18 g mol$^{-1}$) with temperature (dashed line).

### 3.5.3   UV/VIS spectroscopic data of compound $C_{12}$-40

The UV/VIS absorption spectrum of compound $C_{12}$-40 in solid state is shown in Figure 118. It exhibits an intense $\pi \rightarrow \pi^*$ ligand centered peak at 314 nm. An intense spin-allowed $^1A_{1g} \rightarrow {}^1T_{2g}$ $d$–$d$ absorption band is located at 380 nm whereas a broad $^1A_{1g} \rightarrow {}^1T_{1g}$ band is centered at 530 nm. The value of the ligand field strength can be calculated from the derived spectroscopic values [376]: $10Dq^{LS} = E(^1T_{1g}) - E(^1A_{1g}) + \{E(^1T_{2g}) - E(^1T_{1g})\}/4 \approx 20$ 700 cm$^{-1}$. The corresponding value of the ligand field strength in the high-spin state is: $10Dq^{HS} = 10Dq^{LS}/1.75 \approx 11\ 800$ cm$^{-1}$.
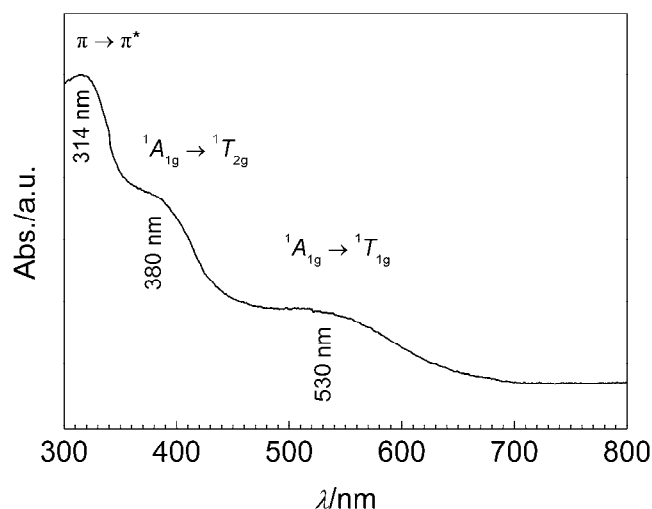


**Figure 118.** The UV/VIS absorption spectrum of compound $C_{12}$-40 in solid state at room temperature.

### 3.5.4   Magnetic properties

The magnetic properties of the compounds **C<sub>n</sub>-40** ($n$ = 4, 6, 8, 10, 12) were measured in both cooling and heating modes in order to detect the influence of the temperature and of the dehydration on the magnetic properties of the compounds. The variation of the product of the molar magnetic susceptibility $\chi_M T$ *vs* $T$ is shown in Figure 119a–e. As one can see, at room temperature the susceptibility of the pristine compounds **C<sub>n</sub>-40** is very near to zero. Mössbauer spectra recorded at 4.2 K confirm that the residual high-spin fraction of iron(II) ions is low in all materials. Upon heating $\chi_M T$ increases abruptly attaining the value of about 3.50 cm$^3$ K mol$^{-1}$ which clearly indicates the occurrence of spin-state change, which is accompanied by a pronounced change of color from purple (low-spin state) to white (high-spin state) (Figure 120). The characteristic temperatures $T_{1/2}$ at which 50 % of the molecules are in the low- and high-spin states, respectively, are near to 330 K in **C<sub>n</sub>-40**. TGA experiments have shown that dehydration takes place in the same temperature region where spin-crossover occurs (see the typical TGA profile in Figure 117). Dehydration of the materials is accomplished at around 360 K. Interplay between dehydration and spin-crossover as observed in these materials was reported in several cases [81, 214].

The magnetic investigation of the dehydrated complexes **C<sub>n</sub>-41** ($n$ = 4, 6, 8, 10, 12; Figure 119a–e) revealed for higher homologues an incomplete spin-transition accompanied by hysteresis and color change in the temperature region of 250–300 K. Around 50 % of iron(II) ions change the electronic configuration as can be inferred from the value of $\chi_M T$ at 200 K for **C<sub>n</sub>-41**. In fact, the Mössbauer spectrum recorded for compound **C<sub>10</sub>-41** at 4.2 K demonstrates that 50 % of the iron(II) ions are in the low-spin state (Figure 126f). Further decrease of the $\chi_M T$ value below 100 K is due to zero-field splitting and possibly antiferromagnetic coupling of the iron(II) atoms remaining in the high-spin state (Chapter 3.2.6). It is worth noting that the temperature and abruptness of the spin-transition and the hysteresis width increase upon increasing $n$, despite non-linearly (Figure 119a–e, Figure 121). Another remarkable fact is that the spin-transition in **C<sub>10</sub>-41** became frozen below *ca.* 250 K. A residual high-spin fraction of *ca.* 50 % is unusual.
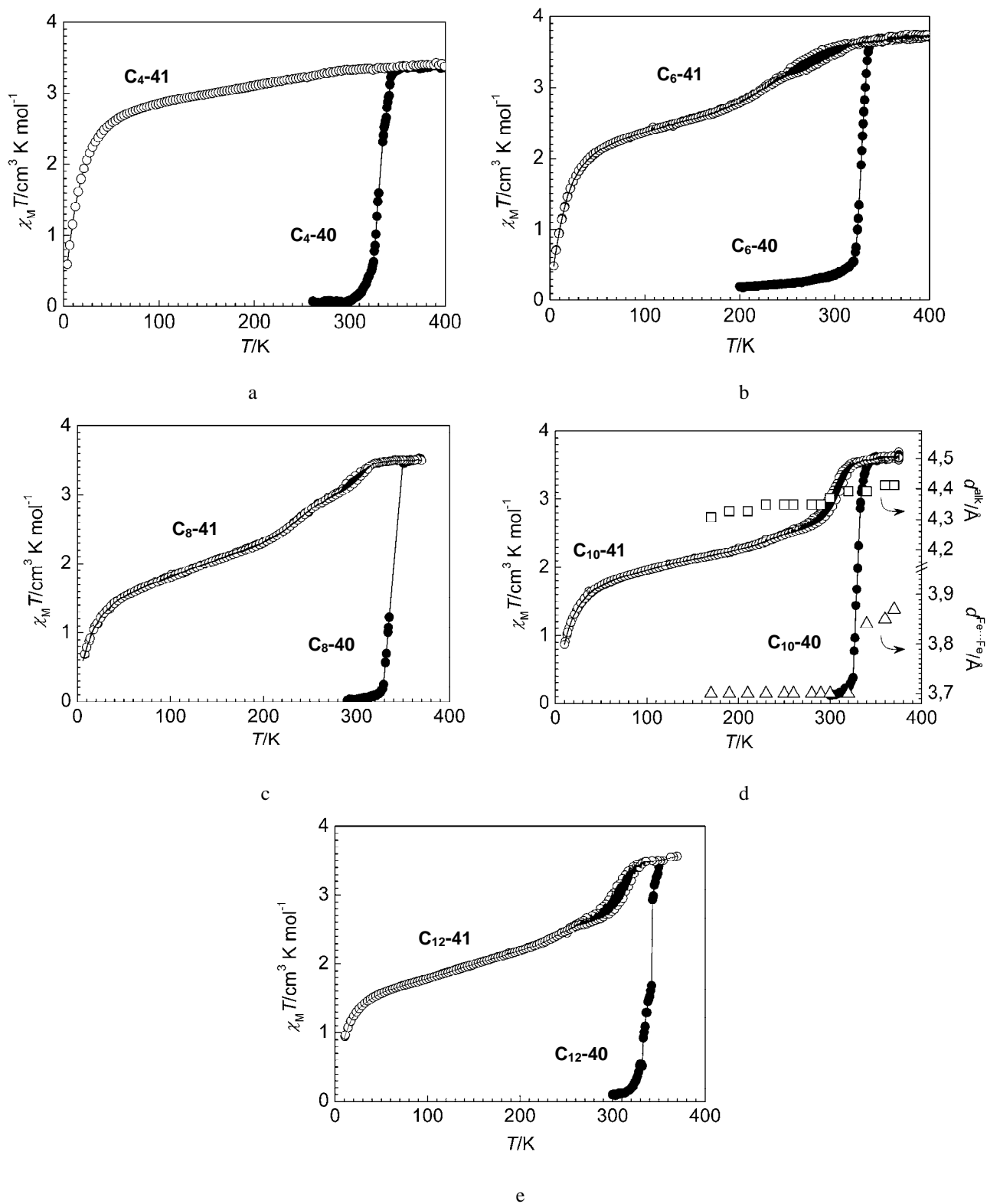
**Figure 119.** Magnetic susceptibility plot $\chi_M T$ *vs* $T$ for a) $C_4$-40, $C_4$-41; b) $C_6$-40, $C_6$-41; c) $C_8$-40, $C_8$-41; d) $C_{10}$-40, $C_{10}$-41. The values $d^{alk}$ (of the alkyl halo) and $d^{Fe\cdots Fe}$ (distance between neighboring iron(II) ions in the polymeric chain) correspond to the compound $C_{10}$-40 during its transformation into $C_{10}$-41; e) $C_{12}$-40, $C_{12}$-41.
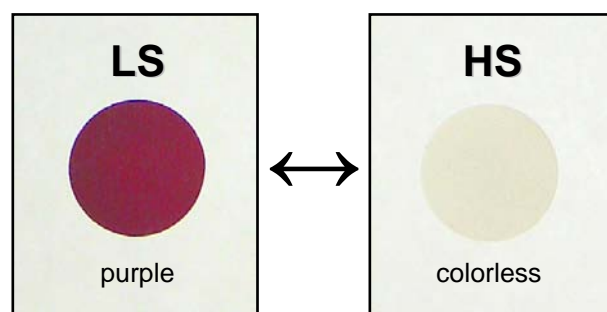
**Figure 120.** Change of color in a film of $C_{10}$-40 at *ca.* 330 K.
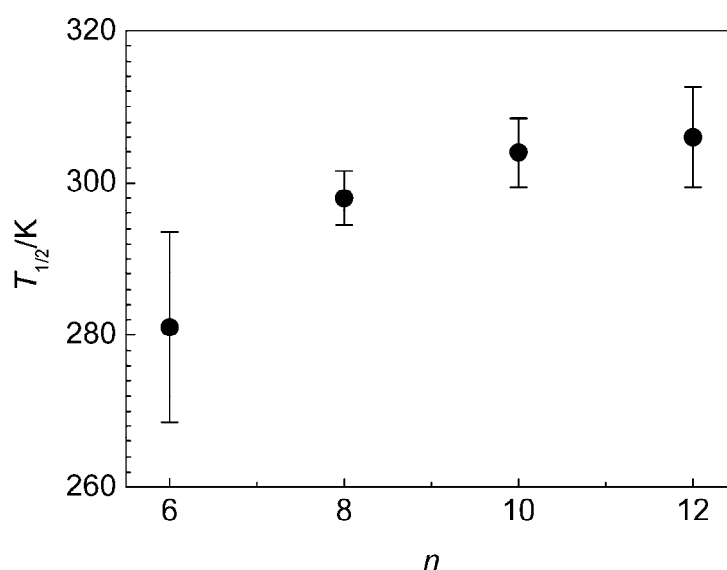


**Figure 121.** Evolution of the parameter $T_{1/2}$ with $n$ in $C_n$-41 with $n = 6, 8, 10, 12$. The length of bars is proportional to the width of the hysteresis loops $\Delta T_{hys}$.

### 3.5.5    XRD data and dynamic light scattering data

The XRD profiles of the complexes $C_n$-40 and $C_8$-40-Zn were measured in the 170–375 K temperature range (Figure 122a–f). The X-ray diffraction patterns of the complexes gave a series of reflections of the two-dimensional hexagonal lattice with up to the seventh reflection {(10), (11), (20), (21), (30), (22) and (31) with the reciprocal spacings at 1, $1/3^{1/2}$, $1/4^{1/2}$, $1/7^{1/2}$, $1/9^{1/2}$, $1/12^{1/2}$ and $1/13^{1/2}$ [371]}. In the XRD patterns of $C_4$-40, $C_6$-40 and $C_8$-40-Zn some additional narrow reflections in the wide-angle region stem from the relatively high crystallinity of the substances. All patterns also have a halo at $d \sim 4.4$ Å ($2\theta \sim 19°$) which corresponds to the disordered alkyl chains. On the basis of these findings a discotic columnar mesophase $Col_h$ has been identified for higher homologues with $n = 8, 10, 12$.

Temperature dependent X-ray measurements were performed on the oriented sample of $C_{10}$-40 prepared *via* extrusion due to its waxy state. In the 2D-WAXS patterns (Figure 123a) the equatorial distribution of the reflections correlates well with a hexagonal ordering with interlayer distance *d* of 29.0 Å (Table 46; the integration plots at different temperatures are shown in Figure 122d). The meridional pair of reflection corresponds to a non-tilted ordering of the disc-like monomeric units (see Figure 115a, b) with a co-facial distance of *ca.* 3.7 Å (corresponds to distance $d^{Fe\cdots Fe}$ along the coordination polymeric chain). Upon heating this reflection is shifted to a lower value ($2\theta \sim 23°$) reflecting an increase of the distance up to nearly 3.9 Å. The discontinuity in the variation of the value (Figure 119d, lower right scale) coincides with the transition of the low-spin iron(II) ions to the high-spin form followed by the magnetic susceptibility. On the other hand, the variation of the alkyl halo at $2\theta \sim 19°$ is negligible (Figure 119d, upper right scale). The partial separation of the broad alkyl reflection into a pair of arks with higher intensity in the equatorial plain indicates that orientation of the alkyl chains preferentially occurs parallel to the axis of the polymeric chain (Figure 123b).

Similar packing in all homologues $C_n$-40 was confirmed on the basis of the dependence of the interlayer distance *d* on the length of alkyl substituents *n* (Figure 124). As is seen, the dependence has a linear character which points out the similar organization of the compounds. The effective size of the coordination core in $C_n$-40 can be determined from a fit of the interlayer spacing *d* *vs* side-chain length *n* which yields a straight line. A linear regression (R = 0.995) gives a slope of 0.92 Å per *n* and an intercept of 18.08 Å which has to be near the size of the coordination core in parent 34 (or 30-Cu), *n* = 0. Assuming that the packing is hexagonal, recalculation using the formula $d^{cc} = 2/3^{1/2}d^{n=0}$ provides the size of the coordination core $d^{cc}$ equal to 20.9 Å which is larger than the value obtained directly from the structure of the copper(II) analogue 30-Cu (19.7 Å). The difference was assigned to the bulkier nature of the anion *p*-tol⁻ in comparison with the triflate and additionally to the different nature of the central ions.

The derived parameter *d* for compounds $C_n$-40 (*n* = 4, 6, 8, 10, 12) and $C_8$-40-Zn are shown in Table 46.

The average length of the polymeric chains in solution was evaluated with dynamic light scattering. For $C_{12}$-40 the determined hydrodynamic radius of the polymeric species in chloroform is nearly 980 Å giving an approximate number or iron(II) ions per chain equal to *ca.* 500.
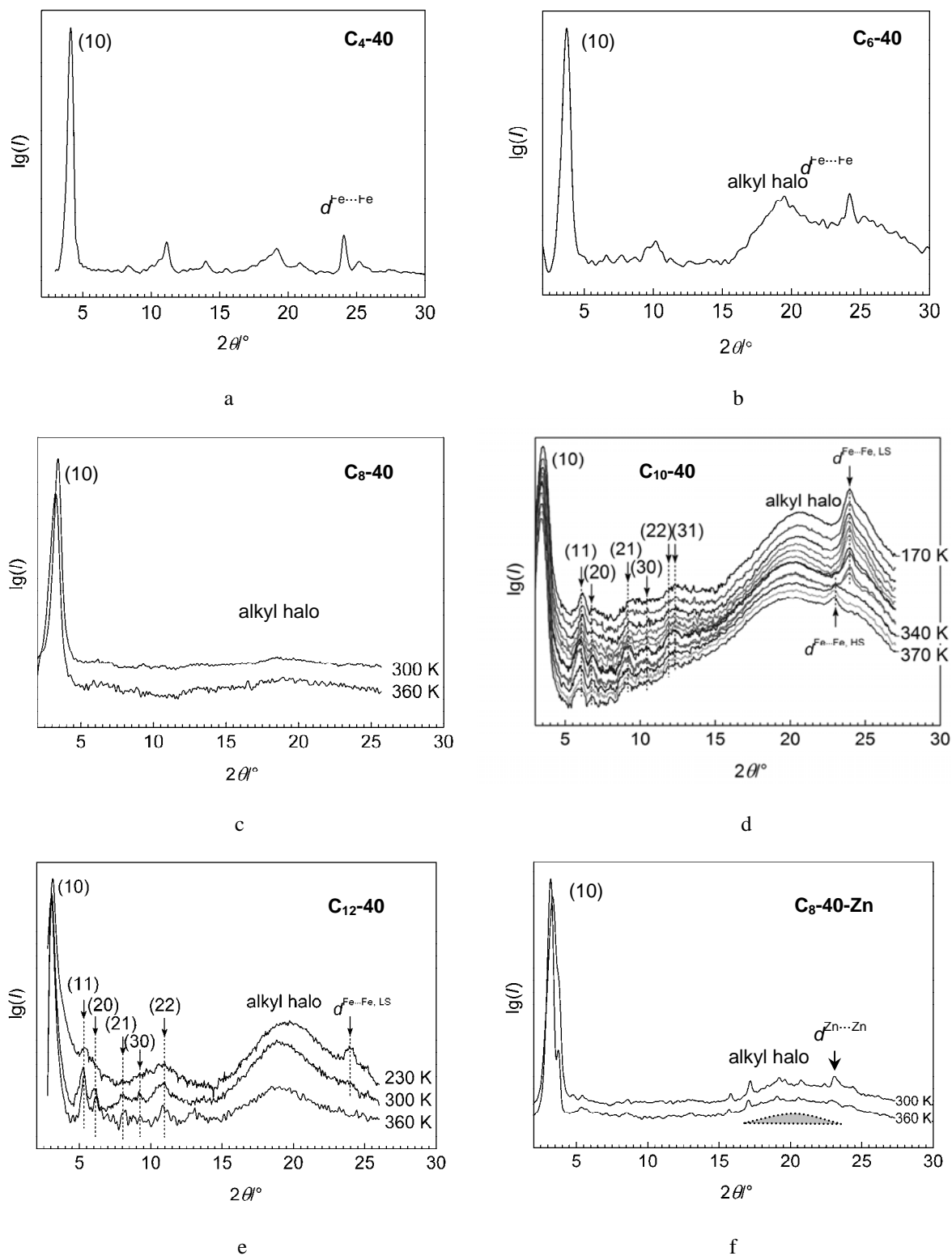
**Figure 122.** XRD profiles of a) **C**$_4$**-40**; b) **C**$_6$**-40**; c) **C**$_8$**-40**; d) **C**$_{10}$**-40**; e) **C**$_{12}$**-40**; f) **C**$_8$**-40-Zn** measured at room temperature (for single profiles) or at temperatures indicated next to the profiles.

a                 b
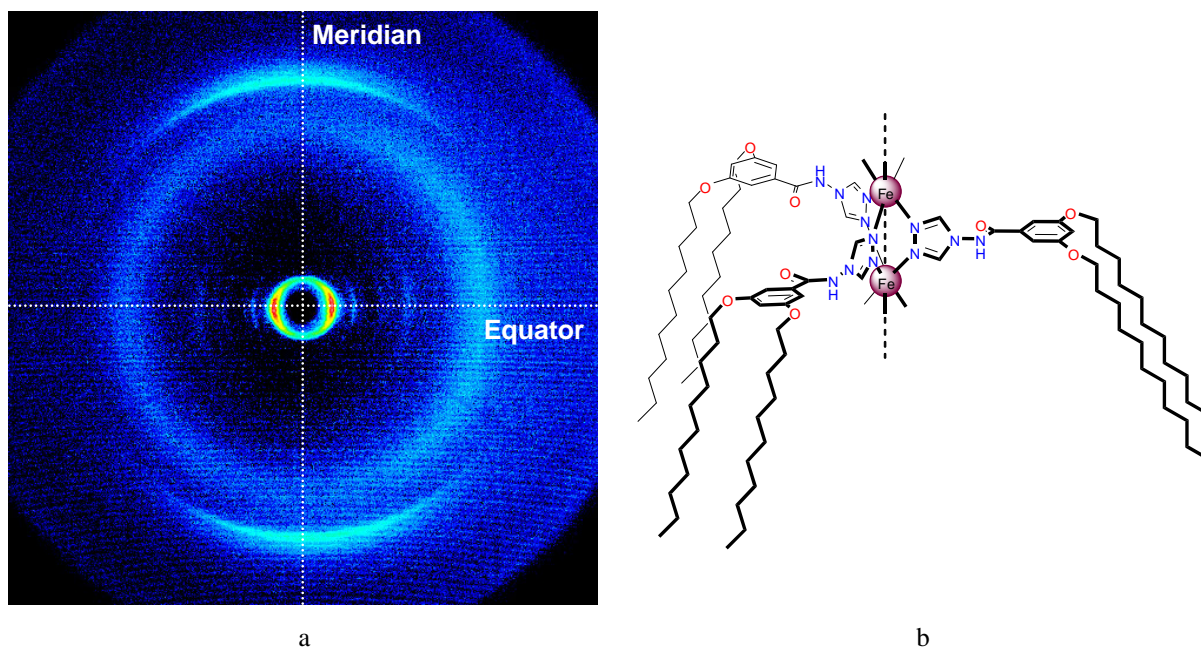
**Figure 123.** a) 2D-WAXS pattern from the oriented sample of $C_{12}$-40 at 260 K. A relatively sharp pair of equatorial reflections along with higher order reflections in the low-angle regime originates from the intercolumnar ordering whereas a pair of weak meridional reflections is due to intracolumnar arrangement of disk-like monomeric units. The diffuse reflection in between is of the liquid-like alkyl chains partially aligned parallel to the polymeric chains; b) Schematic structure of the monomeric unit with the tilt of the alkyl chains close to the direction of the axis of the polymeric chain (dashed line).
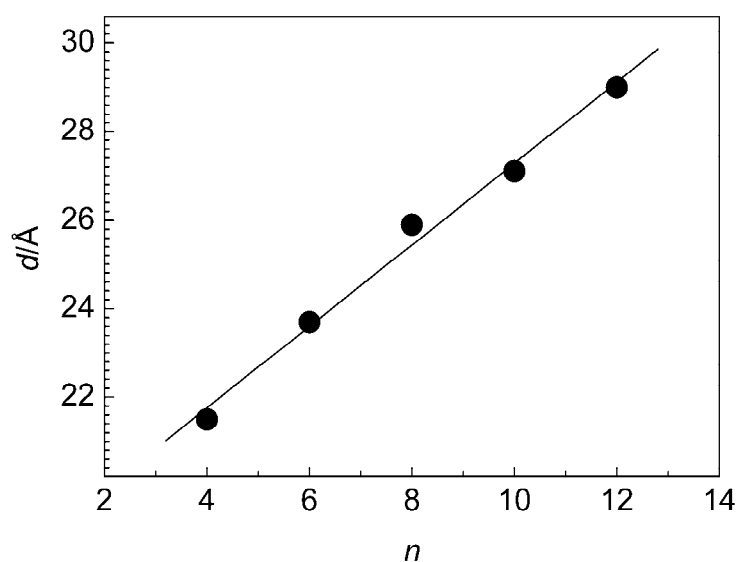


**Figure 124.** Dependence of the interlayer distance $d$ on the length of alkyl chains $n$ in $C_n$-40. Solid line represents the linear fit of the experimental points.

### 3.5.6   DSC and POM data

The DSC experiments performed at a rate of 5 K min$^{-1}$ in closed pans are shown in Figure 125a–e. For compounds $C_4$-40 and $C_6$-40, two broad peaks are observed at temperatures *ca*. 270 and *ca*. 340 K (Figure 125a, b). The thermal dependence of the heat flow for $C_8$-40 and $C_{10}$-40 is similar to each other despite the fact that in these compounds two peaks are observed in the 250–350 K temperature interval (Figure 125c, d). The DSC profile of $C_{12}$-40 contains also an intense peak centered at 270 K attributed to the phase transition (Figure 125e). Anomaly in the profiles near 340 K corresponds to the spin-state change along with the dehydration process, which match with the reported magnetic and TGA data. However, on cooling the rehydration of the samples (because of the closed pans) is observed which resulted in the spin-transition peak of the same energy and at the same temperature as of the pristine compounds. Rehydration is confirmed by the DSC profiles of the zinc analogue $C_8$-40-Zn where the endothermic peaks are observed in the heating and the cooling modes despite the absence of the spin-state change (Figure 125f). The anomalies in the heat flow observed near 480 K and near 580 K for $C_n$-40 (not shown) are assigned to the isotropization and decomposition temperatures, respectively. Realization of the crystalline state in the higher homologues is difficult; only for $C_{12}$-40 was observed an endothermic peak at 270 K with high energy which possibly originates from the transition crystalline $\rightarrow$ columnar hexagonal. However, the XRD data did not confirm any structural change on going from 230 K up to 300 K (see Figure 122e). For the other compounds the broad peak at 270 K could also be associated with the spin-transition of the small fraction of $C_n$-41 which was not rehydrated during cooling in the closed pan or in analogy with compounds $C_n$-36 ($n$ = 8, 10, 12) with the glass transition (vitrification). Since this broad peak is observed in the first heating run of all pristine compounds $C_n$-40 (except $n$ = 4, 6) which are completely low-spin, we accepted the possibility of the glass transition.

Table 46 summarizes the derived thermodynamic parameters $\Delta H^{\text{SCO}}$ and $\Delta S^{\text{SCO}}$ corrected for the enthalpy of the dehydration of the compound $C_8$-40-Zn; the values are in the range of the values expected for iron(II) spin-crossover compounds [41].

To identify the thermotropic liquid crystalline mesomophism of $C_n$-40, a polarizing optical microscopy (POM) was used. For higher homologues with $n$ = 8, 10, 12 the anisotropic texture observed at higher temperatures is ascribed to the discotic mesophase. On warming, isotropization occurs at *ca*. 460 K.
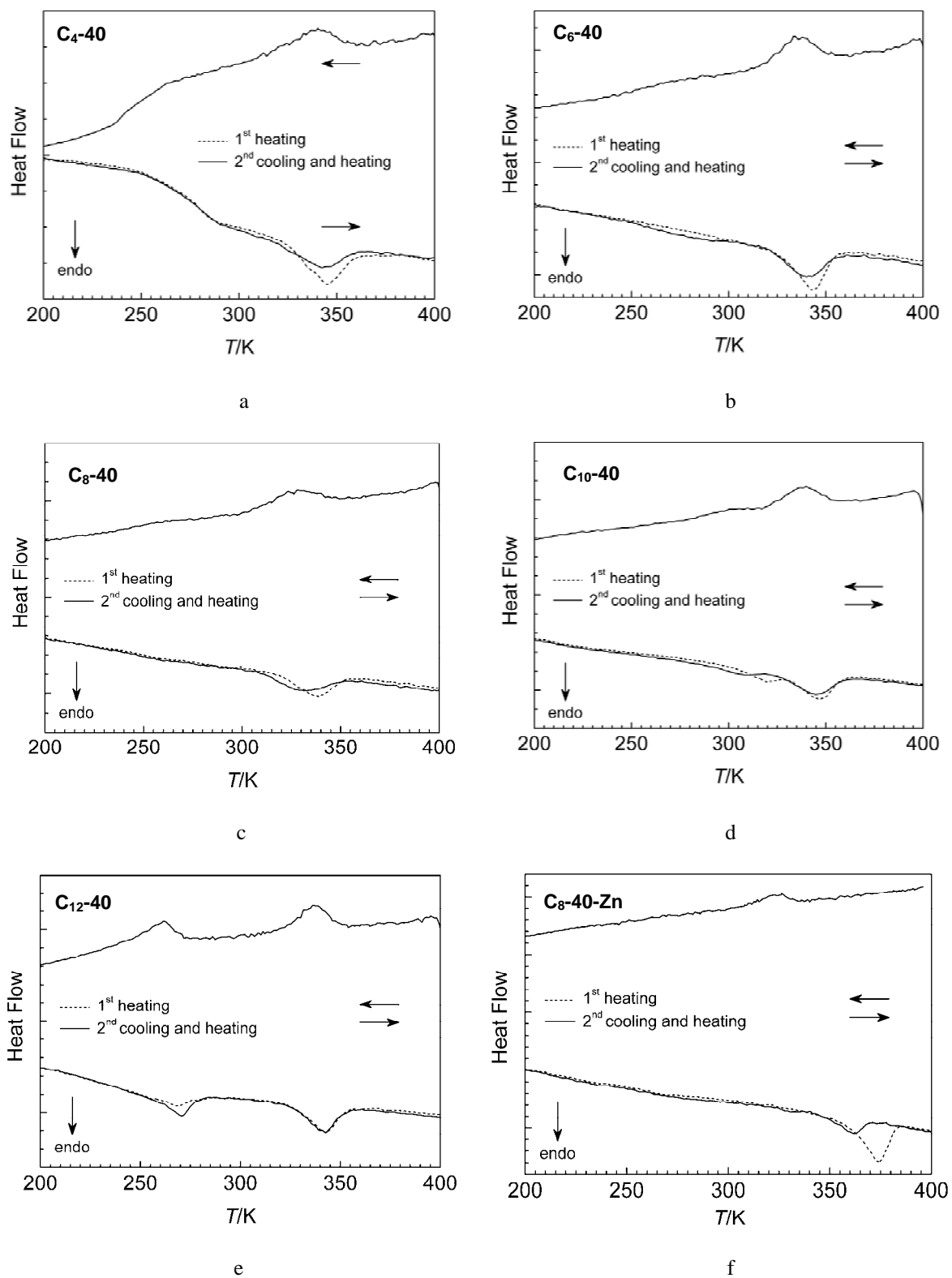
**Figure 125.** DSC profiles in heating and cooling modes for a) **$C_4$-40**; b) **$C_6$-40**; c) **$C_8$-40**; d) **$C_{10}$-40**; e) **$C_{12}$-40**; f) **$C_8$-40-Zn**.

**Table 46.** Interlayer distances $d$, thermal transitions and mesomorphism, enthalpy $\Delta H^{SCO}$ and entropy $\Delta S^{SCO}$ of spin-transition and enthalpy $\Delta H_g$ of glass transition determined by XRD, DSC, TGA and POM for $C_n$-40 and $C_8$-40-Zn.

| Compound | $d$ [Å], 300 K | Transitions [K][a] | $\Delta H^{SCO}$ [kJ mol$^{-1}$][a, c] | $\Delta S^{SCO}$ [J K$^{-1}$ mol$^{-1}$] | $\Delta H_g$ [kJ mol$^{-1}$] |
|---|---|---|---|---|---|
| $C_4$-40 | 21.5 | g $\xrightarrow{270}$ Col$_h$ (LS $\xrightarrow{345}$ HS) $\xrightarrow{469}$ d | 23.8 | 68.0 | 3.2 |
| $C_6$-40 | 23.7 | g $\xrightarrow{275}$ Col$_h$ (LS $\xrightarrow{343}$ HS) $\xrightarrow{424}$ i $\xrightarrow{510}$ d | 25.6 | 74.6 | 3.9 |
| $C_8$-40 | 25.9 | g $\xrightarrow{277}$ Col$_h$ (LS $\xrightarrow{340}$ HS) $\xrightarrow{462}$ i $\xrightarrow{511}$ d | 18.2 | 53.5 | 3.8 |
| $C_{10}$-40 | 27.1 | g $\xrightarrow{295}$ Col$_h$ (LS $\xrightarrow{343}$ HS) $\xrightarrow{460}$ i $\xrightarrow{500}$ d | 17.1 | 49.8 | 3.8 |
| $C_{12}$-40 | 29.0 | g $\xrightarrow{265}$ Col$_h$ (LS $\xrightarrow{341}$ HS) $\xrightarrow{463}$ i $\xrightarrow{510}$ d | 23.8 | 69.7 | 29.3 |
| $C_8$-40-Zn | 26.4 | g $\xrightarrow{265}$ Col$_h$ ($h$ $\xrightarrow{375}$ $dh$ [b]) $\xrightarrow{479}$ i $\xrightarrow{492}$ d | 4.5 [d] | 13.5 [d] | 4.4 |

[a] Data correspond to the first heating run. Decomposition temperature evaluated from the TGA data; [b] $h$ for hydrated, $dh$ for dehydrated; [c] Corrected for the dehydration; [d] Value for the dehydration process.

### 3.5.7 Mössbauer spectroscopy

[57]Fe Mössbauer spectra of the compounds $C_n$-40 and $C_{10}$-41 were recorded at 4.2 K (Figure 126a–f). The parameters derived from least-squares fitting are listed in Table 47. The observed spectra could be fitted using low-spin and high-spin doublets in a ratio of area fractions correlated with the magnetic data at low temperature. The asymmetry of the doublets in the Mössbauer spectra of the low-crystallinity non-substituted triazole-based compounds is the result of the Goldanskii-Koryagin effect due to the anisotropy of the vibrations of iron in the direction parallel and perpendicular to the main axis of the polymeric chains [342]. On the other hand, in compounds $C_n$-40 the texture effect cannot be excluded as an additional source of the pronounced asymmetry (see, for example, Figure 126e). Because of the wax-like nature of the compounds $C_n$-40 the mechanical stress was applied in order to get homogenous thickness of the samples which was not achievable by other methods. As it is known from the 2D-WAXS data, the mechanical stress leads to orientation of the polymeric species. This can also lead to the asymmetry effect of the Mössbauer doublets which is usually observed for the crystalline samples with the plate- or needle-like form of the crystals [44, 114, 377-379].

The relatively low population of the high-spin fraction in the pristine compounds points out the polymeric structure of the compounds with the bridging mode of the triazole units.
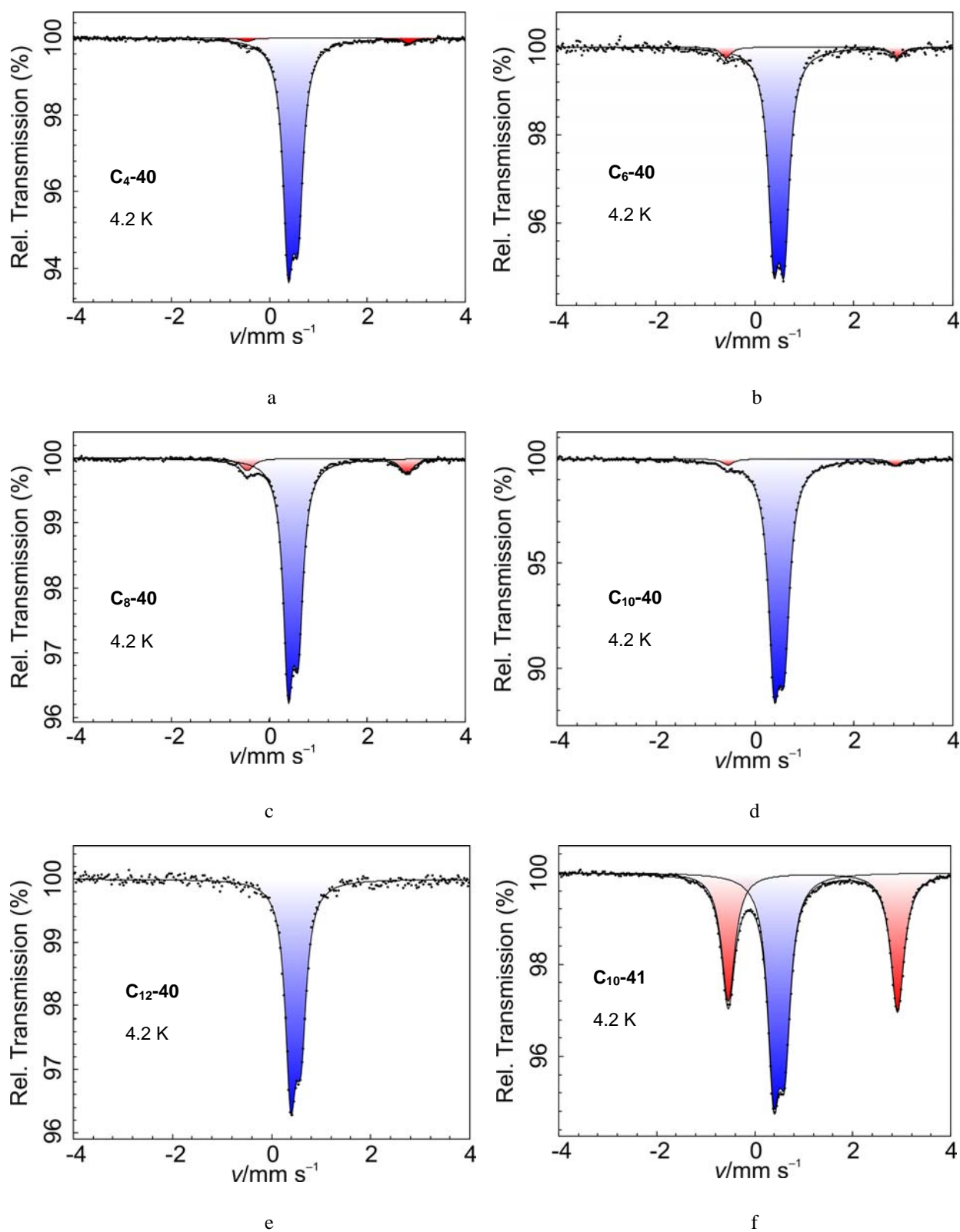
**Figure 126.** Mössbauer spectra of: a) **$C_4$-40**; b) **$C_6$-40**; c) **$C_8$-40**; d) **$C_{10}$-40**; e) **$C_{12}$-40**; f) **$C_{10}$-41** at 4.2 K.

**Table 47.** Mössbauer parameters, isomer shift ($\delta$, relative to $\alpha$-iron), quadrupole splitting ($\Delta E_Q$), half-width of the lines ($\Gamma_{1/2}$) and percentage of the multiplet populations in the high-spin (HS) and low-spin (LS) states (*A*) for $C_n$-40 (*n* = 4, 6, 8, 10, 12) and $C_{10}$-41.

| Compound | *T* [K] | Spin state | $\delta$ [mm s$^{-1}$] | $\Delta E_Q$ [mm s$^{-1}$] | $\Gamma_{1/2}$ [mm s$^{-1}$] | *A* [ %] |
|---|---|---|---|---|---|---|
| $C_4$-40 | 4.2 | LS | 0.48(0) | 0.20(0) | 0.12(0) | 97.7(6) |
|  |  | HS | 1.19(4) | 3.30(8) | 0.12(5) | 2.3(8) |
| $C_6$-40 | 4.2 | LS | 0.49(0) | 0.21(0) | 0.13(0) | 94.3(14) |
|  |  | HS | 1.15(6) | 3.45(12) | *0.13* | 5.7(12) |
| $C_8$-40 | 4.2 | LS | 0.49(1) | 0.21(0) | 0.12(0) | 90.7(5) |
|  |  | HS | 1.18(1) | 3.26(2) | 0.17(1) | 9.3(7) |
| $C_{10}$-40 | 4.2 | LS | 0.49(1) | 0.20(0) | 0.13(0) | 96.6(4) |
|  |  | HS | 1.15(2) | 3.39(6) | *0.13* | 3.4(3) |
| $C_{12}$-40 | 4.2 | LS | 0.49(0) | 0.21(1) | 0.13(0) | 100 |
| $C_{10}$-41 | 4.2 | LS | 0.49(0) | 0.23(0) | 0.15(1) | 53.4(3) |
|  |  | HS | 1.19(0) | 3.45(0) | 0.17(1) | 46.6(4) |

The values given in italics were fixed during the fitting.

### 3.5.8 Discussion

The polymeric chain-like structure of the compounds $C_n$-40 was confirmed by IR spectroscopy (retaining the $C_{2v}$ symmetry by triazole units), magnetic and Mössbauer studies (low residual low spin fraction at low temperatures). For compound $C_{12}$-40 the dynamic light scattering data gave the average number of iron(II) ions per a chain equal to be *ca*. 500. According to the XRD data, the compounds adopt columnar polymeric structure with hexagonal ordering in the lattice. Due to sufficiently long alkyl chains (*n* > 6) they generate a liquid crystalline phase identified as columnar hexagonal phase (Col$_h$). Upon heating compounds $C_n$-40 release one water molecule per a monomeric unit undergoing simultaneously an abrupt spin-state change from the low-spin state to the high-spin state which was also possible to follow by temperature dependent XRD measurements. Heating up in the magnetometer revealed a modification of the magnetic properties being different for different homologues. The anhydrous compound $C_4$-41 did not show any decrease of the susceptibility due to spin-crossover. Higher homologues $C_n$-41 (*n* = 6, 8, 10, 12), however, showed an incomplete spin-transition with $T_{1/2}$ centered at *ca*. 300 K. In general, the increase of *n* increased the value $T_{1/2}$ (Figure 121) similarly to compounds $C_n$-37 (Figure 105).

The question about the role of the anion *p*-tol in the reappearance of the spin-transition in the anhydrous compounds can be answered by comparing the properties in the series $C_n$-41 and $C_n$-37. The temperature of the transition in the later practically coincides with that of the pristine compounds $C_n$-36 with only a slight shift of the transition to lower

temperature. In contrast, upon dehydration of compound $C_4$-40 into $C_4$-41 the spin-transition disappears similarly to the parent compounds 34 and 35. This allows one to conclude that the anion $p$-tol does not reside between triazole units and is not immobilized by the hydrogen bonds CH···O···HC (the oxygen atom O belongs to the $SO_3^-$-group of the anion $p$-tol$^-$) as is supposed to be the case with the triflate anion in $C_n$-37 (see Figure 116b). Instead, the realization of the spin-transition in $C_n$-41 is probably induced by the alkyl substituents of the triazole ligands. The IR data show that the alkyl chains in the shorter homologues with $n = 4$, 6 are in a rather disordered state, but the relative population of the disordering (or *gauche* kinks) deceases with increasing $n$. Establishing the new structure with lengthening of chains governs the evolution of the magnetic properties in the series $C_n$-41 from $n = 4$ up to 12. While the shorter homologue $C_4$-40 still retains a similarity in the structural and magnetic aspects with the parent compound 34, the higher homologues $C_{10}$-40 and $C_{12}$-40 possess incomplete spin-transition along with the definite columnar mesomorphism at room temperature. The intermediate homologues $C_6$-40 and $C_8$-40 show a gradual change of the spin-transition properties between the two boundary cases.

The temperature of vitrification in the samples $C_8$-41, $C_{10}$-41 and $C_{12}$-41 changes non-linearly with the alkyl chain length with the highest temperature being observed for the $C_{10}$-41 homologue. The vitrification, however, is not reflected by the magnetic properties. Indeed, the value of $T_{1/2}$ gradually increases with the length of the alkyl substituents (Figure 121). We can conclude that in contrast to the compound $C_{12}$-37, where the phase transition is reflected by the hysteresis loop, the spin-transition in $C_{10}$-41 is not affected by the vitrification which means that the structural reorganization is minor. In the compound $C_{12}$-41 the phase transition is too low in temperature to modify in any way the magnetic behavior of the compound. The hysteresis of the magnetic properties is therefore the feature resulting from the operation of the liquid crystallinity alone.

### 3.5.9   Summary

1. The chemical modification of the parent compound 34 afforded a family of alkylated compounds $C_n$-40 ($n = 4$, 6, 8, 10, 12) which show modified spin-crossover properties and liquid crystallinity (for $n = 8$, 10, 12);

2. The heating of compounds $C_n$-40 is accompanied by loss of one molecule of water per formula unit which generates anhydrous compounds $C_n$-41;

3.  As a result of the ability of liquid crystals to form thin layers, it is possible to prepare thermochromic films of **C$_{10}$-40** which under sealed conditions are purple at room temperature and almost colorless above the spin-change temperature (*ca*. 330 K);

4.  It appeares that spin-crossover in **C$_n$-40** occurs in the temperature range at which the materials exhibit a columnar hexagonal mesophase Col$_h$ which is confirmed by the DSC, XRD and POM data;

5.  Appearance of a narrow hysteresis loop in the higher anhydrous homologues **C$_n$-41** with $n = 8$, 10, 12 is due to the liquid crystalline properties of the compounds.

## 3.6  Cumulative table of the one-dimensional systems

| Parent compound | | ► | Mesogenic compound | | |
|---|---|---|---|---|---|
| *Code* | s | A⁻ | *Code* | *Ligand* | s |
| **30** | 2 | | **C₄-36** | $C_4$-*tba* | 0.5 |
| **31** | 0 | $CF_3SO_3^-$ | **C₄-37** | | 0 |
| | | | **C₆-36** | $C_6$-*tba* | 0.5 |
| | | | **C₆-37** | | 0 |
| | | | **C₈-36** | $C_8$-*tba* | 0.5 |
| **30-Cu** | 3 | | **C₈-37** | | 0 |
| | | | **C₁₀-36** | $C_{10}$-*tba* | 0.5 |
| | | | **C₁₀-37** | | 0 |
| | | | **C₁₂-36** | $C_{12}$-*tba* | 0.5 |
| | | | **C₁₂-37** | | 0 |
| **32** | 3 | | **C₄-38** | $C_4$-*tba* | 1 |
| **33** | 0 | $BF_4^-$ | **C₄-39** | | 0 |
| | | | **C₆-38** | $C_6$-*tba* | 1 |
| | | | **C₆-39** | | 0 |
| | | | **C₈-38** | $C_8$-*tba* | 1 |
| | | | **C₈-39** | | 0 |
| | | | **C₁₀-38** | $C_{10}$-*tba* | 1 |
| | | | **C₁₀-39** | | 0 |
| | | | **C₁₂-38** | $C_{12}$-*tba* | 1 |
| | | | **C₁₂-39** | | 0 |
| **34** | 3 | | **C₄-40** | $C_4$-*tba* | 1 |
| **35** | 0 | *p*-tol⁻ | **C₄-41** | | 0 |
| | | | **C₆-40** | $C_6$-*tba* | 1 |
| | | | **C₆-41** | | 0 |
| | | | **C₈-40** | $C_8$-*tba* | 1 |
| | | | **C₈-41** | | 0 |
| | | | **C₁₀-40** | $C_{10}$-*tba* | 1 |
| | | | **C₁₀-41** | | 0 |
| | | | **C₁₂-40** | $C_{12}$-*tba* | 1 |
| | | | **C₁₂-41** | | 0 |
| | | | **C₈-40-Zn** | $C_8$-*tba* | 1 |

# 4    General discussion

According to Sorai, phase transitions taking place in condensed matter manifest themselves as concerted effects of molecular structure, intermolecular interactions, and molecular motions [380]. Well-known phase transitions include the order-disorder, displacive and reconstructive types. The order-disorder type phase transition involves a change in the positional and orientational alignment of molecular or spin axes [381]. The displacive-type phase transition concerns the displacement of atomic or molecular positions preserving the existing bonds [381]. The reconstructive transition is the most drastic and involves considerable atomic movements [381]. Since intramolecular electronic energy is much greater than intermolecular potential energy, the change in the structure of a molecule is negligibly small when phase transitions take place [380]. However, in some molecule-based materials, the change in the electronic state is strongly coupled with a change in the lattice. One of such types occurs in transition-metal complexes with thermally driven transition between high- and low-spin states, which is always accompanied by pronounced structural modifications originating from the different volume of the coordination polyhedron in the two states.

The main question of the present thesis is the reversed problem, *i.e.* can a structural phase transition govern spin-change in a spin-crossover compound? It is possible to answer this question in part on the basis of the reported data dealing with the solid state spin-crossover materials. Among the nearly 2000 reports on the spin-crossover phenomenon cited in the ISI Web of Knowledge Data Base [382] over the last forty years nearly 40 describe synchronously occurring spin-transition and phase-transition with change of space group or disorder of the lattice components. As is now widely accepted, the occurrence of an independent or induced structural phase-transition of the reconstructive type is not a prerequisite for the observation of the spin-transition [41, 86, 383, 384]. The structural transformation which compounds undergo during the spin-transition by itself is a displacive phase transition which in favorable cases is efficient enough for the propagation of the cooperative interactions through the lattice and observation of all kinds of the spin-crossover transitions (abrupt, gradual, with hysteresis *etc.*) [41]. In some cases, however, it can trigger the change of the space-group, but in general for systems where simultaneously spin- and structural transitions are observed the question about the primary effect arises, *i.e.* the structural phase transition induces the spin-transition or vice versa leads to a "hen and egg" like problem. At least in some of the systems like those described in refs. [385-388] the structural phase transition was determined not to be the driving force, but only the factor

which modulates the character of the transition making it more steep up to the appearance of hysteresis which follows the structural transformation. Similarly, in the case of a very large hysteresis like in the systems [Fe(PM-Pea)$_2$(NCS)$_2$], [Fe(2-pic)$_3$]Cl$_2$·H$_2$O and [Co(C$_{14}$-terpy)$_2$](BF$_4$)$_2$ a crystallographically significant phase transitions is held responsible for the spin-transition [59, 103, 180]. For the rest of the systems the problem is seemingly unsolvable [180, 388].

Another type of phase transition, namely the order-disorder phenomenon was discussed in the spin-crossover literature since the report of Mikami *et al.* about the disorder of the solvent molecules in the spin-transition complex [Fe(2-pic)$_3$]Cl$_2$·EtOH (2-pic = 2-(aminomethyl)pyridine) [389]. The structurally determined disorder of the ethanol molecule was suggested to trigger the two-step spin-transition which later was confirmed in more precise studies [22, 389, 390]. Other types of disorder involve anions [391-396] and ligand moieties [393, 396]. It was suggested that in these cases, the modification of the ligand field strength upon cooperative ordering of the lattice components provides an intrinsic impulse for the initiation of the spin-crossover and observation of hysteresis loops or abrupt spin-state change.

Close interconnectivity of the phase transitions and the related macroscopic properties can also be found in molecular organic and metallorganic magnets where the change in the magnetic response is a measure of the inter- or intra-molecular interaction between paramagnetic centers. It intimately correlates with the adopted structure, therefore if the phase transition takes place, the magnetic properties follow structural changes. For example, the solid-state radical-based materials usually exhibit the Curie-Weiss paramagnetism at high temperatures, because their magnetic exchange interactions are weak in general [397-400]. When the temperature is lowered, the exchange interactions increase, and some of the systems undergo magnetic ordering, just like inorganic magnetic materials. Some other materials undergo a structural phase transition toward a less paramagnetic low-temperature phase, reflecting their strong spin-lattice interactions. Since these phase transitions are of the first-order, they always are accompanied by thermal hysteresis [381]. The most prominent examples reported recently are l,3,5-trithia-2,4,6-triazapentalenyl (TTTA) (Figure 127a) and spiro-biphenalenyl neutral radicals with the hysteresis loops centered around room temperature [401, 402]. Additionally TTTA is reported to exhibit pronounced thermochromism form green-yellow to purple [401]. Magnetic bistability accompanied by the structural transition has also been found in the manganese–iron Prussian blue analogues exhibiting an electron transfer transition between a Mn(II)($S = 5/2$)–CN–Fe(III)($S = 1/2$) high-

temperature phase ($F\bar{4}3m$) and a Mn(III)($S = 2$)–CN–Fe(II)($S = 0$) low-temperature phase ($I\bar{4}m2$) with a thermal hysteresis of 116 K (Figure 127b) [403]. Similarly, several reported binuclear and polymeric azide complexes show modifications of the magnetic response through the phase transition [404-406]. The full X-ray analysis of the binuclear system in two phases revealed a modification in the bridging geometry of the azido group, which switches the antiferromagnetic coupling between the constituting nickel(II) ions (Figure 127c) [407]. Analogously, the order-disorder transition in the metal-organic radical dithiolene complex was found to be responsible for the discontinuity observed in the magnetic response [408, 409]. The structural data revealed changes in the relative disposition of the radical moieties within the lattice which alternated the amplitude of the interaction between them. Numerous other examples also confirm that the reason for the observed anomalies in the magnetic susceptibly (or another property) of compounds possessing phase transitions is the modification of the relative disposition of the lattice components and therefore the degree of their interactions [410-419].
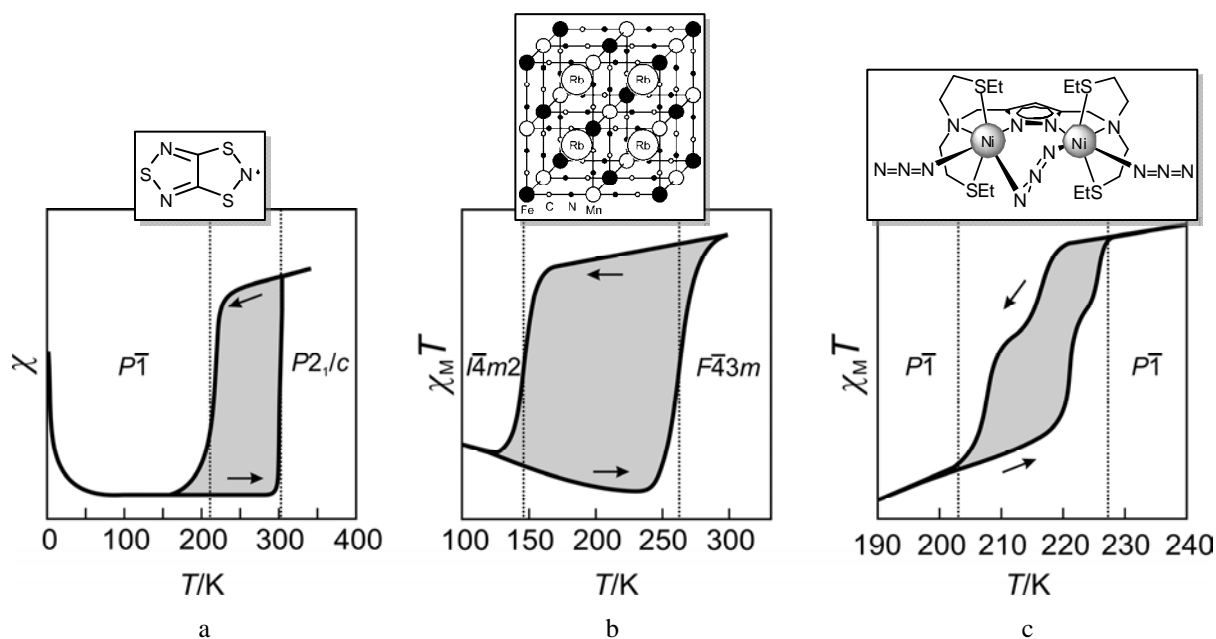


**Figure 127.** Examples of the molecular systems with the coupled structural phase transition and magnetic properties: a) TTTA (l,3,5-trithia-2,4,6-triazapentalenyl) [401]; b) $Rb_xMn[Fe(CN)_6]_{(x+2)/3} \cdot zH_2O$ [403]; c) $[LNi_2(N_3)_3]$ (L = 3,5-((bis(2-ethylthioethyl)amino)methyl)pyrazolato) [407].

The phenomenon of polymorphism in spin-crossover compounds also serves as convincing evidence of how important the character of the crystal packing, in particular the intermolecular contacts, for the spin-crossover in the solid state is. The characterization of iron(II) spin-crossover polymorphs concerned mostly the thiocynate complexes with different

heterocyclic ligands [101-105]. In the polymorphs I and II of the compound [Fe(PM-BiA)$_2$(NCS)$_2$] small and apparently insignificant structural changes were found to modify the magnetic behavior [104]. The polymorph I undergoes an abrupt spin-transition at 170 K, while the polymorph II undergoes a gradual transition centered around 205 K. The main difference in the two structures is that form I has a slightly more distorted FeN$_6$ octahedron and shorter, weak, intermolecular S···HC hydrogen-bonding contacts than the form II (S belongs to one NCS group; the CH group is part of a phenyl ring from a neighboring molecule). For the related systems [Fe(PM-X)$_2$(NCS)$_2$] (X = substituent), a direct correlation between the length of this contact in the room temperature high-spin crystal packing and the abruptness of the transition deduced from the magnetic curves was found [104, 180]. As stated by Guionneau *et al.*, this result constitutes a direct experimental proof of the correlation between structural and magnetic features [180]. It demonstrates further the fundamental role of intermolecular contacts in spin-crossover compounds. For instance, only polymorph A of [Fe(bt)$_2$(NCS)$_2$] (bt = 2,2′-di-2-thiazoline) shows a spin-transition centered at 175 K (with hysteresis), while the polymorph B remains high-spin down to liquid helium temperature. This discrepancy in the magnetic behavior was ascribed to the different space groups adopted by the polymorphs and the resulting different motifs of the intermolecular contacts, specifically the S···S contacts [105] (Figure 128a). Other important examples of structurally characterized polymorphism has been described in the literature, for instance, the three polymorphs of the *fac*-[Fe(dppa)(NCS)$_2$] complex (dppa = 3-aminopropyl)bis(2-pyridylmethyl)amine) [102], the two polymorphs of the system [Fe(abpt)$_2$(NCX)$_2$] (abpt = 4-amino-3,5-bis(pyridin-2-yl)-1,2,4-triazole and X = S or Se) [107, 420] (Figure 128b) and the three polymorphs of {Fe[(*p*-IC$_6$H$_4$)B(3-Mepz)$_3$]$_2$} [108]. Comparison of the crystal structures of the polymorphs showed that the differences in the spin-transition behavior are due to crystal packing effects and small changes in the geometry of the complex molecules (Figure 128a, b). The role of the hydrogen bond network has also been pointed out, for instance in the study of salicylidene based iron(II) complexes for which modifications of such a network are held responsible for the special features of the spin-transition [98, 421]. The triazole system [Fe(Htrz)$_3$(BF$_4$)$_2$] characterized in the form of the so-called α- and β-phases provides also an example of the possibility to transform polymorphs into each other by heating above the threshold temperature [92].

Changes of lattice vibrations as direct consequence of structural divergence are seemingly responsible factors governing different spin-transition behavior in different polymorphs. According to the variable temperature IR and Raman data supported by DFT

calculation the distribution of the entropy gain in spin-crossover iron(II) compounds is approximately as follows: nearly 27 % is the share of the spin entropy, 40 % is the contribution of the vibration-related entropy change mainly due to the metal-ligand skeletal vibrational modes and the rest of 33 % is attributed to changes in lattice vibrations perturbed by intermolecular interactions [46, 47]. The variation of the lattice indispensably changes the latter which leads to the change of the spin-crossover properties.
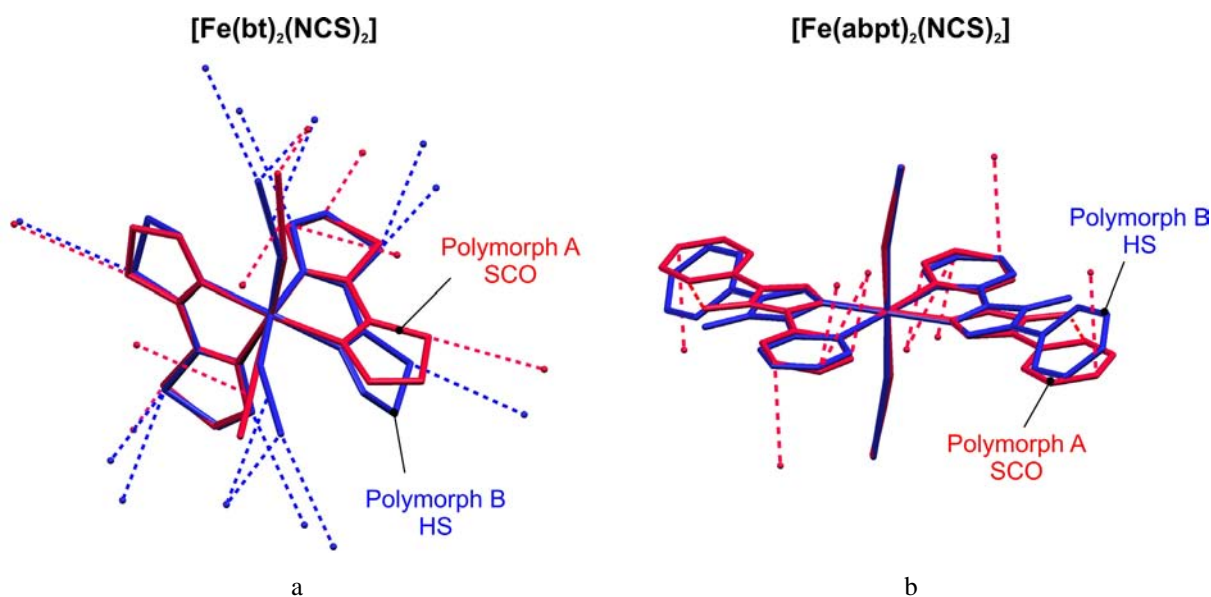


**Figure 128.** a) Minimized overlay of molecules $[Fe(bt)_2(NCS)_2]$ polymorph A (red) with spin-crossover properties, and polymorph B (blue), high-spin; b) Projection of the minimized overlay of molecules $[Fe(abpt)_2(NCS)_2]$, polymorph A (red) with spin-crossover properties and polymorph B (blue), high-spin. Dashed lines emphasize different motifs of intermolecular contacts for the polymorphs. Adopted from [105, 107, 420].

Even knowing much about the paramount role of the intermolecular contacts in influencing properties of the bulk materials and the ability to modify them through phase transitions, does not help much the researchers to create new materials with required properties, in particular with the defined temperature of the transitions. All reported solid-state systems are more or less unique since they were mostly obtained sporadically. Thus the available experimental data have singular importance because they cannot be usually extended to create new even slightly modified systems. In this sense the use of the solid → mesophase transitions instead of solid → solid transitions is a more promising approach for the control of the structure-coupled properties in a new generation of the thermo-responsive molecular systems. The switching between the two states in such materials can be controlled by the melting temperature of the compound which in turn is defined by the easily

controllable chemical structure. In the case of the metallomesogens the melting point depends on the length of the alkyl substituents. In the odd/even series of the homologous compounds, the temperature of the transition changes in a predictable way with lengthening of the alkyl chains [129] (see Chapter 1.4.3). In addition, the fine tuning of the melting temperature can be achieved by mixing of neighbor homologues [255].

A large number of new iron(II)-based mononuclear and polymeric metallomesogens has been described in the Chapters 2 and 3 of the present thesis. Each compound was firstly examined in the non-alkylated form with the goal to determine the spin-crossover properties excluding the influence of the alkoxy substituents. Alkylation of the parent compounds caused appearance of the relatively low-temperature melting and mesomorphic properties. In the following the reasons responsible for the observed influence of the phase transition on the magnetic properties of the alkylated compounds in the region of the phase transition will be discussed.

As was mentioned in the Chapter 1.3.4, in the solid state the ligand field strength of the spin-crossover compounds is governed by a number of factors. They can be divided into two groups. The first group includes those inherent variables which are defined by the chemical nature of the compound: type of the ligand, its substituents, type of the anion, crystal solvent and dimensionality. These are "inherent parameters" which cannot be changed by the external perturbation without degradation or irreversible chemical modification of the material. To the second group belong "structure-determined parameters". These are readily identifiable hydrogen bonds and π-π interactions which shape the pattern of the strong intermolecular contacts between the complex molecules. Other kinds of the structure-dependent interactions include electrostatic and van der Waals types taken together as weak interactions. The structure-determined parameters can be changed in course of a phase transition. The intermolecular contacts modify the electronic structure of the ligand and transmit information about the spin-state through the lattice. Any modification of these contacts, *e.g.* due loss of solvent or phase transitions will lead to changes in the structure-dependent properties of the compound. One more source of the different behavior in different phases is the structure-induced deformation of the complex molecule or of the ligand (Figure 128a, b). The cumulative scheme of the parameters is depicted in Figure 129.

Any kind of the phase transition changing the patterns of the intermolecular contacts must be accompanied by the change in the character of the structure-related properties in spin-crossover compounds. The melting is admittedly is accompanied by the decrease of the cooperativity. It is easy to imagine assuming increase of the volume during melting which
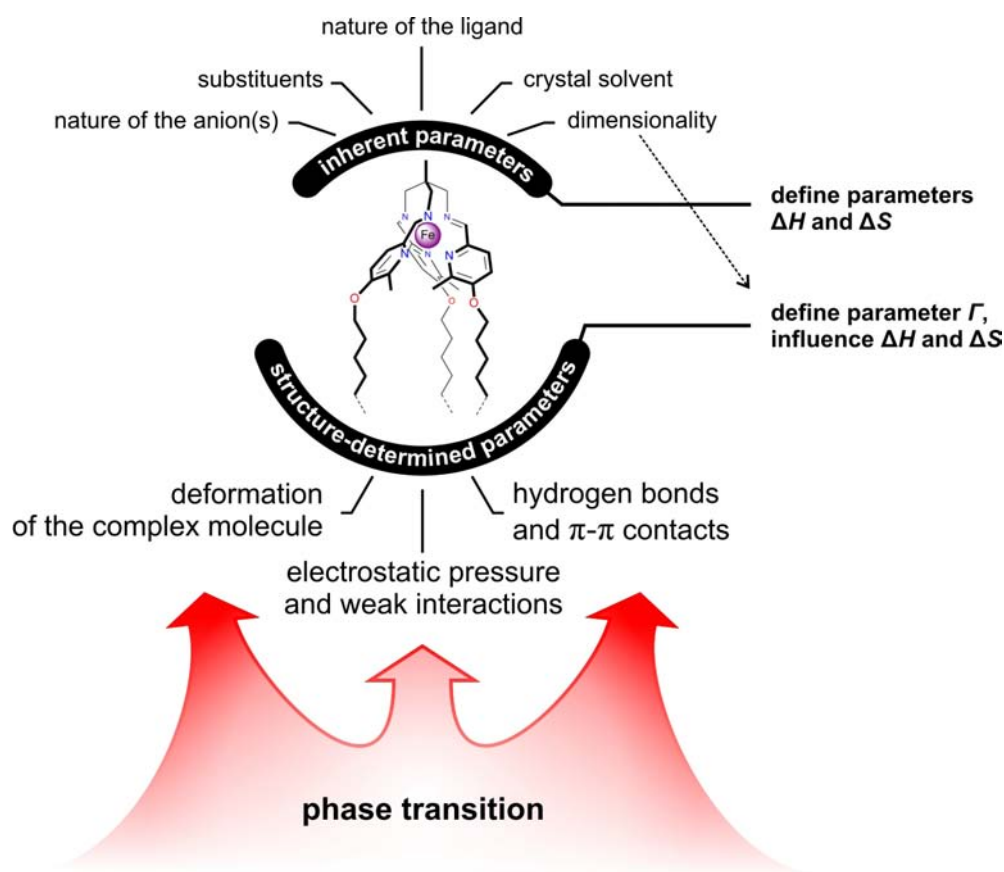
**Figure 129.** Parameters influencing the transition properties in spin-crossover compounds.

means increase of distances between molecules and the following decrease of the contacts which mediate interactions between spin-crossover centers. Therefore one can expect stabilization of the non-cooperative spin-transition in the molten state and of the cooperative spin-transition in the solid state. To the case of the different cooperativity in two phases is corresponding the change of the parameter $\Gamma$ alone, whereas concomitant change of the enthalpy $\Delta H$ and entropy $\Delta S$ would mean difference in the critical temperature $T_{1/2}$ in the two phases too.

Three types of interplay between spin-crossover and solid $\rightarrow$ mesophase phase transitions can be expected. The first one is type $i$ with coupled transitions. Members belonging to this group are compounds $C_n$-**14** ($n = 16, 18, 20$). In these compounds before the phase transition $Cr \rightarrow S_A$ takes place, the magnetic susceptibility is insensitive to the variation of temperature, which means that the structure is of the type which blocks spin-transition below the melting point. This implies that the hypothetical temperature of the spin-transition in the solid state $T_{1/2}^{\text{solid}}$ is much above 400 K (Curve 1, Figure 130a). Nevertheless, melting of the alkyl chains in these compounds modifies the structure in a way, that the molten samples show spin-transition above the melting point. The reason for this is the pronounced
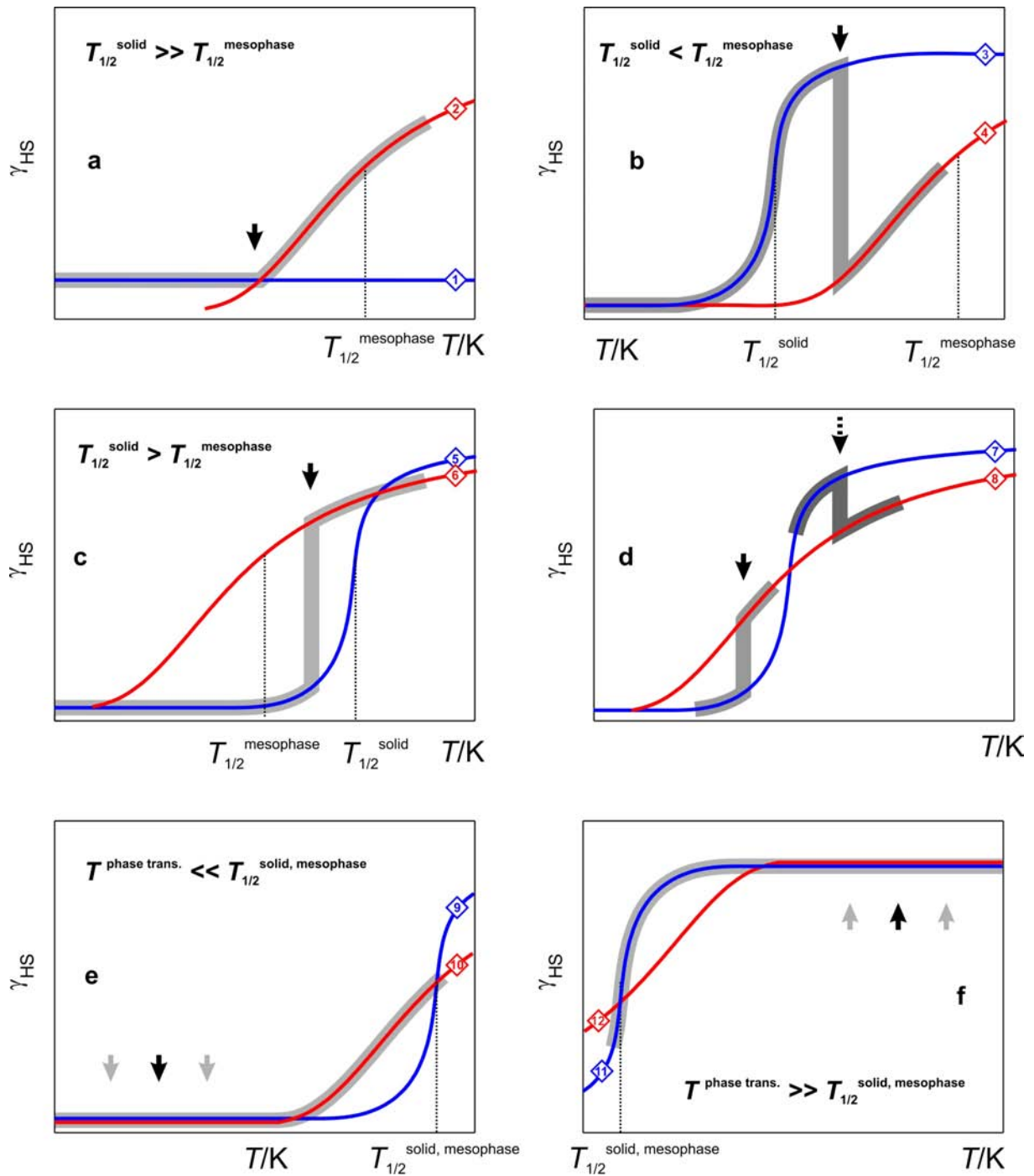
**Figure 130.** Plots a), b), c), d), e) and f) illustrate transitions from solid-like behavior (blue) to the mesophase-like behavior (red). The bold grey curves show the resultant macroscopic responses with the abrupt change of the behavior at the point of the phase transition (back bold arrow). The curves 1–12 were simulated using Slichter-Drickamer model with different parameters of the enthalpy and entropy, which define the values $T_{1/2} = \Delta H / \Delta S$ in solid state and mesophase. The cooperativity parameters for the solid state curves 1, 3, 5, 7, 9, 11 and for the mesophase curves 2, 4, 6, 8, 10, 12 obey inequality $\Gamma^{\text{solid}} > \Gamma^{\text{mesophase}}$, *i.e.* in the mesophase spin-transition is always less cooperative and therefore more gradual.

change of the intermolecular contacts which is evident from the difference in thickness of the ionic bilayers of the liquid crystalline and solid samples determined from the XRD data (the estimated value is *ca.* 6 Å). The amplitude of the structural transformation implies a change of all thermodynamical parameters, the cooperativity $\Gamma$, the entropy and enthalpy of the spin-transition. In the molten state the cooperativity can approximate liquid-like behavior which is typical for spin-equilibrium compounds (curve 2, Figure 130a). The observed spin-state change in the system **C$_{18}$-26** can be described in the same way.

In the case of the compounds **C$_n$-27** ($n$ = 12, 14, 16) the fitting of the magnetic curves before and after the phase transition sheds light on the changes which the systems undergo. As follows from the data, the melting decreases the parameter $\Gamma$ that correlates with the moderate variation of the ionic bilayers due to the phase transition (the difference in the thickness is *ca.* 1 Å). Also the enthalpy and entropy are somewhat changed, which define inequality $T_{1/2}^{\text{solid}} < T_{1/2}^{\text{mesophase}}$. The spin-state change in **C$_n$-27** ($n$ = 12, 14, 16) induced by melting corresponds to the change of more cooperative curve 3 to the less cooperative curve 4 (Figure 130b). The superheating and supercooling on melting and solidification, respectively, cause the appearance of hysteresis of the structural transformation which is followed by the magnetic response.

In the triazole-based compound **C$_{12}$-37** the phase transition was also found to modify the hysteresis loop making it asymmetric in comparison with the homologues with shorter alkyl chains. The change is less pronounced because of the small variation of the structure as is evidenced by the variation of the interlayer distance *d*.

Conclusions can be drawn about the importance of the structural transformation due to the phase transition. The larger the variation of the structure, the more significant is the difference in the intermolecular contacts in the two phases and the more pronounced are differences in the properties of the molten system compared to the crystalline one. In the mononuclear systems the amplitude of the variation of the ionic bilayers is a measure of the structural transformation which leads to the modification of the spin-crossover properties.

Fujigaya *et al.* claimed that the driving of the spin-state change occurred by the phase transition in three reported compounds [211]. The simulation of the magnetic data with the Slichter-Drickamer model in both phases of one of those is shown in Figure 135, Chapter 6.3, which leads to the transition type *i* shown in Figure 130c where $T_{1/2}^{\text{solid}} > T_{1/2}^{\text{mesophase}}$. Hayami *et al.* reported the cobalt(II) system exhibiting the spin-state change in the region of the melting [422]. The system can be an example of the type *i* illustrated in Figure 130d where the phase transition causes a pronounced change of the cooperativity $\Gamma$ and of the

parameter $T_{1/2}$. The simulation of the reported data with the Slichter-Drickamer model in both phases is shown in Figure 136, Chapter 6.4. We can also note, that the phase transition illustrated in Figure 130d by dashed arrow, *i.e* above $T_{1/2}^{\text{solid}}$, would lead to the behavior similar to that shown in Figure 130b.

In systems of the type *ii* both the spin-transition and the solid → mesophase transition coexist in the same temperature region but are not coupled. To these belong the compounds $\mathbf{C_n\text{-}13}$ ($n$ = 16, 18, 20), which are insensitive to the melting, but not to the release of crystal water. In compounds $\mathbf{C_{18}\text{-}24}$, $\mathbf{C_n\text{-}37}$ ($n$ = 8, 10) and $\mathbf{C_n\text{-}41}$ ($n$ = 8, 10, 12) the spin-transition is practically unaffected by the phase transition. This stems from the insignificance of the structural modification as shown by the XRD data.

The type *iii* is comprised by the systems where the two transitions are too far separated in temperature and therefore are not coupled. The spin-transition can be located much above in temperature resulting in low-spin behavior of the compound up to 400 K ($\mathbf{C_{18}}$-**7**: $T^{\text{phase transition}}$ ~ 380 K, $T_{1/2}^{\text{mesophase}}$ >> 400 K) or can be located much lower (for example, $\mathbf{C_{18}}$-**19**: $T^{\text{phase transition}}$ ~ 380 K, $T_{1/2}^{\text{solid}}$ = 133 K). The first case is exemplified by curves 9 and 10 shown in Figure 130e. Despite some possible modification of the intermolecular contacts and change of the curve from the solid-like curve 9 to the less cooperative mesophase-like curve 10, the transition temperature $T_{1/2}$ is still too high to cause any feasible changes in the magnetic response around the melting point. Similarly the case of the low temperature spin-crossover metallomesogens insensitive to high-temperature phase transition is explained (Figure 130f). The mononuclear iron(III) system reported by Galyametdinov *et al.* [229] and iron(II) systems reported by Hayami *et al.* [230-232] and [423], as well as polymeric one-dimensional systems investigated by Bodenthin *et al.* [366] also match type *iii* (Figure 130e, f) since the independent spin-transition and phase transition take place in different temperature regions.

We can conclude from the four archetypal transitions shown in Figure 130a–d, that in order to observe the interplay of the phenomena it is necessary for the system to exhibit spin-transition at least in one of the phases with the parameter $T_{1/2}$ located not far from the temperature of the solid → mesophase phase transition (Figure 130a) or inside of the "loop" defined by the solid-like and mesophase-like curves (Figure 130b, c, d).

The cumulative scheme of the metallomesogens $\mathbf{C_n\text{-}7}$–$\mathbf{C_n\text{-}29}$ and $\mathbf{C_n\text{-}36}$–$\mathbf{C_n\text{-}41}$ is shown in Figure 131.

**Spin-crossover
and phase transition
in metallomesogens
$C_n$-7–$C_n$-29 and $C_n$-36–$C_n$-41**

| Type *i* | Type *ii* | Type *iii* | |
|---|---|---|---|
| Coupled phenomena | Coexisting phenomena | Uncoupled phenomena | |
| $C_{16}$-14 | $C_{18}$-10 | $C_{18}$-7 | $C_{12}$-8 |
| $C_{18}$-14 | $C_{18}$-11 | $C_{18}$-9 | $C_{18}$-12 |
| $C_{20}$-14 | $C_{16}$-13 | $C_{16}$-15 | $C_{18}$-15 |
| $C_{18}$-26 | $C_{18}$-13 | $C_{20}$-15 | $C_{18}$-16 |
| $C_{12}$-27 | $C_{20}$-13 | $C_{18}$-17 | $C_{18}$-18 |
| $C_{14}$-27 | $C_{18}$-29 | $C_{12}$-19 | $C_{18}$-19 |
| $C_{16}$-27 | $C_8$-37 | $C_{18}$-20 | $C_{20}$-21 |
| $C_{17}$-27 | $C_{10}$-37 | $C_{18}$-22 | $C_{20}$-23 |
| $C_{18}$-27 | $C_8$-38 | $C_{18}$-24 | $C_{18}$-25 |
| $C_{20}$-27 | $C_{10}$-38 | $C_8$-39 | $C_{10}$-39 |
| $C_{18}$-29 | $C_{12}$-38 | $C_{12}$-39 | |
| $C_{12}$-37 | $C_8$-40 | | |
| | $C_{10}$-40 | | |
| | $C_{12}$-40 | | |
| | $C_8$-41 | | |
| | $C_{10}$-41 | | |
| | $C_{12}$-41 | | |

**Figure 131**. Classification of the metallomesogens $C_n$-7–$C_n$-41 according to the proposed three types of interplay *i*, *ii* and *iii* between spin-crossover and phase transition.

We can additionally note, that the proposed explanation of the abrupt change of the magnetic susceptibility by the jump-like transition from one type of the curve to another one is of general character and can be also applied for the explanation of the properties of other magnetic materials with undergo phase transitions, for example, of those shown in **Figure 127**a, b, c.

# 5   Summary and perspectives

## 5.1  Summary

Tripodand-based complexes **1**–**6** of the general formula [Fe(L)](A)$_2$, were prepared, where L is the derivative of a symmetric triamine and of a heterocyclic aldehyde, and A is ClO$_4^-$ or BF$_4^-$. Detailed structural and spectroscopic investigations of the complexes were carried out together with the magnetic characterization. It was found that the compounds possess spin-crossover behavior (**1**), adopt high-spin (**2**) or low-spin (**3**–**6**) states. On the basis of the detailed variable-temperature X-ray structural data of **1** it was confirmed that the magnetic response is closely related to the observed structural transformations, in particular to the distortion of the coordination polyhedron FeN$_6$ and the modification of the intermolecular contacts. Comparative analysis of the obtained structural data together with those of the reported analogous complexes **A** and **B** led to the conclusion about the applicability of the parent complexes for further chemical modifications.

Covalent grafting mesogenic groups to the coordination cores of the parent mononuclear low-spin and spin-crossover compounds **B**, **1**, **3**, **4**, **5** and **6**, afforded compounds **C$_n$-7**–**C$_n$-29** of the general formula [Fe(C$_n$-L)](A)$_2$·sH$_2$O, where C$_n$-L is the derivative of a symmetric triamine and of an alkylated pyridine-based aldehyde, $n$ is the number of carbon atoms in the alkyl chains which can be 6, 10, 12, 14, 16, 17, 18 or 20; s $\geq$ 0, and A is ClO$_4^-$, BF$_4^-$, F$^-$, Cl$^-$, Br$^-$, I$^-$, SiF$_6^{2-}$, SO$_4^{2-}$ or C$_{18}$TOS$^-$ (for more details about the chemical composition and the relation of the parent compounds and their alkylated derivatives see Cumulative table in Chapter 2.9). In comparison with the parent complexes the spin-crossover properties of the alkylated derivatives are substantially modified. The type of the modification was found to be dependent on the properties of the parent system and the nature of the used anion, however, the general tendency is the destabilization of the low-spin state at the favor of spin-crossover or high-spin behavior below 400 K. The structural insight revealed the micro-segregated layered organization with the separated ionic bilayers composed of the coordination head-groups and anions, and the separate alkyl substituents forming the paraffinic sublattice in the inter-bilayer space. The effect of the alkylation of the parent compounds consists first of all in the change of the lattice to a two-dimensional lamellar one preserving significant intermolecular contacts only within the ionic bilayers. The latter served as an argument for the observed decrease of the cooperativity of the spin-transition in the compounds **C$_n$-19** ($n$ = 6, 12, 18) which are alkylated analogues of the parent compound **1**.

The comprehensive analysis of the structural and thermodynamic data in the homologous series of the compounds $C_n$-14 ($n$ = 16, 18, 20) and $C_n$-27 ($n$ = 12, 14, 16) pointed at the mechanism of the interplay between the structural modification on melting and the induced anomalous change of the magnetic properties. The phase transition of the alkyl chains from more ordered crystalline state to less ordered quasi-liquid state causes the structural perturbation of the ionic bilayers with the longitudinal displacement or tilt of the coordination head-groups and the consequent change of the intermolecular contacts. In the case of the series $C_n$-27 ($n$ = 12, 14, 16), the fit of the magnetic curves in the two phases could be interpreted as an evidence of the weaker cooperativity in the mesophase. The extent of the structural modification was found to be decisive for the character of the change. In turn the phase transition changes from low-spin to spin-crossover behavior ($C_n$-14) or from more cooperative to less cooperative spin-transition behavior ($C_n$-27). In the context of the Slichter-Drickamer model, the phase transition is supposed to alter the thermodynamical parameters of enthalpy, entropy, and cooperativity of the spin-transition. It was also found that within the series $C_n$-14 ($n$ = 16, 18, 20) and $C_n$-27 ($n$ = 12, 14, 16) the temperature of the phase transition (melting point) and of the observed magnetic anomaly is a function of the chain length defined by $n$, and it increases with increasing $n$. The coincidence of transition temperatures of both phenomena unambiguously confirms the direct influence of the structural transformation on the spin-transition properties of the compounds.

A family of one-dimensional spin-crossover polymers **30–35** with general formula [{Fe($tba$)$_3$}A$_2$]·sH$_2$O [$tba$ = N-(4$H$-1,2,4-triazol-4-yl)benzamide; s ≥ 0; A = CF$_3$SO$_3^-$, BF$_4^-$, tosylate] was synthesized and characterized using a series of spectroscopic methods, X-ray powder diffraction, magnetic susceptibility measurements and differential scanning calorimetry. The copper analogue of **30**, [{Cu($tba$)$_3$}(CF$_3$SO$_3$)$_2$]·3H$_2$O (**30-Cu**), was also synthesized and its crystal structure solved at 293 K.

The alkylation of the one-dimensional spin-crossover parent compounds **30–35** afforded the alkylated derivatives $C_n$-**36**–$C_n$-**41** of the general formula [Fe($C_n$-$tba$)$_3$](A)$_2$·sH$_2$O, $C_n$-$tba$ = 3,5-bis(alkoxy)-$N$-(4$H$-1,2,4-triazol-4-yl)benzamide; $n$ = 4, 6, 8, 10, 12; s ≥ 0,   and A = CF$_3$SO$_3^-$, BF$_4^-$ or tosylate (for more details about the chemical composition and the relation of the parent compounds and their derivatives see Cumulative table in Chapter 3.6). In comparison with the mononuclear systems, the polymeric mesogens of iron(II) are less sensitive to the glass transition, which was attributed to the moderate concomitant variation of the structure. Nevertheless, the observed increase of the magnetic hysteresis with lengthening of the alkyl substituents was ascribed to the interplay of the

structural reorganization of the coordination core due to spin-crossover with the structural delay in the spatial reorganization of the mesogenic substituents.

The classification of mononuclear $C_n$-**7**–$C_n$-**29** and polymeric $C_n$-**36**–$C_n$-**41** metallomesogens according to the interactions between the structural- and the spin-transition and analysis of the data on the reported spin-crossover metallomesogens led to the separation of three types, namely:

Type *i*: systems with coupling between the electronic structure of the iron(II) ions and the mesomorphic behavior of the substance;

Type *ii*: systems where both transitions coexist in the same temperature region but are not coupled due to competition with the dehydration or due to negligible structural transformation;

Type *iii*: systems where both transitions occur in different temperature regions and therefore are uncoupled.

In the mononuclear iron(II) $C_n$-**7**–$C_n$-**29** and polymeric $C_n$-**36**–$C_n$-**41** metallomesogens, systems of the types *i*, *ii* and *iii* were isolated. It is found that in the systems where the structural changes influence the spin-state of the iron(II) centers (type *i*) and those where both transitions coexist in the same temperature region but are not coupled (type *ii*) are equally common with those of type *iii* among the metallomesogens under study.

The iron(II) metallomesogens present spin-transition accompanied by change of color. The mononuclear metallomesogens change the coloration from dark red-violet (low-spin) to red or orange (high-spin) while the one-dimensional ones from purple (low-spin) to almost colorless (high-spin). By virtue of the semi-fluid nature of the mesogens it was possible to prepare the compounds $C_n$-**40** ($n = 8, 10, 12$) as thin films.

Fine-tuning, in particular regarding the temperature at which the spin-transition occurs with hysteresis properties responsible for the memory effect, are still a major challenge towards practical implementation of spin-crossover materials into technical devices. A possible answer to the problem could be the creation of new materials in which the spin-crossover transition is coupled with another transition easily controllable by external stimuli. In the present thesis we have shown the viability of the approach realized in the mesogenic systems with coupled phase- and spin-transitions.

.

## 5.2 Perspectives

The future activity in the area of the spin-crossover metallomesogens can be developed towards creation of new systems on the basis of the present results. To our opinion, the mononuclear systems are preferable because of several advantages in comparison with the high-dimensional systems. First of all, occurrence of a real phase transition solid $\rightarrow$ mesophase with substantial reorganization of the structure is more probable than the less drastic glass transition which is typical for the polymeric liquid crystalline systems. In this sense, even more preferable is the real melting to the isotropic phase omitting the mesophase which would mean complete breakage of the static intermolecular contacts with the highest possible structural difference between the two phases. The rational pre-design of the organic ligands in a way which can favor the formation of strong hydrogen bonds between coordination heads and anions in the solid metallomesogenic compounds would be preferable in view of the known strong determining influence of such bonds on the spin state of the iron(II) compounds. The relatively high melting temperatures of the systems presented in this thesis are caused by the ionic nature of them. New systems could be with reduced charge of the coordination head-groups or neutral which can be achieved by introducing anionic groups into the ligands. Another approach towards the decrease of the melting temperature is the use of branched alkyl chains instead of normal alkyl chains or preparation of asymmetrically substituted mesogenic systems. Control of the spin state by light induced ligand isomerization in the mesophase is also potentially interesting. This can be achieved by introducing the organic N=N or C=C groups into the ligation units. The ultimate goal in the area of the spin-crossover metallomesogens is the switching of the spin state utilizing sensitivity of liquid crystalline phases to external electric and magnetic fields.

# 6 Appendix

## 6.1 Mössbauer spectrum of 2-ClO₄ at 80 K

The spectrum of **2-ClO₄** measured at 80 K is very similar to that of **2** (with $BF_4^-$ anion) (Figure 132), however, it is composed of only one slightly asymmetric doublet with parameters $\delta = 1.11(1)$ mm s$^{-1}$, $\Delta E_Q = 3.94(1)$ mm s$^{-1}$ and $\Gamma_{1/2} = 0.15(1)$ (note, the relative population of the small bump in the central part of the spectrum was estimated to have relative population of *ca.* 2 %, therefore it was excluded from the final fitting).
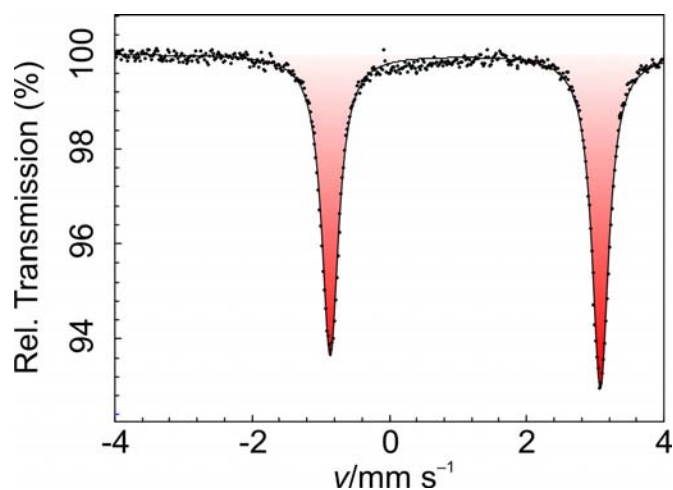


**Figure 132.** Mössbauer spectrum of **2-ClO₄** at 80 K.

## 6.2 Crystal structure of [Zn{*tren*(5-HO-*py*)₃}](NO₃)₂

The complex **[Zn{*tren*(5-HO-*py*)₃}](NO₃)₂** can serve as a model of the high-spin coordination head-groups in the alkylated *tren*-based systems reported in Chapter 2.5 due to similarity of the distances Zn–N with those usually found in iron(II) high-spin complexes. It was obtained by condensation of the three equivalents of 5-hydroxy-picolinaldehyde with triamine *tren* in presence of one equivalent of the zinc nitrate. The molecular structure of the complex (Figure 133) is similar to the structure of [Zn{*tren*(*py*)₃}](BF₄)₂ reported previously [194].
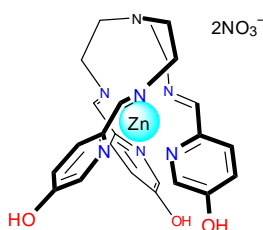


**Figure 133.** Schematic molecular structure of **[Zn{*tren*(5-HO-*py*)₃}](NO₃)₂**.

The coordination polyhedron of the zinc ion in [Zn{*tren*(5-HO-py)₃}](NO₃)₂ is best described as a strongly distorted trigonal antiprizm [$\theta$ = 45.58(9)°, $\Sigma$ = 102.29(10)°] (Figure 134a). The tris[4-(5-hydroxy-2-pyridyl)-3-aza-3-butenyl]amine ligand *tren*(5-HO-*py*)₃ coordinates to the metal centre through the three pyridine and three imino N atoms, each set of atoms forming two almost parallel triangles; the metal ion is located between these two planes. The average values for the Zn–N$^{py}$ and the Zn–N$^{im}$ bond lengths are 2.265(3) and 2.133(3) Å, respectively. The tertiary bridging N7 atom lies on the pseudo $C_3$–axis of the molecule and is situated 2.974(3) Å from the Zn center. The crystal packing is formed by *L* and *D* antipodes arranged in layers (Figure 134b). Molecules are involved into strong hydrogen bonding settled between hydroxyl groups and nitrate anions [2.569(3)–2.890(3) Å].

a              b
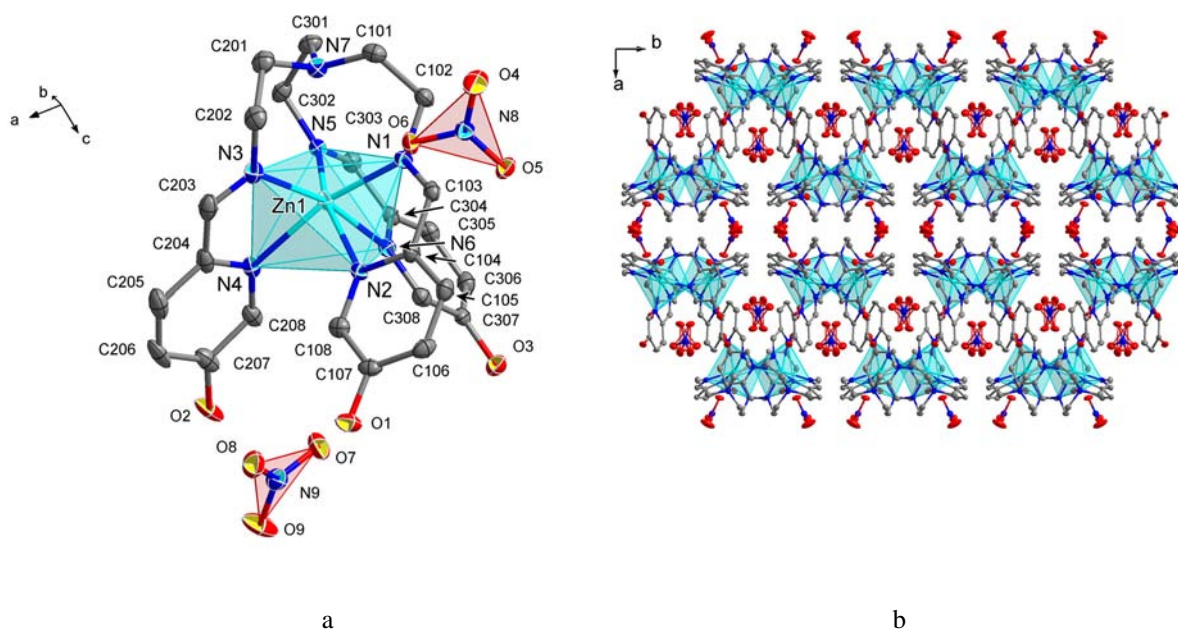
**Figure 134.** a) Molecular structure of **[Zn{*tren*(5-HO-*py*)₃}](NO₃)₂**. Hydrogen atoms are omitted for clarity. Displacement ellipsoids are shown at 50 % probability level; b) Projection of the molecular packing along the *c* axis.

The unit cell parameters and refinement details are presented in Table 48.

**Table 48.** Crystallographic data and refinement details for **[Zn{*tren*(5-HO-*py*)₃}](NO₃)₂**.

| | | | |
|---|---|---|---|
| Empirical formula | C$_{24}$H$_{27}$N$_9$O$_9$Zn | $F(000)$ | 2728 |
| Formula weight | 650.90 | $\theta$ range for data collection [°] | 1.48 to 27.49 |
| Temperature [K] | 100(2) | Index ranges | $-27 \le h \le 36$ |
| Wavelength [Å] | 0.71073 | | $-13 \le k \le 10$ |
| Crystal system | monoclinic | | $-24 \le l \le 22$ |
| Space group | *C*2/c | Reflections collected | 11941 |
| $a$ [Å] | 28.0587(12) | Independent reflections | 5160 |
| $b$ [Å] | 10.3677(2) | Data/restraints/parameters | 5160/0/388 |
| $c$ [Å] | 19.1322(8) | Goodness-of-fit, $F^2$ | 1.072 |
| $\beta$ [°] | 101.277(2) | Final *R* indices [$I > 2\sigma(I)$] | $R1 = 0.0344$, |
| Volume [Å$^3$] | 5458.2(3) | | $wR2 = 0.0889$ |
| Z | 8 | *R* indices (all data) | $R1 = 0.0516$, |
| $\rho$ [g cm$^{-3}$] | 1.634 | | $wR2 = 0.1041$ |
| Absorption coefficient [mm$^{-1}$] | 2.328 | $\rho_{min}$, $\rho_{max}$ [e Å$^{-3}$] | $-0.588$, 0.519 |

## 6.3 Fitting of the magnetic data of [Fe(C$_8$-*tba*)$_3$](ClO$_4$)$_2$ with the Slichter-Drickamer model

The spin-crossover system [Fe(C$_8$-*tba*)$_3$](ClO$_4$)$_2$ was reported by Fujigaya *et al.* [211]. It exhibits a spin-state change at *ca*. 270 K supposedly due to the phase transition.

The fit of the magnetic data was performed with the Slichter-Drickamer model in the ranges 70–270 K (solid state curve, blue) and 290–350 K (mesophase curve, red) (Figure 135), where according to the reported DSC and magnetic data no anomalies were detected [211]. It was assumed that $\gamma_{HS} = 1$ corresponds to $\chi_M T = 3.5$ cm$^3$ K mol$^{-1}$. The system is of the particular case in which $\Gamma^{solid} = \Gamma^{mesophase} = 0$. The change in the magnetic response at the phase transition temperature is due to the inequality $T_{1/2}^{\,solid} > T_{1/2}^{\,mesophase}$. The underestimation of the entropy values is seemingly due to the reported magnetic data which are uncorrected for the diamagnetic contributions.
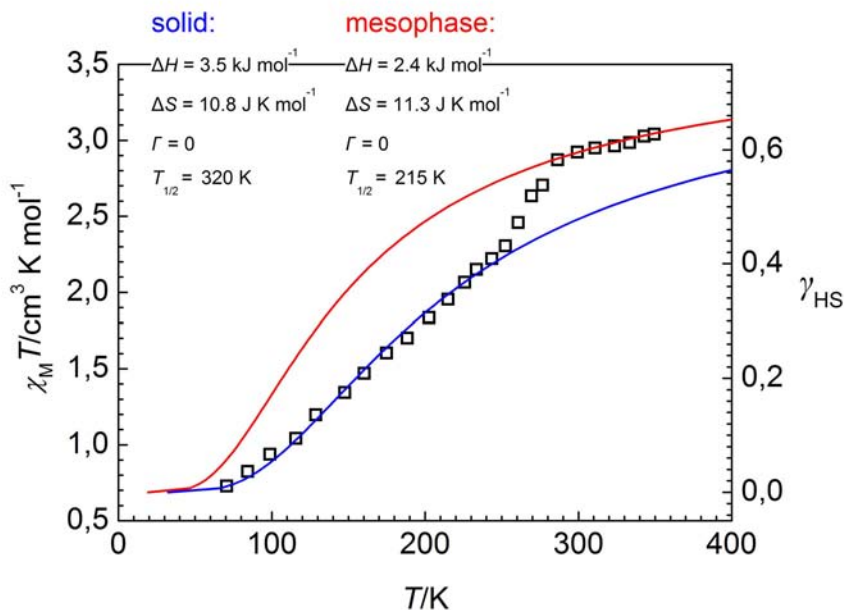


**Figure 135.** Fitting of the magnetic data of the mesogenic compound [Fe(C$_8$-*tba*)$_3$](ClO$_4$)$_2$ reported in ref. [211].

## 6.4 Fitting of the magnetic data of [Co(C$_5$C$_{12}$C$_{10}$-terpy)$_2$](BF$_4$)$_2$ with the Slichter-Drickamer model

The mesomorphic spin-crossover compound [Co(C$_5$C$_{12}$C$_{10}$-terpy)$_2$](BF$_4$)$_2$ [C$_5$C$_{12}$C$_{10}$-terpy = 4-(6-nonyloctadecyloxy)-2,6-di(2-pyridyl)pyridine] was reported by Hayami *et al*. [422]. It exhibits a spin-state change with a thermal hysteresis loop $\Delta T_{hys} = 4$ K at the liquid-crystal transition temperature.

The fit of the magnetic data was performed with the Slichter-Drickamer model in the temperature regions 100–267 K (solid state curve, blue) and 295–400 K (smectic mesophase curve, red) (Figure 136), where according to the reported DSC data no anomalies in the heat flow were detected. It was assumed that $\gamma_{HS} = 1$ corresponds to $\chi_M T = 2.8$ cm$^3$ K mol$^{-1}$ [424]. Although only limited ranges of the experimental points are available for the fitting and the obtained numerical values have to be interpreted with care, the less cooperative character of the spin-transition in the smectic mesophase is evident.
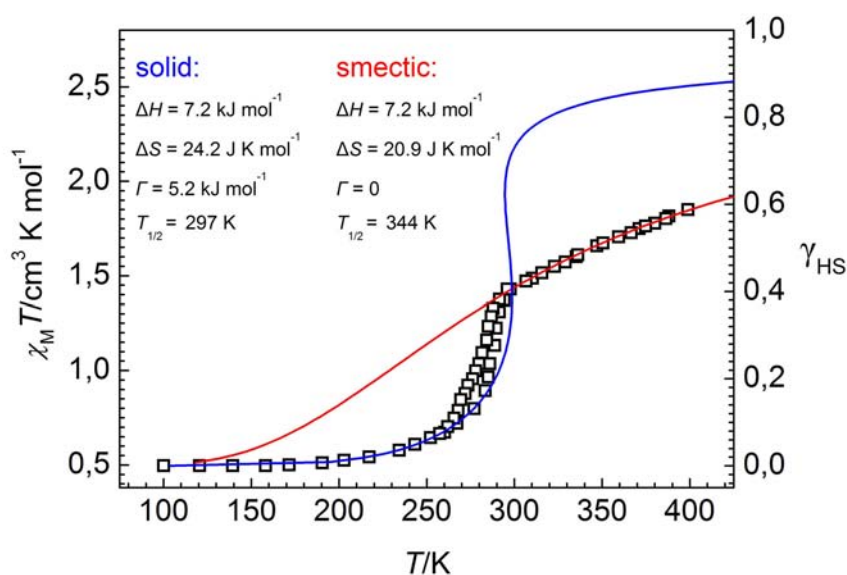


**Figure 136.** Fitting of the magnetic data of the mesogenic compound [Co(C$_5$C$_{12}$C$_{10}$-terpy)$_2$](BF$_4$)$_2$ reported in ref. [422].

## 6.5  Physical methods

### 6.5.1  X-ray single crystal diffraction

The X-ray diffraction experiment is the easiest way to obtain precise structural data of a crystalline spin-crossover substance [425]. It requires a source of X-ray radiation consisting of a metal anode (Cu or Mo) which emits radiation when irradiated with high-energy electrons. A monochromator selects radiation of the required wavelength and a beam passes through a long, thin collimator tube, for producing a parallel beam with the spot of limited cross-section. The sample is a single crystal, typically about 0.1–0.3 mm in each direction, mounted on a goniometer head, which allows precise change of the position and orientation of the crystal. The recorder is either a camera, or a detector and counter (Figure 137).
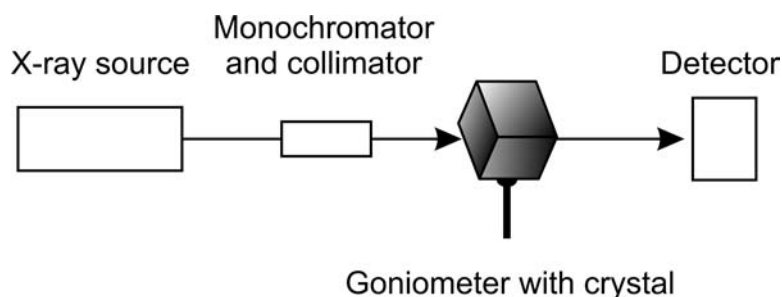


**Figure 137.** Schematic set up for X-ray single crystal diffraction experiment.

The determination of symmetry properties and measurement of cell parameters are carried out at an early stage of the structural study. Once the intensities of reflections are known and various corrections applied for absorption, extinction *etc.*, it should be possible to reconstruct a map of electron density in the cell. Two methods are used to achieve this and thereby solve the structure. One method is to calculate Patterson maps, which represent all interatomic vectors in the cell. A Patterson function is therefore the three-dimensional equivalent of a radial distribution curve (similar to EXAFS curve, for example). For simple structures, it is possible to work from this to the arrangement of the atoms particularly if one atom is much heavier than the others so that the vector involving that atom stands out clearly. Thus the heavy-atom method of solving structures is useful, particu1arly for transition metal complexes, which often have one atom much heavier than the rest. An alternative strategy is so-called direct method, which is based on two fundamental physical principles. First, the

electron density in the unit cell cannot be negative at any point, and so the large majority of possible sets of values for the phases of the various structure factors are not allowed. A random set of phases should give positive and negative regions in the electron density map with equal probability. Secondly, the electron density in the cell is not randomly distributed, but is mainly concentrated in small areas which are identified as atoms. A consequence of these two principles is that for certain sets of reflections having particular combination of Miller indices, there are theoretical probability relationships among their phases. Thus phases can be assigned to some reflections, usually most intense, and hence the position of some or all of the heaviest atoms can be located. Once atoms are in more-or-less the right places, least squares refinement adjust coordinates and vibrational parameters. The steps necessary to solve a crystal structure are briefly outlined in Table 49.

**Table 49.** A typical X-ray crystal structure determination procedure.

| Steps | Obtained information | Program |
|---|---|---|
| **Data collection and data reduction** ▼ | Cell parameters $a$, $b$, $c$, $\alpha$, $\beta$, $\gamma$; $hkl$-list | |
| **Data reduction, space group determination, absorption correction** ▼ | | Xprep |
| **Trial solution by Direct method ↔ Patterson method** ▼ | Localization of non-hydrogen atoms | SHELXS97, Sir92, Sir2004 |
| **Least squares refinement: isotropic refinement anisotropic refinement H-atoms refinement** ▼ | Improving the quality of the structural model: refinement of the atom coordinates and displacement parameters until convergence, localization of hydrogen atoms | SHELXL97, Crystals |
| **Analysis of refined solution** ▼ | | |
| **Final structure** | | Mercury, Diamond, CrystalMaker, Ortep, Platon |

### 6.5.2   X-ray diffraction analysis

X-ray diffraction techniques have traditionally been very useful in the study of both metal-containing and metal-free liquid crystals [426]. Among them, X-ray diffraction is the most widely used method. The X-ray diffraction pattern of a liquid crystal phase affords several types of information depending on the angular region investigated. In general, two regions are examined in the pattern:

▪ The small-angle maxima are due to intermolecular interferences along the director in the case of elongated molecules of calamitic mesogens or along a direction perpendicular to the director in the case of flattened discotic mesogens, and correspond to long distances (tens of Å). Periodic distances $d$ in the structure, such as the interlayer spacing, are calculated from these maxima by applying Bragg's law

$$n\lambda = 2d\sin\theta \tag{19}$$

where n is an integer, $\lambda$ the X-ray wavelength, and $\theta$ the diffraction angle. From Bragg's law, it follows that there is a reciprocal relationship between the separation of the planes $d$ in real space and the diffraction angle $\theta$ in the X-ray pattern. Therefore, the larger the distance $d$, the smaller the angle $\theta$. In general, the $d$ value calculated from Bragg's law corresponds roughly to the molecular length in calamitic compounds and to the molecular diameter in discotic compounds. For smectic and columnar mesophases, in which the structure consists of a periodic arrangement of layers or columns, respectively, a certain number of peaks are observed in the scattered intensity. In smectic phases equidistant peaks are observed which correspond to layered structure of the mesophase with ratio of spacings $1 : 2 : 3 : 4\ldots$ for reflections (10), (20), (30), (40)… of a lamellar smectic phase (S) or columnar lamellar phase (Col$_L$) [371]. In columnar phases the spacing ratio of the small-angle maxima are characteristic of the type of columnar packing. Thus ratios of $1 : 1/3^{1/2} : 1/4^{1/2} : 1/7^{1/2} : 1/9^{1/2}\ldots$ for the $d$ spacings of the (10), (11), (20), (21), (30), … reflections are observed in a hexagonal columnar phase (Col$_h$) [371].
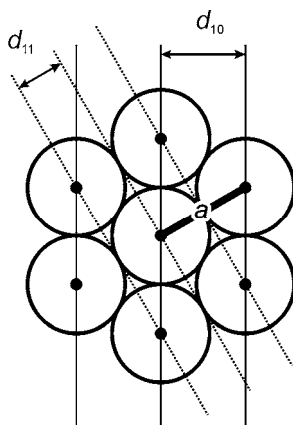


**Figure 138.** In a hexagonal lattice, the $d$ spacings of the (10) and (11) reflections show the characteristic ratio $1 : 1/3^{1/2}$.
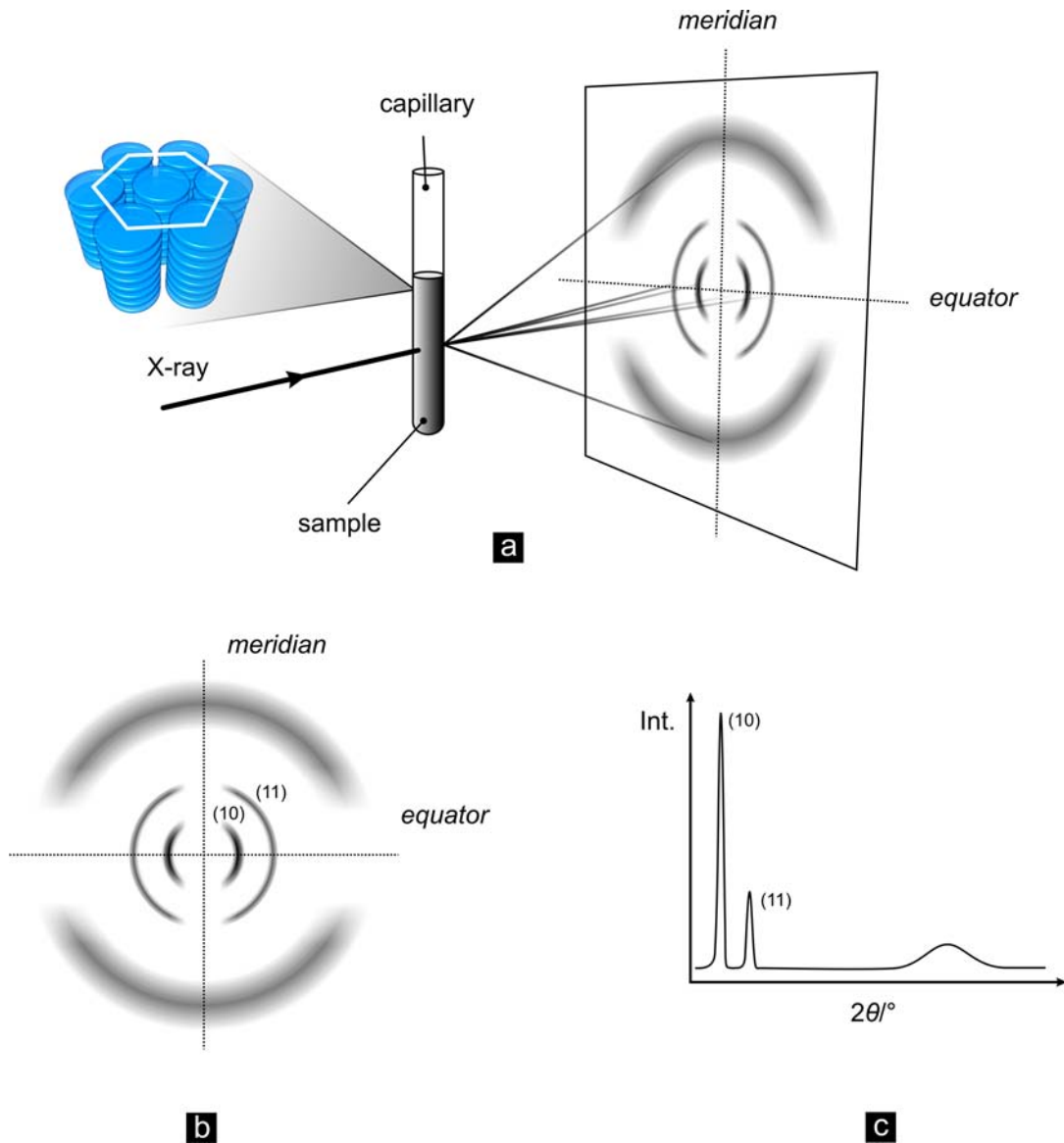
**Figure 139.** a) Experimental setup for the X-ray experiment; b) Typical 2D-WAXD diffraction pattern of a columnar hexagonal phase (Col$_h$); c) 360° integration plot of b).

As can also be seen in Figure 138, the $d_{hk}$ spacings (in which $h$ and $k$ are the Miller indices of the associated reflection) are related to diameter of the column $a$ (the lattice constant) according to equation

$$\frac{1}{d_{hk}^2} = \frac{4}{3}\frac{h^2 + k^2 + hk}{a^2} \tag{20}$$

which gives

$$a = 2d_{10}/3^{1/2} \tag{21}$$

▪ The wide-angle maxima are due to intermolecular interferences in the direction perpendicular to the director in the case of calamitics or along the director in the case of

discotics, and correspond to short distances (typically between 3 and 6 Å). In general, these distances correspond roughly to the molecular width in calamitic compounds and to the molecular thickness in discotic compounds. The wide-angle maxima are diffuse for those mesophases in which the molecular packing perpendicular to the director is liquid-like, such as nematic, smectic A and C phases. On the other hand, the wide-angle peaks are sharp for smectic phases other than A and C, in which there is two-dimensional order within the layer. In the case of columnar phases, the wide-angle peaks are more or less sharp depending on the extent to which the stacking order of the mesogenic cores extends along the column long axis. Additionally for mesophases in the wide-angle region a broad peak (halo) is usually observed, which corresponds to the liquid-like order of the alkyl chains with the corresponding spacing ~4.6 Å.

The simplest way to observe the various diffraction peaks is to employ a powder sample, that is, a sample which is composed of very many microdomains, each with a random orientation [274]. In the diffractogram obtained by 2D-WAXS (two-dimensional <u>W</u>ide <u>A</u>ngle <u>X</u>-ray <u>S</u>cattering) method, each diffraction maximum is averaged to give a ring centered around the incident beam. Diffraction patterns recorded on aligned samples provide more precise information about the local arrangement of the molecules. Alignment is usually achieved by the application of electric or magnetic fields or by mechanical shearing on a surface when the mesophase is viscous. In the X-ray pattern of an aligned sample, each ring splits into two arcs or crescents whose angular extension depends on the degree of orientational order (Figure 139a). Thus, one kind of information that can be obtained from this type of pattern is an estimation of the degree of orientation. The higher the degree of orientational order of the molecules, the more concentrated is the scattered intensity. Usually, in X-ray patterns from oriented samples, the region of the pattern parallel to the direction of alignment of the molecular axes is called the *meridian*, whereas the region of the pattern perpendicular to the direction of alignment is called the *equator* (Figure 139a, b). Thus, the diffraction maxima situated along the meridian are due to interferences along the director, and this means that for calamitic mesogens the meridional maxima appear at small angles (long distances), while for discotics they appear at wide angles (short distances). On the other hand, the equatorial maxima correspond to lateral intermolecular interferences, and thus they appear at wide angles (short distances) for calamitic mesogens and at small angles (long distances) for discotics. Integration of a two-dimensional diffractogram gives a plot where $2\theta$ values are plotted *vs* intensity (Figure 139c).

### 6.5.3   EXAFS and XANES spectroscopies

The primary effect of X-ray absorption is the excitation of the electrons from deep core levels of a selected atom by the absorption a photon. Depending on the photon energy, various physical processes can lead to different features in the X-ray absorption spectrum. It corresponds to excitation of a $1s$ electron. Such a spectrum is commonly divided in two regions, the X-ray Absorption Near Edge Structure (XANES) part and the Extended X-ray Absorption Fine Structure (EXAFS) part (Figure 140). When the energy of the photon is less than the $1s$ binding energy $E_B$, electronic transition to the first empty states occur. The transition to the first empty $3d$ molecular levels contributes to the band observed below the main edge in the region called *pre-edge*. Increasing in energy of the photons (but still $E < E_B$) leads to a sharp increase of the absorption coefficient called *edge*. When energy becomes more than $E_B$, a photoelectron is emitted with a kinetic energy $E_c$ and transition to a continuum states occurs. If the photoelectron is excited into the continuum with a high kinetic energy, the mean free path is small and a single scattering process takes place. This region, starting from about 50 eV after the edge, is the EXAFS region. EXAFS is sensitive to short-range order and gives the radial distribution function around the absorber up to 4 or 5 Å at room temperature. At low kinetic energies the XANES region is located. It can be used to extract structural and electronic information on a selected atom, complementary to the ones coming from EXAFS. The major advantage of the techniques is that they do not rely on long range crystallographic order.
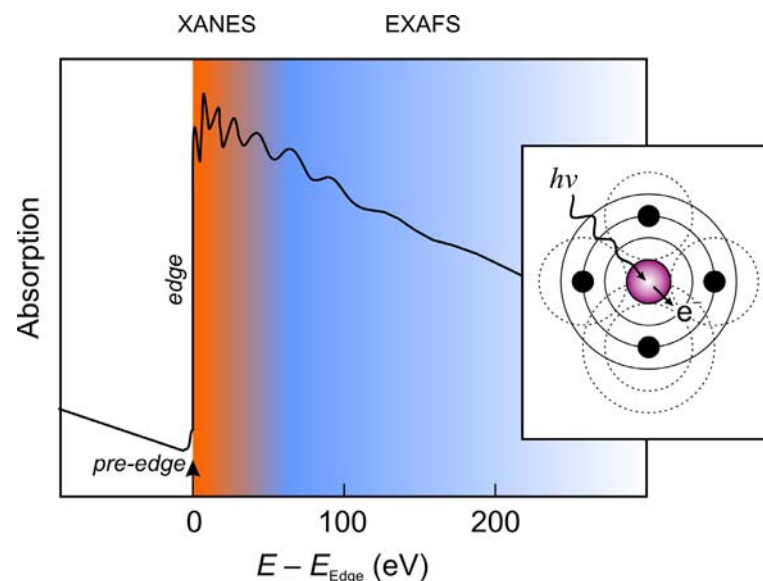


**Figure 140.** *K*-edge absorption spectrum with XANES and EXAFS regions. The inset shows schematicaly the radial portion of the photoelectron wave. The solid line indicates the outgoing portion, and the dashed lines indicate portions of the scattered wave from the surrounding atoms.

*Selection rules.* The transition induced by radiation is governed by atomic selection rules. In the frame of the selection rules, the transition at $K$-edge [$1s$ ($l = 0$) $\rightarrow$ $4p$ ($l = 1$)], $L_1$-edge [$2s$ ($l = 0$) $\rightarrow$ $4p$ ($l = 1$)] and $L_{2,3}$-edge [$2p$ ($l = 1$) $\rightarrow$ $3d$ ($l = 2$) and $2p$ ($l = 1$) $\rightarrow$ $4s$ ($l = 0$)] are allowed due to $\Delta l = \pm 1$. The transition $1s$ ($l = 0$) $\rightarrow$ $3d$ ($l = 2$) is forbidden (*i.e.* pre-edge region) [427].

*XANES.* The changes in the shape of the spectrum can be analyzed following the so-called "branching ratio". It is the ratio of the integrated intensities of the $L_3$ ($2p \rightarrow 3d$) edge to the sum of the integrated intensities of the $L_3$ and $L_2$ ($2p \rightarrow 4s$) edges. The high-spin states show a higher branching ratio than the low-spin states. This means, that the relative area of the $L_2$ edge increases during the transition from high-spin to low-spin states due to rearrangement of the $d$-electrons. The observed shift to high energy ($\sim 3$ eV) in the $K$-edge ($1s \rightarrow 4p$, where $4p$ has antibonding character and is centered on the metal) upon transition high-spin $\rightarrow$ low-spin is the result of the shortening metal–ligand (*e.g.* Fe–N) distances and enhancement of the hybridization with the suitable orbitals of the donor atoms (*e.g.* N($2p$) in case of the FeN$_6$ chromophore) [428].

*EXAFS.* The EXAFS part of the spectrum corresponds to the region starting from about 50 eV after the edge up to 1000 eV and above. In this energy range electrons are ejected in the material with a kinetic energy equal to the ionization energy. The oscillations observed in the EXAFS spectrum originate from the existence of the neighbors. For an isolated atom the photoelectron can be represented as an outgoing wave as shown in Figure 140 (inset) by the solid lines. The surrounding atoms will scatter the outgoing waves as indicated by the dashed lines. The final state is the superposition of the outgoing and scattered waves.

If $\mu_0(k)$ is the absorption coefficient of the isolated atom ($k$ is the wave vector associated to the ejected electron) and $\mu(k)$ the absorption coefficient measured in the solid, the $\chi(k)$ EXAFS signal is equal to

$$\chi(k) = \frac{\mu(k) - \mu_0(k)}{\mu_0(k)} \tag{22}$$

The modulations of the absorption coefficient are due to the interference of the outgoing wave and the waves scattered by the neighbor atom.

In the single scattering approximation which is valid for most cases, one considers the singular path "to and back" between the absorber atom and a neighbor.

For $K$-edge, in the plane wave approximation, the $\chi(k)$ expression is the sum of damped sinusoids

$$\chi(k) \propto \sum_j \frac{N_j}{kR_j^2} A_j(k) \exp(-2k^2\sigma_j^2) \exp(\frac{2R_j}{\lambda(k)}) \sin[2kR_j + \Phi_{i,j}(k)] \qquad (23)$$

where

- $j$ is the shell of the $N_j$ atomic scatters at the $R_j$ distance;

- $\Phi_{i,j}(k)$ is the total phase shift introduced by the atomic potentials for a scattering by the $j$ atom;

- $A_j(k)$ is the amplitude of the wave scattered by the $j$ atom. The parameters $\Phi_{i,j}(k)$ and $A_j(k)$ can be obtained experimentally from the EXAFS spectra of model compounds. Theoretical parameters are tabulated [429].

- $\exp(\frac{2R_j}{\lambda(k)})$ is a damping factor due to the loss effect by inelastic scattering. $\lambda(k)$ is the mean free path of the photoelectron;

- $\exp(-2k^2\sigma_j^2)$ is also a damping factor. $\sigma_j$ is the Debye-Waller factor, which represents the static disorder and the thermal vibrations; $k = [2m_e(E - E_0)/\hbar^2]^{1/2}$ (in $\mathring{A}^{-1}$), where $m_e$ is mass of electron, $E_0$ is the energy threshold;

- $2kR_j + \Phi_{i,j}(k)$, the argument of the sine, represents the phase shift between the outgoing wave and the back-scattered one.

We can distinguish two kinds of parameters:

- the electronic parameters: $\Phi_{i,j}(k)$, $A_j(k)$ and $\lambda(k)$;

- the structural parameters: $N_j$, $R_j$ and $\sigma_j$.

The knowledge of the electronic parameters allows to obtain the structural ones.

***Data analysis* [428].** The analysis of the experimental EXAFS spectra includes several steps.

1. *Extraction of the EXAFS signal $\chi(k)$*

This standard analysis includes linear pre-edge background removal with a linear or Victoreen function [430] applied to the pre-edge region and extrapolated then to the EXAFS energy range (Figure 141a). The atomic absorption is simulated, calculating a monotonous curve that is adjusted at the middle of the EXAFS oscillation. $\mu_0(E)$ is simulated by a polynomial function (5 or 6 degree) (Figure 141b). Thereafter a Lengeler-Eisenberg spectrum normalisation is applied [431]. According to Equation (22), the value $\chi(k)$ can be calculated and the EXAFS oscillation can be obtained (Figure 141c).

2. *Fourier transform of the $\chi(k)$ signal*

The EXAFS signal is then transformed according to Equation (23). The radial distribution function $F(R)$ is calculated by Fourier transformation of $k^3w(k)\chi(k)$, where $w(k)$ is

a Kaiser-Bessel apodization window [432-434] (Figure 141d). In the Fourier transform, each peak corresponds to a shell of neighbors around the absorber. When the shell is well separated, a simple inverse Fourier transform of one peak allows to isolate the contribution of one shell to the EXAFS spectrum (Figure 141e).
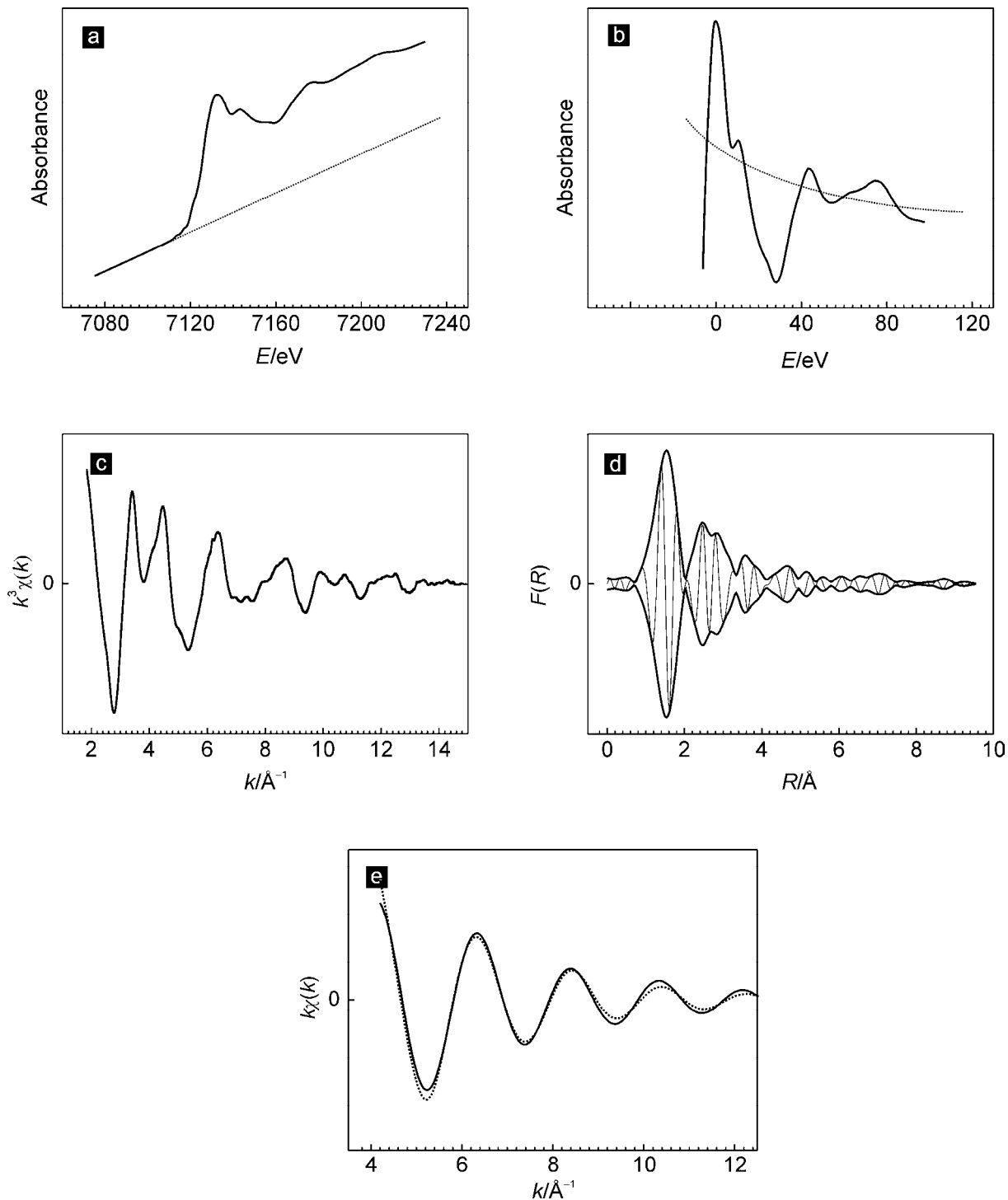


**Figure 141.** EXAFS data processing: a) Pre-edge extrapolation; b) Calculated background curve (dashed line) to extract the EXAFS signal; c) The normalized EXAFS plotted *vs* $k$; d) Fourier transforms of the EXAFS spectrum including the modulus and imaginary parts; e) The experimental (solid) and calculated (dashed) curves for the filtered Fourier signal.

3.    *Simulation of the signal of the first coordination shell*

Using Equation (23) and the atomic parameters $\Phi_{i,j}(k)$, $A_j(k)$ calculated or extracted from a model system, one can obtain the structural parameters: $N$, the number of neighbors, $R$, the absorber-neighbors distance and $\sigma$, the Debye-Waller factor (Figure 141e). Typically, the expected error is $\pm 0.02$ Å for the distances.
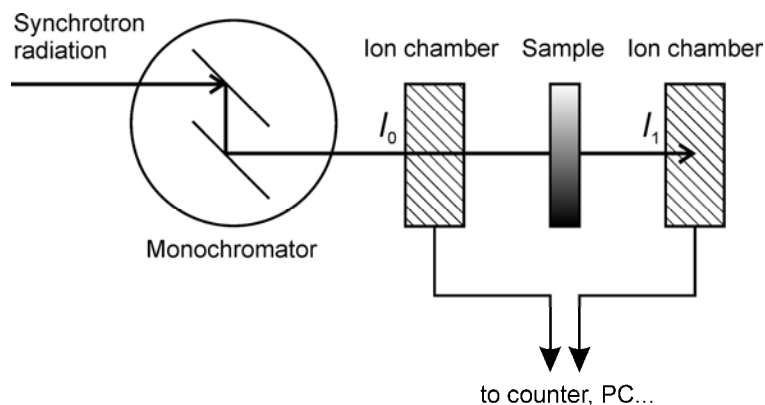


**Figure 142.** Schematic layout of an EXAFS spectrometer. Adopted from [428].

***Description of the experiment.*** The schematic layout of the EXAFS spectrometer is shown in Figure 142. As a source of the suitable radiation synchrotrons are served [*e.g.* DESY, Hamburg]. Synchrotron radiation is emitted by relativistic electrons or positrons accelerated in storage rings. The data is collected in a transmission mode. The energy of the monochromatic beam is turned using a double reflection from single crystals and the Bragg's law. The incident ($I_0$) and transmitted ($I_1$) X-ray intensities are recorded at sequential incident X-ray energies. The relationship between the absorbance A and the linear absorption coefficient $a$ of a sample of sickness $d$ is given by Beer's law: A $= ad = \ln(I_0/I_1)$. The intensities are measured using ion chambers.

### 6.5.4    Magnetic measurements

Although the spin-crossover process in iron(II) compounds manifests itself in a number of ways (spectroscopic-, structural-, dielectric properties *etc*.) the main characterization method of spin-crossover compounds is the measurement of the magnetic susceptibility as a function of temperature. This arises from the fundamental difference in the magnetic properties of the low-spin (total spin $S = 0$) and high-spin ($S = 2$) forms of the compounds. Below is given a short introduction into the field of the molecular magnetism.

If a substance is placed in a field of $H$ then $B$, the magnetic induction, is given by $H$ plus a contribution $4\pi M$ due to the substance itself:

$$B = H + 4\pi M \tag{24}$$

where $M$ is the magnetization per unit volume.

Dividing Equation (24) by $H$ we obtain:

$$\mu = 1 + 4\pi\chi_V \tag{25}$$

where $\mu$ and $\chi_V$ are the permeability and susceptibility per unit volume which may be considered dimensionless. For convenience the magnetic susceptibility per gram ($\chi_g$) and per mole ($\chi_M$) are used: $\chi_g = \chi_V/\rho$ (in $cm^3\,g^{-1}$) and $\chi_M = \chi_g M_w$ (in $cm^3\,mol^{-1}$).

The molecular susceptibility is the algebraic sum of the diamagnetic contribution ($\chi_M^D$) and two positive paramagnetic contributions ($\chi_M^P$ and $\chi_M^{TIP}$):

$$\chi_M = \chi_M^D + \chi_M^P + \chi_M^{TIP} \tag{26}$$

The diamagnetism is due to the interaction of the magnetic field with the motion of the electrons in their orbits. It is sufficient to specify that $\chi_M^D$ is independent of the temperature and the strength of the applied field. To estimate this contribution, the tabulated Pascal's constants are used or for a rough estimation of the diamagnetic contribution the formula $\chi_M^D = 0.5 M_w 10^{-6}\,cm^3\,mol^{-1}$ [3]. The paramagnetic contribution $\chi_M^P$ is due to unpaired electron spins outside filled shells (*e.g.* four unpaired electrons in iron(II), high-spin). The third contribution $\chi_M^{TIP}$ describes the temperature independent paramagnetism which arises from a mixing into the ground state wave function of the exited states that are *not* thermally populated. For low-spin iron(II) ion ($^1A_{1g}$) the contribution $\chi_M^{TIP}$ is *ca.* $10^{-4}\,cm^3\,mol^{-1}$ [21].

For paramagnetic materials without interactions between paramagnetic centers, the empirically determined *Curie law* is valid:

$$\chi = \frac{C}{T} \tag{27}$$

with the *Curie* constant

$$C = \frac{N_A g^2 \mu_B^2}{3 k_B} S(S+1) \tag{28}$$

where $T$ is the absolute temperature, $N_A$ the Avogadro number, $g$ the Lande factor, the Bohr magneton $\mu_B = e\hbar/2m_e$, $k_B$ Boltzmann's constant, and $S$ the total spin.

The effective magnetic moment is defined as

$$\mu_{eff} = \sqrt{\frac{3 k_B}{N_A \mu_B^2}} \sqrt{\chi T} = 2.83\sqrt{\chi T} \tag{29}$$

Accounting Equations (27, 28 and 29), this leads to

$$\mu_{\text{eff}} = g\sqrt{S(S+1)} \text{ B.M.} \tag{30}$$

where $\mu_{\text{eff}}$ is expressed in units of Bohr magnetons (B.M.). For paramagnetic materials $\mu_{\text{eff}}$ is temperature independent.

For many paramagnetic substances, a more exact relationship is

$$\chi = \frac{C}{T - \Theta} \tag{31}$$

where $\Theta$ is the Curie-Weiss constant, which is positive for ferromagnetic and negative for antiferromagnetic compounds.

In the field of spin-crossover compounds the magnetic data is usually represented in the form of $\chi_{\text{M}}T$ *vs* $T$. Depending on the properties of the particular compound five types of the magnetic curves are typically distinguishable: gradual, abrupt, stepwise, incomplete, or one with hysteresis [41]. In the case of incomplete spin-transition in the low temperature region a sharp drop of the susceptibility caused by zero-field splitting is usually observed. In the case of iron(II) ions with the $3d^6$ electronic configuration, the electrostatic field of the ligands partially resolves the degeneracy of the $m_{\text{s}}$ states. The energy scheme includes two doubly degenerate levels with $m_{\text{s}} = \pm 1$ and $\pm 2$ with corresponding energies $D$ and $4D$ ($D \sim 10 \text{ cm}^{-1}$), respectively, above the non-degenerate ground state ($m_{\text{s}} = 0$). Thermal population of these energetic levels leads to variation of the macroscopic susceptibility $\chi_{\text{M}}T$ at low temperatures [435].

The susceptibility of spin-crossover compounds can be measured by force (Gouy-, Faraday balances) and flux-sensing (VSM and SQUID) magnetometers [436]. The Gouy and Faraday methods require that magnetic materials be placed in an inhomogeneous magnetic field. A displacement force depends on both the magnetization and the field gradient so that measurements of the force gives direct information on the magnetic susceptibility of the sample [435]. In the Gouy method the sample is placed in a long cylindrical tube which is suspended from an analytical balance. The sample tube is positioned between the poles of a magnet such that one end is in a region of homogeneous field and the other in zero-field. A paramagnetic material experiences an increase in weight while a diamagnetic substance a decrease in weight as a result of the displacement force exerted on the sample. A large amount of material is required and the uniformity of the sample is important. The Faraday method requires specially designed pole faces to place a small uniform sample in a region where the product of the field times the field gradient is constant. The method is more sensitive and highly reproducible, therefore requires a small amount of material [435].

Flux-sensing magnetometers are based on the principle that a moving or changing magnetic moment induces a current in a detection coil. By extracting the sample from one coil to another, an absolute value of the magnetic moment can be obtained. The principle of the Vibrating Sample Magnetometry (VSM) method implies that the sample is rapidly oscillating between the detection coils. The use of the phase-sensitive detectors allows to achieve high sensitivity of the method approaching that of the Faraday method [436].

For characterization of materials presented in this thesis a SQUID (Superconducting Quantum Interference Device) flux magnetometer was used. A SQUID magnetometer is an electrical device that is capable of amplifying small changes in magnetic field. When coupled to a suitable detection system, the SQUID electrical circuitry becomes the measuring probe of a superconductor magnetometer. The basic SQUID consisting of a small loop of superconducting material in which one or more weak links – Josephson junction – are interposed (Figure 143a). A weak link is essentially a point in the loop at which the critical current for the destruction of the superconducting state is severely reduced.
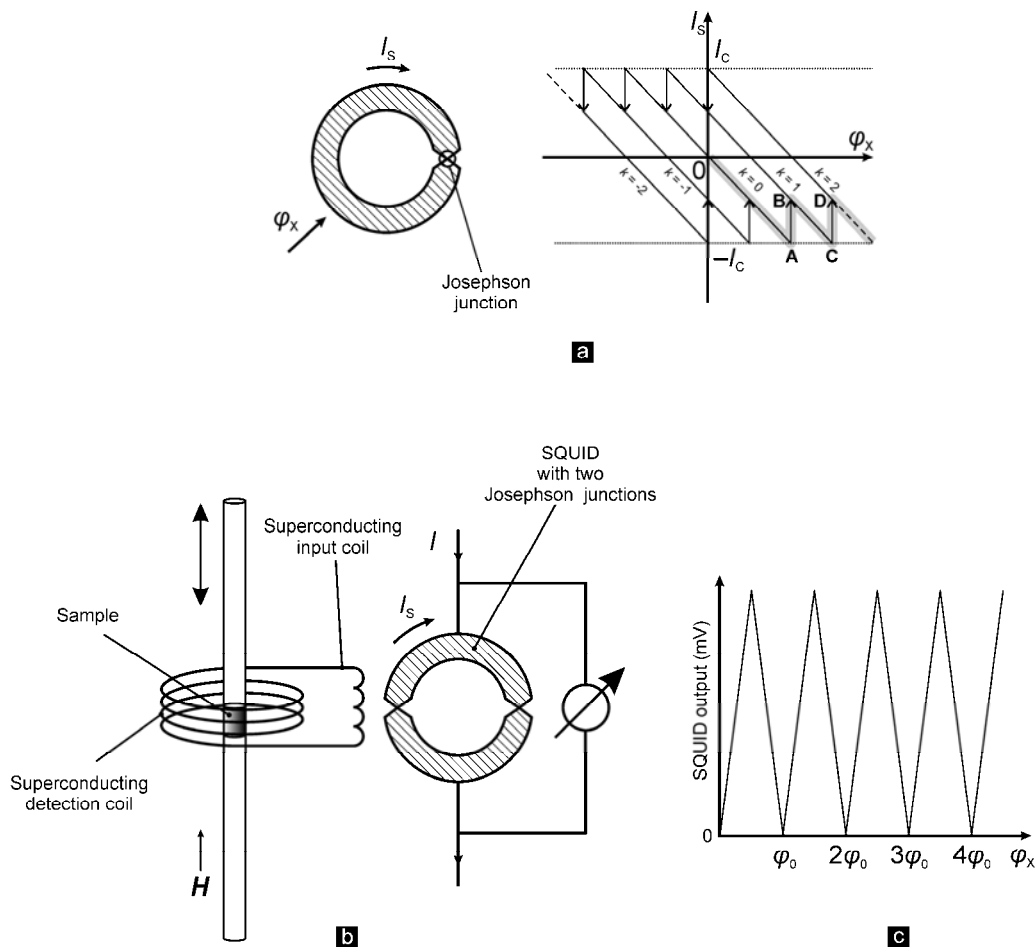


**Figure 143.** a) Schematic representation of the response of a SQUID with one Josephson junction to an applied flux. The grey line shows oscillation of the current with increasing magnetic flux; b) Simplified magnetometer with SQUID with two Josephson junctions; c) SQUID output voltage as a sample is moved inside the detection coil. Adopted from [436, 437].

When a metal becomes superconducting some of its electrons form Cooper pairs obeying Bose-Einstein statistics which leads to the quantization requirement. This restriction leads in turn to the circulating current in a superconducting ring being a periodic function of an applied magnetic flux. An equation describing the magnetic state of the superconductive loop can be written as:

$$\varphi = k\varphi_0 \qquad\qquad (32)$$

where $\varphi$ is the flux, $k$ may take only integral values, and $\varphi_0$ is the flux quantum, $\varphi_0 = h/2e = = 2.07 \cdot 10^{-7}$ Wb. If there exists a magnetic field with a component perpendicular to the plane of the superconducting ring, an external flux $\varphi_X$, proportional to the field and a function of the device geometry, will be present.

The complete analysis of a Josephson junction includes treating of tunneling effect governed by the equation $I = I_c \sin \Delta \kappa$ ($I_c$ is critical supercurrent, and $\Delta \kappa$ is the phase difference of the superconducting wave function across the junction) which is shunted by a normal resistance $R$ and where interference of the waves takes place. A simpler explanation of the behavior is given below.

It is well known that superconductors can only support a finite supercurrent. Above the critical current $I_c$, an electric field can exist in the material and flux penetration occurs. In the particular case, a flux will be able to enter or leave the ring when the circulating current is high enough to cause the weak link to go into resistive mode. A diagrammatic representation of the response of a loop containing a weak link to an applied magnetic flux is shown in Figure 143a, where the solid lines being the allowed states of the loop [437]. The origin of the periodic response of the SQUID is now apparent. Starting at the origin 0, a steadily increasing flux will cause the SQUID to follow the path 0A, the circulating current growing from zero to $I_c$. If the process is continued, the SQUID must undergo a transition into the resistive mode, which causes a decrease of the current, and then as a result transition to a neighbor $k$-state ($\Delta k = \pm 1$) (see Figure 143a). The work done is thought to appear as the energy of a rapidly damped oscillation at the natural resonant frequency of the ring, about $10^{10}$ Hz. An improved response can be obtained with a SQUID containing two weak links in the superconducting ring (Figure 143b, c). Magnetic fields can be sensed digitally by counting the number of oscillations which take place in the output when the field changes [436].

The Evans method is used for measurements of the spin-equilibrium of dissolved spin-crossover complexes. It is based on the NMR method. The frequency at which proton resonance occurs depends on the magnetic environment of the proton and changes in this environment produce corresponding changes in the resonance frequency. If a change of the

environment is caused by the presence of a paramagnetic solute, it should by possible to relate the susceptibility of this to the change in the resonance frequency of the proton. This is the basis of the Evans method in which the resonance frequency of a standard substance in solution is compared to that of the same substance in an otherwise pure solvent [438].

### 6.5.5   Mössbauer spectroscopy

Mössbauer spectroscopy also know as recoilless nuclear resonance of $\gamma$-rays, involves nuclear transitions which result from the absorption of $\gamma$-rays by the sample [202]. This transition is characterized by a change in the nuclear spin quantum number, $I$. The conditions for absorption depend upon the electronic density about the nucleus, and characteristics of the spectra obtained are related to the symmetry of the compound. As a result, structural and valence state information can be obtained.

The energy $E_\gamma$ of the $\gamma$-quantum emitted by a free atom is given by equation:

$$E_\gamma = E_0 + E_D - E_R \tag{33}$$

where $E_0$ is the difference in energy between excited and ground states of the source nucleus: $E_0 = E_e - E_g$; $E_D$ is the Doppler shift due to translational motion of the nucleus and $E_R$ is the recoil energy of the nucleus (Figure 144a). According to the formula $E_R = E_\gamma^2/2mc^2$, where $m$ is the mass of the nucleus, $E_\gamma$ is the energy of emitted $\gamma$-quanta (14.4 keV for $^{57}$Fe), $c$ is the velocity of light. For $^{57}$Fe nuclide, the recoil energy is 0.002 eV.

Analogously, the energy of the resonantly absorbed $\gamma$-quantum is given by:

$$E_\gamma = E_0 + E_D + E_R \tag{34}$$

In this case, $E_R$ is added because the exciting $\gamma$-quantum must have energy necessary to compensate the recoil effect of the absorbing nucleus. The quantity $E_D$ has the same significance as before, and the value of $E_R$ is assumed to be the same for the source and the sample.

In the solid state the situation is different. In the lattice a Mössbauer active atom is more or less rigidly bound so that the mass of the absorbing nucleus in a crystal is effectively that of the crystal. Because of the large mass of the crystal, the recoil effect is sufficiently reduced (Figure 144b), however, the resonant absorption (Figure 144c) in the solids can also lead to excitation of the lattice vibrations (phonons). There is a certain probability $f$ that no lattice excitation (*i.e.* zero-phonon process) takes place during $\gamma$-emission or $\gamma$-absorption

process. *f* is called *recoil-free fraction* (or *Debye-Waller-*, or *Lamb-Mössbauer factor*) and denotes the fraction of nuclear transitions which occur without recoil.
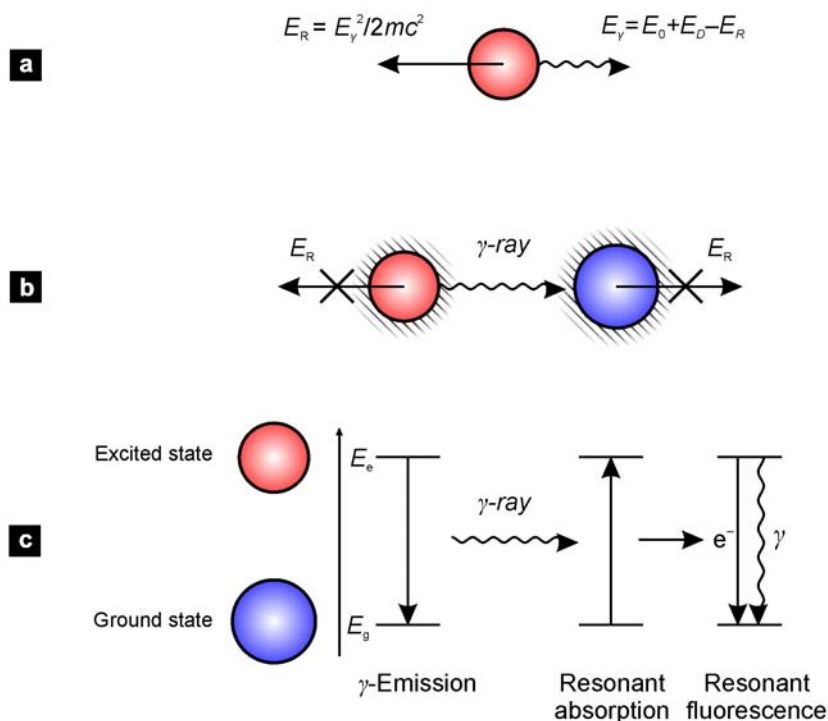


**Figure 144.** a) Emission of a *γ*-quantum of energy $E_\gamma$ from an excited nuclear state of a free nucleus; b) Recoilless emission and absorption of a *γ*-quantum by two nuclei in solids; c) Schematized representation of nuclear resonance absorption of *γ*-rays (Mössbauer effect) and nuclear resonance fluorescence.

The Debye model in the low-temperature approximation ($T < \Theta_D$) leads to the expression for the recoil-free fractions:

$$f = \exp\left[ -\frac{E_R}{k_B \Theta_D}\left( \frac{3}{2} + \frac{\pi^2 T^2}{\Theta_D^2} \right) \right] \tag{35}$$

where $\Theta_D := \hbar\omega_D/k_B$ – Debye-temperature; $\omega_D$ represents the Debye frequency of the oscillator. One can consider $\Theta_D$ as a measure for the strength of the bonds between the Mössbauer atom and the lattice. It is high (> room temperature) for metallic materials and low (< room temperature) for soft compounds, including coordination and metalorganic ones.

We can notice:

a)  *f* increases with decreasing recoil energy;

b)  *f* increases with decreasing temperature;

c)  *f* increases with increasing Debye temperature $\Theta_D$;

Recoilless resonant absorption ($E_R \to 0$) is necessary for maximum overlap of the emission line and absorption line (Figure 145).
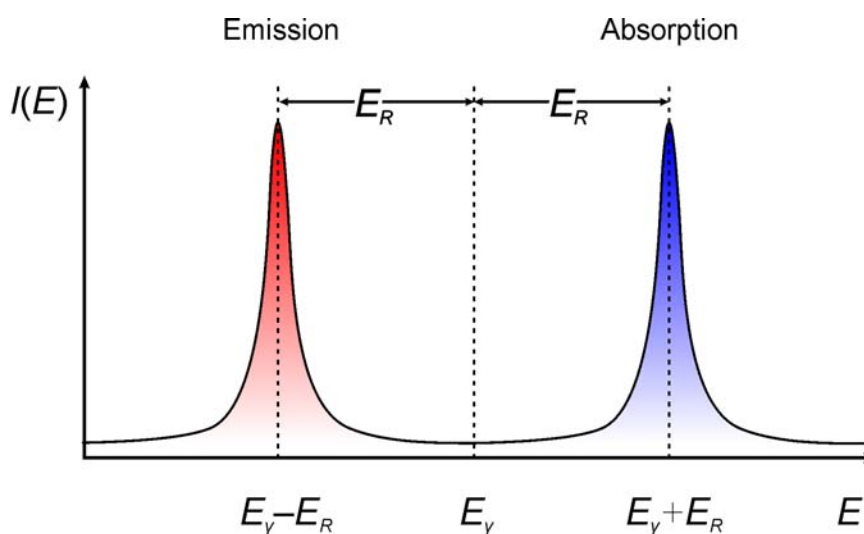


**Figure 145.** Energy shift of an emission line and an absorption line by $E_R$ because of the recoil effect.
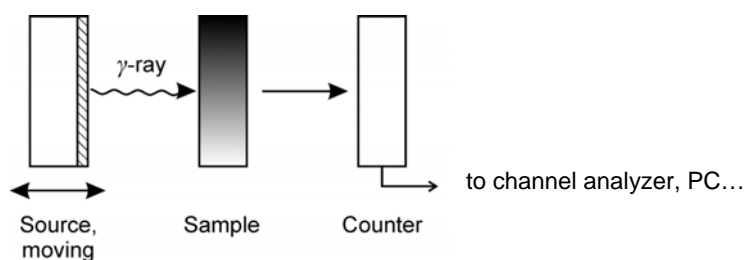


**Figure 146.** Schematic illustration of the experimental arrangement for Mössbauer spectroscopy experiments (transmission geometry).

If the source and the absorber consist of different materials, the resonance effect may be perturbed due to electric and magnetic *hyperfine interactions* between the nuclei and electric and magnetic fields set up by electrons interacting with the nuclei. Such hyperfine interactions can shift and split degenerate nuclear levels resulting in several transition lines (Figure 147). The perturbation energies are of the order of $10^{-8}$ eV, which shifts the transition lines away from each other such that the overlap decreases or disappears entirely. The overlap can be restored again by the Doppler effect, *i.e.* by moving the absorber (generally kept fixed) and the source (generally mounted on a vibrator) relative to each other (Figure 146). In the case of $^{57}$Fe spectroscopy, Doppler velocities of up to a few mm s$^{-1}$ are sufficient to make up for the perturbing hyperfine interaction energies and bring emission and absorption lines to

resonance. The hyperfine interaction energy $\Delta E_h$ (of interest) is correlated with the Doppler velocity $v$ via $\Delta E_h = (v/c)E_\gamma$ and can be measured in this way. The plot of the relative transmission of the γ-radiation as a function of the Doppler velocity $v$ is called the Mössbauer spectrum (see Figure 147a–d).
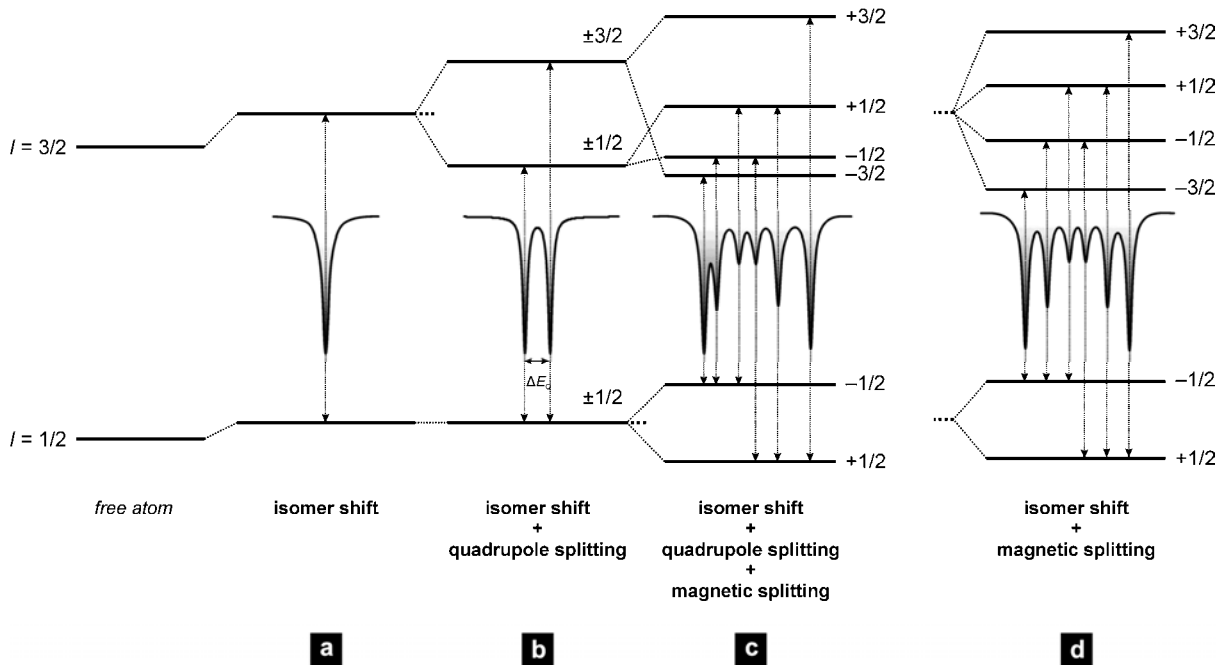


**Figure 147.** a) Isomer shift of the nuclear levels in $^{57}$Fe due to monopole interaction between the nuclear charge and electrons at the nucleus without changing the degeneracy, and the resultant Mössbauer singlet; b) Additional quadrupole splitting of the excited states level into two sublevels by electronic quadrupole interaction, and the resultant Mössbauer doublet; c) Additional magnetic dipole splitting (nuclear Zeeman effect) and the resultant asymmetric Mössbauer sextet (the selection rules: $\Delta m_I = 0, \pm 1$. Energy levels are shown arbitrary); d) Only monopole interaction and magnetic dipole splitting are active giving a symmetric Mössbauer sextet.

Two kinds of hyperfine interactions observed in a Mössbauer spectrum and important in the context of the present thesis are:

***Electric monopole interaction*** between protons of the nucleus and electrons penetrating the nuclear field. The observable Mössbauer parameter is the isomer shift $\delta$. This shift appears in the spectrum as the difference between the position of the centroid of the resonance signal and zero Doppler velocity.

The isomer shift is given by the following expression:

$$\delta = E_A - E_S = \text{const} \cdot (\rho_A - \rho_S)(R_e{}^2 - R_g{}^2) \tag{36}$$

where const = $\frac{2}{3}\pi Ze^2$, $E_A$ and $E_S$ are the energy differences between ground and excited states of the source and absorber, respectively; $\rho_A$ and $\rho_S$ are s-electronic densities of the source and absorber, respectively, and $R_e$ and $R_g$ are nuclear radii in the excited state (e) and the ground states (g) (for $^{57}$Fe: $(R_e - R_g)/R_g$ = –0.2 %, *i.e.* there is a contraction of the nucleus upon excitation).

The isomer shift depends directly on the *s*-electron densities (as sum of all *s*-electron shells), which have a finite probability of overlapping with the nuclear charge density and thus interacting with it, but may be influenced indirectly via shielding effects of *p*-, *d*- and *f*-electrons, which are not capable of penetrating the nuclear field.

The most valuable information derived from isomer shift data refers to the valence state of a Mössbauer-active atom embedded in a solid material.

For $^{57}$Fe, the isomer shift becomes more negative due to:

a)   $\sigma$-donor- (*e.g.* H$^-$) and $\pi$-acceptor- (*e.g.* NO$^+$) properties of the ligand;

b)   an increase in oxidation state of the metal centre [$\delta$(Fe$^I$) > $\delta$(Fe$^{VI}$)];

c)   spin state [*e.g.* for iron(II): $\delta$(HS, $S$ = 2) > $\delta$(LS, $S$ = 0)].

***Electric quadrupole interaction*** between the nuclear quadrupole moment and an inhomogeneous electric field at the nucleus.

A quadrupole moment arises due to an elliptic charge distribution in the nucleus with $I \geq 1$. In a non-spherical electric field, the different orientations of the nucleus are not equienergetic.

If the electric field gradient (EFG) is non-zero, for instance due to a non-cubic valence electron distribution and/or non-cubic lattice site symmetry, electric quadrupole interaction splits the degenerate $I$ = 3/2 level into two substates with magnetic spin quantum numbers m$_I$ = ± 3/2 and ± 1/2. The energy difference between the two substates $\Delta E_Q$ is observed in the spectrum as the separation between the two resonance lines (see Figure 147b).

These two resonance lines in the spectrum refer to the two transitions between the two substates of the split excited state and the unsplit ground state. The ground state with $I$ = 1/2 has no quadrupole moment and remains therefore unsplit, but still is twofold degenerate. The same holds for the two substates of the excited $I$ = 3/2 level, which are still twofold degenerate after electric quadrupole interaction. This degeneracy can be lifted by magnetic dipole interaction (Zeeman effect) (Figure 147c, d).

The quadrupole splitting depends on the electric field gradient $q$, the quadrupole moment of the nucleus $Q$ and the quantum numbers $I$ and m$_I$. In the case of axial symmetry the quadrupole splitting energy is:

$$\Delta E_Q = e^2 qQ \frac{3m_I^2 - I(I+1)}{4I(2I-1)} \tag{37}$$

There are two sources which can contribute to the total EFG:

$$(EFG)^{total} = (EFG)^{val} + (EFG)^{lat} \tag{38}$$

where $(EFG)^{val}$ is the *valence electron contribution* due to anisotropic (non-cubic) electron distribution in the valence shell of the Mössbauer atom, and $(EFG)^{lat}$ is the *lattice contribution* due to non-cubic distribution of distant charges (or dipoles) surrounding the Mössbauer atom.

The electric quadrupole splitting depends on:

a) oxidation state;

b) spin state [*e.g.* for iron(II): $\Delta E_Q(HS, S = 2) > \Delta E_Q(LS, S = 0)$ ] and

c) local symmetry of the Mössbauer atom [$\Delta E_Q(D_{4h}) > \Delta E_Q(O_h)$].

### 6.5.6   DSC and phase transitions

Molecular compounds exhibiting phase transitions can be characterized by calorimetric methods. Calorimetric studies play a significant role in providing information on energy effects of spin-crossover in coordination compounds and solid-solid and solid-liquid crystal phase transitions and complement structural information from X-ray or magnetic investigations [439-441]. The vast majority of thermal information concerns calorimetric data on the enthalpy, $H$, the entropy, $S$, or specific heat capacity, $C_p$.

The origin of the structural transformation is the transition between two phases. The phase is defined as a homogeneous, macroscopic volume of matter, separated by well-defined surfaces. The relative stability of a phase is determined by the difference in the Gibbs free energy,

$$G = H - TS \tag{39}$$

Provided the entropy $S$ is finite, the contribution of the term $TS$, at low temperature, to the free energy of a phase is negligible. Consequently, the condition of stability is decided by the difference in energy of the phases, the more stable being the state of lower energy. For spin-state transitions, this is in general the low-spin state, for liquid crystalline compounds the more ordered states. At the transition temperature $T_c$ (or $T_{1/2}$ for spin-crossover compounds), the free energies of the two phases are equal, $\Delta G = G_H - G_L = 0$ and thus $\Delta H = T_c \Delta S$. At sufficiently high temperatures, the term $TS$ in Equation (39) will dominate, and the stable phase will be that of greater entropy. In general, therefore, the high-temperature phase should show a higher disorder than the low-temperature phase.

A classification of phase transitions proposed by Ehrenfest is based on the lowest derivative of the Gibbs free energy which shows a discontinuity. Following Equation (39), it is

$$dG = Vdp - SdT \tag{40}$$

The first derivatives of $G$ with respect to temperature $T$ and pressure $p$ are entropy $S$ and volume $V$, respectively, whereas one of the second derivatives is $C_p/T$.

Accordingly, a *first-order transition* would be one in which a first derivative of the Gibbs free energy, that is, volume or entropy, is discontinuous. Since $\Delta S = \Delta H/T_c$, a discontinuity in the entropy implies a non-zero latent heat $\Delta H$. An additional characteristic feature of a first-order transition is thermal hysteresis. In this case the transition does not occur at the true critical temperature $T_c$ where the free energies $G_H$ and $G_L$ of the two phases are exactly equal, but rather at a higher and lower temperature, usually denoted $T_c\uparrow$ and $T_c\downarrow$. Some superheating or supercooling is required for the transition to take place. The width of the hysteresis is defined by the metastable region between the two temperatures, $\Delta T_{hys} = T_c\uparrow - T_c\downarrow$. Thermal hysteresis is an intrinsic property understandable in terms of domain formation or nucleation theory. A *second-order transition* would be characterized by a discontinuity in a second derivative of the free energy $G$, *i.e.* $C_p/T$. In particular, second-order transitions show neither latent heat nor hysteresis. For second-order phase transitions it is mandatory that there is a group-subgroup relation between the two space groups. Some transitions that have some-times been considered as second-order show a logarithmic behavior of the heat capacity and are actually *lambda transitions* (in $^4$He, $^3$He). Also, many transformations are of mixed order, showing characteristics of both first- and second-order transitions.

An alternative classification of phase transitions into structural categories is often employed. The most common structural types of transition are the following [193, 381, 442]:

*Reconstructive transitions* involve changes of the nearest neighbors and are therefore associated with extensive breaking of bonds. Such transitions take place at a fixed temperature, require in general a large latent heat, and may thus be sluggish. The transformation begins at a nucleation site, which may be a site with a vacancy in the crystal. There, the movement of the atoms sets in and is followed by the growth of the nucleus and the reconstruction of the structure. Bonds of the old structure are broken and new bonds of the growing new structure are joined at the boundary between the two phases, while atoms perform the necessary diffusion. Group-subgroup relations between the space groups are of no importance in this kind of phase transition. Such conversions are always first-order transitions.

*Displacive transitions* are characterized by small atomic displacements, by the definite direction of these displacements, and by breaking or rejoining only intermolecular bonds (*e.g.* hydrogen bonds) but no primary chemical bonds. The transitions may be but need not be a second-order transition. Most of the solid spin-crossover compounds show this type of the transition.

*Order-disorder transitions* are usually second-order transitions. They occur because the perfect order in a solid is not realized at any temperature except 0 K. In this transition, the system changes from a near perfectly ordered to a disordered state. Three types of transition are:

- *Positional disordering* arises in materials where two or more different kinds of sites exist for the atoms or molecules (in liquid crystals).

- *Orientational disordering* arises in materials where more than one different orientation is possible (in plastic crystals). Can be first-order.

- *Conformational disorder* is observed in linear, flexible molecules which can show chain mobility that leaves the position and orientation of the molecule unchanged, but introduces large-amplitude conformational motion about the chain axis (in conformationally disordered crystals (condis) crystals) [440].

- *Disordering of electronic spins* arises in ferromagnetic materials because of thermal agitation and also arises in antiferromagnetic materials where spins are aligned in two sublattices so that a zero magnetic moment results. Related are the ferroelectric-paraelectric transitions, which involve electrical dipoles.

The entropy change for any type of order-disorder transition is essentially configurational and is given as $\Delta S = R\ln(N_1/N_2)$, were $N_1$ and $N_2$ are the number of configurations in the disordered and the ordered states.

Finally, *dilatational* or *martensitic transitions* are generated by atomic displacements that are so large that the environments of most atoms are changed in the process. These transitions are rapid and involve a considerable shear of the unit cell (in metals, alloys).

The *glass transition* is a much more subtle transition than the types of the transitions described above. In the case of an amorphous glass, the structure is the same as that of a liquid, but the changes in position, orientation, and conformational state of the molecules are stopped. Such a liquid-to-solid transformation occurs at the glass transition temperature, $T_g$. The thermal response during glass transition is closer by the manifestation to the second-order transitions, however, glass transition is a non-equilibrated process and is dependent on the

heating/cooling rate [443]. The glass transition is revealed by a slight inflection in the baseline on the DSC signal rather than a true peak which is seen for other types of phase transitions.
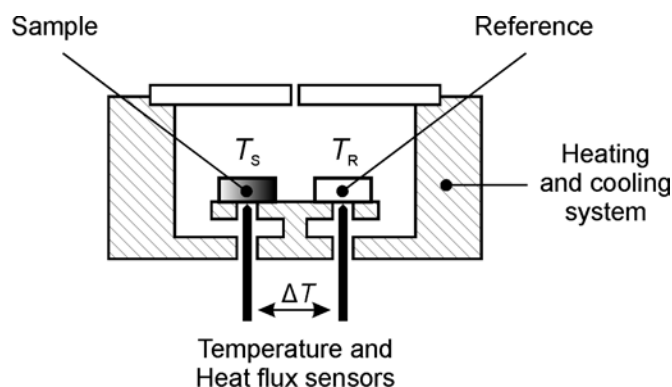


**Figure 148.** Simplified DSC measuring head.

Figure 148 illustrates the measuring head of a modern heat-flux DSC facility. The internally heated furnace is connected to cooling rods and the controlled temperature is applied to the bottom of the chamber, producing a regulated temperature. The temperature is measured continuously, and a differential technique is used to assess the heat flow into the sample and to equalize incidental heat gains and losses between reference and sample. The heat-flow rate into the sample is proportional to $\Delta T = T_R - T_S$.

Differential Scanning Calorimetry (DSC) is by far the most commonly used thermal technique for studying heat effects in spin-crossover and liquid crystalline compounds. It is a very useful and sensitive survey technique for discovering phase transitions and for determining the qualitative magnitude of thermal features. An accurate definition of DSC is the measurement of the change of the difference in the heat flow rate to the sample and to a reference sample while they are subjected to a controlled temperature program [443].

### 6.5.7   Dynamic light scattering

Dynamic light scattering is one of the most convenient methods used to determine the size of particles [444]. Shining a coherent monochromatic laser beam onto a solution with spherical particles in Brownian motion causes a Doppler shift when the light hits the moving particle, changing the wavelength of the incoming light. This change is related to the size of the particle. It is possible to compute the sphere size distribution and give a description of the

motion of the particle in the medium, measuring the diffusion coefficient of the particle and using the correlation function.

If we assume that the particles used in the experiment are of the spherical form, then it is possible to apply the Stokes-Einstein relation and hence have a formula that gives the diffusion constant:

$$D = \frac{k_\mathrm{B}T}{6\pi\eta_0 R_h} \tag{41}$$

where $R_h$ is the hydrodynamic radius, $\eta_0$ is the viscosity of the solvent. Since from the light scattering it is possible to obtain information about the position of the particles, through Equation (41), it is easy to get the radius of the particles.
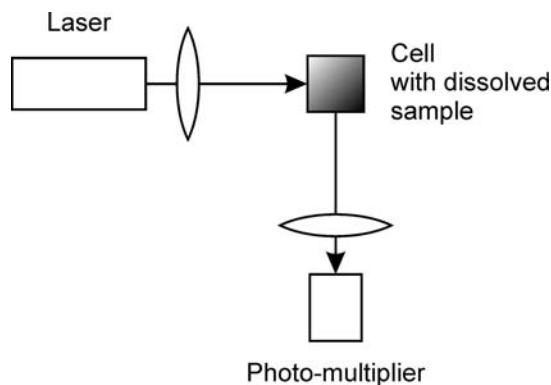


**Figure 149.** Schematic set up of dynamic light scattering experiment.

The schematic set up is illustrated in Figure 149. As is seen, the laser passes through a collimator lens and then hits the cell with the solution. The light is scattered and detected by a photomultiplier that transforms a variation of intensity into a variation of voltage. The photomultiplier is positioned at a scattering angle of 90°. The data are then processed using a computer.

### 6.5.8 Polarizing optical microscopy

The most widely used technique of liquid crystal phase identification is Polarizing Optical Microscopy (POM), which reveals that each different liquid crystal phase has a distinct optical texture [445, 446].

In general, it is easy to see if a pale-colored material possesses any liquid crystal phases by simple examination of a sample as it is being heated and cooled. Liquid crystal

samples appear opaque because of director fluctuations in the bulk non-aligned sample. Accordingly, the opaque appearance combined with some degree of fluidity signifies the presence of a liquid crystal phase in a pure sample. The clarification of the nature of the liquid crystalline phase needs a more selective method, *i.e.* polarizing microscopy.
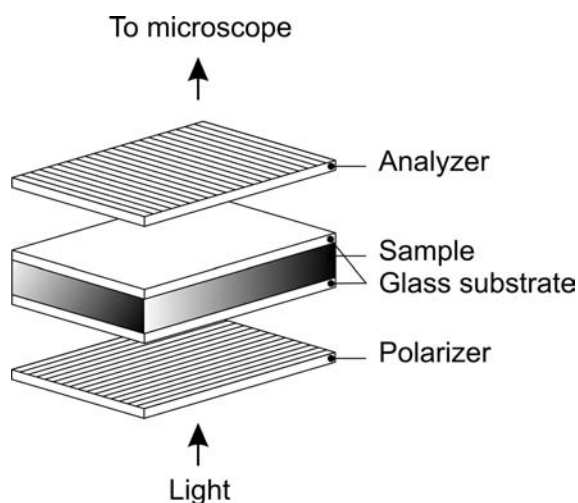


**Figure 150.** Simplified scheme of the polarizer stage.

The identification of mesophases through POM usually involves the magnified view of a thin sample of a mesogenic material sandwiched between a glass microscope slide and a glass coverslip (Figure 150). The microscope slide of material is usually placed in a stage, which can be accurately temperature-controlled, between polarizers which are crossed at 90° to each other. The manner in which the molecules are arranged within the phase can be detected by analysis of the microscopic *defect texture*. Since the polarizers in the microscope are crossed at 90° to each other, then with no sample in place light is extinguished and so blackness is seen. Similarly, if an isotropic liquid is analyzed, the polarized light remains unaffected by the sample (*isotropic*) and so no light passes through the analyzer. However, when an anisotropic, birefringent medium is present, light is not extinguished and an optical texture appears that gives information relating to the arrangement of the molecules within the medium. When analyzing mesophases by POM, the texture that is revealed depends upon how the sample is aligned, in addition to being dependent upon the phase structure of the sample. There are two basic forms of alignment for liquid crystalline compounds, *homeotropic* and *homogeneous* (also called planar or horizontal [446]). Homeotropic alignment is achieved when the molecules are oriented with their long axes orthogonal to the supporting substrate. By this orientation polarized light is unaffected by the material, therefore light cannot pass through the analyzer. In homogeneous alignment the constituent molecules of the liquid

crystal phase are oriented parallel to the supporting substrates. In practice, POM for phase identification is carried out on glass slides that are not treated to obtain any particular alignment. Accordingly, both types of alignment often occur at various positions of the microscope slide and the alignment seen is dependent upon the thickness of the sample. Thin samples tend to generate homeotropic alignment whereas thicker samples tend to give some regions of homeotropic alignment and some regions of homogeneous alignment.

The nematic phase is the least ordered liquid crystal phase which is easy to identify by POM. The high degree of disorder of the phase structure means high fluidity of the phase. Therefore, dust particles within the sample are seen to undergo intense Brownian motion. On heating a nematic sample, homogeneous alignment is often induced close to the clearing point just before the isotropic liquid produces a completely optically extinct texture. At this point the phase appears most colorful (schlieren texture) (Figure 151a). For optical extinction to occur the molecules must be aligned in the direction of either of the two crossed polarizers. In the nematic phase, the alignment of the molecules can often converge to a point (a point defect). The molecules can align in this manner in a number of different ways causing defects called two-brush and four-brush schlieren. The chiral nematic phase (N*) has a structure similar to the achiral nematic phase except the reduced symmetry of the phase caused by the gradual rotation of the molecular director to describe a helix. When viewed by optical polarizing microscopy, the N* phase can exhibit characteristic fingerprint texture (Figure 151b).

The identification of the type of smectic liquid crystal phase by optical polarizing microscopy is possible because the different structural arrangements of each phase are revealed by a different defect texture for each phase. The smectic A ($S_A$) phase exhibits two characteristic textures: i) by homeotropical alignment the polarized light is extinguished and the texture appears completely black, which is very typical for ionic mesogens [128]; ii) when the molecules are not aligned homeotropically, the phase structure adopts a focal-conic fan texture (Figure 151c), which arises because of an energetically favorable packing of the lamellar structure to give a system of curved, equidistant layers. The smectic C ($S_C$) phase is a tilted smectic phase in which the constituent molecules are tilted at a temperature dependent angle with respect to the layer normal. Two textures are exhibited by an $S_C$ phase: i) the broken focal-conic fan texture identical to that of the $S_A$ phase and ii) a schlieren texture similar to that exhibited by the nematic phase (but only with four-brush defect points). The highly ordered quasi-crystalline smectic mesophases (B, J, G, E, K, H) can easily be

distinguished from the genuine liquid crystal phases by examining the defect textures. In the crystalline smectic mesophases, long range order is seen in the form of grain boundaries.
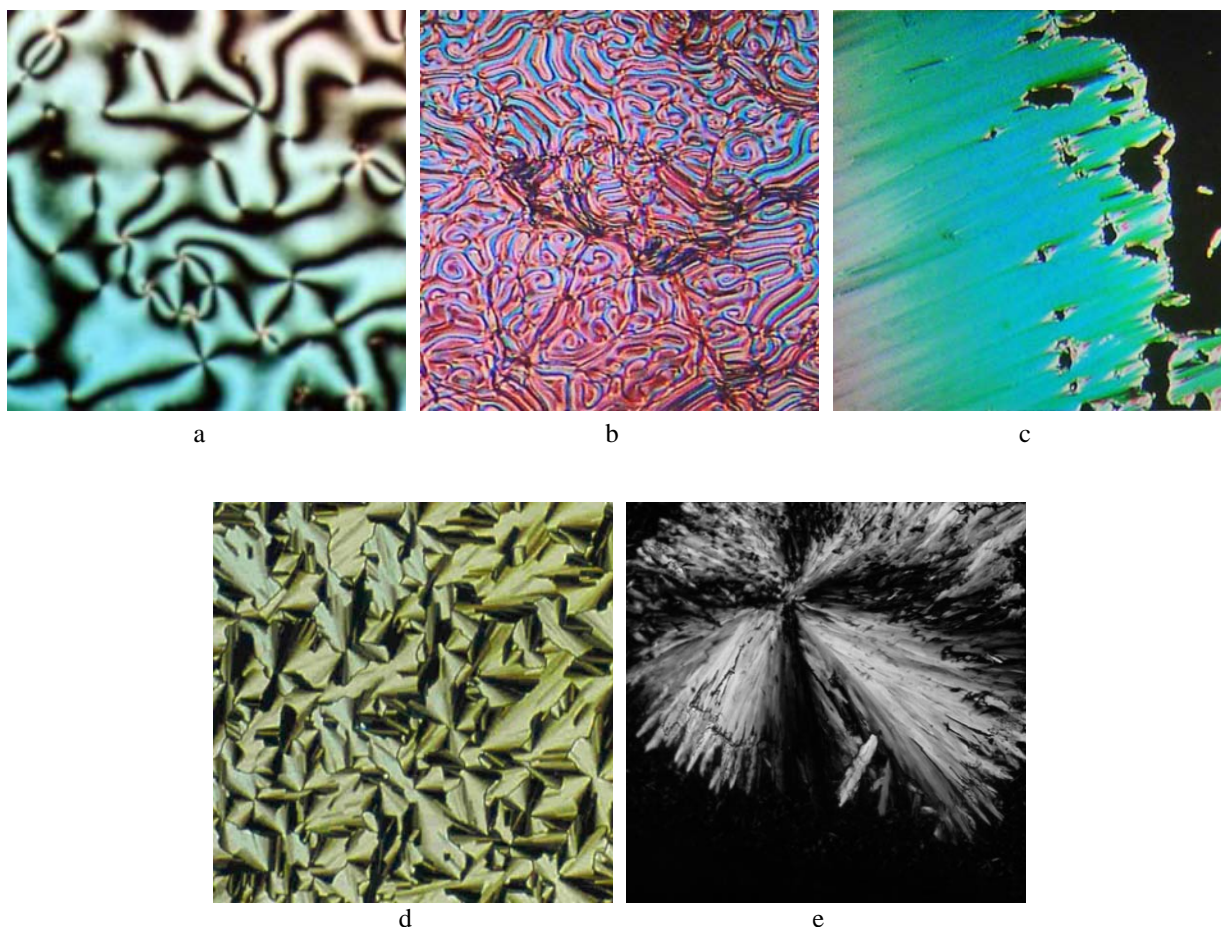


**Figure 151**. a) Schlieren texture of nematic liquid crystals [447]; b) Fingerprint texture of the chiral nematic (cholesteric) liquid crystal phase [445]; c) Focal-conic fan texture and homeotropic texture of the smectic A liquid crystal phase [445]; d) Fan-shaped focal conic texture of columnar hexagonal phase [371]; e) Broken fan-like texture of a lamellar columnar mesophase [371].

For columnar hexagonal $Col_h$ mesophases, conic fan-shaped (pseudofocal conic) and focal textures (Figure 151d) are characteristic. However, the problem often occurs that only small domains are formed that could not be attributed to a typical texture. The textures of the columnar lamellar mesophase ($Col_L$) are similar to the textures of calamitic smectic phases. Typically, broken fan-like textures with large domains (Figure 151e) can be observed for $Col_L$ phases.

### 6.5.9   UV/VIS spectroscopy

Thermal spin-crossover is always accompanied by a color change (thermochromism), *e.g.* iron(II) complexes generally change from weakly colored in the high-spin state to more deeply colored in the low-spin state [21, 41, 448]. For example, tetrazole and triazole complexes of iron(II) are nearly white in the high-spin state and purple in the low-spin state [60, 315]. Therefore, the optical spectrum in the UV/visible region differs drastically for the two spin states and proves to be well suited to follow the spin-transition qualitatively and quantitatively [60]. From the Tanabe-Sugano diagram (Figure 3, top) for an octahedral $d^6$ complex one sees that in the region left of the crossover point $\Delta_c$, the $^5T_2$ term is the ground state, only one spin-allowed transition, namely $^5T_2 \rightarrow {}^5E$, can be expected here. To the right of the crossover point, $^1A_1$ is the ground state term. Two spin-allowed transitions, *viz.* $^1A_1 \rightarrow {}^1T_1$ and $^1A_1 \rightarrow {}^1T_2$, are predicted to appear in the UV/visible region at considerably higher energies than that of the high-spin absorption band. In complexes with strong metal-to-ligand charge transfer (MLCT), the weak $d$–$d$ transitions are severely obscured by charge-transfer bands, however, the position of these bands and intensity also are spin-state dependent [150].

## 6.6 Analytical methods

### 6.6.1 CHN analysis

Elemental analysis on carbon, hydrogen and nitrogen (CHN) is the most essential investigation performed to characterize and prove the elemental composition of organic and coordination metal-containing compounds [449]. The principle of the method is based on the analysis of the combustion gases. During a standard procedure, precisely weighed samples in lightweight tin capsules are dropped at preset times into a combustion tube (at 1000° C), through which a constant stream of helium is maintained. Just prior to sample introduction the helium stream is replaced by pure oxygen for a brief period. The sample is instantaneously burned followed by intense oxidation of the tin capsule at 1800° C (flash combustion). The resulting combustion gases are passed over catalysts to ensure complete oxidation and absorption of halogens and other interferences. Excess oxygen is removed as the gases are swept through a reduction tube containing copper at 650° C. Any oxides of nitrogen are reduced to nitrogen gas. Finally the gases are separated on a chromatographic column into nitrogen (N), carbon dioxide (C) and water vapor (H) and quantitatively measured by a detecting system.

### 6.6.2 IR spectroscopy

Infrared (IR) spectroscopy is one of the most common spectroscopic techniques used for characterization of organic and inorganic compounds [425]. It is based on the fact that different functional groups due to different inherent symmetry and different nature of the constituting atoms exhibit different vibrations at characteristic frequencies of IR radiation which can be used for qualitative and quantitative analysis.

The general rule connects the number of the vibrational degrees of freedom F and the number of atoms N in a molecule by the relation:

$$F = 3N - 6 \tag{42}$$

In addition to a number of distinct vibrations, the wavenumber $\omega$ of the absorbed radiation is given by Hook's law:

$$\omega = \frac{1}{2\pi c} \sqrt{f \frac{m_A + m_B}{m_A \cdot m_B}} \tag{43}$$

where $c$ is the velocity of light, $f$ is force constant, $m_A$ and $m_B$ are the masses of the bonded atoms. It is seen, that the heavier the atoms involved in the bond, the lower the absorption frequency should be and the weaker is the bond, the lower the frequency is. This is especially important for spin-crossover compounds, in which transition from low-spin to high-spin state decreases the absorption frequency of the bonds Fe–N due to occupation of the antibonding $e_g$ orbitals [439]. The IR technique can also be used to derive the LS:HS ratio by analyzing multi-temperature data of spin-crossover compounds [209, 450, 451].

The vibrations of an individual molecule in the gas or liquid phase are subject only to the symmetry based on its own intrinsic point symmetry. But when a molecule resides in a crystal it is subject to the symmetry restrictions arising out of its crystalline environment. The latter effect can be successfully applied to analyze the packing effects in long-chained molecules and as well to probe the conformation and environment of complex hydrocarbon-chain assemblies [248-250].

Usually, IR absorption information is presented in the form of a spectrum with wavelength or wavenumber *vs* absorption intensity.

### 6.6.3   NMR spectroscopy

Nuclear Magnetic Resonance (NMR) is selective absorption of high-frequency radio waves by atomic nuclei that are subjected to an appropriately strong stationary magnetic field [425]. Nuclei with nuclear spin $I > 0$ are influenced by a strong magnetic field which exerts a force that causes them to precess. When the natural frequency of the precessing nuclear magnets corresponds to the frequency of a weak external radio wave striking the material, energy is absorbed from the radio wave. This selective absorption, called resonance, is the essential principle of the method. Because the energy of the absorbed radiation depends on the environment around the absorbing nucleus in a molecule, NMR spectroscopy provides the most valuable structural information of all the spectroscopic techniques used in chemistry. Especially valuable are proton magnetic resonance spectroscopy (^{1}H NMR), which measures the resonances due to energy absorption by hydrogen atoms in organic compounds, and carbon-13 magnetic resonance spectroscopy, which yields the resonances due to absorption by atoms of carbon-13 (^{13}C NMR). In the present work both NMR methods were used for the characterization of organic intermediates.

### 6.6.4   Mass spectrometry

Mass spectrometry (MS) is an analytical technique that is used to identify unknown compounds, quantify known materials and elucidate the structural and physical properties of ions [425, 452].

A mass spectrometer is an instrument that can separate charged atoms or molecules according to their mass-to-charge ratio ($m/z$). Relative molecular masses of organic compounds and complex species can be measured in this way and the instrument is also capable of generating structural information.
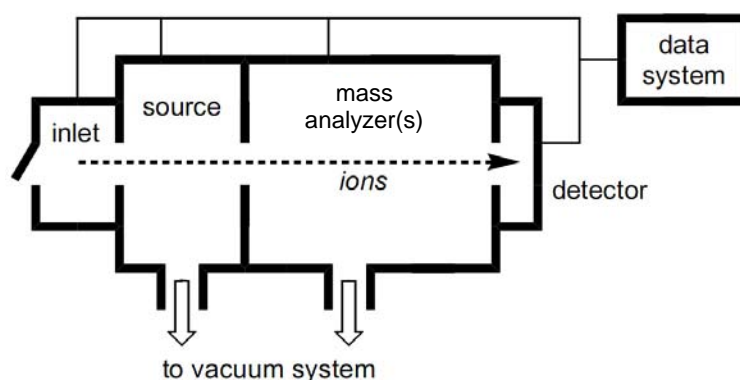


**Figure 152.** Schematic layout of a mass spectrometer. Adopted from [452].

The sample is introduced into the mass spectrometer, which is generally kept under high vacuum ($10^{-5}$ mBar) (Figure 152). Compounds are converted into gas phase molecules either before or during the charging or ionization process, which takes place in the ion source.

Many types of ionization modes are available: the type of compound to be analyzed and the specific information required determines which ionization mode is the most suitable. Methods suitable for characterization of complex molecules are field desorption (FD) and electrospray ionization (ESI) ones. The ions produced in the ionizer are repelled out of the ion source and accelerated towards the analyzer region. Although both positive and negative ions may be generated at the same time, one polarity is chosen and either positive or negative ions are analyzed and recorded. Molecules that do not ionize, *i.e.* remain neutral, are pumped away and are not detected.

The two most common types of mass analyzers are field and time-of-flight (TOF) methods [452]. Field instruments utilize the behavior of charged particles moving through field regions. Sector instruments incorporate an electromagnetic field and (usually) an electric field (for energy focusing). Quadrupole and ion trap instruments incorporate a combination of

radio-frequency and direct-current fields. Ions entering a field experience a deflecting force, depending on the strength of the field and the mass-to-charge ratio of the ion. By scanning the field strength all the ions produced in the ion source are sequentially focused at the detector. The resulting pattern obtained is called mass spectrum. In time-of-flight instruments the time taken for an ion to travel a set distance is measured very accurately. The time taken for the ion to reach the detector is directly related to the mass-to-charge ratio.

### 6.6.5 Termogravimetric analysis

The basis of the method is simple [440]. It consists in a comparison of the force exerted by gravity on the two masses to be compared, using for example a beam balance as is shown schematically in Figure 153. The main calculation from a direct measurement of mass is to establish the number of lost moles of the compound or element in question during heating up the sample. This is achieved by dividing by the molar mass, $M_w$. In order to identify the mass flux, an analysis technique, such as IR spectroscopy, or exclusion chromatography, or mass spectrometry can be coupled to the furnace.
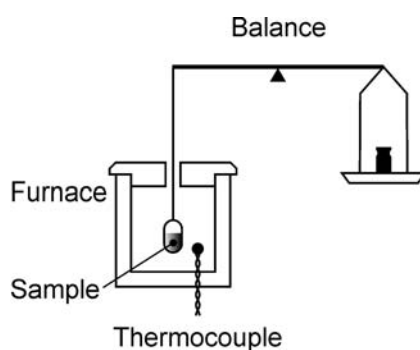


**Figure 153.** Schematic for a thermogravimetric experiment.

## 6.7  Experimental section

### 6.7.1  Physical and analytical methods

**Chemicals and solvents.** The chemicals and solvents were obtained from the companies Sigma-Aldrich, Fluka and Acros and used as obtained. THF was freshly distilled over potassium prior to use.

**X-ray single crystal diffraction.** The data were collected using an Oxford Diffraction KM-4 $\kappa$ diffractometer with a Sapphire3 CCD detector and graphite-monochromated Mo $K_\alpha$ radiation (0.71073 Å). The crystals were mounted on a quartz glass capillary and cooled by a cold dry nitrogen gas stream (Oxford Cryosystems equipment). The temperature stability was ±0.1 K. Accurate cell parameters were determined and refined using the program *CrysAlis CCD* (Version 1.171.29; Oxford Diffraction Ltd, Wrocław, Poland). For the integration of the collected data the program *CrysAlis RED* was used (Version 1.171.29; Oxford Diffraction Ltd, Wrocław, Poland). The structure was solved using direct method with SHELXS97 [453] or Sir92 [454] or Sir2000 software [455], and then the solution was refined with SHELXL97 [453]. All non-H atoms were refined with anisotropic displacement factors.

In the structure of **2** the tetraflouroborate anion is disordered over two positions, with about 40:60 populations of both. The bond length and angle similarity restraints were applied in order to ensure tetrahedral symmetry, and average B–F distances were refined freely (the value, 1.352(13) Å, is consistent with the literature value of 1.36 Å [42]).

In the structure of **4** one hydrogen atom of the water molecule O1w was not localized.

In the structure **C$_6$-19** one of the perchlorate anions is disordered over two positions, with about 50:50 populations of both. The ratio does not change with temperature.

**X-ray Absorption Data Recording and Processing.** The Fe $K$-edge XANES (X-ray absorption near-edge structures) and EXAFS (extended X-ray absorption fine structures) spectra were recorded in the conventional transmission mode on beamline A1 at the German Electron Synchrotron, DESY, Hamburg. The spectrum was recorded from 6970 to 7997 eV. The energy scale at the iron $K$-edge was calibrated with the strong absorption peak of metallic iron foil at 7111.2 eV. A water-cooled Si(111) channel-cut crystal was employed as a monochromator. The intensities of the incident and transmitted X-rays were recorded using ionization chambers. The mass of the sample was calculated to obtain a product $a{\times}d$ of about 2.5 for energies just above the absorption $K$-edge of iron ($a$ is the linear absorption coefficient

and $d$ is the thickness of the pellet). The calculated amount of the sample was ground, mixed with crystalline cellulose and pressed into a 13 mm diameter and about 1 mm thickness pellet. The temperature of the experiment was 80 K. For this purpose a closed-cycle He cryostat was used and the temperature was measured with a Si diode placed close to the sample. Data acquisition time for each data point was 1 s. EXAFS data analysis was performed with the program *EXAFS98* [433, 434]. This standard analysis includes linear pre-edge background removal, a Lengeler-Eisenberg spectrum normalization, and reduction from the absorption data $\mu(E)$ to the EXAFS spectrum $\chi(k)$ with the energy threshold, taken at the absorption maximum (7130 ± 1 eV). The radial distribution function $F(R)$ was calculated by Fourier transformation of $k^3 w(k)\chi(k)$ in the 2–14 Å$^{-1}$ range; $w(k)$ is a Kaiser-Bessel apodization window with smoothness coefficient $\tau = 3$. After Fourier filtering, the first single-shell Fe–N$_6$ was fitted in the 4–12 Å$^{-1}$ range to the standard EXAFS formula, in a single scattering scheme. The curve-fitting analysis for the first coordination sphere of the iron was performed with *Round Midnight* [432] code after Fourier filtering in the 0.7–2.0 Å range of the EXAFS spectrum. Spherical-wave theoretical amplitudes and phase shifts calculated by the *McKale* [429, 456] code were used. Since theoretical phase shifts were used, we fitted the energy threshold $E_0$ ($\Delta E_0$). The goodness of fit is given by:

$$\rho(\%) = \frac{\Sigma\left[k\chi_{\exp}(k) - k\chi_{th}(k)\right]^2}{\Sigma\left[k\chi_{\exp}(k)\right]^2} \tag{44}$$

**X-ray diffraction (XRD) analysis.** X-ray powder diffraction measurements were carried out with a Seifert TT3300 diffractometer (monochromatic Cu K$_\alpha$ radiation) or a STOE STADI 2 diffractometer, equipped with a linear position-sensitive detector (STOE mini PSD) in the range of $2\theta = 1$–30°. 2D-WAXS measurements were conducted using a CCD camera (Bruker GADDS) in the range of $2\theta = 2$–30°. The patterns were recorded with vertical orientation of the sample axis and with the beam perpendicular to the sample.

**Magnetic measurements.** Variable-temperature magnetic susceptibility measurements were recorded with a Quantum Design MPMS2 SQUID susceptometer equipped with a 7 T magnet, operating in standard procedure at 1 T and at temperatures in the range 4–400 K. The susceptometer was calibrated with metallic palladium. Measurements were performed on finely ground samples (15–30 mg). The magnetic data were corrected for the sample holder and the diamagnetic contribution. During the LIESST experiment, the sample was irradiated at 4 K with light of $\lambda = 514$ nm (25 mW cm$^{-2}$) until saturation of the magnetic moment was reached. Then irradiation was switched off and $\chi_M T$ *vs* $T$ was recorded in the warming mode at a rate of 2 K/min up to 300 K. At temperatures greater than 70 K,

$\chi_M T$ increases following the spin-transition curve observed for each compound which was used for the calibration of the LIESST curve. The least squares fitting of the experimental curves with Slichter-Drickamer model was performed with the program Origin 7.0.

**Mössbauer spectroscopy.** Mössbauer spectra were recorded in transmission geometry with a [57]Co/Rh source kept at room temperature and a conventional spectrometer operating in the constant-acceleration mode. The samples were sealed in Plexiglass sample holders and mounted in a nitrogen-bath cryostat. The Recoil 1.03a Mössbauer Analysis Software was used to fit the experimental spectra.

**DSC measurements.** DSC measurements were performed on a Mettler model DSC 822e calibrated with metallic indium and zinc. DSC profiles were recorded on the samples encapsulated in an aluminum pan (5–10 mg) at the rate of 5, 7 or 10 K min$^{-1}$ and analyzed with Netzsch Proteus software. An overall accuracy of 0.2 K in the temperature and 2 % in the heat flow has been estimated.

**Dynamic light scattering.** Dynamic light scattering (DLS) was performed with an argon ion laser (Stabilite 2060-04, λ 514 nm, Spectra-Physics), a SP-125 goniometer, and an ALV-5000 multiple-τ digital correlator. The temperature was kept constant at 293 K for light scattering measurements. Each sample was analyzed at two concentrations 1 mmol l$^{-1}$ and 2 mmol l$^{-1}$.

**Polarizing optical microscopy.** The temperatures and textures of phase transitions were determined with a polarization microscope, equipped with a hot stage and with temperature control of better than ± 0.5 K.

**Infrared spectroscopy.** The IR spectra of the solid samples were recorded at 293 K in the range of 400–4000 cm$^{-1}$ using a Bruker Tensor 27 Spectrometer. The bands were assigned using the literature data.

**CHN analysis.** Elemental analyses on C, H, N (and S) were done on a Foss Heraeus Vario EL Analyzer. In several cases for iron(II) carbon-rich metallomesogenic complexes the elemental analysis yielded somewhat lower percentage (~1 %) of carbon due to the formation of refractory materials during the combustion, however, the percentage of hydrogen and nitrogen was still in the tolerance range.

**NMR spectroscopy.** ^{1}H NMR spectroscopic measurements were done in deuterated solvents on an Advance DRX Bruker 400 MHz Spectrometer with use of the solvent proton or carbon signal as an internal standard.

**UV/VIS spectroscopy**. UV/VIS spectra were recorded at room temperature on a Perkin-Elmer Lambda 9 spectrophotometer in solution ($CH_2Cl_2$, $CH_3CN$, $CH_3OH$) in transmission mode.

**Mass spectrometry.** Mass spectra were recorded on Finnegan MAT 95 (Field Desorption, FD), Micromass Q-TOF2 (Electro Spray Ionization, ESI) and on Finnegan MAT 212 mass spectrometer (EI). The identified peaks are given for the most abandoned isotopes.

**TGA measurements.** TGA analysis in tandem with MS EI spectroscopy on a [18]$^+$ ion was done on a Mettler Toledo S500 facility or Mettler Toledo S851.

### 6.7.2   Preparation of the mononuclear systems

*Synthesis of the precursors*

**Scheme 1.** Synthesis of 5-(alkoxy)picolinaldehyde.
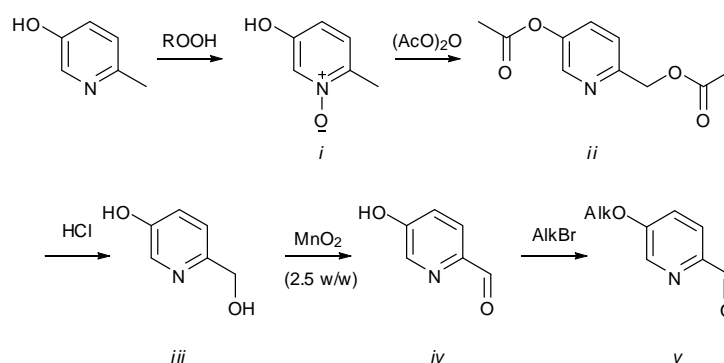


**5-hydroxy-2-methylpyridine-1-oxide (*i*).** 5-hydroxy-2-methylpyridine (54.4 g, 0.5 mol) was suspended in 1.5 L of chloroform and a solution of *m*-chlorperbenzoic acid (103.0 g, 0.596 mol) in a sufficient amount of chloroform was added with stirring during 6 h and left overnight. Then the solvent was evaporated and the obtained solid was dissolved in hot ethanol at 50 °C. A sufficient amount of diisopropyl ether was added to initialize crystallization. The crystalline precipitate (5-hydroxy-2-methylpyridine-1-oxide) was filtered off and the organic phase was dried in a rotor evaporator. The obtained solid was dissolved in minimum amount of chloroform and left in a fridge for several hours. The formed crystals (*m*-chlorbenzoic acid) were filtered off and the filtrate was dried in a rotor evaporator, the solid residue was one more crystallized from ethanol/diisopropyl ether to provide the rest of 5-hydroxy-2-methylpyridine-1-oxide. Two portions of the product were combined and recrystallized from hot ethanol. Yield 51.66 g (83 %).

MS EI (rel. int.): $m/z$ 125.1 $[M]^+$ (96 %), 108.1 $[M\text{-}O]^+$ (100 %); $^1$H NMR (400 MHz, MeOH-d$^4$): δ (ppm) 7.88 (1H, d, J = 2.7 Hz, PyH), 7.27 (1H, d, J = 8.6 Hz, PyH), 7.00 (1H, dd, J = 2.7, 8.6 Hz, PyH), 2.37 (3H, s, CH$_3$); $^{13}$C NMR (100 MHz , CDCl$_3$ + DMSO d$^6$): δ (ppm) 160.8, 145.8, 134.5, 132.3, 121.1, 22.9; FT-IR (KBr; cm$^{-1}$): 3421br ν(O–H), 1461 ν(Py); Calcd for C$_6$H$_7$NO$_2$: C, 57.59, H, 5.64, N, 11.19. Found C, 57.68, H, 5.70, N, 11.24.

**6-(hydroxymethyl)pyridin-3-ol (*iii*).** 6-methylpyridin-3-ol 1-oxide (50.0 g, 0.4 mol) was boiled in 0.5 L of acetic anhydride at 120 °C during 3 h under N$_2$. After cooling the product mixture was subjected to rotor evaporation, the rest was purified by dissolving in boiling n-hexane. The yield of crude 6-[(acetyloxy)methyl]pyridin-3-yl acetate (*ii*) is 83.47 g (95 %).

Crude 6-[(acetyloxy)methyl]pyridin-3-yl acetate (80 g, 0.38 mol) was dissolved in conc. HCl (200 ml) and boiled over a period of 24 h. After cooling the solution was evaporated and dissolved in water, then it was neutralized with sufficient amount of sodium hydroxide. The precipitated sodium chloride was filtered off, and the filtrate was evaporated to give a dark residue which was taken up with boiling acetonitrile (3 × 50 ml). Fractions were combined and evaporated to dryness; the residue was recrystallized from acetonitrile. Yield 18.24 g (39 %). MS EI (rel. int.): $m/z$ 125.1 $[M]^+$ (96 %), 108.1 $[M–O]^+$ (100 %); $^1$H NMR (400 MHz, CDCl$_3$ + DMSO-d$^6$): δ 7.97 (1H, d, J = 8.5 Hz,PyH), 7.31 (1H, d, J = 2.7Hz, PyH), 7.19 (1H, dd, J = 2.7, 8.5 Hz, PyH) 4.54 (2H, s, CH$_2$); $^{13}$C NMR (100 MHz, CDCl$_3$ + DMSO-d$^6$): δ 155.2, 152.1, 137.5, 125.4, 123.4, 65.3;  Calcd for C$_6$H$_7$NO$_2$: C, 57.59, H, 5.64, N, 11.19. Found C, 57.59, H, 5.64, N, 11.18.

**5-(hydroxy)picolinaldehyde (*iv*).** To 6-(hydroxymethyl)pyridin-3-ol  (4.9 g, 39.8 mmol) dissolved in *i*-PrOH was added 2.5 times its weight of active MnO$_2$. The reaction mixture was stirred and refluxed for 2 h and then after cooling transferred into a centrifuge. The organic layer was decanted, the inorganic cake of manganese oxide was washed by suspending with alcohol and the procedure of centrifugation was repeated. The organic solutions were combined and evaporated to dryness. The obtained yellow-brown powder was recrystallized from boiling water to provide analytically pure 5-(hydroxy)picolinaldehyde. Yield 2.9 g (60 %). MS EI (rel. int.): $m/z$ 123.1 $[M]^+$ (100 %), 95.1 $[M\text{-}CO]^+$ (92 %); $^1$H NMR (400 MHz, DMSO-d$^6$): δ 9.76 (1H, s, CHO), 8.25 (1H, d, J = 2.7Hz, PyH$^6$), 7.78 (1H, d, J = 8.5 Hz, PyH$^2$) 7.27 (1H, dd, J = 2.7, 8.5 Hz, PyH$^3$); $^{13}$C NMR (100 MHz, DMSO-d$^6$): δ 191.7 (CHO), 157.8, 144.5, 138.8, 123.8, 122.2; FT-IR (KBr; cm$^{-1}$): 2849, 2754 ν(C–H), 1698 ν(C=O).  Calcd for C$_6$H$_5$NO$_2$: C, 58.54, H, 4.09, N, 11.38. Found C, 58.69, H, 4.14, N, 11.46.

**Standard procedure for 5-(alkoxy)picolinaldehyde (*v*).** 5-(hydroxy)-picolinaldehyde (1 g, 8.123 mmol), anhydrous potassium carbonate (1.12 g, 8.123 mmol), n-alkylbromide (8.123 mmol) were stirred vigorously in dry *N,N*-dimethylformamide (30 ml) at 100 °C for 4 h. After cooling excess of water was added and the formed precipitate was filtered off and recrystallized from ethanol. The isolated crystalline solid was dried *in vacuo* providing an analytically pure product.

**5-(hexyloxy)picolinaldehyde** (from n-hexylbromide, 1.33 g) was used in further syntheses without purification.

**5-(hexadecyloxy)picolinaldehyde.** n-Hexadecylbromide (2.46 g); yield 2.59 g (92 %). MS EI (rel. int.): $m/z$ 347.3 $[M]^+$ (62 %); $^1$H NMR (400 MHz, CDCl$_3$): δ (ppm) 10.00 (1H, s, CHO), 8.44 (1H, d, $J$ = 2.4 Hz, PyH$^6$), 7.97 (1H, d, $J$ = 8.5Hz, PyH$^2$), 7.30 (1H, dd, $J$ = 2.4, 8.5Hz, PyH$^3$), 4.11 (2H, t, $J$ = 6.5 Hz, OC$H_2$), 1.86 (2H, quin, $J$ = 6.5 Hz, OCH$_2$C$H_2$) 1.63–1.1 (26H, m, CH$_2$), 0.89 (3H, t, $J$ = 6.5 Hz, CH$_3$); $^{13}$C NMR (100 MHz, CDCl$_3$): δ (ppm) 191.9 (CHO), 158.4, 145.9, 138.6, 123.2, 120.2, 68.7, 31.7, 29.4–28.7 (m), 25.6, 22.5, 13.9; FT-IR (KBr; cm$^{-1}$): 2923, 2850 ν(C–H), 1704 ν(C=O); Calcd for C$_{22}$H$_{37}$NO$_2$: C, 76.03, H, 10.73, N, 4.03. Found C, 76.04, H, 10.63, N, 4.04.

**5-(octadecyloxy)picolinaldehyde.** n-Octadecylbromide (2.71 g); yield 2.74 g (90 %). MS EI (rel. int.): $m/z$ 374.3 $[M]^+$ (83 %), 346.3 $[M-CHO]^+$ (100 %); $^1$H NMR (400 MHz, CDCl$_3$): δ 9.91 (1H, s, CHO), 8.34 (1H, d, $J$ = 2.4 Hz, PyH$^6$), 7.91 (1H, d, $J$ = 8.5 Hz, PyH$^2$), 7.24 (1H, dd, 2.4, 8.5 Hz, PyH$^3$), 4.05 (2H, t, $J$ = 6.5 Hz, OC$H_2$), 1.80 (2H, quin, $J$ = 6.5 Hz, OCH$_2$C$H_2$) 1.50–1.10 (18H, m, CH$_2$), 0.85 (3H, t, $J$ = 6.5 Hz, CH$_3$); $^{13}$C NMR (100 MHz, CDCl$_3$): δ 191.9 (CHO), 158.4, 145.9, 138.6, 123.1, 120.2, 68.7, 31.7, 29.5-29.1 (m), 28.7, 25.6, 22.5, 13.9; FT-IR (KBr; cm$^{-1}$): 2923, 2850 ν(C–H), 1705 ν(C=O); Calcd for C$_{24}$H$_{41}$NO$_2$: C, 76.75, H 11.00, N 3.73. Found C, 76.89, H, 10.97, N, 3.73.

**5-(eicosyloxy)picolinaldehyde.** n-Eicosylbromide (2.94 g); yield 2.71 g (94 %). MS EI (rel. int.): $m/z$ 403.4 $[M]^+$ (83 %); $^1$H NMR (400 MHz, CDCl$_3$): δ (ppm) 10.00 (1H, s, CHO), 8.43 (1H, d, $J$ = 2.4 Hz, PyH$^6$), 7.96 (1H, d, $J$ = 8.5Hz, PyH$^2$), 7.29 (1H, dd, $J$ = 2.4, 8.5 Hz, PyH$^3$), 4.11 (2H, t, $J$ = 6.5 Hz, OC$H_2$), 1.84 (2H, quin, $J$ = 6.5 Hz, OCH$_2$C$H_2$) 1.63–1.1 (34H, m, CH$_2$), 0.89 (3H, t, $J$ = 6.5 Hz, CH$_3$); $^{13}$C NMR (100 MHz, CDCl$_3$): δ (ppm) 191.9 (CHO), 158.4, 145.9, 138.6, 123.2, 120.2, 68.7, 31.7, 29.4–28.7, 25.6, 22.5, 13.9; FT-IR (KBr; cm$^{-1}$): 2922, 2849 ν(C–H), 1704 ν(C=O); Calcd for C$_{26}$H$_{45}$NO$_2$: C, 77.37, H, 11.24, N, 3.47. Found C, 77.51, H, 11.38, N, 3.49.

**Scheme 2.** Synthesis of 6-methyl-5-(alkoxy)picolinaldehyde.
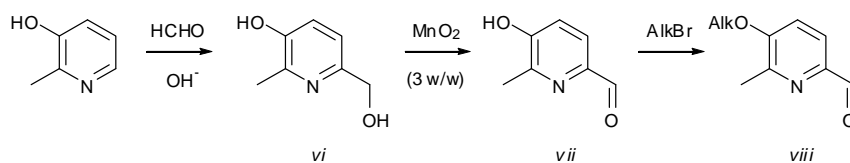


**3-Hydroxy-6-hydroxymethyl-2-methylpyridine (*vi*).** A mixture of 3-hydroxy-2-methylpyridine (5 g, 4.58 mmol), 30 ml of 10 % sodium hydroxide in 15 ml of water and 5 ml of 34 % formalin (aqueous formaldehyde solution) was refluxed for 2 h. An additional amount of 34 % formalin (5 ml.) was added and the reflux is continued for additional 2 h. The mixture was acidified with acetic acid and the resulting precipitate was filtered off and washed twice with acetone. The filtrate was evaporated to dryness and the residue was repeatedly extracted with hot acetone. The extract was evaporated to give crude 3-hydroxy-6-hydroxymethyl-2-methylpyridine as a solid that was recrystallized from hot methanol to provide analytically pure white crystalline substance. Yield 1.62 g (25 %).

MS EI (rel. int.): *m/z* 139.1 [M]$^+$ (100 %), 122.1 [M–OH]$^+$ (11 %), 110.1 [M–CO]$^+$ (83 %); $^1$H NMR (400 MHz, D$_2$O): δ (ppm) 7.82 (2H, m, PyH$^{2+3}$), 4.47 (2H, s, PyC*H*$_2$OH), 2.33 (3H, s, PyCH$_3$); $^{13}$C NMR (100 MHz, D$_2$O): δ (ppm) 155.9, 144.8, 142.7, 127.4, 121.9, 61.45, 15.86; FT-IR (KBr; cm$^{-1}$): 3100 br ν(OH), 2941, 2885 ν(C–H), 1467 ν(Py); Calcd for C$_7$H$_9$NO$_2$: C, 60.42, H, 6.52, N, 10.07. Found C, 60.31, H, 6.43, N, 10.35.

**6-methyl-5-(hydroxy)picolinaldehyde (*vii*).** To 3-Hydroxy-6-hydroxymethyl-2-methylpyridine (1.62 g, 11.64 mmol) dissolved in *i*-PrOH was added 3 times its weight of active MnO$_2$. The reaction mixture stirred and refluxed for 2 h and then after cooling subjected to centrifugation. Thereafter the transparent organic layer was decanted; the remaining inorganic cake was washed by suspending with alcohol and the procedure of centrifugation was repeated. The organic solutions were combined and evaporated to dryness. The obtained yellow-brown powder was recrystallized from boiling water to provide analytically pure 6-methyl-5-(hydroxy)picolinaldehyde. Yield 1.51 g (95 %).

MS EI (rel. int.): *m/z* 137.0 [M]$^+$ (56 %), 109.1 [M-CO]$^+$ (100 %); $^1$H NMR (400 MHz, CD$_3$OD): δ (ppm) 9.84 (1H, s, CHO), 7.78 (1H, d, J = 8.3 Hz, PyH$^2$), 7.22 (1H, d, J = 8.3 Hz, PyH$^3$), 2.49 (3H, s, PyCH$_3$); $^{13}$C NMR (100 MHz, CD$_3$OD): δ (ppm) 191.0 (CHO), 156.2, 147.9, 143.7, 122.5, 120.3, 17.2; FT-IR (KBr; cm$^{-1}$): 3300 br ν(O–H), 2919, 2863 ν(C–H), 1649 ν(C=O); Calcd for C$_7$H$_7$NO$_2$: C, 61.31, H, 5.14, N, 10.21. Found C, 61.29, H, 5.20, N, 10.32.

**Standard procedure for 6-methyl-5-(alkoxy)picolinaldehyde (*viii*).** The same procedure was used as for 5-(alkoxy)picolinaldehyde starting from 6-methyl-5-(hydroxy)picolinaldehyde (1 g, 7.30 mmol), n-alkylbromide (7.30 mmol), potassium carbonate (1 g, 7.30 mmol) and dry *N,N*-dimethylformamide (30 ml).

**6-methyl-5-(hexyloxy)picolinaldehyde** (from n-hexylbromide, 1.20 g), **6-methyl-5-(decyloxy)picolinaldehyde** (from n-decylbromide, 1.61 g) and **6-methyl-5-(dodecyoxy)picolinaldehyde** (from n-dodecylbromide, 1.82 g) were used in further syntheses without purification.
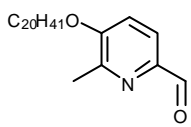
**6-methyl-5-(tetradecyloxy)picolinaldehyde.** n-Tetradecylbromide (2.02 g); yield 2.38 g (98 %). MS EI (rel. int.): *m/z* 333.1 $[M]^+$ (8 %); $^1$H NMR (400 MHz, CDCl$_3$): δ (ppm) $^1$H (CDCl$_3$): δ 9.98 (1H, s, CHO), 7.85 (1H, d, J = 8.6 Hz, PyH$^2$), 7.16 (1H, d, J = 8.6 Hz, PyH$^3$), 4.07 (2H, t, J = 6.5 Hz, OC*H*$_2$), 2.56 (3H, s, PyCH$_3$), 1.87 (2H, quin, J = 6.5 Hz, OCH$_2$C*H*$_2$) 1.53–1.10 (22H, m, CH$_2$), 0.89 (3H, t, J = 6.5 Hz, CH$_3$); $^{13}$C NMR (100 MHz, CDCl$_3$): δ (ppm) 192.2 (CHO), 156.7, 149.8, 144.3, 121.8, 116.1, 68.4, 31.7, 29.4–29.0 (m), 28.7, 25.8, 22.5, 19.2, 13.9; FT-IR (KBr; cm$^{-1}$): 2918, 2853 ν(C–H), 1691 ν(C=O);  Calcd for C$_{21}$H$_{35}$NO$_2$: C, 75.63, H, 10.58, N, 4.20. Found C, 75.24, H, 10.15, N, 4.21.

**6-methyl-5-(hexadecyloxy)picolinaldehyde.** n-Hexadecylbromide (2.23 g); yield 2.58 g (98 %). MS EI (rel. int.): *m/z* 361.1 $[M]^+$ (9 %); $^1$H NMR (400 MHz, CDCl$_3$): δ (ppm) 9.98 (1H, s, CHO), 7.85 (1H, d, J = 8.6 Hz, PyH$^2$), 7.16 (1H, d, J = 8.6 Hz, PyH$^3$), 4.07 (2H, t, J = 6.5 Hz, OC*H*$_2$), 2.58 (3H, s, PyCH$_3$), 1.87 (2H, quin, J = 6.5 Hz, OCH$_2$C*H*$_2$) 1.63–1.10 (26H, m, CH$_2$), 0.90 (3H, t, J = 6.5 Hz, CH$_3$); $^{13}$C NMR (100 MHz, CDCl$_3$): δ (ppm) 192.2 (CHO), 156.7, 149.7, 144.3, 121.8, 116.0, 68.4, 31.7, 29.4–28.7 (m), 25.8, 22.5, 19.2, 13.9; FT-IR (KBr; cm$^{-1}$): 2922, 2850 ν(C–H), 1689 ν(C=O);  Calcd for C$_{23}$H$_{39}$NO$_2$: C, 76.40, H, 10.87, N, 3.87. Found C, 76.85, H, 10.62, N, 3.85.

**6-methyl-5-(heptadecyloxy)picolinaldehyde.** n-Heptadecyl-bromide (2.33 g); yield  2.60 g (95 %). MS EI (rel. int.): *m/z* 375.2 $[M]^+$ (89 %); $^1$H NMR (400 MHz, CDCl$_3$): δ (ppm) $^1$H (400 MHz, CDCl$_3$): δ 9.98 (1H, s, CHO), 7.85 (1H, d, J = 8.4 Hz, PyH$^2$), 7.17 (1H, d, J = 8.4, PyH$^3$), 4.08 (2H, t, J = 6.4 Hz, OC*H*$_2$), 2.57 (3H, s, PyCH$_3$), 1.85 (2H, quin, J = 6.4 Hz, OCH$_2$C*H*$_2$) 1.63–1.20 (28H, m, CH$_2$), 0.90 (3H, t, J = 6.4 Hz, CH$_3$); $^{13}$C NMR (100 MHz, CDCl$_3$): δ (ppm) 192.2 (CHO), 156.7, 149.7, 144.3, 121.8, 116.1, 68.4, 31.7, 29.5–29.0 (m), 28.7, 25.8, 22.5, 19.2, 13.9; FT-IR (KBr;

$cm^{-1}$): 2916, 2850 $\nu$(C–H), 1690 $\nu$(C=O); Calcd for $C_{24}H_{41}NO_2$: C, 76.75, H, 11.00, N, 3.73. Found C, 76.60, H, 10.99, N, 3.55.

**6-methyl-5-(octadecyloxy)picolinaldehyde.** n-Octadecylbromide (2.43 g); yield 2.44 g (86 %). MS EI (rel. int.): $m/z$ 389.3 $[M]^+$ (96 %), 360.3 $[M-CHO]^+$ (100 %); ^{1}H NMR (400 MHz, $CDCl_3$): $\delta$ (ppm) 9.92 (1H, s, CHO), 7.79 (1H, d, J = 8.4Hz, PyH[2]), 7.10 (1H, d, J = 8.4Hz, PyH[3]), 4.00 (2H, t, J = 6.4 Hz, OC*H*$_2$), 2.50 (3H, s, PyC*H*$_3$), 1.81 (2H, quin, J = 6.4 Hz, OCH$_2$C*H*$_2$), 1.50–1.21 (30H, m, C*H*$_2$), 0.83 (3H, t, J = 6.4 Hz, C*H*$_3$); ^{13}C NMR (100 MHz, $CDCl_3$): $\delta$ (ppm) 192.2 (CHO), 156.7, 149.7, 144.3, 121.7, 116.1, 31.7, 29.5–29.0 (m), 28.7, 25.7, 22.5, 19.2, 13.9; FT-IR (KBr; $cm^{-1}$): 2916, 2850 $\nu$(C–H), 1690 $\nu$(C=O), 1456 $\nu$(Py); Calcd for $C_{25}H_{43}NO_2$: C, 77.07, H, 11.12, N, 3.60. Found C, 77.12, H, 11.34, N, 3.46.

**6-methyl-5-(eicosyloxy)picolinaldehyde.** n-Eicosylbromide (2.63 g); yield 2.86 g (94 %). MS EI (rel. int.): $m/z$ 417.0 $[M]^+$ (21 %); ^{1}H NMR (400 MHz, $CDCl_3$): $\delta$ (ppm) 9.98 (1H, s, CHO), 7.85 (1H, d, J = 8.4 Hz, PyH[2]), 7.16 (1H, d, J = 8.4, PyH[3]), 4.07 (2H, t, J = 6.4 Hz, OC*H*$_2$), 2.57 (3H, s, PyC*H*$_3$), 1.87 (2H, quin, J = 6.4 Hz, OCH$_2$C*H*$_2$) 1.63–1.20 (34H, m, CH$_2$), 0.85 (3H, t, CH$_3$); ^{13}C NMR (100 MHz, $CDCl_3$): $\delta$ (ppm) 192.2 (CHO), 156.7, 149.7, 144.2, 121.8, 116.1, 68.4, 31.7, 29.5–29.0 (m), 28.7, 25.8, 22.5, 19.2, 13.9; FT-IR (KBr; $cm^{-1}$): 2918, 2850 $\nu$(C–H), 1691 $\nu$(C=O); Calcd for $C_{27}H_{47}NO_2$: C, 77.64, H, 11.34, N, 3.35. Found C, 77.52, H, 11.37, N, 3.19.

**Scheme 3.** Synthesis of *cis,cis*-1,3,5-triamincyclohexane



        *ix*                *x*
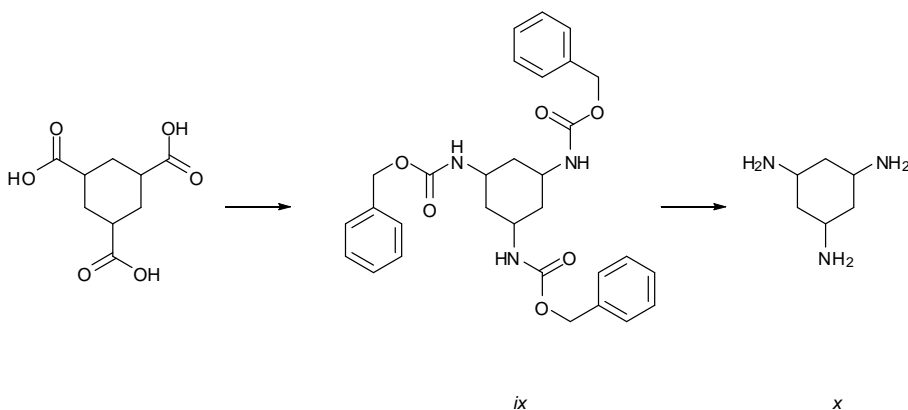
***cis,cis*-1,3,5-tris(*N*-(benzyl)carbamate)cyclohexane (*ix*).** *cis,cis*-1,3,5-Cyclo-hexanetricarboxylic acid (8.0 g, 37 mmol) was washed into a round-bottomed flask with benzene (300 mL) and Et$_3$N (15.6 mL, 112 mmol) was added followed by phosphoric acid diphenyl ester azide (30.85 g, 0.112 mol). The mixture was stirred for 0.5 h at room temperature and then refluxed for 0.5 h. Benzyl alcohol (13.34 g, 123.5 mmol) was added and the solution was refluxed for 18 h. After cooling to ambient temperature, the product was

collected by vacuum filtration, washed with minimal amount of cold benzene, and dried under vacuum to leave 6.0 g (30.5 %). MS EI: *m/z* 424.2 [M-$C_7H_7O$]$^+$ (3 %). Calcd. for $C_{30}H_{33}N_3O_6$: C, 67.77; H, 6.27; N, 7.91. Found: C, 67.72, H, 6.37, N, 7.77.

**cis,cis–1,3,5–cyclohexanetriamine (*tach*) (*x*).** To solution HBr/AcOH (33 %, 50ml) in a round-bottom flask was added with stirring *cis,cis*-1,3,5-tris(*N*-(benzyl)carbamate)cyclohexane (6.0 g, 11.3 mmol). Immediately after the addition of the reagent, carbon dioxide began to develop. The mixture was allowed to be stirred at room temperature for 1 h and 50 ml of dry ether was added to precipitate formed amine hydrobromide. The suspension was centrifuged, organic layer decanted and the rest was washed with ether (50ml) then centrifugation one more repeated. Obtained hydrobromide salt was washed with ethanol to remove colored impurities. Finally, triamine hydrobromide was dried *in vacuo*. Yield of *cis,cis*-1,3,5-cyclohexanetriamine·3HBr·0.5$H_2O$ (*tach*·3HBr·0.5$H_2O$) 4.10 g (95 %).

ESI MS (rel. int.): *m/z* 130.2 [M+H]$^+$ (6 %); $^1$H NMR (400 MHz, $D_2O$): δ (ppm) 3.47 (1H, m, N-C*H*), 2.43 (1H, d, J = 9.8 Hz, CH), 1.58 (1H, dq, J = 11.9 Hz, CH); $^{13}$C (100 MHz, $D_2O$): δ (ppm) 45.2, 32.3; FT-IR (KBr; cm$^{-1}$): 3400br ν(O–H), 3000br ν($N^{quart}$–H), 2965, 2890 ν(C–H); Calcd for $C_6H_{20}Br_3N_3O_{0.5}$: C 18.92, H 5.03, N 11.03. Found C, 19.20, H, 5.24, N, 10.98.
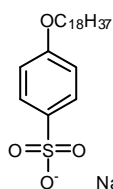
**$NaC_{18}TOS·H_2O$** (sodium 4-(octadecyloxy)benzenesulfonate). Sodium salt of *p*-phenolsulfonic acid (8.40 g, 42.8 mmol) and sodium hydroxide (1.71 g, 4.71 mmol) were dissolved under agitation in 20 ml of water. After a hot ethanol solution (*ca*. 30 ml) of n-octadecylbromide (11.7 g, 47.1 mmol) was added and the mixture was allowed to react under reflux for 17 h. Sodium hydroxide (1.8 g, 45.0 mmols) in 5 ml of water was added after termination of the reaction, and heating reflux was carried out for another 2 h. Then, the solvent was distilled off under reduced pressure, and water was added. The desired compound was obtained by filtration and drying *in vacuo*. FT-IR (KBr; cm$^{-1}$): 3400br ν(O–H), 2918, 2850 ν(C–H), 1185 ν(S–O); Calcd for $C_{24}H_{43}NaO_5S$: C, 61.77, H, 9.29, S, 6.87. Found C, 62.07, H, 9.39, S, 6.45.

*Synthesis of complexes*

**General procedure for the parent complexes.** A batch of an aldehyde and the calculated amount of iron(II) salt were dissolved in water, a stoichometric amount of a triamine was added which was immediately accompanied by intensive coloration. The

mixture was stirred for 15 min and then transferred into a fridge and left at 4°C over night. The crystalline precipitate was filtered off, washed with water and air dried. Recrystallization in a thermostat from boiling water provided crystalline material in quantitative yield with sufficiently good quality for the single-crystal X-ray analysis.

**1.** *tren* (0.1 g, 0.68 mmol), 6-methylpicolinaldehyde (0.25 g, 2.04 mmol), $Fe(ClO_4)_2 \cdot xH_2O$ (0.17 g, 0.68 mmol); Calcd for $C_{27}H_{33}Cl_2FeN_7O_8$: C, 45.65, H, 4.68, N, 13.80. Found C, 45.48, H, 4.67, N, 13.86.

**1-Zn.** *tren* (0.1 g, 0.68 mmol), 6-methylpicolinaldehyde (0.25 g, 2.04 mmol), $Zn(ClO_4)_2 \cdot 6H_2O$ (0.25 g, 0.68 mmol); Calcd for $C_{24}H_{24}Cl_2N_6O_8Zn$: C, 45.05, H, 4.62, N, 13.62. Found C, 44.78, H, 4.70, N, 13.65.

**2.** *tach* $\cdot$ 3HBr $\cdot$ 0.5H$_2$O (0.2 g, 0.52 mmol) was neutralized with 1.56 ml of 1*M* NaOH working in aqueous medium. Then the water mixture of 4*H*-imidazole-5-carbaldehyde (0.15 g, 1.56 mmol) and $Fe(BF_4)_2 \cdot 6H_2O$ (0.18 g, 0.52 mmol) was added. Calcd for $C_{18}H_{21}B_2F_8FeN_9$: C, 36.47, H, 3.57, N, 21.26. Found C, 36.46, H, 3.57, N, 21.36.

**2-ClO$_4$.** *tach* $\cdot$ 3HBr $\cdot$ 0.5H$_2$O (0.2 g, 0.52 mmol) was neutralized with 1.56 ml of 1*M* Na*OH* working in aqueous medium. Then the water mixture of 4*H*-imidazole-5-carbaldehyde (0.15 g, 1.56 mmol) and $Fe(ClO_4)_2 \cdot xH_2O$ (0.13 g, 0.52 mmol) was added. MS ESI (rel. int.): 518 $[M+ClO_4]^+$ (100 %), 418 $[M–H]^+$ (90 %), 210 $[M]^{++}$ (18 %). Calcd for $C_{18}H_{21}Cl_2FeN_9O_8$: C, 34.97, H, 3.42, N, 20.39. Found C, 34.90, H, 3.44, N, 20.25.

**3.** *tach* $\cdot$ 3HBr $\cdot$ 0.5H$_2$O (0.2 g, 0.52 mmol) was neutralized with 1.56 ml of 1*M* NaOH working in aqueous medium. Then the water mixture of picolinaldehyde (0.17 g, 1.56 mmol) and $Fe(ClO_4)_2 \cdot xH_2O$ (0.13 g, 0.52 mmol) was added. Calcd for $C_{24}H_{24}Cl_2FeN_6O_8$: C, 44.26, H, 3.71, N, 12.90. Found C, 43.99, H, 3.90, N, 12.80.

**4.** *tame* (0.1 g, 0.85 mmol), 4*H*-imidazole-5-carbaldehyde (0.24 g, 2.55 mmol), $Fe(ClO_4)_2 \cdot xH_2O$ (0.22 g, 0.85 mmol). Calcd for $C_{17}H_{22}Cl_2FeN_9O_{8.5}$: C, 33.19; H, 3.60; N, 20.49. Found C, 33.19, H, 3.48, N, 20.98.

**5.** *tame* (0.1 g, 0.85 mmol), picolinaldehyde (0.27 g, 2.55 mmol), $Fe(ClO_4)_2 \cdot xH_2O$ (0.22 g, 0.85 mmol); recrystallized from CH$_3$CN/Acetone. Calcd for $C_{23}H_{24}Cl_2FeN_6O_8$: C, 43.22, H, 3.78, N, 13.15. Found C, 43.58, H, 3.91, N, 13.52.

**6.** *tame* (0.1 g, 0.85 mmol), 6-methylpicolinaldehyde (0.31 g, 2.55 mmol), $Fe(ClO_4)_2 \cdot xH_2O$ (0.22 g, 0.85 mmol); recrystallized from CH$_3$CN/Acetone. Calcd for $C_{26}H_{30}Cl_2FeN_6O_8$: C, 45.84, H, 4.44, N, 12.34. Found C, 46.01, H, 4.13, N, 12.39.

**[Zn{*tren*(5-HO-*py*)$_3$}](NO$_3$)$_2$.** *tren* (0.198 g, 0.136 mmol), 5-hydroxy-picolinaldehyde (0.5 g, 0.406 mmol), $Zn(NO_3)_2 \cdot 6H_2O$ (0.403 g, 0.136 g) in ethanol;

recrystallized from methanol. ESI MS (rel. int.): $m/z$ 587 $[M+NO_3]^+$ (17 %), 524 $[M–H]^+$ (100 %) 264 $[M]^{++}$ (18 %). Calc for $C_{24}H_{27}N_9O_9Zn$: C, 44.28, H, 4.18, N, 19.37. Found C, 44.20, H, 4.28, N, 19.27.

**General procedure for alkoxy-substituted systems.** A batch of an alkylated aldehyde and stoichometric amount of a triamine were dissolved in ethanol, calculated amount of iron(II) salt was added which was immediately accompanied by intensification of coloration. The mixture was allowed to stir for 15 min and then subjected into a fridge at 4°C overnight. Formed crystalline precipitate was filtered off, washed with ethanol and dried *in vacuo*. Dehydrated compounds were obtained by heating the pristine compounds in an evacuated flask at 130 °C for 30 min or during the control experiment in the SQUID facility.

**C$_6$-7.** *tren* (0.05 g, 0.34 mmol), excess of crude 5-(hexyloxy)picolinaldehyde, Fe(ClO$_4$)$_2$·xH$_2$O (0.087 g, 0.34 mmol). Calcd for $C_{42}H_{63}Cl_2FeN_7O_{11}$: C, 52.07, H, 6.55, N, 10.12. Found C, 51.98, H, 6.53, N, 10.09.

**C$_{18}$-7.** *tren* (0.05 g, 0.34 mmol), 5-(octadecyloxy)picolinaldehyde (0.38 g, 1.02 mmol), Fe(ClO$_4$)$_2$·xH$_2$O (0.087 g, 0.34 mmol). Calcd for $C_{78}H_{135}Cl_2FeN_7O_{11}$: C, 63.57, H, 9.23, N, 6.65. Found C, 63.45, H, 8.82, N, 6.46.

**C$_{12}$-8.** *tren* (0.05 g, 0.34 mmol), 5-(dodecyloxy)picolinaldehyde (0.3 g, 1.02 mmol), Fe(BF$_4$)$_2$·6H$_2$O (0.11 g, 0.34 mmol); recrystallized from CHCl$_3$/EtOH at –40 °C over a period of two weeks. Calcd for $C_{60}H_{99}B_2F_8FeN_7O_3$: C, 60.26, H, 8.34, N, 8.20. Found C, 60.35, H, 8.76, N, 8.33.

**C$_{18}$-9.** *tren* (0.05 g, 0.34 mmol), 5-(octadecyloxy)picolinaldehyde (0.38 g, 1.02 mmol), Fe(BF$_4$)$_2$·6H$_2$O (0.11 g, 0.34 mmol); Calcd for $C_{78}H_{136}B_2F_8FeN_7O_{3.5}$: C, 64.28, H, 9.41, N, 6.73. Found C, 64.12, H, 9.52, N, 6.83.

**C$_{18}$-10.** *tren* (0.05 g, 0.34 mmol), 5-(octadecyloxy)picolinaldehyde (0.38 g, 1.02 mmol), FeSO$_4$·7H$_2$O in H$_2$O (0.095 g, 0.34 mmol); Calcd for $C_{78}H_{143}FeN_7O_{11}S$: C, 64.93; H, 9.99; N, 6.80; S, 2.22. Found C, 65.27, H, 9.53, N, 6.80, S, 2.32.

**C$_{18}$-11.** tren (0.05 g, 0.34 mmol), 5-(octadecyloxy)picolinaldehyde (0.38 g, 1.02 mmol), FeBr$_2$ (0.073 g, 0.34 mmol), TlF in EtOH/H$_2$O (0.15 g, 0.68 mmol). After mixing of components white precipitate of TlBr was filtered off, solution evaporated, the rest recrystallized from hot EtOH. Calcd for $C_{81}H_{148}F_2FeN_7O_{6.5}$: C, 68.09, H, 10.40, N, 7.13. Found C, 68.32, H, 10.42, N, 6.54.

**C$_{16}$-13.** tren (0.05 g, 0.34 mmol), 5-(hexadecyloxy)picolinaldehyde (0.35 g, 1.02 mmol), FeCl$_2$·4H$_2$O (0.07 g, 0.34 mmol). Calcd for $C_{72}H_{130}Cl_2FeN_7O_{6.5}$: C, 65.29, H, 9.89, N, 7.40. Found C, 65.63, H, 9.81, N, 7.31.

**C$_{18}$-13.** tren (0.05 g, 0.34 mmol), 5-(octadecyloxy)picolinaldehyde (0.38 g, 1.02 mmol), FeCl$_2$·4H$_2$O (0.07 g, 0.34 mmol). Calcd for C$_{78}$H$_{142}$Cl$_2$FeN$_7$O$_{6.5}$: C, 66.50, H, 10.16, N, 6.96. Found C, 66.74, H, 10.47, N, 6.69.

**C$_{20}$-13.** tren (0.05 g, 0.34 mmol), 5-(icosyloxy)picolinaldehyde (0.41 g, 1.02 mmol), FeCl$_2$·4H$_2$O (0.07 g, 0.34 mmol). Calcd for C$_{84}$H$_{154}$Cl$_2$FeN$_7$O$_{6.5}$: C, 67.58, H, 10.40, N, 6.57. Found C, 67.83, H, 10.12, N, 6.47.

**C$_{18}$-16.** *tren* (0.05 g, 0.34 mmol), 5-(octadecyloxy)picolinaldehyde (0.38 g, 1.02 mmol), FeBr$_2$ (0.073 g, 0.34 mmol); Calcd for C$_{78}$H$_{141}$Br$_2$FeN$_7$O$_6$: C, 62.55; H, 9.56, N, 6.55. Found C, 62.15; H, 9.33; N, 6.43.

**C$_{18}$-17.** In MeOH/CHCl$_3$ medium, *tren* (0.05 g, 0.34 mmol), 5-(octadecyloxy)picolinaldehyde (0.38 g, 1.02 mmol), Fe(ClO$_4$)$_2$·xH$_2$O (0.087 g, 0.34 mmol), KI (0.11 g, 0.68 mmol). Calcd for C$_{78}$H$_{135}$I$_2$N$_7$O$_3$: C, 61.29, H, 8.90, N, 6.41. Found C, 61.83, H, 8.84, N, 6.26.

**C$_{18}$-18.** *tren* (0.05 g, 0.34 mmol), 5-(octadecyloxy)picolinaldehyde (0.38 g, 1.02 mmol), Fe(BF$_4$)$_2$·6H$_2$O (0.11 g, 0.34 mmol), NaC$_{18}$TOS·H$_2$O in hot EtOH/H$_2$O (0.32 g, 0.68 mmol). Calcd for C$_{126}$H$_{219}$FeN$_7$O$_{12}$S$_2$: C, 70.58, H, 10.30, N, 4.57, S, 2.99. Found C, 70.39, H, 10.71, N, 4.41, S, 3.25.

**C$_6$-19.** *tren* (0.05 g, 0.34 mmol), excess of crude 6-methyl-5-(hexyloxy)picolinaldehyde, Fe(ClO$_4$)$_2$·xH$_2$O (0.087 g, 0.34 mmol). Calcd for C$_{45}$H$_{69}$Cl$_2$FeN$_7$O$_{11}$: C, 53.47; H, 6.88; N, 9.70. Found C, 53.72, H, 6.53, N, 9.82.

**C$_{12}$-19.** *tren* (0.05 g, 0.34 mmol), excess of crude 5-(dodecyloxy)picolinaldehyde, Fe(ClO$_4$)$_2$·xH$_2$O (0.087 g, 0.34 mmol). Calcd for C$_{45}$H$_{69}$Cl$_2$FeN$_7$O$_{11}$: C, 60.73, H, 8.57, N, 7.51. Found C, 59.79, H, 8.37, N, 7.74.

**C$_{18}$-19.** *tren* (0.05 g, 0.34 mmol), 6-methyl-5-(octadecyloxy)picolinaldehyde (0.40 g, 1.02 mmol), Fe(ClO$_4$)$_2$·xH$_2$O (0.087 g, 0.34 mmol). Calcd for C$_{78}$H$_{135}$Cl$_2$FeN$_7$O$_{11}$: C, 63.57, H, 9.23, N, 6.65. Found C, 63.73, H, 9.27, N, 6.66.

**C$_{18}$-20.** *tren* (0.05 g, 0.34 mmol), 6-methyl-5-(octadecyloxy)picolinaldehyde (0.40 g, 1.02 mmol), Fe(BF$_4$)$_2$·6H$_2$O (0.11 g, 0.34 mmol. Calcd for C$_{81}$H$_{141}$B$_2$F$_8$FeN$_7$O$_3$: C, 65.27, H, 9.54, N, 6.58. Found C, 64.68, H, 9.27, N, 6.75.

**C$_{20}$-21.** *tren* (0.05 g, 0.34 mmol), 6-methyl-5-(icosyloxy)picolinaldehyde (0.43 g, 1.02 mmol), FeCl$_2$·4H$_2$O (0.07 g, 0.34 mmol), [NBu$_4$][PF$_6$] (0.26 g, 0.68 mmol). Calcd for C$_{87}$H$_{153}$F$_{12}$FeN$_7$O$_3$P$_2$: C, 61.79, H, 9.12, N, 5.80. Found C 61.48, H, 9.05, N, 5.78.

**C$_{18}$-22.** *tren* (0.05 g, 0.34 mmol), 6-methyl-5-(octadecyloxy)picolinaldehyde (0.40 g, 1.02 mmol), FeSiF$_6$·6H$_2$O (0.11 g, 0.34 mmol). Calcd for C$_{81}$H$_{141}$F$_6$FeN$_7$O$_3$Si: C, 66.68, H, 9.74, N, 6.72. Found C, 66.70, H, 9.31, N, 6.21.

**C$_{20}$-23.** *tren* (0.05 g, 0.34 mmol), 6-methyl-5-(icosyloxy)picolinaldehyde (0.43 g, 1.02 mmol), FeSO$_4$·7H$_2$O in H$_2$O (0.095 g, 0.34 mmol). Calcd for C$_{87}$H$_{159}$FeN$_7$O$_{10}$S: C, 67.37, H, 10.33, N, 6.32, S, 2.07. Found C, 67.41, H, 10.33, N, 6.60, S, 2.05.

**C$_{18}$-24.** *tach*·3HBr·0.5H$_2$O (0.1 g, 0.26 mmol) was neutralized with MeONa (0.042 g, 0.78 mmol), 5-(octadecyloxy)picolinaldehyde (0.29 g, 0.78 mmol), FeCl$_2$·4H$_2$O (0.052 g, 0.26 mmol), NaC$_{18}$TOS·H$_2$O in hot EtOH/H$_2$O (0.24 g, 0.52 mmol). Calcd for C$_{126}$H$_{218}$FeN$_6$O$_{13}$S$_2$: C, 70.55, H, 10.24, N, 3.92, S, 2.99. Found C, 70.70, H, 9.76, N, 3.45, S, 3.51.

**C$_{18}$-25.** *tame* (0.025 g, 0.215 mmol), 5-(octadecyloxy)picolinaldehyde (0.24 g, 0.645 mmol), FeCl$_2$·4H$_2$O (0.042 g, 0.215 mmol), NaC$_{18}$TOS·H$_2$O in hot EtOH/H$_2$O (0.2 g, 0.43 mmol); Calcd for C$_{125}$H$_{216}$FeN$_6$O$_{12}$S$_2$: C, 70.98, H, 10.29, N, 3.97, S, 3.03. Found C, 70.86, H, 9.70, N, 4.22, S, 2.61.

**C$_6$-26.** *tame* (0.05 g, 0.43 mmol), excess of crude 6-methyl-5-(hexyloxy)picolinaldehyde, Fe(ClO$_4$)$_2$·xH$_2$O (0.11 g, 0.43 mmol). Calcd for C$_{44}$H$_{66}$Cl$_2$FeN$_6$O$_{11}$: C, 53.83, H, 6.78, N, 8.56. Found C, 53.45, H, 6.75, N, 8.50.

**C$_{18}$-26.** *tame* (0.025 g, 0.215 mmol), 6-methyl-5-(octadecyloxy)picolinaldehyde (0.25 g, 0.645 mmol), Fe(ClO$_4$)$_2$·xH$_2$O (0.055 g, 0.215 mmol. Calcd for C$_{80}$H$_{138}$Cl$_2$FeN$_6$O$_{11}$: C, 64.63, H, 9.36, N, 5.65. Found C, 64.27, H, 8.89, N, 5.59.

**C$_{10}$-27**. *tame* (0.05 g, 0.43 mmol), excess of crude 6-methyl-5-(decyloxy)picolinaldehyde, Fe(BF$_4$)$_2$·6H$_2$O (0.145 g, 0.43 mmol). Calcd for C$_{56}$H$_{90}$B$_2$F$_8$FeN$_6$O$_3$: C, 59.80, H, 8.06, N, 7.47. Found C, 59.78, H, 7.73, N, 7.41.

**C$_{12}$-27.** *tame* (0.05 g, 0.43 mmol), excess of crude 6-methyl-5-(dodecyloxy)picolinaldehyde, Fe(BF$_4$)$_2$·6H$_2$O (0.145 g, 0.43 mmol. Calcd for C$_{62}$H$_{102}$B$_2$F$_8$FeN$_6$O$_3$: C, 61.60, H, 8.50, N, 6.95. Found C, 60.60, H, 8.49, N, 6.84.

**C$_{14}$-27**. *tame* (0.025 g, 0.215 mmol), 6-methyl-5-(tetradecyloxy)picolinaldehyde (0.21 g, 0.645 mmol), Fe(BF$_4$)$_2$·6H$_2$O (0.078 g, 0.215 mmol). Calcd for C$_{68}$H$_{114}$B$_2$F$_8$FeN$_6$O$_3$: C, 63.16, H, 8.89, N, 6.50. Found: C, 63.76, H, 8.62, N, 6.50.

**C$_{16}$-27**. *tame* (0.025 g, 0.215 mmol), 6-methyl-5-(hexadecyloxy)picolinaldehyde (0.23 g, 0.645 mmol), Fe(BF$_4$)$_2$·6H$_2$O (0.078 g, 0.215 mmol). Calcd for C$_{74}$H$_{126}$B$_2$F$_8$FeN$_6$O$_3$: C, 64.53, H, 9.22, N, 6.10. Found C, 64.34, H, 9.01, N, 6.11.

**C$_{17}$-27**. *tame* (0.025 g, 0.215 mmol), 6-methyl-5-(heptadecyloxy)picolinaldehyde (0.24 g, 0.645 mmol), Fe(BF$_4$)$_2$·6H$_2$O (0.078 g, 0.215 mmol). Calcd for C$_{77}$H$_{132}$B$_2$F$_8$FeN$_6$O$_3$: C, 65.16, H, 9.37, N, 5.92. Found C, 65.25, H, 9.44, N, 5.85.

**C$_{18}$-27**. *tame* (0.025 g, 0.215 mmol), 6-methyl-5-(octadecyloxy)picolinaldehyde (0.25 g, 0.645 mmol), Fe(BF$_4$)$_2$·6H$_2$O (0.078 g, 0.215 mmol). Calcd for C$_{80}$H$_{138}$B$_2$F$_8$FeN$_6$O$_3$: Calcd for C$_{80}$H$_{138}$B$_2$F$_8$FeN$_6$O$_3$: C, 65.75, H, 9.52, N, 5.75. Found: C, 65.03, H, 9.30, N, 5.85.

**C$_{20}$-28.** *tame* (0.025 g, 0.215 mmol), 6-methyl-5-(icosyloxy)picolinaldehyde (0.26 g, 0.645 mmol), Fe(BF$_4$)$_2$·6H$_2$O (0.078 g, 0.215 mmol);   Calcd for C$_{86}$H$_{152}$B$_2$F$_8$FeN$_6$O$_4$: C, 66.06, H, 9.80, N, 5.37. Found C, 66.60, H, 9.56, N, 5.75.

**C$_{18}$-29.** *tame* (0.025 g, 0.215 mmol), 6-methyl-5-(octadecyloxy)picolinaldehyde (0.25 g, 0.645 mmol), FeCl$_2$·4H$_2$O (0.042 g, 0.215 mmol), NaC$_{18}$TOS·H$_2$O in hot EtOH/H$_2$O (0.2 g, 0.43 mmol); Calcd for C$_{128}$H$_{224}$FeN$_6$O$_{13}$S$_2$: C, 70.68, H, 10.38, N, 3.86, S, 2.95. Found C, 70.73; H, 9.84; N, 4.01; S, 3.20.


### 6.7.3   Preparation of the one-dimensional systems


**General procedure for iron(II) and zinc(II) salts.** Iron or zinc powder was dissolved, with heating, in a stoichiometric amount of aqueous solution of the corresponding acid. By cooling a crystalline precipitate was formed. It was filtered off and air dried, providing the analytically pure iron or zinc salt in a quantitative yield.

**Fe(CF$_3$SO$_3$)$_2$·6H$_2$O.** Calcd for C$_2$H$_{12}$F$_6$FeO$_{12}$S$_2$: C, 5.20, H 2.62, S, 13.88. Found C, 5.25, H, 2.60, S, 13.89.

**Fe(p-tol)$_2$·6H$_2$O.** (*p*-tol = tosylate, 4-CH$_3$-(C$_6$H$_4$)SO$_3^-$) Calcd for C$_{14}$H$_{26}$FeO$_{12}$S$_2$: C, 33.21, H, 5.18, S, 12.67. Found C, 33.34, H, 4.89, S, 12.95.

**Zn(p-tol)$_2$·6H$_2$O.** Calcd for C$_{14}$H$_{26}$O$_{12}$S$_2$Zn: C, 32.59, H, 5.08, S, 12.43. Found C, 32.51, H, 4.93, S, 12.61.

**Cu(CF$_3$SO$_3$)$_2$·6H$_2$O.** Copper (II) hydroxyde obtained by precipitation of copper(II) sulfate and sodium hydroxide, was dissolved in a hot aqueous solution of trifluorosulfonic acid. By cooling, blue crystals were formed. They were filtered off and air dried, providing analytically pure salt in a quantitative yield. Calcd for C$_2$H$_{12}$CuF$_6$O$_{12}$S$_2$: C, 5.11, H, 2.57, S, 13.65. Found C, 5.07, H, 2.67, S, 13.92.

**Scheme 3.** Synthesis of *N*-4*H*-1,2,4-triazol-4-ylbenzamides (*tba*).
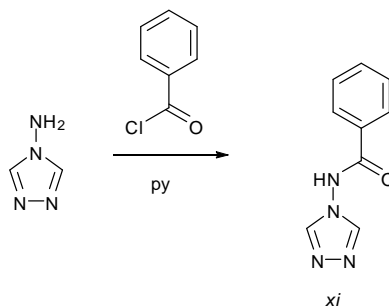


***N*-4*H*-1,2,4-triazole-4-ylbenzamide (*tba*) (*xi*).** A suspension of 4-amino-4*H*-1,2,4-triazole (4.2 g, 50 mmol) and benzoyl chloride (7.0 g, 50 mmol) in dry pyridine (100 ml) was refluxed for 24 h, the solvents were removed *in vacuo* to provide a cream-colored solid which was dissolved in hot water (100 ml), neutralized with sodium bicarbonate until no further effervescence was observed. On cooling, a white precipitate was obtained which was filtered and washed with water and finally re-crystallized from ethanol to give 6.48 g of *tba* (Yield: 69 %).

MS EI: 188.2 [M]$^+$ (2 %), 105.0 [M–trzNH]$^+$ (100 %); $^1$H NMR (400 MHz, DMSO-d$^6$): δ (ppm) 12.1 (1H, br s, N*H*), 8.73 (2H, s, CH of trz), 7.89 (2H, dd, J = 1.36, 7.20 Hz, ph*H*), 7.61 (1H, tt, J = 1.36, 7.20 Hz, ph*H*), 7.52 (2H, t, J = 7.2Hz, ph*H*); FT-IR (KBr; cm$^{-1}$): 3113 ν(CH of trz), 2000-1750 ν(ph), 1674 ν(C=O); Calcd for C$_9$H$_8$N$_4$O: C, 57.44, H, 4.28, N, 29.77. Found C, 57.41, H, 4.24, N, 29.81.

**Scheme 4.** Synthesis of 3,5-dialkoxy-*N*-4*H*-1,2,4-triazol-4-ylbenzamides (C$_n$-*tba*).
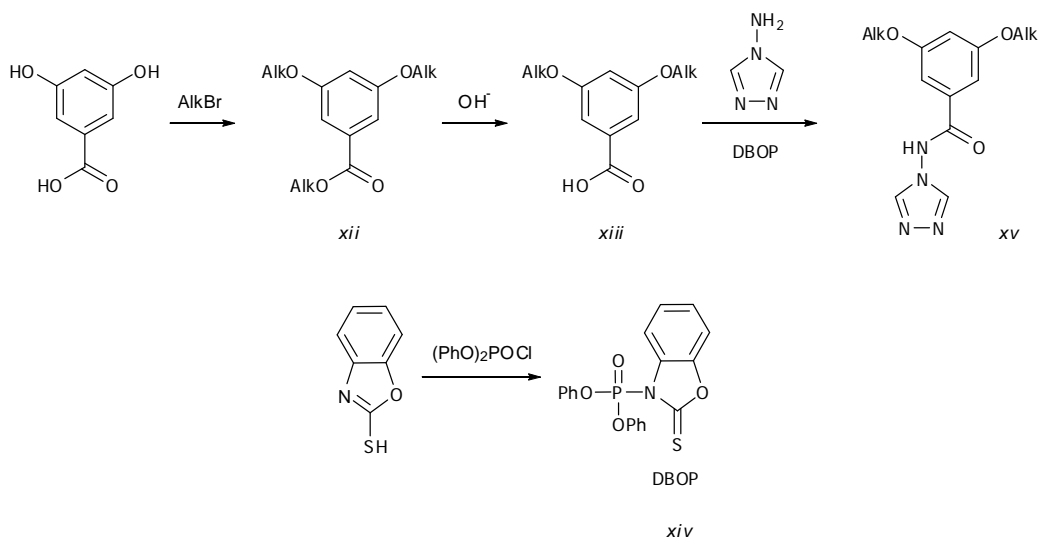
**General procedure for 3,5-dialkoxybenzoic acid (*xiii*).** Potassium 3,5-dihydroxobenzoate (5.46 g, 28.4 mmol), n-alkylbromide (85.2 mmol), anhydrous $K_2CO_3$ (7.88 g, 56.8 mmol), tetrabutylammonium bromide (0.3 g, 0.3 mmol) and pinch of $TiO_2$ as a catalyst were mixed in a flask and heated for 2 h with stirring at 120 °C in a solventless condition. After cooling the product was extracted with $CHCl_3$, filtered and the solvent distilled off under reduced pressure which provided crude alkyl-3,5-bis(alkoxy)benzoate (*xii*). The resulting compound was suspended in a solution of KOH (4 g, 71.4 mmol) in ethanol/water solution (19:1, 100 ml) and heated under reflux for 1 h. The reaction mixture was cooled to room temperature and brought to pH = 5 with 10 % *v/v* formic acid. The 3,5-dialkoxybenzoic acid precipitated upon further cooling was filtered and then recrystallized from hot ethanol before being dried in air to yield a white crystalline solid.
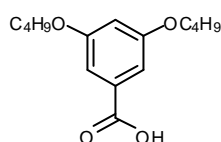
**3,5-dibutyloxybenzoic acid**. n-Butylbromide (11.70 g); yield 3.25 g (43 %); MS EI (rel. int.): *m/z* 266.2 [M]$^+$ (57 %); $^1$H NMR (400 MHz, $CDCl_3$): δ (ppm) 7.07 (2H, d, J = 2.4 Hz, phH), 6.77 (t, 1H, J = 2.4 Hz, phH), 4.02 (4H, t, J = 7.0 Hz, OC*H$_2$*), 1.71 (4H, m, OCH$_2$C*H$_2$*), 1.45 (4H, m, CH$_2$), 0.94 (6H, t, J = 7.0 Hz, CH$_3$); Calcd for $C_{15}H_{22}O_4$: C, 67.64, H, 8.33; Found C, 67.39, H, 8.31.
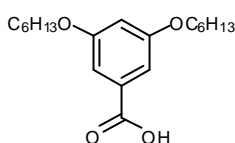
**3,5-dihexyloxybenzoic acid**. n-hexylbromide (14.00 g); yield 4.39 g (48 %); MS EI (rel. int.): *m/z* 322.1 [M]$^+$ (36 %); $^1$H NMR (400 MHz, $CDCl_3$): δ 7.14 (2H, d, J = 2.1 Hz, phH), 6.63 (1H, t, J = 2.1 Hz, phH), 3.91 (4H, t, J = 6.8 Hz, OC*H$_2$*), 1.72 (4H, m, OCH$_2$C*H$_2$*), 1.30 (12H, m, CH$_2$), 0.85 (6H, t, J = 6.8 Hz, CH$_3$); Calcd for $C_{19}H_{30}O_4$: C, 70.77, H, 9.38. Found C, 70.84, H, 9.39.
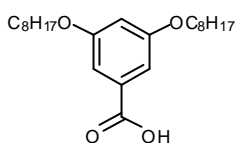
**3,5-dioctyloxybenzoic acid**. n-octylbromide (16.50 g); yield 6.23 g (58 %); MS EI (rel. int.): *m/z* 378.2 [M]$^+$ (65 %); $^1$H NMR (400 MHz, $CDCl_3$): δ (ppm) 7.25 (2H, d, J = 2.3 Hz, phH), 6.71 (1H, d, J = 2.3 Hz, phH), 4.00 (4H, t, J = 7.0 Hz, OC*H$_2$*), 1.81 (4H, quin, J = 7.0 Hz, OCH$_2$C*H$_2$*), 1.48-1.35 (20H, m, CH$_2$), 0.92 (6H, t, J = 7.0 Hz, CH$_3$); Calcd for $C_{23}H_{38}O_4$: C, 72.98, H, 10.12. Found C, 72.85, H, 10.21.
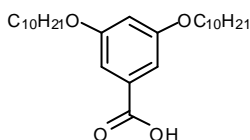
**3,5-dodecyloxybenzoic acid**. n-decylbromide (18.84 g); yield 6.54 g (53 %); MS EI (rel. int.): *m/z* 434.3 [M]$^+$ (100 %); $^1$H NMR (400 MHz, $CDCl_3$): δ (ppm) 7.24 (2H, d, J = 2.3 Hz, phH), 6.70 (1H, d, J = 2.3 Hz, phH), 4.00 (4H, t, J = 7.0 Hz, OC*H$_2$*), 1.82 (4H, quin, J = 7.0 Hz, OCH$_2$C*H$_2$*), 1.49-1.35 (28H, m, CH$_2$), 0.90 (6H, t, J = 7.0 Hz, CH$_3$); Calcd for $C_{27}H_{46}O_4$: C, 74.61, H, 10.67. Found C, 74.51, H, 10.63.
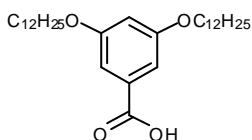
**3,5-didodecyloxybenzoic acid.** n-dodecylbromide (21.23 g); yield 9.47 g (68 %); MS EI (rel. int.): $m/z$ 490.2 [M]$^+$ (100 %); $^1$H NMR (400 MHz, CDCl$_3$): δ (ppm) 7.23 (2H, d, J = 2.3 Hz, ph*H*), 6.71 (1H, d, J = 2.3 Hz, ph*H*), 3.98 (4H, t, J = 7.0 Hz, OC*H*$_2$), 1.81 (4H, quin, J = 7.0 Hz, OCH$_2$C*H*$_2$), 1.49-1.35 ( 36H, m, CH$_2$), 0.90 (6H, t, J = 7.0 Hz, CH$_3$); Calcd for C$_{31}$H$_{54}$O$_4$: C, 75.87, H, 11.09. Found C, 75.89, H, 11.01.
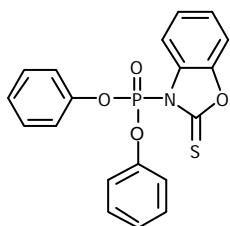
**Diphenyl(2,3-dihydro-2-thioxo-3-benzoxazoleyl)phosphate** (*xiv*). To a solution of 2-mercaptobenzoxazlole (4.53 g, 30 mmol) and triethylamine (4.2 ml, 30 mmol) in benzene (35 ml) was added dropwise at room temperature with stirring a solution of diphenyl phosphochloridate (6.2 ml, 30 mmol) in benzene (10 ml). The addition was completed in 30 min, and stirring was continued at room temperature for an additional 1.5 h. Triethylamine hydrochloride was removed by filtration and the solvent was distilled off *in vacuo*. The sirup-like residue was dissolved with stirring in boiling n-hexane, turbid solution decanted and subjected into fridge overnight. The procedure was repeated several times to provide colourless or slightly violet block crystals. Yield 5.9 g (52 %).

MS EI (rel. int.): $m/z$ 383.0 [M]$^+$ (100 %); $^1$H NMR (400 MHz, CDCl$_3$): δ (ppm) 7.41–7.23 (m); $^{13}$C (CDCl$_3$, 100 MHz): δ (ppm) 180.1 (C=S), 148.3, 147.4, 131.8, 131.7, 125.9, 125.3, 123.9, 114.6, 109.9; FT-IR (KBr; cm$^{-1}$): 1284 ν(P=O), 1178, 979 ν(C–O–P); Calcd for C$_{19}$H$_{14}$NO$_4$PS: C, 59.53, H, 3.68, N, 3.65, S, 8.36. Found C, 59.40, H, 3.16, N, 3.74, S, 8.39.

**General procedure for 3,5-dialkoxy-*N*-4*H*-1,2,4-triazol-4-ylbenzamide (C$_n$-*tba*)** (*xv*). Two equivalents of 4-amino-1,2,4-triazole (1 g, 11.89 mmol) was added at room temperature to a THF solution of a mixture of corresponding dialkobenzoic acids (15.45 mmol), triethylamine (1.56 g, 15.45 mmol) and diphenyl-(2,3-dihydro-2-thioxo-3-benzoxazoleyl)phosphate (5.13 g, 15.45 mmol). The mixture was refluxed for 30 min and allowed to cool at room temperature and then resulting solution was evaporated to dryness. The residue was subjected to column chromatography using CHCl$_3$/MeOH (gradient from 100/0 to 97/3) as eluent. The second fraction was collected and evaporated to dryness to give 3,5-dialkoxy-*N*-4*H*-1,2,4-triazol-4-ylbenzamide as white waxy solid that was then recrystallized from methanol.
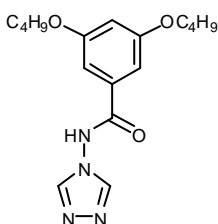
**3,5-dibutyloxy-*N*-4*H*-1,2,4-triazol-4-ylbenzamide.** 3,5-di(butyloxy)benzoic acid (4.11 g); yield 2.84 g (72 %). MS EI (rel. int.): $m/z$ 332.1 [M]$^+$ (48 %); $^1$H NMR (400 MHz, DMSO-d$^6$): δ (ppm) 12.0 (1H,

br, NH), 8.76 (2H, s, TrzH), 7.07 (2H, d, J = 2.4 Hz, phH), 6.77 (t, 1H, J = 2.4 Hz, phH), 4.02 (4H, t, J = 7.0 Hz, OC$H_2$), 1.71-1.45 (8H, m, CH$_2$), 0.94 (6H, t, J = 7.0 Hz, CH$_3$); FT-IR (KBr; cm$^{-1}$): 3115 $\nu$(C–H$_{trz}$), 2956, 2934, 2871 $\nu$(C–H), 1673 $\nu$(C=O); Calcd for C$_{17}$H$_{24}$N$_4$O$_3$: C, 61.43, H, 7.28, N, 16.86. Found C, 61.31, H 7.24, N 16.73.
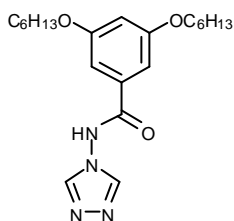
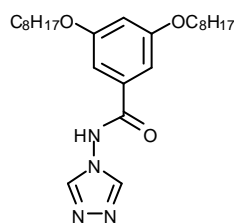**3,5-dihexyloxy-*N*-4*H*-1,2,4-triazol-4-ylbenzamide.** 3,5-di(hexyloxy)benzoic acid (4.98 g); yield 3.14 g (68 %). MS EI (rel. int.): *m/z* 388.0 [M]$^+$ (84 %); $^1$H NMR (400 MHz, CDCl$_3$): δ (ppm) 12.1 (1H, br, NH), 8.17 (2H, s, TrzH), 7.14 (2H, d, J = 2.1 Hz, phH), 6.63 (1H, t, J = 2.1 Hz, phH), 3.91 (4H, t, J = 6.8 Hz, OCH$_2$), 1.72 (4H, quin, J = 6.8 Hz, OCH$_2$C$H_2$), 1.30 (12H, m, CH$_2$), 0.85 (6H, t, J = 6.8 Hz, CH$_3$); FT-IR (KBr; cm$^{-1}$): 3117 $\nu$(C–H$_{trz}$), 2935, 2858 $\nu$(C–H), 1686 $\nu$(C=O); Calcd for C$_{21}$H$_{32}$N$_4$O$_3$: C 64.92, H 8.30, N 14.42. Found C, 64.76, H, 8.52, N, 14.10.

**3,5-dioclyloxy-*N*-4*H*-1,2,4-triazol-4-ylbenzamide.** 3,5-di(octyloxy)benzoic acid (5.87 g); yield 3.70 g (70 %). MS EI (rel. int.): *m/z* 444.3 [M]$^+$ (53 %); $^1$H NMR (400 MHz, CDCl$_3$): δ (ppm) 8.20 (2H, s, TrzH), 7.17 (2H, d, J = 2.0 Hz, phH), 6.63 (1H, t, J = 2.0 Hz, phH), 3.98 (4H, t, J = 7.0 Hz, OC$H_2$), 1.77 (4H, quin, J = 7.0 Hz, OCH$_2$C$H_2$), 1.48-1.36 (20H, m, CH$_2$), 0.88 (6H, t, J = 7.0 Hz, CH$_3$); FT-IR (KBr; cm$^{-1}$): 3116 $\nu$(C–H$_{trz}$), 2923, 2853 $\nu$(C–H), 1671 $\nu$(C=O); Calcd for C$_{25}$H$_{40}$N$_4$O$_3$: C, 67.53, H, 9.07, N, 12.60. Found C, 67.51, H, 9.16, N, 12.55.
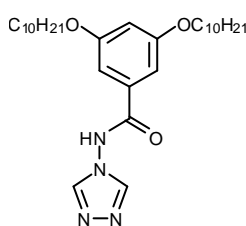
**3,5-didecyloxy-*N*-4*H*-1,2,4-triazol-4-ylbenzamide.** 3,5-di(decyloxy)benzoic acid (6.71 g); yield 4.22 g (71 %). MS EI (rel. int.): *m/z* 500.3 [M]$^+$ (26 %); $^1$H NMR (400 MHz, CDCl$_3$): δ (ppm) 8.20 (2H, s, TrzH), 7.11 (2H, d, J = 2.0 Hz, phH), 6.69 (1H, t, J = 2.0 Hz, phH), 3.98 (4H, t, J = 7.0 Hz, OC$H_2$), 1.77 (4H, quin, J = 7.0 Hz, OCH$_2$C$H_2$), 1.48-1.32 (28H, m, CH$_2$), 0.89 (6H, t, J = 7.0 Hz, CH$_3$); FT-IR (KBr; cm$^{-1}$): 3116 $\nu$(C–H$_{trz}$), 2921, 2851 $\nu$(C–H), 1671 $\nu$(C=O); Calcd for C$_{29}$H$_{48}$N$_4$O$_3$: C, 69.56, H, 9.66, N, 11.19. Found C, 69.43, H, 9.45, N, 11.21.
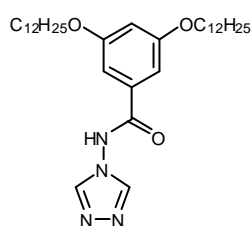
**3,5-didodecyloxy-*N*-4*H*-1,2,4-triazol-4-ylbenzamide.** 3,5-di(dodecyloxy)benzoic acid (7.58 g); yield 5.30 g (80 %). MS EI (rel. int.): *m/z* 556.4 [M]$^+$ (16 %); $^1$H NMR (400 MHz, CDCl$_3$): δ (ppm) 8.23 (2H, s, TrzH), 7.17 (2H, d, J = 2.0 Hz, phH), 6.69 (1H, t, J = 2.0 Hz, phH), 3.98 (4H, t, J = 7.0 Hz, OC$H_2$), 1.77 (4H, quin, J = 7.0 Hz, OCH$_2$C$H_2$), 1.48-1.35 (36H, m, CH$_2$), 0.88 (6H, t, J = 7.0 Hz, CH$_3$); FT-IR (KBr; cm$^{-1}$): 3115

ν(C–H$_{trz}$), 2921, 1851 ν(C–H), 1670 ν(C=O); Calcd for C$_{33}$H$_{56}$N$_4$O$_3$: C, 71.18, H, 10.14, N, 10.06. Found C, 71.19, H, 10.02, N, 10.05.

### *Synthesis of complexes*

**General procedure.** To a hot methanolic solution of 3,5-dialkoxy-*N*-4*H*-1,2,4-triazol-4-ylbenzamide or *N*-4*H*-1,2,4-triazol-4-ylbenzamide was added a methanolic solution of the MA$_2$·6H$_2$O (M = Cu, Zn or Fe; A = *p*-tol$^-$, CF$_3$SO$_3$$^-$, BF$_4$$^-$). The mixture was refluxed for 5 min, then concentrated by evaporating and allowed to cool to room temperature. The precipitate of a complex was filtered off and dried in air. Dehydrated compounds were obtained by heating the pristine compounds in an evacuated flask at 130 °C (400 K) for 30 min or during the control experiment in the SQUID facility.

**30.** *tba* (0.122 g, 0.648 mmol), Fe(CF$_3$SO$_3$)$_2$·6H$_2$O (0.1 g, 0.216 mmol); Calcd for C$_{29}$H$_{28}$F$_6$FeN$_{12}$O$_{11}$S$_2$: C, 36.49, H, 2.96, N, 17.61, S, 6.72. Found C, 36.10, H, 2.93, N, 17.21, S, 6.95.

**30**-**Cu.** *tba* (0.120 g, 0.648 mmol), Cu(CF$_3$SO$_3$)$_2$·6H$_2$O (0.1 g, 0.213 mmol); Calcd for C$_{29}$H$_{32}$CuF$_6$N$_{12}$O$_{13}$S$_2$: C 34.89, H 3.23, N 16.84, S 6.42. Found C, 35.03, H, 3.11, N, 16.55, S, 6.24.

**32.** *tba* (0.167 g, 0.888 mmol), Fe(BF$_4$)$_2$·6H$_2$O (0.1 g, 0.296 mmol); Calcd for C$_{27}$H$_{30}$B$_2$F$_8$FeN$_{12}$O$_6$: C, 38.24, H, 3.57, N, 19.82. Found C 38.02, H, 3.56, N, 19.87.

**34.** *tba* (0.113 g, 0.6 mmol), Fe(*p*-tol)$_2$·6H$_2$O (0.1 g, 0.2 mmol); Calcd for C$_{41}$H$_{44}$FeN$_{12}$O$_{12}$S$_2$: C, 48.43, H, 4.36, N, 16.53, S, 6.31. Found C, 47.61, H, 4.50, N, 16.20, S 6.65.

**C$_4$-36.** C$_4$-*tba* (0.215 g, 0.648 mmol), Fe(CF$_3$SO$_3$)$_2$·6H$_2$O (0.1 g, 0.216 mmol); Calcd for C$_{53}$H$_{73}$F$_6$FeN$_{12}$O$_{15.5}$S$_2$: C, 46.80, H, 5.41, N, 12.36, S, 4.71. Found C, 46.53, H, 5.22, N, 12.03, S, 4.39.

**C$_6$-36.** C$_6$-*tba* (0.251 g, 0.648 mmol), Fe(CF$_3$SO$_3$)$_2$·6H$_2$O (0.1 g, 0.216 mmol); Calcd for C$_{65}$H$_{97}$F$_6$FeN$_{12}$O$_{15.5}$S$_2$: C, 51.08, H, 6.40, N, 11.00, S, 4.20. Found C, 51.02, H, 6.84, N, 10.59, S, 4.30.

**C$_8$-36.** C$_8$-*tba* (0.288 g, 0.648 mmol), Fe(CF$_3$SO$_3$)$_2$·6H$_2$O (0.1 g, 0.216 mmol); Calcd for C$_{77}$H$_{121}$F$_6$FeN$_{12}$O$_{15.5}$S$_2$: C, 54.50, H, 7.19, N, 9.91, S, 3.78. Found C, 54.63, H, 7.18, N, 9.80, S, 3.62.

**C$_{10}$-36.** C$_{10}$-*tba* (0.324 g, 0.648 mmol), Fe(CF$_3$SO$_3$)$_2$·6H$_2$O (0.1 g, 0.216 mmol); Calcd for C$_{89}$H$_{145}$F$_6$FeN$_{12}$O$_{15.5}$S$_2$: C, 57.31, H, 7.84, N, 9.01, S, 3.44. Found C, 57.36, H, 8.19, N, 9.12, S, 3.12.

**C$_{12}$-36.** C$_{12}$-*tba* (0.36 g, 0.648 mmol), Fe(CF$_3$SO$_3$)$_2$·6H$_2$O (0.1 g, 0.216 mmol); Calcd for C$_{101}$H$_{169}$F$_6$FeN$_{12}$O$_{15.5}$S$_2$: C, 59.66, H, 8.38, N, 8.27, S, 3.15. Found C, 59.96, H, 8.54, N, 8.28, S, 3.27.

**C$_4$-38.** C$_4$-*tba* (0.295 g, 0.888 mmol), Fe(BF$_4$)$_2$·6H$_2$O (0.1 g, 0.296 mmol); Calcd for C$_{51}$H$_{74}$B$_2$F$_8$FeN$_{12}$O$_{10}$: C, 49.21, H, 5.99, N, 13.50. Found C, 49.20, H, 6.29, N, 13.20.

**C$_6$-38.** C$_6$-*tba* (0.344 g, 0.888 mmol), Fe(BF$_4$)$_2$·6H$_2$O (0.1 g, 0.296 mmol); Calcd for C$_{63}$H$_{98}$B$_2$F$_8$FeN$_{12}$O$_{10}$: C, 53.55, H, 6.99, N, 11.90. Found C, 53.18, H, 6.81, N, 11.66.

**C$_8$-38.** C$_8$-*tba* (0.395 g, 0.888 mmol), Fe(BF$_4$)$_2$·6H$_2$O (0.1 g, 0.296 mmol); Calcd for C$_{75}$H$_{122}$B$_2$F$_8$FeN$_{12}$O$_{10}$: C, 56.97, H, 7.78, N, 10.63. Found C, 56.50, H, 7.42, N, 10.51.

**C$_{10}$-38.** C$_{10}$-*tba* (0.444 g, 0.888 mmol), Fe(BF$_4$)$_2$·6H$_2$O (0.1 g, 0.296 mmol); Calcd for C$_{87}$H$_{146}$B$_2$F$_8$FeN$_{12}$O$_{10}$: C, 59.72, H, 8.41, N, 9.61. Found C, 59.89, H, 8.37, N, 9.37.

**C$_{12}$-38.** C$_{12}$-*tba* (0.494 g, 0.888 mmol), Fe(BF$_4$)$_2$·6H$_2$O (0.1 g, 0.296 mmol); Calcd for C$_{99}$H$_{170}$B$_2$F$_8$FeN$_{12}$O$_{10}$: C, 62.00, H, 8.93, N, 8.76. Found C, 61.87, H, 8.68, N, 8.47.

**C$_4$-40.** C$_4$-*tba* (0.222 g, 0.6 mmol), Fe(*p*-tol)$_2$·6H$_2$O (0.1 g, 0.2 mmol); Calcd for : C, 55.23, H, 6.28, N, 11.89, S, 4.54; Found C, 55.42, H, 6.06, N, 12.32, S, 4.23.

**C$_6$-40.** C$_6$-*tba* (0.259 g, 0.6 mmol), Fe(*p*-tol)$_2$·6H$_2$O (0.1 g, 0.2 mmol); Calcd for C$_{77}$H$_{112}$FeN$_{12}$O$_{16}$S$_2$: C, 58.47, H, 7.14, N, 10.63, S, 4.05. Found C, 58.51, H, 7.19, N, 10.16, S, 4.09.

**C$_8$-40.** C$_8$-*tba* (0.296 g, 0.6 mmol), Fe(*p*-tol)$_2$·6H$_2$O (0.1 g, 0.2 mmol); Calcd for C$_{89}$H$_{136}$FeN$_{12}$O$_{16}$S$_2$: C, 61.08, H, 7.83, N, 9.60, S, 3.66. Found C, 61.43, H, 7.98, N, 9.60, S, 3.78.

**C$_{10}$-40.** C$_{10}$-*tba* (0.334 g, 0.6 mmol), Fe(*p*-tol)$_2$·6H$_2$O (0.1 g, 0.2 mmol); Calcd for C$_{101}$H$_{160}$FeN$_{12}$O$_{16}$S$_2$: C, 63.23, H, 8.41, N, 8.76, S, 3.34. Found C, 63.93, H, 8.81, N, 8.51, S, 3.48.

**C$_{12}$-40.** C$_{12}$-*tba* (0.371 g, 0.6 mmol), Fe(*p*-tol)$_2$·6H$_2$O (0.1 g, 0.2 mmol); Calcd for C$_{113}$H$_{184}$FeN$_{12}$O$_{16}$S$_2$: C, 65.04, H, 8.89, N, 8.05, S, 3.07. Found C, 65.44, H, 8.71, N, 7.69, S, 3.29.

**C$_8$-40-Zn.** C$_8$-*tba* (0.258 g, 0.582 mmol), Zn(*p*-tol)$_2$·6H$_2$O (0.1 g, 0.194 mmol); Calcd for C$_{89}$H$_{136}$N$_{12}$O$_{16}$S$_2$Zn: C, 60.75, H, 7.79, N, 9.55, S, 3.64. Found C, 60.93, H, 8.02, N, 9.92, S, 3.68.

## References

[1]     J.-M. Lehn, *Supramolecular Chemistry. Concepts and Perspectives*, VCH, Weinheim, **1995**.

[2]     J. W. Steed, J. L. Atwood, *Supramolecular Chemistry*, John Wiley & Sons, Chichester, **2000**.

[3]     O. Kahn, *Molecular Magnetism*, VCH, New York, **1993**.

[4]     S. Kitagawa, R. Kitaura, S.-i. Noro, *Angew. Chem., Int. Ed. Engl.* **2004**, *43*, 2334-2375.

[5]     T. K. Maji, R. Matsuda, S. Kitagawa, *Nature Materials* **2007**, *6*, 142-148.

[6]     H. Hayashi, A. Cote, H. Furukawa, M. O'Keeffe, O. Yaghi, *Nature Materials* **2007**, *6*, 501-506.

[7]     E. Coronado, J. R. Galan-Mascaros, C. J. Gomez-Garcia, V. Laukhin, *Nature* **2000**, *408*, 447-449.

[8]     E. Coronado, P. Day, *Chem. Rev.* **2004**, *104*, 5419-5448.

[9]     T. Inabe, H. Tajima, *Chem. Rev.* **2004**, *104*, 5503-5533.

[10]    R. Kato, *Chem. Rev.* **2004**, *104*, 5319-5346.

[11]    O. Kahn, J. P. Launay, *Chemtronics* **1988**, *3*, 140-151.

[12]    B. L. Feringa, *Molecular Switches*, Wiley-VCH, Weinheim, **2001**.

[13]    J.-P. Sauvage (ed.), *Struct. Bonding (Berlin)* **1999**, *v. 99*.

[14]    T. R. Kelly (ed.), *Top. Curr. Chem.* **2005**, *v. 262*.

[15]    V. Balzani, A. Credi, F. Raymo, J. F. Stoddart, *Angew. Chem., Int. Ed. Engl.* **2000**, *39*, 3348-3391.

[16]    L. Cambi, L. Szegö, *Ber. Deutsch. Chem. Ges.* **1931**, *64* 2591-2598.

[17]    L. Cambi, L. Szegö, *Ber. Deutsch. Chem. Ges.* **1933**, *66*, 656-661.

[18]    L. Cambi, L. Malatesta, *Ber. Deutsch. Chem. Ges.* **1937**, *70*, 2067-2078.

[19]    O. Kahn, C. Kröber, C. Jay, *Adv. Mater.* **1992**, *4*, 718-728.

[20]    P. Gütlich, *Struct. Bonding (Berlin)* **1981**, *44*, 83-195.

[21]    P. Gütlich, A. Hauser, H. Spiering, *Angew. Chem., Int. Ed. Engl.* **1994**, *33*, 2024-2054.

[22]    D. Chernyshov, M. Hostettler, K. W. Törnroos, H. B. Bürgi, *Angew. Chem., Int. Ed. Engl.* **2003**, *42*, 3825-3830.

[23]    M. Hostettler, K. W. Törnroos, D. Chernyshov, B. Vangdal, H. B. Bürgi, *Angew. Chem., Int. Ed. Engl.* **2004**, *43*, 4589-4594.

[24]    J. A. Real, A. B. Gaspar, M. C. Munoz, P. Gütlich, V. Ksenofontov, H. Spiering, *Top. Curr. Chem.* **2004**, *233*, 167-193.

[25]    S. Brooker, P. G. Plieger, B. Moubaraki, K. S. Murray, *Angew. Chem., Int. Ed. Engl.* **1999**, *38*, 408-410.

[26]    R. Herchel, R. Boca, M. Gembicky, J. Kozisek, F. Renz, *Inorg. Chem.* **2004**, *43*, 4103-4105.

[27]    R. Sieber, S. Decurtins, H. Stoeckli Evans, C. Wilson, D. Yufit, J. A. K. Howard, S. C. Capelli, A. Hauser, *Chem.-Eur. J.* **2000**, *6*, 361-368.

[28]    K. S. Murray, C. J. Kepert, *Top. Curr. Chem.* **2004**, *233*, 195-228.

[29]    S. Floquet, S. Salunke, M. L. Boillot, R. Clement, F. Varret, K. Boukheddaden, E. Riviere, *Chem. Mater.* **2002**, *14*, 4164-4171.

[30]    G. J. Halder, C. J. Kepert, B. Moubaraki, K. S. Murray, J. D. Cashion, *Science* **2002**, *298*, 1762-1765.

[31]    J. A. Real, E. Andres, M. C. Muñoz, M. Julve, T. Granier, A. Bousseksou, F. Varret, *Science* **1995**, *268*, 265-267.

[32]    S. M. Neville, B. Moubaraki, K. S. Murray, C. J. Kepert, *Angew. Chem., Int. Ed. Engl.* **2007**, *46*, 2059-2062.

[33]    N. Moliner, M. C. Munoz, S. Létard, X. Solans, N. Menendez, A. Goujon, F. Varret, J. A. Real, *Inorg. Chem.* **2000**, *39*, 5390-5393.

[34]  M. Nihei, L. Q. Han, H. Oshio, *J. Am. Chem. Soc.* **2007**, *129*, 5312-5313.

[35]  C. Faulmann, S. Dorbes, W. G. de Bonneval, G. Molnar, A. Bousseksou, C. J. Gomez-Garcia, E. Coronado, L. Valade, *Eur. J. Inorg. Chem.* **2005**, 3261-3270.

[36]  C. Faulmann, S. Dorbes, J. A. Real, L. Valade, *J. Low Temp. Phys.* **2006**, *142*, 261-266.

[37]  K. Takahashi, H. B. Cui, Y. Okano, H. Kobayashi, Y. Einaga, O. Sato, *Inorg. Chem.* **2006**, *45*, 5739-5741.

[38]  C. Faulmann, K. Jacob, S. Dorbes, S. Lampert, I. Malfant, M. L. Doublet, L. Valade, J. A. Real, *Inorg. Chem.* **2007**, *46*, 8548-8559.

[39]  P. Bamfield, *Chromic Phenomena. The Technological Applications of Colour Chemistry*, RSC, Cambridge, **2001**.

[40]  M. Blanca Ros, in *Metallomesogens* (Ed.: J. L. Serrano), VCH, Weinheim, **1996**, pp. 419-481.

[41]  P. Gütlich, H. A. Goodwin, *Top. Curr. Chem.* **2004**, *233*, 1-47.

[42]  *Cambridge Structural Data Base*, **February 2008**.

[43]  J. A. Real, A. B. Gaspar, M. C. Muñoz, *Dalton Trans.* **2005**, 2062-2079.

[44]  M. Sorai, J. Ensling, P. Gütlich, *Chem. Phys.* **1976**, *18*, 199-209.

[45]  T. Nakamoto, A. Bhattacharjee, M. Sorai, *Bull. Chem. Soc. Jpn.* **2004**, *77*, 921-932.

[46]  A. Bousseksou, J. J. McGarvey, F. Varret, J. A. Real, J. P. Tuchagues, A. C. Dennis, M. L. Boillot, *Chem. Phys. Lett.* **2000**, *318*, 409-416.

[47]  J. P. Tuchagues, A. Bousseksou, G. Molnar, J. J. McGarvey, F. Varret, *Top. Curr. Chem.* **2004**, *235*, 85-103.

[48]  D. A. Shultz, in *Magnetism: Molecules to Materials II: Molecule-Based Materials.* (Eds.: J. S. Miller, M. Drillon), Wiley-VCH, Weinheim, **2002**, pp. 281-306.

[49]  D. T. Shay, G. P. A. Yap, L. N. Zakharov, A. L. Rheingold, K. H. Theopold, *Angew. Chem., Int. Ed. Engl.* **2005**, *44*, 1508-1510.

[50]  D. T. Shay, G. P. A. Yap, L. N. Zakharov, A. L. Rheingold, K. H. Theopold, *Angew. Chem., Int. Ed. Engl.* **2006**, *45*, 7870.

[51]  E. K. Byrne, D. S. Richeson, K. H. Theopold, *Chem. Commun.* **1986**, 1491-1492.

[52]  E. K. Byrne, K. H. Theopold, *J. Am. Chem. Soc.* **1989**, *111*, 3887-3896.

[53]  J. Zarembowitch, C. Roux, M. L. Boillot, R. Claude, J. P. Itie, A. Polian, M. Bolte, *Mol. Cryst. Liq. Cryst.* **1993**, *234*, 247-254.

[54]  C. Roux, J. Zarembowitch, B. Gallois, T. Granier, R. Claude, *Inorg. Chem.* **1994**, *33*, 2273-2279.

[55]  M. L. Boillot, A. Sour, P. Delhaes, C. Mingotaud, H. Soyer, *Coord. Chem. Rev.* **1999**, *192*, 47-59.

[56]  M. L. Boillot, J. Zarembowitch, A. Sour, *Top. Curr. Chem.* **2004**, *234*, 261-276.

[57]  Y. Garcia, P. J. van Koningsbruggen, E. Codjovi, R. Lapouyade, O. Kahn, L. Rabardel, *J. Mater. Chem.* **1997**, *7*, 857-858.

[58]  P. J. van Koningsbruggen, Y. Garcia, E. Codjovi, R. Lapouyade, O. Kahn, L. Fournes, L. Rabardel, *J. Mater. Chem.* **1997**, *7*, 2069-2075.

[59]  S. Hayami, Y. Shigeyoshi, M. Akita, K. Inoue, K. Kato, K. Osaka, M. Takata, R. Kawajiri, T. Mitani, Y. Maeda, *Angew. Chem., Int. Ed. Engl.* **2005**, *44*, 4899-4903.

[60]  O. Kahn, J. Martinez, *Science* **1998**, *279*, 44-48.

[61]  R. N. Muller, L. Vander Elst, S. Laurent, *J. Am. Chem. Soc.* **2003**, *125*, 8405-8407.

[62]  A. Bousseksou, K. Boukheddaden, M. Goiran, C. Consejo, M. L. Boillot, J. P. Tuchagues, *Phys. Rev. B* **2002**, *65*, 172412.

[63]  S. Kimura, Y. Narumi, K. Kindo, M. Nakano, G. Matsubayashi, *Phys. Rev. B* **2005**, *72*, 064448.

[64]  N. Shimamoto, S. Ohkoshi, O. Sato, K. Hashimoto, *Chem. Lett.* **2002**, *31*, 486-487.

[65] A. Bousseksou, G. Molnar, P. Demont, J. Menegotto, *J. Mater. Chem.* **2003**, *13*, 2069-2071.

[66] S. Bonhommeau, G. Molnar, A. Galet, A. Zwick, J. A. Real, J. J. McGarvey, A. Bousseksou, *Angew. Chem., Int. Ed. Engl.* **2005**, *44*, 4069-4073.

[67] A. Bousseksou, G. Molnar, *C. R. Chim.* **2003**, *6*, 1175-1183.

[68] A. Bousseksou, G. Molnar, G. Matouzenko, *Eur. J. Inorg. Chem.* **2004**, 4353-4369.

[69] P. Mounaix, N. Lascoux, J. Degert, E. Freysz, A. Kobayashi, N. Daro, J. F. Létard, *Appl. Phys. Lett.* **2005**, *87*, 244103.

[70] S. Bonhommeau, T. Guillon, L. M. L. Daku, P. Demont, J. S. Costa, J. F. Létard, G. Molnar, A. Bousseksou, *Angew. Chem., Int. Ed. Engl.* **2006**, *45*, 1625-1629.

[71] T. Guillon, S. Bonhommeau, J. S. Costa, A. Zwick, J. F. Létard, P. Demont, G. Molnar, A. Bousseksou, *Phys. Status Solidi A-Appl. Mat.* **2006**, *203*, 2974-2980.

[72] H. L. Schläfer, G. Gliemann, *Einfürung in die Liganfeldtheorie*, Akademische Verlagsgeselschaft, Frankfurt/Main, **1967**.

[73] R. Claude, J. A. Real, J. Zarembowitch, O. Kahn, L. Ouahab, D. Grandjean, K. Boukheddaden, F. Varret, A. Dworkin, *Inorg. Chem.* **1990**, *29*, 4442-4448.

[74] P. Spacu, M. Teodorescu, G. Filotti, P. Telnic, *Z. Anorg. Allg. Chem.* **1972**, *392*, 88-92.

[75] K. Madeja, E. König, *J. Inorg. Nucl. Chem.* **1963**, *25*, 377-385.

[76] E. W. Müller, H. Spiering, P. Gütlich, *Chem. Phys. Lett.* **1982**, *93*, 567-571.

[77] J. A. Real, B. Gallois, T. Granier, F. Suez-Panama, J. Zarembowitch, *Inorg. Chem.* **1992**, *31*, 4972-4979.

[78] M. Sorai, J. Ensling, K. M. Hasselbach, P. Gütlich, *Chem. Phys.* **1977**, *20*, 197-208.

[79] G. Ritter, E. König, W. Irler, H. A. Goodwin, *Inorg. Chem.* **1978**, *17*, 224-228.

[80] S. Hayami, R. Moriyama, Y. Shigeyoshi, R. Kawajiri, T. Mitani, M. Akita, K. Inoue, Y. Maeda, *Inorg. Chem.* **2005**, *44*, 7295-7297.

[81] J. Kröber, E. Codjovi, O. Kahn, F. Groliere, C. Jay, *J. Am. Chem. Soc.* **1993**, *115*, 9810-9811.

[82] J. A. Real, M. C. Muñoz, E. Andres, T. Granier, B. Gallois, *Inorg. Chem.* **1994**, *33*, 3587-3594.

[83] R. Hernandez-Molina, A. Mederos, S. Dominguez, P. Gili, C. Ruiz-Perez, A. Castineiras, X. Solans, F. Lloret, J. A. Real, *Inorg. Chem.* **1998**, *37*, 5102-5108.

[84] W. Vreugdenhil, J. H. Van Diemen, R. A. G. De Graaff, J. G. Haasnoot, J. Reedijk, A. M. Van der Kraan, O. Kahn, J. Zarembowitch, *Polyhedron* **1990**, *9*, 2971-2979.

[85] P. Gütlich, H. Köppen, H. G. Steinhäuser, *Chem. Phys. Lett.* **1980**, *74*, 475-480.

[86] B. Gallois, J. A. Real, C. Hauw, J. Zarembowitch, *Inorg. Chem.* **1990**, *29*, 1152-1158.

[87] Z. J. Zhong, J. Q. Tao, Z. Yu, C. Y. Dun, Y. J. Liu, X. Z. You, *J. Chem. Soc., Dalton Trans.* **1998**, *3*, 327-328.

[88] Y. Garcia, P. Guionneau, G. Bravic, D. Chasseau, J. A. K. Howard, O. Kahn, V. Ksenofontov, S. Reiman, P. Gütlich, *Eur. J. Inorg. Chem.* **2000**, *7*, 1531-1538.

[89] M. Thomann, O. Kahn, J. Guilhem, F. Varret, *Inorg. Chem.* **1994**, *33*, 6029-6037

[90] J. J. A. Kolnaar, G. van Dijk, H. Kooijman, A. L. Spek, V. G. Ksenofontov, P. Gütlich, J. G. Haasnoot, J. Reedijk, *Inorg. Chem.* **1997**, *36*, 2433-2440.

[91] C. Jay, F. Groliere, O. Kahn, J. Kröber, *Mol. Cryst. Liq. Cryst.* **1993**, *234*, 255-262.

[92] J. Kröber, R. Audière, R. Claude, E. Codjovi, O. Kahn, J. G. Haasnoot, F. Crolière, C. Jay, A. Bousseksou, J. Linares, F. Varret, A. Gonthier-Vassal, *Chem. Mater.* **1994**, *6*, 1404-1412.

[93] F. Armand, C. Badoux, P. Bonville, A. Ruaudel-Teixier, O. Kahn, *Langmuir* **1995**, *11*, 3467-3472.

[94] A. Michalowicz, J. Moscovici, B. Ducourant, D. Cracco, O. Kahn, *Chem. Mater.* **1995**, *7*, 1833-1842.

[95]   K. Nakano, N. Suemura, S. Kawata, A. Fuyuhiro, T. Yagi, S. Nasu, S. Morimoto, S. Kaizaki, *Dalton Trans.* **2004**, 982-988.

[96]   K. Yoneda, K. Adachi, S. Hayami, Y. Maeda, M. Katada, A. Fuyuhiro, S. Kawata, S. Kaizaki, *Chem. Commun.* **2006**, 45-47.

[97]   Y. Garcia, O. Kahn, L. Rabardel, B. Chansou, L. Salmon, J. P. Tuchagues, *Inorg. Chem.* **1999**, *38*, 4663-4670.

[98]   L. Salmon, A. Bousseksou, B. Donnadieu, J. P. Tuchagues, *Inorg. Chem.* **2005**, *44*, 1763-1773.

[99]   E. König, K. Madeja, J. K. Watson, *J. Am. Chem. Soc.* **1968**, *90*, 1146-1153.

[100]  E. König, K. Madeja, *Inorg. Chem.* **1967**, *6*, 48-57.

[101]  A. Ozarowski, B. R. McGarvey, A. B. Sarkar, J. E. Drake, *Inorg. Chem.* **1988**, *27*, 628-635.

[102]  G. S. Matouzenko, A. Bousseksou, S. Lecocq, P. J. van Koningsbruggen, M. Perrin, O. Kahn, A. Collet, *Inorg. Chem.* **1997**, *36*, 5869-5879.

[103]  P. Guionneau, J. F. Létard, D. S. Yufit, D. Chasseau, G. Bravic, A. E. Goeta, J. A. K. Howard, O. Kahn, *J. Mater. Chem.* **1999**, *9*, 985-994.

[104]  M. Marchivie, P. Guionneau, J. F. Létard, D. Chasseau, *Acta Crystallogr., Sect. B: Struct. Sci.* **2003**, *59*, 479-486.

[105]  A. Galet, A. B. Gaspar, M. C. Muñoz, G. Levchenko, J. A. Real, *Inorg. Chem.* **2006**, *45*, 9670-9679.

[106]  N. Moliner, A. B. Gaspar, M. C. Muñoz, V. Niel, J. Cano, J. A. Real, *Inorg. Chem.* **2001**, *40*, 3986-3991.

[107]  A. B. Gaspar, M. C. Muñoz, N. Moliner, V. Ksenofontov, G. Levchenko, P. Gütlich, J. A. Real, *Monatsh. Chem.* **2003**, *134*, 285-294.

[108]  D. L. Reger, J. R. Gardinier, M. D. Smith, A. M. Shahin, G. J. Long, L. Rebbouh, F. Grandjean, *Inorg. Chem.* **2005**, *44*, 1852-1866.

[109]  P. Ganguli, P. Gütlich, E. W. Mueller, W. Irler, *J. Chem. Soc., Dalton Trans.* **1981**, *2*, 441-446.

[110]  E. W. Müller, H. Spiering, P. Gütlich, *Inorg. Chem.* **1984**, *23*, 119-120.

[111]  M. S. Haddad, W. D. Federer, M. W. Lynch, D. N. Hendrickson, *Inorg. Chem.* **1981**, *20*, 131-139.

[112]  M. S. Haddad, M. W. Lynch, W. D. Federer, D. N. Hendrickson, *Inorg. Chem.* **1981**, *20*, 123-131.

[113]  C. P. Slichter, H. G. Drickamer, *J. Chem. Phys.* **1972**, *56*, 2142-2160.

[114]  S. Decurtins, P. Gütlich, C. P. Köhler, H. Spiering, A. Hauser, *Chem. Phys. Lett.* **1984**, *105*, 1-4.

[115]  A. Hauser, *Coord. Chem. Rev.* **1991**, *111*, 275-290.

[116]  A. Hauser, *Chem. Phys. Lett.* **1986**, *124*, 543-548.

[117]  A. Hauser, A. Vef, P. Adler, *J. Chem. Phys.* **1991**, *95*, 8710-8717.

[118]  F. Reinitzer, *Monatsh. Chem.* **1888**, *9*, 421-441.

[119]  F. Reinitzer, *Liq. Cryst.* **1989**, *5*, 7-18.

[120]  D. Blunk, K. Praefcke, V. Vill, in *Handbook of Liquid Crystals, Vol. 3* (Eds.: D. Demus, J. Goodby, G. W. Gray, H.-W. Spiess, V. Vill), Wiley-VCH, Weinheim, **1998**, pp. 305-340.

[121]  D.-K. Yang, S.-T. Wu, *Fundamentals of Liquid Crystal Devices*, John Wiley & Sons, New York, **2006**.

[122]  I. C. Sage, in *Handbook of Liquid Crystals, Vol. 1* (Eds.: D. Demus, J. Goodby, G. W. Gray, H.-W. Spiess, V. Vill), Wiley-VCH Weinheim, **1998**, pp. 731-762.

[123]  J. W. Goodby, in *Handbook of Liquid Crystals, Vol. 2A* (Eds.: D. Demus, J. Goodby, G. W. Gray, H.-W. Spiess, V. Vill), Wiley-VCH, Weinheim, **1998**, pp. 3-21.

[124]  S. Kumar, *Chem. Soc. Rev.* **2006**, *35*, 83-109.

[125]  D. Vorländer, *Z. Physik. Chem.* **1923**, *105*, 211–254.

[126]  J. L. Serrano, in *Metallomesogens* (Ed.: J. L. Serrano), VCH, Weinheim, **1996**, pp. 23-29.

[127]  S. A. Hudson, P. M. Maitlis, *Chem. Rev.* **1993**, *93*, 861-885.

[128]  K. Binnemans, *Chem. Rev.* **2005**, *105*, 4148-4204.

[129]  A. I. Kitaigorodski, *Organic Chemical Crystallography*, Consultants Bureau, New York, **1961**.

[130]  W. Weissflog, A. Wiegeleben, S. Diele, D. Demus, *Cryst. Res. Technol.* **1984**, *19*, 583-591.

[131]  D. Demus, in *Handbook of Liquid Crystals, Vol. 1* (Eds.: D. Demus, J. Goodby, G. W. Gray, H.-W. Spiess, V. Vill), Wiley-VCH, Weinheim, **1998**, pp. 133-187.

[132]  A. P. Polishchuk, T. V. Timofeeva, *Russ. Chem. Rev.* **1993**, *62*, 291-321.

[133]  O. Roubeau, J. M. A. Gomez, E. Balskus, J. J. A. Kolnaar, J. G. Haasnoot, J. Reedijk, *New J. Chem.* **2001**, *25*, 144-150.

[134]  P. Coronel, A. Ruaudel-Teixier, A. Barraud, O. Kahn, *Mater. Res. Soc. Symp. Proc. (Adv. Org. Solid State Mater.)* **1990**, *173*, 537-541.

[135]  A. Ruaudel-Teixier, A. Barraud, P. Coronel, O. Kahn, *Thin Solid Films* **1988**, *160*, 107-115.

[136]  F. Lions, K. V. Martin, *J. Am. Chem. Soc.* **1957**, *79*, 1572-1575.

[137]  W. O. Gillum, R. A. D. Wentworth, R. F. Childers, *Inorg. Chem.* **1970**, *9*, 1825-1832.

[138]  W. M. Reiff, *J. Am. Chem. Soc.* **1973**, *95*, 3048-3050.

[139]  R. A. D. Wentworth, P. S. Dahl, C. J. Huffmann, W. O. Gillum, W. E. Streib, J. C. Huffman, *Inorg. Chem.* **1982**, *21*, 3060-3063.

[140]  E. B. Fleischer, A. E. Gebala, D. R. Swift, P. A. Tasker, *Inorg. Chem.* **1972**, *11*, 2775-2784.

[141]  C. Mealli, E. C. Lingafelter, *J. Chem. Soc., Chem. Commun.* **1970**, 885.

[142]  M. A. Hoselton, L. J. Wilson, R. S. Drago, *J. Am. Chem. Soc.* **1975**, *97*, 1722-1729.

[143]  L. J. G. Wilson, D.; Hoselton, M. A. , *Inorg. Chem.* **1975**, *14*, 2968-2975.

[144]  M. A. Hoselton, R. S. Drago, L. J. Wilson, N. Sutin, *J. Am. Chem. Soc.* **1976**, *98*, 6967-6969.

[145]  M. S. Lazarus, M. A. Hoselton, T. S. Chou, *Inorg. Chem.* **1977**, *16*, 2549-2553.

[146]  E. V. Dose, M. A. Hoselton, N. Sutin, M. F. Tweedle, L. J. Wilson, *J. Am. Chem. Soc.* **1978**, *100*, 1141-1147.

[147]  W. H. R. Batschelet, N. J., *Inorg. Chem.* **1983**, *22*, 2083-2087.

[148]  P. Adler, H. Spiering, P. Gütlich, *J. Phys. Chem. Solids* **1989**, *50*, 587-597.

[149]  A. J. Conti, C. L. Xie, D. N. Hendrickson, *J. Am. Chem. Soc.* **1989**, *111*, 1171-1180.

[150]  W. S. Hammack, A. J. Conti, D. N. Hendrickson, H. G. Drickamer, *J. Am. Chem. Soc.* **1989**, *111*, 1738-1741.

[151]  J. E. Monat, J. K. McCusker, *J. Am. Chem. Soc.* **2000**, *122*, 4092-4097.

[152]  G. Brewer, C. Luckett, *Inorg. Chim. Acta* **2005**, *358*, 239-245.

[153]  I. Morgenstern-Badarau, F. Lambert, J. P. Renault, M. Cesario, J. D. Marechal, F. Maseras, *Inorg. Chim. Acta* **2000**, *297*, 338-350.

[154]  M. Yamada, M. Ooidemizu, Y. Ikuta, S. Osa, N. Matsumoto, S. Iijima, M. Kojima, F. Dahan, J. P. Tuchagues, *Inorg. Chem.* **2003**, *42*, 8406-8416.

[155]  H. Ohta, Y. Sunatsuki, M. Kojima, S. Iijima, H. Akashi, N. Matsumoto, *Chem. Lett.* **2004**, *33*, 350-351.

[156]  Y. Sunatsuki, H. Ohta, M. Kojima, Y. Ikuta, Y. Goto, N. Matsumoto, S. Iijima, H. Akashi, S. Kaizaki, F. Dahan, J. P. Tuchagues, *Inorg. Chem.* **2004**, *43*, 4154-4171.

[157]  C. Brewer, G. Brewer, G. Patil, Y. Q. Sun, C. Viragh, R. J. Butcher, *Inorg. Chim. Acta* **2005**, *358*, 3441-3448.

[158] G. Brewer, M. J. Olida, A. M. Schmiedekamp, C. Viragh, P. Y. Zavalij, *Dalton Trans.* **2006**, 5617-5629.

[159] C. Brewer, G. Brewer, R. J. Butcher, E. E. Carpenter, L. Cuenca, A. M. Schmiedekamp, C. Viragh, *Dalton Trans.* **2005**, 3617-3619.

[160] G. Brewer, C. Luckett, L. May, A. M. Beatty, W. R. Scheidt, *Inorg. Chim. Acta* **2004**, *357*, 2390-2396.

[161] C. Brewer, G. Brewer, C. Luckett, G. S. Marbury, C. Viragh, A. M. Beatty, W. R. Scheidt, *Inorg. Chem.* **2004**, *43*, 2402-2415.

[162] M. J. Hardie, C. A. Kilner, M. A. Halcrow, *Acta Crystallogr. Sect. C-Cryst. Struct. Commun.* **2004**, *60*, M177-M179.

[163] H. Z. Lazar, T. Forestier, S. A. Barrett, C. A. Kilner, J. F. Létard, M. A. Halcrow, *Dalton Trans.* **2007**, 4276-4285.

[164] C. T. Brewer, G. Brewer, R. J. Butcher, E. E. Carpenter, A. M. Schmiedekamp, C. Viragh, *Dalton Trans.* **2007**, 295-298.

[165] P. G. Sim, E. Sinn, *J. Am. Chem. Soc.* **1981**, *103*, 241-243.

[166] Y. Garcia, P. Gütlich, *Top. Curr. Chem.* **2004**, *234*, 49-62.

[167] H. Toftlund, J. J. McGarvey, *Top. Curr. Chem.* **2004**, *233*, 151-166.

[168] H. Toftlund, S. Yde-Andersen, *Acta Chem. Scand., A* **1981**, *35*, 575-585.

[169] J. K. Mccusker, H. Toftlund, A. L. Rheingold, D. N. Hendrickson, *J. Am. Chem. Soc.* **1993**, *115*, 1797-1804.

[170] H. R. Chang, J. K. McCusker, H. Toftlund, S. R. Wilson, A. X. Trautwein, H. Winkler, D. N. Hendrickson, *J. Am. Chem. Soc.* **1990**, *112*, 6814-6827.

[171] C. R. Goldsmith, R. T. Jonas, A. P. Cole, T. D. P. Stack, *Inorg. Chem.* **2002**, *41*, 4642-4652.

[172] D. J. Rudd, C. R. Goldsmith, A. P. Cole, D. P. Stack, K. O. Hodgson, B. Hedman, *Inorg. Chem.* **2005**, *44*, 1221-1229.

[173] L. Christiansen, D. N. Hendrickson, H. Toftlund, S. R. Wilson, C. L. Xie, *Inorg. Chem.* **1986**, *25*, 2813-2818.

[174] H. A. Goodwin, *Top. Curr. Chem.* **2004**, *233*, 59-90.

[175] A. N. Vedernikov, G. A. Shamov, V. N. Solomonov, *Zh. Obshchei Khim.* **1999**, *69*, 1144-1158.

[176] T. Bowen, R. P. Planalp, M. W. Brechbiel, *Bioorg. Med. Chem. Lett.* **1995**, *6*, 807-810.

[177] J. F. Létard, P. Guionneau, L. Rabardel, J. A. K. Howard, A. E. Goeta, D. Chasseau, O. Kahn, *Inorg. Chem.* **1998**, *37*, 4432-4441.

[178] J. Kusz, H. Spiering, P. Gütlich, *J. Appl. Crystallogr.* **2001**, *34*, 229-238.

[179] J. Kusz, H. Spiering, P. Gütlich, *J. Appl. Crystallogr.* **2004**, *37*, 589-595.

[180] P. Guionneau, M. Marchivie, G. Bravic, J. F. Létard, D. Chasseau, *Top. Curr. Chem.* **2004**, *234*, 97-128.

[181] K. W. Törnroos, M. Hostettler, D. Chernyshov, B. Vangdal, H. B. Bürgi, *Chem.-Eur. J.* **2006**, *12*, 6207-6215.

[182] E. Trzop, M. B. L. Cointe, H. Cailleau, L. Toupet, G. Molnar, A. Bousseksou, A. B. Gaspar, J. A. Real, E. Collet, *J. Appl. Crystallogr.* **2007**, *40*, 158-164.

[183] P. Guionneau, C. Brigouleix, Y. Barrans, A. E. Goeta, J. F. Létard, J. A. K. Howard, J. Gaultier, D. Chasseau, *Comptes Rendus Acad. Sci. Ser. II C* **2001**, *4*, 161-171.

[184] P. Guionneau, M. Marchivie, Y. Garcia, J. A. K. Howard, D. Chasseau, *Phys. Rev. B* **2005**, *72*, 214408.

[185] A. L. Thompson, A. E. Goeta, J. A. Real, A. Galet, M. C. Muñoz, *Chem. Commun.* **2004**, 1390-1391.

[186] V. Niel, A. L. Thompson, M. C. Muñoz, A. Galet, A. S. E. Goeta, J. A. Real, *Angew. Chem., Int. Ed. Engl.* **2003**, *42*, 3760-3763.

[187] V. Niel, A. L. Thompson, A. E. Goeta, C. Enachescu, A. Hauser, A. Galet, M. C. Muñoz, J. A. Real, *Chem.-Eur. J.* **2005**, *11*, 2047-2060.

[188] A. Galet, M. C. Muñoz, J. A. Real, *Chem. Commun.* **2006**, 4321-4323.

[189] A. Galet, M. C. Muñoz, V. Martinez, J. A. Real, *Chem. Commun.* **2004**, 2268-2269.

[190] P. Guionneau, M. Marchivie, G. Bravic, J. F. Létard, D. Chasseau, *J. Mater. Chem.* **2002**, *12*, 2546-2551.

[191] J. Kusz, H. Spiering, P. Gütlich, *J. Appl. Crystallogr.* **2000**, *33*, 201-205.

[192] M. G. B. Drew, C. J. Harding, V. McKee, G. G. Morgan, N. J., *J. Chem. Soc., Chem. Commun.* **1995**, 1035-1038.

[193] E. König, *Prog. Inorg. Chem.* **1987**, *35*, 527-622.

[194] R. M. Kirchner, C. Mealli, M. Bailey, N. Howe, L. P. Torre, L. J. Wilson, L. C. Andrews, N. J. Rose, E. C. Lingafelter, *Coord. Chem. Rev.* **1987**, *77*, 89-163.

[195] E. König, *Struct. Bonding (Berlin)* **1991**, *76*, 51-152.

[196] A. Galet, V. Niel, M. C. Muñoz, J. A. Real, *J. Am. Chem. Soc.* **2003**, *125*, 14224-14225.

[197] J. A. Real, A. B. Gaspar, V. Niel, M. C. Muñoz, *Coord. Chem. Rev.* **2003**, *236*, 121-141.

[198] V. Ksenofontov, A. B. Gaspar, G. Levchenko, B. Fitzsimmons, P. Gütlich, *J. Phys. Chem. B* **2004**, *108*, 7723-7727.

[199] H. Toftlund, *Coord. Chem. Rev.* **1989**, *94*, 67-108.

[200] H. L. Chum, J. A. Vanin, M. I. D. Holanda, *Inorg. Chem.* **1982**, *21*, 1146-1152.

[201] S. Schenker, A. Hauser, W. Wang, I. Y. Chan, *J. Chem. Phys.* **1998**, *109*, 9870-9878.

[202] P. Gütlich, R. Link, A. Trautwein, *Mössbauer Spectroscopy and Transition Metal Chemistry*, Springer, Berlin, **1978**.

[203] M. Marchivie, P. Guionneau, J. A. K. Howard, G. Chastanet, J. F. Létard, A. E. Goeta, D. Chasseau, *J. Am. Chem. Soc.* **2002**, *124*, 194-195.

[204] Y. Z. Voloshin, O. A. Varzatskii, A. I. Stash, V. K. Belsky, Y. N. Bubnov, I. I. Vorontsov, K. A. Potekhin, E. V. Polshin, M. Y. Antipin, *Polyhedron* **2001**, *20*, 2721-2733.

[205] M. Ijjaali, C. Venturini, R. Gerardin, B. Malaman, C. Gleitzer, *Eur. J. Solid State Inorg. Chem.* **1991**, 984-998.

[206] R. Krishnamurty, W. B. Schaap, *J. Chem. Educ.* **1969**, *46*, 799-810.

[207] K. Nakamoto, *Infrared and Raman Spectra of Inorganic and Coordination Compounds*, 5th ed., John Wiley and Sons, New York, **1997**.

[208] Y. Ikuta, M. Ooidemizu, Y. Yamahata, M. Yamada, S. Osa, N. Matsumoto, S. Iijima, Y. Sunatsuki, M. Kojima, F. Dahan, J. P. Tuchagues, *Inorg. Chem.* **2003**, *42*, 7001-7017.

[209] C. L. Zilverentant, G. A. van Albada, A. Bousseksou, J. G. Haasnoot, J. Reedijk, *Inorg. Chim. Acta* **2000**, *303*, 287-290.

[210] N. Suemura, M. Ohama, S. Kaizaki, *Chem. Commun.* **2001**, 1538-1539.

[211] T. Fujigaya, D. L. Jiang, T. Aida, *J. Am. Chem. Soc.* **2003**, *125*, 14690-14691.

[212] E. Codjovi, L. Sommier, O. Kahn, C. Jay, *New J. Chem.* **1996**, *20*, 503-505.

[213] G. M. Bankroft, *Mössbauer spectroscopy. An introduction for inorganic chemists and geochemists*, McGraw-Hill, London, **1973**.

[214] Y. Garcia, J. Moscovici, A. Michalowicz, V. Ksenofontov, G. Levchenko, G. Bravic, D. Chasseau, P. Gütlich, *Chem.-Eur. J.* **2002**, *8*, 4992-5000.

[215] D. L. Reger, C. A. Little, M. D. Smith, A. L. Rheingold, K. C. Lam, T. L. Concolino, G. J. Long, R. P. Hermann, F. Grandjean, *Eur. J. Inorg. Chem.* **2002**, 1190-1197.

[216] J. J. A. Kolnaar, M. I. de Heer, H. Kooijman, A. L. Spek, G. Schmitt, V. Ksenofontov, P. Gütlich, J. G. Haasnoot, J. Reedijk, *Eur. J. Inorg. Chem.* **1999**, *5*, 881-886.

[217] J. Fleisch, P. Gütlich, K. M. Hasselbach, *Inorg. Chim. Acta* **1976**, *17*, 51-54.

[218]  T. C. Gibb, *J. Chem. Soc. (A)* **1968**, 1439-1444.

[219]  R. H. Herber, in *Chemical Mössbauer Spectroscopy* (Ed.: R. H. Herber), Plenum, New York, **1984**, pp. 199-216.

[220]  D. Onggo, H. A. Goodwin, *Aust. J. Chem.* **1991**, *44*, 1539-1551.

[221]  C. M. Harris, S. Kokot, H. R. H. Patil, E. Sinn, H. Wong, *Aust. J. Chem.* **1972**, *25*, 1631-1643.

[222]  I. Gladstone, N. J. Rose, E. C. Lingafelter, *Inorg. Chem.* **1986**, *25*, 1516-1518.

[223]  Y. Z. Voloshin, E. V. Polshin, A. Y. Nazarenko, *Hyperfine Interact.* **2002**, *141-142*, 309-320.

[224]  A. Y. Nazarenko, E. V. Polshin, Y. Z. Voloshin, *Mendeleev Commun.* **1993**, 45-47.

[225]  O. Kahn, *J. Chim. Phys. Phys.-Chim. Biol.* **1988**, *85*, 1113-1118.

[226]  H. Soyer, C. Mingotaud, M. L. Boillot, P. Delhaes, *Langmuir* **1998**, *14*, 5890-5895.

[227]  H. Soyer, C. Mingotaud, M. L. Boillot, P. Delhaes, *Thin Solid Films* **1998**, *329*, 435-438.

[228]  J. F. Létard, O. Nguyen, H. Soyer, C. Mingotaud, P. Delhaes, O. Kahn, *Inorg. Chem.* **1999**, *38*, 3020-3021.

[229]  Y. Galyametdinov, V. Ksenofontov, A. Prosvirin, I. Ovchinnikov, G. Ivanova, P. Gütlich, W. Haase, *Angew. Chem., Int. Ed. Engl.* **2001**, *40*, 4269-4271.

[230]  S. Hayami, K. Danjobara, K. Inoue, Y. Ogawa, N. Matsumoto, Y. Maeda, *Adv. Mater.* **2004**, *16*, 869-872.

[231]  S. Hayami, K. Danjobara, S. Miyazaki, K. Inoue, Y. Ogawa, Y. Maeda, *Polyhedron* **2005**, *24*, 2821-2827.

[232]  S. Hayami, N. Motokawa, A. Shuto, N. Masuhara, T. Someya, Y. Ogawa, K. Inoue, Y. Maeda, *Inorg. Chem.* **2007**, *46*, 1789-1794.

[233]  P. J. Alonso, in *Metallomesogens* (Ed.: J. L. Serrano), VCH, Weinheim, **1996**, pp. 387-417.

[234]  W. Hass, W. A. König, *Liebigs Ann. Chem.* **1982**, 1615-1622.

[235]  E. J. J. Blanz, F. A. French, J. R. DoAmaral, D. A. French, *J. Med. Chem.* **1970**, *13*, 1124-1130.

[236]  T. Jen, J. S. Frazee, M. S. Schwartz, C. Kaiser, *J. Med. Chem.* **1977**, *20*, 1258-1262.

[237]  Z. S. Piao, L. Wang, Z. Z. Zhao, *Chin. Chem. Lett.* **2003**, *14*, 1119-1122.

[238]  P. Gütlich, J. Jung, H. Goodwin, in *Molecular Magnetism: From Molecular Assemblies to the Devices* (Ed.: E. Coronado), Kluwer Academic Publishers, **1996**, pp. 327-378.

[239]  J. N. Israelachvili, D. J. Mitchell, B. W. Ninham, *J. Chem. Soc., Faraday Trans. 2* **1976**, *72*, 1525-1568.

[240]  E. Terazzi, S. Suarez, S. Torelli, H. Nozary, D. Imbert, O. Mamula, J.-P. Rivera, E. Guillet, J.-M. Bénech, G. Bernardinelli, R. Scopelliti, B. Donnio, D. Guillon, J.-C. G. Bünzli, C. Piguet, *Adv. Funct. Mater.* **2006**, *16*, 157-168.

[241]  C. Tschierske, *J. Mater. Chem.* **1998**, *8*, 1485-1508.

[242]  E. Terazzi, S. Torelli, G. Bernardinelli, J.-P. Rivera, J.-M. Bénech, C. Bourgogne, B. Donnio, D. Guillon, D. Imbert, J.-C. G. Bünzli, A. Pinto, D. Jeannerat, C. Piguet, *J. Amer. Chem. Soc.* **2005**, *127*, 888-903.

[243]  E. Terazzi, J.-M. Bénech, J.-P. Rivera, G. Bernardinelli, B. Donnio, D. Guillon, C. Piguet, *J. Chem. Soc., Dalton Trans.* **2003**, 769-772.

[244]  D. W. Bruce, *Acc. Chem. Res.* **2000**, *33*, 831-840.

[245]  K. Binnemans, L. Jongen, C. Gorller-Walrand, W. D'Olieslager, D. Hinz, G. Meyer, *Eur. J. Inorg. Chem.* **2000**, 1429-1436.

[246]  R. G. Snyder, *J. Mol. Spectrosc.* **1961**, *7*, 116-144.

[247]  S.-H. Park, C. E. Lee, *Chem. Mater.* **2006**, *18*, 981-987.

[248] R. A. MacPhail, H. L. Strauss, R. G. Snyder, C. A. Elliger, *J. Phys. Chem.* **1984**, *88*, 334-341.

[249] M. Borja, P. K. Dutta, *J. Phys. Chem* **1992**, *96*, 5434-5444.

[250] C. Almirante, G. Miniony, G. Zerbi, *J. Phys. Chem* **1986**, *90*, 852-859.

[251] P. Krumholtz, *J. Amer. Chem. Soc.* **1953**, *75*, 2163-2166.

[252] L. G. Vanquickenborne, K. Pierloot, *Inorg. Chem.* **1981**, *20*, 3673-3677.

[253] F. M. Van Meter, H. M. Neumann, *J. Amer. Chem. Soc.* **1976**, *98*, 1388-1394.

[254] L. Jongen, B. Goderis, I. Dolbnya, K. Binnemans, *Chem. Mater.* **2003**, *15*, 212-217.

[255] D. L. Dorset, *Crystallography of the polymethylene chain: an inquiry into the structure of waxes* Oxford University Press, Oxford, New York, **2005**.

[256] K. Saito, M. Ikeda, M. Sorai, *J. Therm. Anal. Cal.* **2002**, *70*, 345-352.

[257] M. Sorai, K. Saito, *Chem. Rec.* **2003**, *3*, 29-39.

[258] E. F. Marques, H. D. Burrows, M. da Miguel Graca, *J. Chem. Soc., Faraday Trans.,* **1998**, *94*, 1729-1736.

[259] "Thermochemical Radii", in *CRC Handbook of Chemistry and Physics*, 85th ed. (Ed.: D. R. Lide), CRC Press, Boca Ranot, FL, **2005**, pp. 12-31 - 12-35.

[260] R. Hogg, R. G. Wilkins, *J. Chem. Soc.* **1962**, 341-350.

[261] R. N. Sylva, H. A. Goodwin, *Aust. J. Chem.* **1967**, *20*, 479-496.

[262] G. A. Renovitch, W. A. Baker, Jr., *J. Am. Chem. Soc.* **1967**, *89*, 6377-6378.

[263] G. Lemercier, M. Verelst, A. Boussekssou, F. Varret, J. P. Tuchagues, (Ed.: O. Kahn), Kluwer, Dordrecht, **1996**, pp. 335-356.

[264] Y. Garcia, P. J. van Koningsbruggen, R. Lapouyade, L. Rabardel, O. Kahn, M. Wieczorek, R. Bronisz, Z. Ciunik, M. F. Rudolf, *Comptes Rendus Acad. Sci. Ser. II C* **1998**, *1*, 523-532.

[265] N. V. Bausk, S. B. Erenburg, L. N. Mazalov, L. G. Lavrenova, V. N. Ikorskii, *J. Struct. Chem.* **1994**, *35*, 509-516.

[266] S. B. Erenburg, N. V. Bausk, L. G. Lavrenova, V. A. Varnek, L. N. Mazalov, *Solid State Ionics* **1997**, *101*, 571-577.

[267] G. Lemercier, N. Brefuel, S. Shova, J. A. Wolny, F. Dahan, M. Verelst, H. Paulsen, A. X. Trautwein, J. P. Tuchagues, *Chem.-Eur. J.* **2006**, *12*, 7421-7432.

[268] M. C. Gimenez-Lopez, M. Clemente-Leon, E. Coronado, F. M. Romero, S. Shova, J. P. Tuchagues, *Eur. J. Inorg. Chem.* **2005**, 2783-2787.

[269] K. Binnemans, L. Jongen, C. Bromant, D. Hinz, G. Meyer, *Inorg. Chem.* **2000**, *39*, 5938-5945.

[270] E. König, G. Ritter, H. A. Goodwin, *Chem. Phys.* **1973**, *1*, 17-26.

[271] E. König, G. Ritter, S. K. Kulshreshtha, *Chem. Rev.* **1985**, *85*, 219-234.

[272] E. C. Constable, G. Baum, E. Bill, R. Dyson, R. van Eldik, D. Fenske, S. Kaderli, D. Morris, A. Neubrand, M. Neuburger, D. R. Smith, K. Wieghardt, M. Zehnder, A. D. Zuberbuhler, *Chem.-Eur. J.* **1999**, *5*, 498-508.

[273] J. Jeftić, R. Hinek, S. C. Capelli, A. Hauser, *Inorg. Chem.* **1997**, *36*, 3080-3087.

[274] J. M. Seddon, in *Handbook of Liquid Crystals, Vol. 1* (Eds.: D. Demus, J. Goodby, G. W. Gray, H.-W. Spiess, V. Vill), Wiley-VCH, Weinheim, **1998**, pp. 635-680.

[275] R. Blinc, B. Zeks, J. Seliger, B. Lozar, J. Slak, A. Levstik, C. Filipic, V. Zagar, G. Lahajnar, F. Milia, G. Chapuis, *J. Chem. Phys.* **1979**, *71*, 2118-2130.

[276] M. S. Akanni, E. K. Okoh, *Thermochim. Acta* **1992**, *208*, 1-41.

[277] R. C. Vickery, *J. Mol. Spectrosc.* **1958**, *2*, 308-331.

[278] C. G. Bazuin, D. Guillon, A. Skoulios, A. M. Amorim da Costa, H. D. Burrows, C. F. G. C. Geraldes, J. J. C. Teixeira-Dias, E. Blackmore, G. J. T. Tiddy, *Liq. Cryst.* **1988**, *3*, 1655-1670.

[279] J. F. Nagle, *Ann. Rev. Phys. Chem.* **1980**, *31*, 157-195.

[280] P. J. Flory, *Statistical Mechanics of Chain Molecules*, Wiley, New York, **1988**.

[281]  J. F. Nagle, M. Goldstein, *Macromolecules* **1985**, *18*, 2643-2652.

[282]  L. Salem, *J. Chem. Phys.* **1962**, *37*, 2100-2113.

[283]  B. Bahadur, *J. Chem. Phys.* **1977**, *67*, 3272-3273.

[284]  P. G. de Gennes, *The physics of liquid crystals*, Clarendon Press, Oxford, **1974**.

[285]  D. Dunmur, K. Toriyama, in *Handbook of Liquid Crystals, Vol. 1A* (Eds.: D. Demus, J. Goodby, G. W. Gray, H.-W. Spiess, V. Vill), Wiley-VCH, Weinheim, **1998**, pp. 204-214.

[286]  F. Hardouin, M. F. Achard, G. Sigaud, H. Gasparoux, *Mol. Cryst. Liq. Cryst.* **1977**, *39*, 241-257.

[287]  Y. Galyametdinov, M. A. Athanassopoulou, K. Griesar, O. Kharitonova, E. A. Soto Bustamante, L. Tinchurina, I. Ovchinnikov, W. Haase, *Chem. Mater.* **1996**, *8*, 922-926.

[288]  Y. G. Galyametdinov, W. Haase, L. Malykhina, A. Prosvirin, I. Bikchantaev, A. Rakhmatullin, K. Binnemans, *Chem.-Eur. J.* **2001**, *7*, 99-105.

[289]  P. J. Alonso, M. L. Sanjuan, P. Romero, M. Marcos, J. L. Serrano, *J. Phys. Condens. Matter.* **1990**, *2*, 9173-9182.

[290]  S. Chandrasekhar, B. K. Sadashiva, B. S. Srikanta, *Mol. Cryst. Liq. Cryst.* **1987**, *151*, 93-107.

[291]  B. Borchers, W. Haase, *Mol. Cryst. Liq. Cryst.* **1991**, *209*, 319-328.

[292]  I. G. Bikhantaev, Y. G. Galyametdinov, I. V. Ovchinnikov, *Zh. Strukt. Khim.* **1987**, *28*, 61-67.

[293]  A.-M. Giroud-Godquin, J.-M. Latour, J.-C. Marchon, *Inorg. Chem.* **1985**, *24*, 4452-4454.

[294]  P. Maldivi, A.-M. Giroud-Godquin, J.-C. Marchon, *Chem. Phys. Lett.* **1989**, *157*, 552-555.

[295]  A.-M. Giroud-Godquin, P. M. Maitlis, *Angew. Chem., Int. Ed. Engl.* **1991**, *30*, 375-402.

[296]  P. Maldivi, D. Guillon, A.-M. Giroud-Godquin, J. C. Marchon, H. Abied, H. Dexpert, A. Skoulios, *J. Chim. Phys.* **1989**, *86*, 1651-1664.

[297]  J. C. Marchon, P. Maldivi, A.-M. Giroud-Godquin, D. Guillon, A. Skoulios, D. P. Strommen, *Philos. Trans. R. Soc. London* **1990**, *A330*, 109-116.

[298]  W. Haase, B. Gehring, B. Borchers, *Mat. Res. Soc. Symp. Proc.* **1990**, *175*, 249-255.

[299]  S. Nakatsuji, H. Anzai, *J. Mater. Chem* **1997**, *7*, 2161-2174.

[300]  S. Nakatsuji, H. Ikemoto, H. Akutsu, J. Yamada, A. Mori, *J. Org. Chem.* **2003**, *68*, 1708-1714.

[301]  S. Nakatsuji, T. Amano, H. Akutsu, J. Yamada, *J. Phys. Org. Chem.* **2006**, *19*, 333-340.

[302]  S. Nakatsuji, M. Mizumoto, H. Ikemoto, H. Akutsu, J.-I. Yamada, *Eur. J. Org. Chem.* **2002**, 1912-1918.

[303]  T. Tayagaki, A. Galet, G. Molnar, M. C. Muñoz, A. Zwick, K. Tanaka, J. A. Real, A. Bousseksou, *J. Phys. Chem. B* **2005**, *109*, 14859-14867.

[304]  J. Jung, G. Schmitt, L. Wiehl, A. Hauser, K. Knorr, H. Spiering, P. Gütlich, *Z. Phys. B: Condens. Matter* **1996**, *100*, 523-534.

[305]  H. Constant-Machado, J. Linares, F. Varret, J. G. Haasnoot, J. P. Martin, J. Zarembowitch, A. Dworkin, A. Bousseksou, *J. Phys. I* **1996**, *6*, 1203-1216.

[306]  L. G. Lavrenova, V. N. Ikorskii, V. A. Varnek, I. M. Oglezneva, S. V. Larionov, *J. Struct. Chem.* **1993**, *34*, 960-965.

[307]  J. P. Martin, J. Zarembowitch, A. Bousseksou, A. Dworkin, J. G. Haasnoot, F. Varret, *Inorg. Chem.* **1994**, *33*, 6325-6333.

[308]  P. Ganguli, P. Gütlich, E. W. Müller, *Inorg. Chem.* **1982**, *21*, 3429-3433.

[309]  P. Gütlich, R. Link, H. G. Steinhäuser, *Inorg. Chem.* **1978**, *17*, 2509-2514.

[310]  B. Weber, F. A. Walker, *Inorg. Chem.* **2007**, *46*, 6794-6803.

[311] N. Ortega-Villar, A. L. Thompson, M. C. Muñoz, V. M. Ugalde-Saldivar, A. E. Goeta, R. Moreno-Esparza, J. A. Real, *Chem.-Eur. J.* **2005**, *11*, 5721-5734.

[312] L. L. Martin, K. S. Hagen, A. Hauser, R. L. Martin, A. M. Sargeson, *J. Chem. Soc., Chem. Commun.* **1988**, *19*, 1313-1315.

[313] J. K. Beattie, *Adv. Inorg. Chem.* **1988**, *32*, 1-53.

[314] O. Roubeau, J. G. Haasnoot, E. Codjovi, F. Varret, J. Reedijk, *Chem. Mater.* **2002**, *14*, 2559-2566.

[315] P. J. van Koningsbruggen, *Top. Curr. Chem.* **2004**, *233*, 123-149.

[316] J. G. Haasnoot, in *Magnetism: A Supramolecular Function* (Ed.: O. Kahn), Kluwer Academic Publishers, Dordrecht, **1996**, pp. 299-321.

[317] G. P. Haasnoot, *Coord. Chem. Rev.* **2000**, *200-202*, 131-185.

[318] J. G. Haasnoot, G. Vos, W. L. Groeneveld, *Z. Naturforsch., B: Chem. Sci.* **1977**, *32*, 1421-1430.

[319] L. G. Lavrenova, V. N. Ikorskii, V. A. Varnek, I. M. Oglezneva, S. V. Larionov, *Koord. Khim.* **1986**, *12*, 207-215.

[320] L. G. Lavrenova, V. N. Ikorskii, V. A. Varnek, I. M. Oglezneva, S. V. Larionov, *Koord. Khim.* **1990**, *16*, 654-661.

[321] J. A. Real, H. Bolvin, A. Bousseksou, A. Dworkin, O. Kahn, F. Varret, J. Zarembowitch, *J. Am. Chem. Soc.* **1992**, *114*, 4650-4658.

[322] O. Kahn, E. Codjovi, *Philos. Trans. R. Soc. Lond. Ser. A-Math. Phys. Eng. Sci.* **1996**, *354*, 359-379.

[323] K. H. Sugiyarto, H. A. Goodwin, *Aust. J. Chem.* **1994**, *47*, 263-277.

[324] K. Boukheddaden, J. Linares, H. Spiering, F. Varret, *Eur. Phys. J. B* **2000**, *15*, 317-326.

[325] C. Cantin, J. Kliava, A. Marbeuf, D. Mikaïlitchenko, *Eur. Phys. J. B* **1999**, *12*, 525-540

[326] L. G. Lavrenova, N. G. Yudina, V. N. Ikorskii, V. A. Varnek, I. M. Oglezneva, S. V. Larionov, *Polyhedron* **1995**, *14*, 1333-1337.

[327] S. Toyazaki, M. Nakanishi, T. Komatsu, N. Kojima, D. Matsumura, T. Yokoyama, *Synth. Met.* **2001**, *121*, 1794-1795.

[328] M. Verelst, L. Sommier, P. Lecante, A. Mosset, O. Kahn, *Chem. Mater.* **1998**, *10*, 980-985.

[329] A. Michalowicz, J. Moscovici, O. Kahn, *J. Phys. IV France* **1997**, *7*, 633-635.

[330] V. P. Sinditskii, V. I. Sokol, A. E. Fogel'zang, M. D. Dutov, V. V. Serushkin, M. A. Porai-Koshits, B. S. Svetlov, *Russ. J. Inorg. Chem.* **1987**, *32*, 1149-1152.

[331] K. Drabent, Z. Ciunik, *Chem. Commun.* **2001**, 1254-1255.

[332] M. B. Bushuev, L. G. Lavrenova, Y. G. Shvedenkov, A. V. Virovets, L. A. Sheludyakova, S. V. Larionov, *Russ. J. Inorg. Chem.* **2007**, *52*, 46-51.

[333] Y. Garcia, V. Niel, M. C. Muñoz, J. A. Real, *Top. Curr. Chem.* **2004**, *233*, 229-257.

[334] Y. Garcia, P. J. van Koningsbruggen, R. Lapouyade, L. Fournes, L. Rabardel, O. Kahn, V. Ksenofontov, G. Levchenko, P. Gütlich, *Chem. Mater.* **1998**, *10*, 2426-2433.

[335] T. Fujigaya, D. L. Jiang, T. Aida, *J. Am. Chem. Soc.* **2005**, *127*, 5484-5489.

[336] M. B. Bushuev, L. G. Lavrenova, V. N. Ikorskii, Y. G. Shvedenkov, V. A. Varnek, L. A. Sheludyakova, S. V. Larionov, *Russ. J. Coord. Chem.* **2004**, *30*, 284-290.

[337] N. V. Bausk, S. B. Erenburg, L. G. Lavrenova, L. N. Mazalov, *J. Struct. Chem.* **1995**, *36*, 925-931.

[338] V. A. Varnek, L. G. Lavrenova, *J. Struct. Chem.* **1995**, *36*, 104-111.

[339] S. B. Erenburg, N. V. Bausk, V. A. Varnek, L. G. Lavrenova, *J. Magn. Magn. Mater.* **1996**, *158*, 595-596.

[340] O. Kahn, L. Sommier, E. Codjovi, *Chem. Mater.* **1997**, *9*, 3199-3205.

[341] V. A. Varnek, L. G. Lavrenova, *J. Struct. Chem.* **1994**, *35*, 842-850.

[342]  V. A. Varnek, L. G. Lavrenova, *J. Struct. Chem.* **1995**, *36*, 97-103.

[343]  V. A. Varnek, L. G. Lavrenova, *J. Struct. Chem.* **1997**, *38*, 850-852.

[344]  A. Narayanan, D. R. Chapman, S. P. Upadhyaya, L. Bauer, *J. Heterocycl. Chem.* **1993**, *30*, 1405-1412.

[345]  Y. Garcia, P. J. van Koningsbruggen, G. Bravic, P. Guionneau, D. Chasseau, G. L. Cascarano, J. Moscovici, K. Lambert, A. Michalowicz, O. Kahn, *Inorg. Chem.* **1997**, *36*, 6357-6365.

[346]  Y. Garcia, P. J. van Koningsbruggen, G. Bravic, D. Chasseau, O. Kahn, *Eur. J. Inorg. Chem.* **2003**, 356-362.

[347]  J. A. Real, I. Castro, A. Bousseksou, M. Verdaguer, R. Burriel, M. Castro, J. Linares, F. Varret, *Inorg. Chem.* **1997**, *36*, 455-464.

[348]  C. Hannay, M. J. Hubin-Franskin, F. Grandjean, V. Briois, J. P. Itie, A. Polian, S. Trofimenko, G. J. Long, *Inorg. Chem.* **1997**, *36*, 5580-5588.

[349]  T. Yokoyama, Y. Murakami, M. Kiguchi, T. Komatsu, N. Kojima, *Phys. Rev. B: Condens. Matter* **1998**, *58*, 14238-14244.

[350]  S. B. Erenburg, N. V. Bausk, L. G. Lavrenova, L. N. Mazalov, *Nucl. Instrum. Methods Phys. Res., Sect. A* **2000**, *448*, 351-357.

[351]  S. B. Erenburg, N. V. Bausk, L. G. Lavrenova, L. N. Mazalov, *J. Magn. Magn. Mater.* **2001**, *226*, 1967-1969.

[352]  P. Gütlich, G. Goodwin (eds.), *Top. Curr. Chem.* **2004**, *vv. 233, 234, 235*.

[353]  V. Niel, J. M. Martinez-Agudo, M. C. Muñoz, A. B. Gaspar, J. A. Real, *Inorg. Chem.* **2001**, *40*, 3838-3839.

[354]  Y. Garcia, V. Ksenofontov, P. Gütlich, *Hyperfine Interact.* **2002**, *139*, 543-551.

[355]  L. G. Lavrenova, V. N. Ikorskii, V. A. Varnek, I. M. Oglezneva, S. V. Larionov, *Koord. Khim.* **1996**, *22*, 357.

[356]  M. Ueda, A. Kameyama, K. Hashimoto, *Macromolecules* **1988**, *21*, 19-24.

[357]  Y. Azefu, H. Tamiaki, R. Sato, K. Toma, *Bioorg. Med. Chem. Lett.* **2002**, *10*, 4013-4022.

[358]  O. Roubeau, B. Agricole, R. Clérac, S. Ravaine, *J. Phys. Chem. B* **2004**, *108*, 15110-15116.

[359]  O. Roubeau, A. Colin, W. Schmitt, R. Clérac, *Angew. Chem., Int. Ed. Engl.* **2004**, *43*, 3283-3286.

[360]  O. Roubeau, E. Natividad, B. Agricole, S. Ravaine, *Langmuir* **2007**, *23*, 3110-3117.

[361]  S. W. Lee, J. W. Lee, S. H. Jeong, I. W. Park, Y. M. Kim, J. I. Jin, *Synth. Met.* **2004**, *142*, 243-249.

[362]  S.-H. Jeong, K.-N. Kim, J. S. Kang, C. S. Hong, D. H. Choi, J.-I. Jin, I.-W. Park, M. G. Kim, *Mol. Cryst. Liq. Cryst.* **2007**, *471*, 3-10.

[363]  K. Kuroiwa, T. Shibata, S. Sasaki, M. Ohba, A. Takahara, T. Kunitake, N. Kimizuka, *J. Polym. Sci. Pol. Chem.* **2006**, *44*, 5192-5202.

[364]  R. Saf, G. Schwarzenbacher, C. Mirtl, G. Hayn, J. Hobisch, K. Gatterer, *Macromol. Rapid Commun.* **2004**, *25*, 911-915.

[365]  Y. Bodenthin, U. Pietsch, J. Grenzer, T. Geue, H. Mohwald, D. G. Kurth, *J. Phys. Chem. B* **2005**, *109*, 12795-12799.

[366]  Y. Bodenthin, U. Pietsch, H. Mohwald, D. G. Kruth, *J. Am. Chem. Soc.* **2005**, *127*, 3110-3114.

[367]  Y. Bodenthin, G. Schwarz, Z. Tomkowicz, A. Nefedov, M. Lommel, H. Mohwald, W. Haase, D. G. Kurth, U. Pietsch, *Phys. Rev. B* **2007**, *76*, 064422.

[368]  G. Zerbi, G. Conti, G. Minoni, S. Pison, A. Bigotto, *J. Phys. Chem.* **1987**, *91*, 2386-2393.

[369]  G. Vos, R. A. Le Febre, R. A. G. De Graaff, J. G. Haasnoot, J. Reedijk, *J. Am. Chem. Soc.* **1983**, *105*, 1682-1683.

[370] G. Vos, R. A. G. De Graaff, J. G. Haasnoot, A. M. Van der Kraan, P. De Vaal, J. Reedijk, *Inorg. Chem.* **1984**, *23*, 2905-2910.

[371] S. Laschat, A. Baro, N. Steinke, F. Giesselmann, C. Hägele, G. Scalia, R. Judele, E. Kapatsina, S. Sauer, A. Schreivogel, M. Tosoni, *Angew. Chem., Int. Ed. Engl.* **2007**, *46*, 4832-4887.

[372] B. Glüsen, W. Heitz, A. Kettner, J. H. Wendorff, *Liq. Cryst.* **1996**, *20*, 627-633

[373] K. Binnemans, J. Sleven, S. De Feyter, F. C. De Schryver, B. Donnio, D. Guillon, *Chem. Mater.* **2003**, *15*, 3930-3938.

[374] B. A. Leita, B. Moubaraki, K. S. Murray, J. P. Smith, J. D. Cashion, *Chem. Commun.* **2004**, 156-157.

[375] N. Kojima, S. Toyazaki, M. Itoi, Y. Ono, W. Aoki, Y. Kobayashi, M. Seto, T. Yokoyama, *Mol. Cryst. Liq. Cryst.* **2002**, *376*, 567-574.

[376] A. B. P. Lever, *Inorganic Electronic Spectroscopy*, Elsevier, Amsterdam, **1984**.

[377] E. König, G. Ritter, S. K. Kulshreshtha, J. Waigel, H. A. Goodwin, *Inorg. Chem.* **1984**, *23*, 1896-1902.

[378] E. König, G. Ritter, S. K. Kulshreshtha, N. Csatary, *Inorg. Chem.* **1984**, *23*, 1903-1910.

[379] P. Gütlich, A. Hauser, *Coord. Chem. Rev.* **1990**, *97*, 1-22.

[380] M. Sorai, *Bull. Chem. Soc. Jpn.* **2001**, *74*, 2223-2253.

[381] C. N. R. Rao, K. J. Rao, *Phase Transitions in Solids*, McGraw-Hill, New York, **1978**.

[382] http://isiknowledge.com

[383] L. Wiehl, G. Kiel, C. P. Köhler, H. Spiering, P. Gütlich, *Inorg. Chem.* **1986**, *25*, 1565-1571.

[384] V. Petrouleas, J. P. Tuchagues, *Chem. Phys. Lett.* **1987**, *137*, 21-25.

[385] A. J. Conti, R. K. Chadha, K. M. Sena, A. L. Rheingold, D. N. Hendrickson, *Inorg. Chem.* **1993**, *32*, 2670-2680.

[386] E. König, G. Ritter, S. K. Kulshreshtha, J. Waigel, L. Sacconi, *Inorg. Chem.* **1984**, *23*, 1241-1246.

[387] C. C. Wu, J. Jung, P. K. Gantzel, P. Gütlich, D. N. Hendrickson, *Inorg. Chem.* **1997**, *36*, 5339-5347.

[388] J. Kusz, P. Gütlich, H. Spiering, *Top. Curr. Chem.* **2004**, *234*, 129-153.

[389] M. Mikami, M. Konno, Y. Saito, *Chem. Phys. Lett.* **1979**, *63*, 566-569.

[390] D. Chernyshov, N. Klinduhov, K. W. Törnroos, M. Hostettler, B. Vangdal, H. B. Bürgi, *Phys. Rev. B* **2007**, *76*, 014406.

[391] J. Fleisch, P. Gütlich, K. M. Hasselbach, W. Müller, *Inorg. Chem.* **1976**, *15*, 958-961.

[392] J. M. Holland, J. A. McAllister, Z. B. Lu, C. A. Kilner, M. Thornton-Pett, M. A. Halcrow, *Chem. Commun.* **2001**, 577-578.

[393] G. S. Matouzenko, A. Bousseksou, S. A. Borshch, M. Perrin, S. Zein, L. Salmon, G. Molnar, S. Lecocq, *Inorg. Chem.* **2004**, *43*, 227-236.

[394] V. A. Money, J. Elhaik, I. R. Evans, M. A. Halcrow, J. A. K. Howard, *Dalton Trans.* **2004**, 65-69.

[395] E. König, G. Ritter, S. K. Kulshreshtha, S. M. Nelson, *Inorg. Chem.* **1982**, *21*, 3022-3029.

[396] G. S. Matouzenko, D. Luneau, G. Molnar, N. Ould-Moussa, S. Zein, S. A. Borshch, A. Bousseksou, F. Averseng, *Eur. J. Inorg. Chem.* **2006**, 2671-2682.

[397] S. J. Blundell, F. L. Pratt, *J. Phys.: Condens. Matter* **2004**, *16*, R711-R828.

[398] D. B. Amabilino, J. Veciana, in *Magnetism: Molecules to Materials II: Molecule-Based Materials.* (Eds.: J. S. Miller, M. Drillon), Wiley-VCH, Weinheim, **2002**, pp. 1-51.

[399] H. Iwamura, K. Inoue, in *Magnetism: Molecules to Materials II: Molecule-Based Materials.* (Eds.: J. S. Miller, M. Drillon), Wiley-VCH, Weinheim, **2002**, pp. 61-108.

[400] P. M. Lahti, in *Carbon-based magnetism* (Eds.: T. Makarova, F. Palacio), Elsevier, Amsterdam, **2006**, pp. 23-53.

[401] W. Fujita, K. Awaga, *Science* **1999**, *286*, 261-262.

[402] M. E. Itkis, X. Chi, A. W. Cordes, R. C. Haddon, *Science* **2002**, *296*, 1443-1445.

[403] S.-i. Ohkoshi, T. Matsuda, H. Tokoro, K. Hashimoto, *Chem. Mater.* **2005**, *17*, 81-84.

[404] A. Escuer, R. Vicente, J. Ribas, X. Solans, *Inorg. Chem.* **1995**, *34*, 1793-1798.

[405] F. A. Mautner, R. Cortes, L. Lezama, T. Rojo, *Angew. Chem., Int. Ed. Engl.* **1996**, *35*, 78-80.

[406] M. Monfort, J. Ribas, X. Solans, M. Font-Bardia, *Inorg. Chem.* **1996**, *35*, 7633-7638.

[407] G. Leibeling, S. Demeshko, S. Dechert, F. Meyer, *Angew. Chem., Int. Ed. Engl.* **2005**, *44*, 7111-7114.

[408] O. Jeannin, R. Clérac, M. Fourmigué, *J. Am. Chem. Soc.* **2006**, *128*, 14649-14656.

[409] O. Jeannin, R. Clérac, M. Fourmigué, *Cryst. Eng. Commun.* **2007**, *9*, 488-495.

[410] A. J. Banister, N. Bricklebank, I. Lavender, J. M. Rawson, C. I. Gregory, B. K. Tanner, W. Clegg, M. R. J. Elsegood, F. Palacio, *Angew. Chem., Int. Ed. Engl.* **1996**, *35*, 2533-2535.

[411] T. M. Barclay, A. W. Cordes, N. A. George, R. C. Haddon, M. E. Itkis, M. S. Mashuta, R. T. Oakley, G. W. Patenaude, R. W. Reed, J. F. Richardson, H. Zhang, *J. Am. Chem. Soc.* **1998**, *120*, 352-360.

[412] X. Ren, Q. Meng, Y. Song, C. Hu, C. Lu, X. Chen, Z. Xue, *Inorg. Chem.* **2002**, *41*, 5931-5933.

[413] X. Ren, Q. Meng, Y. Song, C. Lu, C. Hu, *Inorg. Chem.* **2002**, *41*, 5686-5692.

[414] J. L. Brusso, O. P. Clements, R. C. Haddon, M. E. Itkis, A. A. Leitch, R. T. Oakley, R. W. Reed, J. F. Richardson, *J. Am. Chem. Soc.* **2004**, *126*, 14692-14693.

[415] J. L. Brusso, O. P. Clements, R. C. Haddon, M. E. Itkis, A. A. Leitch, R. T. Oakley, R. W. Reed, J. F. Richardson, *J. Am. Chem. Soc.* **2004**, *126*, 8256-8265.

[416] X. M. Ren, H. Okudera, R. K. Kremer, Y. Song, C. He, Q. J. Meng, P. H. Wu, *Inorg. Chem.* **2004**, *43*, 2569-2576.

[417] A. Alberola, R. J. Collis, S. M. Humphrey, R. J. Less, J. M. Rawson, *Inorg. Chem.* **2006**, *45*, 1903-1905.

[418] W. Fujita, K. Awaga, R. Kondo, S. Kagoshima, *J. Am. Chem. Soc.* **2006**, *128*, 6016-6017.

[419] X. M. Ren, S. Nishihara, T. Akutagawa, S. Noro, T. Nakamura, *Inorg. Chem.* **2006**, *45*, 2229-2234.

[420] N. Moliner, M. C. Muñoz, S. Létard, J. F. Létard, X. Solans, R. Burriel, M. Castro, O. Kahn, J. A. Real, *Inorg. Chim. Acta* **1999**, *291*, 279-288.

[421] L. Salmon, B. Donnadieu, A. Bousseksou, J. P. Tuchagues, *Comptes Rendus Acad. Sci. Ser. II C* **1999**, *2*, 305-309.

[422] S. Hayami, R. Moriyama, A. Shuto, Y. Maeda, K. Ohta, K. Inoue, *Inorg. Chem.* **2007**, *46*, 7692-7694.

[423] S. Hayami, N. Motokawa, A. Shuto, R. Moriyama, N. Masuhara, K. Inoue, Y. Maeda, *Polyhedron* **2007**, *26*, 2375-2380.

[424] S. Hayami, K. Hashiguchi, G. Juhasz, M. Ohba, H. Okawa, Y. Maeda, K. Kato, K. Osaka, M. Takata, K. Inoue, *Inorg. Chem.* **2004**, *43*, 4124-4126.

[425] E. A. V. Ebsworth, D. W. H. Rankin, S. Cradock, *Structural Methods in Inorganic Chemistry*, Blackwell Scientific Publications, Oxford, **1987**.

[426] J. Barberá, in *Metallomesogens* (Ed.: J. L. Serrano), VCH, Weinheim, **1996**, pp. 325-348.

[427] A. Bianconi, in *X-Ray Absorption: Principles, Applications, Techniques of EXAFS, SEXAFS and XANES* (Eds.: D. C. Koningsberger, R. Prins), John Wiley & Sons, New York, **1988**, pp. 573-662.

[428]  C. Cartier Dit Moulin, V. Briois, P. Lagarde, F. Villain, M. Verdaguer, in *Introduction to Physical Techniques in Molecular Magnetism: Structural and Macroscopic Techniques* (Eds.: F. Palacio, E. Ressouche, J. Schweizer), Universidad de Zaragoza, Zaragoza, **1999**, pp. 251-283.

[429]  A. G. McKale, B. W. Veal, A. P. Paulikas, S.-K. Chan, G. S. Knapp, *J. Am. Chem. Soc.* **1988**, *110*, 3763-3768.

[430]  D. E. Sayers, B. A. Bunker, in *X-Ray Absorption: Principles, Applications, Techniques of EXAFS, SEXAFS and XANES* (Eds.: D. C. Koningsberger, R. Prins), John Wiley & Sons, New York, **1988**, pp. 221-253.

[431]  B. Lengeler, P. Eisenberger, *Physical  Review B* **1980**, *21*, 4507-4520.

[432]  A. Michalowicz, in *Logiciels pour la Chimie*, Société Française de Chemie, Paris, **1991**, p. 116.

[433]  A. Michalowicz, in *Logiciels pour la Chimie*, Société Française de Chemie, Paris, **1991**, p. 102.

[434]  A. Michalowicz, *J. Phys. IV France* **1997**, *7*, 235.

[435]  L. R. Carlin, *Magnetochemistry*, Springer, Berlin, **1986**.

[436]  C. Paulsen, in *Introduction to Physical Techniques in Molecular Magnetism: Structural and Macroscopic Techniques* (Eds.: F. Palacio, E. Ressouche, J. Schweizer), Universidad de Zaragoza, Zaragoza, **1999**, pp. 51-76.

[437]  S. J. Swithenby, *Contemp. Phys.* **1974**, *15*, 249-267.

[438]  D. F. Evans, *J. Chem. Soc.* **1959**, 2003-2005.

[439]  M. Sorai, S. Seki, *J. Phys. Chem. Solids* **1974**, *35*, 555-570.

[440]  B. Wunderlich, *Thermal Analysis of Polymeric Materials*, Springer, Berlin, **2005**.

[441]  J. Thoen, in *Handbook of Liquid Crystals, Vol. 1* (Eds.: D. Demus, J. Goodby, G. W. Gray, H.-W. Spiess, V. Vill), Wiley-VCH, Weinheim, **1998**, pp. 310-333.

[442]  U. Müller, *Inorganic Structural Chemistry*, 2nd ed., John Wiley & Sons, Chichester, **2006**.

[443]  G. W. H. Höhne, W. F. Hemminger, H.-J. Flammersheim, *Differential Scanning Calorimetry* 2nd ed., Springer, Berlin, **2003**.

[444]  W. Schärtl, *Light Scattering from Polymer Solutions and Nanoparticle Dispersions*, Springer, Berlin, **2007**.

[445]  P. J. Collings, M. Hird, *Introduction to Liquid Crystals. Chemistry and Physics*, Taylor & Francis, London, **1997**.

[446]  Y. Bouligand, in *Handbook of Liquid Crystals, Vol. 1* (Eds.: D. Demus, J. Goodby, G. W. Gray, H.-W. Spiess, V. Vill), Wiley-VCH, Weinheim, **1998**, pp. 406-453.

[447]  Adopted from http://home.cc.umanitoba.ca/~hegmannt/index.htm

[448]  A. Hauser, *Top. Curr. Chem.* **2004**, *233*, 49-58.

[449]  D. C. Harris, *Quantitative Chemical Analysis*, 7 ed., Freeman, New York, **2007**.

[450]  J. H. Takemoto, B. Hutchinson, *Inorg. Nucl. Chem. Lett.* **1972**, *8*, 769-772.

[451]  J. H. Takemoto, B. Hutchinson, *Inorg. Chem.* **1973**, *12*, 705-708.

[452]  W. Henderson, J. S. McIndoe, *Mass Spectrometry of Inorganic, Coordination and Organometallic Compounds: Tools–Techniques–Tips*, John Wiley & Sons, Chichester, **2005**.

[453]  G. M. Sheldrick, *SHELXS97 and SHELXL97*, University of Göttingen, Germany, **1997**.

[454]  A. Altomare, G. Cascarano, C. Giacovazzo, A. Guagliardi, M. C. Burla, G. Polidori, M. Camalli, *J. Appl. Crystallogr.* **1994**, *27*, 435.

[455]  M. C. Burla, M. Camalli, B. Carrozzini, G. L. Cascarano, C. Giacovazzo, G. Polidori, R. Spagna, *J. Appl. Crystallogr.* **2003**, *36*, 1103.

[456]  A. G. McKale, G. S. Knapp, S. K. Chan, *Phys. Rev. B* **1986**, *33*, 841-846.

## List of publications

[1]     A. B. Gaspar, V. Ksenofontov, M. Seredyuk, P. Gütlich, *Coord. Chem. Rev.* **2005**, *249*, 2661-2676.

[2]     M. Seredyuk, A. B. Gaspar, V. Ksenofontov, S. Reiman, Y. Galyametdinov, W. Haase, E. Rentschler, P. Gütlich, *Hyperfine Interact.* **2005**, *166*, 385-390.

[3]     M. Seredyuk, A. B. Gaspar, V. Ksenofontov, S. Reiman, Y. Galyametdinov, W. Haase, E. Rentschler, P. Gütlich, *Chem. Mater.* **2006**, *18*, 2513-2519.

[4]     M. Seredyuk, A. B. Gaspar, J. Kusz, G. Bednarek, P. Gütlich, *J. Appl. Crystallogr.* **2007**, *40*, 1135-1145.

[5]     M. Seredyuk, A. B. Gaspar, M. C. Muñoz, M. Verdaguer, F. Villain, P. Gütlich, *Eur. J. Inorg. Chem.* **2007**, 4481-4491.

[6]     M. Seredyuk, M. Haukka, I. O. Fritsky, H. Kozłowski, R. Krämer, V. A. Pavlenko, P. Gütlich, *Dalton Trans.* **2007**, 3183-3194.

[7]     M. Seredyuk, A. B. Gaspar, V. Ksenofontov, Y. Galyametdinov, J. Kusz, P. Gütlich, *J. Amer. Chem. Soc.* **2008**, *130*, 1431-1439.

[8]     M. Seredyuk, A. B. Gaspar, V. Ksenofontov, Y. Galyametdinov, J. Kusz, P. Gütlich, *Adv. Func. Mater.* **2008**, accepted, DOI: 10.1002/adfm.200800049.

[9]     I. S. Jahro, D. Onggo, Ismunandar, S. I. Rahayu, M. C. Muñoz, A. B. Gaspar, M. Seredyuk, P. Gütlich, J. A. Real, *Inorg. Chim. Acta* **2008**, submitted.

[10]    M. Seredyuk, A. B. Gaspar, V. Ksenofontov, Y. Galyametdinov, F. Villain, M. Verdaguer, P. Gütlich, *Inorg. Chem.* **2008**, accepted, DOI: 10.1021/ic006266.